Noble Gas Analysis of Volcanic Glass Particles: A Better Understanding of Volcano Degassing and Implications for Ar/Ar Dating of Eruptions

Thesis

Noble gas analysis of volcanic glass particles: a better understanding of volcano degassing and implications for Ar/Ar dating of eruptions

Thesis submitted for the degree of Doctor of Philosophy by

Simone Cogliati

School of Environment, Earth and Ecosystem Sciences

The Open University

May 2019

"Fatti non foste a viver come bruti ma per seguir virtute e canoscenza"

Dante, Commedia, Canto XXVI

"*…The human mind is only capable of absorbing a few things at a time. We see what is taking place in front of us in the here and now, and cannot envisage simultaneously a succession of processes……..We observe a fraction of the process, like hearing the vibration of a single string in an orchestra of supergiants….. above and below, beyond the limits of perception or imagination, thousands and millions of simultaneous transformations are at work, interlinked like a musical score by mathematical counterpoint…*"

Stanislaw Lem – Solaris, 1961.

Abstract

Noble Gases (NG) have been investigated extensively in a variety of volcanic materials, however, few efforts have been made to study their incorporation, partition and release to and from subaerial volcanic glass. In this study, ^{4}He, ^{22}Ne, ^{36}Ar, ^{40}Ar, trapped in different subaerial volcanic glass types, are used to characterize magmatic reservoirs, to study volcanic processes, to investigate the degassing and evolution of volcanic systems and to understand the implications for the Ar/Ar system.

Glass shards from silicic tuffs interbedding basaltic lavas of the Columbia River Basalt Group (CRBG - Washington, U.S.) yielded accurate, precise Ar/Ar ages ($12.00\pm0.24_{2\sigma}$ Ma, $11.37\pm0.15_{2\sigma}$ Ma, $10.67\pm0.21_{2\sigma}$ Ma, $10.70\pm0.18_{2\sigma}$ Ma, $10.77\pm0.18_{2\sigma}$ Ma). These were used to indirectly constrain better the timing of eruption of two Formations of the CRBG and to aid the correlation of the tuffs with their eruptive centre (Bruneau-Jarbidge) in the Central Snake River Plain.

NG in Pele's hairs and tears were used to monitor the degassing of Masaya volcano (Nicaragua) between 2015 - 2016. The variations of the NG in the samples were attributed to the upward migration of a gas-rich magma from depth in 2015. The NG abundances in single particles are controlled by sample vesicularity and by solubility and diffusion fractionation of the gas prior eruption.

Pre-, syn- and post-eruptive processes interplay and superimpose upon each other, complicating the interpretation of Ar/Ar ages and NG abundances in pumice glass particles. The NG variations in glass particles from different portions of a pumice fall and an ignimbrite from the Eras Formation (Tenerife) are attributed to a "stratified" magma chamber with respect to NG, and, to diffusion fractionation processes that acted during pumice cooling. Glass particles failed to provide Ar/Ar ages and no relationships were observed between Ar degassing and Ar/Ar ages produced from different portions of the eruptive sequence.

This study has been funded by The Open University and by the NERC - Deep Volatiles Consortium.

Dedicated to D.

For what you never had and for what

this world has taken from you

Acknowledgements

I would like to thank my main supervisors Sarah Sherlock and Alison Halton for giving me the opportunity to realise my dream to be a scientist, for their invaluable help and continuous support. I really appreciate what you have done for me during these last three (almost four) years.

I would like to thank who was directly and indirectly involved in this project: Simon Kelley, Tiffany Barry, Mike Branney and Steve Blake.

I thank James Malley for his technical help in the Ar/Ar laboratory, for his music and for the fabulous discussions around sci-fi, universe, movies, literature and much more.

I thank Sam Hammond and Giulia Degli Alessandrini for their help and assistance with the electron microprobe, Michelle Higgins and Kay Green for their effort in preparing thin sections from extremely fragile materials, and Tom Knott for his guidance in XRF sample preparation and for XRF analyses.

The Ar/Ar laboratory (The Open University) and the NERC - Deep Volatiles consortium are thanked for having funded this research.

Finally, I would like to thank the *TEMINEL s.r.l.*, my Love, my future wife and the "Junk BoyZ" for their priceless support during my entire career.

Table of content

Chapter 5: NG behaviour and partitioning in young pumice glass during plinian eruptions and implications for Ar/Ar ages 119-214

Lists of figures

Chapter 2

Chapter 3

Chapter 4

4.1 Cooling rates and temperatures of Pele's tear. ……..…….....…….....…….....

Chapter 5

Lists of tables

Chapter 2

Chapter 3

Chapter 4

Chapter 5

Chapter 1:
Introduction

1.1 Introduction

Noble gases (NG - He, Ne, Ar, Kr, Xe) are inert incompatible trace elements widely used as geochemical tracers to study a variety of magmatic processes. Several studies have investigated NG abundance and isotopic signature in a variety of volcanic products (e.g. lavas, pumice) of variable compositions (from basaltic to rhyolitic) in order to unravel magma sources, magma contamination and differentiation and to investigate evolution and degassing of many volcanic systems (Yamamoto and Burnard, 2004; Burnard et al., 2004; Macpherson et al., 2005; Flude et al., 2018).

Rather than being retained in crystals, the NG preferentially partition in melt and bubbles during degassing, due to diffusion and to their different solubilities (e.g. Carrol and Stolper, 1993; Carroll and Draper, 1994; Aubry et al., 2013). For this reason the study of NG in volcanic glass (and bubbles) is fundamental when investigating the degassing history of a magmatic system.

Many studies focused on the investigation of NG trapped in submarine glasses derived from MORB basalts in order to better understand mantle evolution and degassing (Burnard, 1999, 2001; Moreira and Sarda 2000; Ballentine and Barfod, 2000; Sarda and Moreira 2002; Yamamoto and Burnard, 2004; Burnard et al., 2002, 2004, Yamamoto and Burnard, 2004; Aubry et al., 2013; Moreira and Kurz, 2013). In spite of the large amount of data and studies on mechanisms that controls NG fractionation, and isotopic abundance, in this type of glass, only a few papers have addressed which factors control NG incorporation into, and release from, subaerial glasses. The majority of the studies have focused on Ar behaviour in obsidians (Flude et al., 2010, 2018), only 3 studies exist on the incorporation of air-derived NG in pumice glass (Pinti et al., 1999; Ruzie and Moreira, 2010, Clay et al., 2011) while none exist on other types of glass (e.g. Pele's hairs and tears, lava glass matrix, ash shards).

Volcanic glass has also found some limited use in K/Ar and Ar/Ar geochronology as a source of information on the age and duration of volcanic events. The first K/Ar studies conducted on glassy submarine pillow basalts failed to provide reliable ages (Funkhouser et al., 1968; Dalrymple and Moore, 1968). After a few encouraging results obtained using rhyolitic ash beds and glassy rhyolitic lava (Drake et al., 1980; McDougall, 1994), many

other studies attempted, with either limited success or none, to use different types of volcanic glass for Ar/Ar dating volcanic eruptions (Cheilletz et al., 1992; Flude et al., 2008, 2010, 2018; Bigazzi et al., 2005, 2008; Clay et al., 2011), to constrain ages of volcano-ice interactions for paleo-environments reconstruction (McGarvie et al., 2007; Nyland et al., 2013; Clay et al., 2015; Flude et al., 2010, 2018), to determine ages of hominoids migration dating obsidian tools (Cerling et al., 1985; Vogel et al., 2006; Morgan et al., 2009) and to understand possible relationships between volcanic eruptions and local or global environmental changes and climate changes (McGarvie et al., 2007).

Despite some promising results there persist some major problems in determining accurate and precise Ar/Ar ages from volcanic glass: rapid alteration; hydration and devetrification of the glass; retention of excess Ar due to incomplete degassing of the glass, and, Ar isotopes fractionation (Cheilletz et al., 1992, Clay et al., 2011, 2015; Flude et al., 2018).

Glass alteration - Due to its metastable nature at surface conditions, volcanic glass is particularly susceptible to weathering, devitrification and hydration when exposed to surface conditions after its eruption. These processes cause chemical and structural modification of the glass leading to aqueous-SiO_2 and alkali loss (Na, K, Mg and Ca) (Palomar et al., 2017, 2019). In particular, a significant decrease in K and Ar can lead to spurious incorrect Ar/Ar ages (Fisher, 1971; Kaneoka, 1970, 1972; Cerling et al., 1985; Flude et al., 2018). Glass alteration is enhanced in highly vesicular glass (e.g. pumice) where post-emplacement processes (e.g. vapour phase alteration, exposure to marine coastal environment) can scavenge alkalis and Ar (as well other NG) from the sample (Clay et al., 2011). The deposition of secondary minerals (e.g. K-feldspar and cristobalite) within open pores by gas escaping or fluid circulation (superficial or hydrothermal) or the formation of alteration minerals (e.g. clays, zeolite, chlorite, sericite) can instead add alkalis and Ar to the glass. The degree of weathering of a glass, and relative element mobility during alteration processes, can be detected using specific alteration indices. The Chemical Index of Alteration (CIA- Nesbitt and Young, 1982) is particularly suited to assess alteration and weathering of volcanic glass. Its value increases as weathering increases with the optimal fresh value of ≤ 50 and the optimal weathered value of 100. CIA is usually calculated from electron microprobe data using the following formula from Nesbitt and Young (1982): $CIA= [Al_2O_3/(Al_2O_3+CaO^*+Na_2O+K_2O)]\times100$ (oxides are considered from Wt % data).

Excess Ar (Ar_E) - One of the problems that affects the Ar/Ar dating technique is the presence of Ar_E within samples (e.g. Kelley, 2002). This is the portion of ^{40}Ar neither radiogenic ($^{40}Ar^*$ - derived from ^{40}K decay) or atmospheric ($^{40}Ar_{atm}$) that is incorporated into the sample during magmatic or post-depositional processes. The presence of Ar_E in volcanic rocks can result in the artificial elevation of the $^{40}Ar/^{39}Ar$ ratio and therefore an artificial increase in the age (e.g. Sherlock and Kelley, 2002; Sherlock et al., 1999). Ar_E can be detected by carefully scrutinising and comparing the shape of age spectra and the inverse isochrons (see appendix A1.5) by using a laser core-rim measurement approach (Sherlock and Kelley, 2002; Sherlock et al., 2003; Sherlock et al., 2009). However, this is not applicable for volcanic glass where a clear core / rim doesn't exist or extremely small samples are analysed.

In volcanic glass, Ar_E can be present due to the incomplete degassing of the sample with ^{40}Ar inherited from the magma chamber and retained in isolated bubbles (Ar is extremely incompatible in melts – Lux, 1987; Carrol and Stolper, 1993; Carroll and Draper, 1994). Ar_E can also be introduced into the sample through diffusion during the interaction of the glass with hydrothermal or meteoric hot fluids with a non-atmospheric Ar signature ($^{40}Ar/^{36}Ar$ of atmospheric Ar = 298.56±0.31 - Lee et al, 2006). The presence of secondary alteration minerals substituting for the glass can be another source of Ar_E.

Incomplete atmospheric equilibration – At the moment of eruption, a volcanic material that is in equilibrium with an atmospheric reservoir at 1 atm is expected to have a $^{40}Ar/^{36}Ar$ ratio equivalent to that of air (298.56±031, Lee et al., 2006). However, lower ratios have been frequently observed in different types of volcanic glasses (obsidian, pumice). These sub-atmospheric $^{40}Ar/^{36}Ar$ ratios have been associated with kinetic mass fractionation of Ar isotopes (e.g. Vogel et al., 2006; Morgan et al., 2009), incomplete equilibration of the glass with the atmosphere during quenching (Morgan et al., 2009; Clay et al., 2015), incorporation of ^{36}Ar from host rocks with an air-like signature assimilated into the magma prior to eruption (Kaneoka, 1980) and to post-eruptive hydration of the glass with preferential incorporation of ^{36}Ar derived from meteoric water (Kaneoka, 1994; Flude et al., 2018). Sub-atmospheric $^{40}Ar/^{36}Ar$ ratios can compromise the use of age spectra in Ar/Ar dating, violating the assumption that the sample has an atmospheric Ar ratio at the moment of their eruption. Moreover sub-atmospheric ratios complicate the interpretation of inverse isochrons and the determination of their true $^{36}Ar/^{40}Ar$ ratios (e.g. Morgan et al. 2009; Flude et al., 2018).

A similar problem can be caused also by interferences at mass 36 during analysis. It has been noted that when a MAP-215-50 mass spectrometer is used to perform Ar/Ar

analyses the ion detector is not able to distinguish between the true peak of ^{36}Ar and the peak of $^{1}H^{35}Cl$ and $^{12}C_3$ (Flude et al., 2018). This could affect the correct determination of the true concentration of the ^{36}Ar precluding a precise characterization of the $^{39}Ar/^{40}Ar$ ratio when the inverse isochron (see A1.5.2) is used to determine the age of the sample (Flude et al., 2018).

All these problems are enhanced when young glass (< 1 Ma) is dated. Young volcanic rocks contain very small amount of radiogenic $^{40}Ar^*$ with respect to the non-radiogenic component. For this reason any minimal depletion in the $^{40}Ar^*$ due to ^{40}Ar-loss (or K-loss) as a results of glass alteration can lead to erroneous young ages while even a small Ar_E content will increase the total ^{40}Ar leading to anomalously old ages. In this context it is clear that understanding which factors control the retention and degassing of Ar in subaerial volcanic glass is fundamental in order to recover precise, accurate and stratigraphically consistent Ar/Ar ages from this material.

1.2 Aim and objectives

The overall aim of this study is to extend our knowledge on which factors control the behaviour of noble gases in different sub-aerial volcanic glass types during degassing, and, what information noble gases can provide to help to model the *evolution of volcanic* systems and the implications for dating volcanic rocks by the Ar/Ar technique.

The objectives are to:

1) Determine whether glass shards within tuff layers interbedding lavas provide better Ar/Ar age constraints for the timing and duration of basaltic volcanism in Large Igneous Provinces and develop preparation and analytical protocols in order to test this.

2) Determine how noble gas measurements of Pele's hairs and tears can be used as a tool to understand degassing and magmatic evolution of a persistently degassing volcanic system – Masaya volcano.

3) Determine how noble gases behave and partition within and between an ash-fall deposit and an ignimbrite of the same eruptive sequence derived from a plinian eruption in the Bandas del Sur (Tenerife) in addition to understanding the impact of Ar degassing on Ar/Ar ages.

4) Discuss implications for Ar/Ar dating with particular regard given to the understanding of the presence of excess Ar and sub-atmospheric Ar ratios in volcanic glass in light of their importance for determining precise and accurate Ar/Ar ages.

In meeting these objectives a range of techniques have been applied to establish the factors that control the noble gases, and in particular Ar, for those materials that are of a sufficient age to be dated by this technique. Pre-eruptive, syn-eruptive and post-eruptive factors and processes are considered and discussed in detail:

- Gas variations in the magma chamber (Chapter 4);
- Chemistry of the magma (Chapter 4 and 5);
- Glass vesicularity and NG fractionation (Chapter 3, 4 and 5);
- Cooling time, rate, dimension of the glass particles (Chapter 4 and 5);
- emplacement mechanism (Chapter 4 and 5);
- Alteration of the glass (Chapter 3, 4 and 5);

1.3 Thesis layout

Chapter 1 provides a brief introduction explaining the reasons for studying NG degassing and Ar/Ar ages in subaerial volcanic glass and highlighting problems and limitation of the applicability of the Ar/Ar dating method to silicic glasses. Aims and objectives of the thesis are also listed together a brief description of the thesis layout including the rationales of each project in which it is divided.

Chapter 2 is written in two sections. The first provides information on the aims and research strategies for each part of the thesis while the second provides general information on the analytical techniques (e.g. thin section, electron microprobe, XRF) used in this study including sample preparation procedures. Detailed information on sample preparation for Noble Gas mass spectrometry and Ar/Ar analyses and analytical conditions for each project are also provided. More general information on theoretical principles of the Ar/Ar technique are in Appendix A1.

Chapter 3 explores the possibility to return precise ages from K-rich glass shards derived from ash-rich silicic deposits interlayering basaltic lavas in the upper part of the Columbia River Basalt Group (CRBG), NW USA. The new ages are discussed in terms of precision and accuracy, as well as in the context of previously reported Ar/Ar ages from the investigated section of the CRBG. The ages produced are then compared with the most precise Ar/Ar ages in the published literature, derived from sanidines from older silicic interbeds in the CRBG.

Chapter 4 investigates ^{4}He, ^{22}Ne, ^{36}Ar and ^{40}Ar behaviour in Pele's hairs and tears from Masaya volcano testing the possibility to use this type of glass as a new tool to track the behaviour of persistent degassing volcanoes. Chemistry, petrography and vesicularity of the samples are investigated in detail in order to understand which factors control variation in the NG abundance in a short period of time (days) and in a longer time period (1 year). Sources of atmospheric contamination are also discussed and a model that explains the behaviour of the Masaya volcano between 2015 and 2016 is proposed.

Chapter 5 explores which factors control the NG signature, retention and degassing in pumice glass particles derived from the Eras eruption in Tenerife and how these processes influence the quality of Ar/Ar ages obtainable from pumice glass. This is done by comparing chemistry, mineral abundance and types, textures, Ar/Ar ages and NG

composition of pumice glass particles from different portions (base and top) of a plinian fall deposit and of an ignimbrite. Two models that explain the degassing behaviour of pumices from the considered eruption are proposed and discussed considering field evidence and theoretical knowledge on NG degassing in pumices during a plinian eruption. NG and Ar/Ar ages were obtained also from sanidines recovered from the same portions of the two deposits. The results are compared with those from pumice glass particles and discussed in relation to degassing processes.

Chapter 6 provides a synthesis of the data discussed in Chapter 3, 4, 5 according to the aims and goals of the thesis set out at its beginning. In this chapter are synthetized common factors (primary and secondary) controlling NG in different types of volcanic glass. The different sources of $^{40}Ar_E$ and atmospheric contamination are described and the implications of these for Ar/Ar dating of different types of glass are considered. NG degassing models for treated volcanic systems are also summarised and compared.

Chapter 7 summarises the main findings of the thesis including models for NG degassing during eruption and the newly obtained Ar/Ar ages. It proposes also future lines of research in order to continue to investigate those factors controlling NG in volcanic glass, the relationships between Ar degassing, the Ar/Ar system and Ar/Ar ages in volcanic glass.

Chapter 2:

Research strategy and methodology

2.1 Introduction

This chapter is divided into two main sections: the first provides information on the aims and research strategies of each strand of the thesis (section 2.2); the second gives a general overview of sample preparation procedures and analytical techniques used in the three strands (section 2.3).

Different types of volcanic glasses with different origins and ages (Figure 2.1) were characterised by a wide range of analytical techniques with respect to their petrographic and textural features, major and trace element compositions, noble gas (NG) contents and ages of eruption (Table 2.1 – 2.2 – 2.3). All the analyses and sample preparations were personally performed at The Open University unless otherwise indicated.

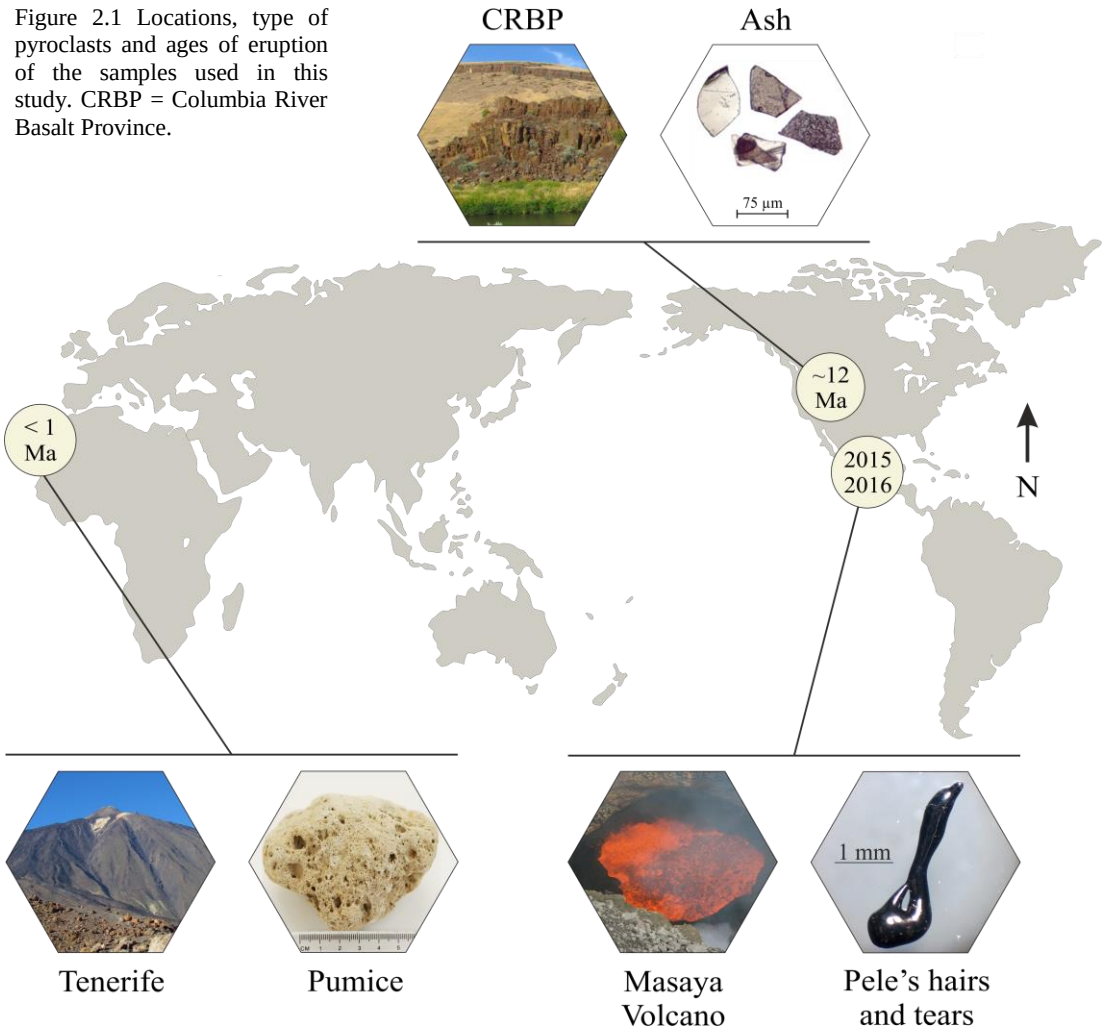

Figure 2.1 Locations, type of pyroclasts and ages of eruption of the samples used in this study. CRBP = Columbia River Basalt Province.

2.2 Aims and research strategies

The first part of this research (Chapter 3) explores the possibility of returning precise Ar/Ar ages from K-rich glass shards derived from ash-rich silicic deposits interlayering basaltic lavas. This was with the specific aim of providing an additional, more precise and indirect way, of determining the age of eruption of basalts whilst overcoming some of the notorious problems related to the application of the Ar/Ar dating technique to basaltic material (see section 3.3).

The volcanic glass shards for Ar/Ar dating were derived from six silicic tuffs interlayering the Columbia River Basalt Group (CRBG – Washington, U.S.). The tuffs were originally collected, described and provided by Dr. Alena Ebinghaus (Aberdeen University).

Bulk-rock compositions of the tuffs were taken from Ebinghaus et al. (2015), with the exception of only one sample (PRD-1-2A) that was analysed in this study.

The glass shards were carefully separated from the unwanted materials, prepared for Ar/Ar dating (see 2.3.4.1) and analysed by step-heating laser fusion mass spectrometry (see 2.3.4.2). For a couple of samples (AR-1-6A, MA-1-5M) multiple aliquots were analysed in order to assess the analytical reproducibility which formed a test for the reliability of the method. The obtained ages were examined relative to the stratigraphic position of the samples and compared with the available Ar/Ar ages of the upper and lower basalts.

Table 2.1 Information on the silicic tuffs interlayering the CRBG used in this study and of the techniques used for their investigation.

Sample	Date of Collection	Coordinates		XRF	Ar/Ar dating
		Latitude	Longitude		
Rhyolitic ashes from the Columbia River Basalt Province (Washington, U.S.A)					
BJ-1-10	N.A	46.199933	-119.713433		X
SRD-1-2	N.A	46.127350	-119.845400		X
MA-1-5M	N.A	46.777583	-119.913317		X
AR-1-6A	N.A	46.064583	-118.956550		X
PRD-1-2A	N.A	45.998400	-119.350467	X	X
U-1-2	N.A	46.912700	-120.505967		X

The second part of this research (Chapter 4) investigates the possibility of using the NG trapped in Pele's hairs and tears as a tracer of active magmatic processes. The ability of these vesiculated glassy particles to preserve NG after their eruption was explored and applied to the study of the degassing behaviour of the Masaya volcano (Nicaragua). The chemistry and the vesicularity of the glass were studied in order to determine which factors could have controlled and influenced the NG signature of the particles.

Pele's hairs and tears from the Masaya volcano were collected by Kerry Reid (former student at The Open University) in two separate field campaigns, in March 2015 and March 2016, during the on-going activity at the Santiago pit crater. In 2016 Pele's hairs and tears were sampled every two days for a total of 10 consecutive days. This collection strategy was specifically designed to investigate the NG isotopic variations on a long period of time (1 year - from 2015 to 2016) and on a shorter time scale (10 days). The use of 'zero age' samples was necessary to ensure that the NG signature obtained from mass spectrometry analyses was not obscured by the presence of radiogenic isotopes, like ^{4}He and ^{40}Ar, derived from the radioactive decay of $^{235,238}U$-^{232}Th and ^{40}K, respectively. Moreover, the use of samples collected just after their eruption minimized alteration due to extended exposure to acidic volcanic gases or by post-eruptive hydration (Moune et al., 2007).

Before each collection, the collecting site was swept-up in order to remove any glass particle derived from previous eruptions. This has ensured that only fresh samples, deriving from the on-going activity, were picked-up for the analyses. Golden-like altered strands were avoided while dark-black Pele's hairs and tears were put in plastic bags and labelled. Despite these precautions, it is impossible to exclude the possibility that old fresh-looking Pele's hairs and tears, remobilised by the wind from surrounding areas, were not incorporated into the collection. Once back to the University the samples were stored, for at least a few months up to 1 year, in a dry environment at room temperature until their preparation for the analyses. This was designed to minimise the alteration of the glass at ambient temperature (Fearn et al., 2004).

Pele's hairs and tears of different shapes, dimensions and dates of collection were studied by thin section in order to determine if their mineral abundance and assemblage had changed through time. Thin section microphotographs together with backscatter images were used to characterise the interior structure of the particles in terms of shape and abundance of the vesicles and variations of the vesicularity in samples collected in a different period of time. This was specifically to aid the interpretation of the NG data because of the relevance of vesicle abundance in controlling the concentration and fractionation of NG in volcanic glass (Burnard et al., 2004).

Major element compositions of the glass were investigated, in collaboration with Kerry Reid (former student at The Open University), by electron microprobe analyses in order to assess for any chemical variation among samples erupted in different periods of time. The Chemical Alteration Index (CIA, Nesbitt and Young, 1982) was calculated for each analysed spot and used to determine if the chemistry of the glass reflects the original magma composition or it is the result of secondary alteration processes. Particular attention was given to the variation of the Si because its relevance in controlling NG solubility in volcanic glass (Carroll and Draper 1994).

Single grain total fusion NG mass spectrometry was used to study the NG abundance (^{4}He, ^{22}Ne, ^{36}Ar, ^{40}Ar) in the samples (see 2.3.4). The results of the analyses of samples collected in different periods of time were compared, discussed and interpreted in the context of magmatic degassing. The $^{4}He/^{40}Ar^{*}$ isotopic ratio was used as an index for magma degassing while the $^{40}Ar/^{36}Ar$ ratio was used as a proxy of air contamination and of the presence of excess ^{40}Ar ($^{40}Ar_{E}$).

The results of thin section, backscatter images and electron microprobe analyses were compared with previous studies on Pele's hairs and tears and, in particular, with the study of Moune et al. (2007) on similar samples from the Masaya volcano. Petrographic, textural and chemical data were coupled with NG data in order to understand which factors control the incorporation, partition and release of the NG in volcanic glass during degassing events. The results of the experiments were compared with published data on the recent degassing activity of the Masaya volcano in order to verify the reliability of the information get from the NG data on its degassing behaviour.

Table 2.2 Information on the Pele's hairs and tears from Masaya volcano and of the techniques used for their investigation.

Sample	Date of Collection	Coordinates		Thin section	Backscatter images	EMPA	NG-MS
		Latitude	Longitude				
Basaltic Pele's hairs and tears from the Masaya volcano (Nicaragua)							
KS15-03	03-2015	11.985698	-86.172155	X	X	X	X
KS-03-11L	03-03-2016	11.982519	-86.169299	X	X	X	X
KS-03-10S	03-03-2016	11.982560	-86.169388	X	-	X	X
KS-13-4L	13-03-2016	11.986586	-86.169900	X	-	X	X
KS-13-10L	13-03-2016	11.982560	-86.169388	X	X	X	X

The third part of this research (Chapter 5) combines together elements presented and discussed in the two previous sections exploring the hypothesis that the quality of the Ar/Ar ages derived from volcanic materials is directly correlated with the degassing history experienced during and / or after their eruptions.

Here, the NG were used as a proxy of magmatic degassing; their concentration and fractionation was studied in vesiculated glass and alkali feldspars derived from pumices collected at different stratigraphic levels within two types of pyroclastic deposits (fall, ignimbrite) emplaced during a single continuous plinian eruption. This approach was designed to study how the NG partition during the different stages of an eruption and how / if the NG composition of the samples is related to the different mechanisms of emplacement of the two deposits. Sample vesicularity and degree of alteration of the glass are also investigated. In this way, this study pursues the investigation of those factors controlling the partition, incorporation and release of NG in volcanic glass and crystals during degassing events. Of particular interest for this research, because of their use in Ar/Ar dating, are the ^{36}Ar and ^{40}Ar isotopes. A better understanding of how the Ar_{atm} and $^{40}Ar^*$ behave, fractionate and distribute in volcanic glass and alkali feldspars is essential for assessing the quality of the Ar/Ar ages derived from these materials. This is particularly important when young samples with low radiogenic ^{40}Ar contents, and particularly sensitive to $^{40}Ar_E$ incorporation, are used for Ar/Ar dating purposes.

With these factors in mind, young (< 1 Ma) visually fresh pumices of different colours and textures from the Eras Formation (Tenerife) were collected at its type locality (28.188243, -16.431851), along the entire outcrop (~20 m long), at the base and at the top of the basal fall and of the overlaying ignimbrite. The samples were taken at a minimum distance of 15 cm from the basal and upper contacts of the Formation and at the same distance from the fall-ignimbrite interface. This was designed to reduce the likelihood of picking up extraneous materials from an upper/lower layer. Due to the complexity of the depositional mechanisms, it is not possible to completely exclude contamination from a different layer, especially where the fall and the ignimbrite are in contact.

The pumices were described in the field in terms of their stratigraphic position within the outcrop, colour, texture and crystal content. Those samples with similar macroscopic characteristics and stratigraphic position were grouped together and put in separate plastic bags. Each bag, referring to a different group of samples, was labelled with a specific code indicating the type of deposit from where the pumices were collected (F = fall, I = ignimbrite), the position of the samples within the deposit (1 = lower part, 2-3 = upper part) and the colour of the specimens (A = grey, B = light green, C = dark green, D = banded dark green). Once back to the University the samples were stored, for at least a

few months up to 1 year, in a dry environment at room temperature until their preparation for analysis.

The pumices were investigated with respect to their mineral assemblage and internal texture by thin section analyses. Petrographic similarities and differences between samples of the same colour and texture, but collected at different stratigraphic levels, were used in order to assess for the homogeneity of the groups established in the field. Thin sections were also used to inspect for the presence of alteration phases related to post-eruption weathering. Thin section microphotographs together with electron backscatter images were used to characterise the pumice vesicularity. This was specifically to aid the interpretation of the NG data because of the relevance of the vesicles abundance in controlling the concentration and fractionation of the NG in volcanic glass (Burnard et al., 2004).

Pumices of between 2 cm and 10 cm and belonging to the same group were mixed and prepared for the analysis. For group A two aliquots were prepared from the same mixture; one was used for XRF analyses only, whereas from the other one were picked glass and alkali feldspars for electron microprobe, NG analysis and Ar/Ar dating. This has ensured the best opportunity for comparing the results of all analyses.

For all the groups, XRF bulk major and trace element compositions were determined in order to investigate the presence of any chemical variability among samples of different groups, and, among samples of the same group but collected in different portions of the eruptive sequence. Bulk-rock analyses have also helped to identify those samples with the highest K content more suitable for Ar/Ar dating.

Major elements by electron microprobe analyses were studied in glass and alkali feldspars derived from pumices of group A. Particular attention was given to the variations of the Si and K because their importance for interpreting NG and Ar/Ar dating results. The CIA was calculated for each analysis performed on pumice glasses in order to determine if their composition had been modified by alteration processes. Between two and four *in-situ* analyses for each sanidine were performed in order to assess the presence of a homogeneous population of crystals and to investigate the existence of any chemical zoning, within selected alkali feldspars, with respect to their K and Si content. This was specifically to aid the interpretation of the NG and Ar/Ar data.

Pumice glass and alkali feldspar from group A were prepared (see 2.3.4.1) and analysed by single grain total fusion NG mass spectrometry (see 2.3.4.2). This was done in order to inspect the variations of the ^{4}He, ^{36}Ar, ^{40}Ar signatures in samples with similar chemistry but collected in different portions of the eruptive sequence. The $^{4}He/^{40}Ar^{*}$ ratio was used as index for sample degassing while the $^{40}Ar/^{36}Ar$ ratio was used as a proxy of air contamination and of the presence of $^{40}Ar_{E}$ within the glass and alkali feldspars.

Ar/Ar dating by laser probe step-heating and single grain total fusion on glass and alkali feldspars from pumices of group A were used to provide, for the first time, the age of the Eras Formation whilst investigating if / how degassing processes influence the ability of these materials to return reliable, precise and accurate Ar/Ar ages.

Haüyne crystals, picked from the pumices of suite D were also dated by laser probe step-heating and single grain total fusion in order to investigate their suitability for dating young silicic volcanic rocks with the Ar/Ar technique. The results were compared with those obtained from pumice glass and alkali feldspars and discussed, altogether, in the context of ^{40}Ar distribution in different types of volcanic materials. The samples were prepared and analysed following procedures listed in sections 2.3.4.1 and 2.3.4.2.

Ar/Ar dating results were compared with available data from previous studies on Tenerife products helping to frame the Eras Formation into the more general evolutionary context of Tenerife.

Table 2.3 Analytical techniques used to study the Eras Formation (Tenerife).

Deposit	Sample	Thin section	Backscatter images	XRF	Probe		NG-MS		Ar/Ar Dating	
					Alkali feldspar	Glass	Alkali feldspar	Glass	Sanidine	Glass
Fall										
F1	A	X	X	X	X	X	X	X	X	X
	B	X		X						
F2	A	X	X	X	X	X	X	X	X	X
	B	X		X						
Ignimbrite										
I1	A	X	X	X	X	X	X	X	X	X
	B	X		X						
	C	X		X						
	D	X		X						
I3	A	X	X	X	X	X	X	X	X	X
	C	X	X	X	X	X				
	D	X	X	X	X	X			Haüyne	X

2.3 Methods

2.3.1 Thin sections and backscatter images analysis

The samples were mounted in epoxy resin blocks and then reduced to thin sections (30 μm) by 'Thin section laboratory' staff at The Open University using internal laboratory procedures. Petrographic analyses were performed using a GX polarised microscope and photomicrographs were acquired using a Qimaging micropublisher digital camera.

Electron backscatter images were taken on thin sections previously polished and gold / carbon coated. The images were acquired with a Zeiss Supra 55VP electron microscope using default settings and ImageJ software (Abramoff et al., 2004) was used for image processing allowing the calculation of the sample vesicularity.

2.3.2 X-ray fluorescence analysis

The samples were crushed in a ceramic mortar until a homogeneous size of ≤63 μm was reached. 10 g of each sample were taken for fusion beads and pellets preparation. The sample preparation was personally performed at The Open University and at the University of Leicester while the analyses and subsequent corrections were performed by Dr. Tom Knot at the University of Leicester.

The Loss On Ignition (LOI) was calculated before the analyses in order to take into account the measurement of those constituents (mainly H_2O and CO_2) that are not detectable by XRF. A few grams of sample powder were put into porcelain crucibles and dried overnight in a furnace at 100^{o}C. Once cooled, they were carefully weighed and ignited in a muffle furnace at a maximum temperature of 950^{o}C. After 2 hours, the samples were removed and left to cool. Once cooled, the samples were re-weighed and the mass of volatiles species lost during the heating process was calculated determining the LOI.

Fusion beads for major elements analyses were prepared mixing, into a platinum crucible, 0.6 ± 0.0001 g of each ignited sample with 3.0319 ± 0.0001 g of lithium tetraborate flux (the exact mass depended on the batch of flux). The crucible was put on a gas burner at 1100°C until its content was completely melted. The fused mixture was swirled twice during the fusion process to homogenise its content and allow gas bubbles to escape. When the sample was completely melted it was spilled into a pre-heated round mould and chilled using a cold air jet. Cooling must be quick enough to prevent crystallization of the sample but not too rapid to cause the sample to crack. After chilling the sample, the glass disc was detached from the mould and the lower surface labelled.

Powder pellets for trace elements analysis were prepared mixing 5-7 g of sample with 11 drops of 7% polyvinylpyrollinade / methyl cellulose binding agent until forming a homogeneous crumbly paste. This mixture was put in a cylindrical steel pellet mould and pressed at 0.15 GPa per sq. inch in a pellet press. The resultant compacted disc (32 mm diameter) was removed from the mould and left to dry in the open air.

XRF bulk-rock analyses were performed using a PANalytical Axios Advanced X-Ray Fluorescence spectrometer (4Kw Rhodium anode end window super sharp ceramic technology X-Ray tube). Instrumental conditions were selected to avoid any significant line overlaps within the usual compositional range of most geological materials. Major elements analyses were performed using the default PANalytical SuperQ conditions while for trace elements the analyses used default parameters within the PANalytical ProTrace software. Trace element correction factors and calibrations for both major and trace elements were done following internal laboratory standard procedures.

2.3.3 Electron microprobe analysis

The samples were mounted in epoxy blocks or prepared as polished thick sections (40 μm) by the 'Thin section laboratory' staff (OU) and then personally carbon coated.

The analyses were conducted with a Cameca SX100 electron microprobe with major elements measured using four wavelength-dispersive detectors. The machine was calibrated against a standard of known composition before the analyses. Standards and analytical conditions were varied for each experiment and are listed in Table 2.4. The overall analytical accuracy, which includes uncertainties in the secondary standard compositions and errors associated with corrections, is closer to ±2% based on repeated analysis of secondary standards. Specific analytical conditions for each experiment are reported in Appendix A3.1 and A4.1.

Table 2.4 Analytical conditions used for electron microbe analyses.

Sample	Beam current	Accelerating voltage	Beam size	Standard
Pele's hairs and tears	20 nA	20 keV	10 μm	VG2
Pumice glass	10 nA	20 keV	1 μm*	NMNH-72854_VG-568
Alkali feldspar	10 nA	20 keV	1 μm	NMNH-72854_VG-568

* This bean size was necessary due to the extremely small and thin structure of the pumice glass.

2.3.4 NG and Ar/Ar Measurements

2.3.4.1 Sample selection and preparation

Before the analyses, tuffs from the CRBG and pumices from Tenerife were crushed in a ceramic mortar, washed with water and sieved in order to separate material of different grain sizes. Pele's hairs and tears from the Masaya volcano were only washed with water and sieved. Different grain sizes were selected for the three projects (Table 2.5) while the same grain size was chosen when NG and Ar/Ar dating experiments were done on the same materials in order to better compare the final results of the analyses.

The selected size fraction was repetitively washed with chloridric acid (HCl), then acetone and finally deionized water, in an ultrasonic bath, in order to remove unwanted materials, adhering to the surfaces of the samples that could potentially alter the results of the analyses. The number of washing cycles and duration of each cycle depended on the cleanliness of the initial material. After each cycle, the samples were dried and carefully observed using a binocular microscope in order to evaluate if another cleaning was necessary. The target materials (glass shards, Pele's hairs and tears, pumice glass, alkali feldspars and haüynes) were handpicked using the binocular microscope. Particular care was taken at this stage to select the optically cleanest materials (without any surface alteration, extraneous particles adhering and visible inclusions) for the analyses. Where necessary, multiple picking passes were required to remove any further unwanted particle from the target material. Description of the microscopic characteristics of the material and micro-photographs were taken at this stage for future reference (presented in sections 3.4.4, 4.5.1 and 5.4.2).

Those samples used for NG analyses were weighed, placed grain by grain in a separate hole of the aluminium sample holder (Figure 2.2 C) and loaded into the ultra-high vacuum extraction line (Figure 2.2 A) of the mass spectrometer using one of the two available sample ports (Figure 2.2 B).

In addition to the sample preparation procedures previously described, those samples for Ar/Ar dating analyses were irradiated. For this purpose, 20-40 mg of sample were wrapped in aluminium foils, labelled and put in an Al cylindrical container together with biotite standard GA1550 (99.738 ± 0.104 Ma - Renne et al., 2011). The standard, used for neutron flux monitoring (in order to calculate the J value which is a function of flux, see Appendix A1), was wrapped in a similar way and regularly spaced between samples (standard every ~10 sample foils) within the cylinder. The samples and the standard were sent for irradiation at the McMaster university nuclear reactor (Canada). Here, they have been put inside a 3MW reactor in position 8D where they have been irradiated after Cd

shielding. Length of irradiation for the different samples was varied in order to obtain the best $^{40}Ar/^{39}Ar$ ratio during the analysis. The difference in the exposure time to irradiation is mainly dependant on the age of the samples, although other factors like the sample chemistry should also be considered in order to reduce the amount of 'unwanted' isotopes generated during the irradiation (see Appendix A1). In the specific case, glass shards from the CRBG are Miocene and needed a longer irradiation time to generate sufficient ^{39}Ar from ^{40}K for the analysis compared to the much younger Tenerife samples (< 1 Ma) that needed much less neutron flux, and thus time, to generate enough Ar isotopes. For these reasons, glass shards have been irradiated for 300 MWH (120 hours) while phonolitic glass, alkali feldspars and haüyne crystals for 12 MWH (4 hours).

Following the irradiation, the samples were safely stored at the reactor until their radiation level drops to a safe threshold. After, they have been shipped-back to the laboratory and safely stored. Before loading the samples into the mass spectrometer the level of radiation was carefully checked in order to provide safe working conditions. Once this has happened, the samples were removed from the foils and then placed in an aluminium sample holder (Figure 2.2 C). Those samples for single grain total fusion were put in separate holes within the sample holder while samples for step heating experiments were distributed in the holder as a single layer of material. Then, the samples were loaded into the ultra-high vacuum extraction line (Figure 2.2 B) of the mass spectrometer using one of the two available sample ports (Figure 2.2 A). After, the samples were heated for 8 hours at 120^{o} C under a 250 W heat lamp in order to accelerate the release of atmospheric gases adsorbed to the sample surfaces and sample port walls. Before the analyses the blank was monitored until a constant minimum value was reached.

Table 2.5 List of the samples prepared for NG and Ar/Ar dating analyses.

Sample	Grain size	NG	Ar/Ar dating	
		Single grain total fusion	Single grain total fusion	Step heating
Glass shards	63 μm			X
Pele's hairs and tears	1000- 500 μm	X		
Pumice glass	250 μm	X	X	X
Alkali feldspars	250 μm	X	X	X
Haüyne	250 μm		X	X

2.3.4.2 Noble gas analysis

Single grain total fusion analyses on Pele's hairs and tears, pumice glass and alkali feldspars were performed using a MAP-215-50 noble gas mass spectrometer using established techniques. A focused continuous SPI 1062 nm fibre infra-red laser (20 W power) was used to extract NG isotopes (^{4}He, ^{22}Ne, ^{36}Ar, ^{40}Ar) from the samples. Two Zr-Al SAES NP10k getters (one working at room temperature, the other one working at 440°C) and an inline cold nitrogen trap were used to capture active gases prior to admission to the mass spectrometer. An ultra-high vacuum system (10^{-9} Torr) provided the lowest blank value within the mass spectrometer. Ion counts were detected by a secondary electron multiplier in peak-hopping mode scanning the peaks at mass 4, 22, 36 and 40. Routine peak centres on ^{4}He and the peak position for masses 22, 36 and 40 were calculated relative to the ^{4}He peak position. During analysis were used the following parameters: 5 minutes gettering time, 10 scan and 10 measurements for each considered isotopes. Peak intensities were automatically calculated, by a LabView routine, extrapolating back to the inlet time to correct for gas adsorption onto the spectrometer walls. A homemade LabView platform, routinely used in the laboratory, was used to control the analytical parameters and to display visually ion count and regression graphs. Background levels of the machine were monitored over the entire duration of the experiments running two blank measurements after every two sample analyses. The daily average blank value was subtracted from the raw data using the in house designed *ArMaDiLo* software (Argon Macro Direct Loader – Schwanethal, 2006). A known volume (0.2 cc) of NG with standard element and isotopic ratios, contained within a specifically designed calibration bottle, was measured before each experiment in order to determine the mass spectrometer sensitivity and mass discrimination value (at 283±2 for ^{40}Ar/^{36}Ar - uncertainty not used in the calculation). Calibration measurements were operated using the same operational routines and analytical conditions used for measuring NG abundances in the samples. Detection limits for the considered isotopes are related to the minimum blank level achievable during the analysis. In order to be reliable an isotopic measurement must be two times over the average blank level of the machine (see tables in the Appendix for average values). The average sensitivity of the mass spectrometer between 2016 and 2018 is 1.21×10^{-9} cc/V for ^{40}Ar, 1.26×10^{-9} cc/V for ^{36}Ar, 4.40×10^{-8} cc/V for ^{4}He and 1.88×10^{-8} cc/V for ^{22}Ne. Table 2.6 shows the Ar isotopic composition and reproducibility of the standard used for calibration measurements between 2016 and 2018.

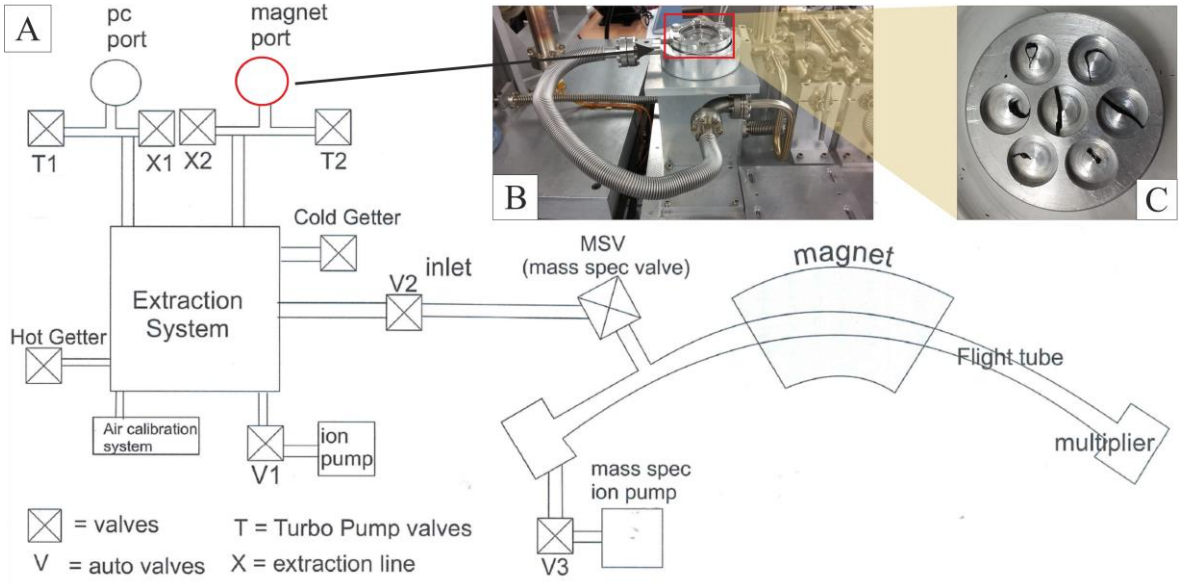

Figure 2.2 A - Scheme of the MAP-215-50 mass spectrometer used in this study for NG and Ar/Ar analyses. B - Detail of the sample port and flexible cable attached to the extraction line system. C - Detail of the aluminium sample holder with Pele's hairs and tears placed each one in a different hole.

Table 2.6 Ar isotopic composition (V) and ratios of the gas standard used for calibration measurements between 2016 and 2018.

	^{40}Ar	±	^{38}Ar	±	^{36}Ar	±	^{40}Ar/^{36}Ar	±	^{38}Ar/^{36}Ar	±
08-2016	2.87959	0.00314	0.00179	0.00010	0.01015	0.00012	283.70	3.37	0.18	0.01
	2.86349	0.00358	0.00207	0.00008	0.01019	0.00008	281.01	2.23	0.20	0.01
	3.12301	0.00231	0.00212	0.00010	0.01091	0.00007	286.25	1.85	0.19	0.01
	3.02473	0.00368	0.00217	0.00013	0.01055	0.00011	286.70	3.01	0.21	0.01
	3.01690	0.00294	0.00203	0.00010	0.01083	0.00013	278.57	3.35	0.19	0.01
	2.87056	0.00782	0.00189	0.00009	0.00986	0.00011	291.13	3.34	0.19	0.01
Average							**284.56**	**2.86**	**0.19**	**0.01**
11-2016	3.62714	0.00898	0.00217	0.00020	0.01334	0.00029	271.90	5.95	0.16	0.02
	3.73077	0.01006	0.00227	0.00014	0.01327	0.00028	281.14	5.98	0.17	0.01
	3.58422	0.00849	0.00229	0.00012	0.01269	0.00035	282.44	7.82	0.18	0.01
	3.59002	0.00745	0.00254	0.00020	0.01262	0.00037	284.47	8.36	0.20	0.02
	3.59498	0.00849	0.00242	0.00028	0.01266	0.00043	283.96	9.67	0.19	0.02
Average							**281.41**	**6.77**	**0.18**	**0.01**
01-2017	3.21611	0.01024	0.00200	0.00021	0.01123	0.00018	286.39	4.68	0.18	0.02
	3.20663	0.00487	0.00244	0.00011	0.01118	0.00026	286.82	6.68	0.22	0.01
	3.26817	0.00823	0.00238	0.00020	0.01178	0.00022	277.43	5.23	0.20	0.02
	3.23009	0.01369	0.00225	0.00009	0.01116	0.00020	289.43	5.33	0.20	0.01
	3.24811	0.01107	0.00212	0.00020	0.01130	0.00014	287.44	3.69	0.19	0.02
Average							**285.50**	**5.12**	**0.20**	**0.01**
08-2017	3.21611	0.01024	0.00200	0.00021	0.01123	0.00018	286.39	4.68	0.18	0.02
	3.20663	0.00487	0.00244	0.00011	0.01118	0.00026	286.82	6.68	0.22	0.01
	3.26817	0.00823	0.00238	0.00020	0.01178	0.00022	277.43	5.23	0.20	0.02
	3.23009	0.01369	0.00225	0.00009	0.01116	0.00020	289.43	5.33	0.20	0.01
	3.24811	0.01107	0.00212	0.00020	0.01130	0.00014	287.44	3.69	0.19	0.02
Average							**285.50**	**5.12**	**0.20**	**0.01**
01-2018	0.82091	0.00267	0.00060	0.00002	0.00282	0.00004	291.10	4.24	0.21	0.01
	2.94102	0.03952	0.00207	0.00002	0.01037	0.00009	283.61	4.54	0.20	0.00
	3.15687	0.02974	0.00204	0.00009	0.01105	0.00012	285.69	4.11	0.18	0.01
	3.04568	0.02020	0.00199	0.00004	0.01099	0.00021	277.13	5.61	0.18	0.01
Average							**284.38**	**4.62**	**0.19**	**0.01**
08-2018	2.61701	0.00405	0.00181	0.00005	0.00950	0.00007	275.47	2.07	0.19	0.01
	2.68125	0.00315	0.00180	0.00007	0.00966	0.00005	277.56	1.47	0.19	0.01
	2.66954	0.00347	0.00182	0.00009	0.00951	0.00006	280.71	1.81	0.19	0.01
	2.71297	0.00413	0.00184	0.00010	0.00955	0.00007	284.08	2.13	0.19	0.01
	2.78758	0.00470	0.00201	0.00007	0.00993	0.00011	280.72	3.15	0.20	0.01
	2.77828	0.00359	0.00191	0.00009	0.00988	0.00011	281.20	3.15	0.19	0.01
Average							**279.96**	**2.30**	**0.19**	**0.01**

2.3.4.3 Ar/Ar dating analysis

Single grain total fusion analyses on standards and on selected samples (Table 2.5) and step-heating experiments on target materials (Table 2.5) were performed using a MAP-215-50 noble gas mass spectrometer (Figure 2.2 A). A focused continuous SPI 1062 nm fibre infra-red laser (20 W power) was used to extract Ar isotopes (^{36}Ar, ^{37}Ar, ^{38}Ar, ^{39}Ar, ^{40}Ar) from the samples. Two Zr-Al SAES NP10k getters (one working at room temperature, the other one working at 440°C) and a cold nitrogen trap was used to capture active gases prior to admission to the mass spectrometer. An ultra-high vacuum system (10^{-9} Torr) provided the lowest blank value within the mass spectrometer. Ions were counted by a secondary electron multiplier in peak-hopping mode with 5 minutes gettering time, 10 scan and 10 measurements for each considered element. Peak intensities were automatically calculated, by a LabView routine, extrapolating back to the inlet time to correct for gas adsorption onto the spectrometer walls. A homemade LabView platform was used to control analytical parameters and to visually display ion count and regression graphs.

In-house *ArMaDiLo* software (Schwanethal, 2006) was used to correct measured data for blank, ^{37}Ar decay, ^{39}Ar decay, atmospheric ^{40}Ar/^{36}Ar ratio (298.56 - Lee et al., 2006) and neutron-induced interference reactions. The following correction factors, based on analyses of Ca and K salts, were applied: $(^{39}Ar/^{37}Ar)_{Ca}$ = 0.00065±0.00000325, $(^{36}Ar/^{37}Ar)_{Ca}$ = 0.000265±0.000001325, and $(^{40}Ar/^{39}Ar)_{K}$ = 0.0085±0.0000425. *ArMaDiLo* was also used for the calculation of the error propagation, J value, ^{40}Ar/^{39}Ar ratio, ^{38}Ar/^{39}Ar ratio, ^{37}Ar/^{39}Ar ratio, ^{40}Ar/^{36}Ar ratio and age of the sample.

The mass spectrometer sensitivity (see section 2.3.4.2) and the mass discrimination value (283±2 for ^{40}Ar/^{36}Ar) were determined with similar procedures used for NG calibration. A known volume (0.2 cc) of NG with standard element and isotopic ratios, contained within a specifically designed calibration bottle, was measured with the same analysis routines and analytical conditions as for samples. A value of 5.543±0.010E^{-10} for the $^{40}K_{tot}$ decay constant (Steiger and Jäger, 1977) and an age of 98.79±0.54 Ma (Renne et al., 1998) for the GA1550 biotite was used in the calculation of the J value. *ArArReCalc* Excel spreadsheet (Koppers et al., 2002) was used to recalculate apparent ages and 1σ error propagation (obtained from *ArMaDiLo*) according to the new age for the GA1550 (99.738±0.104 Ma) and $^{40}K_{tot}$ decay constant (5.5305±0.0135E^{-10}) given by Renne et al. (2011).

Isoplot/Ex V.4.15 Microsoft Excel add-in (Ludwig, 2003) was used for plotting age-spectra and inverse isochrons and calculating plateau ages, inverse isochron ages and

weighted mean ages. Errors on the ages are quoted at 2σ or 95% confidential level including a 0.5% error on the J value. In this study, a plateau age refers to a minimum of three contiguous concordant steps with similar apparent ages at the 95% confidence level and representing a minimum of 50% of the released ^{39}Ar (Fleck et al., 1977). The age spectra and inverse isochrons were used in combination to assess for the presence of $^{40}Ar^{E}$, the recoil of ^{39}Ar and ^{37}Ar, sample alteration and atmospheric contamination.

When an inverse isochron age is calculated using *Isoplot*, the software try to find the best-fitting straight line through the given $^{36}Ar/^{40}Ar$ and $^{39}Ar/^{40}Ar$ ratios. This is done by calculating their probability of fit and applying specific regression models.

Model 1 is used when the probability of fit of the data is more than 15%. In this case the software applies the algorithm of York (1969) to regress the data and to find the best fit line. The model assumes that the errors associated to the data are the only reason the data-points scatter from a straight line. The points are therefore weighted proportional to the inverse square of these errors (taking into account the error correlations). In this case the errors are given at 2σ or 95% confidence level with this last one equivalent to 1.96 times the 1σ internal analytical uncertainty.

In the case of poor fit, when the probability is less than 15%, *Isoplot* gives the possibility to choose to continue to use the *Model 1* for the regression or to use an alternative *Model 2*. When *Model 1* is accepted, *Isoplot* calculates the 95% confidence interval from the observed scatter using the Student's-*t* multiplier to convert from estimated errors to 95%-confidence errors. On the other side, when *Model 2* is used the software assigns equal weights and zero error-correlations to each point. This permits to avoid to weight the points according to analytical errors when some other cause of scatter is involved. In this case the 95% confidence-limit errors are calculated.

When a plateau age is calculated with *Isoplot*, the software use a specific algorithm to find the plateau that include the largest amount of released ^{39}Ar that at the same time satisfies the following criteria: it must be the best statistically-justifiable plateau and plateau-age from the data; it must have at least three contiguous steps comprising more than no less than 30% of the ^{39}Ar (this value is arbitrary and can be changed by the user – default value is 60%); the probability-of-fit of the weighted-mean age of the steps must be greater than 5%; the slope of the error-weighted line through the plateau ages must not be different from zero at 5% confidence level; the ages of the outermost 2 steps for either side of the plateau must not be significantly different (at 1.8 σ) than the weighted-mean plateau age; the outermost 2 steps for either side of the plateau must not have non-zero slopes (at 1.8 σ) with the same sign.

When the Ar/Ar dating analyses were performed on multiple aliquots of the same sample (glass shards – see section 3.4.5), the age of the sample was calculated as the error-weighted mean of the ages. This calculation was used for both isochrons ages and plateau ages with the 2σ analytical uncertainty propagated only from the internal analytical uncertainties. Here again, if the probability of fit is more than 15%, the 95% confidential error is 1.96 times the internal 1σ analytical uncertainty, otherwise it is Student's-*t* times the square root of the Mean Squares of Weighted Deviates (MSWD) if the probability is less than 15 %.

For all the calculated ages the MSWD value is given with the graphs. The MSWD is the ratio of the observed scatter of the points from the best-fitting line to the expected scatter from the assigned errors and error correlations. It provides information on how much the data scatter from the weighted mean value based on the calculated analytical uncertainty. Those ages with MSWD values closer to 1 are weighted preferred, over those with larger values, to represent the true age of the samples. This because if the MSWD is closer to the unity the assigned errors are the only source of scatter. If the MSWD values are much greater than 1 the observed scatter exceeds that predicted by the analytical uncertainties, in other words the data are "overdispersed" and the analytical uncertainties are underestimated or a non-analytical scatter is the source of the deviation from the unity. MSWD values lower than 1 indicate that the observed scatter is less than that predicted by the analytical uncertainties, the data are "underdispersed" and the analytical uncertainties are overestimated or an unrecognized error-correlations exists in for the data.

Chapter 3:

Ar/Ar dating of silicic volcanic glass interbedding the upper Columbia River Basalt Group (Washington, U.S.)

3.1 Introduction

Ar/Ar dating has been used extensively to investigate the timing and temporal evolution of Large Igneous Provinces (LIPs). However, as shown in Barry et al. (2013), the obtained results are not always reliable when any one, or more, of whole-rock, single crystals, groundmass or interstitial glass are analysed.

Ar/Ar age dating of K-rich minerals in silicic tuffs interlayered between basaltic lavas has been demonstrated to produce more precise and accurate, indirect, ages for basaltic lavas (Henry et al., 2006, 2017; Mahood and Benson, 2017). Directed by these outcomes and supported by the encouraging results on Ar/Ar dating of glass (e.g. Bigazzi et al., 2008; Morgan et al., 2009; Nyland et al., 2013), in this chapter, I investigate the ability of K-rich glass shards, found within silicic interlayers, of returning precise and accurate indirect Ar/Ar ages of basalt emplacement. The validity and reliability of the method is assessed by comparing the obtained ages with the stratigraphical position of the interlayers and of the upper and lower basalts and, where available, with K/Ar and Ar/Ar ages from previous studies. The precision of the ages is compared and discussed with respect to the most precise Ar/Ar ages from K-rich minerals found within interlayers from the same area.

Due to the lack of a detailed chronology of lava emplacement and the abundance of ash-rich interlayers I focus this research on glass shards found within ash-rich deposits interlayering the upper part of the Columbia River Basalt Group (CRBG), northwest USA. This section of the Columbia River Flood Basalt Province (CRFBP), unlike other portions of the CRBG, has not been extensively studied using the Ar/Ar dating since the early K/Ar studies (Evernden and James, 1964; McKee et al., 1977). Only four Ar/Ar ages (Duncan, 1983; Reidel et al., 1989; Barry et al., 2013) have been published for this part of the CRBG (15.0 Ma – 6.0 Ma, McKee et al., 1977; Barry et al., 2013). New and precise Ar/Ar ages from this section of the CRBG will help to refine the stratigraphy of the latest phases of the CRFBP volcanism aiding a more precise determination of the timing, frequency and duration of eruptions and their synchronicity with specific eruptive events of the Central Snake River Plain rhyolitic volcanism (CSRP, 12.7 – 5.5 Ma - Bonnichsen et al., 2008).

3.2 Large igneous provinces (LIPs)

LIPs are extensive lava plateaus (up to several kilometres thick) associated with mantle plume fissure eruptions (Campbell, 2005) during which large volumes of basaltic magma (up to 10^3-10^4 km^3) and volcanic gases are erupted within a brief period of time ($<10^6$ years) (Self et al., 2015). Continental silicic LIPs, forming the Earth's biggest ignimbrite plateaus, represent a minority, whereas, basaltic provinces are more widespread and occur in ocean basins (oceanic plateaus) and on continental crust (e.g. the North Atlantic Volcanic Province, the Siberian and Deccan Traps and the Columbia River Flood Basalts Province) (Bryan et al., 2010; Bryan and Ferrari, 2013).

Continental flood basalts (CFBs) are composed of tholeiitic pahoehoe and sheet lavas (Self et al., 1998; Brown et al., 2014), originating from initial Hawaiian-Strombolian-style volcanism characterised by lava fountaining, spatter-fed flows and tephra eruption (Brown et al., 2014). The basaltic lavas are generally composed of plagioclase, clinopyroxene, iron and titanium oxides, minor olivine and sometimes orthopyroxene (Self et al., 2015). More rare occurrences of alkalic, silica-undersaturated and rhyolitic deposits have been found associated with basaltic lavas (Reichow et al., 2005). Hiatuses in the eruptive activity are marked by interbedded lateritic soils, terrestrial, fluvial and lacustrine deposits (Jolley, 1997; Jolley et al., 2008; Halton, 2011; Ebinghaus et al., 2014).

The outpouring of huge volumes of CO_2 and SO_2 during LIP emplacements can cause severe and long-term consequences for climate and biota (Rampino and Self, 1992; Jolley and Widdowson, 2005; Self et al., 2006; Jolley et al., 2008; Tobin et al., 2017). The SO_2 and sulphate aerosols are responsible for global cooling through their ability to reflect and adsorb sunlight (Jolley and Widdowson, 2005; Ernst and Youbi, 2017), whereas the release of CO_2 is accountable for global warming through the increase of the absorption of Earth's radiated heat (Tobin et al., 2017).

The environmental effects of CFB emplacement and their relationship with mass extinctions have been investigated by several studies (e.g. Courtillot, 1999; Wignall, 2001; Courtillot and Renne, 2003; Self et al., 2006; Courtillot et al., 2015; Bond and Grasby, 2017; Ernst and Youbi, 2017). Although this argument is still debated, good correlations between these phenomena have been only found for three of the biggest CFBs erupted during the last 300 Myr. Deccan traps has been linked to the end-Cretaceous extinction (Kelley, 2007; Chenet et al., 2009); the Siberian traps to the Permian-Triassic boundary extinction (Kelley, 2007; Burgess et al., 2014); and the Central Atlantic Magmatic Province to the Triassic-Jurassic extinction (Nomade et al., 2007; Kelley, 2007). Other LIPs of smaller size, like the Columbia River Basalt (CRB), have only been correlated with

minor or more local events that may have had only a limited impact on the global environment (Ebinghaus et al., 2015).

In this context, a more precise determination of the timing and frequency of eruptions and duration of peak activity, and consequently of the total volume of magma erupted and volume of gases released into the atmosphere, are essential factors in determining the role played by continental LIPs in past environmental changes.

3.3 Dating LIP basalts

Several geochronological techniques (K/Ar, Ar/Ar, U/Pb, magnetostratigraphy, palynology) have been used to date the timing and rates of volcanism of LIPs (Evernden and James, 1964; Jolley et al., 2008; Jarboe et al., 2008; Barry et al., 2010; Burgess et al., 2014). Among them, the K/Ar and Ar/Ar techniques have been extensively used but often with limited success. Dating basalts has always been challenging for both K/Ar and Ar/Ar methods due to their low-K contents (K_2O~ 0.1-1.5%) and the ease with which they weather and undergo alteration. Numerous types of material (fresh and altered whole-rock, plagioclase crystals, groundmass, interstitial glass) have been tested in order to provide reliable, precise and accurate ages (Barry et al., 2010). Even when the highest K-content phase (groundmass - K_2O~ 1.5%) has been selected for analysis, the ages are not always consistent (CRBG - Barry et al., 2010; North Atlantic Igneous Province – Halton, 2011).

Contrasting Ar/Ar results have been attributed to contamination and alteration effects including: analysis of xenocrysts (Barry et al., 2010); plagioclase sericitization (Verati and Jourdan, 2013); glass alteration and devitrification with replacement zeolites (Fleck et al., 1977); deposition of secondary minerals (clays, sericite, zeolites) from circulating fluids (Verati and Jourdan, 2014); ^{39}Ar and ^{37}Ar recoil (Koppers et al., 2000; Jourdan et al., 2007) and $^{40}Ar_E$ (Kelley, 2002). Ar/Ar ages obtained for basaltic rocks from LIPs can only be understood if these effects are recognized and taken into account.

The alteration of glass and plagioclase leads to K-loss (and thus ^{40}Ar loss) from their structures, lowering apparent ages. The same situation is caused by the circulation of high-temperature fluids that can promote radiogenic ^{40}Ar loss if the closure temperature of a mineral is exceeded. In contrast, the deposition of secondary minerals and circulation of fluids enriched in ^{40}Ar can introduce $^{40}Ar_E$, artificially elevating the ages. Recoil causes the redistribution and / or loss of the Ar isotopes; in particular the $^{37}Ar_{Ca}$ recoil causes an under-correction of the $^{39}Ar_K$ lowering the apparent ages, while the $^{39}Ar_K$ recoil has the opposite effect (Jourdan et al., 2007).

Some of these problems can be identified and minimised prior to the irradiation, others cannot be overcome and can be recognised only after the analysis (Table 3.1). Sample alteration can be detected prior to the irradiation, through macroscopic and microscopic inspection, and those specimens too altered can then be discarded. Alteration minerals in groundmass and glass adhering to the crystals can be removed by acid-cleaning the samples using HCl, HF and/or HNO_3 (Koppers et al., 2000). Although this method has proved to be effective in reducing alteration, some concerns have arisen through the observation of the formation of "bread-crust" fractures on basalt groundmass after HNO_3-cleaning (Barry et al., 2012). Increasing the sample surface area potentially favours recoil and the incorporation of anomalous concentration of ^{36}Ar into the sample (Clay et al., 2011; Barry et al., 2012). HF cleaning of feldspars has not produced the effects that were observed for basalt groundmass (Wilkinson, 2013). ^{39}Ar and ^{37}Ar recoil can be minimised by in vacuum-encapsulating the samples, in silica vials, prior to irradiation (Dong et al., 1995; Hall et al., 2013). Disturbances of the Ar system due to Ar recoil, $^{40}Ar_E$ and/or the presence of alteration, can only be identified after the irradiation by inspecting the shape of the age spectra and isochrons (Jourdan et al., 2007; McDougall and Harrison, 1999) although step-heating can homogenise and mask these effects such that the age spectra can be erroneously flat (Sherlock & Arnaud, 1999).

After carefully scrutinising the possible source of errors, the resultant ages must be evaluated in relation to the stratigraphical position of the sample and compared with the results coming from independent geochronological methods (e.g. magnetostratigraphy, palynology, U/Pb dating). The application of all these techniques should then leave only the most robust ages.

The usefulness of these good practices has been evaluated and demonstrated by several authors that have reinvestigated the Ar/Ar ages for several LIPs using the aforementioned criteria (Hofmann et al., 2000; Jourdan et al., 2005; Nomade et al., 2007; Barry et al., 2013). These studies show that the duration of a single magmatic event was more restricted than previously thought. This has helped a more precise determination of the time of the eruptions, duration of peak activity and coincidence of LIP eruptions with climate changes and/or mass extinctions.

Table 3.1 List of the problems affecting Ar/Ar ages in basaltic rocks.

Problem	Effect on the Ar system	Action to minimize the problem	How to detect	Effect on the age**
Presence of xenocrysts*	Anomalous high ^{40}Ar	N.A.†	Comparison of the Ar/Ar ages with the stratigraphy	Anomalous old ages
Presence of alteration products *	Loss of K with ^{40}Ar loss	Sample cleaning with HCl, HF, HNO3 prior the irradiation§	Microscopic observation, age spectra shape**	Decrease of the ages
Deposition of secondary minerals *	Anomalous high ^{40}Ar	Sample cleaning with HCl, HF, HNO3 prior the irradiation§	Microscopic observation, age spectra shape**	Decrease of the ages
$^{39}Ar_K$ and $^{37}Ar_{Ca}$ recoil *	Redistribution of Ar isotopes	In vacuum-encapsulation of the sample prior to irradiation#	Age spectra shape**	$^{37}Ar_{Ca}$ recoil lowers the ages $^{39}Ar_K$ recoil increase the ages
Excess ^{40}Ar *	Anomalous high ^{40}Ar	N.A.†	Age spectra shape, isochron Y-intercept**	Increase of the ages
^{40}Ar* loss due to hot circulating fluids*	Loss of ^{40}Ar	N.A.†	Age spectra shape, isochron Y-intercept**	Decrease of the ages

*See text for references.
†N.A = Not applicable.
§Koppers et al., 2000.
#Folan et al., 1992; Dong et al., 1995; Hall et al., 2013.
**McDougall and Harrison, 1999; Jourdan et al., 2007.

3.4 The Columbia River Flood Basalt Province (CRFBP)

3.4.1 Geological background

The CRFBP is the smallest, youngest and best-exposed continental flood basalt province on Earth. With an area of 210,000 km^2 (Reidel at al., 2013), it covers most of Oregon and eastern Washington, western Idaho and part of northern Nevada (Figure 3.1). The CRFBP comprises a series of tholeiitic to basalt-andesitic compound and sheet flood basalt lavas erupted between 16.7 Ma and 5.5 Ma (Jarboe et al., 2008, 2010; Barry et al., 2010, 2013; Reidel at al., 2013; Henry et al., 2017).

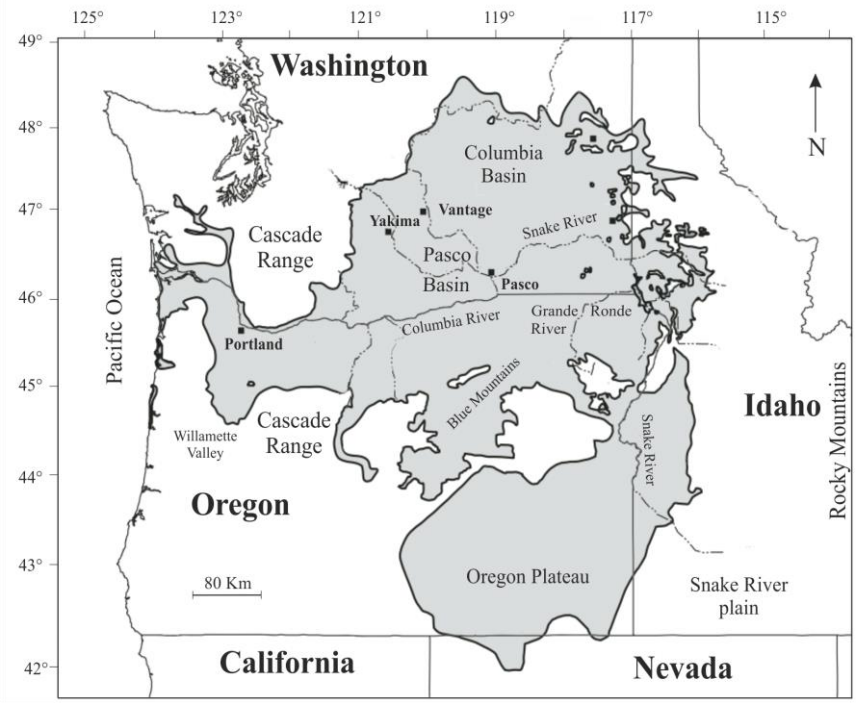

Figure 3.1 Geographical map showing the extent of the Columbia River Flood Basalt Province (CRFBP) in grey (modified from Reidel et al., 2013).

Although several models have been proposed for the origin of the CRFBP (e.g. Liu and Stegman, 2012; Long et al., 2012), the most widely accepted is based on the mantle plume concept (e.g. Camp, 2013; Camp et al., 2013). The CRFBP erupted in a back arc setting between the Cascade volcanic arc (western margin) and the Rocky Mountains (eastern margin). CRFBP eruptions initiated in the Oregon Plateau, contemporaneously with rhyolitic eruptions located at the western margin of the Snake River Plain hotspot track, and then moved northwards towards the Columbia Basin, Cascade arc, Willamette Valley and Coast Range (Reidel et al., 2013). Collectively basaltic lavas erupted in these areas form the Columbia River Basalt Group (CRBG - Swanson et al., 1979; Reidel et al., 2013).

Detailed stratigraphical, geochemical, geochronological and paleomagnetic studies have permitted the development of geochemical and petrogenetic models of this complex volcanic environment (Hooper and Hawkesworth, 1993; Camp and Hanan, 2008; Wolff and Ramos, 2013). Emplacement processes, morphological features (proximal and distal), type of deposits, areal extent and volume of the lavas, as well as the position of feeder vents and dykes have also been established (Self et al., 1996; Camp et al., 2013, 2017; Reidel et al, 2013; Brown et al., 2014). Different Formations and Members of the CRBG have been recognized and distinguished according to their mineral content, chemistry, age and magnetic polarity (Schmincke, 1967; Swanson et al., 1979; Jarboe et al., 2008; Hooper, 2000; Reidel and Tolan, 2013; Wolff and Ramos, 2013; Reidel et al., 2013).

The volcanism started with the eruption of the Steen Basalts (16.9-16.6 Ma, Henry et al., 2006; Jarboe et al, 2008; 2010, Barry et al., 2013) (Figure 3.2). Between 16.7 Ma and 16.0 Ma the activity shifted from south-east to north-east upon which the Imnaha Basalts were erupted (Jarboe et al, 2010; Barry et al., 2010, 2013) (Figure 3.2). The peak of the CRBG activity happened during the Grande Ronde Basalt emplacement (16.0 - 15.6 Ma) when 72% of the total CRBG lava volume was erupted (Barry et al., 2010) (Figure 3.2). A couple of minor eruptions (Prineville Basalt and Picture Gorge Basalt) were contemporaneous to the Grande Ronde Basalt emplacement (Reidel et al., 2013; Barry et al., 2013). The waning phase of the CRBG volcanism is represented by the eruption of Wanapum Basalt (15.6-15.0 Ma – Duncan, 1982; Barry et al., 2010, 2013) and the Saddle Mountain Basalt (15.0-6.0 Ma - McKee et al., 1977; Barry et al., 2010, 2013) (Figure 3.2).

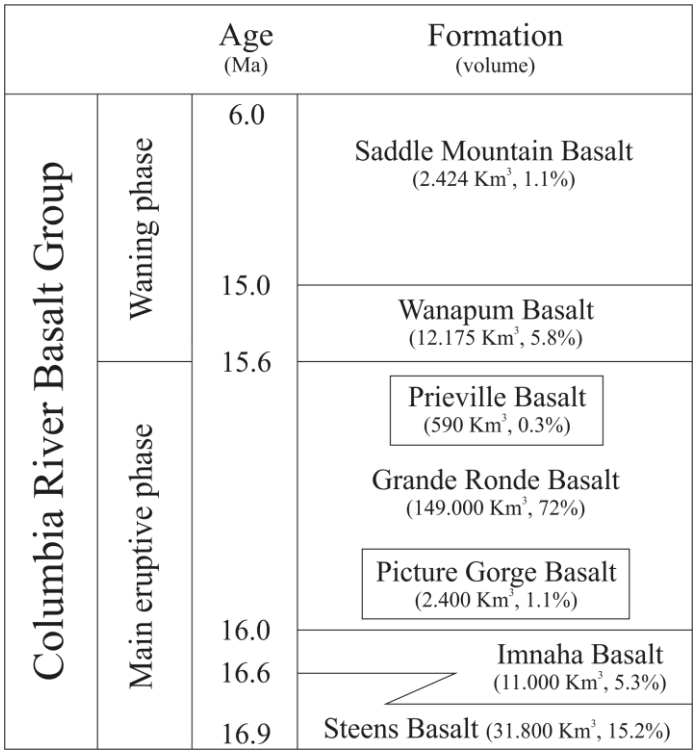

Figure 3.2 Stratigraphy of the Columbia River Basalt Group (CRBG) with relative ages and eruptive volumes given in km^3 and in % in respect to the total erupted volume. Modified from Camp et al. (2017), with relative ages and volumes from Barry et al. (2010, 2013).

Similarly to other LIPs (Jolley, 1997; Jolley et al., 2008; Halton, 2011), hiatuses in eruptive activity are marked by the deposition of lateritic soils, terrestrial, fluvial and lacustrine deposits and primary or reworked air-fall tephra interbedding the CRBG lavas (Schmincke, 1967; Swanson et al., 1979; Fecht et al., 1987; Smith, 1988; Ebinghaus et al., 2014). Thickness and distribution of these sedimentary interbeds are controlled by the duration of volcanic hiatuses, the location of active eruptive centres, the local tectonic activity and the local topography (Smith, 1988; Reidel et al., 2013; Ebinghaus et al., 2014).

The Ellensburg Formation comprises epiclastic and volcanoclastic sedimentary interbeds deposited in the central and western area of the CRBG between 15.6 Ma and 6.5 Ma (Swanson et al., 1979). This Formation has been divided into several members (Figure 3.3) according to their stratigraphic position, composition, relations with the upper and lower lava units and sedimentary facies that include siliciclastic, epiclastic and volcanic facies (Mackin, 1961; Schmincke, 1967; Reidel and Fecht, 1981; Fecht et al., 1987; Smith, 1987; Ebinghaus et al., 2014). Volcanic facies comprise primary pyroclastic deposits, reworked volcaniclastic deposits and agglutinates (Ebinghaus et al., 2014). Primary pyroclastic deposits are ash-fall layers erupted during the Cascade Range and Yellowstone activity and were deposited on exposed CRBG lavas (Smith, 1988; Ebinghaus et al., 2014, 2015); reworked volcaniclastic deposits comprise a mixture of ash shards, pumices, quartz, feldspars and lithic fragments derived from syn-eruptive pyroclasts reworked and re-sedimentated in fluvial and lacustrine environments (Swanson et al., 1979; Smith, 1988; Ebinghaus et al., 2014); agglutinates are basaltic bombs and blocks, occasionally associated with ash-beds or lapilli-beds, that were deposited proximal to the vent or transported and redeposited by fluvial currents not far from their original depocentre. All these deposits can be found in any member of the Ellensburg Formation, alone, or interbedding with sandstones, mudstones and clastic sediments (Ebinghaus et al., 2014).

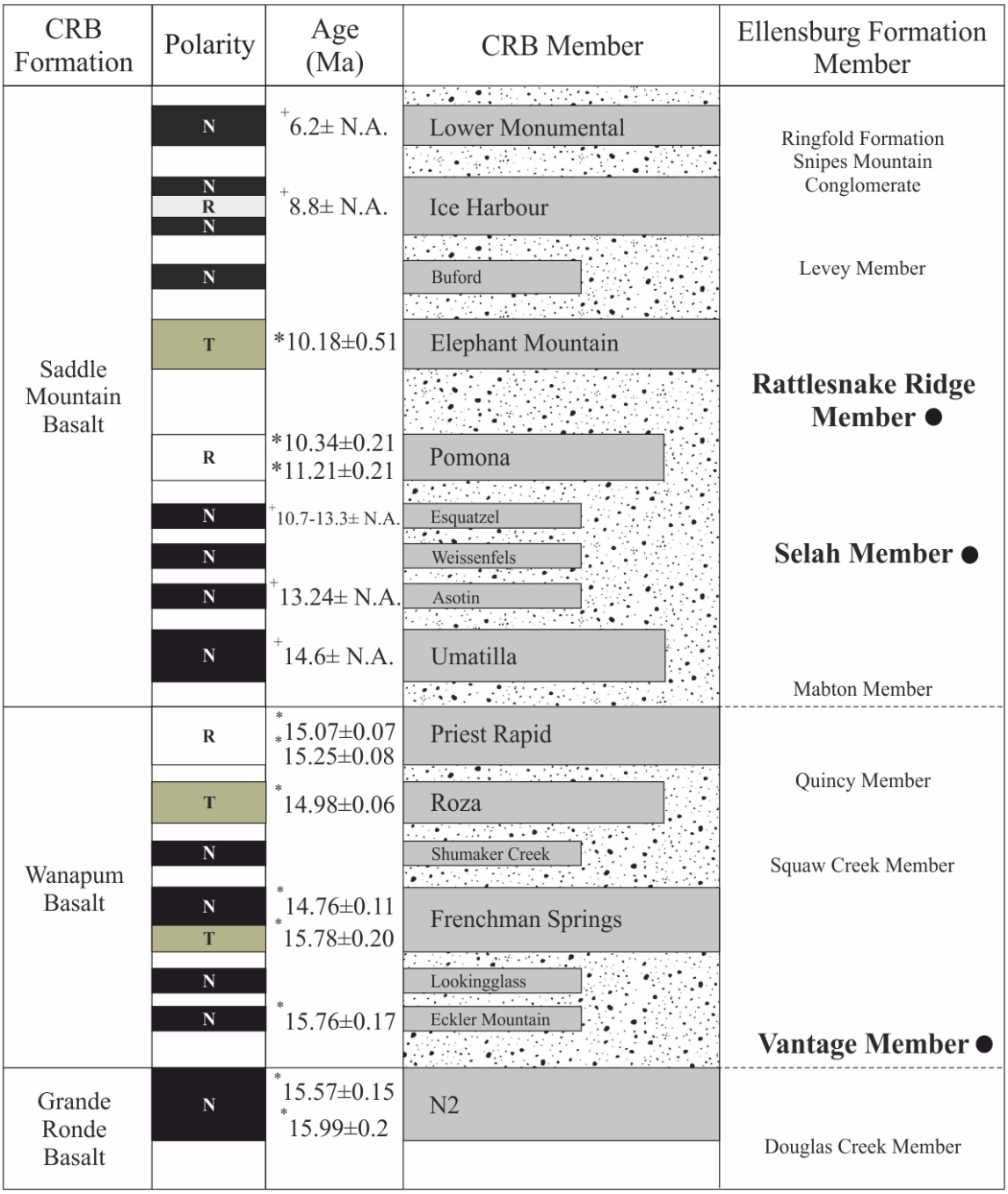

Figure 3.3 Detailed stratigraphic positions and ages of the Columbia River Basalt Members (CRB) of the Wanapum and Saddle Mountain basalts and associated sedimentary interbeds (based on Swanson et al., 1979; Ebinghaus et al., 2014). Black dots represent the stratigraphic position from where the samples of this study were collected. CRBG ages taken from Barry et al. (2013). Where available, the age errors are quoted at the 1σ level. Polarities of the lavas (N = normal, T = transitional, R = reverse) are from Reidel et al. (2013). N.A. = age error not available; * = Ar/Ar age; $^{+}$ = K/Ar age

3.4.2 Age dating attempts

Aphyric CRBG lavas have always been challenging for K/Ar and Ar/Ar dating due to their low feldspar abundance, low K_2O concentrations within plagioclase phenocrysts ($K_2O \leq 0.1\%$) and the highly altered groundmass. Since the earliest K/Ar studies (Evernden and James, 1964; Baksi et al., 1967; Holmgren, 1970; McKee et al., 1977; Swanson et al., 1979) numerous attempts have been made to reconstruct the temporal evolution of the CRBG (Hooper et al. 2002, Jarboe et al., 2008, 2010; Barry et al., 2010, 2013; Camp et al., 2013). During the last two decades, Ar/Ar single grain fusion and step-heating experiments performed on plagioclase, whole rock and groundmass, have been used to achieve more accurate and precise ages (Jarboe et al., 2008, 2010; Barry et al., 2010, 2013; Hooper et al., 2002).

Analysis of plagioclase crystals recovered from the Imnaha, Grande Ronde and Wanapum Basalts failed to provide any plateau ages (Barry et al., 2010 - ages of single incremental steps ranging between 0.4±2.3 Ma and 10.4±7.1 Ma), or, in other cases, once an age was obtained it was discarded because it was not in accordance with the stratigraphy (e.g. Imnaha Basalt: $16.85 \pm 0.21_{1\sigma}$ Ma – Jarboe et al., 2010; Grande Ronde Basalt: $16.5 \pm 1.20_{1\sigma}$ Ma - Lees, 1994).

The plagioclase crystals, identified as disaggregate cognate antecrysts or xenocrysts, display disequilibrium and zoning textures that suggest complex magmatic processes (crystallization-resorption-recirculation-regrowth and crustal contamination) within the magma chamber prior to their eruption (Ramos et al., 2005; Barry et al., 2010; 2012; Ramos et al., 2013). The long-lived residence of plagioclase within the plumbing system and their complex history of crystallization suggest that different proportions of Ar isotopes could have been incorporated, through diffusion, in to the crystal lattice during several stages of growth. Similarly, the circulation of hydrothermal fluids, particularly enriched in Ar isotopes, have favoured the entrapment of multiple populations of fluid inclusions within plagioclase during crystallization (Barry et al., 2012). $^{40}Ar_E$ incorporated into the crystal structures, or within fluid inclusions, as well as ^{40}Ar loss from the crystal lattice could have disturbed the Ar system complicating the age determination (Kelley et al., 1986; Kelley, 2002). In this context, the unreliable ages obtained for plagioclase from the Imnaha, Grande Ronde and Wanapum Basalt must be interpreted as the result of the release of Ar isotopes from multiple reservoirs (melt and fluid inclusions, crystal lattice), with different isotopic signatures, and not representing the true eruption age of the samples.

In contrast, the Steen Basalts were erupted during the first phases of CRBG evolution and so plagioclases in this unit, even if they have been recognised to be antecrysts (Wolff, 2009; Sheth, 2016), were much less affected by complex magmatic processes and by crustal contamination (Ramos et al., 2005; Wolff et al., 2008). Consequently the ages are accurate, reliable and more likely represent the age of lava emplacement (e.g. $16.80\pm0.24_{1\sigma}$ Ma - Jarboe et al., 2008; $16.91 \pm 0.21_{1\sigma}$ Ma - Camp et al., 2013).

More robust, precise and accurate ages for the Imnaha, Grande Ronde and Wanapum Basalts eruption have been obtained by analysing fresh whole-rock matrix and glassy groundmass (e.g. Imnaha Basalt: $16.06 \pm 0.15_{1\sigma}$ Ma - Barry et al., 2010; $16.45\pm 0.11_{1\sigma}$ Ma- Jarboe et al., 2010; Grande Ronde: $15.48 \pm 0.11_{1\sigma}$ Ma - Barry et al., 2010; $15.90\pm 0.10_{1\sigma}$ Ma - Hooper et al., 2002; Wanapum: $14.98 \pm 0.06_{1\sigma}$ Ma - Barry et al., 2013; $15.12\pm 0.19_{1\sigma}$ Ma - Barry et al., 2010).

However, even when an age was determined for the CRBG lavas, and an acceptable precision was achieved ($\pm$ 0.1 Ma $< 1\sigma <$ $\pm$ 0.2 Ma), it was impossible to rule out the possibility that the groundmass had not acquired ^{40}Ar escaping from the large antecrysts during magmatic and/or post-emplacement events (Barry et al., 2010, 2012). This can happen when magma temperature exceeds the closure temperature of the coexisting minerals, promoting the diffusion of the ^{40}Ar out of the crystals into the grain boundary network with a later incorporation into the groundmass. In this case, the true age of crystallization of the groundmass will be higher than expected because the presence of $^{40}Ar_E$ within it. These phenomena are promoted by hot hydrothermal or aqueous fluids, enriched in Ar isotopes, circulating within the magma chamber during crystallization phases, or throughout the lava after emplacement. These fluids can deposit secondary minerals, hosting high contents of ^{40}Ar and atmospheric ^{36}Ar (if hydrothermal activity occurs after emplacement), that can lead to anomalous high ages if they are not entirely removed before the analysis (Verati and Jourdan, 2013). Hot fluids can also favour the alteration of the groundmass and of the interstitial glass leading to a K-loss (and thus loss of ^{40}Ar) from the samples, lowering the apparent ages. Various degrees of $^{40}Ar_E$ contamination, ^{40}Ar loss and alteration can explain the lower precision on the ages (e.g. Steens Basalt: $16.33\pm0.48_{1\sigma}$ Ma – Colgan et al., 2006; Imnaha Basalt: $15.76\pm0.61_{1\sigma}$ Ma – Duncan, 1983; Grande Ronde Basalt: $15.4\pm0.6_{1\sigma}$ Ma – Hopper et al., 2002; Saddle Mountain Basalt: $10.0\pm0.5_{1\sigma}$ Ma – Duncan, 1983) and ages that do not correspond to the stratigraphy found for some of the CRBG lavas (Barry et al., 2013).

The most precise and accurate Ar/Ar ages for the CRBG have been obtained by Mahood and Benson (2017) and Henry et al. (2006, 2017) who have provided high-

precision and highly-accurate ages for the eruption of the Steens basalts, although indirectly, by dating silicic volcanic rocks and ash-rich layers interbedded between the lavas. These deposits, associated with the rhyolitic–trachytic Snake River Plain volcanism, contain plagioclase, anorthoclase and sodic-sanidine suitable for Ar/Ar dating. Mahood and Benson (2017) report ages for silicic tuffs interlayered between the Steen Basalts that are one order of magnitude more precise than those attainable by analysing basaltic groundmass anorthoclase - $16.596\pm0.018_{1\sigma}$ Ma, $16.639\pm0.021_{1\sigma}$ Ma; plagioclase - $16.495\pm0.024_{1\sigma}$ Ma, $16.542\pm0.079_{1\sigma}$ Ma, $16.499\pm0.052_{1\sigma}$ Ma; sanidine $16.389\pm0.064_{1\sigma}$ Ma, $16.479\pm0.021_{1\sigma}$ Ma). Even more precise results have been achieved by Henry et al. (2017) dating tuffs of the Oregon Canyon and Trout Creek overlaying the Steen Basalt lavas in the McDermitt caldera area ($16.49\pm0.015_{1\sigma}$ Ma, $16.57\pm0.001_{1\sigma}$ Ma, $16.517\pm0.015_{1\sigma}$ Ma). These results reinforce the idea that accurate and precise, indirect, ages for the CRBG are achievable.

Despite the type of material used to constrain the timing and duration of the CRBG eruption, and the level of precision and accuracy reached, some problems still remain. Even when reliable ages were determined they do not always cross-correlate, as would be expected, with the paleomagnetic record (Barry et al., 2013). Based on Ar/Ar ages, the Imnaha Basalt erupted between 16.7 Ma and 16.0 Ma in a period of ~ 700,000 years corresponding to five chrons, of different polarity (C5Cn.3n, C5Cn.2r, C5Cn.2n, C5Cn.1r, C5Cn.1n), of the geomagnetic time scale of Gradstein et al. (2004). This is in contrast with the available paleomagnetic data that suggest that the entire sequence was erupted during a single paleomagnetic chron of normal polarity (Barry et al., 2010) leading to the conclusion that two short chrons of reverse polarity are not yet discovered within the Imnaha Basalt (Barry et al., 2013). Another discrepancy is identified by the comparison of the paleomagnetic data recovered from the Grande Ronde Basalt with the total duration of its eruption (~ 420,000 years) (Barry et al., 2013). Four different magnetizations of opposite polarity (R_1-N_1-R_2-N_2) have been recognised within the Grande Ronde Basalt (Swanson et al., 1979), while the Ar/Ar ages suggest that the entire sequence was totally emplaced, between 16.0 Ma and 15.6 Ma, during the early C5Br chron (15.974 Ma – 15.160 Ma - Gradstein et al., 2004) (Barry et al., 2010). Three possible explanations have been proposed by Barry et al. (2013) for the observed inconsistency: the first regards the actual duration of the reversal excursions observed in the Grande Ronde Basalt that could be really short in comparison to the longer duration of the C5Br chron and not been accounted in the geomagnetic time scale; the second evokes a younger age (pre 16 Ma) for the two rapid reversal episodes, of normal polarity, that were observed in the lavas

(C5Cn.2r and C5Cn.1n are currently dated at 16.453 Ma and 15.974 Ma, respectively - Gradstein et al., 2004); the third suggests that the Ar/Ar ages, obtained from Grande Ronde Basalt groundmass, are too young by ~ 0.5 Ma years.

On this basis it is clear that, in order to better constrain the evolution of the CRBG, the identification of good materials to enable us to obtain high-resolution and high-precision ages is a priority. This research follows on from Mahood and Benson (2017) and Henry et al. (2006, 2017) but instead of using K-bearing minerals, silicic glass shards extracted from interbeds between the Saddle Mountains and Wanapum Basalts are used to determine precise ages. This section of the CRBG was selected because of the abundance of ash-rich interlayers and because it has not been extensively studied using Ar/Ar dating. With this in mind new and precise Ar/Ar ages will help to refine the stratigraphy of the latest phases of the CRFBP volcanism.

3.4.3 Sample description

Volcanic glass shards for Ar/Ar dating are derived from six samples originally collected by Dr. Alena Ebinghaus (Aberdeen University) from volcanoclastic ash-rich layers within the Rattlesnake Ridge, Selah and Vantage Members of the Ellensburg Formation (Figure 3.3 - Table 3.2) in the Pasco Basin area (Figure 3.4).

All six samples display similar characteristics (Table 3.2). They are compacted ash-rich siltstones mainly composed of volcanic glass, dispersed minerals (quartz, biotite, alkali-feldspar, amphibole, apatite and zircon) and minor detrital components. The samples are alkaline to sub-alkaline rhyolites (Ebinghaus et al., 2015) and display Chemical Index of Alteration (CIA - Nesbitt and Young, 1982) of between 57.53 and 60.52, slightly above the optimal value of 50 for unaltered material (Table 3.3). Sample U-1-2 has the lowest K_2O content (2.8%) and shows the highest value for the CIA index of 72.62 (Table 3.3).

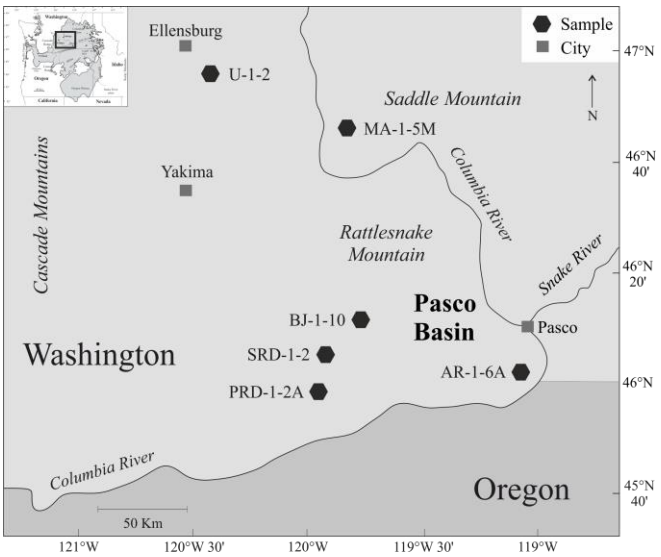

Figure 3.4 Field locations of samples analyzed in this study - Coordinate system refers to WGS84 – UTM 11N (see Ebinghaus et al., 2014 and 2015 for initial analyses of samples).

Table 3.2 Location, stratigraphic position and description of the samples.

Sample	Coordinates	CRBG upper basalt	Ellensburg Formation interbed	CRBG lower basalt	Sample colour	Glass colour	Depositional setting
	Latitude Longitude	(Member)	(Member)	(Member)			
BJ-1-10	46.199933 -119.713433	Elephant Mountain	Rattlesnake Ridge	Pomona	Grey	Transparent	Fluvial
SRD-1-2	46.127350 -119.8454	Elephant Mountain	Rattlesnake Ridge	Pomona	Grey	Transparent	Fluvial
MA-1-5M	46.777583 -119.913317	Elephant Mountain	Selah	Priest Rapids	White	Transparent	Lacustrine
AR-1-6A	46.064583 -118.95655	Pomona	Selah	Umatilla	Black	Dark brown	Unknown
PRD-1-2A	45.998400 -119.350467	Pomona	Selah	Umatilla	Black	Dark brown	Unknown
U-1-2	46.912700 -120.505967	Frenchman Springs	Vantage	Grande Ronde N2	Beige	Transparent, dark brown	Unknown

Table 3.3 Bulk composition of the samples.

Sample	BJ-1-10*	SRD-1-2*	MA-1-5M*	AR-1-6A*	PRD-1-2A†	U-1-2*
Major oxides (Wt %)						
SiO_2	76.42	75.71	75.82	74.01	72.12	74.33
$Al2O_3$	12.10	12.77	12.56	12.90	11.96	14.67
K_2O	6.04	5.73	5.94	5.84	5.41	2.80
Na_2O	2.16	1.67	1.40	1.66	2.18	1.70
FeO	2.10	2.28	2.23	2.87	2.50	3.31
CaO	0.74	0.93	1.21	0.91	0.78	1.03
MgO	0.16	0.55	0.37	1.33	0.58	1.31
TiO_2	0.23	0.25	0.40	0.39	0.32	0.75
MnO	0.04	0.09	0.04	0.04	0.04	0.03
P_2O_5	0.02	0.02	0.04	0.04	0.04	0.08
CIA	57.53	60.52	59.47	60.52	58.85	72.62
Trace Elements (ppm)						
Ni	2.16	9.16	3.44	10.94	N.D. §	25.96
Cr	5.41	1.32	7.02	8.04	N.D.	71.91
Sc	4.45	5.68	7.98	7.98	N.D.	15.03
V	9.42	22.95	20.60	76.94	N.D.	107.69
Ba	646.34	693.79	1048.17	817.95	N.D.	822.19
Rb	223.75	208.44	237.42	186.68	N.D.	131.12
Sr	32.64	41.86	70.72	57.36	N.D.	271.64
Zr	502.09	524.92	576.25	595.16	N.D.	486.56
Y	97.28	93.98	69.21	64.51	N.D.	35.69
Nb	60.37	60.51	55.51	58.08	N.D.	29.47
Ga	28.09	27.42	25.54	24.87	N.D.	24.87
Cu	6.26	9.64	5.88	8.39	N.D.	22.53
Zn	98.19	96.32	60.87	63.25	N.D.	119.36
Pb	34.04	34.58	31.13	30.27	N.D.	17.56
La	108.83	106.61	89.83	91.48	N.D.	50.43
Ce	227.66	232.21	183.28	187.09	N.D.	91.58
Th	39.94	40.61	35.20	36.19	N.D.	13.35
Nd	83.28	78.50	66.60	65.43	N.D.	38.61
U	11.12	8.48	9.36	6.83	N.D.	3.96
Cs	1.80	1.27	3.39	2.65	N.D.	3.82

Note: All the data are normalised at 100% total.
* Data from Ebinghaus et al. (2015), † New data provided in this study.
§ N.D. No Data

3.4.4 Methods

The samples were crushed, washed with water and sieved (Figure 3.5 A-C). The material remaining in the 63 μm sieve (Figure 3.5 D) was washed with HCl, then acetone and finally deionized water, in an ultrasonic bath, in order to remove unwanted materials adhering to the surfaces of the glass shards. Particular care was taken at this stage to select the cleanest and most transparent glass particles for the analysis. After a careful inspection, with a binocular microscope, only shards without visible altered surfaces and extraneous particles adhering to them were handpicked and used for the analyses (Figure 3.5 E-F).

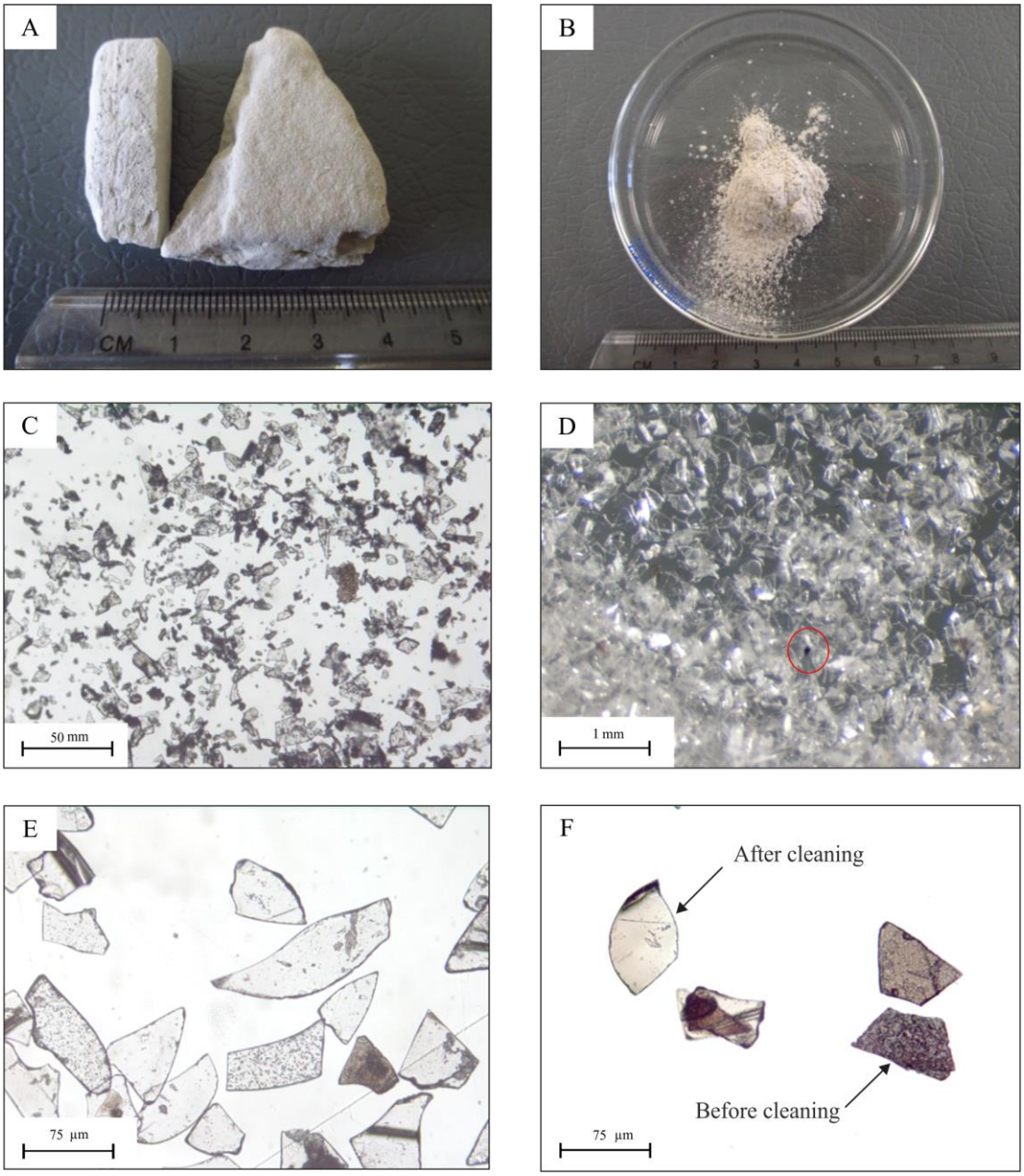

Figure 3.5 Light photographs showing various stages of sample preparation (example: sample MA-1-5M). A - Sample prior to processing. B - Sample ground using a ceramic mortar. C – Transmitted light photograph under binocular microscope of glass shards of different dimension after grinding and prior the sieving and cleaning stage. D - Transmitted light photograph under binocular microscope of glass shards of uniform size (63 μm) with extraneous dark materials (in the black circle). E - Glass shards remaining after the first pick selection. F - Transmitted light photograph under binocular microscope. On the right glass shards before acid cleaning. Visible small dark dots on shard surface represent some impurities or material adhering to their surface. On the left clear and transparent glass shards after the cleaning stage.

The samples were then prepared for irradiation and Ar/Ar analysis as outlined in Chapter 2. Analysis of AR-1-6A and MA-1-5M samples were, respectively, performed on three and two separate aliquots in order to assess the analytical reproducibility and to test the reliability of the method.

The results of the analysis were interpreted using age spectra and inverse isochrons. In order to obtain more statistically valid inverse isochrons, any negative $^{40}Ar/^{36}Ar$ ratios were excluded during the calculation of an isochron age. The same exclusion was applied to those steps, at low or high temperature, that were not included in the plateau age calculations. This approach has enabled the direct comparison of the plateau and isochron ages. When plateau ages and isochron ages derived from the same samples were compared, those with MSWD closer to 1 were statistically preferred to represent the age of eruption of the sample. Where two ages with similar MSWD values were compared, the age with lower 2σ uncertainty was preferred over the other one.

Once an age was obtained its validity was carefully scrutinised following the criteria listed in Barry et al. (2013), enabling the direct comparison of the new ages with those recently published in a review of the CRBG Ar/Ar ages (Barry et al., 2013). The analytical reproducibility was assessed as evidence of the reliability of the methods and the resulting ages. Weighted mean ages derived from the different aliquots were calculated. Age spectra and isochrons were used to assess for the presence of excess ^{40}Ar, the recoil of ^{39}Ar, sample alteration and atmospheric contamination. Finally, all the ages were examined relative to the stratigraphic position of the samples and compared with the published ages of the corresponding upper and lower lavas.

Table 3.4 Plateau ages calculated using different parameters for the $^{40}K_{tot}$ decay constant and age of the standard.

Sample	Plateau age calculated with ArMaDiLo default values (± 2σ - Ma)	Recalculated plateau age using ArArReCalc (± 2σ - Ma)	Relative variation
BJ-1-10	10.56±0.21	10.67±0.21	
SRD-1-2	10.59±0.18	10.70±0.18	
MA-1-5M_1	10.32±0.77	10.42±0.77	
MA-1-5M_2	10.68±0.18	10.79±0.18	0.98%
AR-1-6A_1	11.53±0.21	11.64±0.21	
AR-1-6A_2	11.19±0.18	11.30±0.18	
AR-1-6A_3	11.27±0.22	11.42±0.22	
PRD-1-2A	11.89±0.24	12.00±0.24	
U-1-2	No plateau	No plateau	N.A

The 2σ includes a 0.5% error for the J value. The following parameters were used in ArMaDiLo for the age calculation: $5.543±0.010E^{-10}$ for the $^{40}Ktot$ decay constant (Steiger & Jager, 1977) and an age of 98.79±0.54 Ma (Renne et al., 1998) for the GA1550 biotite. The following parameters were used in ArArReCalc for the age calculation: $5.5305±0.0135E^{-10}$ for the 40Ktot decay constant (Renne et al., 2011) and an age of 99.738±0.104 Ma for the GA1550 biotite (Renne et al., 2011).

3.4.4 Results

Five of the six samples yielded ages and the results are summarised in Table 3.5 and displayed in age spectra and inverse isochron diagrams (Figure 3.6-3.9). All the reported errors are quoted at the 2σ level. The entire dataset of Ar isotopes extracted from the samples during step-heating experiments with associated analytical errors, average blank values and J values, is reported in Appendix A2.1.

Table 3.5 Plateau and isochron ages for the analysed samples with relative $^{39}Ar^*$ comprised within plateau, $^{40}Ar/^{36}Ar$ isochron intercepts and MSWD values.

Sample	Plateau age ± 2σ (Ma)	MSWD	$^{39}Ar^*$ (%)	Isochron age ± 2σ (Ma)	MSWD	$^{40}Ar/^{36}Ar$	Weighted mean age ± 2σ (Ma)
BJ-1-10	**10.67±0.21**	0.72	89.6	10.13±0.92	0.53	317±120	N.A
SRD-1-2	**10.70±0.18**	0.99	100	10.65±0.28	1.14	293±32	N.A
MA-1-5M_1	10.42±0.77	1.6	93.6	11.60±3.70	1.7	208±120	Age spectra **10.77±0.18** MSWD = 0.88
MA-1-5M_2	10.79±0.18	1.5	84.5	10.80±1.30	1.9	294±83	Isochron 10.9±1.2 MSWD = 0.17
AR-1-6A_1	11.64±0.21	0.70	92.1	11.51±0.47	0.85	326±170	Age spectra 11.44±0.44
AR-1-6A_2	11.30±0.18	0.91	80.9	11.30±0.21	0.91	251±78	MSWD = 3.0
AR-1-6A_3	11.42±0.22	0.23	93.2	11.38±0.37	0.19	253±140	Isochron **11.34±0.17*** MSWD = 0.36
PRD-1-2A	**12.00±0.24**	0.31	75.4	11.86±0.85	0.35	320±190	N.A
U-1-2	No plateau	N.A.	N.A.	108.70±8.6	42	617±130	N.A

Note: In bold preferred ages for the considered samples. * The weighted mean of the isochron ages has lower MSWD but higher probability of fit (P = 0.70) than the weighted mean of plateau ages (P = 0.048).

Experiments performed on three aliquots of AR-1-6A sample (see Figure 3.6) yielded plateau ages that are all within error: 11.64±0.21 Ma, 11.30±0.18 Ma and 11.42±0.22 Ma, including 92.1 %, 80.9% and 93.6% of the ^{39}Ar respectively. The relative inverse isochron ages of 11.51±0.47 Ma, 11.30±0.21 Ma and 11.38±0.37 Ma have, respectively, atmospheric $^{40}Ar/^{36}Ar$ intercepts of 326±170 Ma, 251±78 Ma and 253±140. A weighted mean age of 11.44±0.44 Ma (95% conf. level) is calculated for the plateau ages and a weighted mean age of 11.34±0.17 Ma is calculated for the isochron ages (Figure 3.9).

The two different aliquots of MA-1-5M (see Figure 3.7) yielded indistinguishable ages when compared at the 2σ level. MA-1-5M_1 has a plateau age of 10.42±0.77 Ma including 93.6% of the released ^{39}Ar and MA-1-5M_2 of 10.79±0.18 Ma including 84.5% of the released ^{39}Ar. For MA-1-5M_1 the inverse isochron age, based on 11 of 16 degassing steps, is 11.6±3.7 Ma with an atmospheric ^{40}Ar/^{36}Ar ratio of 208±120. For MA-1-5M_2 the isochron age is based on 7 of 10 degassing steps and is 10.8±1.3 Ma with an atmospheric ^{40}Ar/^{36}Ar ratio of 294±83 (2σ). The weighted mean of plateau ages of the two aliquots is 10.77±0.18 Ma and the weighted mean of isochron ages is 10.9±1.2 Ma (Figure 3.9). MA-1-5M has higher 2σ uncertainties than the other samples, which we attribute to the higher analytical uncertainties (1σ), lower amount of ^{39}Ar and ^{40}Ar and relatively higher amount of ^{36}Ar and ^{37}Ar released during the analysis (see Table 3.7). This could be attributed to the slightly higher Ca content of the sample than the other samples (1.21% - Table 3.3).

The plateau and isochron ages of BJ-1-10 (see Figure 3.8) are indistinguishable at the 2σ confidence level. The plateau age of 10.67±0.21 Ma is calculated based on 9 of 11 degassing steps and it includes 86.6% of the released ^{39}Ar. The related inverse isochron yielded an age of 10.13±0.92 Ma with a ^{40}Ar/^{36}Ar ratio of 317±120.

SRD-1-2 (see Figure 3.8) yielded a plateau age of 10.70±0.18 Ma comprising 100% of the released ^{39}Ar and based on 11 degassing steps. The inverse isochron age is 10.65±0.28 Ma with an intercept at the atmospheric ^{40}Ar/^{36}Ar ratio of 293±32. As for the previous sample the plateau age and isochron age are concordant at the 2σ confidence level.

PRD-1-2A (see Figure 3.8) yielded concordant plateau and isochron ages at the 2σ level, with a plateau age of 12.00±0.24 Ma including 75.4% of the released ^{39}Ar and based on 9 of 11 degassing steps, and an isochron age of 11.86±0.85 Ma with an atmospheric ^{40}Ar/^{36}Ar ratio of 320±190.

U-1-2 (see Figure 3.7) is the only sample that failed to provide a plateau age and the ages decrease from 185±2.8 Ma to 108±0.7 Ma. The inverse isochron age is 108.2±8.6 Ma with a ^{40}Ar/^{36}Ar intercept at 617±130.

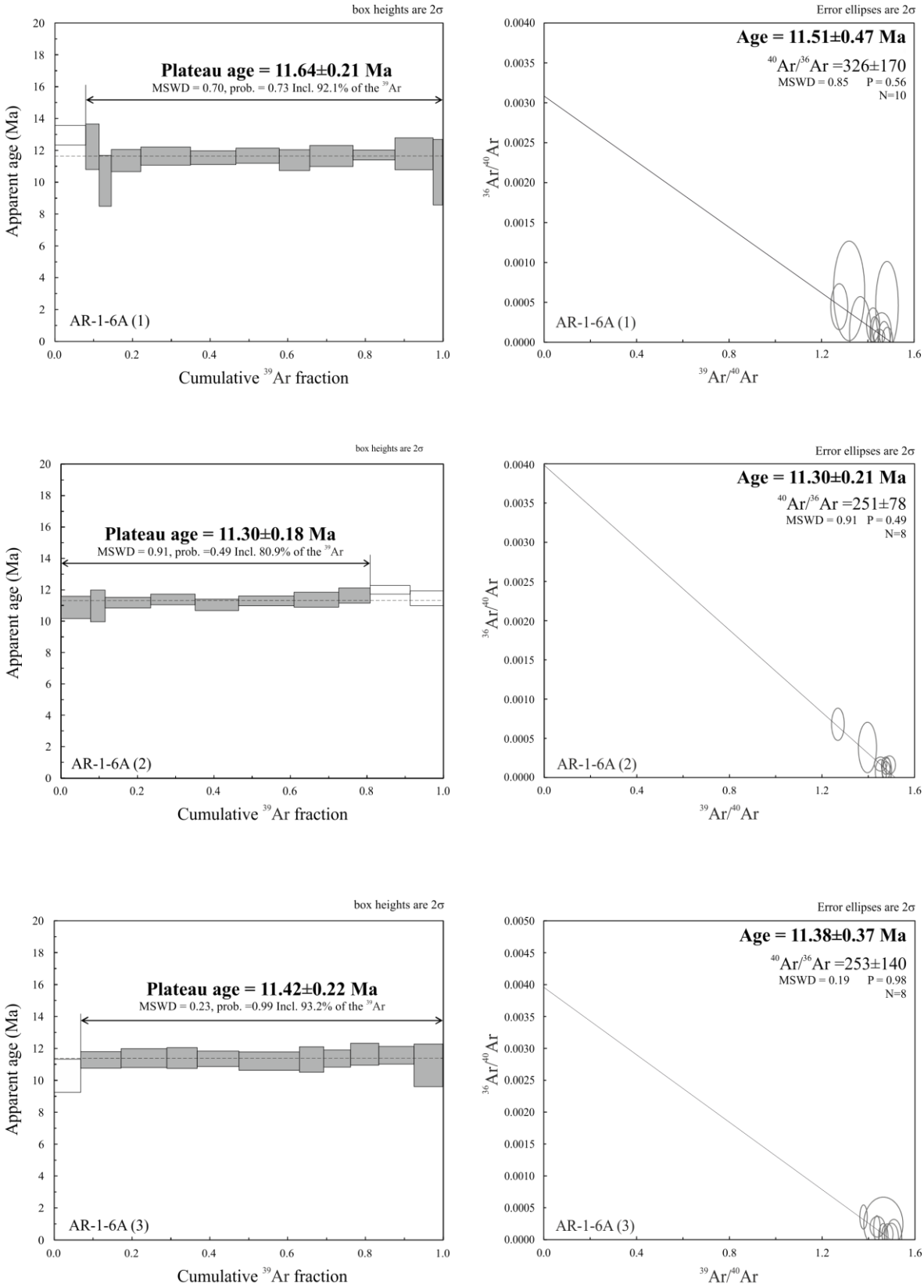

Figure 3.6 Age spectra and isochrons for step heating experiments on sample AR-1-6A. All ages are reported at 2σ level.

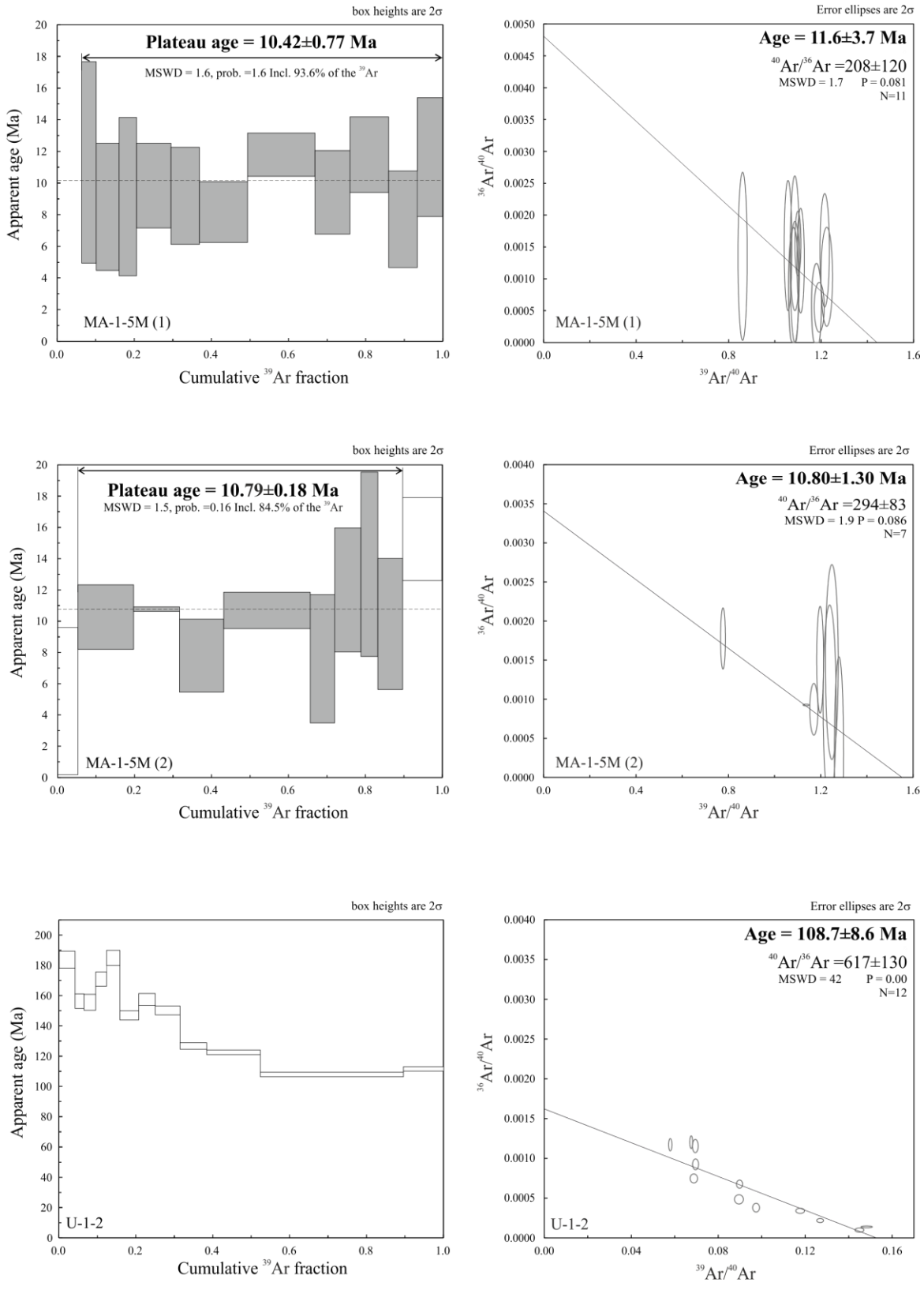

Figure 3.7 Age spectra and isochrons for step heating experiments on samples MA-1-5M and U-1-2. All ages are reported at 2σ level. First steps for MA-1-5M_1 are not represented because having negative values.

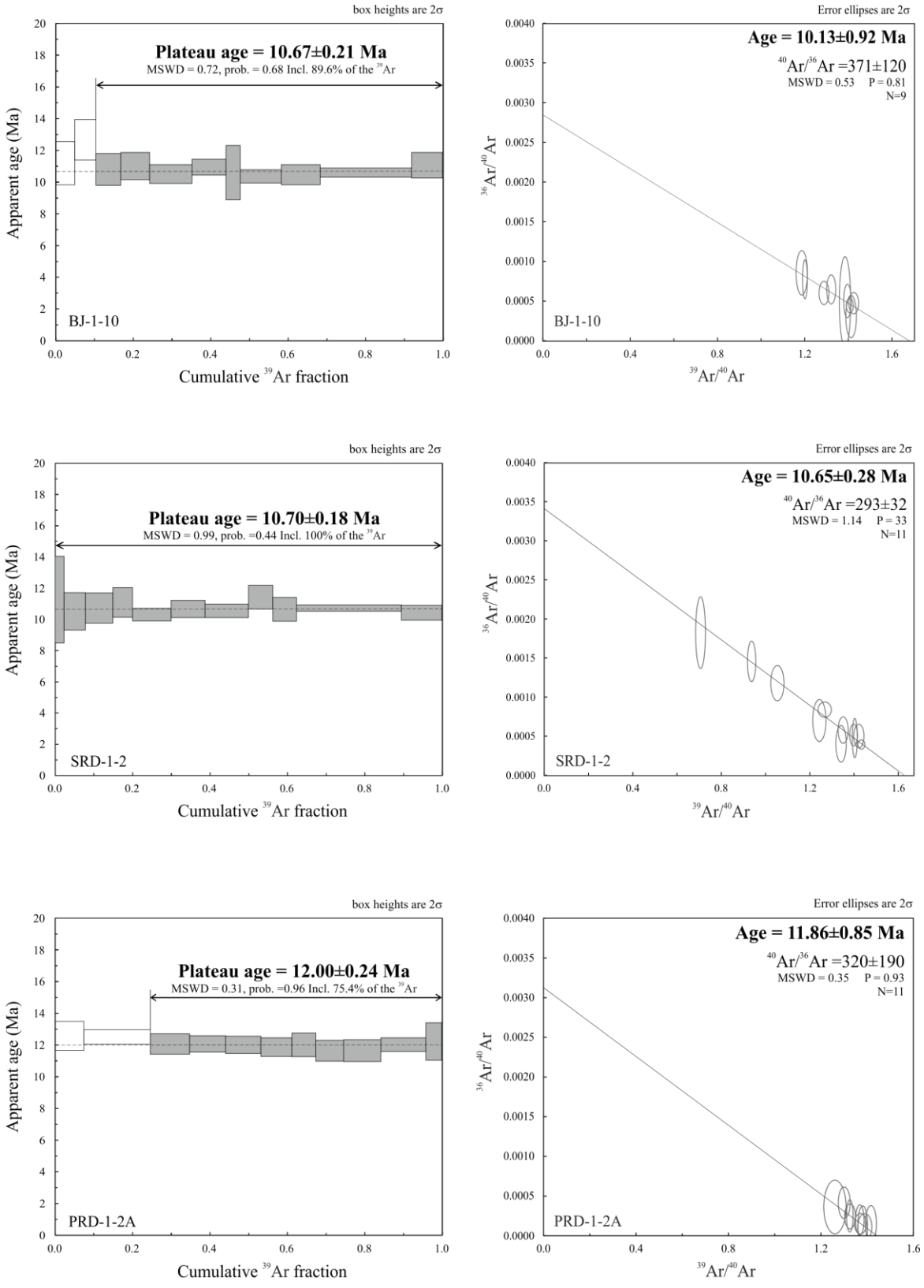

Figure 3.8 Age spectra and isochrons for step heating experiments on samples BJ-1-10, SRD-1-2 and PRD-1-2A. All ages are reported at 2σ level.

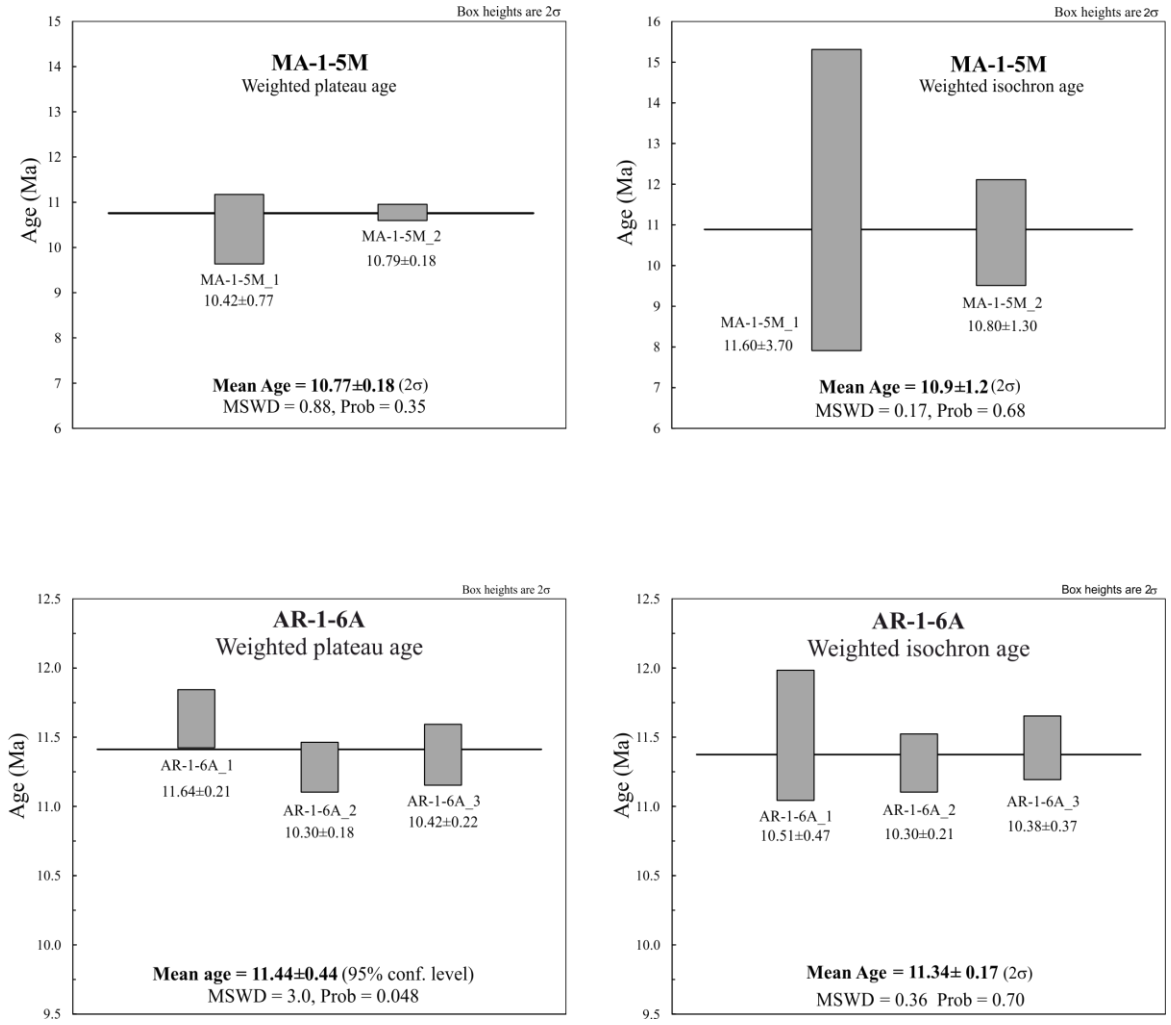

Figure 3.9 Weighted mean plateau and isochron ages for MA-1-5M and AR-1-2A.

Table 3.6 Average values for Ar isotopes in comparison with isochron and plateau ages.

Sample	^{39}Ar (cc STP)*	^{40}Ar (cc STP)*	^{36}Ar (cc STP)*	^{40}Ar/^{36}Ar	±	AGE (Ma)	±2σ (Ma)	AGE (Ma)	±2σ (Ma)
AR-1-6A_1	616.43	437.84	0.07	326	170	11.64	0.21	11.51	0.47
AR-1-6A_2	999.88	691.57	0.12	251	78	11.3	0.18	11.30	0.21
AR-1-6A_3	704.73	487.03	0.10	211	81	11.42	0.22	11.38	0.37
BJ-1-10	276.47	217.23	0.14	369	50	10.67	0.22	10.15	0.43
MA-1-5M_1	116.01	109.98	0.14	208	120	10.42	0.77	11.60	3.70
MA-1-5M_2	212.73	198.50	0.25	294	83	10.79	0.18	10.80	1.30
PRD-1-2A	286.69	220.58	0.06	320	190	12.00	0.24	11.86	0.85
SRD-1-2	392.20	304.87	0.21	293	32	10.70	0.18	10.65	0.28
U-1-2	187.16	1686.18	0.79	617	130	108.70	8.6	108.70	8.60

*Data quoted as cc STP x 10^{-12}.

3.4.6 Discussion

3.4.6.1 Ar/Ar dating of volcanic ash

The method used to date glass shards is reliable and robust on the basis of the accurate, precise and statistically valid ages presented here: the isochron and plateau ages are consistent and comparable at the 2σ level. The results are reproducible and consistent when multiple aliquots were analysed (see AR-1-6A_2 and AR-1-6A_3 where isochron and plateau ages are closely aligned and within error). The minor differences in total gas isochron ages and plateau ages of different aliquots in MA-1-5M and AR-1-6A, and the MSDW values, can be attributed to different factors: the heterogeneous distribution of ^{40}Ar within the sample; the incorporation of altered glass in the aliquot; the presence of micro fluid inclusions within glass shards; the presence of minor amounts of clay, or other K-bearing minerals, within the sample even after its preparation.

The scattered results obtained for U-1-2 are ascribed to the presence of unwanted materials that were not completely removed during sample preparation, muscovite and quartz probably not purely volcanic in origin. This was assessed after a careful inspection of the material prepared for analysis but not sent for irradiation. The extraneous materials, of unknown origin, but likely detrital, could be much older than the ash shards and contain high amount of radiogenic ^{40}Ar, due to their older age, that could compromise a correct age determination. Moreover, muscovite and quartz have been recognised as natural hosts for $^{40}Ar_E$ (Kelley et al., 1986; Qiu et al., 2011) that, if present in the detrital grains, could contribute to the extreme elevation in the ages observed in U-1-2. The presence of $^{40}Ar_E$ within weathered areas of muscovite crystals associated to defects in crystal lattice (there is evidence for phengite - white mica – in a metamorphic terrain, De Jong et al., 2001) or trapped within fluid inclusion in quartz grains (Qiu et al., 2011) could explain the highly scattered anomalously old apparent ages in the age spectra. Anomalous quantities of $^{40}Ar_E$ can be introduced into fluid inclusions by hydrothermal and metamorphic fluids (Kelley et al., 1986; Qiu et al., 2011).

Aside from U-1-2, all the age-spectra have flat plateaus with only a few steps rejected from the age calculation. Rejected steps with negative or lower apparent ages with respect to the plateau could be related to a possible ^{40}Ar-loss caused by the alteration or hydration of small areas of the sample surface (MA-1-5M_1 and MA-1-5M_2) that were not possible to detect at the microscopic level due to the small size of the shards. Rejected steps with higher apparent ages (at low- and high-temperature release steps), with respect to the plateaus, could reflect the presence of $^{40}Ar_E$ released from micro fluid inclusions (not detectable by microscopic observation) (McDougall and Harrison, 1999).

The plateau ages display 2σ errors of between 0.18 Ma and 0.24 Ma with higher error of 0.77 Ma observed for MA-1-5M_1. A negative correlation exists between the amount of ^{40}Ar and ^{39}Ar released during the analysis and the 2σ error of plateau ages. Larger uncertainties are associated to those samples with low concentration of ^{40}Ar and ^{39}Ar (Table 3.6). Similar observations can be made relating to the 2σ uncertainties of the isochron ages.

Aside from U-1-2 that display a $^{40}Ar/^{36}Ar$ ratio of 617±130, all the other inverse isochrons display atmospheric $^{40}Ar/^{36}Ar$ ratios at the 2σ confidence level (Figure 3.10). The extremely high atmospheric $^{40}Ar/^{36}Ar$ ratio observed for U-1-2 can be explained by the presence of $^{40}Ar_E$ within fluid inclusion in quartz grains not removed during the sample preparation stage. The minimum $^{40}Ar/^{36}Ar$ ratios in AR-1-6A_2, AR-1-6A_3 and MA-1-5M_1 samples can be related to hydration and alteration of the glass and heat transfer for lava emplacement that could have introduced or removed different proportion of ^{36}Ar and ^{40}Ar from the glass. Without other evidence is not possible to discriminate between these processes and can only suggest possible mechanisms. Although these samples have lower absolute $^{40}Ar/^{36}Ar$ values than the atmosphere, this seems not to have caused any particular disturbance to the determination of the age as demonstrated by the concordance between plateau ages and isochron ages; so the given ages must see as representative of the actual eruption age of the ashes.

High 2σ uncertainties on the $^{40}Ar/^{36}Ar$ ratio are related to those isochrons where almost all the data clump close to the X-intercept ($^{39}Ar/^{40}Ar$ value) rather than to be spread on a 2-point mixing line (PRD-1-2A, BJ-1-10 and AR-1-6A samples). This can be explained by the low content of ^{36}Ar in the samples and the little variation of the ^{39}Ar released for each step of the analysis. Lower errors are detected for those isochrons with higher data dispersion (SRD-1-2, MA-1-5M_2). MA-1-5M_1 has a high 2σ uncertainty associated to the Y-intercept ($^{36}Ar/^{40}Ar$ value) and the data points are more dispersed than for other samples. This can be attributed to the elevated 1σ analytical uncertainty associated to each individual step.

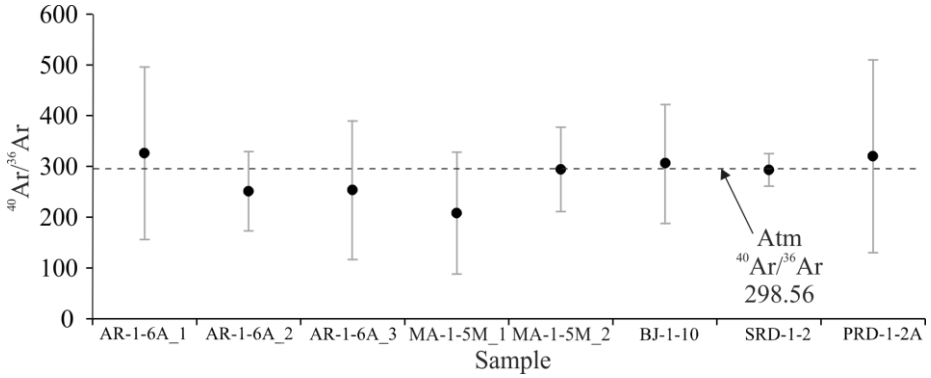

Figure 3.10 $^{40}Ar/^{36}Ar$ ratios for the analyzed samples. U-1-2 is omitted in order to emphasize differences in the $^{40}Ar/^{36}Ar$ ratios of the other samples. Atmospheric $^{40}Ar/^{36}Ar$ = 298.56 (Lee et al., 2006).

All the samples display ages that are consistent with the stratigraphy at 2σ analytical uncertainty. The plateau ages are considered to more accurately represent the eruption age to due to their better statistics (MSWD closer to 1 and higher probability of fit) and higher precision when compared to the isochron ages. The plateau ages can be considered reliable only because all the samples display an atmospheric $^{40}Ar/^{36}Ar$ ratio within 2σ uncertainty. For AR-1-6M, the weighted mean of isochron ages is preferred due to its better statistics (MSWD of 0.35, probability of fit of 0.70) compared to the weighed mean of plateau ages (MSWD of 3.0, probability of fit of 0.048).

PRD-1-2A (12.00±0.24 Ma) and AR-1-6M (11.34±0.17 Ma) yielded precise ages that are in good agreement with their stratigraphic position within the Selah Member (Ellensburg Formation) between Umatilla (12.4 ± N.A. - 15.5 ± N.A. – probable age of 14.6 Ma ± N.A. - U.S. Energy Research and Development Administration, N.A. = not available) and Pomona Basalts (11.21±0.21 - 10.34±0.21 Ma - Barry et al., 2013).

BJ-1-10 (10.67±0.21 Ma), SRD-1-2 (10.70±0.18 Ma) and MA-1-5M (10.77±0.18 Ma) are within error at the 2σ level. The ages are in good agreement with the stratigraphic position of the samples within the Rattlesnake Ridge Member (Ellensburg Formation) between the Pomona Basalt (11.21±0.21 Ma – Barry et al., 2013) and the Elephant Mountain Basalt (10.18±0.51 Ma – after Barry et al., 2013). Despite this, at this level of precision (±0.2 - 0.1 Ma - 2σ), it is not possible to resolve the ages without an external control. For this reason, the relative stratigraphic position (Table 3.2), chemistry (Table 3.2) and age (Table 3.4) of the samples are used to assess if the three samples represent the products of the same eruption. BJ-1-10 (10.67±0.21 Ma) and SRD-1-2 (10.70±0.18 Ma) are from a fluvial deposit within the Rattlesnake Ridge Member and display similar chemical signatures with Zr/SiO_2 ratio of 6.5 and 6.9, Nb/Zr ratio of 0.12 and 0.11, Zr/Ba ratio of 0.77 and 0.75, TiO_2 of 0.23 Wt% and 0.25 Wt%, respectively. MA-1-5M (10.77±0.18 Ma) is from a lacustrine deposit within the lower portion of the Rattlesnake Ridge Member where it merges with the Selah Member. It has a distinctive chemical signature respect to BJ-1-10 and SRD-1-2 with Zr/SiO_2 ratio of 7.6, Nb/Zr ratio of 0.09, Zr/Ba ratio of 0.54 and TiO_2 of 0.40 Wt%.

In light of these data, I suggest that BJ-1-10 and SRD-1-2 can be correlated to the same eruptive event while MA-1-5M belongs to a different episode that occurred closely spaced in time after the eruption of the other two. More systematic analysis and even more precise ages would be needed in order to fully resolve the ages between these samples, but, this chapter demonstrates that the method works well and these new data can be used to determine the age and rate of emplacement of the basaltic lavas in the CRBG.

3.4.6.2 Precision of the Ar/Ar ages

The Ar/Ar ages presented here have uncertainties (1σ) ranging between 0.12 Ma and 0.085 Ma (1.0 - 0.7 % of the total age). These results are almost one order of magnitude more precise than those previously reported for whole-rock (±0.7 - 0.2 Ma - 1σ) and plagioclase (±0.4 - 0.1 Ma - 1σ) and in good agreement with the most precise ages obtained from lava groundmass (±0.1 - 0.05 Ma - 1σ) (Barry et al., 2013).

Higher precision has been achieved for plagioclase (±0.07 - 0.02 Ma - 1σ), Na-sanidine (±0.06 - 0.02 Ma - 1σ) and anorthoclase (±0.02 - 0.01 Ma - 1σ) recovered from the Steens Basalt interbeds (Mahood and Benson, 2017). These results fully propagate analytical errors, interference reaction errors and J value uncertainties into the 1σ model error. In order to obtain such level of precision, the results of multiple single grain fusion analysis, with 1σ model error between ±0.013 Ma and ±2.77 Ma, have been averaged during the calculation of the weighted mean of inverse-isochron ages. Feldspar crystals (500-710 μm grain size) used by Mahood and Benson (2017) have been prepared using a Frantz magnetic separator and then cleaned in an ultrasonic bath for a minimum of 3 hours with deionized water. A CO_2 laser has been used for single crystal fusion experiments and a Nu-Noblesse mass spectrometer has been used to analyse the isotopic composition of the gas extracted from the crystals. Inverse isochron ages, for an average of 25 grains per sample, have been calculated using a decay constant of $5.543*10^{-10}$ a^{-1} (Steiger and Jäger, 1977), an age for the Fish Canyon sanidine of 28.02 Ma (Renne et al., 1998), and atmospheric air $^{40}Ar/^{36}Ar$ ratio of 298.56 (Lee et al., 2006). No information is available about blank values during the experiments and about the weight of the material used for each single grain fusion experiment.

The best results, in terms of precision (±0.03 - 0.006 Ma - 1σ), have been obtained by averaging the results of multiple single grain fusion analysis of sanidines found within the oldest interbeds of the Steens Basalts around the McDermitt Caldera area (Henry et al., 2006, 2017) and include analytical uncertainties, interference reactions errors and uncertainties on the J value. The ages from single analysis have 1σ uncertainties of between ± 0.006 Ma and ± 0.13 Ma including analytical uncertainty only, without incorporating the uncertainties relating to interference reactions or J-value. These results are derived from the analysis of crystals prepared using magnetic and density mineral separation and cleaned with 5% HF for ~1 h. Single crystal Ar/Ar analyses have been performed with a single collector MAP-215-50 mass spectrometer and, those with higher precision, with a multicollector Argus VI mass spectrometer. All the ages have been calculated relative to the Fish Canyon Tuff sanidine standard at 28.201 Ma (Kuiper et al.,

2008) using a total ^{40}K decay constant of $5.463e^{-10}$ a^{-1} (Min et al., 2000). No information is available about the type of laser used, the blank values during the experiments, the grain sizes of the crystals and the weight of the material for each single grain fusion experiment.

The results of Mahood and Benson (2017) and Henry et al. (2017) are not directly comparable with those presented in this study because the different methods used to calculate the age and the relative uncertainties, but the volcanic glass here investigated has the potential to return ages with similar high precision due to its relatively high K content (ranging from 5.4 to 6.0 wt %), low levels of alteration and hydration and $^{40}Ar/^{36}Ar$ of atmospheric value at the 2σ confidence level. An improvement in precision and accuracy of the Ar/Ar ages from glass shards could be achieved by the following:

- *The analysis of multiple aliquots* will provide the opportunity to enhance the precision of the weighted mean ages as demonstrated by averaging the results of three aliquots for AR-1-2A.
- *Increasing the amount of material in each aliquot* will result in increased ^{39}Ar and ^{40}Ar signals that will decrease the internal analytical uncertainty.
- *Improve the sample preparation and cleaning.* Removing all the extraneous material (alteration products, non-glassy material) from the sample and selecting even more pristine glass shards would help to obtain better results.
- *The use of multicollector mass-spectrometer (e.g. Argus, Nu-Noblesse)* has been proven to be more efficient, in respect to single collector mass-spectrometer (MAP-215-50, VG3600), to return highly precise ages (2σ < 1%) for different type of materials (feldspars, basaltic groundmass, impact glass) of different ages (200 Ka – 30 Ma), grain size (500 μm - 180 μm) and sample weight (116-12 mg) (Mark et al., 2009; Henry et al., 2017). Although these studies have confirmed the superior ability to provide ultra-high precise Ar/Ar ages, this is not always true when small amount (20 mg) of fine-grained samples (63 μm) are analysed. With such small sample weights the use of multicollector mass spectrometer is of no advantage over the use of a single collector instrument because of the analytical uncertainty inherent in detector cross-calibration (as confirmed by J Saxton, Nu-Instruments).

  It is unlikely that the high precision on the ages for small (30-40 mg) and fine-grained (63 μm) volcanic ash shards can be achieved only by using multicollector mass spectrometers. Instead, it is proposed that the best way to achieve reliable, accurate and precise ages is still an optimal sample selection and the analysis of multiple aliquots of material that take in account of sample heterogeneities and yielding a more representative age of the entire sample.

3.4.6.3 Volcanological implications

The new ages for the five samples from the Selah and Rattle Snake Ridge Members of the Ellensburg Formation can be used to better constraint the ages of lavas emplacement and the duration of volcanic hiatuses (Figure 3.11).

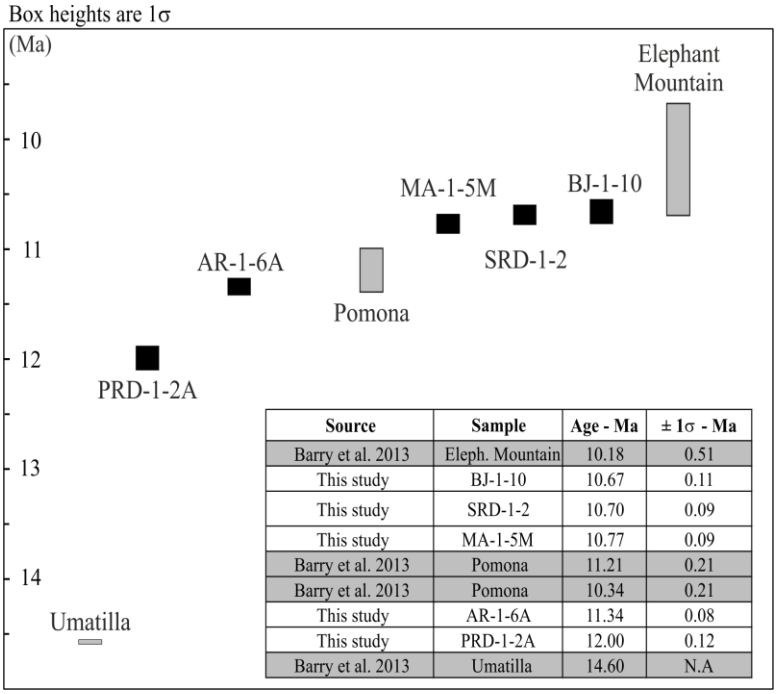

Source	Sample	Age - Ma	± 1σ - Ma
Barry et al. 2013	Eleph. Mountain	10.18	0.51
This study	BJ-1-10	10.67	0.11
This study	SRD-1-2	10.70	0.09
This study	MA-1-5M	10.77	0.09
Barry et al. 2013	Pomona	11.21	0.21
Barry et al. 2013	Pomona	10.34	0.21
This study	AR-1-6A	11.34	0.08
This study	PRD-1-2A	12.00	0.12
Barry et al. 2013	Umatilla	14.60	N.A

Figure 3.11 Stratigraphic relationships between ages of the Saddle Mountain Basalt (Barry et al., 2013), ages of the ash layers investigated in this study and ages of the Cougar Point Tuff (CPT) (Bonnichsen et al., 2008). All the ages are quoted at 2σ level. Basalt ages recalculated after the new age for the Fish Canyon Sanidine of Renne et al. (2011) – 28.294±0.08 Ma – are indistinguishable from those calculated by Barry et al. (2013) with the value given by Jourdan and Renne (2007) of 28.03±0.036 Ma. The age error for the Umatilla Basalt is not available and the error bar is only for illustrative scope. Magnetic polarity of the Columbia River Basalt Group (CRBG) lavas are from Reidel et al. (2013) whereas for the CPT are from Bonnichsen et al. (2008). Magnetic polarity of the ash layers are not available.

The age of 12.00±0.24 Ma for PRD-1-2A is consistent with the position of the sample within the Selah Member below the Pomona Basalt. Considering the age of 11.34±0.17 Ma from the top of the Selah Member just below Pomona Basalt, and an age of 14.6±N.A Ma for the Umatilla Basalt it is confirmed that a hiatus of ~ 3.3 Ma exists between the Umatilla and Pomona Basalt eruptions as previously assessed by Barry et al. (2013).

The new ages of 10.77±0.18 Ma, 10.70±0.18 Ma and 10.67±0.21 Ma from ash layers between the Pomona and Elephant Mountain Basalts, suggest a total duration of < 500 Ka years for the deposition of the Rattlesnake Ridge Member as previously proposed by Ebinghaus et al. (2015). These ages helps to better constraint the eruption age of the Elephant Mountain Basalt that was previously dated at 10.18±0.51 Ma (Duncan, 1983). In particular, the age of 10.67±0.21 for an ash layer from the middle portion of the interbed leaves to suggest that the Elephant Mountain Basalt could be younger than ~ 10.5 Ma and, consequently, the time interval between Elephant Mountain and Pomona could be much longer than 500 Ka.

Given the consistency of the ages and the stratigraphic position of the samples, the age of 10.34±0.21 Ma (Barry et al., 2013) for Pomona Basalt seems to be too young and out of stratigraphic order. This interpretation is supported by the absence of any stratigraphical evidence of the synchronous eruption of the Pomona and Elephant Mountain Basalts. Moreover, magnetostratigraphic data position the Pomona Basalt within a reverse polarity and the Elephant Mountain Basalt within a normal-transitional polarity indicating that, if a second eruptive episode for the Pomona Member happened, it should have a magnetic signature similar to the Elephant Mountain. Because no other studies have observed these similarities, a synchronicity of the two events is unlikely. This conclusion is supported by the ages from two ash layers either side of the Pomona Member of 11.34±0.17 Ma and of 10.77±0.18 Ma respectively, and in good agreement with the older age of 11.21±0.21 Ma for the eruption of Pomona Basalt (Duncan 1983). However, the possibility that the Pomona Basalt erupted in two different periods separated by a hiatus of ~ 1 Ma cannot be ruled out. In this scenario, the ages of Duncan (1983) and Barry et al. (2013) should be considered valid leading to two possible scenarios: the first evokes a much younger age for Elephant Mountain Basalt that should be erupted after Pomona emplacement, the second implies that Pomona Basalt was contemporaneously erupted during the first stages of Elephant Mountain Basalt emplacement. Without any additional stratigraphical constraint and age data discriminating between these two scenarios is not possible and it is preferred a more simple explanation of a single eruptive pulse of the Pomona basalt at around 11.21±0.21 Ma (Duncan, 1983).

Ebinghaus et al. (2015) have correlated the ashes in this study with products of the Yellowstone volcanism comparing Nb-Zr-Y, Zr/SiO2 and Nb/Zr ratios, obtained from XRF analysis of the samples, with the composition of the Yellowstone lavas. Using this information combined with the Ar/Ar ages obtained in this study it is possible to correlate the ash layers with the deposits of the Bruneau-Jarbidge (BJ) eruptive centre in the Central Snake River Plain (Figure 3.12). The BJ includes nine rhyolitic welded ignimbrites, erupted between 12.82±0.03 Ma and ~ 10.5 (collectively named Cougar Point Tuff – CPT), and a series of younger intracaldera rhyolitic lavas (Bonnichsen and Citron, 1982; Bonnichsen et al., 2008). CPT units are designated as follows: III (12.66±0.02 Ma), V (12.07±0.04 Ma), VII (11.81±0.03 Ma), IX (11.56±0.07 Ma), X (~11.3 Ma), XI (11.22±0.07 Ma), XII (~11.1 Ma), XIII (10.79±0.04 Ma), and XV (~10.5 Ma).

The age of 12.00±0.24 Ma is in good agreement with the age of 12.07±0.04 Ma obtained for CPT V (Bonnichsen et al., 2008). However, at this level of precision and without any additional chemical analysis on glass shards, it is impossible to exclude a possible correlation with CPT VII (11.81±0.03 Ma - Bonnichsen et al., 2008). A better

correlation has been identified between the ash layer just below the Pomona Basalt (11.34±0.17) with CPT XI (11.22±0.07 - Bonnichsen et al., 2008; 11.36±0.07 Ma – Ellis et al., 2012). The ages of 10.77±0.18 Ma, 11.70±0.18 Ma and 10.67±0.21 Ma for the three ash layers within the Rattlesnake Ridge member correlate well, at the 2σ level, with the ages provided for the CPT XIII (10.82±0.06, 10.80±0.06 and 10.75±0.07 with an average of 10.79±0.04 Ma) by Bonnichsen et al. (2008). Given the variation in composition of the samples analysed in this study (e.g. TiO_2 of 0.23 Wt%, 0.25 Wt% and 0.40 Wt%) and according to Bonnichsen et al., (2008), the different ages seems to reflect multiple eruptive events which occurred over a short time span that are indistinguishable at the 2σ level (Figure 3.13).

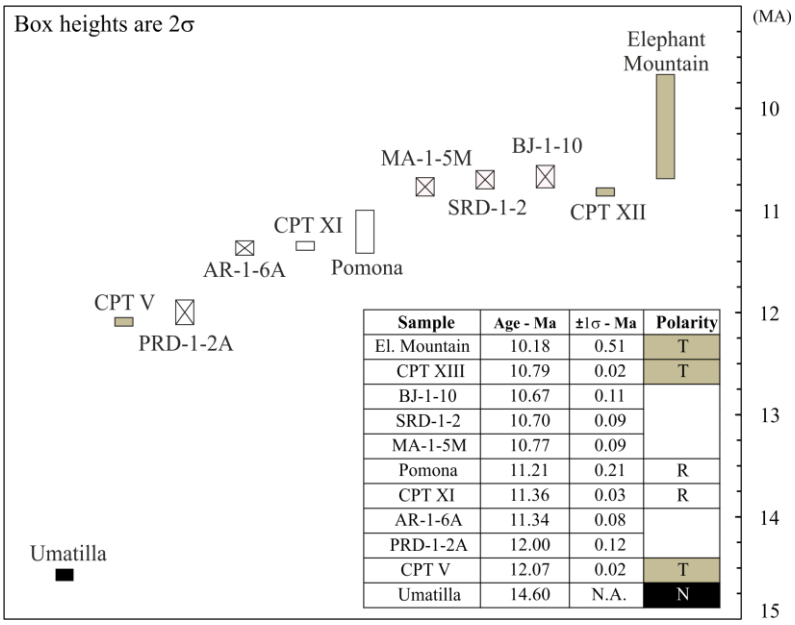

Sample	Age - Ma	±1σ - Ma	Polarity
El. Mountain	10.18	0.51	T
CPT XIII	10.79	0.02	T
BJ-1-10	10.67	0.11	
SRD-1-2	10.70	0.09	
MA-1-5M	10.77	0.09	
Pomona	11.21	0.21	R
CPT XI	11.36	0.03	R
AR-1-6A	11.34	0.08	
PRD-1-2A	12.00	0.12	
CPT V	12.07	0.02	T
Umatilla	14.60	N.A.	N

Figure 3.12 Stratigraphic relationships between ages of the Saddle Mountain Basalt (Barry et al., 2013), ages of the ash layers investigated in this study and ages of the CPT (CPT V and CPT XIII from Bonnichsen et al., 2008; CPT XI from Ellis et al., 2012). Magnetic polarity of CRBG lavas are from Riedel et al. (2013) whereas for the CPT are from Bonnichsen et al. (2008).

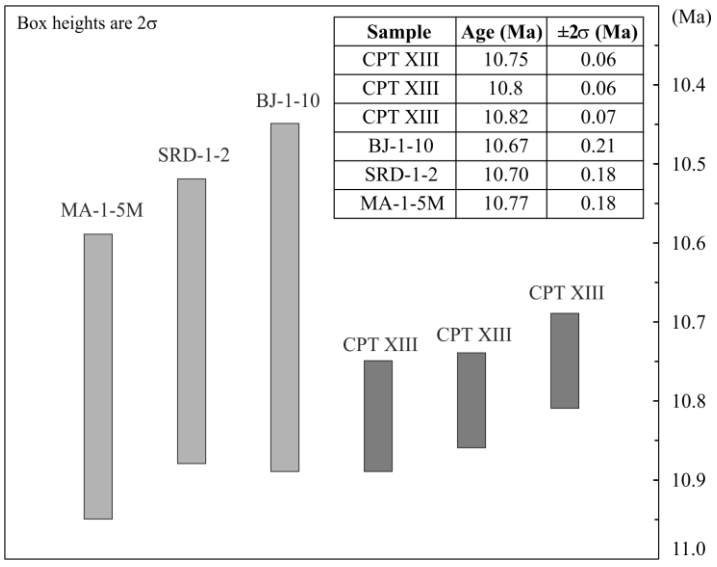

Sample	Age (Ma)	±2σ (Ma)
CPT XIII	10.75	0.06
CPT XIII	10.8	0.06
CPT XIII	10.82	0.07
BJ-1-10	10.67	0.21
SRD-1-2	10.70	0.18
MA-1-5M	10.77	0.18

Figure 3.13 Comparison between the ages of Cougar Point Tuff (CPT) XIII (Bonnichsen et al., 2008) and ages provided in this study for three ash layers of the Rattlesnake Ridge member (Ellensburg Formation).

3.4.7 Conclusions

Accurate and precise Ar/Ar ages were obtained for silicic volcanic glass shards derived from volcanic tuffs interlayering the CRBG. Whilst sample preparation is highly challenging, this study demonstrates that the method is robust on the basis of the reproducibility and consistency of the ages when multiple sample aliquots were analysed. The ages are accurate, stratigraphically consistent and in good agreement with Ar/Ar ages provided for the upper and lower lavas (Duncan, 1983; Barry et al., 2013).

These glass shards have $^{40}Ar/^{36}Ar$ of atmospheric value at the 2σ confidence level, it seems that they didn't suffer from any ^{40}Ar loss and ^{39}Ar recoil and are free from $^{40}Ar_E$ unlike other materials used for Ar/Ar dating of volcanic eruptions (e.g. sanidine, plagioclase, groundmass, whole-rock). This last point is a clear advantage over using, for example, plagioclase and sanidine, that have been proven to host significant amounts of excess ^{40}Ar (Renne et al., 1997; Kelley, 2002; Layer and Gardner, 2001; Sumino et al., 2008). Moreover, using glass shards for Ar/Ar dating avoids the problem of inadvertently analysing xenocrysts and antecrysts that often exist in volcanic systems (Renne et al., 2012; Sheth, 2016). For these reasons, I suggest that volcanic glass shards should be more widely investigated and, potentially used, for producing reliable and precise indirect Ar/Ar ages for CRBG lava emplacement and any other LIPs for which there are silicic ash-bearing interbeds (e.g. North Atlantic Igneous province - Jolley and Bell, 2002).

The new ages obtained in this study have provided better constraint on the timing of the emplacement of the Pomona and Elephant Mountain Basalts helping to critically assess previous Ar/Ar ages from lavas overlain and underlain the ash beds. The results of this study has allowed the correlation of ash layers with at least three major eruptions (CPT V, XI, XIII) of the Bruneau-Jarbidge eruptive centre in the CSRP. More highly precise Ar/Ar ages from the shards, coupled with geochemical analysis of the glass and detailed field studies of the distribution and stratigraphy of the interbeds, could be used to better correlate the ashes with their source. This will help to resolve correlation problems where no direct contacts between basalts are observed, or, where the stratigraphic relationships between lavas cannot be determined (e.g. Jolley et al., 2002, 2008). A refined stratigraphy will aid a better estimate of the timing of lavas emplacement and eruptive hiatus between their eruption.

I see also promising use of Ar/Ar dating of glass shards in archaeology where Ar/Ar dating ash layers overlaying and/or underlying human artefacts will permit to better comprehend the ages of hominoids migrations and civilization and, possibly, their relations with volcanic eruptions.

3.4.8 Final remarks:

More experiments are required in order to improve the precision, over and above the data reported here, of Ar/Ar ages for volcanic ash shards recovered from CRBG interbeds. This can be achieved by analysing multiple aliquots of samples with bigger volumes of the cleanest material. The importance of cleaning procedures and the removal of unwanted material cannot be underestimated for obtaining such good results.

Although the Ar/Ar ages obtained in this study seem not affected by Ar recoil, I recommend to in vacuum-encapsulate the samples in silica vials prior to irradiation in order to minimise any problem related to this phenomenon. Because Ar loss due to alteration and hydration is another problem that can affect the Ar/Ar ages when glass is used for dating purposes, I suggest the use of electron microprobe and Nano-SIMS in order to determine the alteration indexes and the water content of the samples.

At the moment it is not possible to know a priori which sample might be expected to provide unreliable Ar/Ar ages. Only by using detailed chemical analysis to evaluate the degree of alteration of the samples, and only performing a careful sample preparation it is possible to select samples that are more likely to provide stratigraphically consistent and reliable ages. However, because Ar recoil, excess Ar and kinetic fractionation of ^{40}Ar and ^{36}Ar are not detectable and evaluable prior Ar/Ar analysis it is still possible that even fresh and pure glass shards yield neither accurate nor precise Ar/Ar ages. Understanding better the systematics of the K-Ar system in volcanic glass is a beneficial goal to aim for, given its importance for obtaining reliable indirect Ar/Ar ages for basalt emplacement.

The comparison of the Ar/Ar ages derived from glass shards with Ar/Ar ages from other K-bearing materials found within the same units (e.g. sanidine) can be seen as a good way to assess for the good quality of the ages recovered from the volcanic glass.

I recommend the importance of a stratigraphical revision of the entire Saddle Mountain Basalt section. Currently, the old K/Ar ages seem to be unhelpful in trying to refine the timing, duration (and gas emissions) of basaltic eruptions during the middle-late Miocene. Coupling highly precise Ar/Ar dating of ash layers with ages coming from basaltic lavas will permit to better determine contemporaneous events happening during the waning phase of the CRBG emplacement and the related climatic consequences on the surrounding environment.

Because volcanic interlayers can be found in different volcanic settings and because ash shards are preserved even in the more distal volcanic and volcanoclastic deposits, I propose the application of the methodology presented in this study to more widely and not only restricted to the investigation of the evolution of LIPs.

Chapter 4:

Noble gas in Pele's hairs and tears: a new tool to track the behaviour of persistent degassing volcano tested using the Masaya volcano (Nicaragua)

4.1 Introduction

Noble Gases (NG) have been used extensively to investigate the degassing of volcanic systems by inspecting different type of minerals, volcanic rocks and glass as primary sources of information (Yamamoto and Burnard, 2004; Burnard et al., 2004; Macpherson et al., 2005). However, not all types of volcanic materials have been equally considered. Amongst those less common volcanic materials yet to receive full consideration are Pele's hairs and tears and, at the time of writing, no studies exist that explores their NG concentrations, variations and isotopic compositions.

Pele's hairs and tears are millimetre size glassy particles derived from the fast-quenching of low-viscosity magmas erupted during fire-fountain Strombolian and Hawaiian eruption of many basaltic volcanoes (Heiken, 1972; Moune et al., 2007; Cannata et al., 2012; Porritt et al., 2012). These pyroclasts have been observed worldwide but they are specifically associated with the activity of many persistent degassing volcanoes (e.g. Hawaii, Etna, Masaya, Erta' Ale, Villarica).

These volcanic systems constantly release heat, energy and gases (e.g. H_2O, CO_2, SO_2, HCl, HF at rates of hundreds of tons/year) through an open vent, from which significant volumes of magma degas and cool over a long period of time (hundreds to thousands of years) without being erupted. These volcanoes (e.g. Masaya, Etna, Sakurajima, Erebus, Erta 'Ale, Nyiragongo) alternate between periods of intense activity and periods of quiescence characterised by fumarole fields (Momotombo - Menyailov et al., 1986), lava lakes (Erebus, Erta' Ale, Nyiragongo, Masaya - Harris et al., 1999) and intense passive degassing (Etna - Allard, 1997; Masaya – Rymer et al., 1998).

Among others, Masaya Volcano (11.984°N, 86.161°W - south-western Nicaragua) has been characterised by intense passive degassing activity during the last 2 centuries (Rymer et al., 1998). Since 1853 five degassing crises occurred causing enormous problems to the local communities (Stoiber et al., 1986; Rymer et al., 1998; Delmelle et al., 2002).

Acid rains caused by the high release of acidic volcanic gases into the atmosphere, and long-time exposure to volcanic gases have had a negative impact on the local economy and on human health (Delmelle et al., 2002). In order to understand the causes and the environmental and social impacts of the persistent degassing of the Masaya volcano, several studies have investigated its degassing evolution, gas plume composition (H_2O, CO_2, SO_2, HCl, HF), rate of degassing and amount of gases released into the atmosphere (e.g. Stoiber et al., 1986; Delmelle et al., 1999; Burton et al., 2000; Williams-Jones et al., 2003; De Moor et al., 2013; De Moor et al., 2017; Aiuppa et al., 2018; Stix et al., 2018). Despite this enormous effort there is still no study of NG concentrations and variations in the erupted products, neither in the plume, nor in the fumarole gases.

Given these premises, instead of using major gases as source of information, this study aims to explore the possibility of tracking active degassing processes at Masaya volcano using NG trapped in Pele's hairs and tears. Due to their high cooling rate (Porritt et al., 2012), these glassy pyroclasts could be able to retain volcanic gases from before the effects of post-eruptive degassing, providing a new tool to study and monitor the evolution of persistent degassing volcanoes.

For this study, Pele's hairs and tears were collected in 2015 and in 2016 at Masaya volcano directly after their eruption. The samples were characterised petrographically, texturally and chemically. ^{4}He, ^{22}Ne, ^{36}Ar, ^{40}Ar were measured by NG mass spectrometry providing, for the first time, information on the NG concentration and variations in Masaya products. The ease of access to the collection site and the abundance of fresh samples have represented two substantial benefits for this research. The appearance of a lava lake between the first and second collections has provided the opportunity to monitor NG during a specific volcanic event. The use of virtually fresh 'zero age' samples has permitted: (A) an investigation of factors controlling the NG retention within fast-quenched, low-viscosity volcanic glass, potentially not affected by post-eruptive alteration and hydration; (B) the study of the behaviour of Ar isotopes in the context of excess Ar within volcanic glass that hasn't experienced any radioactive decay of ^{40}K that could interfere with the detection of possible small variations in the $^{40}Ar^{*}$ content.

4.2 Pele's hairs and tears

4.2.1 Origin and volcanic context

Pele's hairs and tears (known also as 'achneliths' - Walker and Croasdale, 1972) are glassy brown-black millimetre to micrometer size pyroclasts emitted during fire-fountaining Strombolian to Hawaiian eruptions of many basaltic volcanoes such as Hawaii, Etna, Masaya, Reunion, Erta' Ale, Azores, Villarica, Stromboli and Erebus (Heiken, 1972; Duffield et al., 1977; Heiken and Wohletz, 1985; 1991; Toutain et al., 1995; Moune et al., 2007; Harpel et al., 2008; Martin et al., 2008; Cannata et al., 2012; Porritt et al., 2012). Pele's hairs and tears have also been found associated with hydrovolcanic and submarine eruptions (Heiken, 1972; Clague et al., 2003; Harpel et al., 2008; Cannata et al., 2012) or to vent/dike complexes like the Joseph Creek vent complex (Grande Ronde Basalt) in the Columbia River Basalt Province (Reidel and Tolan, 1992; Camp et al., 2017).

4.2.2 Morphology and external characteristics

Pele's hairs and tears have fluidal morphologies with a black glassy external surface (Duffield et al, 1977; Moune et al, 2007; Porritt et al., 2012; Carracedo et al., 2016) that sometimes can be orange to red as a result of discoloration due to the oxidation of the glass (Porritt et al., 2012). Open cavities on the exterior of Pele's hairs and tears are created by bubble bursting while irregular bulges and protrusions were observed related to crystals and/or bubbles just below the surface (Porritt et al., 2012; Moune et al., 2007).

Pele's hairs are long straight, bent and/or bifurcate cylindrical thin fibres with a diameter variable of between 1 μm and 500 μm even in a single strand (Moune et al., 2007; Duffield et al., 1977). Knots and protrusions along their length have been attributed to the presence of crystals in the glass that were not able to deform and stretch with the melt during eruption (Moune et al., 2007; Duffield et al., 1977). Surficial crusts observed on Pele's hairs are thought to have been deposited by the gas cloud through which the particles have been transported before their deposition (Duffield et al, 1977).

Pele's tears are between 20 mm and 150 μm in diameter (Porritt et al., 2012; Moune et al., 2007; Carracedo et al., 2016) and have more complex morphologies. They can be perfectly spherical or elongated, displaying tear-drop like or rod like shapes (Porritt et al., 2012; Moune et al., 2007; Carracedo et al., 2016). Pele's tears can be found alone, attached to the edges of a Pele's hairs, adhering to their surface or within vesicles (Moune et al., 2007; Duffield et al., 1977). Their external surface can be smooth with a vitreous lustre (Carracedo et al., 2016; Porritt et al., 2012), rough (Moune et al., 2007), ribbed (Porritt et

al., 2012) or with flow lines (Carracedo et al., 2016). Rough surfaces have been attributed to particles colliding during transport in the plume after their quenching (Heiken, 1972; Moune et al., 2007).

4.2.3 Internal characteristics

Internally, Pele's hair display small round vesicles, and elongated and tubular vesicles stretched parallel to the major axis of the particles (Duffield et al., 1977; Moune et al., 2007; Cannata et al., 2012).

Internally Pele's tears are characterised by isolated round vesicles that occasionally are coalescent (Porritt et al., 2012; Moune et al., 2007; Carracedo et al., 2016). Slightly stretched vesicles have been found in some particularly elongated tears (Carracedo et al., 2016). Vesicles mostly contain H_2O and CO_2 (Muenow, 1963; Duffield et al., 1977), range between 0.7–0.5 mm to 10-20 μm in diameter (Porritt et al., 2012; Carracedo et al., 2016) and represent the 5% - 40% of the total volume of the samples (Carracedo et al., 2016). In some small clasts (< 0.4 mm) vesicles are totally absent (Carracedo et al., 2016). Porritt et al. (2012), analysing the internal texture of two Pele's tears from Kilauea Iki (Hawaii) using the FOAM software (Shea et al., 2010), have calculated a vesicularity of between 21.3 % and 42.5 %. These values are comparable with the two calculated bulk density vesicularities, 34 % and 40 % respectively, obtained for the same samples (Porritt et al., 2012). These percentages are much lower than those obtained by Stovall et al. (2012) for any other pyroclasts from the same eruption (scoria and pumices have a vesicularity of between 55 % and 90 %) leading to the suggestion that Pele's tears could represent the state of magma at the point of initial fragmentation (Porritt et al., 2012).

4.2.4 Petrography and chemical composition

Pele's hairs and tears are composed of a dark brown sideromelane vesiculated glass and microphenocrysts (≤ 2 mm) of olivine (Porritt et al., 2012; Carracedo et al., 2016), clinopyroxene (Carracedo et al., 2016) and/or plagioclase (Moune et al., 2007). Pele's hairs are crystal poor (Duffield et al., 1977, Cannata et al., 2012) while Pele's tears display a crystal content that can vary from < 2 % (Kilauea Iki Volcano - Porritt et al., 2012) to 35 % (Las Herrerias Volcano - Carracedo et al., 2016).

The glass is basaltic in composition with SiO_2 ranging from between 46 Wt% and 58 Wt% (Ladle, 1978; Moune et al., 2007; Cannata et al 2012; Porritt et al., 2012; Stovall et al., 2012). Only pyroclasts found in tephra deposits from the Las Herrerias Volcano have a more nephelinitic composition with SiO_2 of about 41 Wt % (Carracedo et al., 2016).

Electron microprobe analyses of some Pele's hairs and tears from Masaya Volcano have highlighted the existence of a chemical gradient in major elements in the glass. For the first 10 μm of the external walls of the particles, from the edge towards the core the Na, K, Ca, Mg, Al, Fe increase while Si decreases from 81.7 Wt. % (rim – altered glass) to 50.9 Wt. % (core – fresh glass) (Moune et al., 2007). The origin of this alteration rim has been interpreted as the result of the interaction of the basaltic glass with acidic volcanic gasses after its eruption and particle deposition (Spadaro et al., 2002; Moune et al., 2007). The degree of the alteration is strictly related to the time of exposure of the glass to these volcanic gases (Spadaro et al., 2002; Moune et al., 2007). Sublimates (20 μm of diameter) of carbonates, sulphates, sulphur and hydrocarbons, particularly enriched in Cl, Na, Ca, K and Al (Moune et al, 2007), have been found adhering to the external walls of both hairs and tears, within small cavities left by bubble bursting and within open-air tubular vesicles in Pele's hairs (Duffield et al, 1977; Moune et al, 2007; Carracedo et al., 2016).

4.2.5 Formation processes and modelling

Pele's hairs and tears are formed during the first stages of fragmentation of low-viscosity basaltic magma (Zimanowski et al., 1997; Porritt et al., 2012). Their morphology is controlled by the size of the particles and their trajectory inside the fountain, surface tension, crystallization time vs. vesiculation, viscous melt relaxation, initial temperature of the melt and its physical proprieties (viscosity, density, volatiles solubilities and glass transition temperature), cooling rate and acceleration of the melt drops after eruption (Walker and Croasdale, 1972; Heiken, 1972; Zimanowski et al., 1997; Porritt et al., 2012).

From the genetic point of view Pele's hairs are formed when the spurting velocity of the magma in the magmatic conduit is high, whereas Pele's tears form when it is relatively low (Shimozuru, 1994). At the top of the volcanic conduit, when the spurting velocity is high, the basaltic glass is stretched and the Pele's hairs are produced. Spherical vesicles, formed during the exolution of volatiles before the eruption, are trapped within the particles, stretched and elongated (Moune et al., 2007). These vesicles can be singles, coalescents or multiples and display an elongation axis parallel to the maximum elongation of the particle (Duffield et al., 1977). After that, the spurting velocity decreases and a syn-eruptive "second exolution episode" may happen forming spherical bubbles before quenching of the Pele's hairs (Moune et al., 2007). Pele's tears are formed at this time (Moune et al., 2007). This is why only spherical bubbles have been detected within the tears and both spherical and elongated vesicles have been observed within hairs (Duffield et al., 1977; Moune et al., 2007; Porritt et al., 2012; Villermaux, 2012; Cannata et al.,

2012). Zimanowski et al. (1997) performed analogue experiments on basalt melt fragmentation by air injection and have calculated an air ejection speed of between 75 m/s and 100 m/s for the formation of Pele's hairs and a lower rate (< 75 m/s) for the formation of Pele's tears. There is not a defined value for the lower rate it is just noted that 75 m/s is the threshold value.

Porritt et al. (2012) modelled the cooling rate and history of Pele's tears with different dimensions (1- 5 mm) erupted during the 1959 fountain eruption at Kilauea Iki (Hawaii). They have considered an exit velocity of the melt from the vent equivalent to 110 m/s, a maximum height of the fountain of ~580 m, a thermal diffusivity of $3x10^{-6}$ m^2/s, an eruption temperature (T_e) of 1150°C, a hot-zone (incandescent part of the fountain) temperature of 900°C and an ambient air temperature of 25°C. Eruption temperature, temperature of the hot-zone and maximum height of the fountain have been taken from Richter et al. (1970) that have determined these parameters from photographs and videos of the eruption; the exit velocity of the melt has been modelled using the 'Eject!' model for ballistic trajectories (Mastin, 2001). Particles smaller than 2 mm are able to quickly equilibrate with air following a simple step-wise cooling history from T_e to T_{amb}. Larger particles (>10 mm) will have a more complex cooling history because the rim and the core will not equilibrate with the hot-zone and air in the same way and at the same time (Table 4.1, Figure 4.1) (Porritt et al., 2012). This difference in the temperature directs whether the rim of the pyroclast will respond in a brittle or ductile way and whether its core will be able to further vesiculate (Porritt et al., 2012) leading to the formation of coalescent vesicles or episodes of second exolution (Moune et al., 2007; Carracedo et al., 2016).

In this context the morphology of the particles and the vesicle size and content are strictly related to the size of the pyroclasts and their residence time within the hot-zone of the fountain (Porritt et al., 2012). The larger the melt drops and the more time they stay within the hot-zone of the fountain, the more they will vesiculate. Small particles (< 2 mm) tend to be spherical while bigger particles (> 5 mm) tend to have a tear-drop shape and even bigger pyroclasts (20 mm) appear more elongated and rarely preserve a tear-drop shape (Porritt et al., 2012). These observations indicate that if big particles stay within the hot zone for longer, and thus above T_g, they are able to ductilely deform and acquire more complex shapes. Whenever they exit to the hot-zone of the fountain their temperature quickly decrease below T_g and the viscous recovery of the melt to a sphere is blocked (Carracedo et al., 2016).

In particular, particles of 1 mm radius completely cool below the transition temperature of the basaltic glass (T_g = 650° C) after 0.1 s and equilibrate with ambient air after 0.25 s (Table 4.1). Bigger particles will require more time to reach the T_g and

equilibrate (Table 4.1); a 5 mm radius sphere will be completely below T_g in 1.25 s and equilibrated with air temperature in 5 s while pyroclasts of 10 mm radius will require 20 s to cool down to the ambient temperature (Porritt et al., 2012) (Figure 4.1). The cores of these big pyroclasts remain at the temperature of eruption (T_e) for 5 s allowing melt relaxation and further bubble expansion (Porritt et al., 2012). Degassing of magma, variation in vesiculation, crystallization and chemical variation, coalescence and transport processes of the particles (Zimanowski et al., 1997) and the not pure ballistic flight trajectory of the particles (Porritt et al., 2012) are other factors that are not included in the calculation that can interfere with the formation and cooling of these particles.

Table 4.1 Parameters used by Porritt et al. (2012) for calculating the cooling rate and temperatures of a sphere (Pele's tears) of different radius with time required to equilibrate the particle with T_g and T_{amb}.

Particle radius	Heat transfer coefficient	T at rim after 1 s	T at core after 1 s	Time to equilibrate from T_e to T_g	Time to equilibrate from T_e to T_{amb}
mm	W/m^2K	°C	°C	s	s
1	6544	25	25	0.1	0.25
2	3781	25	25	-	-
5	2124	110	806	1.25	5
10	1571	197	1150	-	20
T_e = 1200 °C, T_{amb} = 25 °C					

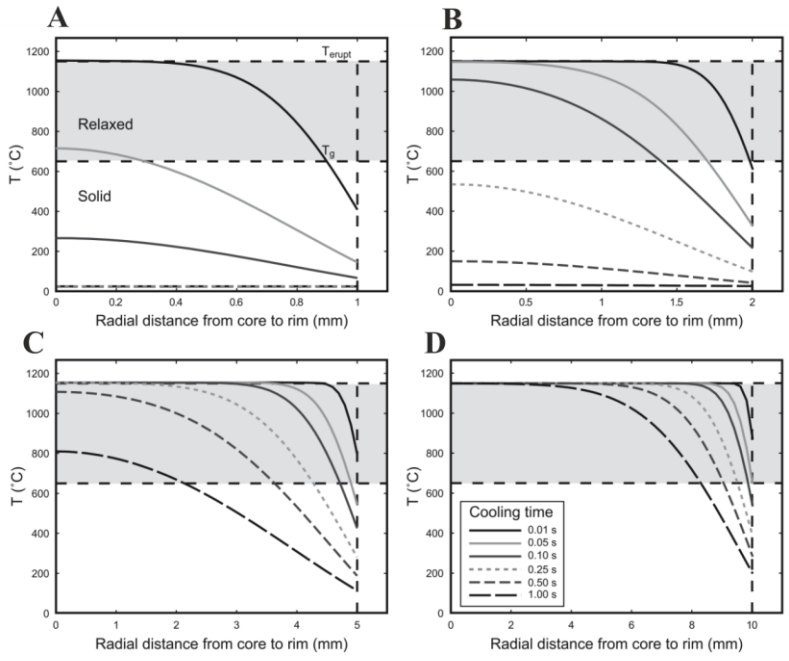

Figure 4.1 Plots of cooling rate and temperature variations from the core to the rim of spherical particles (Pele's tears) of different sizes: (A) 1 mm radius, (A) 2 mm radius, (C) 5 mm radius and (D) 10 mm radius (Porritt et al., 2012).

4. 3 Case study: The Masaya Volcano

As shown in section 4.2, several papers have investigated the external and internal morphological features (Duffield et al., 1977; Moune et al. 2007, Porritt et al., 2012; Carracedo et al., 2016), petrography and geochemical compositions (Ladle, 1978; Moune et al., 2007; Cannata et al 2012; Porritt et al., 2012; Stovall et al., 2012; Carracedo et al., 2016) and formation processes (Shimozuru, 1994; Zimanowski et al., 1997; Moune et al., 2007; Porritt et al., 2012) of Pele's hairs and tears but little attention has been given to the use of these particles as tracers of magmatic processes (Villemant, 2009). In this regard this study aims to contribute to use Pele's hairs and tears as tracer of active degassing processes. With this in mind Pele's hairs and tears recently erupted from the Masaya Volcano were used.

4.3.1 Geological background

Masaya Volcano is located at 11.984°N 86.161°W in south-western Nicaragua, 20 km south of the capital Managua. It is one of the 18 Nicaraguan volcanoes of the Central American Volcanic Front, a volcanic chain running along the western margin of the Caribbean plate from Costa Rica through Nicaragua, El Salvador and Guatemala (Whattman and Stern, 2015). The tectonic and volcanic activity in this area is related to the subduction of the Cocos Plate beneath the Caribbean Plate along the Mesoamerican trench (Van Wyk de Vries, 1993; Whattman and Stern, 2015).

The Masaya shield volcano developed within Las Sierras caldera on a series of basaltic ignimbrites erupted during the collapse of the pre-existing Las Sierra shield volcano (0.3 – 0.27 Ma) (Bice, 1980; Van Wyk de Vries, 1993; Walker et al., 1993). Basaltic lavas and tephra erupted around 0.7 Ma and 0.35 Ma have been associated with this first magmatic phase (*Proto-Masaya*) (Walker et al., 1993).

After the construction of the *Proto-Masaya* edifice, a NW-SE elongated summit caldera (6 Km x 11.5 Km wide) – Masaya caldera (Figure 4.2) – formed as the result of a series of basaltic plinian eruptions (McBirney, 1956; Crenshaw et al., 1982). 8 Km^3 of ignimbrite, tephra and pyroclastic surge deposits erupted at this stage. These volcanic products have been divided into four main groups: San Antonio Tephra – 0.6 Ma (Pérez and Freundt, 2006; Pérez et al., 2009), Masaya Triple Layer – 0.21 Ma (Williams, 1983; Bice, 1980, 1985), Masaya Tuff and Ticuantepe Lapilli – 0.18 Ma (Pérez and Freundt, 2006; Kutterolf et al., 2007).

The post-caldera activity is represented by the eruption of scoria, ash and lavas from a series of pyroclastic cones (e.g. Nindirì, Masaya, Cerro Montoso, Media Luna, Arenoso,

Comalito) formed along rim-fault structures (Caravantes González et al., 2019) (Figure 4.2). Vertical collapses of the Masaya and Nindirì crater floors have created San Fernando, Masaya, Nindirì, Santiago and San Pedro pit craters (Figure 4.3) (Rymer et al., 1998; Harris, 2009). In particular, historical lavas have been erupted as fissure eruptions in 1772 from the San Fernando crater and as a lava lake overflow in 1670 from the Nindirì crater (McBirney, 1956; Walker et al., 1993; Rymer et al., 1998).

The most recent activity is confined to the Santiago pit crater (Nindirì cone) and is dominated by small Strombolian eruptions, passive degassing and lava lake formation (Rymer et al., 1998; Stoiber et al., 1986; Williams-Jones et al., 2003) (Figure 4.3). Explosive activity, related to hydrothermal-magma interaction, has produced blocks, bombs, juvenile ash and vesiculated scoria (Bulletin of the Global Volcanism Network, 1970-2018). Pele's hairs and tears have been found in association with fire fountaining episodes during periods of lava lake formation in 1965 - 1969, 1972 - 1979, 1989, and 1993 - 1994 and 2015 - 2018 (Bulletin of the Global Volcanism Network, 1970-2018).

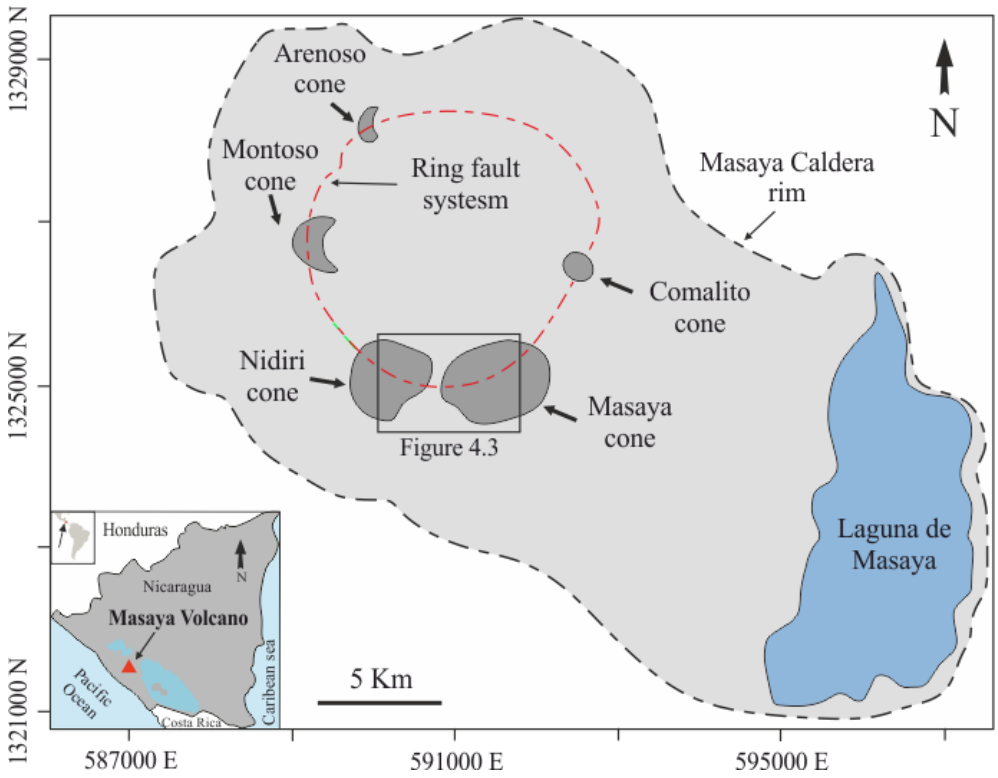

Figure 4.2 Schematic illustration of the Masaya caldera (Black dashed line). Dark grey circles are the cinder cones, with relative names, sited within the Masaya caldera. Red dashed line is the estimated surface trace of the ring faults along which the cones are located (Caravantes González et al., 2019). UMT zone 16P, UMT grid in m.

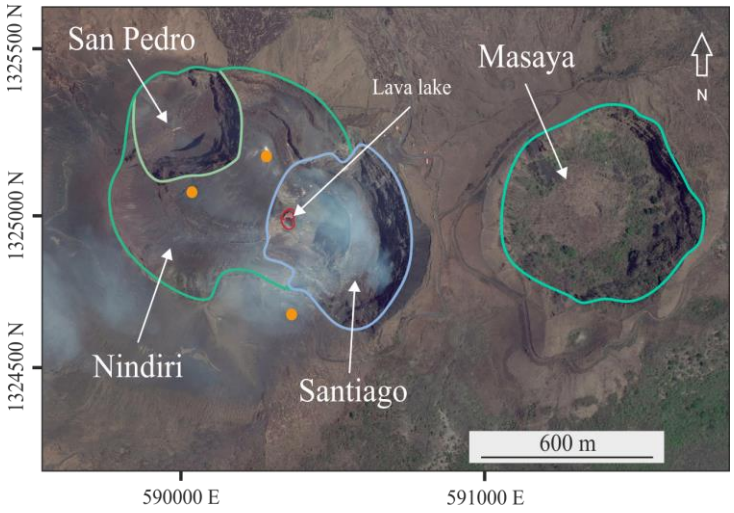

Figure 4.3 Location and stratigraphic relationships of the main pit craters in the summit area of the Masaya caldera. Only Santiago pit crater is active with the formation of a lava lake (red circle). Orange dots are the sampling sites. Image taken from Google Earth. UMT zone 16P, UMT grid in m.

4.3.2 Petrography and geochemistry of Masaya products

Lavas and pyroclastic rocks from Masaya volcano range from basaltic to basaltic-andesitic in composition and are composed of phenocrysts of plagioclase, clinopyroxene and micro-phenocrysts of magnetite and by a groundmass with similar composition (Walker et al., 1993). Olivine phenocrysts have been found only in pre-caldera lavas whereas they are absent from post-caldera products (Walker et al., 1993). Major and trace elements analyses and $^{87}Sr/^{86}Sr$ ratios have revealed no crustal contamination for post-caldera products and a 15 - 30% assimilation of acidic igneous rocks for the pre-caldera deposits (Walker, 1993). In particular, the analyses show low $A1_2O_3$, high FeO* and very high concentration of large-ion lithophile elements in comparison to the other Nicaraguan lavas (Walker, 1993; Atlas et al., 2011). Higher $^{87}Sr/^{86}Sr$ ratios and ^{10}Be concentration have also been detected (Walker, 1989; Walker et al., 1993). Variations in the MgO, TiO_2 content and FeO*/MgO ratio have been considered as the expression of medium and long-term changes in the magma chemistry (Walker et al., 1993). K, B and Ba enrichments coupled with high CaO/AI_2O_3 and B/Zr ratio have been related to the interaction of a magma with mantle origin with fluids derived from the dehydration of the subducted slab (Atlas et al., 2011). Analyses of melt inclusions in phenocrysts of Masaya lavas have highlighted low H_2O (< 0.5 wt.%), S and Cl (<300 ppm) concentration as well as high CO_2 values (up to ~ 6000 ppm) compared to others arc products (Walker et al., 1993; Atlas et al., 2011). These data have been correlated to: crustal and subduction contamination and fractional crystallization in a large, shallow and degassed magma chamber that is mixed by vigorous convective movements; magma recycling into a deep reservoir where magma mixes with more primitive material coming from deeper levels; multi stage degassing occurring even after the melt entrapment within the crystals (Walker et al., 1993; Delmelle et al., 1999; Atlas et al., 2011).

4.3.3 Degassing of Masaya volcano

Several structural, geophysical and geochemical studies have investigated the Masaya plumbing system in order to understand the causes and the sources of its continuous degassing (Stoiber et al., 1986; Walker et al., 1993; Rymer et al., 1998; Delmelle et al., 1999; Duffel et al., 2003; Williams-Jones et al., 2003; Stix, 2007; Harris, 2009; Martin et al., 2010; Atlas et al.; 2011; Mauri et al., 2012; Spampinato and Salerno, 2012; De Moor et al., 2013, 2017; Aiuppa et al., 2018; Stix et al., 2018; Stephens and Wauthier, 2018; Caravantes González et al., 2019).

A shallow reservoir, periodically recharged by a deeper source, has been identified at 1-3 km depth below Santiago and San Pedro craters (Métaxian et al., 1997; Williams-Jones et al., 2003) (Figure 4.4). This reservoir provides highly vesiculated and gas-rich magma to a superficial accumulation zone sited 200 m beneath Santiago crater (Rymer et al., 1998; Williams-Jones et al., 2003) (Figure 4.4). This zone is directly linked to the surface through an open vent (Stix, 2007) from which the most of Masaya gases are released (Figure 4.4). Soil and flank diffusive degassing, fumarole degassing and the release of gases through other minor structures (buried faults, Comalito crater), are also responsible for the degassing of the Masaya magmatic system (Mauri et al., 2012; De Moor et al., 2013). Since the formation of the Santiago crater (1853) at least five cyclical degassing events have occurred. The most recent one began in May 1993 and continues to date (Stoiber et al., 1986; Rymer et al., 1998; Delmelle et al., 1999; Duffell et al., 2003). Given the results of gas rate emission studies it seems that Masaya is close to the minimum of its degassing cycle (Williams-Jones et al., 2003; Martin et al., 2010) and that 10 km^3 of magma has been degassed during last 150 years (Rymer et al., 1998). Since 1993 the composition of the plume has remained relatively stable with respect to H_2O, SO_2, CO_2, HCl and HF gas fluxes (Martin et al., 2010). This suggests a particular stability of the shallow magma system (Martin et al., 2010) supporting the idea that an open-degassing system with a stable deeper source that releases volatiles to a shallow reservoir exists and controls the activity of Masaya volcano (Stix, 2007).

According to Delmelle et al. (1999) it seems that the chemical and physical state of the reservoirs control the timescale between these degassing events. Convective overturns of the magma in the shallow reservoir, rather than the intrusion of new magma within the magma chamber, are the causes of these degassing cycles (Rymer et al., 1998; Harris et al., 1999; Williams-Jones et al., 2003; Caravantes González, 2013). Gravity measurements have clearly shown an active convective system below the Masaya volcano (Caravantes González, 2013). At the base of these convective cycles there are complex processes

occurring between the shallow and surface reservoir as well as within the conduit that links these two parts of the plumbing system (Stix, 2007) (Figure 4.4). Fresh, low density, gas-rich magma rises from deep levels within the central portion of the conduit. As soon as the magma reaches the surface reservoir it degases, crystallises and starts to sink along the edges of the conduit (Rymer et al., 1998; Stix, 2007; Caravantes González, 2013) (Figure 4.4). The exsolved gases form bubbles that accumulate at the top of the accumulation zone creating a foam layer just a few tens of meters below the surface (Delmelle et al., 1999; Stix, 2007) (Figure 4.4). Gas crises occur when a considerable portion of the foam layer starts to detach from the rest of the reservoir (Delmelle et al., 1999). Pele's hairs and tears could represent portions of the foam layer erupted during periods of intense instability of the shallow reservoir (Stix, 2007).

Deep magma movements or structural adjustments of both shallow and surface reservoirs contribute to destabilising the magmatic system and the foam layer (Rymer et al., 1998; Williams-Jones et al., 2003). Small subterranean vertical collapses of the crater floor coupled with magma fluctuations or major structural modifications of the shallow reservoir can modify both the conduit and the relative vent structure (Rymer et al., 1998; Roche et al., 2001). Vent blocking, vent clearing, variations in the conduit convection or in the magma supply rate lead to periods of increased or decreased volcanic and degassing activity causing the observed gas flux changes and micro-gravity variations (Rymer et al., 1998; Harris et al., 1999; Williams - Jones et al., 2003; Caravantes González, 2013).

An inverse relationship exists between the gas flux fluctuations and micro-gravity variations with micro-gravity decreasing during periods of increased degassing (higher flux rate) and vice versa (Williams-Jones et al., 2003). Short- and long-term variations of degassing rate and micro-gravity have been related to different phenomena that characterise the Masaya volcanic system (Williams-Jones et al., 2003; Caravantes González, 2013). Short-term (1 year) and mid-term (2-5 years) gravity variations have been related to small scale surface processes like cavern filling, magma fluctuations, pit crater collapses and minor/major changes in the foam layer thickness (Caravantes González, 2013). Long-term (>10 year) gravity changes have been linked to deep magma movements or major structural adjustments affecting the entire plumbing system (Caravantes González, 2013).

Specific relationships have been found between the gas flux variations, the magmatism of the volcano and the structural modification of the volcanic system (Williams-Jones et al., 2003). Long-term (years) gas flux variations have been related to the input of a new volatile-rich magma into the shallower reservoir (Williams-Jones et al., 2003; De Moor et al., 2013) that causes variations in the magma supply rate (Spampinato and Salerno, 2012).

Short-term changes (days) have been linked with shallower processes occurring within the conduit or in the shallow reservoir (e.g. variation of the conduit radius, vent blockage and clearing). Shorter-time gas fluctuations (minutes) correlate to rates of gas bubbles/trains of bubbles bursting at the magma surface (Spampinato and Salerno, 2012).

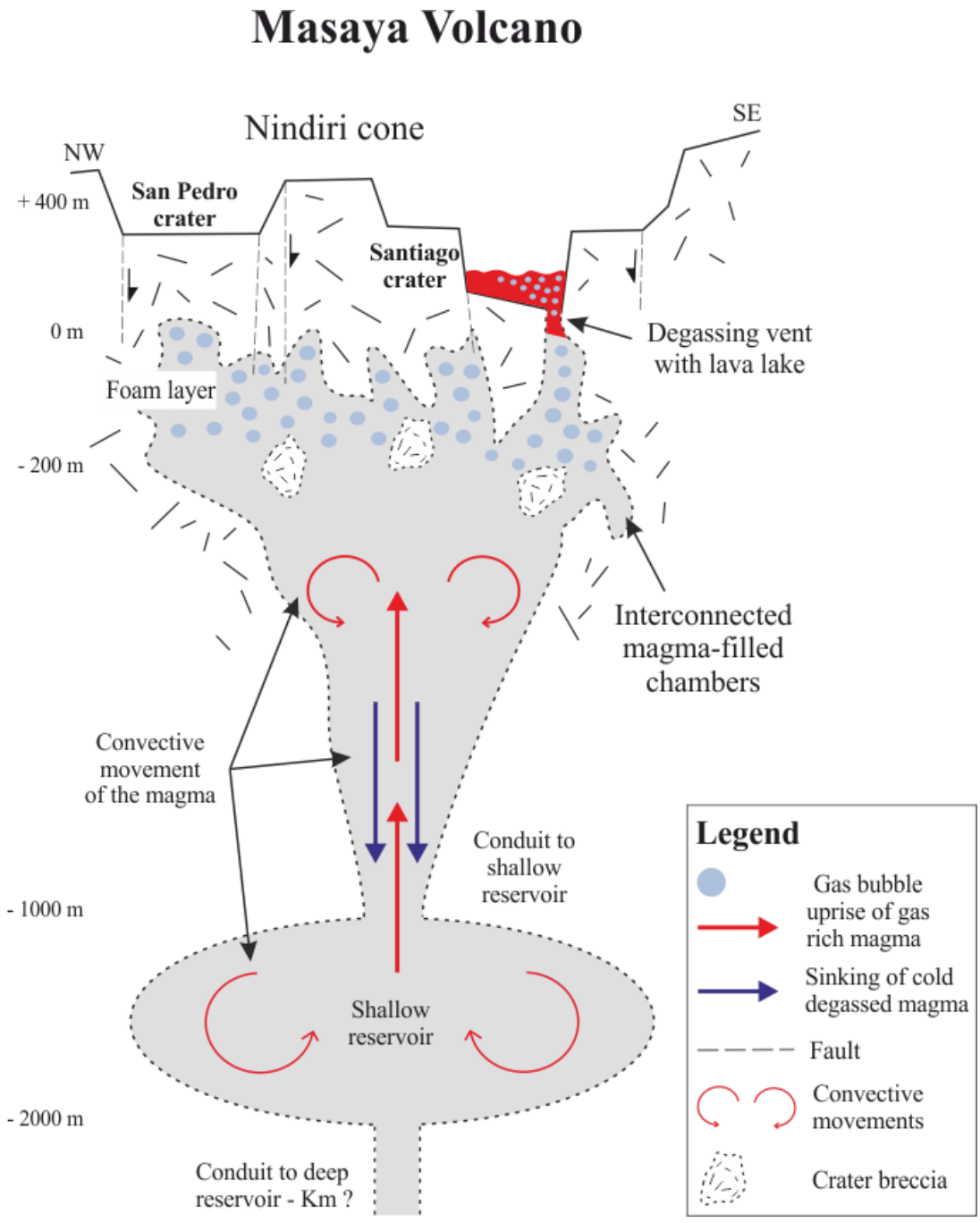

Figure 4.4 Schematic diagram of the Masaya volcano plumbing system (see text for explanation). Modified after Rymer et al. (1998) and Stix (2007).

4.4 Methods

Pele's hairs and tears collected in 2015 (KS15-03) and 2016 (KS16-03, KS16-13) at Masaya Volcano were characterised in terms of their petrography and texture by thin section analyses and backscatter electron images. Mineral contents, external morphologies, the shapes of internal vesicles and the degree of vesicularity of the samples are described in detail. In order to determine the vesicularity backscatter images were produced from carbon coated thin sections. The obtained images were loaded into Corel Draw software the limits of the bubbles and of the external margins of the particles were better defined. After that ImageJ software was used to calculate the areas of the vesicles and of the entire particle that, in turn, were used to determine the total vesicularity of the samples.

Major element compositions of the glass were determined by electron microprobe analysis and the Chemical Alteration Index (CIA) was calculated for each analysed spot in order to inspect the degree of alteration of the glass. Areas of single vesicle in the samples and electron microprobe data together with calibration information are reported in detail in Appendix A3.1, A3.2 and A3.3, respectively.

NG (^{4}He, ^{22}Ne, ^{36}Ar and ^{40}Ar) compositions and isotope ratios were investigated by single grain fusion noble gas mass spectrometry analyses of Pele's hairs and tears with dimensions of ~1-2 mm. ^{4}He, ^{22}Ne and ^{40}Ar were measured for 129 particles while ^{36}Ar was measured only for 54 samples. Images of the samples loaded in the sample holder were taken before the analyses for comparison between morphology of the samples and NG concentration.

More specific information and technical details of each technique are given in Chapter 2.

Table 4.2 analytical techniques used to study Pele's hairs and tears collected at Masaya volcano in 2015 and 2016 with location of the collecting point.

Sample	Date of collection	Coordinates	Thin section	Backscatter images	Electron microprobe	NG-MS
KS15-03	Mar-15	11.985698 -86.172155	X	X	X	X
KS-03-11L	03/03/2016	11.982519 -86.169299	X	X	X	X
KS-03-10S	03/03/2016	11.982560 -86.169388	X		X	X
KS-13-4L	13/03/2016	11.986586 -86.169900	X		X	X
KS-13-10L	13/03/2016	11.982560 -86.169388	X	X	X	X

4.5 Sample characterisation

4.5.1 Macroscopic and microscopic features

Pele's hairs and tears in this study display similar fluidal morphological, textural and petrographical characteristics reported for the same type of material derived from other volcanoes (Cannata et al., 2012; Porritt et al., 2012) and, in particular, with those samples investigated by Moune et al. (2007) collected at Masaya volcano.

In this study the Pele's hairs are up to 5 cm long and up to 1 mm thick and have tubular and cylindrical shapes that sometimes display bends and bifurcations (Figure 4.5 A). Some of them display small bulges on the surface associated with the presence of small microcrystals along their length (Figure 4.5 C).

Pele's tears are between 5 mm and 0.5 mm in size with respect to their maximum elongation axes. They can be spherical (Group A in Figure 4.5 B), tear-drop like/oblate spheroidal (Group B in Figure 4.5 B) or elongated (Group C in Figure 4.5 B) and can be found alone as single particles or attached to the edges of intact Pele's hairs.

The majority of the samples collected in 2015 are covered by a yellowish crust that could be associated to sulphur sublimates resulting from glass-plume interaction. Once cleaned with acetone the samples displayed a black shiny surface.

In thin section Pele's hairs and tears are composed of a brown transparent sideromelane glass (99 % - 100 %) (Figure 4.5 C-D). Only a few hairs/tears have isolated microcrystals (< 1 %) of plagioclase and/or clinopyroxene (< 50 μm). The glass is pristine and, generally, without devitrification or alteration structures. At the edges of a few Pele's hairs were observed small circular structures that could be areas that have undergone devitrification associated with the interaction of the samples with volcanic gases.

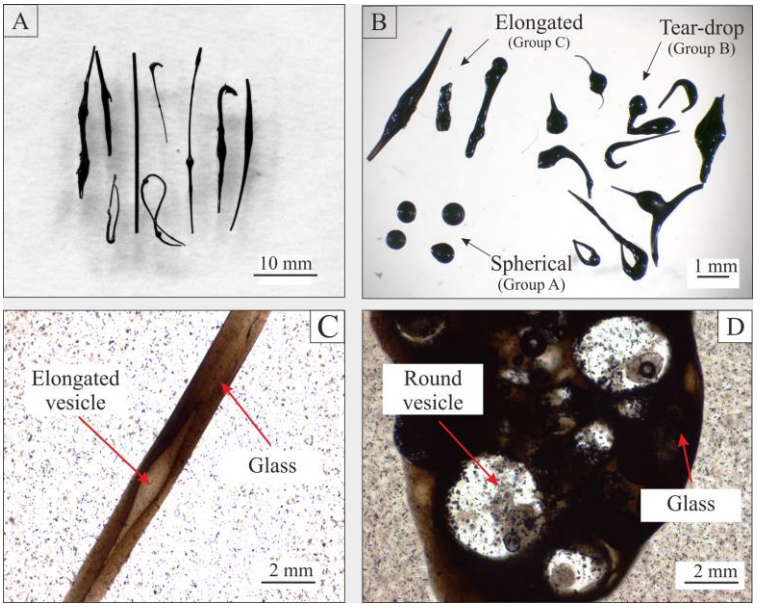

Figure 4.5 A - Pele's hairs with tubular shape and displaying bifurcations. B - Pele's tears with spherical, tear-drop and elongated shapes. C - Thin section of a Pele's hair displaying sideromelane glass and elongated vesicles. D - Thin section of a Pele's tear displaying sideromelane glass and round vesicles.

Internal vesicles vary in size and number without any particular relation to the shape and size of the particles, or, their proximity to the sample surface (Figure 4.13 – 4.15). Elongated vesicles, stretched parallel to the maximum axes of the samples, were observed in Pele's hairs and in Pele's tears of group C (Figure 4.6 A-B) whereas round vesicles were observed only in Pele's tears (Figure 4.7 – 4.9). These pyroclasts display multiple generations of vesicles: a few of them (~ 1%) are composed of pure glass without visible vesicles (Figure 4.7 A) or with only a few round vesicles of less than 100 μm in diameter (Figure 4.7 B); others have only small isolated round vesicles with a diameter equal or less than 50 μm (Figure 4.8 A); others have small isolated round vesicles (<50 μm) and bigger round isolated (150 - 200 μm) (Figure 4.8 B – 4.9 A); the last group is composed of samples having three generations of vesicles: small isolated round vesicles (<50 - 100 μm), bigger isolated round vesicles (100 - 200 μm) and coalescent vesicles (200 x 320 μm) (Figure 4.9 B).

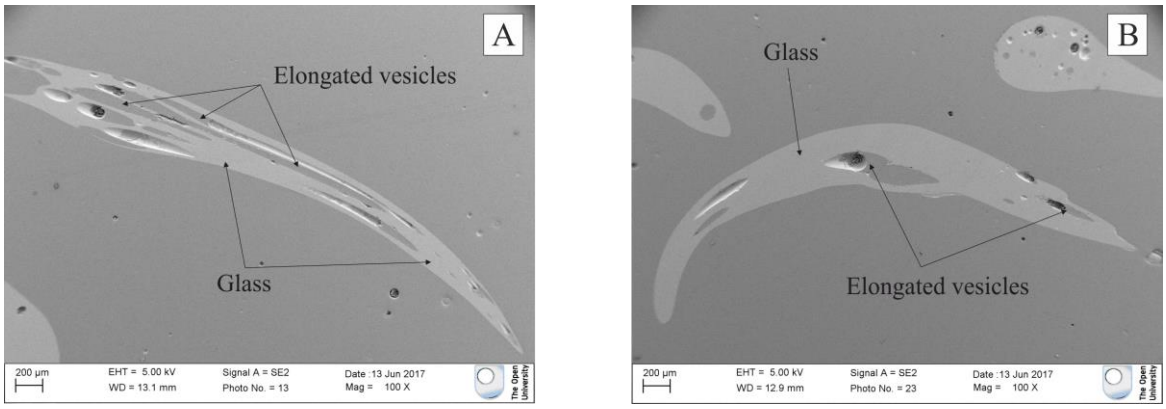

Figure 4.6 A - BSE image of a Pele's hair with elongated vesicles. B - BSE image of a Pele's tear of group C with elongated vesicles

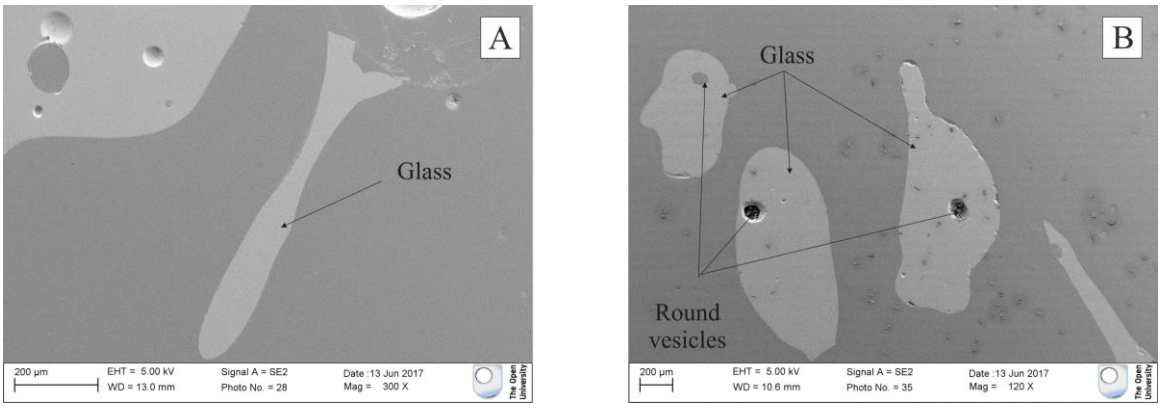

Figure 4.7 A - BSE image of a Pele's tear without vesicles. B - BSE image of a Pele's tears with a few isolated round vesicles.

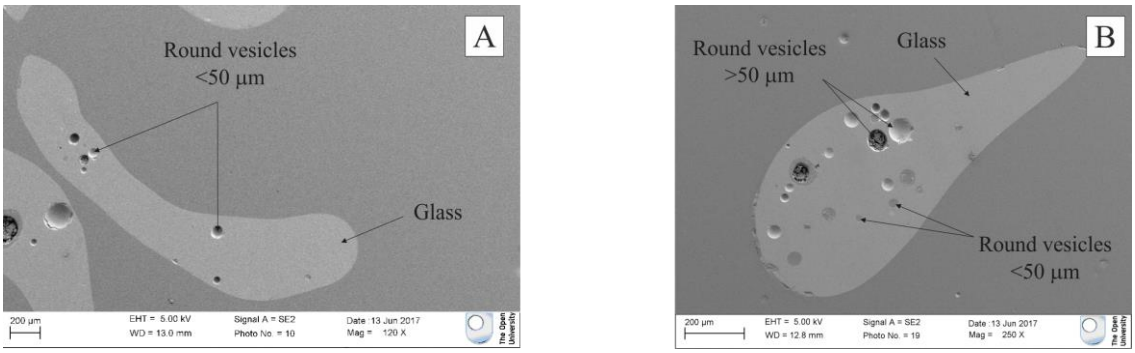

Figure 4.8 A - BSE image of a Pele's tear with only small (<50 µm) isolated round vesicles. B - BSE image of a Pele's tear with isolated round vesicles with dimension lower than 50 µm and isolated vesicles bigger than 50 µm.

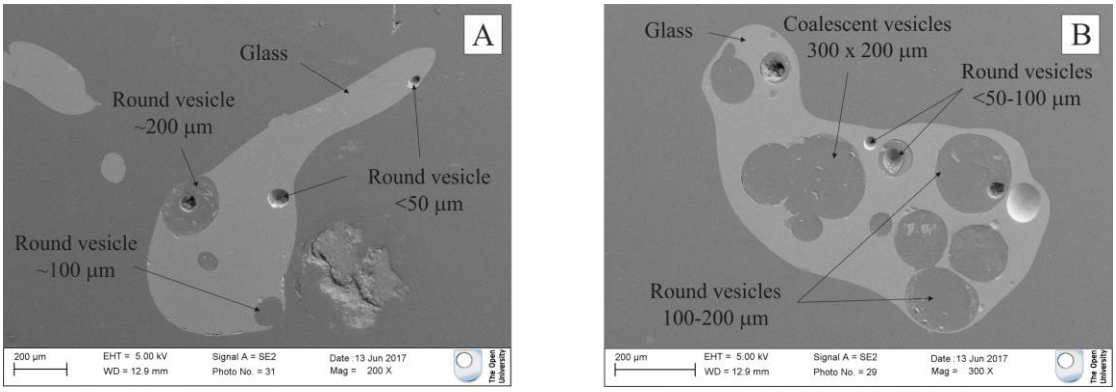

Figure 4.9 A - BSE image of a Pele's tear with small (<50 µm) isolated round vesicles and bigger vesicles (100 - 200 µm). B - BSE image of a Pele's tear with three generation of vesicles: small isolated round vesicles (<50 - 100 µm), bigger isolated round vesicles (100 - 200 µm) and coalescent vesicles (200 x 320 µm).

Sample vesicularity, calculated as the ratio between the area covered by vesicles and the total area of the sample, was determined for ten Pele's hairs and tears from each of the three sample suites collected in this study (KS15-03, KS16-03, KS16-13). The vesicularity varies a lot from one particle to another ranging from 0 % (KS16-03_5) up to 47.6 % (KS16-03_6) (Table 4.3). 10 out of 30 particles have a vesicularity of between 1 % and 10 % (Table 4.3, Figure 4.10). Pyroclasts from sample KS15-03 have a vesicularity of between 1.7 % and 39.4 % with a weighted mean vesicularity of 17.4% (Table 4.3, Figure 4.11, 4.13). Sample KS16-03 has particles with a vesicularity of between 0.0 % and 47.6% with a weighted mean vesicularity of 23.2 % (Table 4.3, Figure 4.11, 4.14). Particles of sample KS16-13 have a vesicularity of between 2.0 % and 35.7 % with a weighted mean vesicularity of 15.3 % (Table 4.3, Figure 4.11, 4.15).

Sample KS15-03 is not only characterised by the highest weighted mean vesicularity but it is also the only one displaying pyroclasts with a vesicularity that is higher than 40 % (Table 4.3, Figure 4.11). This sample, in particular, has only three particles with vesicularity ≤ 10% while sample KS15-13 and KS16-13 have four and five particles, respectively, in this range (Table 4.3, Figure 4.11). The same observation can be made with respect to those particles with vesicularities of between 10% and 20% where sample

KS15-03 has four particles in this range while samples KS15-13 and KS16-13 have only two and one particles, respectively, in this range (Table 4.3, Figure 4.11). Sample KS16-03 has no particles with vesicularity of between 20 % and 30 % but displays two particles with vesicularity of between 30 % and 40 % (Table 4.3, Figure 4.11).

From Figure 4.12 A1 it is possible to observe that for all the three suites the majority of the vesicles (60% - 70%) have an area of between 0 and 5 mm^2. Sample KS16-03 has the greatest variability in term of vesicles dimension with areas of the single vesicles ranging from 0.022 mm^2 up to 190 mm^2 with 80.7 % of them having an area lower than 10 mm^2 (Figure 4.12 A1-A2). Sample KS16-13 has the lowest variability with vesicles ranging from <0.001 mm^2 up to 45 mm^2 with 89.4 % of them having an area lower than 10 mm^2 (Figure 4.12 A1-A2). Sample KS15-03 has vesicles with areas ranging from <0.001 mm^2 to 110 mm^2 and 75.6 % of them are of between <0.001 mm^2 and 10 mm^2 (Figure 4.12 A1-A2). At a closer look bubbles with an area of between 0 mm^2 and 1 mm^2 and of between 3 mm^2 and 3.5 mm^2 are more frequent in samples KS16-13 and KS15-03 while bubbles with an area of between 1 mm^2 and 3 mm^2 and of between 4.5 mm^2 and 5 mm^2 are more frequent in sample KS16-03 (Figure 4.12 A2).

Table 4.3 Vesicularity calculated for each individual grain of samples KS15-03, KS16-03 and KS16-13.

Grain	Sample		
	KS15-03	KS16-03	KS16-13
1	30.44	6.31	22.44
2	1.70	10.57	22.47
3	7.56	10.00	2.46
4	5.89	36.30	23.69
5	17.39	0.00	4.10
6	6.09	47.59	16.77
7	25.66	13.87	10.02
8	39.45	12.93	6.99
9	27.13	34.65	35.67
10	12.70	44.50	2.04
Mean	17.48	23.21	15.35
±St.dev.	12.02	16.36	10.72

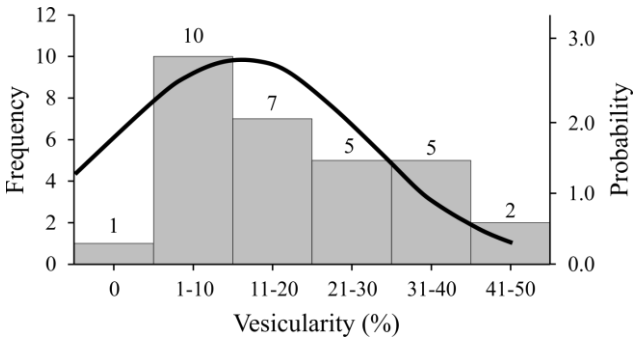

Figure 4.10 Distribution and frequency of sample vesicularity of all the samples analysed in this study. Samples with vesicularity comprised of between 1 % and 10 % are more frequent then samples with higher vesicularity.

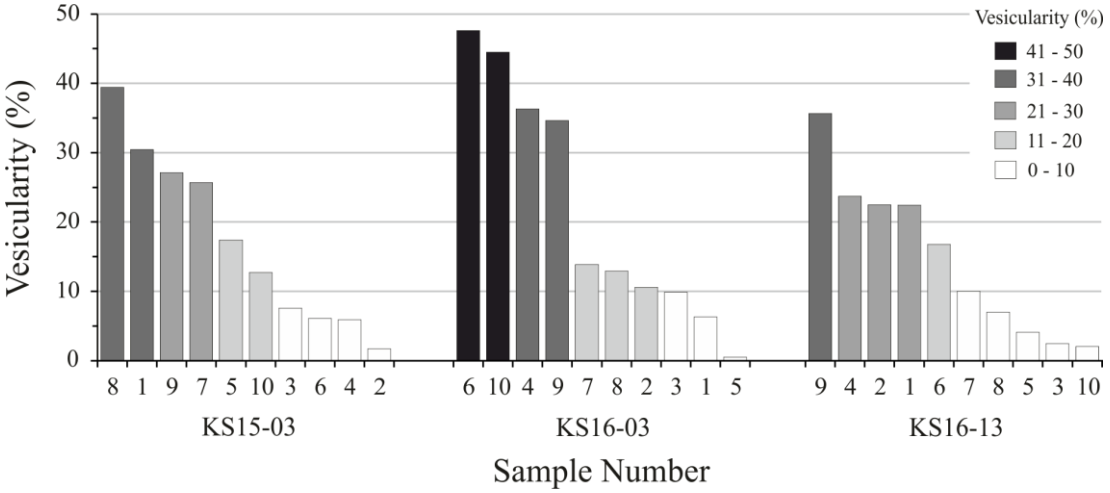

Figure 4.11 Histogram showing the vesicularity of the particles analysed in this study for the three suites of samples collected at Masaya volcano. The number reported on the X-axis refers to the single particle analysed for each of the three suites of samples while on the Y-axis is reported the corresponding vesicularity expressed in % calculated using ImageJ software (Abramoff et al., 2004). Different colours were used to highlight samples with similar vesicularity. Sample N° 5 of KS16-03 has a vesicularity of 0 % so the bar in the diagram is only for illustrative scope and not indicative of a real value.

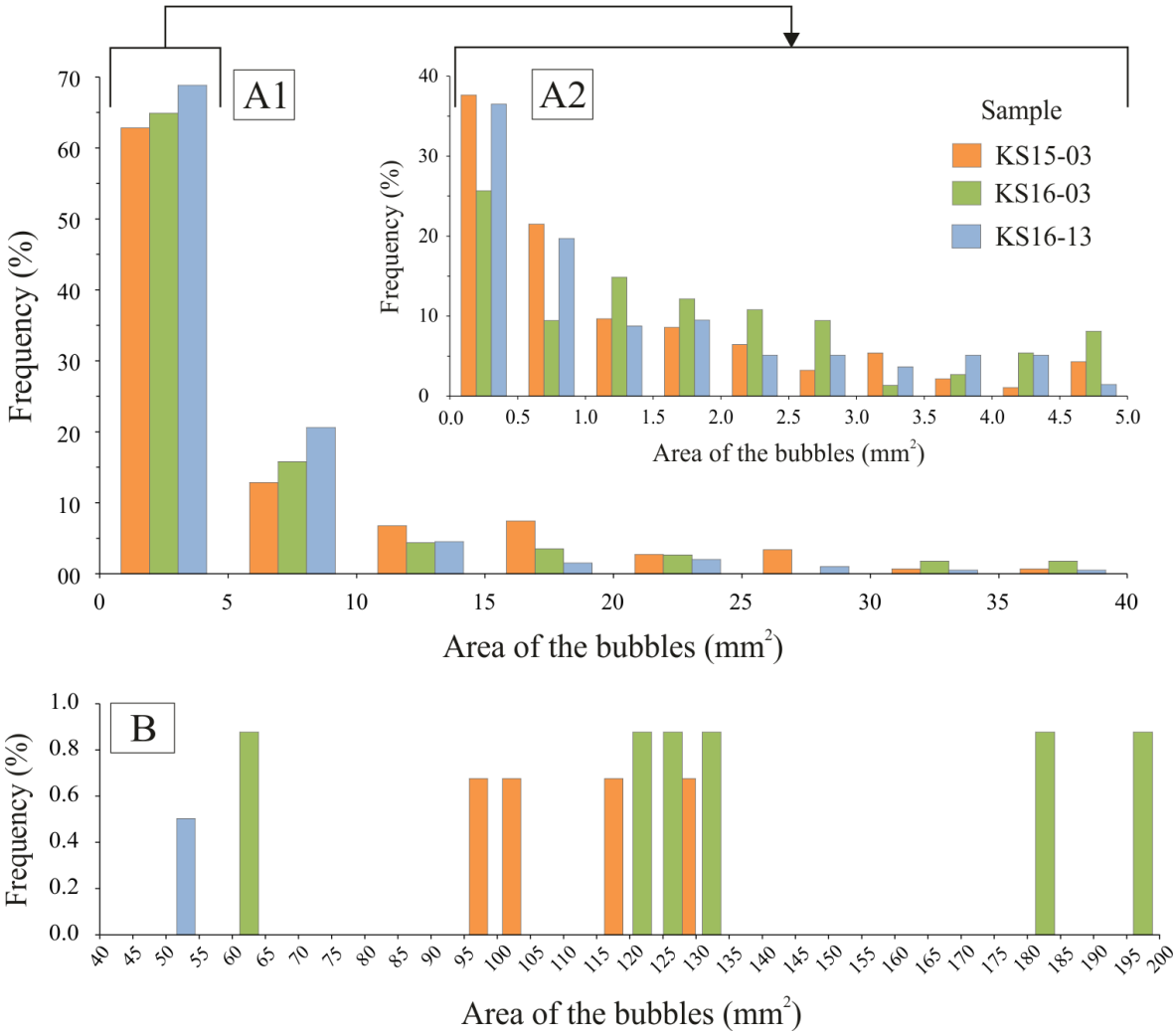

Figure 4.12 Frequency histogram of vesicles with similar internal areas divided for the three sample suites here analysed. The bins represent ranges of areas covered by vesicles. A1 - Areas of between 0 mm^2 and 40 mm^2; A2 - Focus on areas of between 0 mm^2 and 5 mm^2; B - Areas of between 45 mm^2 and 2 mm^2.

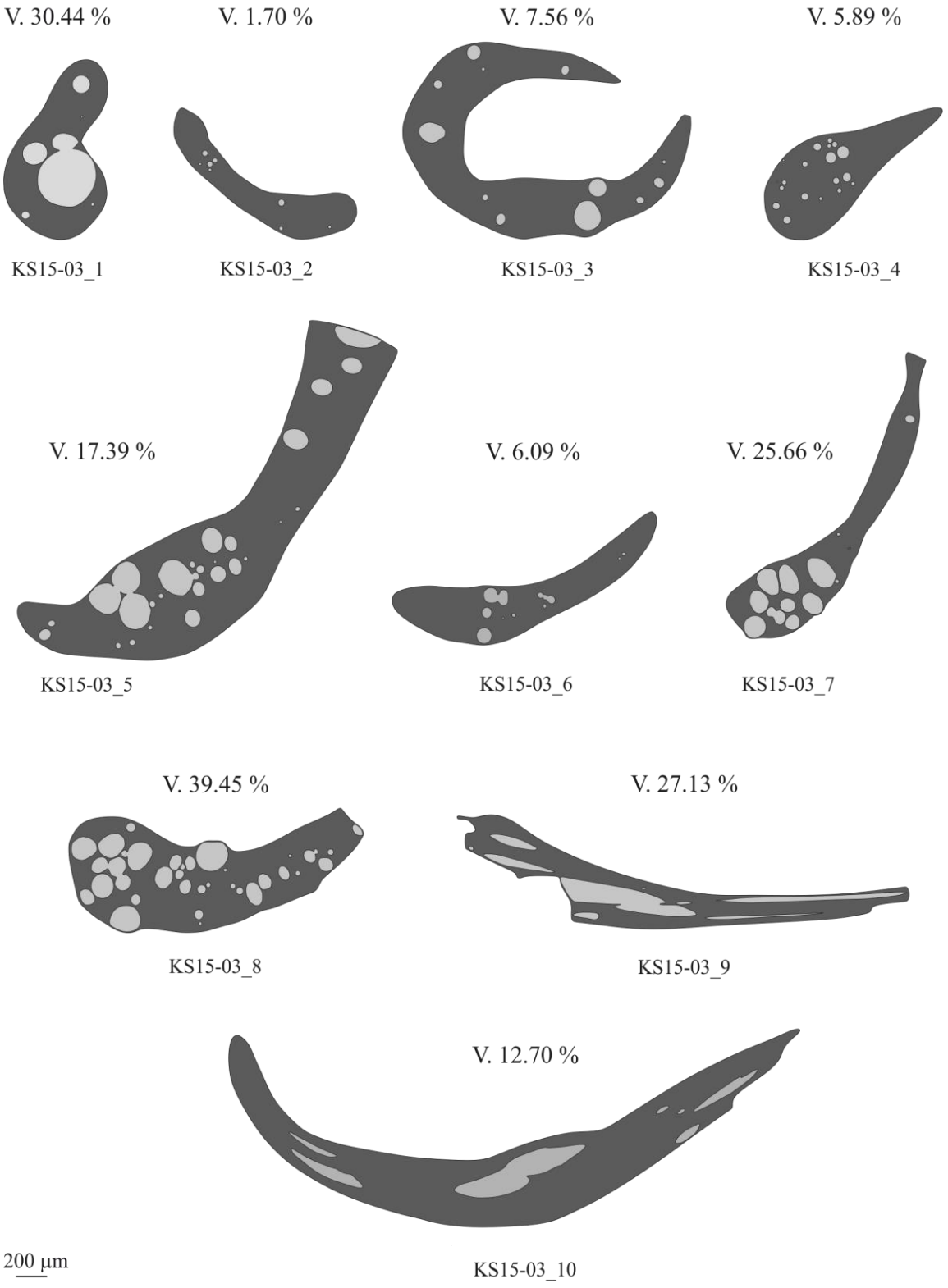

Figure 4.13 Illustrations of particle shapes, vesicles geometry and dimension of Pele's hairs and tears from samples of suite KS15-03. The images were drawn from BSE images and used to calculate the vesicularity of the particles. The scale on the left is the same for all the images. V. = vesicularity.

KS16-03

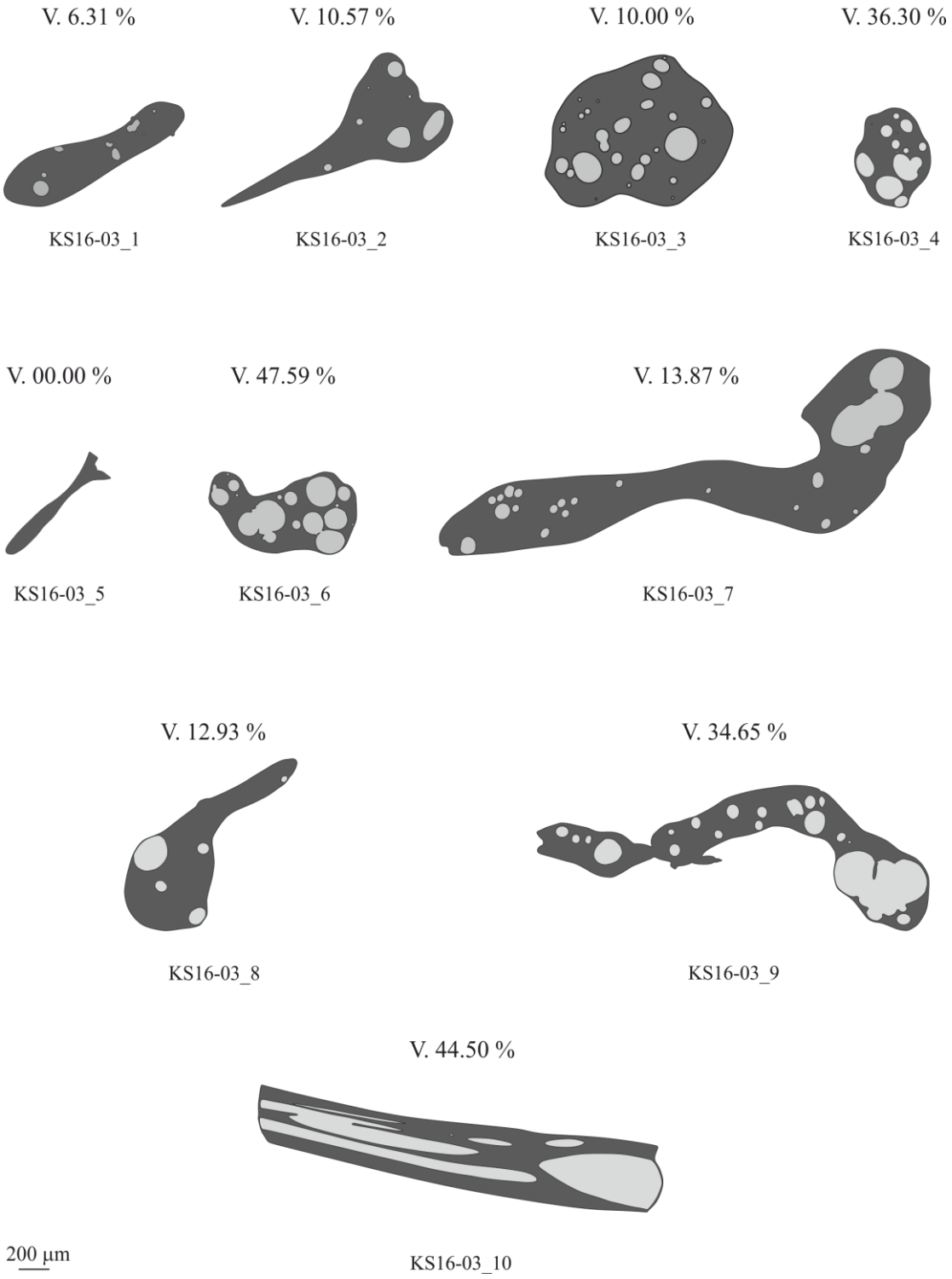

Figure 4.14 Illustrations of particle shapes, vesicles geometry and dimension of Pele's hairs and tears from samples of suite KS16-03. The images were drawn from BSE images and used to calculate the vesicularity of the particles. The scale on the left is the same for all the images. V. = vesicularity.

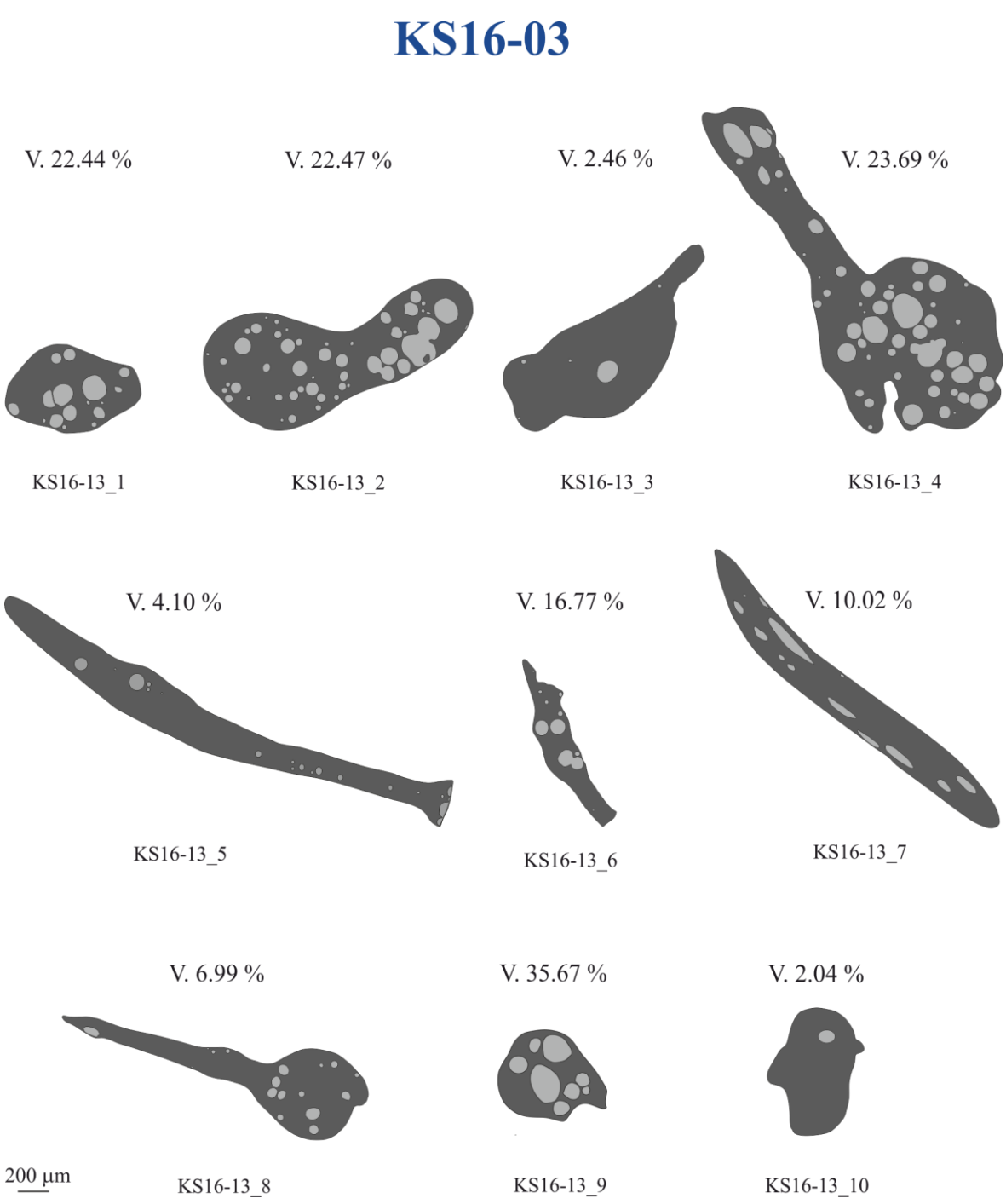

Figure 4.15 Illustrations of particle shapes, vesicles geometry and dimension of Pele's hairs and tears from samples of suite KS16-13. The images were drawn from BSE images and used to calculate the vesicularity of the particles. The scale on the left is the same for all the images. V. = vesicularity.

4.5.2 Chemistry of the glass

The results of 106 electron microprobe analyses demonstrate that Pele's hairs and tears of this study have similar chemistry to those collected at Masaya and analysed by Moune et al. (2007) (Table 4.4). All the samples are basaltic in composition when plotted on a total-alkali-silica diagram (TAS - Le Bas, 1986) with mean SiO_2 values of 51.2±0.4 (KS15-03), 51.7±0.3 (KS16-03) and 51.1±0.4 (KS16-13) and total alkalis of 4.4±0.1 Wt % for all three samples (Table 4.4). Generally speaking, the samples display the same major elements composition (Table 4.4) with only minor variations detected within each dataset (Table 4.4). In particular, minimal variations among the three samples were observed for Mg, Al and Fe, elements previously used to characterise the eruptive cycles of Masaya volcano and as index of fractional crystallization of its products (Walker et al., 1993).

Totals from EMPA are between 97.07 (KS15-03) and 99.58 (KS16-13) and the Chemical index of alteration (CIA, Nesbitt and Young, 1982) values are 50.76±0.27, 50.91±0.35 and 50.72±0.33 for samples KS15-03, KS16-03 and KS16-13, respectively. Electron probe analyses do not show any variation in the Si content or variations in the related index of alteration confirming the pristine condition of the glass previously observed in the thin sections. This condition is also corroborated by the small variations observed for the more mobile elements like K, Na and Ca. In particular, the K is extremely constant with values of 1.44 wt. % for all the analysed samples.

Table 4.4 Chemical composition of Pele's hairs and tears

	KS15-03 (N° 33)		KS16-03 (N° 53)		KS16-13 (N° 20)		Moune et al. (2007)*	
Wt. %	Mean	± St. Dev.	Mean	± St. Dev.	Mean	± St. Dev.	Mean	± St. Dev.
SiO_2	51.25	0.42	51.71	0.35	51.12	0.45	50.90	0.60
Na_2O	2.97	0.10	3.02	0.13	3.01	0.10	2.83	0.18
K_2O	1.44	0.02	1.44	0.03	1.44	0.02	1.39	0.13
CaO	8.89	0.04	8.85	0.10	8.85	0.07	8.81	0.30
MgO	4.87	0.05	4.86	0.07	4.84	0.04	4.67	0.14
MnO	0.25	0.01	0.24	0.01	0.24	0.01	0.25	0.08
FeO	13.46	0.17	13.34	0.25	13.44	0.23	13.80	0.40
Al_2O_3	13.71	0.13	13.81	0.11	13.69	0.11	13.50	0.40
TiO2	1.31	0.06	1.31	0.05	1.34	0.07	1.42	0.13
Cl	0.05	0.03	0.04	0.03	0.04	0.03	-	-
P_2O_5	0.36	0.02	0.36	0.03	0.36	0.02	-	-
SO_3	0.01	0.01	0.01	0.01	0.01	0.01	-	-
Total	98.56	0.52	98.99	0.37	98.38	0.57	97.60	0.80
CIA	50.76	0.27	50.91	0.35	50.72	0.33	-	-

All the data are from microprobe analysis.
*Data from Moune et al. (2007) come from the freshest portion of the samples.

4.5.3 Noble gas (NG)

4.5.3.1 Introduction

The results of NG analyses performed on 129 Pele's hairs and tears picked from samples KS15-03, KS16-03 and KS16-13 are presented here. The analytical uncertainties are expressed at the 1σ level.

Because NG concentrations vary considerably from particle to particle, in the following paragraphs it is only the minimum, maximum and mean values that are presented for each isotope (^{4}He, ^{22}Ne, ^{36}Ar, ^{40}Ar, $^{40}Ar^{*}$) and isotopic ratio ($^{40}Ar/^{36}Ar$, $^{4}He/^{40}Ar^{*}$) from each sample (KS15-03, KS16-03, KS16-13). Data related to individual particles are listed in Tables 4.5 - 4.10 and presented in Figures 4.16 - 4.22.

Data that have negative values after blank correction (due to gas concentrations within error of the background value) or with 1σ analytical uncertainties higher than 100 % of the absolute value are not included in this section. Also excluded are those values of ^{40}Ar for which the ion detector measured an ion count close to 14V. This value represents the saturation point of the ion detector of the MAP-215-50 mass spectrometer used in this study. For this reason the values of ^{40}Ar close to this number are not considered reliable and thus are excluded from further considerations. Measurements of ^{36}Ar collected when the ion detector reached the saturation point (14V) at mass ^{40}Ar are also omitted. These values can't be considered reliable because of the possible interferences caused by a Cl-based compound with mass 36 which is emitted from the detector/detector housing upon saturation. All omitted data are reported, mean blank values, raw data, weight of the samples and calibration data are included in Appendix A3.3 for completeness.

4.5.3.2 ^{4}He isotope

91 samples yielded positive ^{4}He values after blank correction. ^{4}He concentrations vary by three orders of magnitude from $1.03E^{-9}\pm5.64E^{-10}$ cc/g to $1.30E^{-7}\pm2.57E^{-8}$ cc/g Figure 4.16) with analytical uncertainties of between 3% and 93% (Tables 4.5 - 4.7).

- KS15-03 has ^{4}He values ranging between $1.03E^{-9}\pm5.64E^{-10}$ cc/g and $1.03E^{-7}\pm3.02E^{-9}$ cc/g with a mean of $2.48E^{-8}$ cc/g.
- KS16-03 has the greatest variability in terms of ^{4}He contents with values of between $1.30E^{-9}\pm7.44E^{-10}$ cc/g and $1.30E^{-9}\pm2.57E^{-8}$ cc/g with a mean of $2.82E^{-8}$ cc/g.
- KS16-13 has ^{4}He values ranging between $2.67E^{-9}\pm8.10E^{-10}$ cc/g and $3.28E^{-8}\pm9.04E^{-9}$ cc/g. The ^{4}He mean concentration is $1.56E^{-8}$ cc/g and it is the lowest among the analysed samples.

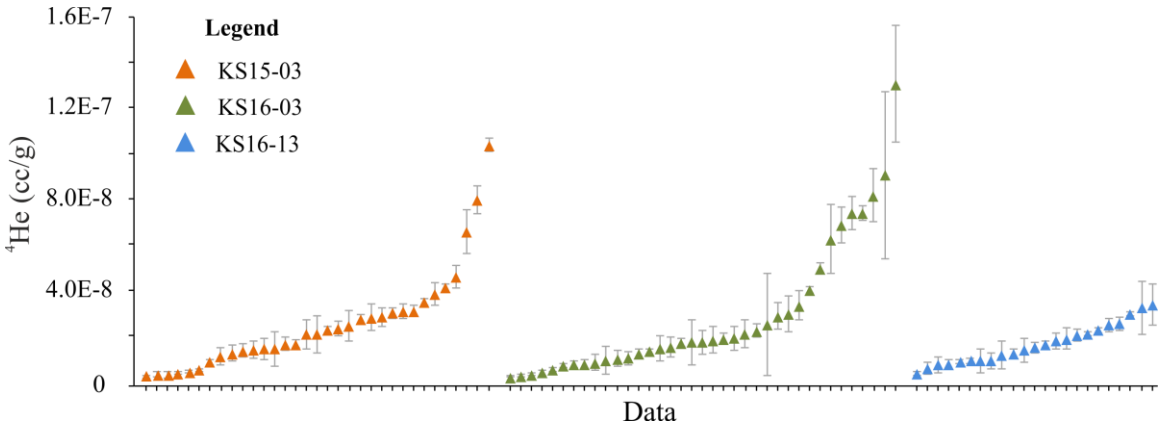

Figure 4.16 Variation of the ^{4}He concentration in Pele's hairs and tears of samples KS15-03, KS16-03 and KS16-13. The data are ordered from the lowest to the highest value and reported at the 1σ level. Error bars if not visible are smaller than the size use to display the data.

4.5.3.3 ^{22}Ne isotope

101 samples yielded positive ^{22}Ne concentrations after blank correction. ^{22}Ne varies of three orders of magnitude from $2.67E^{-10}\pm1.95E^{-10}$ cc/g to $2.38E^{-7}\pm2.85E^{-8}$ cc/g (Figure 4.17). The analytical uncertainties are between 1% and 87% (Tables 4.5, 4.6 and 4.7).

- KS15-03 has the lowest variability with ^{22}Ne values of between $2.67E^{-10}\pm1.95E^{-9}$ cc/g and $3.10E^{-8}\pm1.58E^{-9}$ cc/g with a mean of $7.34E^{-9}$ cc/g.
- KS16-03 has the greatest variability with ^{22}Ne varying from $2.94E^{-10}\pm2.02E^{-10}$ cc/g and $2.38E^{-7}\pm2.85E^{-8}$ cc/g with a mean of $4.25E^{-8}$ cc/g.
- KS16-13 has ^{22}Ne concentrations of between $1.49E^{-9}\pm9.15E^{-10}$ cc/g and $7.54E^{-8}\pm1.05E^{-9}$ cc/g with a mean of $1.06E^{-8}$ cc/g.

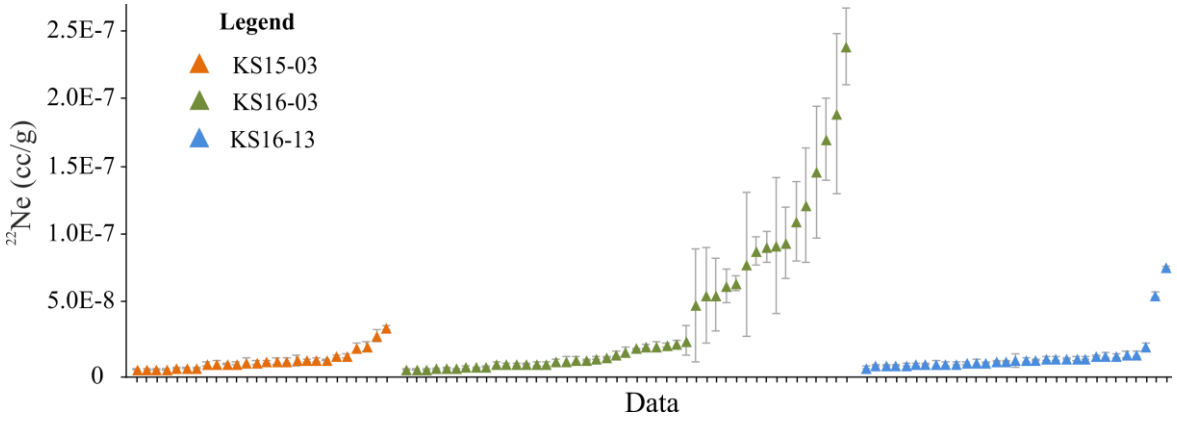

Figure 4.17 Variation of the ^{22}Ne concentration in Pele's hairs and tears of samples KS15-03, KS16-03 and KS16-13. The data are ordered from the lowest to the highest value and reported at the 1σ level. Error bars if not visible are smaller than the size use to display the data.

4.5.3.4 Ar isotopes

^{40}Ar varies by four orders of magnitude between $2.52E^{-9}\pm3.33E^{-10}$ cc/g and $2.51E^{-5}\pm9.29E^{-8}$ cc/g (Figure 4.18) with analytical uncertainties ranging from <1% up to 21% (Tables 4.5, 4.6 and 4.7).

- KS15-03 has ^{40}Ar concentrations in the range of $2.52E^{-9}\pm3.33E^{-10}$ cc/g and $9.52E^{-6}\pm2.31E^{-9}$ cc/g with a mean of $1.81E^{-6}$ cc/g.
- KS16-03 has the maximum variability in term of ^{40}Ar content with values ranging between $7.91E^{-9}\pm2.11E^{-10}$ cc/g and $2.51E^{-5}\pm9.29E^{-8}$ cc/g with a mean of $4.48E^{-6}$ cc/g.
- KS16-13 has the minimum variation; the ^{40}Ar is between $3.22E^{-8}\pm3.07E^{-9}$ cc/g and $6.14E^{-6}\pm3.01E^{-8}$ cc/g with a mean of $1.52E^{-8}$ cc/g.

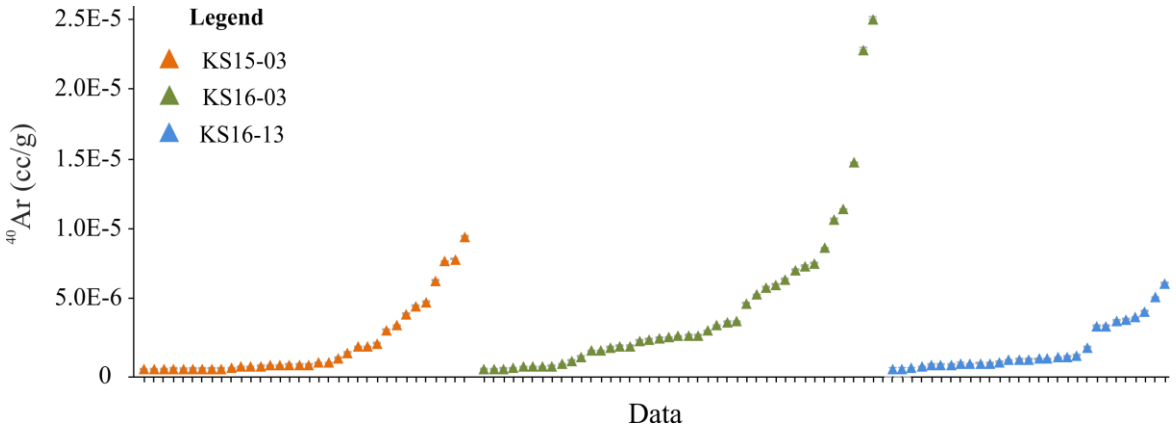

Figure 4.18 Variation of the ^{40}Ar concentration in Pele's hairs and tears of samples KS15-03, KS16-03 and KS16-13. The data are ordered from the lowest to the highest value and reported at the 1σ level. Error bars if not visible are smaller than the size use to display the data.

^{36}Ar concentrations vary by three orders of magnitude, ranging from 5.66E^{-11}±8.08E^{-12} cc/g to 3.04E^{-8}±5.66E^{-10} cc/g (Figure 4.19) with analytical uncertainties of between ~2% and 23% (Tables 4.5, 4.6 and 4.7).

- KS15-03 has ^{36}Ar of between 9.43E^{-11}±2.13E^{-11} cc/g and 3.04E^{-8}±5.66E^{-10} cc/g with a mean of 2.27E^{-9} cc/g.
- KS16-03 has ^{36}Ar content with values ranging between 5.66E^{-11}±8.08E^{-12} cc/g and 2.34E^{-8}±2.17E^{-10} cc/g and a mean of 5.23E^{-9} cc/g.
- KS16-13 has ^{36}Ar values of between 9.70E^{-10}±8.15E^{-11} cc/g and 1.25E^{-8}±1.73E^{-10} cc/g and a mean of 4.09E^{-9} cc/g.

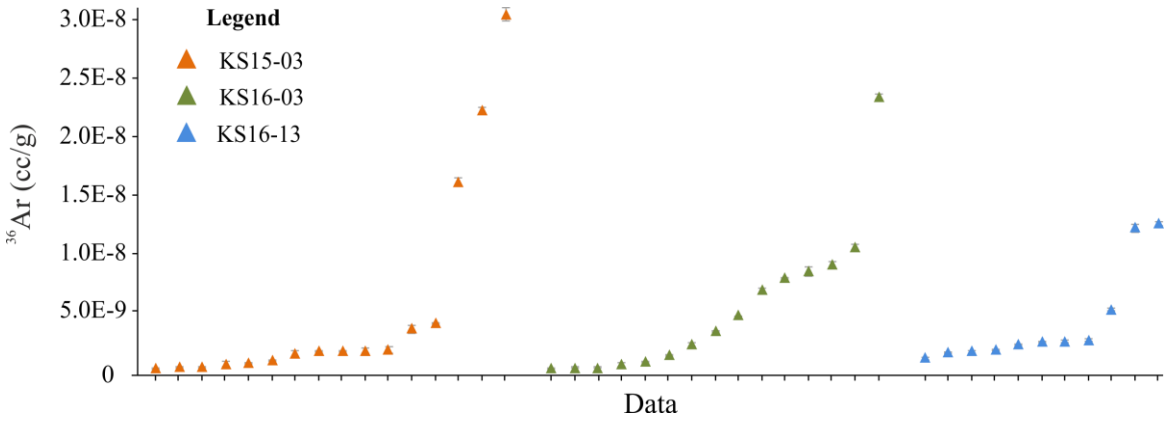

Figure 4.19 Variation of the ^{36}Ar concentration in Pele's hairs and tears of samples KS15-03, KS16-03 and KS16-13. The data are ordered from the lowest to the highest value and reported at the 1σ level. Error bars if not visible are smaller than the size use to display the data.

Only 10 samples, among those for which ^{36}Ar was measured, after atmospheric correction yielded positive $^{40}Ar^*$ values ($^{40}Ar^* = {}^{40}Ar - 298.56 \times {}^{36}Ar$). The $^{40}Ar^*$ ranges between $3.95E^{-9}\pm8.73E^{-10}$ cc/g and $2.86E^{-7}\pm9.05E^{-9}$ cc/g (Figure 4.20) with analytical uncertainties of between 1% and 12% (Tables 4.5, 4.6 and 4.7).

- KS15-03 has the minimum variation with ^{40}Ar values of between $3.95E^{-9}\pm8.73E^{-11}$ cc/g and $4.09E^{-8}\pm3.79E^{-9}$ cc/g with a mean of $1.89E^{-8}$ cc/g.
- Sample KS16-03 has the maximum variability in term of $^{40}Ar^*$ content with values ranging between $9.74E^{-9}\pm9.77E^{-11}$ cc/g and $2.86E^{-7}\pm9.05E^{-9}$ cc/g with a mean of $1.58E^{-7}$ cc/g.
- KS16-13 has $^{40}Ar^*$ values of between $2.01E^{-8}\pm5.84E^{-10}$ cc/g and $7.10E^{-8}\pm1.50E^{-9}$ cc/g with a mean of $4.53E^{-8}$ cc/g.

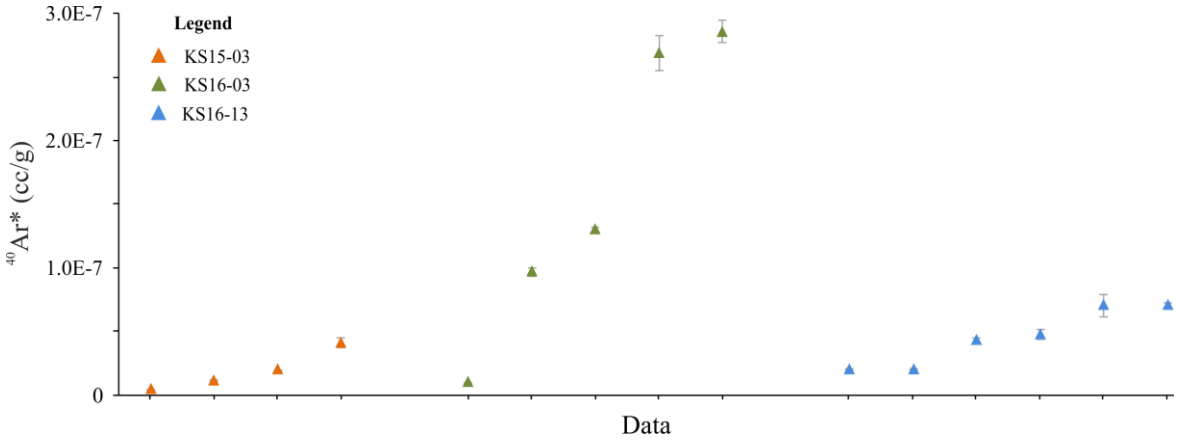

Figure 4.20 Variation of the $^{40}Ar^*$ concentration in Pele's hairs and tears of samples KS15-03, KS16-03 and KS16-13. The data are ordered from the lowest to the highest value and reported at the 1σ level. Error bars if not visible are smaller than the size use to display the data.

4.3.5.5 $^{40}Ar/^{36}Ar$ isotopic ratios

The $^{40}Ar/^{36}Ar$ ratios vary from sub-atmospheric to atmospheric to supra-atmospheric, with values ranging from 111.5±45.5 to 370.9±32.9 (Figure 4.21) with analytical uncertainties of between 1% and 48% (Tables 4.8, 4.9 and 4.10).

- KS15-03 has the highest variability with ratios of between 111.5±45.5 and 352.7±46.3 with a mean of 261.1.
- KS16-03 has ratios of between 128.4±13.9 and 338.3±12.2 with a mean of 271.0.
- KS16-13 has the lowest variation with ratios ranging from 253.7±21.8 to 370.8±32.9 with a mean of 305.6.

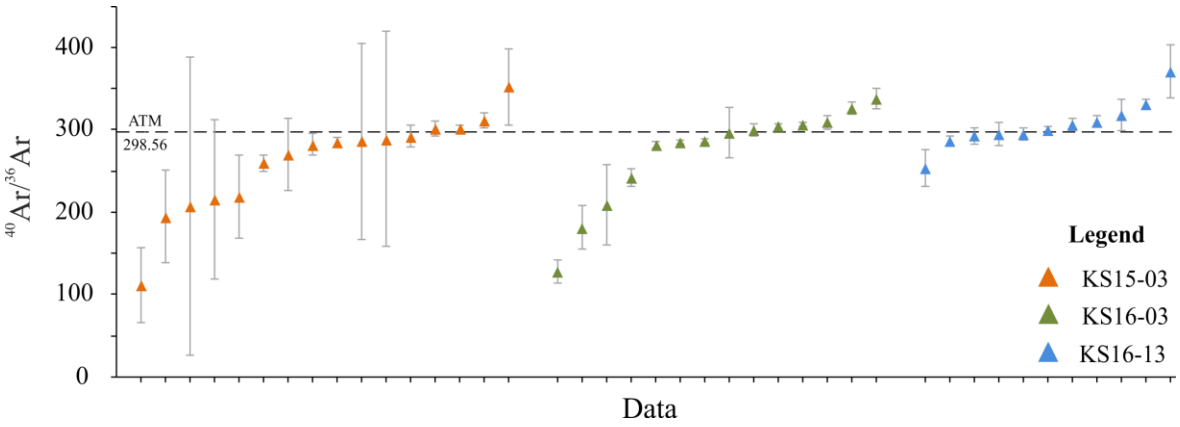

Figure 4.21 Variation of the $^{40}Ar/^{36}Ar$ ratios in Pele's hairs and tears of samples KS15-03, KS16-03 and KS16-13. The data are ordered from the lowest to the highest value and reported at the 1σ level. Error bars if not visible are smaller than the size use to display the data.

4.3.5.6 $^{4}He/^{40}Ar^{*}$ isotopic ratios

The $^{4}He/^{40}Ar^{*}$ ratio is preferred over other isotopic ratios to determine the degree of degassing of the samples for the following reasons:

- During degassing Ar is preferentially segregated in the vesicles while He preferentially remains in the melt (Carrol and Draper, 1994). This different behaviour is controlled by the different solubility of the He and Ar in basaltic melts (Jambon at al., 1986) that, in turn, controls the isotopic fractionation of these two isotopes during magma evolution.
- Because ^{40}Ar can be easily corrected for atmospheric contamination assuming that all the ^{36}Ar comes from the atmosphere ($^{40}Ar^{*} = {}^{40}Ar - 298.56 \times {}^{36}Ar$) and because the considered samples don't contain any radiogenic ^{40}Ar, in the present study any variation of the $^{40}Ar^{*}$ abundance corresponds to a direct variation of the amount of magmatic ^{40}Ar retained in the samples.

In this study it was only possible to determine the $^{4}He/^{40}Ar^{*}$ ratios for 13 particles. The ratios vary from $2.86E^{-2}\pm1.34E^{-2}$ to $5.84E^{-1}\pm2.71E^{-1}$ (Figure 4.22) with analytical uncertainties of between 12% and 57 % (Tables 4.8, 4.9 and 4.10).

- KS15-03 has $^{4}He/^{40}Ar^{*}$ ratios of between $2.32E^{-1}\pm3.03E^{-2}$ and $5.84E^{-1}\pm2.71E^{-1}$ with a mean of $3.74E^{-1}$.
- KS16-03 has ratios ranging from $2.86E^{-2}\pm1.34E^{-2}$ and $2.44E^{-1}\pm7.19E^{-2}$ with a mean of $3.21E^{-1}$.
- KS16-13 has values comprised between $3.76E^{-2}\pm1.14E^{-2}$ and $3.82E^{-1}\pm4.43E^{-2}$ with a mean of $2.39E^{-1}$.

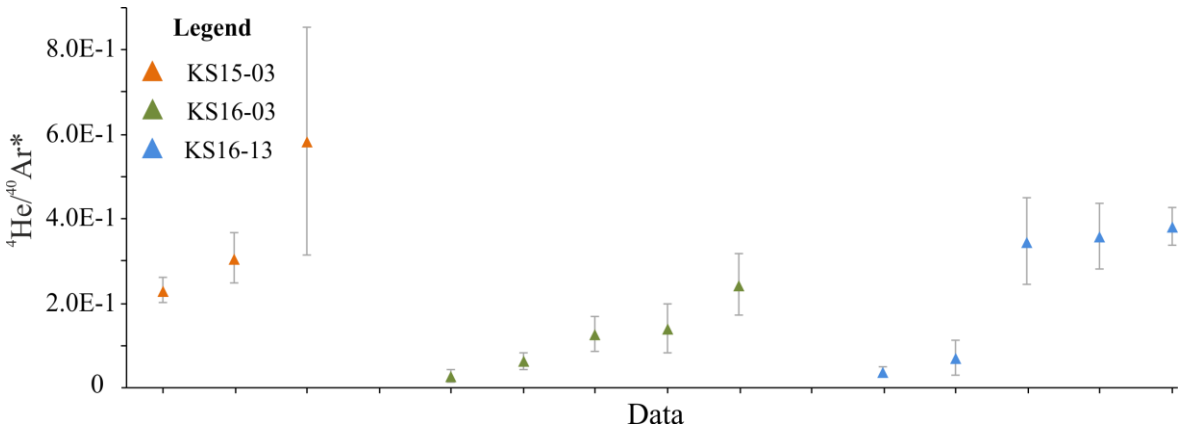

Figure 4.22 Variation of the $^{4}He/^{40}Ar^{*}$ ratios in Pele's hairs and tears of samples KS15-03, KS16-03 and KS16-13. The data are ordered from the lowest to the highest value and reported at the 1σ level. Error bars if not visible are smaller than the size use to display the data.

Table 4.5 NG abundances and isotopic ratios of sample KS15-03.

Sample N°	^{4}He	±	^{22}Ne	±	^{36}Ar	±	^{40}Ar	±	$^{40}Ar^{*}$	±	$^{4}He/^{40}Ar^{*}$	±	$^{40}Ar/^{36}Ar$	±
1	4.1E-8	1.7E-9	9.9E-9	8.0E-10	N.A.	N.A.	2.9E-7	2.0E-9	N.A.	N.A.	N.A.	N.A.	N.A.	N.A.
2	3.4E-8	1.3E-9	4.7E-9	6.2E-10	N.A.	N.A.	-	-	N.A.	N.A.	N.A.	N.A.	N.A.	N.A.
3	3.0E-8	2.2E-9	7.1E-9	8.1E-10	N.A.	N.A.	-	-	N.A.	N.A.	N.A.	N.A.	N.A.	N.A.
4	3.0E-8	3.2E-9	4.1E-9	1.3E-9	N.A.	N.A.	4.0E-6	4.2E-9	N.A.	N.A.	N.A.	N.A.	N.A.	N.A.
5	1.3E-8	2.9E-9	-	-	N.A.	N.A.	2.6E-8	3.1E-9	N.A.	N.A.	N.A.	N.A.	N.A.	N.A.
6	2.9E-8	2.1E-9	5.9E-9	1.0E-9	N.A.	N.A.	1.9E-6	6.2E-9	N.A.	N.A.	N.A.	N.A.	N.A.	N.A.
7	2.2E-8	1.6E-9	7.0E-9	7.3E-10	N.A.	N.A.	1.6E-6	8.7E-9	N.A.	N.A.	N.A.	N.A.	N.A.	N.A.
9	7.8E-9	1.3E-9	4.7E-9	4.4E-10	N.A.	N.A.	-	-	N.A.	N.A.	N.A.	N.A.	N.A.	N.A.
10	2.0E-8	6.2E-9	-	-	N.A.	N.A.	7.7E-6	1.7E-8	N.A.	N.A.	N.A.	N.A.	N.A.	N.A.
11	1.0E-7	3.0E-9	3.1E-8	1.6E-9	N.A.	N.A.	9.5E-6	2.3E-9	N.A.	N.A.	N.A.	N.A.	N.A.	N.A.
12	1.4E-8	4.5E-9	5.4E-9	1.6E-9	N.A.	N.A.	6.1E-8	4.0E-9	N.A.	N.A.	N.A.	N.A.	N.A.	N.A.
13	1.3E-8	3.9E-9	-	-	N.A.	N.A.	3.5E-7	3.7E-9	N.A.	N.A.	N.A.	N.A.	N.A.	N.A.
14	2.4E-8	6.5E-9	-	-	N.A.	N.A.	3.2E-6	4.6E-9	N.A.	N.A.	N.A.	N.A.	N.A.	N.A.
15	1.0E-8	3.8E-9	6.6E-9	1.7E-9	N.A.	N.A.	3.2E-7	1.9E-9	N.A.	N.A.	N.A.	N.A.	N.A.	N.A.
16	7.9E-8	6.1E-9	4.5E-9	2.5E-9	N.A.	N.A.	-	-	N.A.	N.A.	N.A.	N.A.	N.A.	N.A.
17	2.8E-8	5.7E-9	-	-	N.A.	N.A.	1.6E-6	5.9E-9	N.A.	N.A.	N.A.	N.A.	N.A.	N.A.
18	6.5E-8	9.5E-9	6.9E-9	3.8E-9	N.A.	N.A.	2.8E-6	9.2E-9	N.A.	N.A.	N.A.	N.A.	N.A.	N.A.
19	2.0E-8	8.3E-9	5.3E-9	3.7E-9	N.A.	N.A.	4.8E-6	8.1E-9	N.A.	N.A.	N.A.	N.A.	N.A.	N.A.
20	1.4E-8	7.5E-9	-	-	N.A.	N.A.	6.0E-8	3.7E-9	N.A.	N.A.	N.A.	N.A.	N.A.	N.A.
21	2.7E-8	2.3E-9	7.1E-9	1.4E-9	4.9E-10	1.9E-10	-	-	-	-	-	-	-	-
23	1.6E-8	1.9E-9	-	-	1.6E-8	3.4E-10	1.0E-7	2.1E-8	-	-	-	-	206.7	90.5
24	-	-	1.0E-8	1.7E-9	3.0E-8	5.7E-10	4.5E-6	3.2E-8	-	-	-	-	282.3	6.3
25	3.8E-8	5.0E-9	1.6E-8	3.2E-9	3.5E-9	3.6E-10	7.9E-6	6.1E-8	-	-	-	-	259.4	5.2
27	1.2E-8	3.5E-9	6.4E-9	2.3E-9	1.6E-9	2.1E-10	7.7E-7	4.1E-8	-	-	-	-	219.3	25.4
28	2.3E-8	3.3E-9	2.5E-8	4.5E-9	2.2E-8	2.4E-10	3.2E-7	1.8E-8	-	-	-	-	194.8	27.8
29	1.6E-8	2.9E-9	1.7E-8	3.2E-9	1.7E-9	3.0E-10	6.3E-6	1.4E-8	-	-	-	-	285.1	3.1
30	2.8E-8	4.2E-9	-	-	1.4E-9	2.8E-10	1.9E-7	2.2E-8	-	-	-	-	111.5	22.8
31	4.5E-8	4.9E-9	-	-	4.0E-9	2.8E-11	2.9E-7	2.5E-8	-	-	-	-	215.1	48.2
32	3.5E-9	6.8E-10	4.2E-10	2.4E-10	6.0E-10	1.4E-11	1.2E-6	8.7E-10	1.1E-8	1.1E-10	3.1E-1	6.0E-2	301.4	2.1
33	2.9E-9	6.0E-10	2.7E-10	2.1E-10	-	-	1.8E-7	3.2E-10	-	-	-	-	292.1	6.6
34	2.3E-9	1.6E-9	1.4E-9	5.5E-10	1.6E-9	2.3E-11	7.3E-9	5.6E-10	-	-	-	-		
35	4.5E-9	5.8E-10	2.7E-10	2.0E-10	1.6E-9	2.5E-11	4.9E-7	3.7E-10	1.9E-8	4.0E-10	2.3E-1	3.0E-2	310.8	4.5
37	2.3E-9	1.1E-9	1.1E-9	3.5E-10	1.9E-10	3.9E-11	4.9E-7	5.8E-10	4.0E-9	8.7E-11	5.8E-1	2.7E-1	301.0	4.7
38	-	-	-	-	-	-	5.4E-8	7.8E-10	-	-	-	-	286.0	59.3
39	1.0E-9	5.6E-10	-	-	3.2E-9	5.4E-11	3.6E-9	2.0E-10	-	-	-	-	-	-
40	-	-	-	-	7.5E-10	4.9E-11	1.1E-6	8.3E-10	1.2E-7	2.9E-9	-	-	336.3	5.7
41	-	-	1.5E-9	6.8E-10	-	-	2.7E-7	7.7E-10	4.1E-8	3.8E-9	-	-	352.7	23.2
42	-	-	3.9E-10	3.1E-10	2.1E-10	1.7E-11	2.5E-9	3.3E-10	-	-	-	-	-	-
43	-	-	-	-	9.4E-11	2.1E-11	5.7E-8	3.1E-10	-	-	-	-	270.0	21.8
44	-	-	-	-	-	-	2.7E-8	3.6E-10	-	-	-	-	289.0	65.4

Data are expressed as cc/g STP.Analytical uncertainties are at 1 σ level. N.A. = Data not available. Empty spaces indicate data not included in this section with negative values of 1σ > 100 % (see 4.5.3.1).

Table 4.6 NG abundances and isotopic ratios of sample KS16-03.

Sample N°	^{4}He	±	^{22}Ne	±	^{36}Ar	±	^{40}Ar	±	^{40}Ar*	±	^{4}He/^{40}Ar*	±	^{40}Ar/^{36}Ar	±
1 - 10S	9.3E-9	3.5E-9	8.8E-8	1.0E-8	N.A.	N.A.	1.7E-6	4.9E-9	N.A.	N.A.	N.A.	N.A.	N.A.	N.A.
2 - 10S	-	-	2.2E-8	1.1E-8	N.A.	N.A.	1.1E-7	1.1E-9	N.A.	N.A.	N.A.	N.A.	N.A.	N.A.
4 - 10S	4.9E-8	2.6E-9	6.2E-8	1.2E-8	N.A.	N.A.	4.7E-6	5.7E-9	N.A.	N.A.	N.A.	N.A.	N.A.	N.A.
5 - 10S	-	-	9.4E-8	2.6E-8	N.A.	N.A.	8.7E-6	4.7E-9	N.A.	N.A.	N.A.	N.A.	N.A.	N.A.
6 - 10S	1.3E-7	2.6E-8	-	-	N.A.	N.A.	3.1E-6	1.5E-8	N.A.	N.A.	N.A.	N.A.	N.A.	N.A.
7 - 10S	6.2E-8	1.5E-8	5.5E-8	3.5E-8	N.A.	N.A.	2.4E-6	6.9E-9	N.A.	N.A.	N.A.	N.A.	N.A.	N.A.
8 - 10S	1.8E-8	2.3E-9	8.9E-9	5.6E-10	N.A.	N.A.	-	-	N.A.	N.A.	N.A.	N.A.	N.A.	N.A.
9 - 10S	6.9E-9	2.2E-9	7.1E-9	6.2E-10	N.A.	N.A.	2.2E-6	2.2E-8	N.A.	N.A.	N.A.	N.A.	N.A.	N.A.
10 - 10S	3.9E-8	1.5E-9	1.6E-8	3.9E-10	N.A.	N.A.	-	-	N.A.	N.A.	N.A.	N.A.	N.A.	N.A.
11 - 10S	8.4E-9	6.0E-9	4.0E-9	1.2E-9	N.A.	N.A.	2.2E-7	6.9E-9	N.A.	N.A.	N.A.	N.A.	N.A.	N.A.
12 - 10S	1.6E-8	9.9E-9	-	-	N.A.	N.A.	7.4E-6	2.4E-8	N.A.	N.A.	N.A.	N.A.	N.A.	N.A.
13 - 10S	2.9E-8	8.1E-9	4.4E-9	1.6E-9	N.A.	N.A.	1.5E-5	1.5E-8	N.A.	N.A.	N.A.	N.A.	N.A.	N.A.
14 - 10S	1.5E-8	4.4E-9	8.6E-9	9.2E-10	N.A.	N.A.	6.4E-6	1.2E-8	N.A.	N.A.	N.A.	N.A.	N.A.	N.A.
15 - 10S	3.3E-8	6.4E-9	1.3E-8	3.2E-9	N.A.	N.A.	6.0E-6	8.8E-8	N.A.	N.A.	N.A.	N.A.	N.A.	N.A.
16 - 10S	7.4E-8	3.1E-9	1.7E-8	1.5E-9	N.A.	N.A.	-	-	N.A.	N.A.	N.A.	N.A.	N.A.	N.A.
18 - 10S	-	-	-	-	N.A.	N.A.	-	-	N.A.	N.A.	N.A.	N.A.	N.A.	N.A.
19 - 10S	1.8E-8	5.9E-9	7.0E-9	2.6E-9	N.A.	N.A.	2.5E-5	9.3E-8	N.A.	N.A.	N.A.	N.A.	N.A.	N.A.
20 - 10S	2.8E-8	5.8E-9	6.6E-9	3.3E-9	N.A.	N.A.	2.3E-5	1.2E-7	N.A.	N.A.	N.A.	N.A.	N.A.	N.A.
21 - 10S	-	-	-	-	N.A.	N.A.	-	-	N.A.	N.A.	N.A.	N.A.	N.A.	N.A.
1 - 11L	1.6E-8	1.8E-9	6.4E-8	5.4E-9	N.A.	N.A.	-	-	N.A.	N.A.	N.A.	N.A.	N.A.	N.A.
2 - 11L	-	-	-	-	N.A.	N.A.	2.0E-7	3.8E-9	N.A.	N.A.	N.A.	N.A.	N.A.	N.A.
3 - 11L	6.8E-8	8.0E-9	5.5E-8	2.7E-8	N.A.	N.A.	3.5E-6	4.2E-9	N.A.	N.A.	N.A.	N.A.	N.A.	N.A.
4 - 11L	-	-	9.1E-8	1.1E-8	N.A.	N.A.	1.6E-6	2.6E-9	N.A.	N.A.	N.A.	N.A.	N.A.	N.A.
5 - 11L	7.3E-8	7.5E-9	1.7E-7	3.0E-8	N.A.	N.A.	7.6E-6	1.5E-8	N.A.	N.A.	N.A.	N.A.	N.A.	N.A.
6 - 11L	8.1E-8	1.2E-8	9.1E-8	5.0E-8	N.A.	N.A.	5.9E-6	7.6E-9	N.A.	N.A.	N.A.	N.A.	N.A.	N.A.
7 - 11L	-	-	2.4E-7	2.9E-8	N.A.	N.A.	2.4E-6	5.3E-9	N.A.	N.A.	N.A.	N.A.	N.A.	N.A.
8 - 11L	2.4E-8	2.2E-8	1.1E-7	2.9E-8	N.A.	N.A.	1.1E-5	8.9E-9	N.A.	N.A.	N.A.	N.A.	N.A.	N.A.
9 - 11L	-	-	1.2E-7	4.2E-8	N.A.	N.A.	1.7E-6	1.0E-8	N.A.	N.A.	N.A.	N.A.	N.A.	N.A.
10 - 11L	-	-	4.8E-8	4.1E-8	N.A.	N.A.	5.3E-6	1.1E-8	N.A.	N.A.	N.A.	N.A.	N.A.	N.A.
11 - 11L	-	-	7.8E-8	5.3E-8	N.A.	N.A.	1.3E-6	1.3E-8	N.A.	N.A.	N.A.	N.A.	N.A.	N.A.
12 - 11L	-	-	1.9E-7	5.9E-8	N.A.	N.A.	1.1E-5	1.6E-8	N.A.	N.A.	N.A.	N.A.	N.A.	N.A.
14 - 11L	9.0E-8	3.7E-8	1.5E-7	4.9E-8	N.A.	N.A.	2.4E-6	1.1E-8	N.A.	N.A.	N.A.	N.A.	N.A.	N.A.
17 - 11L	9.5E-9	3.0E-9	1.9E-9	9.2E-10	2.2E-8	2.0E-10	-	-	-	-	-	-	-	
18 - 11L	7.7E-9	3.6E-9	4.2E-9	1.2E-9	6.8E-9	2.5E-10	2.3E-6	3.5E-9	2.7E-7	1.4E-8	2.9E-2	1.3E-2	338.3	12.3
19 - 11L	1.1E-8	1.9E-9	4.0E-9	6.0E-10	3.3E-9	4.8E-11	9.4E-7	1.7E-9	-	-	-	-	281.9	4.1
20 - 11L	2.2E-8	2.8E-9	3.9E-9	9.3E-10	2.4E-8	1.0E-10	-	-	-	-	-	-	-	-
21 - 11L	1.8E-8	5.5E-9	3.8E-9	1.8E-9	1.0E-8	2.3E-10	3.4E-6	7.0E-9	2.9E-7	9.1E-9	6.4E-2	1.9E-2	325.8	7.3
23 - 11L	1.7E-8	5.3E-9	1.8E-8	1.9E-9	2.3E-8	2.2E-10	7.1E-6	7.2E-9	1.3E-7	1.7E-9	1.3E-1	4.1E-2	304.1	2.8
24 - 11L	-	-	1.1E-8	2.1E-9	4.5E-10	1.7E-10	1.8E-7	3.6E-9					-	-
25 - 11L	1.4E-8	5.6E-9	5.9E-9	2.4E-9	9.0E-9	2.5E-10	2.8E-6	4.2E-9	9.7E-8	3.7E-9	1.4E-1	5.8E-2	309.3	8.5
26 - 11L	-	-	-	-	8.4E-9	3.6E-10	2.0E-6	8.9E-9	-	-	-	-	242.1	10.5
27 - 11L	2.0E-8	6.3E-9	1.9E-8	2.5E-9	2.2E-9	2.2E-10	6.4E-7	5.0E-9	-	-	-	-	296.7	30.0
28 - 11L	1.2E-8	1.3E-9	2.2E-9	4.5E-10	1.2E-8	5.6E-11	-	-	-	-	-	-	-	-
29 - 11L	2.4E-9	7.0E-10	5.3E-10	1.5E-10	1.3E-9	8.8E-12	3.8E-7	5.3E-10	9.7E-9	9.8E-11	2.4E-1	7.2E-2	306.3	2.2
30 - 11L	6.2E-9	9.4E-10	2.1E-9	1.9E-10	4.6E-9	3.4E-11	1.3E-6	8.7E-10	-	-	-	-	286.8	2.1
31 - 11L	1.3E-9	7.4E-10	4.9E-10	1.5E-10	6.2E-11	6.5E-12	7.9E-9	2.1E-10	-	-	-	-	128.4	13.9
32 - 11L	3.2E-9	1.2E-9	9.8E-10	2.5E-10	6.5E-11	1.5E-11	1.4E-8	3.1E-10	-	-	-	-	208.7	48.4
33 - 11L	1.7E-9	9.3E-10	2.9E-10	2.0E-10	5.7E-11	8.1E-12	1.0E-8	2.8E-10	-	-	-	-	181.1	26.3
34 - 11L	4.3E-9	8.9E-10	1.1E-9	1.9E-10	6.5E-10	1.5E-11	2.0E-7	3.1E-10	-	-	-	-	299.6	7.1
35 - 11L	6.8E-9	1.5E-9	1.0E-9	3.4E-10	7.8E-9	8.0E-11	2.2E-6	1.2E-9	-	-	-	-	285.1	2.9

Data are expressed as cc/g STP. Analytical uncertainties are at 1σ level. N.A. = Data not available. Empty spaces indicate data not included in this section with negative values of 1σ >100 % (see 4.5.3.1).

Table 4.7 NG abundances and isotopic ratios of sample KS16-13.

Sample N°	^{4}He	±	^{22}Ne	±	^{36}Ar	±	^{40}Ar	±	$^{40}Ar^{*}$	±	$^{4}He/^{40}Ar^{*}$	±	$^{40}Ar/^{36}Ar$	±
2 - 4L	2.0E-8	1.1E-9	7.5E-8	1.1E-9	N.A.	N.A.	-	-	N.A.	N.A.	N.A.	N.A.	N.A.	N.A.
3 - 4L	3.2E-8	1.2E-8	1.2E-8	1.8E-9	N.A.	N.A.	3.1E-6	8.5E-8	N.A.	N.A.	N.A.	N.A.	N.A.	N.A.
4 - 4L	3.3E-8	9.0E-9	5.5E-8	1.8E-9	N.A.	N.A.	3.5E-6	6.8E-8	N.A.	N.A.	N.A.	N.A.	N.A.	N.A.
5 - 4L	2.4E-8	3.1E-9	9.8E-9	5.1E-10	N.A.	N.A.	9.9E-7	2.2E-8	N.A.	N.A.	N.A.	N.A.	N.A.	N.A.
6 - 4L	-	-	4.7E-9	1.4E-9	N.A.	N.A.	4.2E-7	5.1E-8	N.A.	N.A.	N.A.	N.A.	N.A.	N.A.
7 - 4L	-	-	8.0E-9	1.5E-9	N.A.	N.A.	3.8E-7	6.8E-8	N.A.	N.A.	N.A.	N.A.	N.A.	N.A.
8 - 4L	-	-	8.4E-9	1.8E-9	N.A.	N.A.	3.2E-8	3.1E-9	N.A.	N.A.	N.A.	N.A.	N.A.	N.A.
9 - 4L	-	-	8.0E-9	1.3E-9	N.A.	N.A.	-	-	N.A.	N.A.	N.A.	N.A.	N.A.	N.A.
10 - 4L	-	-	7.0E-9	5.0E-9	N.A.	N.A.	9.0E-7	8.5E-9	N.A.	N.A.	N.A.	N.A.	N.A.	N.A.
11 - 4L	-	-	1.1E-8	2.5E-9	N.A.	N.A.	6.9E-8	3.9E-9	N.A.	N.A.	N.A.	N.A.	N.A.	N.A.
12 - 4L	-	-	-	-	N.A.	N.A.	8.9E-8	2.6E-9	N.A.	N.A.	N.A.	N.A.	N.A.	N.A.
13 - 4L	-	-	-	-	N.A.	N.A.	7.6E-7	5.5E-9	N.A.	N.A.	N.A.	N.A.	N.A.	N.A.
14 - 4L	2.9E-8	8.0E-10	7.7E-9	3.0E-10	3.6E-8	2.4E-10	-	-	-	-	-	-	-	-
15 - 4L	2.5E-8	2.9E-9	6.7E-9	5.8E-10	5.3E-8	3.0E-10	-	-	-	-	-	-	-	-
16 - 4L	-	-	5.6E-9	6.9E-10	5.2E-9	1.2E-10	1.6E-6	2.5E-9	4.3E-8	1.4E-9			306.9	7.1
17 - 4L	8.5E-9	3.6E-9	3.5E-9	6.8E-10	2.4E-9	4.4E-11	6.9E-7	2.8E-9	-	-	-	-	286.8	5.3
18 - 4L	8.3E-9	1.2E-9	4.1E-9	2.6E-10	2.4E-8	6.3E-11	-	-	-	-	-	-	-	-
20 - 4L	7.0E-9	2.1E-9	-	-	1.7E-9	3.5E-11	5.3E-7	1.8E-9	2.0E-8	5.8E-10	3.5E-1	1.0E-1	310.3	6.4
21 - 4L	1.7E-8	3.4E-9	4.0E-9	1.2E-9	2.4E-9	1.3E-10	7.7E-7	1.3E-8	4.8E-8	3.8E-9	3.6E-1	7.8E-2	318.1	18.3
22 - 4L	5.0E-9	2.8E-9	4.8E-9	8.6E-10	9.7E-10	8.1E-11	3.6E-7	1.0E-8	7.0E-8	8.6E-9	7.2E-2	4.1E-2	370.9	32.9
1 - 10L	1.6E-8	1.5E-9	8.3E-9	7.8E-10	-	N.A.	-	-	N.A.	N.A.	N.A.	N.A.	N.A.	N.A.
2 - 10L	1.1E-8	2.1E-9	3.5E-9	1.1E-9	-	N.A.	-	-	N.A.	N.A.	N.A.	N.A.	N.A.	N.A.
3 - 10L	1.8E-8	4.6E-9	5.3E-9	2.6E-9	-	N.A.	-	-	N.A.	N.A.	N.A.	N.A.	N.A.	N.A.
4 - 10L	2.0E-8	2.7E-9	-	-	-	N.A.	6.1E-6	3.0E-8	N.A.	N.A.	N.A.	N.A.	N.A.	N.A.
5 - 10L	1.4E-8	2.5E-9	4.3E-9	1.4E-9	-	N.A.			N.A.	N.A.	N.A.	N.A.	N.A.	N.A.
7 - 10L	-	-	1.7E-8	2.2E-9	-	N.A.	4.2E-6	3.7E-8	N.A.	N.A.	N.A.	N.A.	N.A.	N.A.
8 - 10L	8.4E-9	5.2E-9	7.3E-9	1.2E-9	-	N.A.	3.4E-7	3.5E-9	N.A.	N.A.	N.A.	N.A.	N.A.	N.A.
9 - 10L	1.1E-8	6.3E-9	1.1E-8	1.6E-9	-	N.A.	3.1E-6	1.2E-8	N.A.	N.A.	N.A.	N.A.	N.A.	N.A.
10 - 10L	-	-	8.4E-9	1.1E-9	-	N.A.	5.1E-6	1.3E-8	N.A.	N.A.	N.A.	N.A.	N.A.	N.A.
11 - 10L	-	-	1.0E-8	2.0E-9	-	N.A.	8.5E-7	5.3E-9	N.A.	N.A.	N.A.	N.A.	N.A.	N.A.
12 - 10L	6.6E-9	3.5E-9	1.5E-9	9.2E-10	-	N.A.	2.1E-7	2.3E-9	N.A.	N.A.	N.A.	N.A.	N.A.	N.A.
13 - 10L	-	-	-	-	-	N.A.	3.2E-7	6.3E-9	N.A.	N.A.	N.A.	N.A.	N.A.	N.A.
15 - 10L	2.7E-9	8.1E-10	3.3E-9	5.6E-10	2.1E-9	3.2E-11	7.1E-7	6.3E-10	7.1E-8	1.5E-9	3.8E-2	1.1E-2	331.9	5.0
16 - 10L	-	-	4.3E-9	2.2E-9	1.5E-9	7.2E-11	4.4E-7	1.8E-9	-	-	-	-	295.1	14.4
17 - 10L	-	-	-	-	1.2E-8	3.0E-10	3.6E-6	9.6E-9	-	-	-	-	295.3	7.4
18 - 10L	2.2E-8	1.2E-9	6.3E-9	6.9E-10	4.0E-8	1.9E-10	-	-	-	-	-	-	-	-
19 - 10L	-	-	-	-	2.5E-9	8.7E-11	7.4E-7	1.8E-9	-	-	-	-	292.7	10.1
20 - 10L	1.3E-8	5.2E-9	-	-	1.5E-9	1.3E-10	3.9E-7	2.9E-9	-	-	-	-	253.7	21.8
21 - 10L	7.8E-9	8.9E-10	3.2E-9	5.9E-10	1.2E-8	1.7E-10	3.7E-6	2.4E-9	2.0E-8	4.0E-10	3.8E-1	4.4E-2	300.2	4.2

Data are expressed as cc/g STP. Analytical uncertainties are at 1σ level. N.A. = Data not available. Empty spaces indicate data not included in this section with negative values of 1σ > 100 % (see 4.5.3.1).

4.5 Discussion

4.5.1 NG variations in Pele's hairs and tears

Combining all the available data it is clear that Pele's hairs and tears in this study have retained NG, in different concentrations and proportions, after their eruption. These vary independently of the shape of the particles.

Looking at the relative abundance of ^{4}He and ^{22}Ne it is possible to recognise two possible main trends that correlate particles with different gas concentrations (Figure 4.23A). Trend 1 has a slope of 3.16 while Trend 2 has a lower slope of 0.64. Correlation coefficients between ^{4}He and ^{22}Ne are 0.90 for both trends. Only a few particles seem to have a more random distribution deviating from the trending lines (Figure 4.23B).

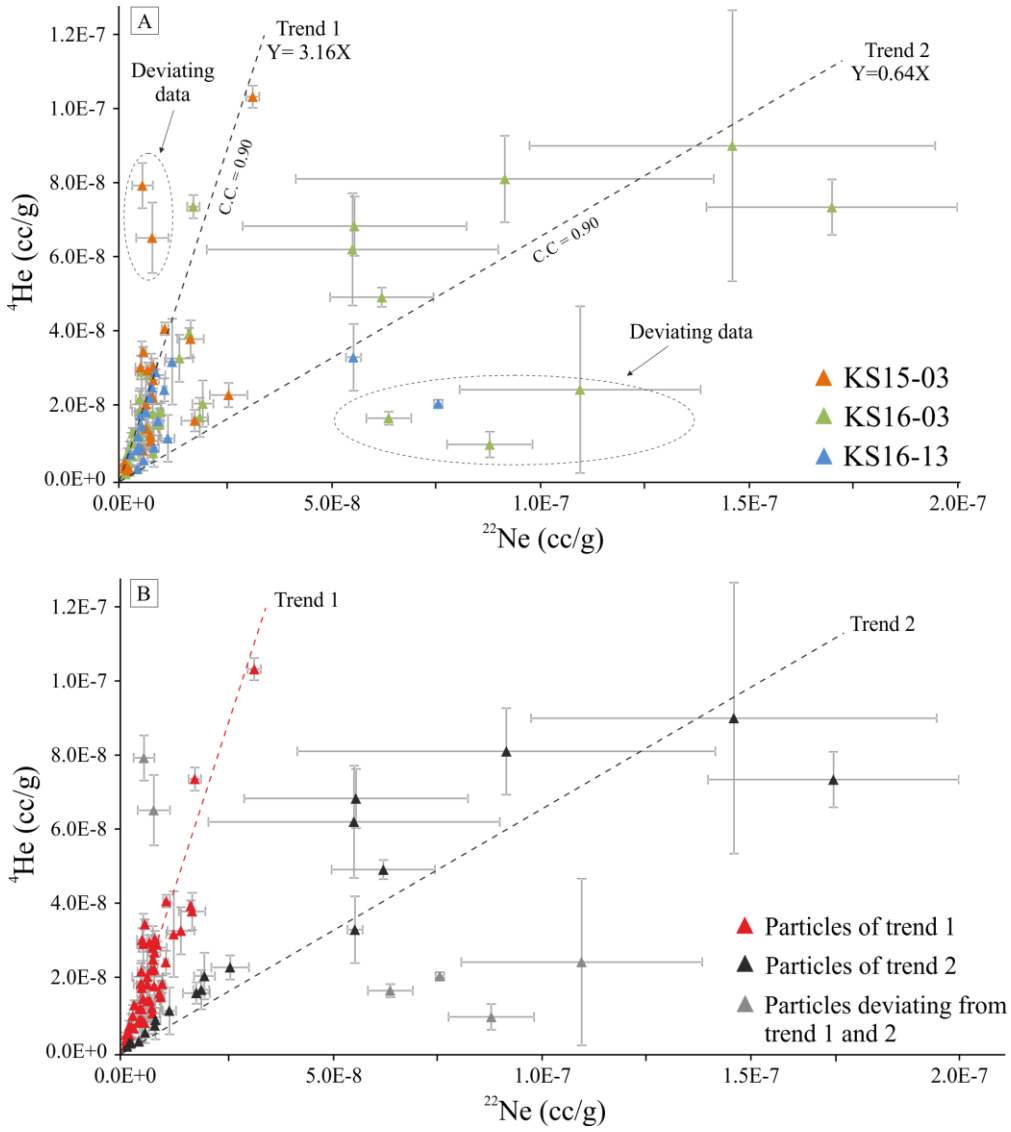

Figure 4.23 A - Variations of the ^{4}He and ^{22}Ne abundances in the analysed samples. Dotted lines indicate two probable trends that correlate the two observed data. Dotted circles refer to isolated particles that are not included in trend 1 and 2. Correlation coefficients (C.C) are of 0.90 revealing a strong positive correlation of the data. B - In different colours those particles belonging to trend 1 and 2. Error bars for A and B are at the 1σ level. If not visible the error bars are smaller than the size of the symbol used to display the data.

Analysing the data in more detail, identifies a separation between particles that have ^{4}He content lower than $4.5E^{-8}$ cc/g and those with higher ^{4}He values. Similarly, particles with ^{22}Ne concentrations higher than $4.0E^{-8}$ cc/g are distinct from those having lower concentrations. From these observations it is possible to split the particles into four groups each of them with a specific and distinct gas compositions (Figure 4.24 A - B):

- Group A has low ^{4}He ($<4.5E^{-8}$ cc/g) and low ^{22}Ne ($<4.0E^{-8}$ cc/g).
- Group B has high ^{4}He ($>4.5E^{-8}$ cc/g) and high ^{22}Ne ($>4.0E^{-8}$ cc/g).
- Group C has high ^{4}He ($>4.5E^{-8}$ cc/g) and low ^{22}Ne ($<4.0E^{-8}$ cc/g).
- Group D has low ^{4}He ($<4.5E^{-8}$ cc/g) and high ^{22}Ne ($>4.0E^{-8}$ cc/g).

Based on this division KS15-03 displays particles belonging to group A and C, KS16-03 has a more variable composition with particles falling in all four groups while KS16-13 has particles falling only in Group A and D.

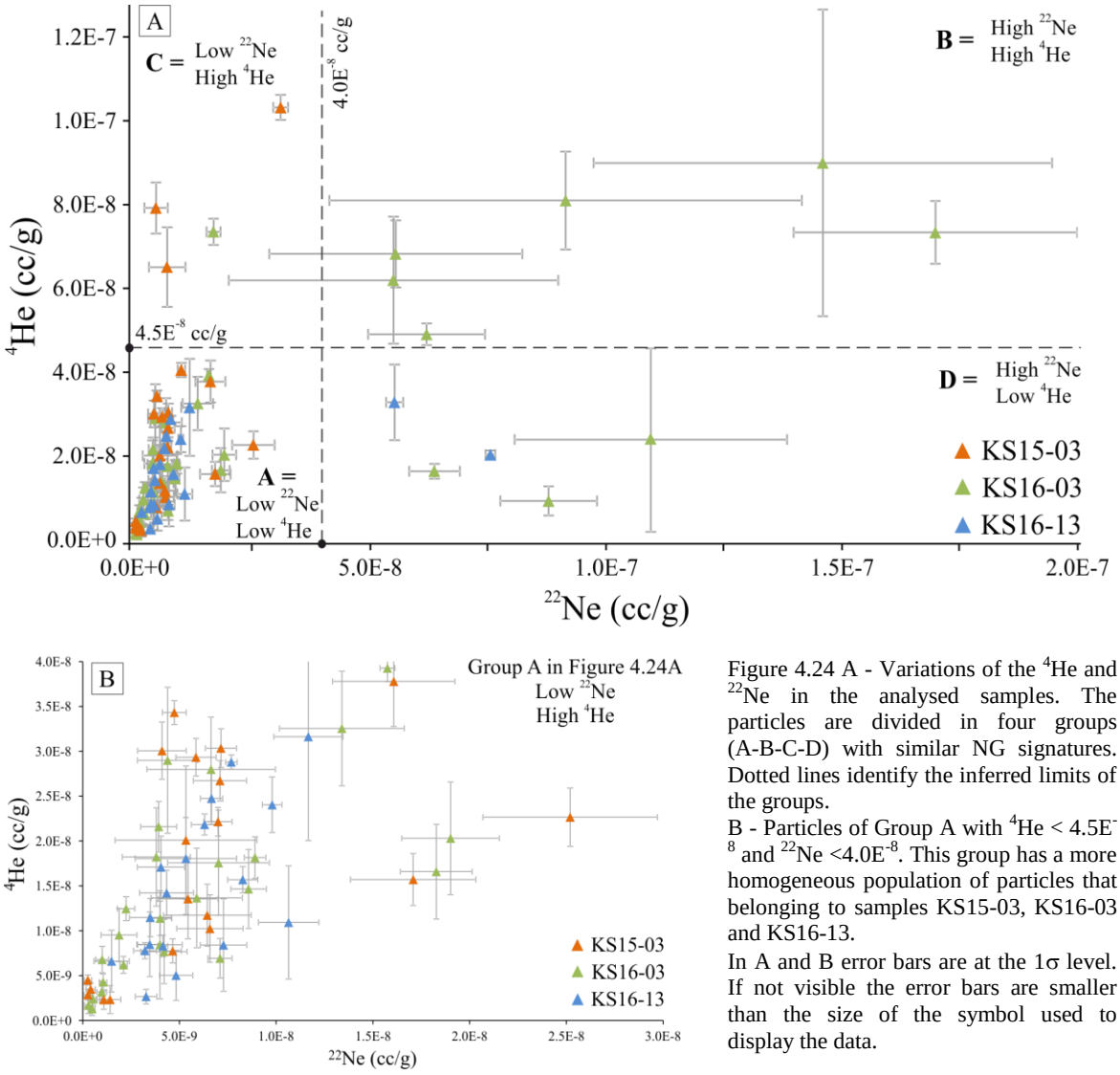

Figure 4.24 A - Variations of the ^{4}He and ^{22}Ne in the analysed samples. The particles are divided in four groups (A-B-C-D) with similar NG signatures. Dotted lines identify the inferred limits of the groups.
B - Particles of Group A with $^{4}He < 4.5E^{-8}$ and $^{22}Ne < 4.0E^{-8}$. This group has a more homogeneous population of particles that belonging to samples KS15-03, KS16-03 and KS16-13.
In A and B error bars are at the 1σ level. If not visible the error bars are smaller than the size of the symbol used to display the data.

Because ^{36}Ar abundances were not measured for particles of Group B, C and D the following paragraphs will focus only on some particles of Group A for those ^{36}Ar was measured. Despite the homogeneity of this group with respect to ^{4}He and ^{22}Ne content, when ^{40}Ar* and ^{4}He/^{40}Ar* ratios are taken in account it is possible to distinguish three populations of particles with distinct NG signatures:

- Population 1 has ^{4}He/^{40}Ar* ratios > 0.2 and ^{40}Ar* content < 5.0E^{-8} cc/g.
- Population 2 has ^{4}He/^{40}Ar* < 0.15 and ^{40}Ar* content > 7.0E^{-8} Cc/g.
- Population 3 has ^{4}He/^{40}Ar* < 0.07 and ^{40}Ar* content > 2.5E^{-7} Cc/g

KS15-03 has only particles that belong to Population 1 (Figure 4.25); KS16-03 has the highest spread in the data with particles belonging to Population 1, Population 2 and Population 3 (Figure 4.25); KS15-13 shows particles with NG signatures of Population 1 and 2 (Figure 4.25).

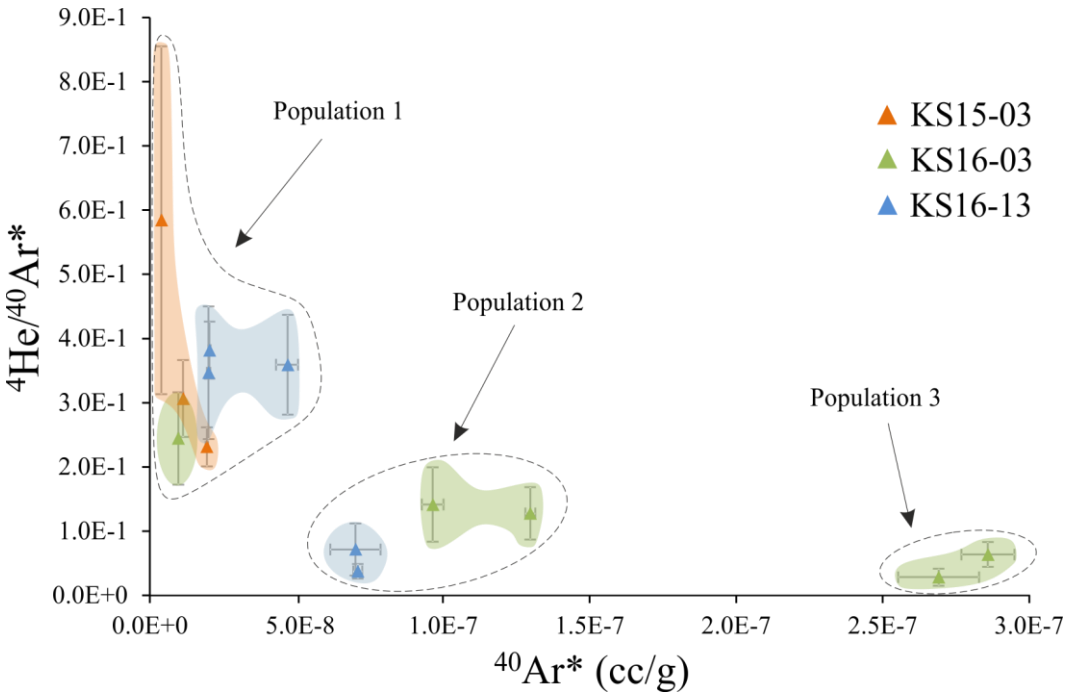

Figure 4.25 Variations of the ^{4}He/^{40}Ar* ratios with respect to ^{40}Ar* abundances. Populations 1, 2 and 3 indicate particles having similar NG composition (see text for explanations). Error bars are at the 1σ level.

Glasses erupted in 2015 (KS15-03) show a uniform composition (Composition 1) while samples erupted in 2016 (KS16-03, KS16-13) display a trimodal distribution. Some particles have NG signatures similar to those glasses erupted in 2015 (Composition 1) while others display a distinctive NG content characterised by lower $^{4}He/^{40}Ar^{*}$ ratios and higher $^{40}Ar^{*}$ content (Composition 2A and 2B) (Figure 4.26).

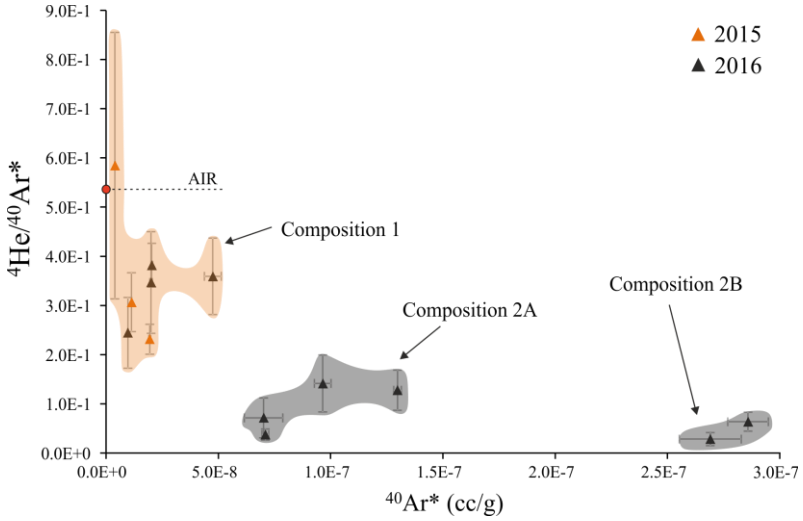

Figure 4.26 Variations of $^{4}He/^{40}Ar^{*}$ with respect to $^{40}Ar^{*}$. The data are divided by year of collection of the samples. Generally speaking, particles collected in 2015 display lower $^{40}Ar^{*}$ and higher $^{4}He/^{40}Ar^{*}$ ratios than those collected in 2016. Some particles collected in 2016 have the same $^{40}Ar^{*}$ content and $^{4}He/^{40}Ar^{*}$ ratios of particles sampled in 2015. Error bars are at the 1σ level. The red dot indicated the He/Ar ratio of the air.

Individual particles display various $^{40}Ar/^{36}Ar$ ratios and ^{36}Ar contents (Figure 4.27). At the 2σ level, KS15-03 and KS16-03 display sub-atmospheric, atmospheric and supra-atmospheric $^{40}Ar/^{36}Ar$ ratios while KS16-13 has only particles with atmospheric and supra-atmospheric $^{40}Ar/^{36}Ar$ ratios. ^{36}Ar is extremely variable in samples KS15-03 and KS16-03 while it is less dispersed for KS16-13.

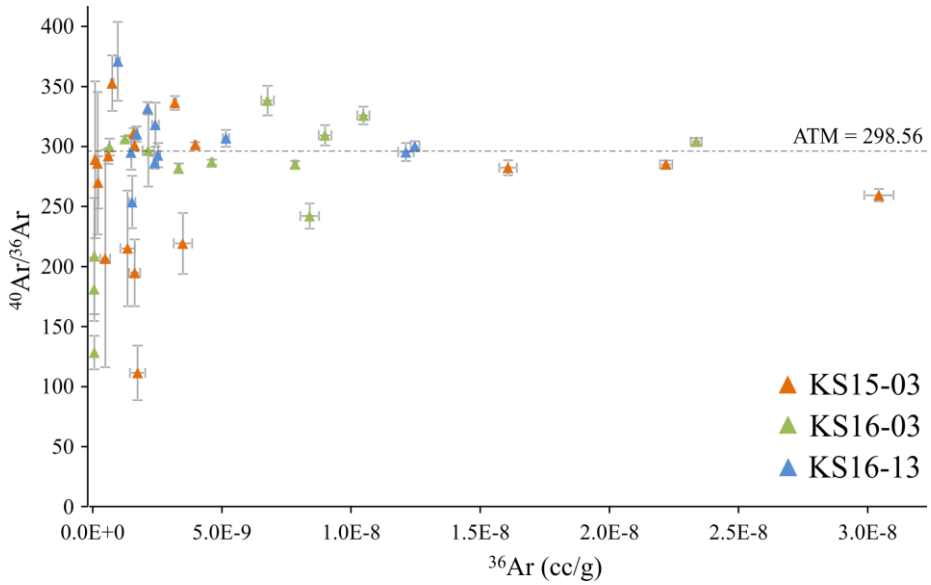

Figure 4.27 Variations of the $^{40}Ar/^{36}Ar$ ratios and ^{36}Ar abundances in samples KS15-03, KS16-03 and KS16-13. It is evident that the particles display sub-atmospheric, atmospheric and supra-atmospheric $^{40}Ar/^{36}Ar$ ratios. Error bars are at the 1σ level. ATM is the $^{40}Ar/^{36}Ar$ ratio of the atmosphere and it is equal to 298.56 (Lee et al., 2006).

When the $^{40}Ar/^{36}Ar$ ratios are plotted against the $^{4}He/^{36}Ar$ ratios it is possible to observe how those data with $^{40}Ar/^{36}Ar$ ratios lower than 200 have also high $^{4}He/^{36}Ar$ ratios (> 13) (Figure 4.28 A). A negative correlation between the two ratios exists for samples KS15-03 and KS16-03. In a correlative graph where the $^{40}Ar/^{36}Ar$ ratios are plotted against the $^{22}Ne/^{36}Ar$ ratios only a weak negative correlation can be observed between the two ratios (Figure 4.28 B). For all the three samples a positive correlation exists between the $^{4}He/^{36}Ar$ and the $^{22}Ne/^{36}Ar$ ratios (Figure 4.28 C).

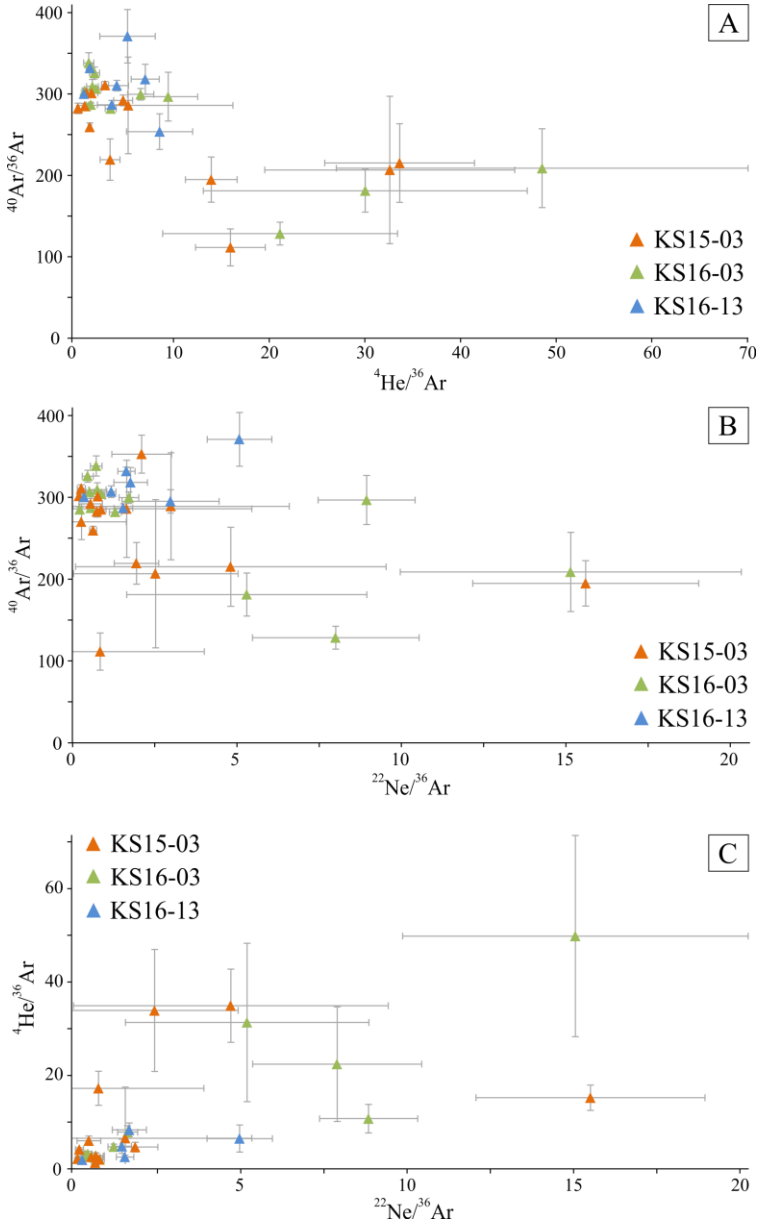

Figure 4.28 Variations of the $^{40}Ar/^{36}Ar$ ratios with respect to $^{4}He/^{36}Ar$ ratios (A) and to $^{22}Ne/^{36}Ar$ ratios (B) in samples KS15-03, KS16-03 and KS16-13. Error bars are at the 1σ level. $^{40}Ar/^{36}Ar$ ratio of 298.5 correspond to the atmospheric value (Lee et al., 2006). C - Variations of the $^{4}He/^{36}Ar$ ratios with respect to $^{22}Ne/^{36}Ar$ ratios. Here, it is clear a positive correlation for all the samples (KS15-03, KS16-03 and KS16-13) between the two isotopic ratios.

In Figure 4.29 (A - B) the ^{4}He and ^{22}Ne isotopes are plotted against the ^{36}Ar in order to investigate in more detail the relationships between the three isotopes. For all the samples some particles display high ^{22}Ne and ^{4}He abundances and high amount of ^{36}Ar while others have high ^{22}Ne and ^{4}He content and low ^{36}Ar abundances or low ^{22}Ne and ^{4}He and progressively high ^{36}Ar content.

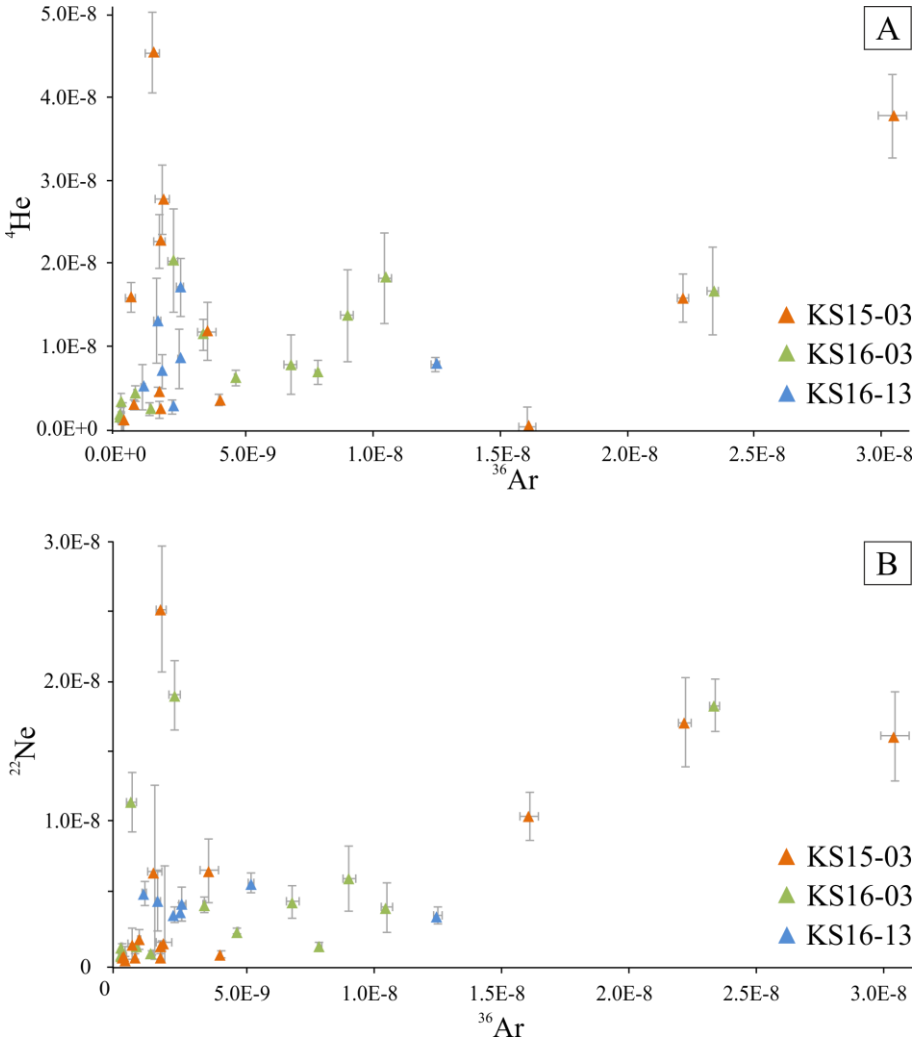

Figure 4.29 Variations of the ^{4}He (A) and ^{22}Ne (B) abundances with respect to ^{36}Ar ratios in samples KS15-03, KS16-03 and KS16-13. Error bars are at the 1σ level.

4.5.2 Reliability of NG data

Because the samples have been collected in different periods of time and analysed after 1 – 2 years after their eruption there is the possibility that the observed $^{4}He/^{40}Ar^{*}$ ratios have been influenced by ^{4}He loss prior to the analyses.

When the date of the analyses and the $^{4}He/^{40}Ar^{*}$ ratios are visualized in the same graphs it is clear that no correlation exists between these factors: samples collected and analysed in different periods of time have comparable $^{4}He/^{40}Ar^{*}$ ratios (see yellow circle in Figure 4.30) as well as samples collected and analysed at the same time have different isotopic ratios (see sample KS16-03 and KS16-13 in Figure 4.30). From this consideration it is possible to assert that the $^{4}He/^{40}Ar^{*}$ ratios have not been influenced by any major ^{4}He loss after the eruption and, for this reason the data can be considered reliable. If ^{4}He loss has occurred it has had only minimal impact on actual $^{4}He/^{40}Ar^{*}$ ratios.

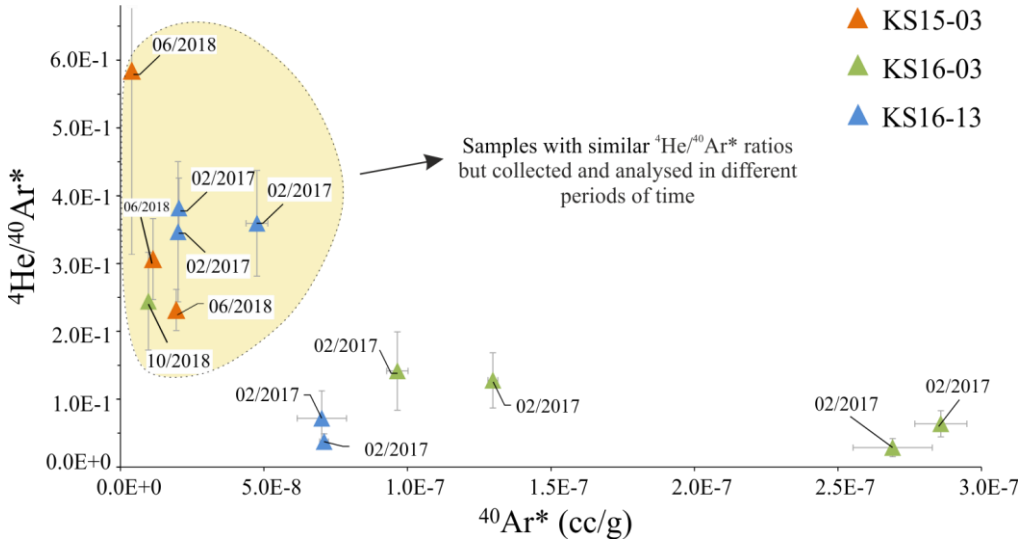

Figure 4.30 Comparison between date of the analyses of the samples and $^{4}He/^{40}Ar^{*}$ ratios. No correlation can be observed between these factors.

A major problem that could affect the reliability of the data get from Pele's hairs and tears is related to the determination of the $^{40}Ar^{*}$. Atmospheric correction is always done in order to derive the $^{40}Ar^{*}$ content of a sample from the measured ^{36}Ar and ^{40}Ar.

When this correction is done for submarine glasses from MORBs and OIBs, which have $^{40}Ar/^{36}Ar$ ratios hundreds / thousands times higher the atmospheric value (e.g. Burnard, 1999, data in Moreira and Kurz, 2013), it does affect only to a lesser extent the interpretation of the data and the calculation of the absolute concentration of the $^{40}Ar^{*}$.

For subaerial volcanic glasses, which have undergone more extensive degassing and Ar mass fractionation, the $^{40}Ar/^{36}Ar$ ratios can be only slightly higher than the atmosphere (this study section 4.3.5.5 and 4.5.1). This creates a problem when the $^{40}Ar^{*}$ abundances

are calculated from the samples and interpreted in the context of magmatic degassing. This is because the atmospheric correction is done on the absolute number given by the $^{40}Ar/^{36}Ar$ ratios without taking into account the analytical uncertainty in the ratios. In this way, a portion of the information provided with the analyses is lost and even samples that display $^{40}Ar/^{36}Ar$ ratios slightly above the atmospheric value of 298.56 (Lee et al., 2006) with elevated 1σ uncertainty will result to have retained $^{40}Ar^*$.

Without critically discussing the analytical uncertainties associated to the $^{40}Ar/^{36}Ar$ ratios in the context of atmospheric correction it is impossible to determine if the variations of the $^{40}Ar^*$ (and $^{4}He/^{40}Ar^*$ ratios) in subaerial volcanic glass are real or related only to a correction artefact.

In section 4.5.1 the $^{40}Ar^*$ values and $^{4}He/^{40}Ar^*$ ratios obtained from pumice glasses in this study are discussed and presented simply applying a pure atmospheric correction ignoring the analytical uncertainties associated to the calculated $^{40}Ar/^{36}Ar$ ratios.

When the $^{40}Ar/^{36}Ar$ ratios with absolute value higher than air are considered at the 1σ level only one sample (N° 21 – KS16-13_10L) has a ratio of atmospheric value within error. Excluding this data from the interpretation, the considerations done in previous section about the variations of the $^{40}Ar^*$ content and $^{4}He/^{40}Ar^*$ ratios in the glassy particles are still valid. When the data are considered at the 2σ level the hyperbolic trend observed when the $^{4}He/^{40}Ar^*$ ratios are plotted against $^{40}Ar^*$ still exists (Figure 4.31) as well as the existence of 2 different NG compositions (2015-like and 2016-like).

All this evidence supports the idea that the variations in the $^{40}Ar^*$ and $^{4}He/^{40}Ar^*$ ratios of Pele's hairs and tears from Masaya volcano are real and not due to an artefact related to a pure atmospheric correction. The data are reliable and can be discussed in the context of volcanic degassing.

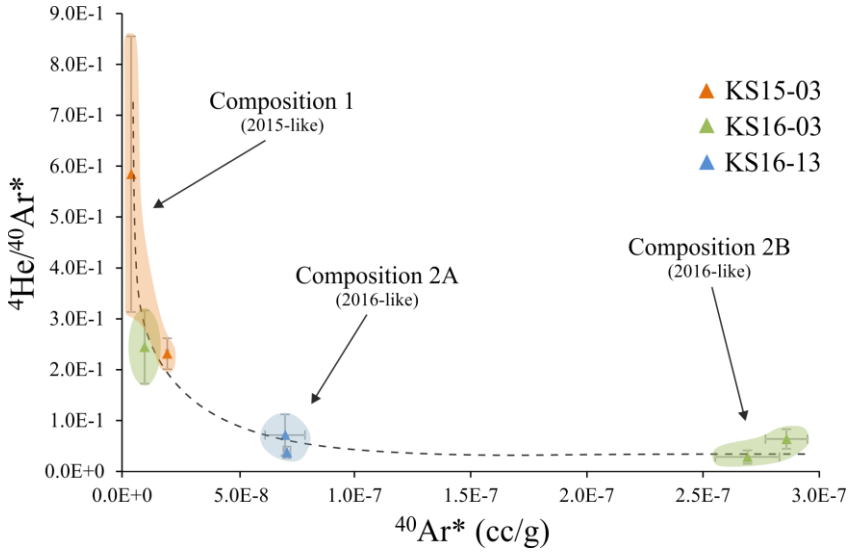

Figure 4.31 Variation of the $^{40}Ar^*$ and $^{4}He/^{40}Ar^*$ in samples having $^{40}Ar/^{36}Ar$ ratio above the atmospheric value of 298.56 (Lee et al., 2006) even at the 2σ level.

4.5.3 Factors controlling NG abundance in Pele's hairs and tears

Before starting to discuss the NG data in the context of magmatic degassing it is necessary to carefully evaluate what other factors could have controlled their abundance in Pele's hairs and tears.

During magmatic processes NG behave as incompatible trace elements preferentially partitioning into melt and bubbles rather than into the crystalline phase (Ozima and Podosek, 2002). Despite this, minerals can retain NG in different concentrations in specific sites such as lattice vacancy defects, crystal boundaries, crystal-melt interfaces and fluid and melt inclusions (Kelley et al., 1986; Brooker et al., 1998; Kelley, 2002). For this reason, any variation in the crystal content of the Pele's hairs and tears must be critically evaluated.

From thin section observations and back-scattered images no differences in crystal abundances were detected in samples collected in subsequent periods of time. The majority of the particles (~ 99%) are crystal free with only a few of them having isolated micro-crystals (see section 4.5.1). With this in mind, I suggest that the amount of NG derived from the crystals can be considered negligible with respect to the total gas trapped into the glass and bubbles. Because the particles are not always transparent it was not possible to detect micro-crystals during sample preparation. Moreover, Because the NG analyses were done by single grain total fusion (see Chapter 2 section 2.3.4.2) it is not possible to separately plot data obtained from crystal-free and crystal bearing particles. For this reason, it is only possible to hypothesize that any large contribution of NG coming from the minerals would result in a distinct NG signature completely different, and thus identifiable, from that which is derived from crystal-free particles.

Another factor that could have influenced the abundance of the NG in Pele's hairs and tears is related to glass chemistry variations.

It has been demonstrated that the solubility of the NG in silicate melt is strictly dependant on the amount of volatiles (H_2O and CO_2) dissolved into the magma (Nuccio and Paonita, 2000) and on the melt chemical composition (Jambon et al., 1986; Lux, 1987; Carroll and Webster, 1994; Carroll and Stolper, 1993). In particular, significant variations of Si, Al and of other network-modifier cations (Ca, K, Mg, Na) can affect the ability of the melt to host NG (Shibata et al., 1998) modifying the number of vacant sites available for NG incorporation (ionic porosity – Carrol and Stolper, 1993).

On a minor scale, post-eruptive alteration and hydration of the glass due to weathering (Fisher and Schmincke, 1984) and/or due to the interaction of the glass with acidic volcanic gases (Spadaro et al., 2002; Moune et al., 2007) can modify the chemistry of the

glass. These processes can favour glass devitrification and the formation of secondary minerals (e.g. palagonite) causing NG loss and/or NG redistribution (Fleck et al., 1977; Cerling et al., 1985).

Pele's hairs and tears in this study have all the same composition especially with regard to Si and Al content. The results of electron microprobe analyses also show that the glass is pristine and not altered. Chemical indices of alteration are around 50 (optimal value for unaltered glass, Nesbitt and Young, 1982) and totals are of between 97.1 and 99.6 indicating only negligible alteration possibly due to minor exposure to plume acidic gases (small devitrification rims were observed in thin sections in some hairs). Based on these considerations, it is possible to exclude that the differences observed in the NG signatures of Pele's hairs and tears in this study are due to major or minor compositional variations of the glass. Because H_2O and CO_2 were not measured in this study it is not possible to comment upon any possible influence that these volatiles have had on the solubility of the NG in the considered samples.

Studies conducted on MORB glass samples have demonstrated that when vesicularity exceeds the 1% level the majority of magmatic NG reside in bubbles rather than in the melt (Carroll and Draper, 1994; Sarda and Moreira, 2002; Aubry et al., 2013). For these reasons, in order to correctly interpret the results of the NG analyses, it is important to critically evaluate possible variations in the degree of vesicularity.

In this study it is difficult to directly correlate the NG variations with the degree of vesicularity of individual Pele's hairs and tears. This is because vesicles analyses were conducted on particles prepared as thin sections and thus not suitable for NG analyses. So, the role played by the vesicles in controlling NG variations can only be discussed in the more general context of degassing processes (see section 4.5.3).

In conclusion, Pele's hairs and tears in this study have all the same chemical composition, are generally crystal free and not affected by post-eruptive alteration. For these reasons the NG abundances in the particles can be discussed only considering magmatic degassing as the primary cause of their variations.

4.5.4 NG variations in the context of magmatic degassing

NG have been frequently used to provide information on degassing histories of volcanic materials including different types of basaltic glasses (Burnard, 1999; Moreira and Sarda 2000; Sarda and Moreira 2002; Yamamoto and Burnard, 2004; Aubry et al., 2013). In this section, the results of the NG analyses are discussed in the context of magma degassing in order to unravel those processes governing NG abundances in Pele's hairs and tears from Masaya volcano. In particular, because the particles are almost crystal free it is possible to interpret the behaviour of the NG as a binary mixing between a gas phase dissolved in the glass and a gas phase in the bubbles.

When the magma migrates to the surface, as a result of a drop in pressure, volatiles (e.g. NG, CO_2, H_2O) separate from the melt forming a distinct gas phase (bubbles). According to their low solubility in silicate melts, the NG readily segregate into the newly-formed bubbles (Carroll and Draper, 1994). In this scenario, the concentration of the NG in the gas phase will be primarily determined by the original gas content of the magma and by the amount of bubbles nucleated during gas-melt separation. The higher the magma vesicularity, the greater the amount of NG partitioned into the bubbles. At vesicularity exceeding 1 vol %, the majority of the magmatic NG will reside in the bubbles instead in the melt (Carrol and Stolper, 1993). For a vesicularity equal to 1 % around 90% of Ar atoms and 40% of He atoms are in the vesicles while at vesicularity $\geq$ 10% more than 99% of Ar atoms and 90% of He atoms are trapped in the gas phase (Aubry et al., 2013).

These differences are related to the rate at which different NG fractionate in bubbles that, in turn, is strictly dependant on their relative solubilities at different pressure. NG solubilities in basaltic melt increase with decreasing atomic mass and increasing the pressure up to 5 GPa (Jambon et al. 1986; Lux, 1987; Carrol and Draper, 1994). Light NG (He, Ne) are more soluble and preferentially remain in the melt compared to heavy NG (Xe, Kr and Ar - less soluble) that preferentially partition into the bubbles (Carrol and Draper, 1994). As a result of this process, bubbles formed during subsequent stages of magma evolution, will incorporate NG with variable fractionated compositions (Burnard, 1999). At high pressure first nucleated bubbles are small and incorporate gas with a more primitive composition. As soon as they migrate upward, they incorporate volatiles through diffusion increasing their size. Vesicles formed at more surface conditions during later stages of magma evolution, with less time to grow, are smaller and are formed from the residue of the volatiles trapped in larger vesicles. These bubbles will preserve a more evolved, fractionated and probably more atmospheric contaminated NG signature (Burnard, 1999, 2001). However, if bubbles formed at high pressure reach the surface

without re-equilibrating with the surrounding magma, they will preserve the least fractionated volatiles. Under these circumstances, when the magma is erupted it will incorporate a mixture of bubbles with different NG compositions. These peculiar NG signatures will be preserved in the sample only if quenching happens really quickly, after eruption, arresting post-eruptive degassing.

This appears to have been the mechanism that operated when Pele's hairs and tears were erupted from Masaya volcano. Multiple generations of bubbles, with different NG signatures, have been trapped within the same portion of magma that, once erupted and quenched, has formed hairs and tears. In this context, the different concentrations of NG detected in individual particles could be related to different degrees of NG fractionation during degassing, and, to variations in the amount of atmospheric contamination as well as in the size of vesicles in different particles.

Variable degrees of fractionation of ^{4}He from ^{22}Ne could be responsible for the alignment of the data along trend 2 in Figure 4.23. Whereas, the alignment of the data along trend 1 can be associated to variable addition and fractionation of atmospheric-derived ^{4}He and ^{22}Ne to the particles. This observation is supported by the fact that trend 1 has a slope of 3.16 that is really close to the value of 3.14 for the $^{4}He/^{22}Ne$ ratio of air.

Because ^{36}Ar is only derived from the atmosphere it is commonly used as a proxy for atmospheric contamination. Looking at Figure 4.29 it is possible to observe that some particles display at the same time high ^{4}He, ^{22}Ne and ^{36}Ar abundances. This observation reinforces the idea that, at least for some particles, the incorporation of atmospheric derived ^{4}He and ^{22}Ne into the magma prior to eruption could be a significant phenomenon that influence the final NG composition of the samples. Data with low ^{36}Ar and high ^{4}He and ^{22}Ne could indicate particles that have incorporated bubbles that are less affected by atmospheric contamination, and thus have preserved a more primitive NG signature.

The few data deviating from the two trends in Figure 4.23 could be interpreted as the result of the incomplete equilibrium fractionation of ^{4}He and ^{22}Ne (deviating data with low ^{4}He and high ^{22}Ne) or related to a more mantle-like signature (deviating data with high ^{4}He and low ^{22}Ne). The presence of micro-crystals with a completely different NG budget, within certain particles, could also be invoked to explain these deviating data.

Such a model involving NG degassing and fractionation, atmospheric contamination and variable sample vesicularities could be valid, in terms of justifying the variations of NG abundances in single Pele's hairs and tears but it does not alone explain the unusual increase in the ^{22}Ne and $^{40}Ar^{*}$ abundances between 2015 and 2016 (Figure 4.23 and 4.24). In fact, the concentrations of NG in samples erupted in subsequent periods of time from an

open-system that is persistently degassing, like Masaya volcano, should decrease through time as a result of gas loss (Sarda and Graham, 1990; Carroll and Draper, 1994).

Among other isotopic ratios, the $^{4}He/^{40}Ar^{*}$ ratio has been widely used to track the degassing of basaltic rocks and glass (e.g. Burnard et al., 2004, Yamamoto and Burnard, 2004; Sarda and Moreira, 2002). In open-systems the $^{4}He/^{40}Ar^{*}$ ratio increases in the residual melt during following stages of degassing (Carroll and Draper, 1994). This happens because $^{40}Ar^{*}$, that is preferentially partitioned into the bubbles with respect to ^{4}He ($He_{solubility}/Ar_{solubility}$ = 9.5; Jambon et al., 1986), is quickly lost from the system after vesiculation. The higher the amount of ^{40}Ar loss (vesicle loss), the more degassed will be the magma and, thus, the higher the $^{4}He/^{40}Ar^{*}$ ratio in the final erupted products (Carroll and Draper, 1994).

In this scenario, a hyperbolic curve with negative slope is expected when the $^{4}He/^{40}Ar^{*}$ ratios and Ar^{*} concentrations are plotted in a correlative graph (Sarda and Moreira, 2002; Burnard et al., 2004) (Figure 4.32 A). In this plot the more degassed samples, depleted in vesicles, will have higher $^{4}He/^{40}Ar^{*}$ ratios and lower $^{40}Ar^{*}$ abundances (melt component). Conversely, the more gas-rich samples, with higher vesicularities, will have lower $^{4}He/^{40}Ar^{*}$ ratios and higher $^{40}Ar^{*}$ content (bubble component) (Burnard et al., 2004; Yamamoto and Burnard, 2004; Moreira and Sarda, 2000; Burnard et al., 2002; Sarda and Moreira, 2002). Sarda and Moreira (2002), studying ridge basalts, suggest that this type of binary mixing between a melt component and a component in vesicles should be related to a degassing mechanism by vesiculation and vesicle loss.

Because the majority of the Pele's hairs and tears in this study are composed only of glass and vesicles (see section 4.5.1) it would be possible to model the behaviour of ^{4}He and $^{40}Ar^{*}$ (and of $^{4}He/^{40}Ar^{*}$ ratios). In theory, because Masaya volcano is continuously degassing, the less degassed samples should be those erupted in 2015 and should be plotted in the lower right area of the graphs (Figure 4.32 A). Conversely, the more degassed samples should have erupted in 2016 and should, therefore, plot in the upper left area of the graph (Figure 4.32 A).

In Figure 4.32 B the trend observed for the data obtained in this study is exactly the opposite of that suggested by the theory modelled in Figure 4.32 A. The $^{40}Ar^{*}$ concentration in the samples generally increases instead of diminishing from 2015 to 2016 and the $^{4}He/^{40}Ar^{*}$ ratios decline instead of increasing. This increase of $^{40}Ar^{*}$ and the decrease of the $^{4}He/^{40}Ar^{*}$ ratios suggest that a recharge event occurred between 2015 and 2016 at Masaya volcano (Figure 4.32 B).

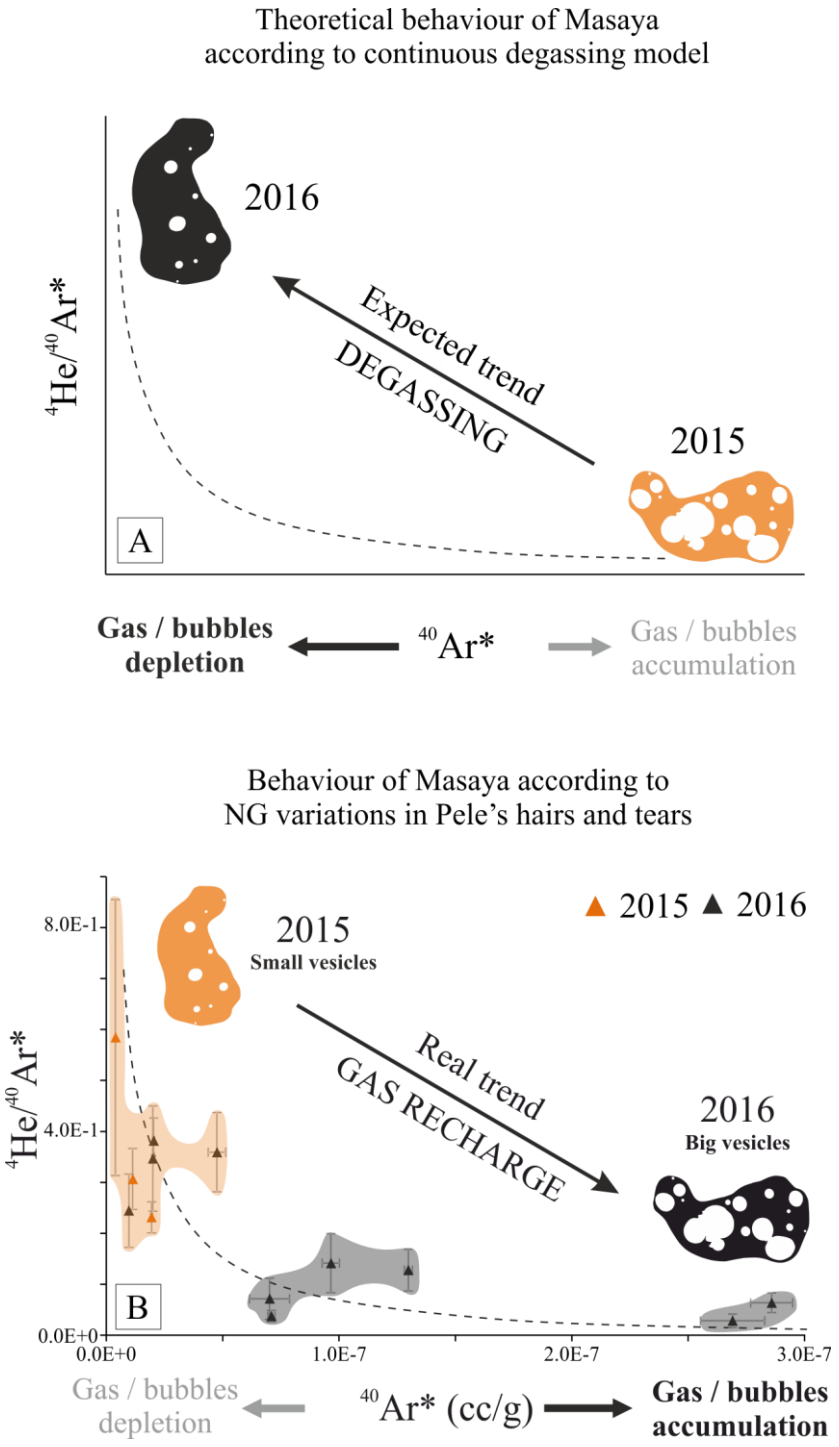

Figure 4.32 A - variations of the $^{4}He/^{40}Ar^{*}$ ratios and $^{40}Ar^{*}$ abundances as expected during a normal degassing event. The $^{4}He/^{40}Ar^{*}$ ratios increase through time and the $^{40}Ar^{*}$ abundances decrease due to gas loss and bubble depletion. The black arrow indicates the theoretical degassing trend. Information are taken and modified from Burnard et al. (2004) and Sarda and Moreira (2002). B - Behaviour of the Masaya volcano according to NG variations in Pele's hairs and tears**.** The black arrow indicates the variations of the $^{4}He/^{40}Ar^{*}$ ratios and $^{40}Ar^{*}$ abundances during the recharge event occurred between 2015 and 2016. The $^{4}He/^{40}Ar^{*}$ ratios decrease between the two collections and the $^{40}Ar^{*}$ abundances increase indicating an accumulation of gases in the reservoir and thus in the particles. Error bars are at the 1σ level. In A and B dotted curved lines indicate a binary mixing between a melt component (high $^{4}He/^{40}Ar^{*}$ ratios and low$^{40}Ar^{*}$) and a component dissolved in vesicles (low $^{4}He/^{40}Ar^{*}$ ratios and high $^{40}Ar^{*}$).

Specifically, 2015 glass display only low $^{40}Ar^*$ concentrations and high $^{4}He/^{40}Ar^*$ ratios (Composition 1 in Figure 4.26) whilst particles erupted in 2016 have two clearly distinct NG signatures. The first is similar to that of the samples erupted in 2015 (low $^{40}Ar^*$ - high $^{4}He/^{40}Ar^*$, Composition 1 in Figure 4.26) and the second is characterised by higher $^{40}Ar^*$ abundances and lower $^{4}He/^{40}Ar^*$ ratios (Composition 2A and 2B in Figure 4.26). This seems to suggest that Pele's hairs and tears erupted in 2016 have incorporated gasses derived from two different reservoirs: one with low NG content (2015-like) and the other one more enriched in gas.

Considering only those samples erupted in 2016 (KS16-03 and KS16-13) with a NG signature of Composition 2 (Figure 4.26), it is possible observe how KS16-03 has particles with higher $^{40}Ar^*$ content than KS16-13 while having similar $^{4}He/^{40}Ar^*$ ratios. As demonstrated by vesicularity analyses in section 4.5.1, KS16-03 displays particles with vesicularities up to 47 % and vesicles with total areas up to 194 mm^2. KS16-13 has particles with a maximum vesicularity of 36 % and vesicles of maximum dimension of 50 mm^2. In this context, the differences in the $^{40}Ar^*$ budget between the two samples could be more likely related to variations of the sample vesicularities and vesicles sizes rather than to variations in the gas supply ($^{40}Ar^*$) from the source region.

Similarly, for ^{22}Ne there are two reservoirs with different NG signatures, and it is also evident from Figure 4.23 where samples erupted in 2015 have only low ^{22}Ne content (Group A and C) while particles erupted in the following year have two distinct ^{22}Ne compositions (Group A, C – Low ^{22}Ne; Group B, D – high ^{22}Ne). Moreover, the same graph shows how ^{22}Ne, similarly to $^{40}Ar^*$, is more abundant in sample KS16-03 than in KS16-13. Although the data for ^{22}Ne are not corrected for air contamination, based on previous discussion on $^{40}Ar^*$ variations, it is possible to suggest that the increase of ^{22}Ne abundances between 2015 and 2016 could be considered as a proper indicator that an increased gas supply (recharge event) occurred between the two collection seasons. This is specifically true for those particles that don't present a correlation between ^{36}Ar and ^{22}Ne.

Taking into consideration all the aforementioned lines of evidences I propose that the increase of the NG abundances in Pele's hairs and tears between 2015 and 2016 could be related to a general change in gas composition occurring within the entire magmatic system. This could be related to a recharge event that has increased the abundance of the NG (^{22}Ne and $^{40}Ar^*$) in the whole magmatic system and, thus, in the final products (e.g. Pele's hairs and tears). Within this broad scale variation in NG abundance, NG abundances in individual particles are, instead, mainly controlled by the variations in the sample vesicularities and degree of NG fractionation.

4.5.5 Ar atmospheric contamination

At the moment of eruption, a volcanic material that is in equilibrium with an atmospheric reservoir at 1 atm is expected to have a $^{40}Ar/^{36}Ar$ ratio equivalent to that of the air (298.56±031, Lee et al., 2006). However, higher and lower ratios have been frequently observed in different types of volcanic glasses (pumices – Kaneoka, 1980; Clay et al., 2011; obsidians - Vogel et al., 2006, Morgan et al., 2009, Clay et al., 2015, Flude et al., 2018; pillow lava rinds – e.g. Kaneoka, 1994) including Pele's hairs and tears in this study. Several processes have been invoked to explain these non-atmospheric Ar signatures.

Supra-atmospheric $^{40}Ar/^{36}Ar$ ratios (Excess ^{40}Ar) have been related to kinetic mass fractionation of Ar isotopes during degassing with preferential ^{36}Ar loss through diffusion (apparent excess ^{40}Ar - Flude et al., 2010, 2018), incomplete degassing of the melt with $^{40}Ar^*$ retained in the sample in excess with respect to the air (Flude et al., 2018), equilibrium of the melt in an environment rich in $^{40}Ar^*$ (Kelley, 2002) and post-eruptive incorporation of $^{40}Ar^*$ derived from hot hydrothermal fluids (Kelley, 2002).

Sub-atmospheric $^{40}Ar/^{36}Ar$ ratios have been associated with kinetic mass fractionation of Ar isotopes (e.g. Vogel et al., 2006; Morgan et al., 2009), incomplete equilibrium of the glass with the atmosphere during quenching (Morgan et al., 2009; Clay et al., 2015), incorporation of ^{36}Ar from host rocks with an air-like signature assimilated into the magma prior to eruption (Kaneoka, 1980) and to post-eruptive hydration of the glass with preferential incorporation of ^{36}Ar derived from meteoric water (Kaneoka, 1994; Flude et al., 2018).

Among others, mass fractionation seems to play a major role in determining the $^{40}Ar/^{36}Ar$ ratios and ^{36}Ar content of volcanic glasses (Kaneoka, 1980; Vogel et al., 2006; Morgan et al., 2009; Brown et al., 2009; Clay et al., 2015; Flude et al., 2018). Mass fractionation is controlled by the different diffusion rates of ^{36}Ar and ^{40}Ar in silicate melt and occurs when the magma interacts and mixes with a reservoir that has an atmospheric Ar signature like air, meteoric water or rocks exposed to surface conditions. Magma interaction with one or more of these reservoirs can occur at depth during magma up rise, at depth or at the surface during magma degassing, during eruption and fragmentation at the vent and after pyroclast deposition if the temperatures of the erupted materials are high enough to allow Ar diffusion. When one of these processes take place Ar migrates from the air-like reservoir into the magma with ^{36}Ar diffusing faster than ^{40}Ar (Morgan et al., 2009; Flude et al., 2018). This happens because the concentration of Ar in air (and water) is higher than in silicate melts ($Ar_{solubility}$ in air >> $Ar_{solubility}$ in basaltic melt, Carroll and Stolper, 1993) and the diffusion of ^{36}Ar is higher than that of ^{40}Ar (Amalberti et al., 2016).

In this scenario, the melt / pyroclast would be enriched in ^{36}Ar, with respect to ^{40}Ar, until equilibrium is reached. If quenching happens before a complete homogenization and equilibration between magmatic and atmospheric Ar, the sample would have a fractionated Ar signature with an 'excess' of ^{36}Ar ($^{36}Ar_E$) with respect to ^{40}Ar. Thus, the final $^{40}Ar/^{36}Ar$ ratio of the sample will be lower than 298.56 (Morgan et al., 2009; Vogel et al., 2006).

According to kinetic theory (Young et al., 2002), if mass fractionation occurs during gas exsolution at depth, it is likely that ^{36}Ar would be preferentially fractionated into the bubbles over ^{40}Ar due to its higher diffusion coefficient. The bubbles would become more enriched in ^{36}Ar with respect to the melt during subsequent stages of degassing and contamination with the amount of ^{36}Ar migrating from the melt into the bubbles depending on its availability in the magmatic system. Following these considerations, it seems plausible that bubbles formed closer to the surface (more exposed to air/water) would be more contaminated by ^{36}Ar while bubbles originated at depth would have an Ar signature more similar to that of the primitive melts from which they have been formed. If bubbles formed at depth migrate upward with a rate faster than the diffusion rate of the ^{36}Ar in the bubbles they will reach the surface without equilibrium preserving a less contaminated Ar signature (Azbel and Tolstikhin, 1989). Under these conditions, once the magma is erupted from the vent it would be a mixture of bubbles equilibrated at different conditions and carrying a different ^{40}Ar and ^{36}Ar budget. If quenching happens rapidly after magma extrusion, as the case of volcanic glass formation, the sample would have a final $^{40}Ar/^{36}Ar$ ratio and ^{36}Ar abundance that would reflects the Ar signature of the trapped vesicles.

In the specific case considered in this study it is plausible that multiple processes have acted to produce the spread in the $^{40}Ar/^{36}Ar$ ratios and ^{36}Ar abundances observed in Masaya volcano Pele's hairs and tears. I suggest that the Ar signatures of these pyroclasts can be ascribed to the inhomogeneous distribution and incorporation of ^{36}Ar within the samples and within the magmatic system coupled with mass fractionation of the Ar isotopes during magma degassing and vesiculation.

In an open-system, like the Masaya volcano, the ^{36}Ar incorporated into the magma may derive from air, meteoric water, hydrothermal fluids circulating within the upper part of the volcano (Mauri, 2009), from wall rocks and portions of the crater floor that collapsed into the reservoir (Rymer et al., 2008) and then assimilated into the magma or from subduction fluids (Bach and Niederman, 1998) derived from the dehydration of the Cocos plate subducting beneath the Caribbean plate (Whattman and Stern, 2015).

As seen in section 4.5.1, Pele's hairs and tears in this study display different vesicularities and have bubbles of different sizes that may have been formed during different stages of magma evolution. In light of previous considerations, I suggest that

small bubbles formed at nearer to surface conditions may have Ar signature more similar to that of the air, while big coalescent bubbles formed at depth, in areas less contaminated by atmospheric Ar and raised without equilibrium, may have preserved a more primitive Ar signature. Here it is proposed that Pele's hairs and tears with different $^{40}Ar/^{36}Ar$ ratios and ^{36}Ar abundances are formed when bubbles, having different proportions of magmatic $^{40}Ar^*$ and ^{36}Ar, are trapped within the same portion of melt during fountaining episodes (Figure 4.33). Fast quenching (0.1 s to 5 s – Porritt et al., 2012) of the melt contribute to arrest the degassing and the fractionation of the Ar isotopes impeding the equilibration of the glass with the atmosphere. After eruption particles that contain a majority of bubbles with an excess of $^{40}Ar^*$ ($^{40}Ar/^{36}Ar$ > air, more primitive signature) would have a final $^{40}Ar/^{36}Ar$ ratio higher than 298.56 while particles that contain a majority of bubbles with an excess of ^{36}Ar ($^{40}Ar/^{36}Ar$ < air) would have sub-atmospheric $^{40}Ar/^{36}Ar$ ratios. Atmospheric ratios that are 'normal' and within error of 298.56 may be associated with non-vesicular glass (most likely equilibrated with air) or with particles that have the majority of their bubbles in equilibrium with air.

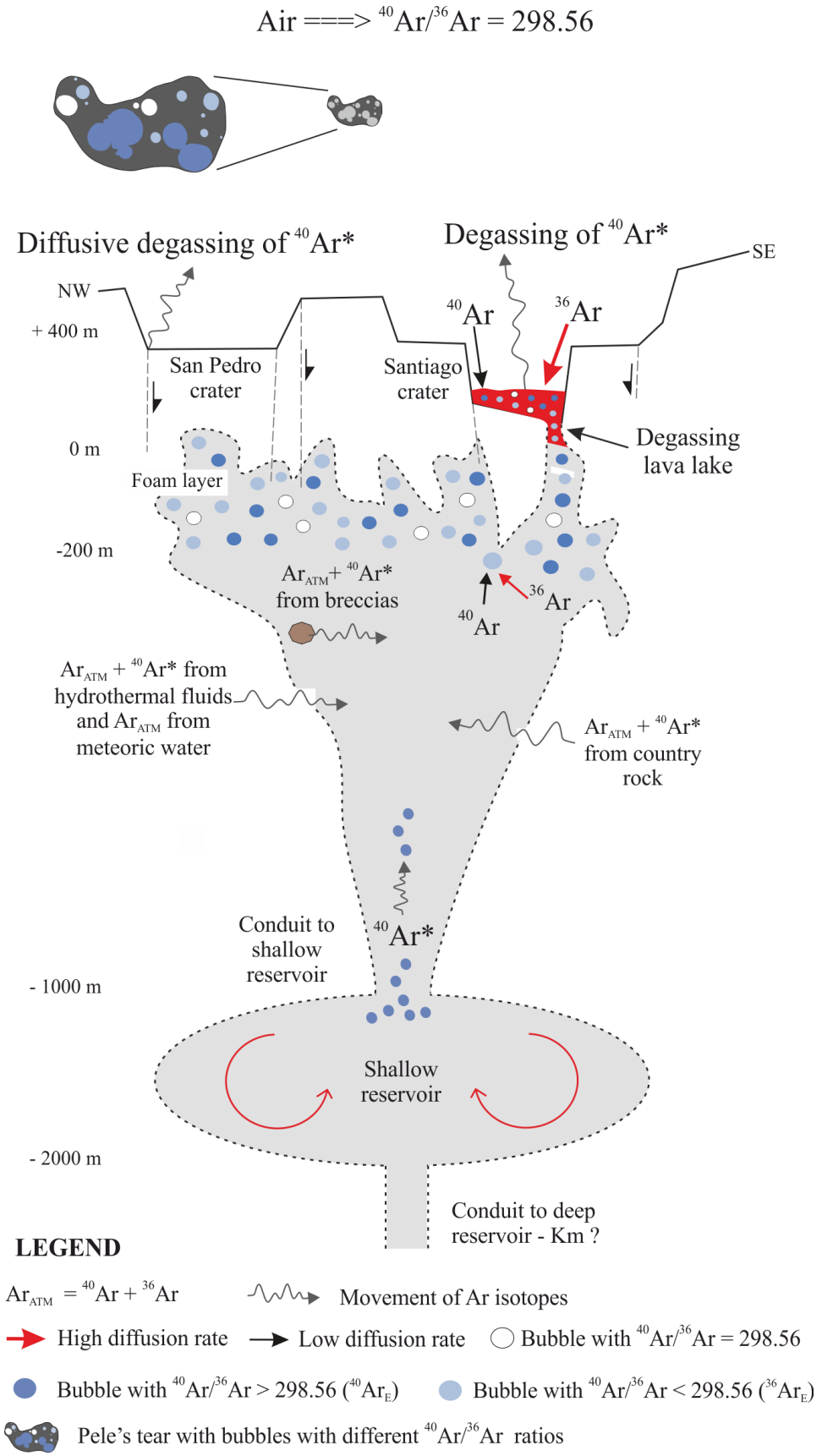

Figure 4.33 Possible source of atmospheric contamination at Masaya volcano and possible mechanisms that are responsible for the variable $^{40}Ar/^{36}Ar$ ratios and ^{36}Ar abundances observed in Pele's hairs and tears of this study. Bubbles formed at different depth, carrying a different ^{36}Ar budget, have been incorporated within hairs and tears erupted at the vent (see text for more specific explanation). Geometry of the Masaya volcano magmatic system is from Rymer et al. (1998) and Stix (2007).

Other processes, not related to the internal dynamics of the Masaya volcano magmatic system, could have influenced the ^{36}Ar abundances and the $^{40}Ar/^{36}Ar$ ratios of Pele's hairs and tears including: (1) Ar_{atm} adsorption at sample surface (Ozima and Podosek 2002); (2) Ar_{atm} incorporated through micro-cracks (Ballentine and Barfod, 2000); (3) incorporation of Ar isotopes during post-eruptive hydration of the glass; (4) analytical artefacts related to the measurement of ^{36}Ar.

(1) Ar_{atm} adsorption was minimised leaving the samples under vacuum (10^{-9} Torr) for at least 4 - 5 days and thus can be considered minimal, if not negligible. The use of heat lamp to speed up the release of adsorbed gas was avoided because it would also degas He from the sample precluding its analysis.

(2) Without specific evidences, in this study it is not possible to completely rule out the possibility that atmospheric Ar (and other NG) may have been also introduced into the samples through micro-cracks after eruption during sample preparation or during the night exposure of the particles to plume gasses.

(3) Based on the pristine nature of the glass of the Pele's hairs and tears (EMPA totals ~ 98.6, CIA ~ 50) it is possible to exclude the post-eruptive incorporation of Ar isotopes following glass hydration to explain the variations of the $^{40}Ar/^{36}Ar$ ratios. This process of Ar contamination is also unlikely as the fact that different $^{40}Ar/^{36}Ar$ ratios are seen from particles from the same sample/collection sites, and where thus exposed to the same weathering conditions. Such distinct isotopic signatures cannot be related to a process that would affect, in the same way, all the samples of a single collection of eruptive material. Moreover, because the samples were collected a maximum of 24 h after their eruption during the dry season is unlikely that weathering processes have acted so fast completely altering the glass chemistry and its NG composition.

Because glass weather even at room temperature and in a brief period of time (hours - days) (Fearn et al., 2004) there is also the possibility that the samples have incorporated atmospheric Ar (and leaked NG) during their storage prior to the analyses (1 to 2 years). On this regard, no relationships were observed between the ^{36}Ar content of the glass and the year of the analysis.

(4) It has been observed that Ar measurements performed with a MAP-215-50 mass spectrometer, like that used in this study, suffer of analytical problems related to the impossibility of the ion detector to fully resolve the peak at mass 36 (Flude et al., 2018). Here, it is not possible to distinguish between the true peak of ^{36}Ar and interferences caused by the presence of $^{1}H^{35}Cl$ and $^{12}C_3$ within the sample (Flude et al., 2018). These interferences could affect the correct determination of the true concentration of the ^{36}Ar precluding a precise characterization of the $^{40}Ar/^{36}Ar$ ratios.

In Pele's hairs and tears Cl can be a constituent of the glass, can be trapped inside isolated vesicles as gas a phase (HCl) and can be derived from plume sublimates adhering to the sample surface (Moune et al., 2007, 2010) which were not completely removed before the analyses. This is because samples for NG analysis are not subjected to a heat lamp, used to expedite the removal of adhered air from the surfaces of samples/sample chamber to be dated by $^{40}Ar/^{39}Ar$ technique. Any heat lamp would also degas He from the sample negating any He analysis.

Based on the results of electron microprobe analyses on glass all the three suites of samples have similar Cl contents (range 0.01 % - 0.11 %).

The presence of volcanic sublimates could be potentially problematic but only for KS15-03 where plume-related deposits were observed on glass surfaces in the form of yellow powder (section 4.5.1). These were not observed for the other two samples. However, sample cleaning in water and acetone may have removed any possible source of contamination. A careful inspection and selection of the samples before the analyses may have further reduced the possibility to analyse contaminated particles.

Because Cl was not measured as a gas phase trapped in individual bubbles it is not possible to comment upon this source of interference. However, in light of the large amounts of Ar released during the analyses, it is hypothesized that any Cl derived from bubbles would have caused only a minor interference to the measured ^{36}Ar content.

Aside from a possible - not verifiable - entrapment of ^{36}Ar during sample preparation, the Ar isotopic ratios and the ^{36}Ar variations observed in Pele's hairs and tears in this study are most likely primary characteristics of the samples inherited from the magmatic system and not related to secondary effects.

4.5.6 Volcanological implications

After ~ 3 years of relatively low activity, characterised only by minor ash eruptions and passive degassing, a new lava lake formed in December 2015 in the Santiago Crater of Masaya volcano. This resurgence had been preceded by a marked increase in seismicity in April 2015, by the eruption of ash from the crater in October 2015 (Global Volcanism Program, 2015 - last episode was recorded in May 2012) and by increased CO_2 degassing in November 2015, just a few weeks before the lava lake appeared (Aiuppa et al., 2018). After its formation the lake started to widen, due to crater floor collapses, until March 2016 when it reached the maximum dimension (Global Volcanism Program, 2016).

According to the results of this study the renewed activity at Masaya seems to correlate with some changes in the gas fluxes that supply the plumbing system. This hypothesis is supported by the clear variation in the NG abundances and signatures detected in Pele's hairs and tears erupted in March 2015 and in March 2016.

Basaltic glass that erupted before the appearance of the lava lake (March 2015) formed from a homogeneous reservoir that has high $^{4}He/^{40}Ar^{*}$ ratios and low $^{40}Ar^{*}$ and ^{22}Ne abundances (pre-lava lake signature). Conversely, samples erupted in 2016 display two different NG signatures. Some hairs and tears have a pre-lava lake NG signature while others show lower $^{4}He/^{40}Ar^{*}$ ratios and higher $^{40}Ar^{*}$ and ^{22}Ne content (Post-lava lake signature).

I propose that the degassing and magmatic activity at Masaya in early 2015, prior to the lava lake formation, was fed only by a gas-poor highly degassed magma (Figure 4.34). Following this, a period of gas-rich magma ascended from depth and reached the surface where it mixed with the degassed magma. This resulted in a reservoir with two distinct gas signatures (Figure 4.34). These upward movements of a buoyant, less dense, gas-rich magma triggered the resurgence of the lava lake. Only at this point basaltic glasses characterised by two different NG signatures were erupted. Small variations in the daily gas supply could have been responsible for the variability of the NG dissolved in samples collected in 2016.

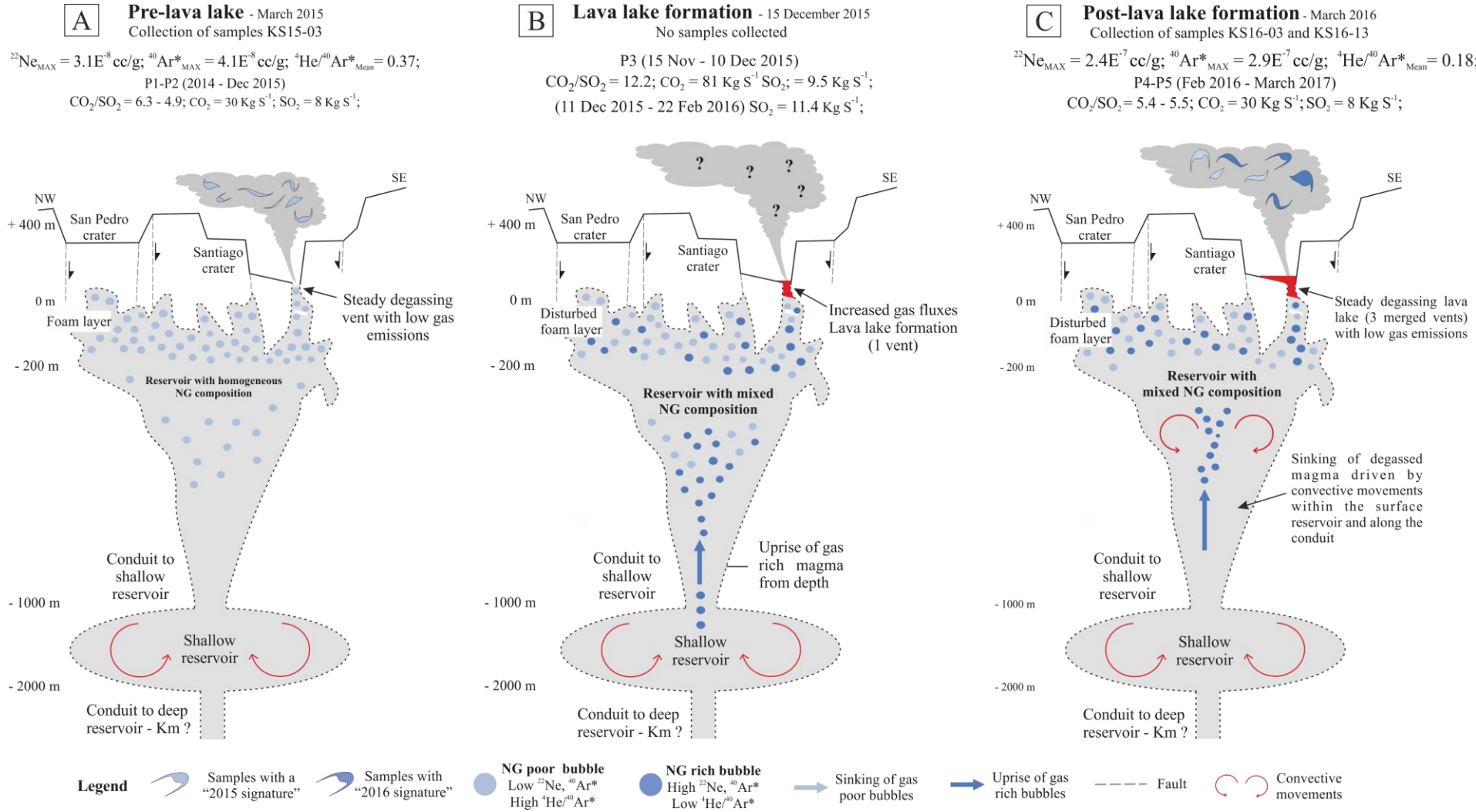

Figure 4.34 Behaviour of the Masaya volcano during the period 2015 – 2016. period 2015 – 2016. A - Before the lava lake appearance only Pele's hairs and tears with low ^{22}Ne and $^{40}Ar^*$ were erupted (March 2015). B - In December 2015 a new batch of gas-rich magma rise from depth causing the formation of the lava lake. C - Convective movements within the upper more superficial portion of the reservoir mixed pre-existing bubbles with low NG content with the new formed bubbles rich in ^{22}Ne and $^{40}Ar^*$. Pele's hairs and tears with different ^{22}Ne and $^{40}Ar^*$ compositions erupted in March 2016. SO_2, CO_2 and CO_2/SO_2 data are from Aiuppa et al. (2018). Geometry of the Masaya volcano magmatic system is from Rymer et al. (1998) and Stix (2007).

This model agrees with the idea that the degassing activity at Masaya is regulated by the existence of a deep reservoir that provides gas-rich magma to the shallow and superficial reservoirs (Rymer et al., 1998; Williams-Jones et al., 2003; Stix, 2007; Atlas et al., 2011; Spampinato and Salerno, 2012).

This has been demonstrated and, again, confirmed by a recent study in which are reported the results of a long term (2014 - 2017) continuous survey of the gas emissions at Masaya. In this study higher than normal CO_2/SO_2 and SO_2 values have been measured in the period between 2014 and 2017 (Aiuppa et al., 2018). CO_2/SO_2 ratios were of 1.5 - 3.5 between 1998 and 2009 (Martin et al., 2010) while, for the five periods of times (P1, P2, P3, P4 and P5) in which the 2014-2017 time series has been divided, the CO_2/SO_2 ratios increased, respectively, up to 6.3±3.1, 4.9±2.0, 12.2±6.3, 5.4±2.1, 5.5±1.9 (Aiuppa et al., 2018). In particular, the highest CO_2/SO_2 ratio of 12.2±6.3 (P3) has been recorded a few weeks prior the formation of the lava lake and the peak of the SO_2 degassing (11.4±5.2 kg/s) has been observed during the phase of lake formation (Aiuppa et al., 2018). Low gas fluxes of P1, P2, P4, P5 intervals have been linked to a gas source equilibrated at low pressure (0.1–10 MPa) while the highest gas fluxes in P3 have been correlated to a much deeper source (0.36–1.4 km) equilibrated at pressures of between 9 – 25 MPa and 15 – 35 MPa (Aiuppa et al., 2018). These observations are concordant with the results of De Moor at al., (2017) that show high CO_2/SO_2 ratio (10.1±1.2) before the appearance of the lava lake followed a decrease in the gas concentrations and related ratios (CO_2/SO_2 = 3.1±0.7).

In this context, the elevated CO_2 and SO_2 fluxes recorded during the peak degassing activity (P3 of Aiuppa et al., (2018) - mid-late November), have been ascribed to a volatile-rich magma, originated at the base of the shallow reservoir, that reached the upper part of the volcanic system in mid-December (Aiuppa et al., 2018). Convective overturn of the magma, within the shallow reservoir and the upper conduit, could have been triggered by density contrasts between the uprising gas-rich magma and the sinking degassed dense magma (Rymer et al., 1998; Williams-Jones et al., 2003; Stix, 2007; Caravantes González, 2013, Aiuppa et al., 2018). The increased gas supply has destabilized the shallow reservoir, enhancing the buoyancy of the magma, and speeding up convective movements within the plumbing system (Aiuppa et al., 2018). This process increased the degassing rate at the vent and caused the upward migration of the magma leading to the reappearance of the lava lake in December 2015 (Aiuppa et al., 2018).

4.6 Conclusions

This study has investigated, for the first time, NG abundances and isotopic ratios of Pele's hairs and tears demonstrating that these glassy pyroclasts are able to retain magmatic NG after eruption. Here, Pele's hairs and tears have been used, with success, to track the behaviour of a persistent degassing volcanic system, Masaya, between March 2015 and March 2016.

Pele's hairs and tears from Masaya have all the same chemistry, are crystal free (~ 99 % of them) and not affected by post-eruptive alteration. The specific methodology designed to collect the pyroclasts, and the fact that they were sampled during the dry season, have been fundamental to obtain pristine unaltered samples optimal for NG analyses.

Pele's hairs and tears from Masaya show a complex mixture of bubbles of different dimensions and shapes. Even within the same collection coexist particles with extremely different vesicularities. This range is comparable with what previously observed in other similar glassy pyroclasts (Porritt et al., 2012; Carracedo et al., 2016).

The variations of the NG abundances in individual hairs and tears are ascribed to the coexistence, within the same particle, of vesicles with different NG budgets. Variable degrees of vesiculation of the melt followed by solubility controlled NG fractionation between melt and bubbles, degassing and atmospheric contamination are the main processes that control the final gas composition of the pyroclasts. NG abundances vary independently of the shape of the particles.

The majority of the hairs and tears have an Ar composition in equilibrium with air ($^{40}Ar/^{36}Ar$ = 298.56 – Lee et al., 2006). Sub-atmospheric and supra-atmospheric Ar compositions were also observed and these are ascribed to different degrees of air contamination before eruption, Ar isotopes kinetic fractionation and incomplete Ar degassing. The extremely fast quench of the melt has favoured the retention of excess $^{40}Ar^*$ within a few particles.

The general decrease of the $^{4}He/^{40}Ar^*$ ratios and the increase of the $^{40}Ar^*$ and ^{22}Ne abundances from 2015 to 2016 suggests that the magmatic reservoir has been enriched in NG at some point between the two collection periods. In the present study this has been linked to the upward migration of a gas-rich magma from depth. This gas-rich magma mixed with the more degassed magma existing in the surface reservoir originating the two different NG signatures observed in Pele's hairs and tears erupted in 2016. These conclusions are supported by the model proposed by Aiuppa et al. (2018) for the degassing behaviour of Masaya volcano during the 2014 - 2017 period.

Given the results of this study, in the specific case of Masaya volcano, I strongly suggest the use of NG mass spectrometry analyses on Pele's hairs and tears in conjunction with other more widely used and well-established techniques (ground based gas sensors, remote sensing) to continue to monitor the behaviour of the volcano.

The ease with which Pele's hairs and tears can be collected in the field, the rapid sample preparation and sample analysis, coupled with the relatively easy and quick interpretation of the results obtained from NG analyses, represent some key benefits of the method here proposed to study the behaviour of Masaya volcano. On this regard, it is important to remember that it can't be underestimated the importance of collecting only pristine samples not affected by alteration. The fresh condition of the glass is an essential requisite in obtaining good results from NG analyses. Weathering and plume-glass interaction could modify the NG concentrations in the samples leading to inaccurate measurements and, therefore, erroneous interpretation of the results and thus of the behaviour of the considered volcanic system.

Taken the recommended precautions (collection of pristine samples, careful sample preparation, evaluation of alteration effects) I propose a wider application of Pele's hairs and tears in the field of geochemistry. Their ability to retain NG (this study) and H_2O and CO_2 (Muenow, 1963; Duffield et al, 1977) could be used to track degassing processes of other persistent degassing systems like, for example, Etna or Hawaii. Moreover, because Pele's hairs and tears are frequently erupted during fire-fountain episodes they could be also used to monitor the degassing of minor events such as the prolonged eruption that occurred at Kilauea along the lower East Rift Zone in May 2018 (USGS, 2018).

Finally, it would be interesting to try to use Pele's hairs and tears in Ar/Ar geochronology. Crushing the samples would release the excess $^{40}Ar^*$ retained in the bubbles leaving only 'vesicle free' glass shards. Using a sufficiently small grain size (see Chapter 3 – 63 μm fraction for silicic ash) for Ar/Ar analysis would reduce the chance of analysing glass contaminated by magmatic $^{40}Ar^*$. However, the non-perfect atmospheric equilibration of the particles, the easy with which glass undergone alteration (Moune et al., 2007; Carracedo et al., 2006) and the low K content of the particles could represent limitations for their use in Ar/Ar geochronology.

4.7 Final remarks

More experiments are required in order to determine the influence of CO_2 and H_2O variations on NG abundances in Pele's hairs and tears from Masaya volcano. In this regard, the extension of the gas analyses to include other major volatiles like H_2O, CO_2, SO_2 and HCl would provide another valuable source of information that, coupled with NG data, would increase our knowledge of the Masaya magmatic system. The use of Fourier-transform infrared spectroscopy (FTIR) or Nano-SIMS (Secondary Ion Mass Spectrometry) would help to solve these research questions.

Although the proposed model for atmospheric contamination seems valid in order to explain the variations in the $^{40}Ar/^{36}Ar$ ratios and ^{36}Ar abundances in sub-aerially erupted basaltic pyroclasts in this study further investigations are required to verify its validity, especially in light of the controversies on the actual location of the atmospheric Ar in basaltic glasses (bubbles vs. matrix glass - Burnard, 1999; Burnard et al., 1997; Raquin et al., 2008; Stroncik and Niedermann, 2016).

The effects of other sources of Ar contamination (adsorption, micro-crack contamination, interferences at mass 36) must be more constrained and understood especially in regard to the possible great influence of these phenomena to alter the $^{40}Ar/^{36}Ar$ ratios when these are really close to the atmospheric value. Any small variation in the ^{36}Ar content due to secondary contamination could compromise a correct determination of $^{40}Ar^*$ abundance and of the final $^{4}He/^{40}Ar^*$ ratios affecting the possibility to correctly interpret degassing processes.

Possible experiments could be undertaken in order to even better characterise the NG content of Pele's hairs and tears include:

- *In-situ* NG analyses of the bubbles of different dimensions would help to unravel the possible variations of NG abundances in vesicles of different dimensions (Burnard et al., 1997; Burnard, 1999).
- The analyses of NG abundances in microcrystals trapped within the Pele's hairs and tears wold help to determine the NG contribution of different crystals to the total NG budget of the particle. This would be necessary in order to determine if the NG contribution derived from crystals is really negligible.
- The analyses of Pele's hairs and tears of different dimensions would clarify if the NG concentrations would have been influenced also by a possible grain size effect related to minimal variations in the dimensions of the particles.

- Modelling the ^{4}He, ^{22}Ne and ^{40}Ar diffusion loss in response to different grain size and temperature of eruption and storage would aid to determine if the observed NG variations are dependent also by these factors.
- Enlarging the spectrum of NG analysed in one run including magmatic derived ^{3}He, ^{20}Ne, ^{21}Ne would help to better characterise the nature of the source region of the magma. This also would help to better understand NG fractionation and air contamination processes (especially from atmospheric derived ^{4}He and ^{22}Ne) occurring at Masaya as well as to reveal possible precursors of a renewed volcanic activity during a period of quiescence. This has already been proved feasible measuring ^{3}He concentrations in corals growth during the eruption at El Hierro in 2011 (Alvarez-Valero et al., 2017).

Chapter 5

NG behaviour and partitioning in young pumice glass during plinian eruptions and implications for Ar/Ar ages

5.1 Introduction

Pumices are highly vesicular glassy pyroclasts produced during fragmentation of a volatile-rich magma during explosive eruptions.

Despite pumices being one of the most common type of pyroclasts, surprisingly, glass separated from these samples has received very little attention in regard to its use in K/Ar and Ar/Ar dating (Drake et al., 1980; Cerling et al., 1985; Pasteels et al., 1986; Clay et al., 2011) and only a few studies have investigated partitioning and variations of NG in this material (Krummenacher, 1970; Bochsler and Mazor, 1975; Kaneoka, 1980; Pinti et al., 1999; Ruzié and Moreira, 2010).

First attempts to date highly vesicular glass with the K/Ar method have been done during the 1980's (Drake et al., 1980; Cerling et al., 1985; Pasteels et al., 1986) and they have been followed by isolated Ar/Ar studies during the last decade (Clay et al., 2011). These studies have demonstrated that can be challenging and almost impossible to provide geological meaningful Ar ages from this type of volcanic material.

Contrasting results have been obtained when glass and co-existing alkali feldspars (more reliable for Ar/Ar dating purposes) have been used to date the same sample (Cerling et al., 1985; Pasteels et al., 1986; Clay et al., 2011). Impossible low / high Ar ages from the glass phase, compared to alkali feldspars and geological evidence, have been ascribed to alteration, hydration and devitrification of the glass (Cerling et al., 1985; Pasteels et al., 1986) or related to the presence of $^{40}Ar_E$ trapped in isolated vesicles (Pasteels et al., 1986; Clay et al., 2011).

Only in one case (Drake et al., 1980) has close agreement between K/Ar ages from pumice glass (e.g. 1.88±0.07, 1.73±0.04) and co-existing feldspars (e.g. 1.89±0.03, 1.74±0.04) has been obtained for samples from lacustrine and fluvial sediments from the Koobi Fora Formation (Lake Turkana, Kenya). However, due to the method used for the analyses and the lack of information on the alteration and hydration state of the glass it is not possible to assess if the samples suffered from any of the aforementioned problems, and thus it is not possible to comment upon the true reliability of the ages.

Cerling et al. (1985), using similar glasses from the Koobi Fora Formation (Lake Turkana, Kenya) as Drake et al (1980), have demonstrated that hydration of the glass can lead to K-loss that can cause anomalously old K/Ar ages due to faster diffusion of K compared to radiogenic Ar. When glass experiences intense degrees of hydration it is also possible to have radiogenic Ar loss and anomalous young Ar ages (Kaneoka, 1972; Foland et al., 1993).

In a recent study Clay et al., (2011) have investigated the Ar system in young fresh phonolitic pumices (age = 668 Ka, CIA < 50, Si = ~ 60 Wt. %) exposed to different weathering conditions, with different degrees of welding and with vesicularity comprised between 10 % and 25 %. They have observed high amount of excess Ar in all the glasses with Ar ages much older (by several Ma) than those from co-existing feldspars and of those reported in previous studies. In particular, they noticed that glasses (and alkali feldspars) derived from pumices with higher vesicularity, and thus that have experienced more intense degassing, have retained less $^{40}Ar_E$ yielding lower ages than glasses from the least vesiculated samples. These age variations were not attributed to a particular loss of K due to weathering or loss of radiogenic Ar due to welding process. Finally, based on the positive correlation between the $^{40}Ar_E$ and air derived ^{36}Ar, Clay et al., (2011) have suggested that incorporation of Ar isotopes into the samples occurred prior to eruption.

These conclusions agree with those of Kaneoka (1980) who attributed the variations in the $^{40}Ar/^{36}Ar$ ratios of pumice glasses to different degrees of mass fractionation and atmospheric gas contamination occurring at shallow levels in the magma chamber. The source of atmospheric contamination was volatiles from shallow crustal materials admixed with the magmatic volatiles. Mass fractionation during magma degassing and the possibility that atmospheric gas is incorporated into the glass during magma cooling were excluded as possible mechanisms of air NG incorporation.

On the other hand, Pinti et al. (1999), have proposed that quenching temperatures, cooling rates of the eruption column and diffusive lengths in pumice (bubble wall thickness) are the main parameters affecting fractionation and incorporation of the air derived ^{20}Ne and ^{36}Ar into pumice. Preferential diffusion of Ne over Ar in pumice bubbles during pumice cooling at the eruption was considered, in that study, as the principal mechanism explaining the excesses of atmospheric ^{20}Ne over ^{36}Ar in the samples. A clear correlation between the number of preserved isolated vesicles and the amount of Ne in pumices was observed by Pinti et al. (1999). Similar conclusions have been reached by other studies investigating Ne and $^{40}Ar^*$ on vesiculated submarine volcanic glasses (e.g. Burnard, 1999, 2001; Sarda and Moreira, 2002; Burnard et al., 2004).

In a later study Ruzié and Moreira (2010) refuted the conclusions of Pinti et al. (1999) proposing that the NG are incorporated and fractionated through diffusion into the bubbles at the moment of fragmentation before eruption. Using a cell model that describes diffusion-induced growth of closely spaced bubbles and using diffusions coefficients for Ar and Ne extrapolated via the Arrhenius law at ambient temperature ($D_{Ne} = 10^{-20}$ cm^2 s^{-1} and $D_{Ar} = 10^{-4}$ cm^2 s^{-1}), Ruzié and Moreira (2010) have demonstrated that below T_g it would be possible to add Ne but not Ar (and other heavy NG) to the pumice via diffusion.

The two previous models have been challenged by Amalberti et al. (2016) who have demonstrated that diffusion NG elemental and mass fractionation may occur also after eruption during pumice cooling at $T > T_g$. They have reached these conclusions modelling the diffusion of Ne and Ar for a pumice with bubble walls of 1 – 10 μm at T = 1100 K and using their new diffusion coefficient for the interested isotopes ($D_{Ne} = 5.1 \times 10^{-10}$ cm^2 s^{-1} and $D_{Ar} = 6.2 \times 10^{-11}$ cm^2 s^{-1}).

Although there is a lack of concordance between these models, it is likely that NG kinetic mass fractionation in pumice may occur at different stages during sample formation exactly as it has been proposed for other volcanic glasses (obsidian – Morgan et al., 2009; MORB – Burnard, 2004).

As seen in this section pumice glass is an extremely challenging material for NG geochemistry and Ar/Ar dating. This can be related to its complex formation and to the processes that it can experience after its eruption (e.g. cooling, gas diffusion in and out, air contamination, deposition, weathering and hydration). In order to more widely use NG trapped in pumices as tracers of magmatic and eruptive processes it is necessary to understand which factors control their behaviour during an explosive eruption. In order to better understand when and if reliable ages can be extracted from this type of glass it is essential to assess the effect of these factors on the quality of Ar/Ar ages derived from it.

Because young materials are even more challenging for Ar/Ar dating, and more susceptible to excess Ar because of their low radiogenic Ar and high atmospheric contamination, I have decided to focus this study on pumices erupted less than 1 Myr during a plinian eruption. Studying NG concentration in pumice glass from different portions of two pyroclastic deposits of the same eruption (Eras Formation – Tenerife, Canary Islands) I aim to comprehend how Ar isotopes distribution and fractionation affect the precision and accuracy of Ar/Ar ages. Co-existing feldspars are also investigated in order to provide a better constraint of the age of the eruption and validate or not the ages obtained from pumice glass.

5.2 Geological background

5.2.1 The Canary Islands

The Canary Islands are an oceanic volcanic chain, 800 Km long and 400 Km wide, located between 100 and 500 Km from the North Western African coast (33 - 27° N and 18–12° W) (Figure 5.1). The Canaries developed on Jurassic oceanic lithosphere (180 Ma - 150 Ma) close to the passive continental margin of the African plate (Carracedo and Day, 2002) and are composed of several seamounts and seven major volcanic islands with ages, of the first subaerial volcanism, generally decreasing from northeast to southwest (Figure 5.1) – Fuerteventura (20.2 Ma), Lanzarote (15.5 Ma), Gran Canaria (14.6 Ma), Tenerife (12 Ma), La Gomera (9.4 Ma), La Palma (1.7 Ma), El Hierro (1.1 Ma) (Guillou et al., 2004).

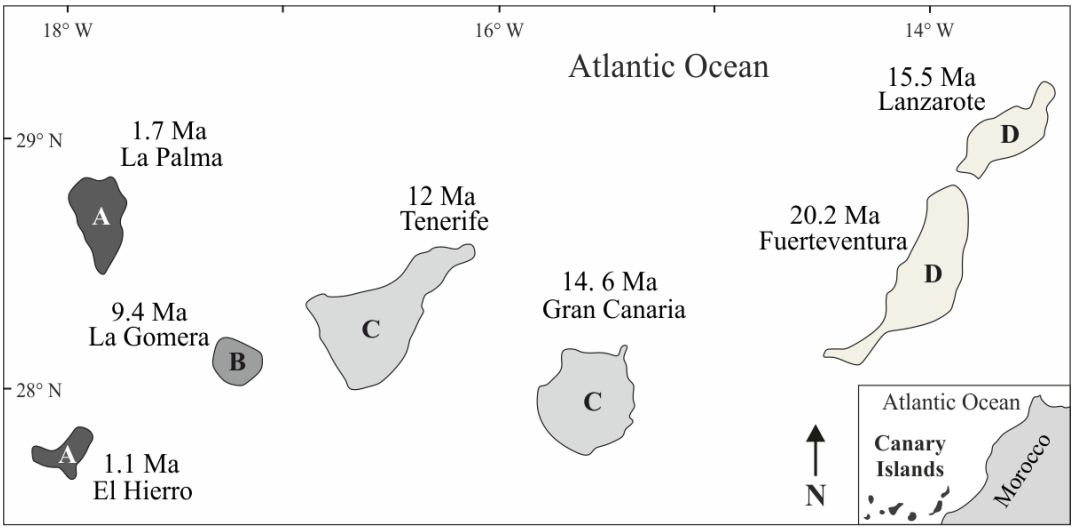

Figure 5.1 Age and location of the Canary Volcanic Province. Each capital letter refers to a different evolutionary stage of the islands: A = shield stage, B = post-shield stage, C = rejuvenation stage, D = erosional stage. Ages from Guillou et al. (2004). Modified after Carracedo and Perez-Torrado, 2013.

Despite the seven islands having a common origin, they display, from E to W, different morphologies and chemistry of the erupted products (Schmincke, 1979; Carracedo et al., 1998, 2002). It is possible to find melilites, nephelinites, basanites, tholeiitic and alkali olivine basalts, tephrites, rhyodacites, rhyolites, pantellerites, comendites, trachytes and phonolites (Carracedo et al., 2002). This geochemical variability is related to the development at shallow levels of evolved magma chambers, to the long living stages of the Canary Islands on old, cold and stable oceanic crust and to the mixture of magma from different reservoirs – lower mantle, lithospheric enriched mantle and asthenospheric depleted mantle (Hoernle and Schmincke, 1993).

It is possible to divide the evolution of the Canaries into five stages on the basis of geomorphological, geochemical and geochronological data. Each stage can be found in at least one of the seven Canary Islands (Guillou et al., 2004; Carracedo and Troll, 2013).

1 - S*ubmarine stage*:

The intrusion of mafic and ultramafic plutonic sheeted dike complexes into marine sediments and the eruption of mainly alkali basaltic pillow lavas create a seamount.

2 - *Shield stage*:

Highly undersaturated rocks (nephelinites and basanites), alkali basalts and transitional tholeiites are erupted forming the first subaerial shield volcanic edifice (El Hierro, La Palma).

3 and 4 - *post-shield* and *rejuvenation stage*:

After a brief period of low activity, characterised by erosion and mass wasting (*post-shield stage* - La Gomera), volcanism restarts with the eruption of more evolved products (*rejuvenation stage* - Tenerife, Gran Canaria). The emission of high volumes of trachytes and phonolites is followed by the emplacement of mafic and evolved alkali-rich volcanic rocks (alkali basalts–basanites–nephelinites to trachytes–phonolites). During this phase the island continues to grow reaching its maximum altitude and complexity (Tenerife).

5 - *Erosional stage*:

When the volcanic activity ceases the erosion and subsidence of the oceanic floor shape the morphology of the island (Lanzarote, Fuerteventura) until atolls and guyots are formed.

The unusual presence of central stratovolcanoes and highly differentiated rocks, shear and compressional structures with uplifted blocks and the almost zero subsidence of the ocean floor make the Canary islands particularly unusual with respect to other oceanic volcanic islands (e.g. Hawaii) (Schmincke, 1979; Carracedo et al., 1998). Several models have been proposed in order to explain these peculiar characteristics (Anguita and Hernan, 2000 - Table 5.1). The most recent and comprehensive is from Anguita and Hernan (2000) which mixes together elements of the previous models providing the best available explanation for the Canary volcanism. According to their model, the magmatic activity in the Canaries is the result of the surface expression of a positive thermal anomaly in the upper mantle beneath the area. This thermal anomaly spreads beneath the Canary Islands, North Africa and Central Europe (Hoernle et al., 1995) and it is thought to be associated with a “fossil” plume related to a remnant portion of a bigger “super-plume” (Wilson, 1997) that reached the upper mantle during the opening of the Central Atlantic Ocean

(May, 1971). Magmatism in the Canary Islands occurs when a system of fractures opens up and provides a pathway for rising magma; amagmatic periods are ascribed to transpressional tectonics during which blocks are uplifted (Anguita and Hernan, 2000). This model supports most of the geological, geophysical and geochemical features observed in the Canary islands such as: the long-time activity of the volcanism, the presence of uplifted blocks in many islands, the similarities between Atlas and Canary magmatism, the decreased volume of the magma after every volcanic cycle, the presence of a hot upper mantle beneath the archipelago, the tectonic structures and the seismicity detected in the area, the absence of a gravity high and bathymetric swell and the differences in the geochemistry of the erupted products.

Table 5.1 Proposed models for the origin of the Canary Islands.

MODEL	AUTHORS	DESCRIPTION
The propagating fracture model	Araña and Ortiz (1991)	The volcanism is a consequence of decompression melting during shear movements occurring along a transcurrent corridor, which connects the Canary islands to the Atlas mountains (Africa). Inactive periods are attributed to compressional tectonics in the same area.
The uplift of tectonic blocks	Anguita and Hernàn (1975)	The eruptions occur during occasional relaxation of the active stress field. This permits the magma to escape to the surface. Compression tectonics is responsible for the observed uplifted blocks outcropping in the Canary archipelago.
The local Canary islands rift model	Fùster (1975)	The model is based on the idea that an active Cenozoic rift exists in the Canary region. This hypothesis is supported by some extensional structures founded in Canary Islands basal complexes.
The classic Canary Islands plume model	Burke and Wilson, (1972); Carracedo et al. (1998)	The model is based on the classical hot spot theory used to explain the origin of the Hawaiian chain.
The blob model	Hoernle and Schmincke (1993)	The model is based on the idea that a blob type (Allègre et al, 1984; White et al, 1993) west-dipping conduit beneath the entire archipelago is responsible for the Canary volcanism. The westward dipping would be produced by the African plate viscous drag.
The upwelling sheet model	Hoernle et al. (1995)	The model explains the Canary volcanism with the presence of a positive thermal anomaly that occupies the upper mantle close to the Canary Archipelago. This anomaly is responsible for mantle melting leading to the Canary volcanism.
The unifying model	Anguita and Hernan (2000)	The model is based on the presence of a positive thermal anomaly in the upper mantle beneath the area associated to a remnant portion of a "super-plume" spreading beneath the Canary Islands, North Africa and Central Europe. Volcanism occurs when fractures opens providing a pathway for rising magma. Quiescent periods are associated to transpression phenomena that are also responsible for the blocks uplifting.

5.2.2 Geology of Tenerife

Tenerife is the biggest island of the Canary Islands. Its geological complexity is the result of a long-lasting evolution of an oceanic volcanic island developed on an old stable Jurassic oceanic crust that, with its relatively slow subsidence rate, has permitted preservation above sea level of all the volcanic products erupted during the last 12 Ma (Guillou et al., 2004; Carracedo et al., 2007).

Between 11.9 Ma and 3.9 Ma mafic shallow intrusive rocks together with alkali basalts, ankaramites, basanites lavas and minor felsic products (Ancochea et al., 1990) were erupted from three coalescent shield volcanoes (Figure 5.2): Roque del Conde in the southwest (11.86±0.17 Ma - 8.95±0.13 Ma), Teno in the west (6.11±0.09 Ma - 5.15±0.07 Ma) and Anaga in the northeast (4.89±0.07 Ma - 3.95±0.06 Ma) (K/Ar and Ar/Ar ages from Guillou et al., 2004). All together the products of these volcanoes form the *Old Basaltic Series* (OBS - Fuster et al., 1968).

From 3.5 Ma to 2.2 Ma (Martí et al., 1994) the eruption of effusive basaltic, trachybasaltic and phonolitic lavas and minor welded and non-welded pyroclastic deposits formed a 2,700 - 3,000 m high and 40 Km wide central shield edifice called Las Canãdas volcano (Araña, 1971) (Figure 5.2).

Between 1.56 Ma and 0.17 Ma minor basaltic and voluminous phonolitic pyroclastic rocks were erupted from the Las Canãdas volcano (Ancochea et al., 1990; Martí et al., 1994; Brown et al., 2003). The large central depression that characterise the central upper part of the Las Canãdas originated at this time from at least three caldera collapse events. Repeated large-volume plinian eruptions, triggered by the intrusion of a mafic magma into a more felsic shallow reservoir (Brown et al., 2003), emptied the shallow magma chamber and caused a series of vertical collapses that resulted in the formation of the central caldera (Martí et al., 1994; Bryan et al., 1998, 2000; Brown et al., 2003). Basaltic activity continued, intermittently, throughout the eruption of lavas interbedding the pyroclastic deposits and with the formation of several basaltic scoria cones at the top and along the flanks of the Las Canãdas (Carracedo et al., 2007). Several gravitational sector and lateral collapses, such as the Güimar landslide at 0.84 Ma and the Orotava landslide at 0.54 Ma - 0.69 Ma (K/Ar ages from Cantagrel et al., 1999), have profoundly modified the morphology of the Las Canãdas volcano.

At 0.15 Ma the eruption of basaltic and tephri-phonolitic to phonolitic products partially infilled the Las Canãdas caldera forming two new stratocones (Teide-Pico Viejo complex) (Araña, 1971; Ablay and Martí 2000; Carracedo et al., 2007) (Figure 5.2).

Thick trachytic, trachy-basaltic and basaltic lavas and the products of a series of scoria cones have also been erupted from a NE, NW and N trending rift fissure-vent system (Figure 5.2) from at least 1.8 Ma to date (Fuster et al., 1968; Ablay and Marti, 2000). The most recent basaltic lava was erupted in 1909 from the NW rift zone (Martí et al., 2008).

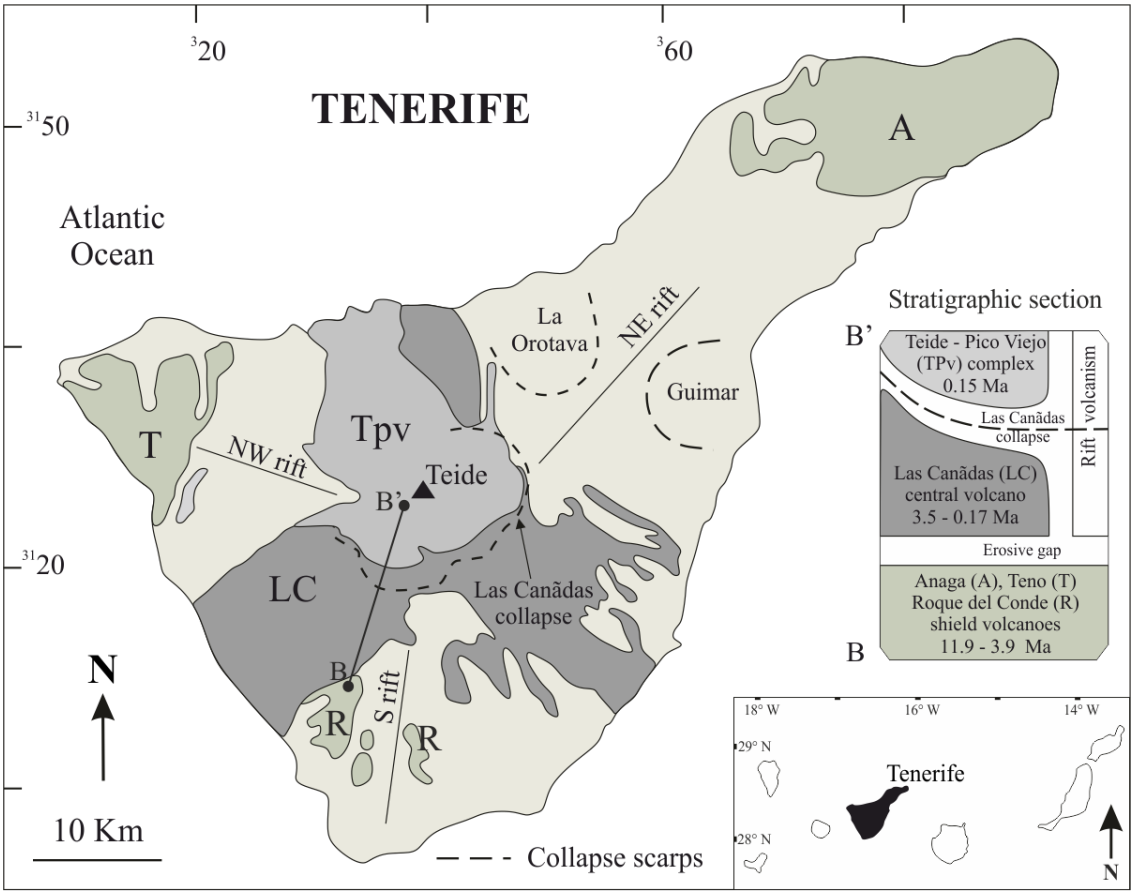

Figure 5.2 Geological map of Tenerife modified from Hoernle and Carracedo (2009). In different colours are shown the three main constructive phases of Tenerife that are summarised in the small inset. Ages are taken from Carracedo and Troll (2013). Coordinate system UMT zone 28R.

5.2.3 Area of research

This study focuses on volcanic products outcropping along the southeastern coastal flank of Tenerife (Bandas del Sur - Figure 5.3). This area, of more than 200 km^2 and extending from El Baul to Aldea Blanca, comprises pyroclastic rocks erupted from the Las Canãdas volcano between 1.6 Ma and 0.17 Ma (Bryan et al., 1998; Brown et al., 2003; Edgar et al., 2007; Dávila-Harris, 2009).

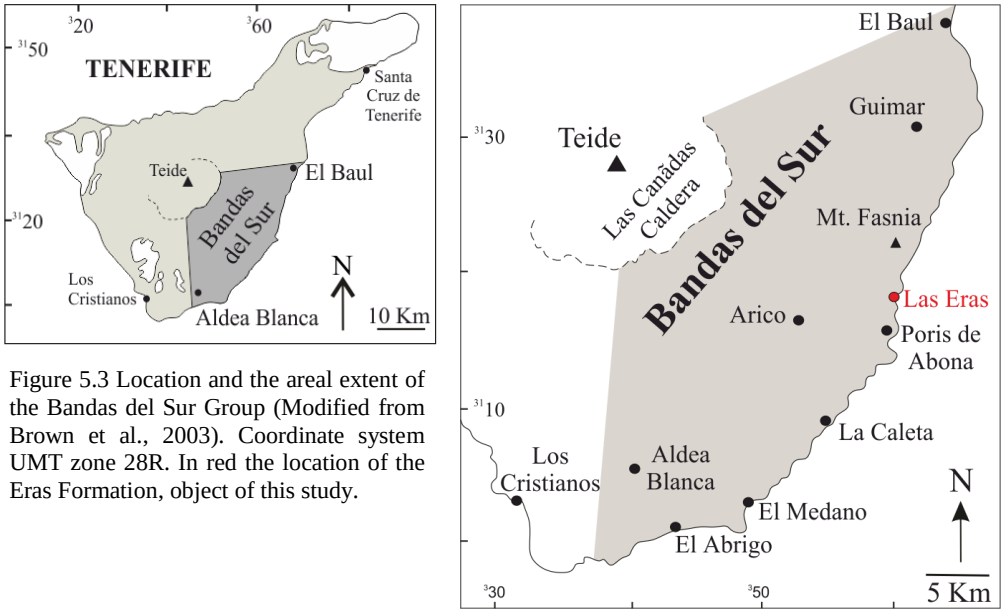

Figure 5.3 Location and the areal extent of the Bandas del Sur Group (Modified from Brown et al., 2003). Coordinate system UMT zone 28R. In red the location of the Eras Formation, object of this study.

The pyroclastic succession (Figure 5.4) overlies basaltic lavas of the previous shield volcanoes and includes: phonolitic ignimbrites (welded and non-welded), ash and pumice fall, phreatomagmatic tuffs, debris-avalanche deposits and flank-erupted scoria cones. Scattered basaltic and phonolitic lavas interlayers the pyroclastic deposits. Epiclastic sandstones, conglomerates and numerous palaeosols, bracketing pyroclastic deposits, testify quiescent periods between eruptions (Bryan et al., 1998; Brown et al., 2003; Dávila-Harris, 2009).

Several stratigraphical and geochronological studies conducted on this pyroclastic sequence (Martí et al., 1994; Bryan et al., 1998, 2002; Huertas et al., 2002; Edgar et al., 2002, 2007; Brown et al., 2003; Dávila-Harris, 2009) together with detailed investigations of single eruptions (Brown and Branney, 2004; Maher, 2006; Smith and Kokelaar, 2013; Dávila-Harris et al., 2013) and correlative studies with offshore and caldera wall deposits (Ancochea et al. 1990; Bryan, et al., 1998; Rodehorst, Schmincke and Sumita, 1998; Smith and Kokelaar, 2013) have allowed a precise definition of the stratigraphy and chronology of the eruptive events that have characterised the second stage of the evolution of the Las Canãdas volcano.

Detailed geochemical studies of the volcanic products outcropping in the Bandas del Sur have also investigated those magmatic processes like fractional crystallization, magma mixing and assimilation that contributed to the great geochemical variability observed in the Tenerife products (Wolff and Storley, 1984; Wolff, 1985; Wolff et al., 2000; Bryan et al., 2002; Stock et al., 2012).

Brown et al., 2003

	Formation	Ar/Ar Age ± 1σ
Upper Bandas del Sur Group	Lava	
	Abrigo Fm.	0.169±0.001
	2 pumice fall units	
	La Caleta Fm	0.221±0.005
	Sabinita Fm.	
	Poris Fm.	0.273±0.005
	Fasnia Fm	0.289±0.006
	Aldea Blanca pumice fall	
	Lava + scoria cone	
	Granadilla Fm.	0.600±0.007
	Abades Fm.	0.596±0.014*
	Lava	
	Arico Fm.	0.668±0.004

Dávila-Harris, 2009

	Formation name	Ar/Ar Age ± 1σ
Lower Bandas del Sur Group	Llano Blanco	
	Eras Fm.	
	Pelada fall deposit	
	Helecho Fm.	0.735±0.005
	Pumice fall deposits	
	Lava	
	Moradas Fm.	0.738±0.004
	Pumice fall	
	Rio Fm.	0.747±0.004
	Pumice fall	
	Monjas Fm.	1.310±0.006
	Mocan Fm	1.494±0.008
	Vallito Fm.	
	Derriscaderos Fm.	1.572±0.007
	Lava	
	Pequeros Fm.	1.577±0.006
	Barco Fm.	1.601±0.008

Figure 5.4 Stratigraphy of the Bandas del Sur Group. Data are from Brown et al. (2003) and Dávila-Harris (2009). *Age is from Bryan, Marti and Cas (1998).

The Eras Formation is one of the several formations outcropping in the Bandas del Sur region. It is exposed between Poris de Abona and Las Eras (type locality, UTM 28R 0359560 E, 3118930 N – in red in Figure 5.3) and comprises a basal phonolitic non-graded pumice fall (1.8 m thick at type section) overlain by a cream-coloured non-welded ignimbrite (10 m thick at type section) (Brown et al., 2003). The ignimbrite is a pumice-rich, lithic-poor, massive and locally diffuse-bedded pumiceous-tuff (Figure 5.5 A) (Brown et al., 2003). The base of the Formation is marked by a soil developed on a series of unnamed pumice falls while its top is marked by a series of lavas, alluvial volcaniclastic sediments and a soil (Brown et al., 2003). Banded and mafic pumices have only been observed in the ignimbrite (Brown et al., 2003). The crystal assemblage of the juveniles is sanidine, plagioclase, biotite and haüyne (Brown et al., 2003). The Eras Formation has been interpreted as the result of a chemically zoned pumice-rich plinian eruption, which has generated a pyroclastic density current along the eastern Bandas del Sur (Brown et al., 2003).

5.3 Methods

Pumices of different colours and textures collected from the Eras Formation type locality during a field campaign in 2016 were studied with different techniques (Table 5.2).

Thin sections and backscatter electron images were used to characterise the samples in terms of their petrography and texture. XRF analyses provided bulk major and trace elements compositions of the samples while major element concentrations for pumice glass and sanidines were investigated by electron microprobe analyses. Chemical Alteration Index (Nesbitt and Young, 1982) was calculated for each analysed spot in order to inspect the degree of alteration of the pumice glass. Data from XRF and electron microprobe analyses are presented and displayed after normalization to 100 %. electron microprobe raw data are listed in Appendix A4.1. Chemical data here are used in support of NG and Ar/Ar data interpretation and will not be discussed in the more general context of chemical variability of the Tenerife products.

Single grain fusion NG (^{4}He, ^{36}Ar and ^{40}Ar) analyses were performed on glass shards and on sanidines picked from pumices, grey in colour, that are common to both fall and ignimbrite deposit. Ar/Ar dating by laser probe step-heating and single grain fusion was performed on glass shards and sanidines picked from the same samples used for the NG analysis. Haüyne crystals, picked from the more mafic pumices, were also dated in order to investigate their suitability for dating young silicic volcanic rocks with the Ar/Ar technique. Raw data of NG and Ar/Ar analyses are listed in Appendix A4.2 and A4.3.

Specific information and technical details of each technique are given in Chapter 2.

Table 5.2 Analytical techniques used to investigate the different juveniles in the Eras Formation.

Deposit	Sample*	Thin section	XRF	Electron microprobe		NG-analysis		Ar/Ar dating	
				Sanidine	Glass	Sanidine	Glass	Sanidine	Glass
Fall									
Base	F1A - Grey	X	X	X	X	X	X	X	X
	F1B - Light-green	X	X						
Top	F2A - Grey	X	X	X	X	X	X	X	X
	F2B - Pale green	X	X						
Ignimbrite									
Base	I1A - Grey	X	X	X	X	X	X	X	X
	I1B - pale green	X	X						
	I1C - Dark green	X	X						
	I1D - Banded dark-green								
Top	I3A - Grey	X	X	X	X	X	X	X	X
	I3C - Dark green	X	X	X	X				
	I3D - Banded dark-green	X	X	X	X			Haüyne X	

* On the right side of the table is illustrated the stratigraphical division of the Eras Formation and the different samples analysed in this study. See text in the following section for the meaning of the designated names.

5.4 Results

5.4.1 Field observations

At its type locality, where the samples of this study were collected, The Eras Formation is composed by a non-graded, locally bedded pumice fall that displays pale grey and green pumices. The fall deposit is overlain by a cream-coloured lithic-poor ignimbrite that is non-welded and has grey, dark green and banded dark green pumices which abundance increases upward. The ignimbrite is generally massive with pumice rich and pumice poor layers alternating throughout the deposit. A paleo soil marks the base of the Eras Formation while a series of volcaniclastic sediments mark the top of the sequence. The pumices are composed of phenocrysts of sanidine biotite and haüyne and are in size of between 0.5 cm and 2 cm in the fall deposit (Figure 5.5 B) while are of between 4 cm and 20 cm in the ignimbrite (Figure 5.5 C). Generally speaking, dark green and banded pumices are bigger than grey pumices when these were collected at the same interval.

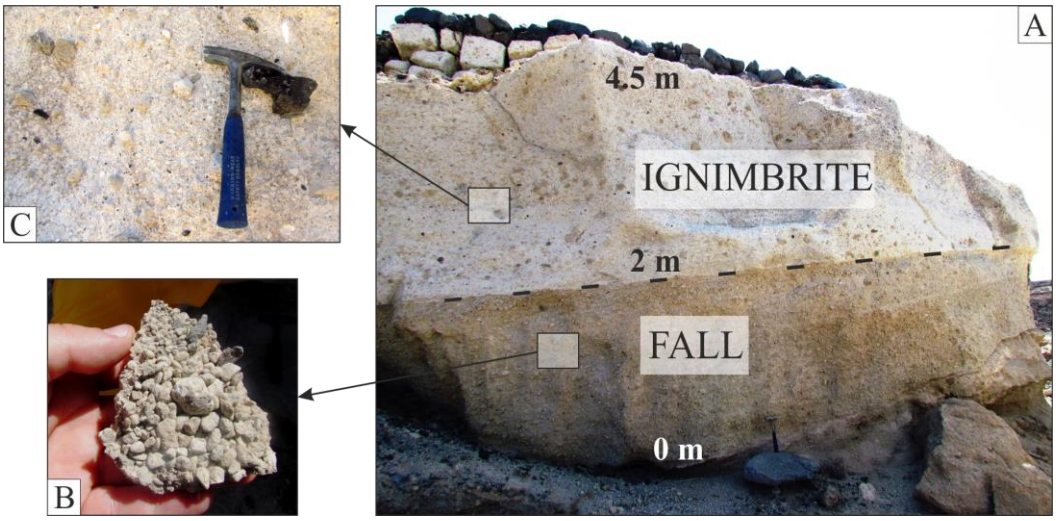

Figure 5.5 A - Sampling location of the Eras Formation. A light-brown basal fall composed of small rounded pumices (B) is overlain by an ignimbrite that is composed of pumices of different colours (C). Dotted line between the fall and the ignimbrite indicates the sharp contact between the two units.

No weathered horizons were observed between the fall and the ignimbrite demonstrating that no time gap exists between their deposition. A sharp contact separates the two units indicating that a possible erosional process has truncated the upper part of the fall deposit. No evidences suggest that a third unit, between the fall and the ignimbrite, has gone missed due to intense erosional processes. Anyway, because the real complexity of the Formation has not yet been identified, it is not possible to completely rule out this possibility. For this reason, the thickness of ~ 4.5 m at the collection locality must be considered the minimum. Due to the limited extension of the outcrop (~ 20 m) no lateral variations were observed. Field observations of the Eras formation in this study match with those from Brown et al. (2003).

5.4.2 Sample characterization:

Different pumices were collected and characterised. According to their colour, mineral abundance and textural characteristics they were divided into four suites (Figure 5.6): A = grey pumices, B = light-green pumices, C = dark-green pumices, D = dark-green banded pumices.

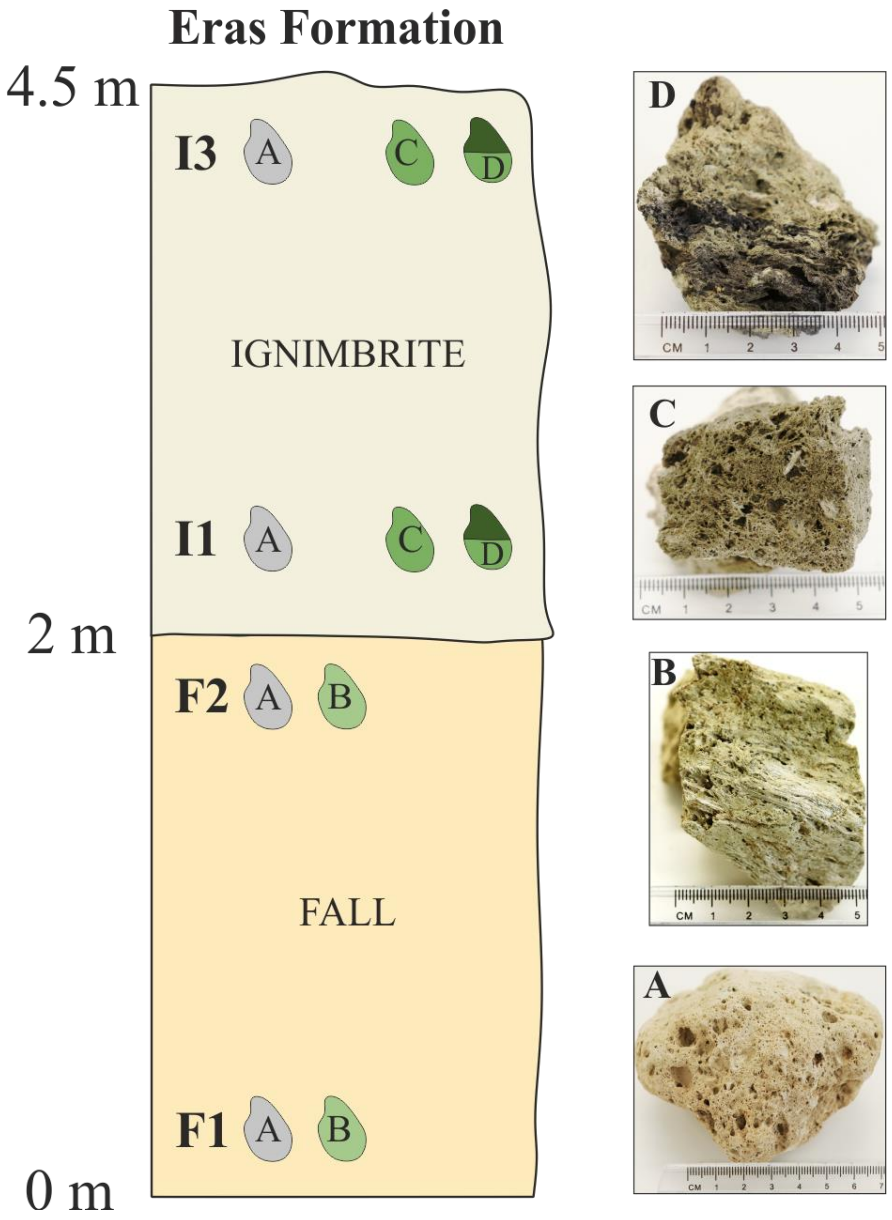

Figure 5.6 Stratigraphic sketch of the Eras Formation with the position (F1, F2, I1, I3) and type of pumices observed and collected in this study. The pumices are grouped into four suites in relation to their colour and texture: A = grey pumices, B = light-green pumices, C = dark-green pumices, D = dark-green banded pumices.

Grey pumices are homogenous in texture and colour and were found throughout the entire sequence (F1A, F2A, I1A, I3A – Figure 5.6). Light-green pumices have similar textures and crystal content abundance to the grey pumices and were observed in the fall deposit (F1B, F2B – Figure 5.6). Dark-green (I1C, I3C) and dark-green banded pumices (I3D) were identified only in the ignimbrite while they are absent in the basal fall (Figure 5.6). Dark-green banded pumices are composed of bands of green and dark-green to black glass (Figure 5.7 C). Grey and light-green pumices are generally smaller in size (~1 - 7 cm) and more altered than the dark-green and dark-green banded pumices that are up to 20 cm in size. The pumice size and abundance of dark-green banded pumices increase towards the top of the ignimbrite. Many grey and light-green pumices display a bright yellowish colour due to the presence of alteration products infilling vesicles or covering their surface.

The samples are composed of a hypocrystalline highly vesiculated glass (Figure 5.7 A-B-C-D). Sample vesicularity decreases from suite A (67 – 80 %), to suite B (60 %), to suite C (45 - 55 %) reaching its minimum in the dark bands of suite D (25 %) (Table 5.4). Small portions (mm in size) of the less vesiculated dark glass can be found dispersed in the grey and light-green pumices.

Crystal content ranges from 5 % to 10 % in suite A, B and C and increases up to 20 - 25 % in the dark bands of suite D (Figure 5.7 C). The mineral assemblage (Table 5.3) is: euedral to subhedral alkali feldspar (~ 85 %, 0.4 - 2.4 mm), Mg-rich biotite (3 - 10 %, 0.4 - 1.2 mm), sodalite/haüyne (1 - 3 %, 0.4 - 2 mm), clinopyroxene (< 1 %, ~ 0.4 mm) and Fe–Ti oxides (1 - 5 %, < 0.1 mm). Apatite was rarely found as inclusions in biotite and pyroxene in the more mafic pumices. Mafic minerals abundance increases from suite A to suite D. The majority of the alkali feldspars are fresh and pristine (Figure 5.7 E) with a few crystals, of bigger dimension (~ 1.8 - 2.4 mm), having altered core or resorbed rims (Figure 5.7 F) found in the ignimbrite pumices; none of them display optical zoning when observed in thin section. Euhedral to elongated fresh and partially altered biotite crystals were found alone and rarely in association with tiny micro-crystals of plagioclase (< 0.1 mm). Glomerophyres of pyroxene, plagioclase (absent as isolated crystals) and oxides are more frequent in the mafic portions of the dark-green banded pumices. Clay minerals, infilling vesicles or substituting the glass, were observed in some areas of the grey and light-green pumices although they were also found in the dark-green samples to a lesser extent.

Table 5.3 Stratigraphic position and petrography each suite of the Eras Formation

Position	Sample	Colour	Vesicularity (%)	Mineral abundance (%)	Mineral assemblage
Ignimbrite					
Top	I3D	Dark-green banded	25	10	>>alkali feldspar > biotite, > sodalite/haüyne < clinopyroxene, < Fe-Ti oxides
	I3C	Dark green	45	5	
	I3A	Grey	75	1-2	
Base	I3D	Dark-green banded	25	10	
	I3C	Dark green	55	5	
	I1A	Grey	80	1-2	
Fall					
Top	F2B	Light-green	61	< 5	>>alkali feldspar > biotite, > sodalite/ haüyne < clinopyroxene, < Fe-Ti oxides
	F2A	Grey	68	1-2	
Base	F1B	Light-green	60	< 5	
	F1A	Grey	67	1-2	

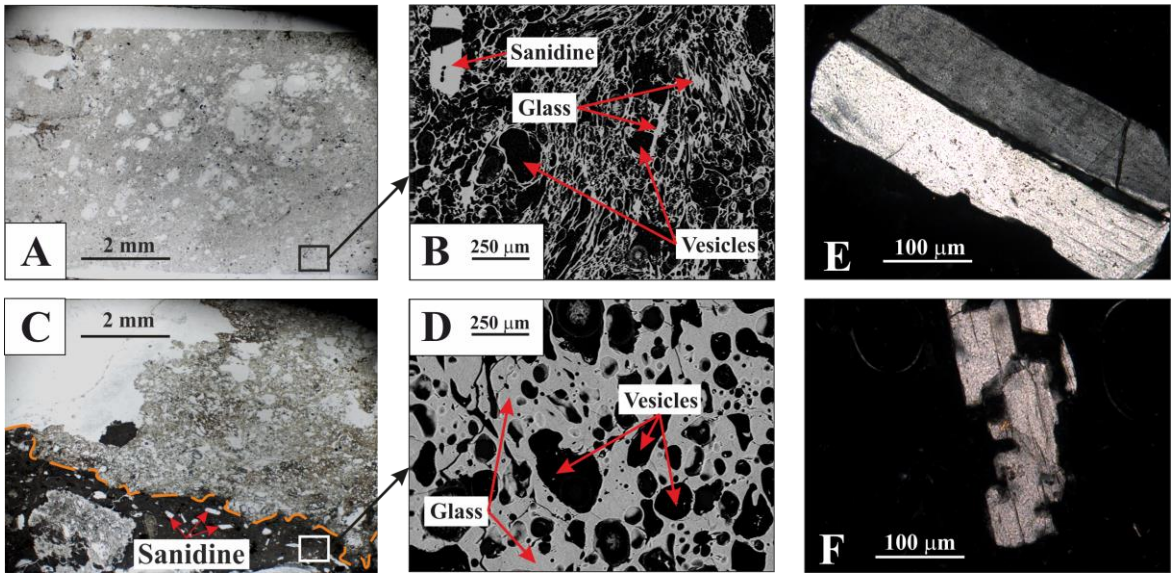

Figure 5.7 Microphotographs (thin sections A, C, E, F and BSI B-D) of pumices from the Eras formation. A-B are from pumices of suite A having low crystal content and high vesicularity. C is from suite D where two types of glass are identifiable. The first is highly vesiculated and with low crystal content (suite A type – upper part of the image) while the other one is less vesiculated and highly crystalline (dark band type – lower portion of the image). D shows a BSI image of the dark band type glass. E shows a pristine sanidine crystal while F shows a feldspar with corroded rims from sample I1A.

5.4.2 XRF Whole-rock geochemistry

The pumices are phonolitic to trachytic in composition (Figure 5.8) when plotted on a total-alkali-silica diagram (TAS - Le Bas, 1986). SiO_2 ranges between 57.97 Wt. % (I3D) and 59.62 Wt. % (F1B) whereas total alkalis are of between 11.98 Wt. % (I3D) and 12.91 Wt. % (I3A) (Table 5.5).

All the samples of the same suite have comparable bulk-rock compositions although some variations exist within suite A (sample I1A, Table 5.5 – Figure 5.9). Suites A and B have higher K, Al and Mn and lower Mg, Fe, Ca, Na, Ti, S and P with respect to suites C and D (Table 5.5). Sample I1A has higher Ca, Ti and P and lower Al and Mn concentrations with respect to the other samples of suite A (Table 5.5 – Figure 5.9). Loss on Ignition (LOI) values are of between 3.96 and 6.21 (Table 5.5) and decrease from suite A to suite D.

With particular reference to suite A, the LOI increases from the base to the top of the eruptive sequence from 4.94 to 6.21; a strong negative correlation exists between the increase of LOI and the decrease of SiO_2 (Correlation Coefficient ρ = - 0.99); a moderate negative correlation exists between LOI and K_2O (ρ = - 0.62) and a strong positive correlation exists between LOI and Na_2O (ρ = 0.97).

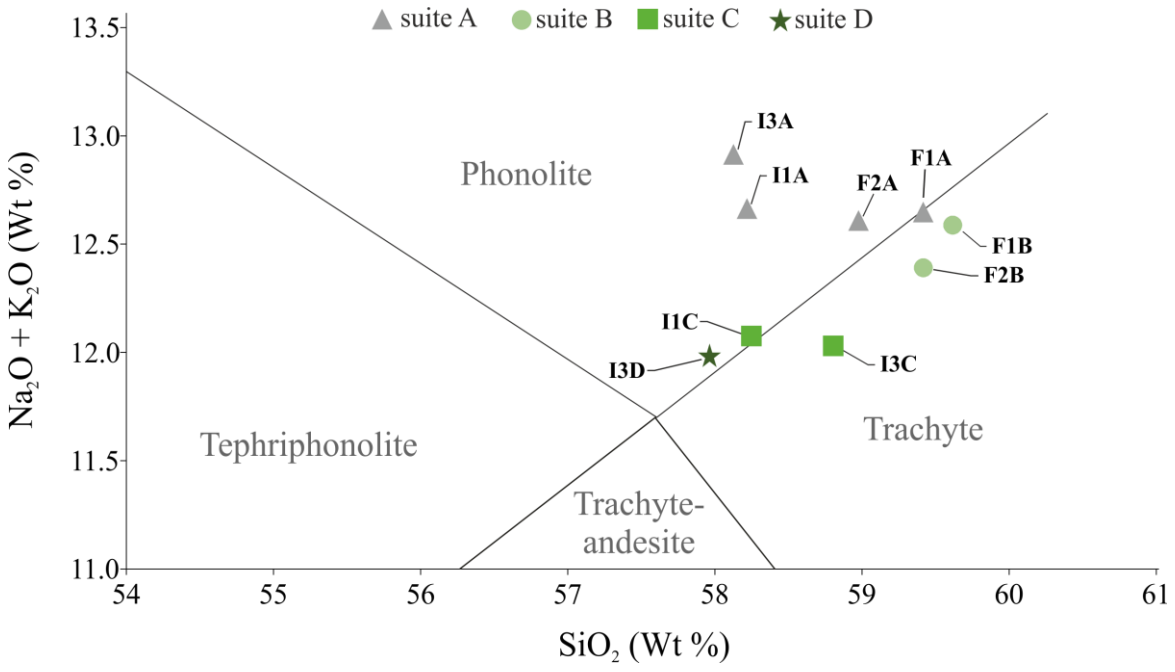

Figure 5.8 XRF whole rock data plotted on a total-alkali-silica plot (Le Bas et al., 1986). Data normalised to 100 %.

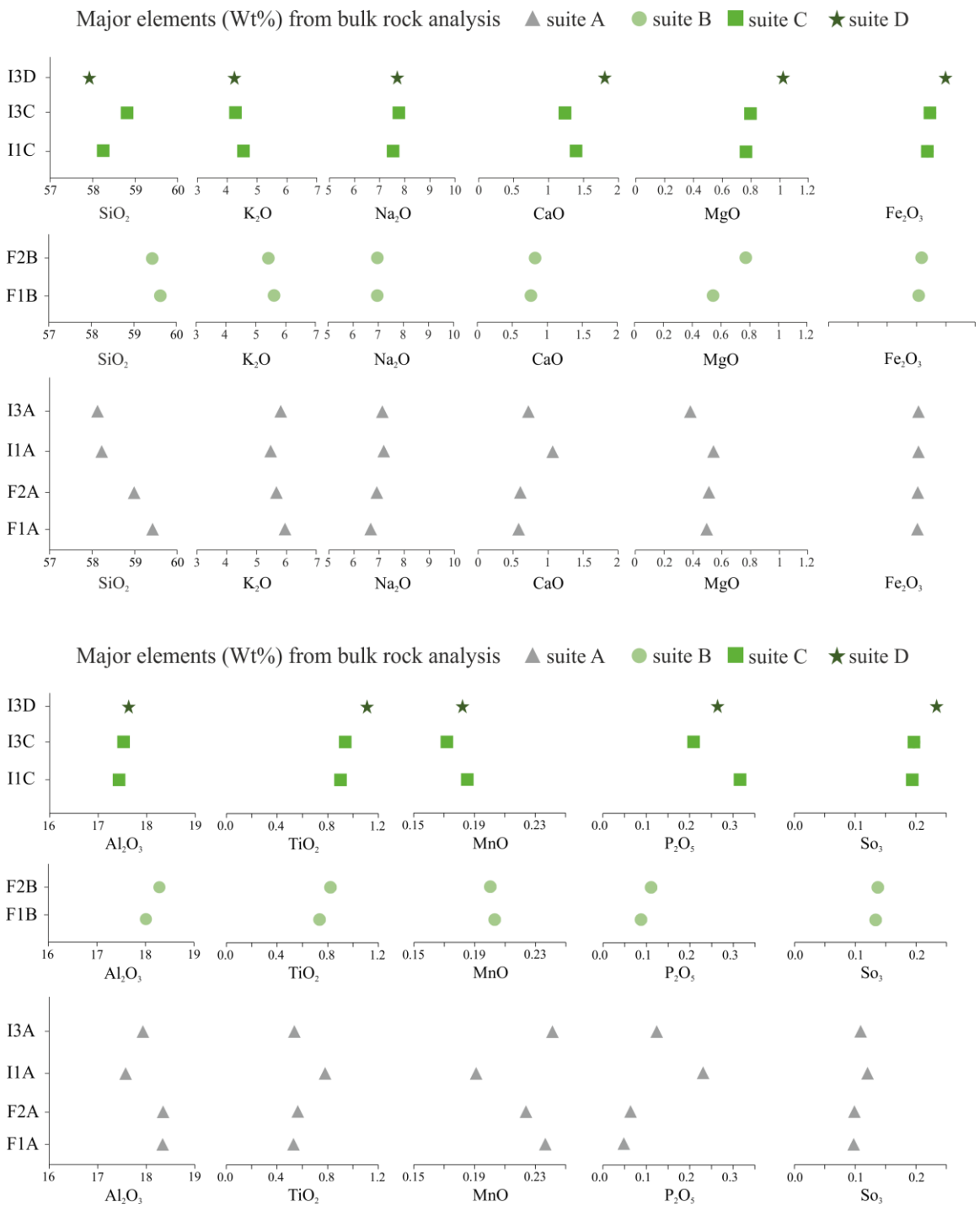

Figure 5.9 Major element compositional variations of the samples with respect to their stratigraphic positions. All the data come from bulk rock analysis. Data normalised to 100 %.

Trace elements display significant variations between samples of different suites (Table 5.5). Among the others Zr, Nb, Rb, Ba and Sr are considered because of their use as indices of mixing, differentiation and fractionational crystallization in Tenerife magmas (Wolff, 1985; Wolff and storey, 1984). The four suites are homogeneous with respect to these elements (Table 5.5) with only sample I1A displaying a composition slightly different, more similar to suite B (Figure 5.10 and 5.11). Zr positively correlates with Nb and Rb (Figure 5.10 A, 5.11 A) and negatively with Sr and Ba (Figure 5.10 B, 5.11 B). In particular, suite A has higher Zr, Nb and Rb and lower Sr and Ba with respect to suite C and D (Figure 5.10 – 5.11).

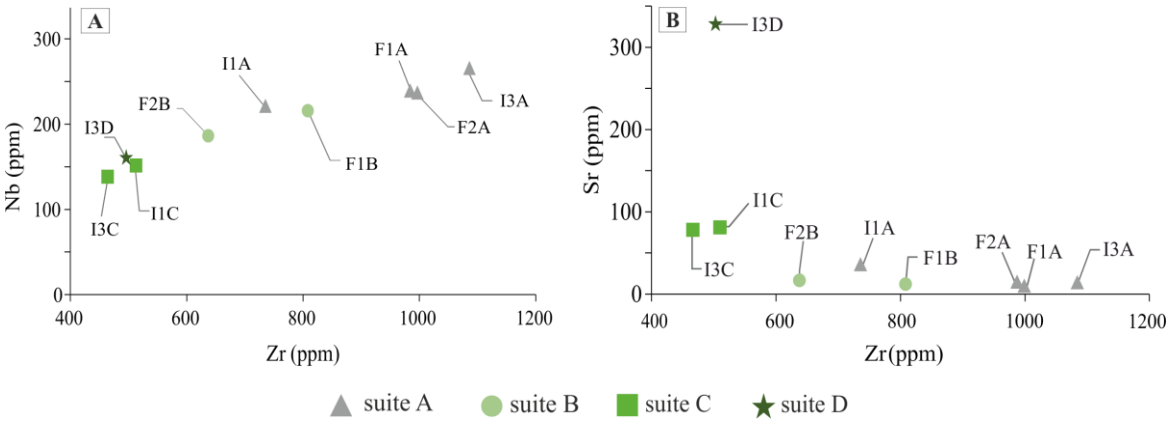

Figure 5.10 Relationships between the Zr and Nb (A) between Zr and Sr (B) in the four suites of samples (A – D).

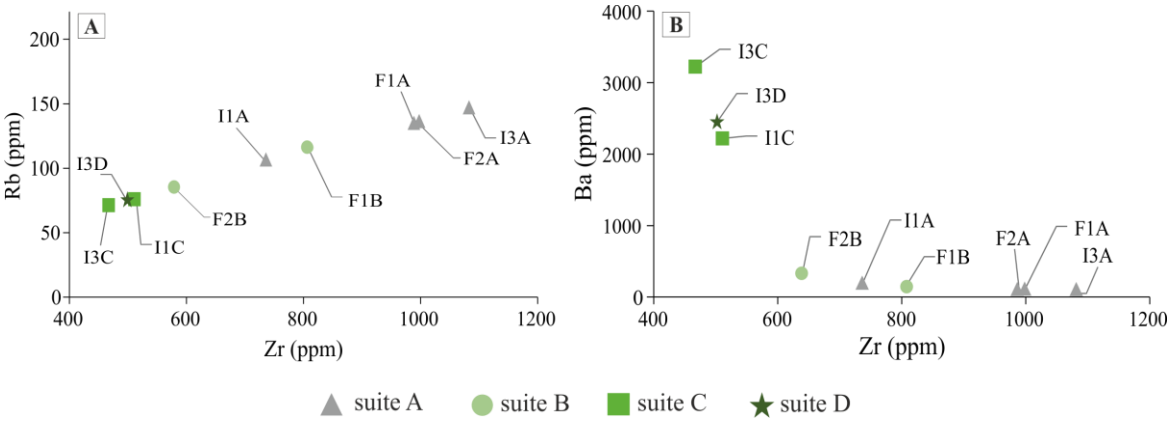

Figure 5.11 Relationships between the Zr and Rb (A) between Zr and Ba (B) in the four suites of samples (A – D).

Table 5.4 Major element abundances of pumices in the Eras Formation. Data are from XRF whole rock analyses.

Sample	F1A	F1B	F2A	F2B	I1A	I1B	I1C	I3A	I3C	I3D
Major Elements (Wt %)										
SiO_2	59.41	59.62	58.98	59.42	58.22	58.23	58.25	58.13	58.80	57.97
TiO_2	0.53	0.73	0.57	0.82	0.78	0.86	0.90	0.54	0.93	1.11
Al_2O_3	18.34	18.01	18.35	18.28	17.57	17.50	17.43	17.92	17.52	17.62
Fe_2O_3	2.99	3.06	3.00	3.16	3.03	3.33	3.32	3.03	3.41	3.94
MnO	0.24	0.20	0.22	0.20	0.19	0.19	0.19	0.24	0.17	0.18
MgO	0.50	0.55	0.51	0.77	0.54	0.70	0.76	0.38	0.79	1.02
CaO	0.57	0.76	0.60	0.82	1.07	1.38	1.40	0.72	1.23	1.80
Na_2O	6.69	6.98	6.93	6.98	7.18	7.67	7.53	7.11	7.76	7.70
K_2O	5.95	5.61	5.66	5.41	5.47	4.67	4.54	5.80	4.27	4.28
P_2O_5	0.05	0.09	0.06	0.11	0.23	0.33	0.32	0.12	0.21	0.26
SO_3	0.10	0.13	0.10	0.14	0.12	0.18	0.19	0.11	0.20	0.23
Total alkali	12.63	12.59	12.59	12.39	12.65	12.34	12.07	12.91	12.03	11.98
LOI	4.94	4.73	5.40	4.74	6.20	5.39	5.61	6.21	5.00	3.96

Note: All the values are normalized to 100%.

Table 5.5 Trace element abundances of pumices in the Eras Formation. Data are from XRF whole rock analyses.

Sample	F1A	F1B	F2A	F2B	I1A	I1B	I1C	I3A	I3C	I3D
Trace elements (ppm)										
As	1.7	1.6	2.0	0.8	2.3	2.8	2.2	2.7	0.5	2.2
Ba	68.0	144.7	61.5	329.3	196.4	1976.1	2237.3	21.8	3223.9	2439.7
Ce	252.4	274.2	252.6	261.7	273.7	209.7	207.3	231.6	177.9	199.0
Cu	0.9	3.0	2.3	1.0	4.4	15.0	4.2	9.8	0.8	3.2
Ga	26.0	25.2	25.7	22.0	22.5	21.2	20.3	28.5	19.5	20.4
La	153.4	152.7	152.0	138.6	138.2	110.7	109.3	139.4	96.5	102.6
Mo	7.5	6.4	7.4	6.0	5.7	6.3	5.8	8.1	5.8	6.5
Nb	236.5	216.4	236.0	185.5	220.5	168.6	151.9	260.0	139.3	153.0
Nd	77.7	97.7	76.2	97.5	105.7	79.6	76.5	67.4	67.8	77.6
Pb	12.0	10.8	11.4	8.7	10.4	8.1	7.7	14.0	6.4	6.1
Rb	136.0	116.0	135.0	97.4	106.9	85.2	76.3	146.4	71.1	75.1
Sn	2.6	3.5	3.0	2.2	5.6	4.9	3.4	6.4	2.3	3.2
Sr	7.2	11.8	13.7	18.1	33.1	82.1	81.4	11.8	78.0	327.6
Th	22.4	18.2	22.6	14.5	15.6	11.8	10.0	24.1	9.5	9.4
U	5.4	4.1	5.5	3.3	4.0	2.8	2.3	5.2	2.3	1.9
V	31.2	33.8	34.1	41.0	38.2	44.1	43.2	28.6	46.9	56.3
W	3.1	1.7	2.6	1.6	1.5	1.0	2.5	<0.9	1.1	<1.0
Y	42.6	46.0	42.9	42.2	54.1	47.7	59.5	46.4	31.6	35.9
Zn	124.7	112.6	124.7	102.1	107.8	107.5	95.6	134.9	89.1	96.9
Zr	997.1	808.2	988.8	638.9	736.1	579.0	510.5	1083.4	466.6	502.9

Note: All the values are normalized to 100%.

5.4.3 Feldspars and glass chemistry

5.4.3.1 Feldspars

268 electron microprobe analyses (Appendix A4.2) were performed on 92 alkali feldspars from Suite A (F1A, F2A, I1A, I3A). Feldspar compositions are in the sanidine range (Or_{37}-Or_{51}) with only a few crystals in the anorthoclase range (Or_{33}-Or_{35}) detected in sample I1A (Figure 5.12).

SiO_2 varies between 64.63 Wt. % and 67.78 Wt. % (Appendix A4.2) with mean values of 66.35±0.40 Wt. % (F1A), 66.24±0.38 Wt% (F2A), 66.39±0.49 Wt% (I1A) and 66.30±0.41 Wt. % (I3A) (Figure 5.13 A – Table 5.6). Generally speaking, the crystals are pretty uniform between the rim and the core with respect to their SiO_2 content (Appendix A4.1). Higher differences were observed at the rim of some crystals were totals are lower than 100.

K_2O varies between 4.50 Wt. % and 7.23 Wt. % (Table A5-2) with mean values of 6.01±0.50 Wt. % (F1A), 6.21±0.38 Wt. % (F2A), 5.89±0.68 Wt. % (I1A) and 6.40±0.34 Wt. % (I3A) (Table 5.6). The crystals at the base of the two deposits have a greater compositional variability than those in the upper portions (Figure 5.12 and 5.13 – Table 5.6). The alkali feldspars display minimal variations, less than 1 Wt. %, between the rim and the core with respect to their K_2O content. This variability increase up to 2 Wt. % in some crystals from sample I3A (Appendix A4.2).

Table 5.6 Major element mean values from EMPA analyses on selected alkali feldspars from suite A.

	F1A		F2A		I1A		I3A	
	Mean	± St. Dev.	Mean	± St. Dev.	Mean	± St. Dev.	Mean	± St. Dev.
N° analysis	80		80		74		34	
Major element (Wt %)*								
SiO_2	66.35	0.40	66.24	0.38	66.39	0.49	66.30	0.41
Na_2O	7.34	0.33	7.39	0.27	7.39	0.40	7.24	0.40
K_2O	6.01	0.50	6.21	0.38	5.89	0.68	6.40	0.34
CaO	0.44	0.18	0.36	0.10	0.47	0.26	0.28	0.08
MgO	0.00	0.01	0.01	0.01	0.00	0.01	0.00	0.01
MnO	0.02	0.03	0.03	0.03	0.02	0.04	0.01	0.02
FeO	0.35	0.16	0.34	0.13	0.30	0.16	0.35	0.10
Al_2O_3	19.41	0.39	19.36	0.22	19.47	0.42	19.34	0.24
TiO_2	0.06	0.05	0.05	0.05	0.05	0.05	0.06	0.05
Cl	0.01	0.02	0.01	0.02	0.01	0.01	0.02	0.02

* All the values were normalised at 100%

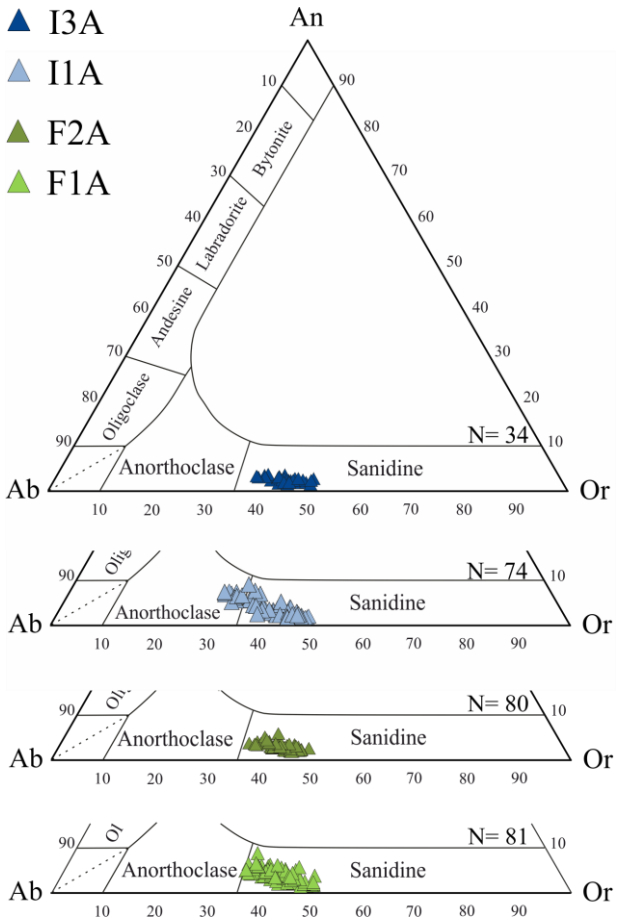

Figure 5.12 Alkali feldspars from samples F1A, F2A, I1A and I3A. The data are shown on a An-Ab-Or feldspar ternary diagram. N is the number of the crystals analysed. Data normalised to 100%.

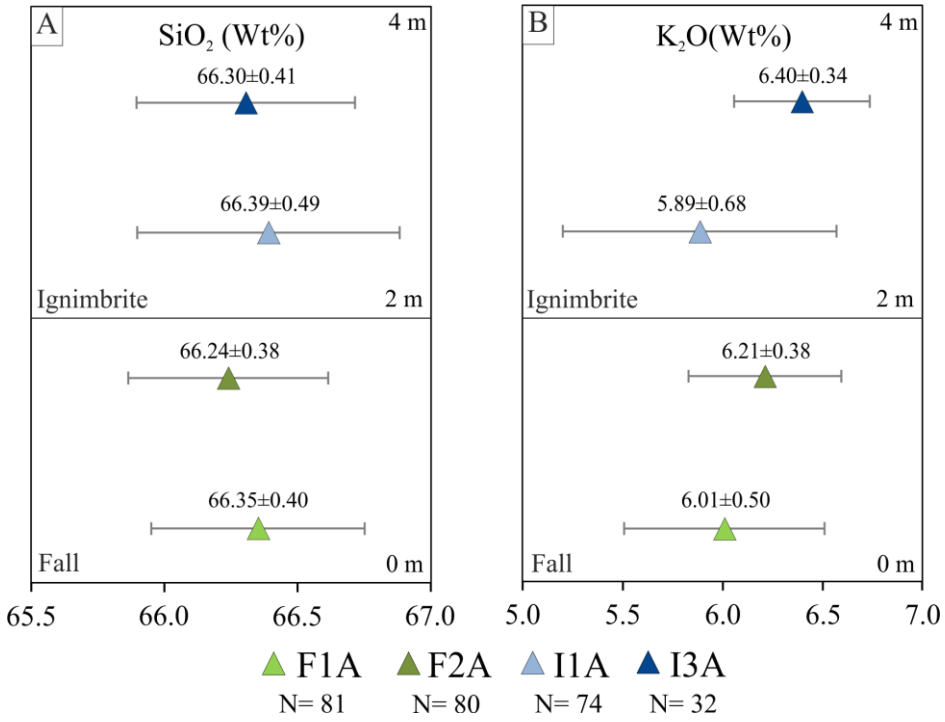

Figure 5.13 SiO_2 (A) and K_2O (B) variations for sanidines of samples F1A, F2A, I1A and I3A. Mean values and standard deviations are from data normalised to 100%.

5.4.3.2 Glass

311 electron microprobe analyses (Appendix A4.2) were performed on pumice glass shards of suite A (F1A, F2A, I1A, I3A). The results show that the glass is mainly trachytic in composition on a total-alkali-silica diagram (Le Bas et al., 1986 – Figure 3.11 A). SiO_2 is of between 60.66 Wt. % and 67.11 Wt. %, total alkalis range between 7.86 Wt. % and 13.15 Wt. % (Figure 5.14, Table 5.7), CIA indexes are of between 59.02 and 71.62 well above the optimal value of 50 for fresh unaltered glass (Nesbitt and Young, 1982) and totals are of between 90 and 99.46 (Appendix A4.2). SiO_2, K_2O, Na_2O and CIA means values of samples from a different stratigraphic positions are all within error when their standard deviations are taken in account (Table 5.7, Figure 5.15 A - D).

For each dataset CIA positively correlates with SiO_2 (ρ = 0.80 to 0.86) and negatively correlates with Na_2O (ρ = - 0.81 to - 0.93). A weak negative correlation is observed between CIA and K_2O for samples F1A and F2A (ρ = - 0.26 and - 0.24, respectively), while a moderate negative correlation exists between the two for samples I1A and I3A (ρ = - 0.45 and - 0.37, respectively).

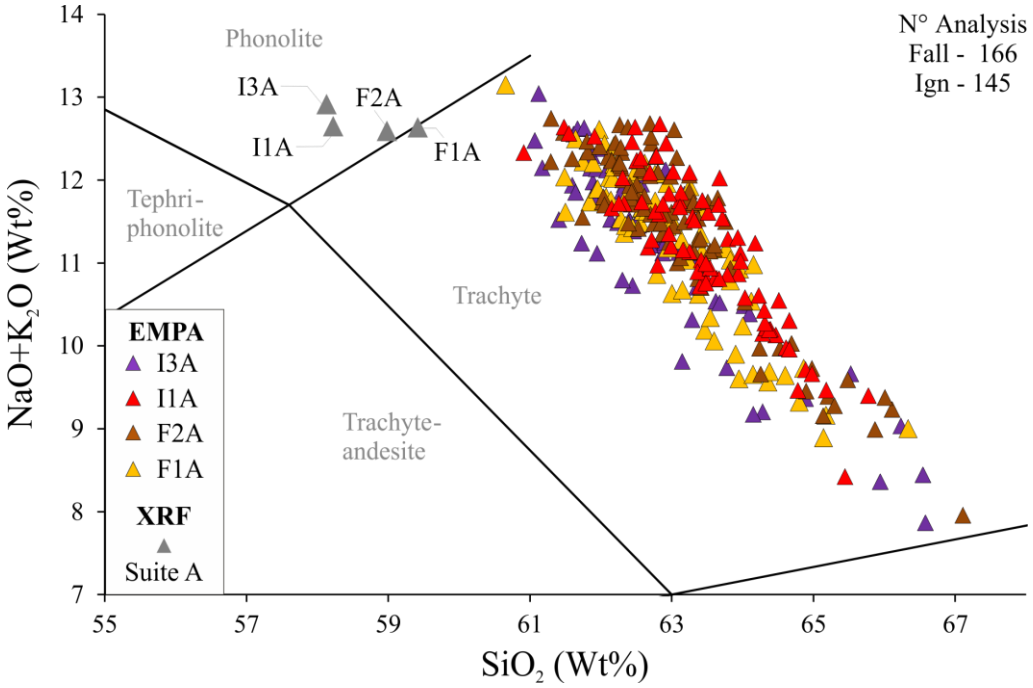

Figure 5.14 EMPA data on individual pumice glass from samples F1A, F2A, I1A and I3A plotted on a total-alkali-silica diagram (Le Bas et al., 1986). Data normalized to 100 %.

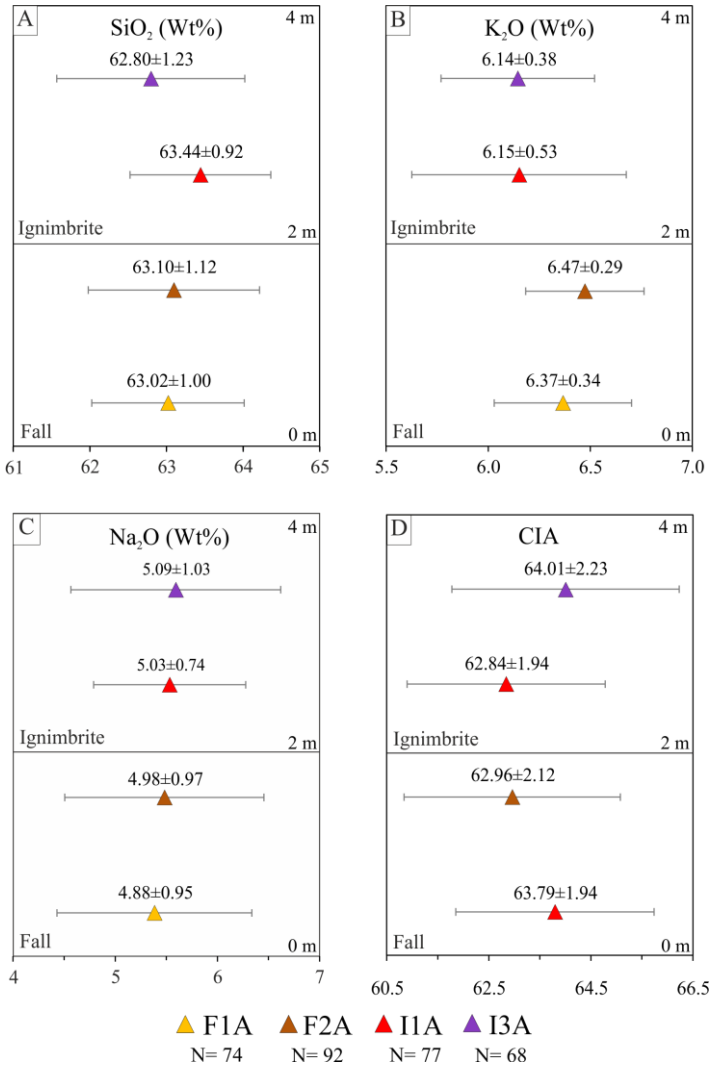

Figure 5.15 SiO_2 (A), K_2O (B), Na_2O (C) and CIA (D) variations for pumice glass of samples F1A, F2A, I1A and I3A. Mean values and standard deviations are from electron microprobe data after totals recalculated to 100%.

Table 5.7 Major element mean values from EMPA on selected pumice glass from suite A.

	F1A		F2A		I1A		I3A	
	Mean	± St. Dev.	Mean	± St. Dev.	Mean	± St. Dev.	Mean	± St. Dev.
N° analysis	74		92		77		68	
Major element (Wt %)*								
SiO_2	63.02	1.00	63.10	1.12	63.44	0.92	62.80	1.23
Na_2O	4.88	0.95	4.98	0.97	5.03	0.74	5.09	1.03
K_2O	6.37	0.34	6.47	0.29	6.15	0.53	6.14	0.38
CaO	0.65	0.18	0.69	0.15	0.85	0.16	0.58	0.13
MgO	0.30	0.04	0.37	0.04	0.39	0.05	0.26	0.04
MnO	0.24	0.07	0.21	0.06	0.20	0.06	0.29	0.07
FeO	2.77	0.37	2.67	0.40	2.77	0.34	3.05	0.40
Al_2O_3	20.91	0.36	20.59	0.36	20.30	0.39	20.94	0.39
TiO_2	0.59	0.10	0.71	0.08	0.78	0.11	0.54	0.07
Cl	0.27	0.05	0.21	0.04	0.19	0.04	0.32	0.05
Total Alkali	11.25	0.95	11.45	1.01	11.18	0.89	11.24	1.08
CIA	63.79	1.94	62.96	2.12	62.84	1.94	64.01	2.23
Totals	94.95	1.34	94.34	1.44	95.52	1.42	96.36	2.20

* Means from data normalized to 100%

5.5 Noble gas (NG) Analysis

Single grain fusion NG analysis (^{4}He - ^{36}Ar - ^{40}Ar) were performed on 115 pumice glass shards and on 109 sanidine crystals derived from pumices of suite A (F1A, F2A, I1A, I3A). Based on the results of the analysis the sanidines and pumice glass can be separated into two different groups with respect to their NG signatures, ^{4}He/^{40}Ar* and ^{40}Ar/^{36}Ar ratios (Figure 5.16 A-B-C). The analytical uncertainties are expressed at the 1σ level.

The sanidines (Group A in Figure 5.16 A) display a ^{4}He mean value of 4.96E^{-7} cc/g while the pumice glass (Group B in figure 5.16 A) has a lower ^{4}He mean value of 2.05E^{-7} cc/g. The ^{40}Ar mean value is lower in the sanidine (9.93E^{-7} cc/g) and higher in the pumice glass (2.16E^{-5} cc/g); the same is observed for the ^{36}Ar mean value that is lower in the sanidines (3.78E^{-9} cc/g) and higher in the pumice glass (7.40E^{-8} cc/g). ^{40}Ar* is lower in the sanidine (1.80E^{-7}) and higher in the glass (9.26E^{-7} cc/g).

The sanidines (Group A in Figure 5.16 B) have higher mean ^{4}He/^{40}Ar* ratios of 9.68 with respect to pumice glass (Group B in Figure 5.16 B) that displays a mean ratio of 0.27. The ^{40}Ar/^{36}Ar mean ratio in the sanidines (Group A in Figure 5.16 C) is of 353.9 while in the pumice glass (Group B in Figure 5.16 C) is of 288.5.

The results of the NG analysis performed on sanidines and on pumice glass are presented and described in more detail in the two following sections. Because NG concentrations vary considerably from sample to sample it is the minimum, maximum and mean values that are presented for each isotope (^{4}He, ^{36}Ar, ^{40}Ar, ^{40}Ar*) and isotopic ratio (^{40}Ar/^{36}Ar, ^{4}He/^{40}Ar*) from each sample. Data of individual samples are listed in Tables 5.8 – 5.15 and presented in Figures 5.17 – 5.28.

Data that have negative values after blank correction (gas concentrations below blank level) or with 1σ analytical uncertainties higher than 100% of the absolute value are not included in this section. All these data, together with mean blank values and calibration measurements, are reported in Appendix A4.3 for completeness.

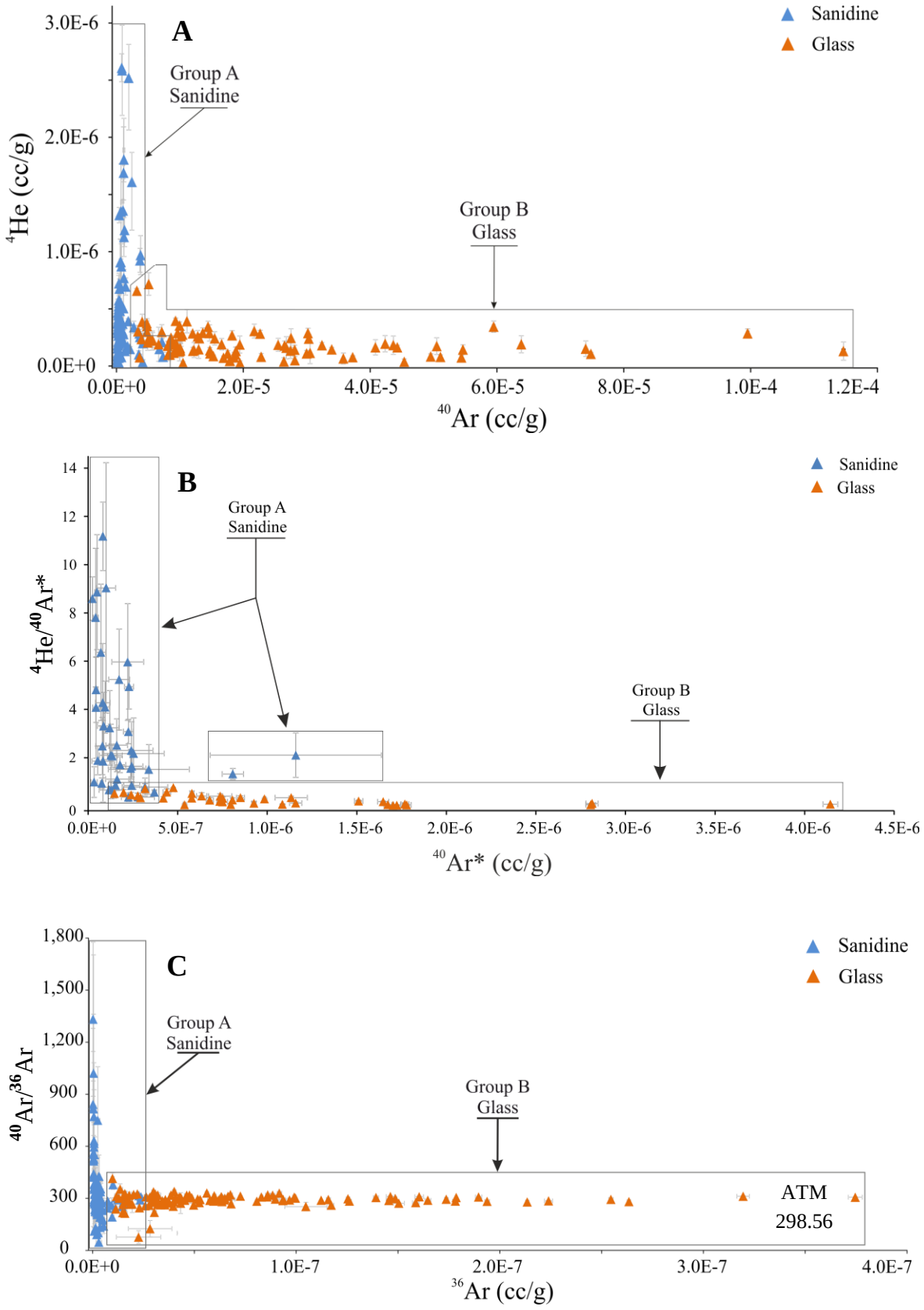

Figure 5.16 A-B-C Isotopic composition and ratios of the analysed sanidines (Group A) and pumice glass (Group B). Data are reported at the 1σ level. Error bars if not visible are smaller than the size of the symbol used to visualize the data point. In B the three data of Group A with ^{4}He/^{40}Ar* of around 90 are not displayed for clarity.

5.5.1 Pumice Glass

5.5.1.1 ^{4}He isotope

96 samples yielded positive ^{4}He values after blank correction. ^{4}He concentrations range between $2.64E^{-8}\pm1.42E^{-8}$ cc/g and $1.36E^{-6}\pm8.60E^{-8}$ cc/g (Figure 5.17) with analytical uncertainties of between 3% and 82% (Tables 5.8 - 5.11).

- F1A has ^{4}He values ranging between $7.55E^{-8}\pm2.74E^{-8}$ cc/g and $1.36E^{-6}\pm8.60E^{-8}$ cc/g with a mean of $3.39E^{-7}$ cc/g.
- F2A has ^{4}He concentrations of between $4.00E^{-8}\pm3.29E^{-8}$ cc/g and $3.74E^{-7}\pm4.04E^{-8}$ cc/g with a mean of $1.87E^{-7}$ cc/g.
- I1A has ^{4}He values ranging between $2.64E^{-8}\pm1.42E^{-8}$ cc/g and $3.54E^{-7}\pm3.04E^{-8}$ cc/g. The ^{4}He mean concentration is $1.59E^{-7}$ cc/g.
- I3A has ^{4}He contents varying of between $3.65E^{-8}\pm2.61E^{-8}$ cc/g and $2.88E^{-7}\pm4.17E^{-8}$ cc/g with a mean of $1.59E^{-7}$ cc/g.

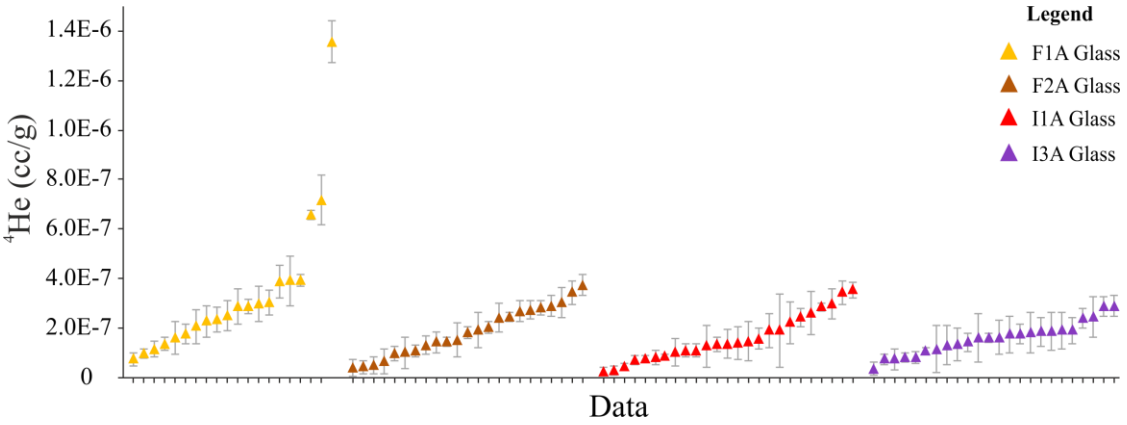

Figure 5.17 Variation of the ^{4}He in pumice glass of samples F1A, F2A, I1A and I3A. The data are ordered from the lowest to the highest value and reported at the 1σ level. Error bars if not visible are smaller than the symbol used to display the data.

5.5.1.2 Ar isotopes

^{40}Ar varies by two orders of magnitude between $1.72E^{-6}\pm7.84E^{-8}$ cc/g and $1.15E^{-4}\pm2.59E^{-7}$ cc/g (Figure 5.18) with analytical uncertainties ranging from <1% up to 11% (Tables 5.8 - 5.11).

- F1A has the minimum variability in term of ^{40}Ar with values ranging between $2.72E^{-6}\pm8.23E^{-9}$ cc/g and $1.47E^{-5}\pm3.60E^{-8}$ cc/g with a mean of $7.04E^{-6}$ cc/g.
- F2A has ^{40}Ar concentrations of between $1.72E^{-6}\pm7.84E^{-8}$ cc/g and $7.40E^{-5}\pm8.08E^{-8}$ cc/g with a mean of $2.40E^{-5}$ cc/g.
- I1A has ^{40}Ar values ranging between $5.64E^{-6}\pm1.99E^{-8}$ cc/g and $3.73E^{-5}\pm2.73E^{-8}$ cc/g. The ^{4}He mean concentration is $1.35E^{-5}$ cc/g.
- I3A has the maximum variability in term of ^{40}Ar content with values of between $1.66E^{-5}\pm2.26E^{-8}$ cc/g and $1.15E^{-4}\pm2.59E^{-7}$ cc/g with a mean of $4.32E^{-5}$ cc/g.

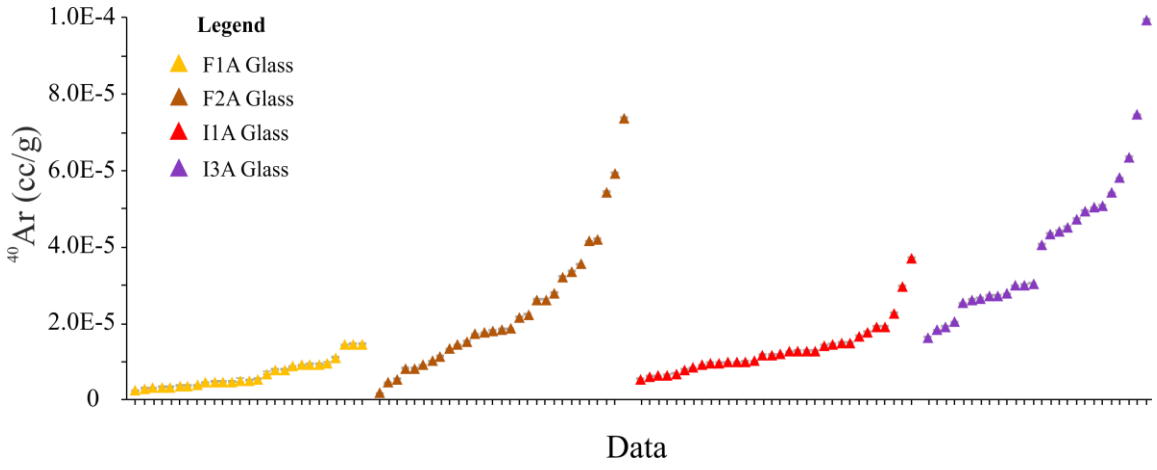

Figure 5.18 Variation of the ^{40}Ar in pumice glass of samples F1A, F2A, I1A and I3A. The data are ordered from the lowest to the highest value and reported at the 1σ level. Error bars if not visible are smaller than the symbol used to display the data.

^{36}Ar varies between 9.80E^{-9}±7.54E^{-10} cc/g and 3.75E^{-7}±3.43E^{-9} cc/g (Figure 5.19) with analytical uncertainties of between <1% and 48% (Tables 5.8 - 5.11).

- F1A has the minimum variability in term of ^{36}Ar with values ranging between 9.80E^{-9}±7.54E^{-10} cc/g and 4.81E^{-8}±1.15E^{-9} cc/g with a mean of 2.45E^{-8} cc/g.
- F2A has ^{36}Ar concentrations of between 1.68E^{-8}±6.16E^{-10} cc/g and 2.63E^{-7}±8.38E^{-10} cc/g with a mean of 8.46E^{-8} cc/g.
- I1A has ^{36}Ar values ranging between 2.02E^{-8}±6.27E^{-10} cc/g and 1.25E^{-7}±8.90E^{-10} cc/g. The ^{4}He mean concentration is 4.64E^{-8} cc/g.
- I3A has the maximum variability in term of ^{36}Ar content with values of between 5.62E^{-8}±7.52E^{-10} cc/g and 3.75E^{-7}±3.43E^{-9} cc/g with a mean of 1.45E^{-7} cc/g.

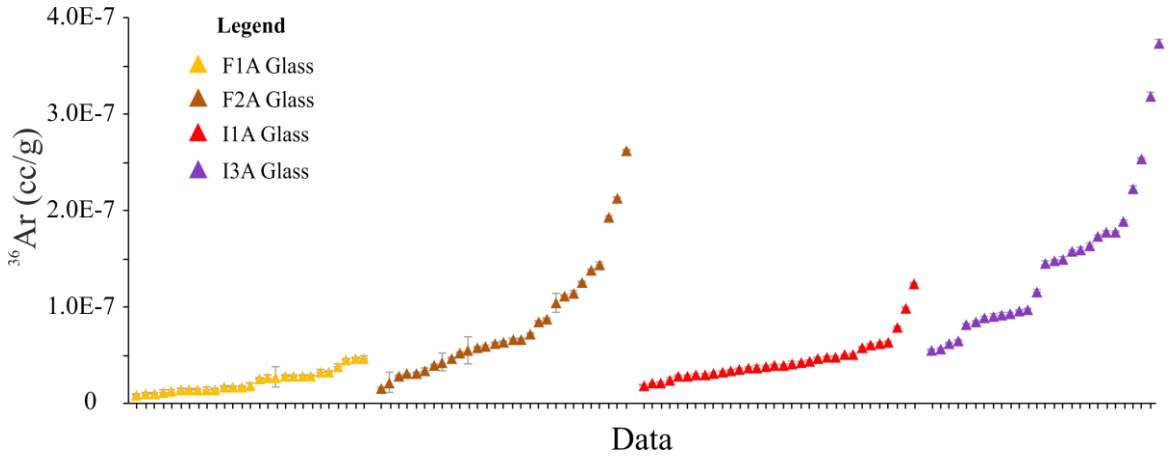

Figure 5.19 Variation of the ^{36}Ar in pumice glass of samples F1A, F2A, I1A and I3A. The data are ordered from the lowest to the highest value and reported at the 1σ level. Error bars if not visible are smaller than the symbol used to display the data.

Only 51 samples, after atmospheric correction, yielded positive $^{40}Ar^*$ values ($^{40}Ar^* = {}^{40}Ar - 298.56 \times {}^{36}Ar$). The $^{40}Ar^*$ ranges between $1.74E^{-8}\pm2.09E^{-9}$ cc/g and $4.14E^{-6}\pm4.09E^{-8}$ cc/g (Figure 5.20) with analytical uncertainties of between 1% and 12% (Tables 5.8 - 5.11).

- F1A has $^{40}Ar^*$ with values ranging between $1.74E^{-8}\pm2.09E^{-9}$ cc/g and $1.13E^{-6}\pm9.02E^{-8}$ cc/g with a mean of $4.56E^{-7}$ cc/g.
- F2A has $^{40}Ar^*$ concentrations of between $4.53E^{-7}\pm7.19E^{-9}$ cc/g and $1.72E^{-6}\pm2.01E^{-8}$ cc/g with a mean of $1.11E^{-6}$ cc/g.
- I1A has $^{40}Ar^*$ values ranging between $7.19E^{-8}\pm7.68E^{-10}$ cc/g and $1.16E^{-6}\pm3.41E^{-8}$ cc/g. The ^{4}He mean concentration is $5.26E^{-7}$ cc/g.
- I3A has $^{40}Ar^*$ values of between $5.79E^{-7}\pm8.33E^{-9}$ cc/g and $4.14E^{-6}\pm4.09E^{-8}$ cc/g with a mean of $1.72E^{-6}$ cc/g.

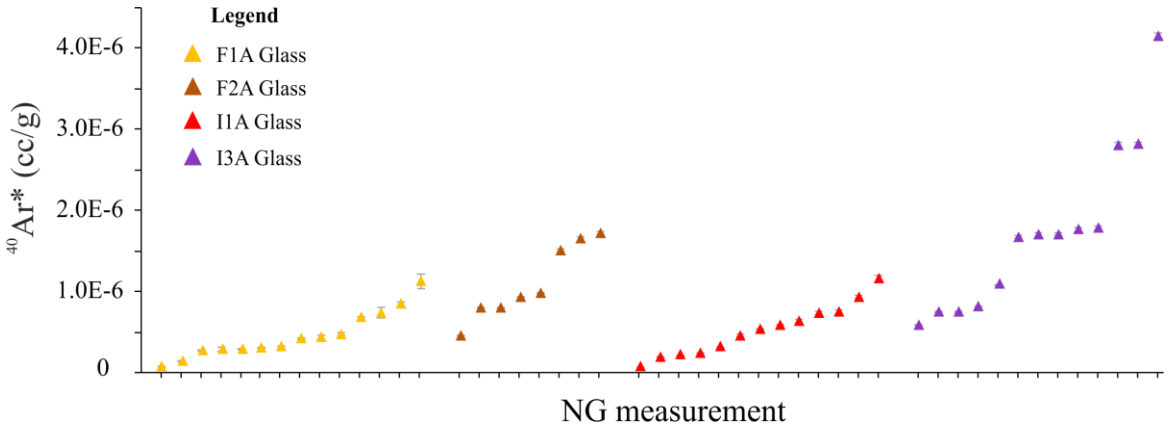

Figure 5.20 Variation of the $^{40}Ar^*$ in pumice glass of samples F1A, F2A, I1A and I3A. The data are ordered from the the lowest to the highest value and reported at the 1σ level. Error bars if not visible are smaller than the symbol used to display the data.

Table 5.8 NG abundances expressed in cc/g STP in glasses of samples F1A and F2A.

N°	^{4}He	±1σ	1σ%	^{36}Ar	±1σ	1σ%	^{40}Ar	±1σ	1σ%	^{40}Ar*	1σ	1σ%
Sample F1A												
1	-	-	-	3.4E-8	1.5E-9	4	9.8E-6	3.0E-7	3	-	-	-
2	-	-	-	1.9E-8	2.9E-9	15	5.2E-6	5.7E-7	11	-	-	-
3	-	-	-	1.3E-8	1.3E-9	10	3.9E-6	2.6E-7	7	1.7E-8	2.1E-9	12
4	-	-	-	1.5E-8	1.0E-9	7	4.9E-6	2.1E-7	4	2.8E-7	2.3E-8	8
5	6.6E-7	2.0E-8	3	1.1E-8	2.8E-10	2	2.7E-6	8.2E-9	0.3	-	-	-
8	-	-	-	2.8E-8	1.1E-8	38	3.5E-6	1.2E-7	3	-	-	-
11	3.0E-7	5.1E-8	17	1.6E-8	1.2E-9	7	3.4E-6	5.9E-8	2	-	-	-
12	2.9E-7	2.8E-8	10	3.4E-8	5.4E-10	2	9.6E-6	3.9E-8	0.4	-	-	-
13	7.5E-8	2.7E-8	36	1.2E-8	5.2E-10	4	3.7E-6	5.9E-8	2	1.5E-7	7.0E-9	5
16	4.0E-7	2.4E-8	6	3.0E-8	6.0E-10	2	9.3E-6	7.0E-8	0.8	4.8E-7	1.0E-8	2
18	1.4E-6	8.6E-8	6	2.8E-8	1.7E-9	6	7.2E-6	2.3E-7	3	-	-	-
19	9.9E-8	1.9E-8	20	2.6E-8	7.8E-10	3	8.1E-6	8.9E-8	1	2.9E-7	9.2E-9	3
21	1.6E-7	6.7E-8	41	2.9E-8	8.2E-10	3	9.5E-6	8.9E-8	0.9	6.8E-7	2.0E-8	3
22	2.4E-7	5.0E-8	21	1.5E-8	7.2E-10	5	3.9E-6	5.9E-8	2	-	-	-
23	-	-	-	1.5E-8	9.9E-10	7	3.2E-6	1.1E-7	3.3	-	-	-
24	2.1E-7	6.9E-8	33	1.9E-8	8.4E-10	5	4.9E-6	9.1E-8	2	-	-	-
25	1.2E-7	3.1E-8	27	2.9E-8	3.8E-10	1	9.1E-6	4.5E-8	0.5	2.8E-7	3.9E-9	1
26	1.4E-7	2.5E-8	18	4.8E-8	3.1E-10	0.6	1.5E-5	3.6E-8	0.2	4.2E-7	2.9E-9	1
27	2.5E-7	6.0E-8	24	1.6E-8	7.3E-10	5	5.2E-6	8.0E-8	2	4.4E-7	2.1E-8	5
28	1.8E-7	3.8E-8	21	2.9E-8	4.6E-10	2	8.1E-6	5.1E-8	0.6	-	-	-
29	2.3E-7	6.5E-8	29	1.8E-8	1.1E-9	6	5.7E-6	8.7E-8	2	3.2E-7	1.9E-8	6
30	3.9E-7	6.6E-8	17	9.8E-9	7.5E-10	8	4.1E-6	8.2E-8	2	1.1E-6	9.0E-8	8
31	2.9E-7	7.1E-8	25	4.6E-8	1.2E-9	3	1.5E-5	9.5E-8	0.6	8.5E-7	2.2E-8	3
32	7.2E-7	9.9E-8	14	1.8E-8	1.1E-9	6	5.1E-6	1.2E-7	2	-	-	-
33	3.0E-7	7.1E-8	24	1.4E-8	1.2E-9	9	4.8E-6	9.5E-8	2	7.4E-7	6.4E-8	9
34	3.9E-7	1.0E-7	26	4.0E-8	1.7E-9	4	1.1E-5	1.3E-7	1	N.A.	N.A.	N.A.
35	-	-	-	4.8E-8	1.1E-9	2	1.5E-5	1.3E-7	0.9	3.1E-7	7.9E-9	3
Sample F2A												
1	-	-	-	4.3E-8	9.5E-9	22	1.2E-5	6.3E-8	0.5	-	-	-
2	-	-	-	2.3E-8	1.1E-8	48	1.7E-6	7.8E-8	5	-	-	-
3	-	-	-	1.0E-7	1.0E-8	10	2.6E-5	6.5E-8	0.2	-	-	-
4	-	-	-	5.6E-8	1.4E-8	26	5.5E-6	9.8E-8	2	-	-	-
6	3.4E-7	4.9E-8	14	2.1E-7	8.2E-10	0.4	5.9E-5	1.8E-7	0.3	-	-	-
7	2.9E-7	4.4E-8	15	4.0E-8	7.2E-10	2	1.4E-5	7.7E-8	0.6	1.6E-6	3.1E-8	2
8	2.7E-7	4.0E-8	15	6.8E-8	6.7E-10	1	1.8E-5	6.8E-8	0.4	-	-	-
9	1.4E-7	4.1E-8	29	1.9E-7	1.1E-9	0.6	5.5E-5	9.5E-8	0.2	-	-	-
10	3.1E-7	6.0E-8	20	6.8E-8	1.0E-9	1	2.2E-5	9.7E-8	0.4	1.5E-6	2.3E-8	2
11	5.0E-8	3.4E-8	68	8.8E-8	1.0E-9	1	2.8E-5	3.5E-8	0.1	1.7E-6	2.0E-8	1
12	4.4E-8	2.7E-8	60	6.4E-8	5.5E-10	0.9	1.8E-5	1.7E-8	0.1	-	-	-
13	2.0E-7	7.1E-8	37	1.4E-7	1.2E-9	0.9	4.2E-5	4.6E-8	0.1	8.1E-7	7.2E-9	1
14	1.5E-7	6.8E-8	44	2.6E-7	8.4E-10	0.3	7.4E-5	8.1E-8	0.1	-	-	-
15	2.7E-7	3.7E-8	13	3.6E-8	8.4E-10	2	1.0E-5	3.6E-8	0.3	-	-	-
16	-	-	-	4.8E-8	7.4E-10	2	1.5E-5	4.7E-8	0.3	4.5E-7	7.2E-9	2
17	1.0E-7	6.3E-8	61	6.0E-8	8.0E-10	1	1.9E-5	4.2E-8	0.2	9.3E-7	1.2E-8	1
18	2.4E-7	5.9E-8	25	5.3E-8	6.3E-10	1	1.5E-5	3.9E-8	0.3	-	-	-
20	2.0E-7	2.5E-8	12	3.2E-8	5.5E-10	2	9.4E-6	3.2E-8	0.3	-	-	-
23	1.1E-7	2.5E-8	23	5.9E-8	5.2E-10	0.9	1.8E-5	3.1E-8	0.2	-	-	-
24	4.0E-8	3.3E-8	82	8.6E-8	6.7E-10	0.8	2.6E-5	4.4E-8	0.2	8.0E-7	6.4E-9	1
25	6.7E-8	4.8E-8	72	1.3E-7	8.5E-10	0.7	3.6E-5	5.9E-8	0.2	-	-	-
26	3.7E-7	4.0E-8	11	1.7E-8	6.2E-10	4	4.8E-6	4.3E-8	0.9	-	-	-
27	-	-	-	1.5E-7	1.3E-9	0.9	4.2E-5	4.8E-8	0.1	-	-	-
28	1.3E-7	3.5E-8	27	6.5E-8	8.7E-10	1	1.9E-5	4.2E-8	0.2	-	-	-
29	2.8E-7	3.0E-8	11	7.3E-8	5.1E-10	0.7	2.3E-5	2.8E-8	0.1	9.8E-7	7.0E-9	1
30	1.0E-7	2.9E-8	29	3.2E-8	5.5E-10	2	8.4E-6	2.3E-8	0.3	-	-	-
31	1.8E-7	2.3E-8	13	1.1E-7	4.5E-10	0.4	3.2E-5	1.7E-8	0.1	-	-	-
33	1.5E-7	1.8E-8	12	1.2E-7	1.0E-9	0.9	3.4E-5	6.5E-8	0.2	-	-	-
34	2.5E-7	1.9E-8	8	3.0E-8	3.1E-10	1	8.6E-6	1.2E-8	0.1	-	-	-

Empty spaces (-) are for data with negative NG concentration after blank / atmospheric correction or with 1σ > 100 %.

Table 5.9 NG abundances expressed in cc/g STP in glasses of samples I1A and I3A.

N°	^{4}He	±1σ	1σ%	^{36}Ar	±1σ	1σ%	^{40}Ar	±1σ	1σ%	^{40}Ar*	1σ	1σ%
Sample I1A												
3	1.1E-7	2.5E-8	23	1.0E-7	5.2E-10	0.5	3.0E-5	4.1E-8	0.1	0.46	0.10	23
4	-	-	-	4.8E-8	4.8E-10	1	1.5E-5	7.3E-8	0.5	-	-	-
5	1.4E-7	5.8E-8	42	3.0E-8	8.5E-10	3	1.0E-5	8.1E-8	0.8	0.12	0.05	42
6	1.6E-7	4.2E-8	26	4.0E-8	6.4E-10	2	1.0E-5	6.3E-8	0.6	-	-	-
8	1.1E-7	2.5E-8	23	4.9E-8	4.9E-10	1	1.5E-5	3.5E-8	0.2	0.56	0.13	23
9	3.4E-7	4.8E-8	14	5.2E-8	6.0E-10	1	1.4E-5	4.7E-8	0.3	-	-	-
10	-	-	-	3.3E-8	9.6E-10	3	8.7E-6	2.9E-8	0.3	-	-	-
11	-	-	-	4.3E-8	6.0E-10	1	1.3E-5	1.2E-8	0.1	-	-	-
12	-	-	-	2.6E-8	9.9E-10	4	6.6E-6	2.8E-8	0.4	-	-	-
13	1.3E-7	8.4E-8	65	3.1E-8	1.1E-9	4	1.0E-5	2.1E-8	0.2	0.17	0.11	65
14	1.9E-7	1.5E-7	78	3.0E-8	9.3E-10	3	6.7E-6	3.5E-8	0.5	-	-	-
15	1.0E-7	5.5E-8	55	3.0E-8	3.7E-10	1	8.2E-6	2.2E-8	0.3	-	-	-
16	-	-	-	4.3E-8	1.0E-9	2	1.3E-5	3.6E-8	0.3	-	-	-
17	2.6E-7	8.9E-8	34	3.2E-8	1.5E-9	5	1.0E-5	3.4E-8	0.3	0.41	0.14	34
18	1.5E-7	8.0E-8	55	5.0E-8	7.5E-10	2	1.3E-5	3.0E-8	0.2	-	-	-
19	1.4E-7	6.6E-8	47	3.8E-8	8.7E-10	2	1.2E-5	2.0E-8	0.2	0.19	0.09	47
20	-	-	-	6.5E-8	6.9E-10	1	1.9E-5	3.3E-8	0.2	-	-	-
21	2.2E-7	8.4E-8	38	2.3E-8	5.6E-10	2	5.6E-6	2.0E-8	0.4	-	-	-
22	1.9E-7	6.8E-8	35	3.6E-8	4.5E-10	1	9.3E-6	1.5E-8	0.2	-	-	-
23	3.0E-7	6.2E-8	21	2.2E-8	4.1E-10	2	7.1E-6	1.7E-8	0.2	0.52	0.11	21
24	4.6E-8	1.3E-8	29	6.2E-8	7.3E-10	1	1.8E-5	4.3E-8	0.2	-	-	-
25	7.2E-8	1.7E-8	23	6.0E-8	6.2E-10	1	1.7E-5	5.6E-8	0.3	-	-	-
26	7.7E-8	1.2E-8	16	1.3E-7	8.9E-10	0.7	3.7E-5	2.7E-8	0.1	-	-	-
27	2.7E-8	1.8E-8	69	6.3E-8	1.0E-9	2	1.9E-5	4.0E-8	0.2	0.05	0.03	69
28	2.6E-8	1.4E-8	54	3.7E-8	4.6E-10	1	1.0E-5	2.5E-8	0.2	-	-	-
29	2.9E-7	1.8E-8	6	4.1E-8	5.6E-10	1	1.2E-5	3.6E-8	0.3	-	-	-
30	8.7E-8	1.0E-8	11	5.2E-8	3.2E-10	0.6	1.5E-5	3.8E-8	0.2	-	-	-
31	3.5E-7	3.0E-8	9	3.6E-8	6.4E-10	2	9.9E-6	4.8E-8	0.5	-	-	-
32	-	-	-	2.0E-8	6.3E-10	3	6.5E-6	2.7E-8	0.4	-	-	-
33	8.1E-8	2.8E-8	34	8.1E-8	6.7E-10	0.8	2.3E-5	7.8E-8	0.3	-	-	-
34	1.3E-7	3.0E-8	23	4.1E-8	6.0E-10	1	1.2E-5	2.8E-8	0.2	-	-	-
35	2.4E-7	3.7E-8	15	4.5E-8	6.0E-10	1	1.3E-5	7.1E-8	0.5	-	-	-
Sample I3A												
1	1.1E-7	1.3E-8	13	2.5E-7	1.1E-9	0.4	7.5E-5	4.4E-8	0.1	-	-	-
2	1.9E-7	5.1E-8	27	5.8E-8	1.1E-9	2	1.7E-5	2.3E-8	0.1	-	-	-
3	2.9E-7	4.0E-8	14	3.2E-7	3.1E-9	1	1.0E-4	1.7E-7	0.2	0.07	0.01	14
4	2.4E-7	3.9E-8	16	9.9E-8	7.2E-10	0.7	3.0E-5	2.2E-8	0.1	0.32	0.05	16
6	7.6E-8	4.3E-8	57	5.6E-8	7.5E-10	1	1.9E-5	3.8E-8	0.2	0.04	0.02	57
7	8.0E-8	1.8E-8	23	1.7E-7	8.6E-10	0.5	5.1E-5	4.3E-8	0.1	-	-	-
8	1.8E-7	4.0E-8	23	9.0E-8	1.5E-9	2	2.7E-5	2.8E-8	0.1	-	-	-
9	1.4E-7	3.8E-8	27	9.7E-8	8.9E-10	0.9	2.8E-5	2.4E-8	0.1	-	-	-
10	1.3E-7	8.0E-8	61	3.7E-7	3.4E-9	0.9	1.1E-4	2.6E-7	0.2	0.05	0.03	61
11	1.9E-7	7.5E-8	40	2.2E-7	2.0E-9	0.9	6.4E-5	7.9E-8	0.1	-	-	-
12	1.9E-7	5.7E-8	31	8.3E-8	7.1E-10	0.9	2.6E-5	3.7E-8	0.1	0.25	0.08	31
13	2.5E-7	8.2E-8	33	9.4E-8	1.1E-9	1	2.8E-5	5.1E-8	0.2	-	-	-
14	-	-	-	1.6E-7	1.5E-9	0.9	4.8E-5	4.9E-8	0.1	-	-	-
15	1.6E-7	9.7E-8	61	9.3E-8	1.6E-9	2	2.7E-5	3.3E-8	0.1	-	-	-
16	1.7E-7	7.3E-8	42	1.8E-7	1.4E-9	0.8	5.0E-5	6.5E-8	0.1	-	-	-
17	-	-	-	6.6E-8	6.6E-10	1	2.1E-5	5.3E-8	0.3	-	-	-
18	-	-	-	1.9E-7	1.6E-9	0.8	5.8E-5	3.7E-8	0.1	-	-	-
19	1.8E-7	8.0E-8	44	1.6E-7	1.6E-9	1	4.4E-5	2.1E-8	0.0	-	-	-
20	1.3E-7	6.7E-8	50	8.6E-8	1.1E-9	1	2.7E-5	3.0E-8	0.1	0.08	0.04	50
21	1.6E-7	6.7E-8	41	1.5E-7	2.7E-9	2	4.1E-5	4.6E-8	0.1	-	-	-
22	1.9E-7	7.5E-8	40	6.3E-8	9.1E-10	1	1.9E-5	2.0E-8	0.1	0.32	0.13	40
23	1.2E-7	9.5E-8	82	1.2E-7	1.1E-9	1	3.1E-5	1.0E-7	0.3	-	-	-
25	3.7E-8	2.6E-8	71	1.5E-7	2.1E-9	1	4.5E-5	7.9E-8	0.2	0.02	0.02	71
26	2.9E-7	4.2E-8	14	9.2E-8	1.1E-9	1	3.0E-5	3.8E-8	0.1	0.10	0.01	15
28	8.3E-8	2.3E-8	28	1.6E-7	2.1E-9	1	5.0E-5	8.4E-8	0.2	0.05	0.01	28
29	1.6E-7	1.9E-8	11	1.5E-7	7.5E-10	0.5	4.4E-5	3.9E-8	0.1	-	-	-
30	7.4E-8	2.0E-8	27	1.8E-7	5.7E-10	0.3	5.4E-5	3.9E-8	0.1	0.07	0.02	27

Empty spaces (-) are for data with negative NG concentration after blank / atmospheric correction or with 1σ > 100 %.

5.5.1.3 $^{40}Ar/^{36}Ar$ isotopic ratios

All the samples have $^{40}Ar/^{36}Ar$ ratios that vary with a perfect Gaussian distribution. Minimum and maximum values are 76.02±36.98 and 414±32.96 (Figure 5.21). Analytical uncertainties are of between <1% and 49% (Tables 5.8 - 5.11).

- F1A has the highest variability with ratios of between 124.7±47.5 and 414.3±33.0 with a mean of 287.9.
- F2A has ratios of between 76.0±37.0 and 339.6±6.4 with a mean of 278.3.
- I1A has ratios of between 218.9±6.8 and 337.2±9.9 with a mean of 289.8.
- I3A has the lowest variation with ratios ranging from 160.3±2.7 to 330.2±4.5 with a mean of 298.7.

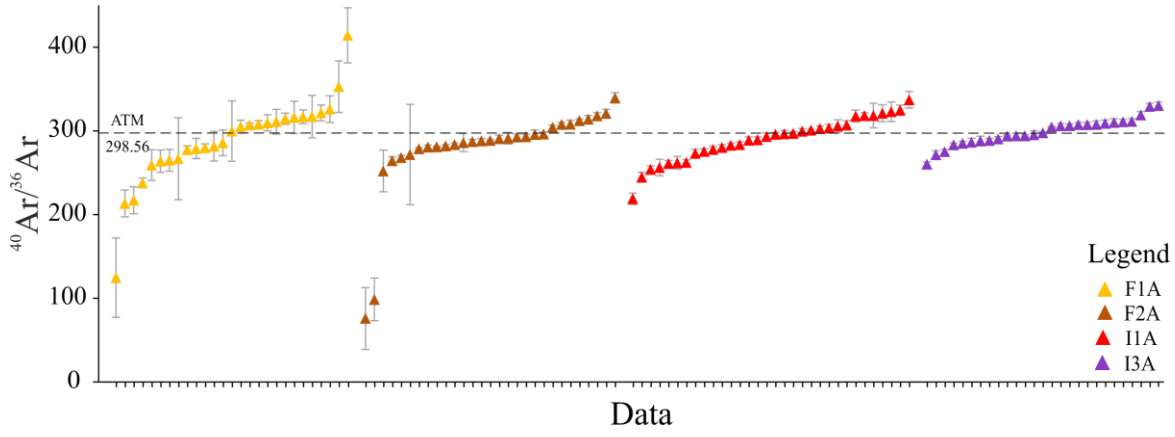

Figure 5.21 Variation of the $^{40}Ar/^{36}Ar$ in pumice glass of samples F1A, F2A, I1A and I3A. The data are ordered from the lowest to the highest value and reported at the 1σ level. Error bars if not visible are smaller than the symbol used to display the data. ATM (Lee et al., 2006).

5.5.1.4 $^{4}He/^{40}Ar^{*}$ isotopic ratios

It was only possible to determine the $^{4}He/^{40}Ar^{*}$ ratios for 13 particles. The ratios vary from 0.021±0.015 to 0.83±0.05 (Figure 5.22) with analytical uncertainties of between 6% and 82% (Tables 5.8 - 5.11).

- F1A has ratios of between 0.24±0.10 and 0.83±0.05 with a mean of 0.46.
- F2A has ratios of between 0.03±0.02 and 0.29±0.03 with a mean of 0.16.
- I1A has ratios of between 0.05±0.03 and 0.56±0.13 with a mean of 0.31.
- I3A has ratios ranging from 0.021±0.015 to 0.32±0.13 with a mean of 0.12.

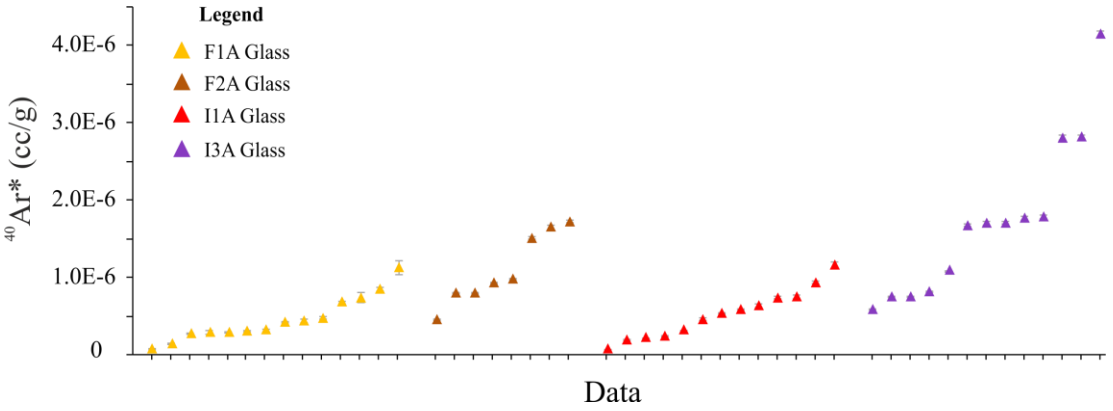

Figure 5.22 Variation of the $^{4}He/^{40}Ar^{*}$ in pumice glass of samples F1A, F2A, I1A and I3A. The data are ordered from the lowest to the highest value and reported at the 1σ level. Error bars if not visible are smaller than the symbol used to display the data.

Table 5.10 Isotopic ratios in glasses of samples F1A and F2A.

Grain	$^{40}Ar/^{36}Ar$	±1σ	1σ%	$^{4}He/^{40}Ar^{*}$	±1σ	1σ%
Sample F1A						
1	286	15	5	-	-	-
2	267	49	18	-	-	-
3	300	36	12	-	-	-
4	317	25	8	-	-	-
5	238	6	2	-	-	-
8	125	47	38	-	-	-
11	213	16	7	-	-	-
12	280	5	2	-	-	-
13	311	15	5	0.51	0.19	37
16	315	7	2	0.83	0.05	6
18	259	18	7	-	-	-
19	310	10	3	0.34	0.07	20
21	322	9	3	0.24	0.10	41
22	264	13	5	-	-	-
23	217	16	7	-	-	-
24	265	13	5	-	-	-
25	308	4	1	0.42	0.11	27
26	307	2	0.7	0.32	0.06	18
27	326	16	5	0.57	0.14	24
28	278	5	2	-	-	-
29	316	19	6	0.71	0.21	29
30	414	33	8	0.34	0.06	19
31	317	8	3	0.34	0.08	25
32	282	18	6	-	-	-
33	353	31	9	0.40	0.10	25
34	279	12	4	-	-	-
35	305	8	3	-	-	-
Sample F2A						
1	272	60	22	-	-	-
2	76	37	49	-	-	-
3	252	25	10	-	-	-
4	99	25	26	-	-	-
6	279	1	0.5	-	-	-
7	340	6	2	0.18	0.03	15
8	268	3	1	-	-	-
9	282	2	0.6	-	-	-
10	321	5	2	0.20	0.04	20
11	318	4	1	0.03	0.02	68
12	281	2	0.9	-	-	-
13	304	3	0.9	0.24	0.09	37
14	281	1	0.3	-	-	-
15	291	7	2	-	-	-
16	308	5	2	-	-	-
17	314	4	1	0.11	0.07	61
18	293	4	1	-	-	-
20	296	5	2	-	-	-
23	296	3	0.9	-	-	-
24	308	2	0.8	0.05	0.04	82
25	284	2	0.7	-	-	-
26	286	11	4	-	-	-
27	287	3	0.9	-	-	-
28	291	4	1	-	-	-
29	312	2	0.7	0.29	0.03	11
30	264	5	2	-	-	-
31	289	1	0.4	-	-	-
33	293	3	0.9	-	-	-
34	288	3	1	-	-	-

Empty spaces (-) are for data derived from NG concentrations with negative values after blank / atmospheric correction or with 1σ > 100 %.

Table 5.11 Isotopic ratios in glasses of samples I1A and I3A.

Grain	$^{40}Ar/^{36}Ar$	±1σ	1σ%	$^{4}He/^{40}Ar^{*}$	±1σ	1σ%
Sample I1A						
3	301	2	0.5	0.46	0.10	22.79
4	318	4	1	-	-	-
5	337	10	3	0.12	0.05	42.32
6	254	4	2	-	-	-
8	303	3	1	0.56	0.13	22.64
9	275	3	1	-	-	-
10	262	8	3	-	-	-
11	304	4	1	-	-	-
12	256	10	4	-	-	-
13	323	12	4	0.17	0.11	65.48
14	219	7	3	-	-	-
15	278	4	1	-	-	-
16	306	7	2	-	-	-
17	318	15	5	0.41	0.14	34
18	261	4	2	-	-	-
19	318	7	2	0.19	0.09	47.28
20	300	3	1	-	-	-
21	245	6	2	-	-	-
22	262	3	1	-	-	-
23	325	6	2	0.52	0.11	21
24	289	3	1	-	-	-
25	284	3	1	-	-	-
26	297	2	0.7	-	-	-
27	307	5	1.7	0.05	0.03	69.25
28	280	3	1	-	-	-
29	296	4	1	-	-	-
30	296	2	0.7	-	-	-
31	273	5	2	-	-	-
32	321	10	3	-	-	-
33	283	3	0.9	-	-	-
34	293	4	1	-	-	-
35	289	4	1	-	-	-
Sample I3A						
1	294	1	0.4	-	-	-
2	288	6	2	-	-	-
3	312	3	1	0.07	0.01	13.87
4	306	2	0.7	0.32	0.05	16.32
6	330	4	1	0.04	0.02	57
7	294	1	0.5	-	-	-
8	295	5	2	-	-	-
9	290	3	0.9	-	-	-
10	306	3	0.9	0.05	0.03	61
11	285	3	0.9	-	-	-
12	308	3	0.9	0.25	0.08	31
13	294	3	1	-	-	-
14	289	3	0.9	-	-	-
15	286	5	2	-	-	-
16	283	2	0.8	-	-	-
17	311	3	1	-	-	-
18	308	3	0.8	-	-	-
19	275	3	1	-	-	-
20	319	4	1	0.08	0.04	50
21	271	5	2	-	-	-
22	308	4	1	0.32	0.13	40
23	260	3	1	-	-	-
25	310	4	1	0.02	0.02	71.44
26	329	4	1	0.10	0.01	14.52
28	309	4	1	0.05	0.01	27.81
29	298	2	0.5	-	-	-
30	305	1	0.3	0.07	0.02	27.03

Empty spaces (-) are for data derived from NG concentrations with negative values after blank / atmospheric correction or with 1σ > 100 %.

5.5.2 Sanidine

5.5.2.1 ^{4}He isotope

98 samples yielded positive ^{4}He values after blank correction. ^{4}He concentrations range between $2.25E^{-8}\pm1.30E^{-8}$ cc/g and $2.61E^{-6}\pm1.22E^{-7}$ cc/g (Figure 5.23) with analytical uncertainties of between 3% and 68% (Tables 5.12 - 5.15).

- F1A has ^{4}He values ranging between $2.85E^{-8}\pm9.25E^{-9}$ cc/g and $1.35E^{-6}\pm4.170E^{-7}$ cc/g with a mean of $3.93E^{-7}$ cc/g.
- F2A has ^{4}He concentrations of between $8.15E^{-8}\pm3.94E^{-8}$ cc/g and $1.32E^{-6}\pm6.75E^{-8}$ cc/g with a mean of $3.39E^{-7}$ cc/g.
- I1A has extremely variable ^{4}He values that range between $2.25E^{-8}\pm1.30E^{-8}$ cc/g and $2.61E^{-6}\pm1.22E^{-7}$ cc/g. The ^{4}He mean concentration is $1.08E^{-6}$ cc/g.
- I3A has ^{4}He contents varying of between $3.47E^{-8}\pm1.74E^{-8}$ cc/g and $7.24E^{-7}\pm8.83E^{-8}$ cc/g with a mean of $3.00E^{-7}$ cc/g.

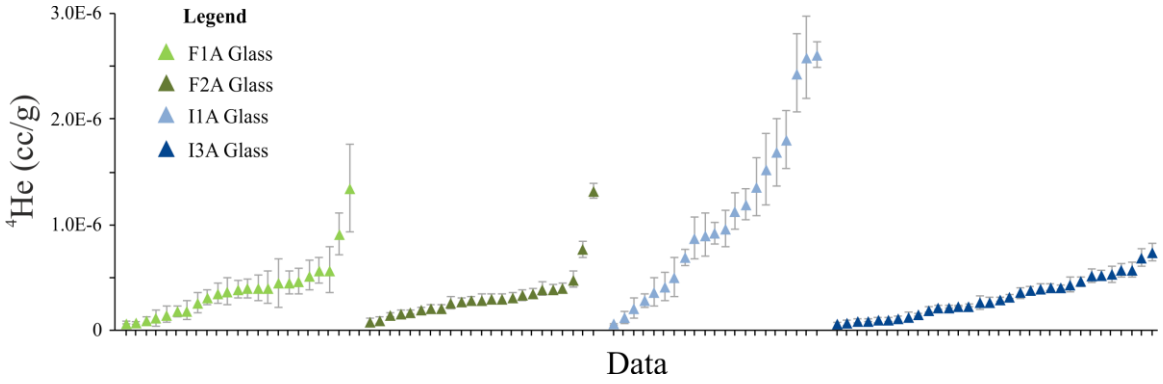

Figure 5.23 Variation of the ^{4}He in sanidine of samples F1A, F2A I1A and I3A. The data are ordered from the lowest to the highest value and reported at the 1σ level. Error bars if not visible are smaller than the symbol used to display the data.

5.5.2.2 Ar isotopes

^{40}Ar varies by three orders of magnitude between $9.60E^{-8}\pm7.81E^{-9}$ cc/g and $1.01E^{-5}\pm1.40E^{-7}$ cc/g (Figure 5.24) with analytical uncertainties ranging from <1% up to 44% (Tables 5.12 - 5.15).

- F1A has ^{40}Ar values ranging between $1.53E^{-7}\pm7.14E^{-9}$ cc/g and $9.17E^{-7}\pm9.21E^{-8}$ cc/g with a mean of $3.79E^{-7}$ cc/g.
- F2A has ^{40}Ar concentrations of between $1.60E^{-7}\pm7.27E^{-9}$ cc/g and $1.01E^{-5}\pm1.40E^{-7}$ cc/g with a mean of $1.85E^{-6}$ cc/g.
- I1A has ^{40}Ar values ranging between $1.07E^{-7}\pm1.43E^{-8}$ cc/g and $3.18E^{-6}\pm1.04E^{-7}$ cc/g. The ^{4}He mean concentration is $1.35E^{-6}$ cc/g.
- I3A has ^{40}Ar values of between $9.60E^{-8}\pm7.81E^{-9}$ cc/g and $4.14E^{-6}\pm1.50E^{-8}$ cc/g with a mean of $6.93E^{-7}$ cc/g.

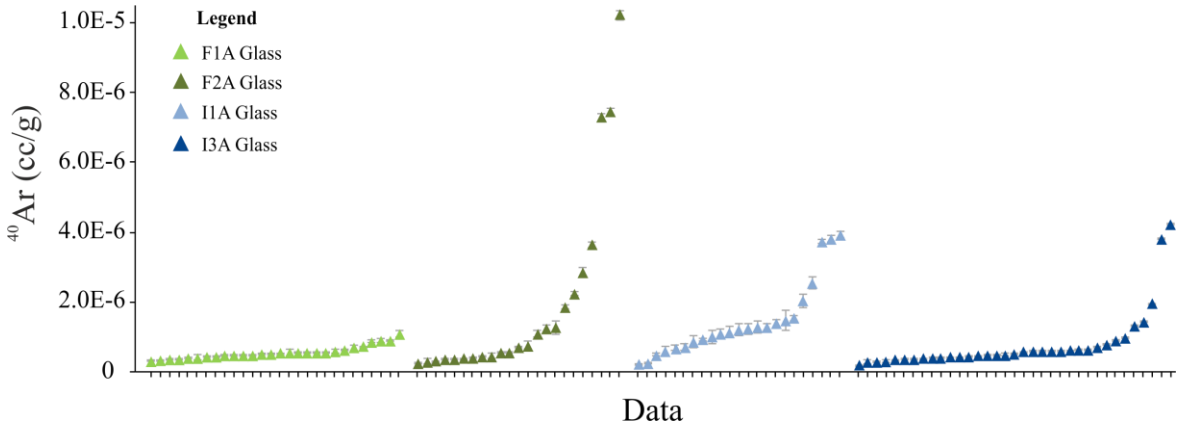

Figure 5.24 Variation of the ^{40}Ar in sanidine of samples F1A, F2A I1A and I3A. The data are ordered from the lowest to the highest value and reported at the 1σ level. Error bars if not visible are smaller than the symbol used to display the data.

94 samples yielded positive ^{36}Ar values after blank correction.^{36}Ar varies between $2.38E^{-10}\pm1.19^{-10}$ cc/g and $2.38E^{-8}\pm5.92E^{-10}$ cc/g (Figure 5.25) with analytical uncertainties of between 2% and 75% (Tables 5.12 - 5.15).

- F1A has ^{36}Ar values ranging between $2.69E^{-10}\pm8.97E^{-11}$ cc/g and $3.70E^{-9}\pm1.23E^{-9}$ cc/g with a mean of $1.38E^{-9}$ cc/g.
- F2A has ^{36}Ar concentrations of between $3.84E^{-8}\pm1.54E^{-10}$ cc/g and $2.38E^{-8}\pm5.92E^{-10}$ cc/g with a mean of $5.45E^{-9}$ cc/g.
- I1A has ^{36}Ar values ranging between $1.67E^{-9}\pm8.34E^{-10}$ cc/g and $1.23E^{-8}\pm4.84E^{-10}$ cc/g. The ^{4}He mean concentration is $5.23E^{-9}$ cc/g.
- I3A has ^{36}Ar content of between $2.38E^{-10}\pm1.19E^{-10}$ cc/g and $1.50E^{-8}\pm2.57E^{-10}$ cc/g with a mean of $2.63E^{-9}$ cc/g.

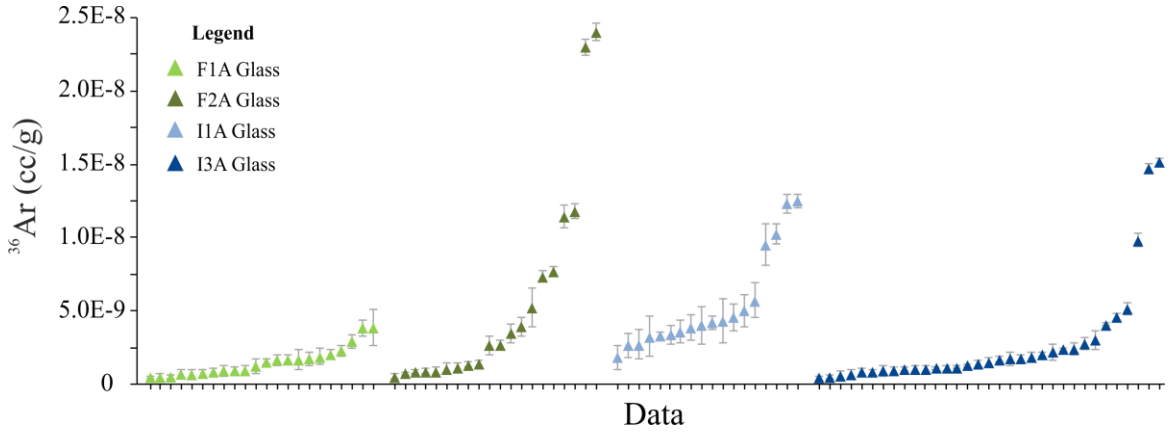

Figure 5.25 Variation of the ^{36}Ar in sanidine of samples F1A, F2A I1A and I3A. The data are ordered from the lowest to the highest value and reported at the 1σ level. Error bars if not visible are smaller than the symbol used to display the data.

Only 47 samples, after atmospheric correction, yielded positive $^{40}Ar^*$ values ($^{40}Ar^* = {}^{40}Ar - 298.56 \times {}^{36}Ar$). The $^{40}Ar^*$ ranges between $3.68E^{-9}\pm1.30E^{-8}$ cc/g and $1.16E^{-6}\pm6.66E^{-7}$ cc/g (Figure 5.26) with analytical uncertainties of between 4% and 95% (Tables 5.12 - 5.15).

- F1A has $^{40}Ar^*$ with values ranging between $3.36E^{-8}\pm1.79E^{-8}$ cc/g and $2.78E^{-7}\pm9.28E^{-8}$ cc/g with a mean of $1.08E^{-7}$ cc/g.
- F2A has $^{40}Ar^*$ concentrations of between $4.46E^{-8}\pm1.01E^{-8}$ cc/g and $3.70E^{-7}\pm1.07E^{-8}$ cc/g with a mean of $1.62E^{-7}$ cc/g.
- I1A has $^{40}Ar^*$ values ranging between $1.40E^{-8}\pm3.65E^{-9}$ cc/g and $1.16E^{-6}\pm4.78E^{-8}$ cc/g. The ^{4}He mean concentration is $3.63E^{-7}$ cc/g.
- I3A has $^{40}Ar^*$ content with values of between $3.68E^{-9}\pm7.41E^{-10}$ cc/g and $3.39E^{-7}\pm2.27E^{-7}$ cc/g with a mean of $1.43E^{-7}$ cc/g.

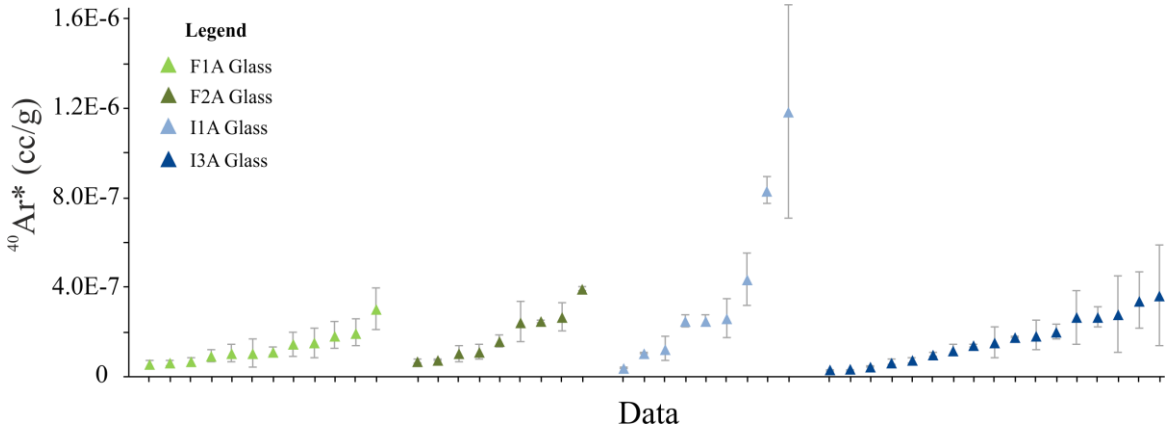

Figure 5.26 Variation of the $^{40}Ar^*$ in sanidine of samples F1A, F2A I1A and I3A. The data are ordered from the lowest to the highest value and reported at the 1σ level. Error bars if not visible are smaller than the symbol used to display the data.

Table 5.12 NG abundances expressed in cc/g STP in sanidines of samples F1A and F2A.

N°	^{4}He	±1σ	1σ%	^{36}Ar	±1σ	1σ%	^{40}Ar	±1σ	1σ%	^{40}Ar*	1σ	1σ%
Sample F1A												
4	3.3E-8	1.2E-8	36	1.1E-9	5.0E-10	45	3.6E-7	1.0E-7	27	3.4E-8	1.8E-8	53
5	-	-	-	2.8E-9	4.6E-10	17	9.2E-7	9.2E-8	10	9.0E-8	1.7E-8	19
6	-	-	-	1.6E-9	4.6E-10	29	5.1E-7	9.2E-8	18	3.8E-8	1.3E-8	35
7	-	-	-	1.5E-9	2.7E-10	18	4.0E-7	5.4E-8	14	-	-	-
10	2.8E-8	9.3E-9	33	7.8E-10	3.5E-10	45	2.3E-7	7.0E-8	31	-	-	-
11	1.0E-7	3.0E-8	30	2.7E-10	9.0E-11	33	3.6E-7	4.3E-9	1	2.8E-7	9.3E-8	33
12	4.1E-7	1.2E-7	30	2.2E-9	3.6E-10	17	4.4E-7	1.7E-8	4	-	-	-
13	3.2E-7	6.9E-8	22	1.4E-9	2.1E-10	15	3.1E-7	9.5E-9	3	-	-	-
14	1.8E-7	5.1E-8	28	3.6E-10	1.5E-10	43	1.5E-7	7.1E-9	5	4.5E-8	1.9E-8	43
15	1.5E-7	8.0E-8	52	3.2E-10	2.4E-10	75	1.8E-7	1.1E-8	6	8.3E-8	6.3E-8	75
16	4.5E-7	1.1E-7	23	8.4E-10	3.1E-10	38	3.2E-7	1.5E-8	5	7.1E-8	2.7E-8	38
17	1.9E-7	8.5E-8	44	-	-	-	3.8E-7	1.2E-8	3	-	-	-
18	4.7E-7	1.2E-7	25	1.5E-9	3.4E-10	23	1.9E-7	1.6E-8	8	-	-	-
19	3.7E-7	1.2E-7	33	-	-	-	1.5E-7	1.7E-8	11	-	-	-
20	3.5E-7	9.6E-8	28	5.7E-10	2.9E-10	50	2.5E-7	1.3E-8	5	8.1E-8	4.1E-8	50
21	1.4E-6	4.2E-7	31	3.7E-9	1.2E-9	33	7.1E-7	5.9E-8	8	-	-	-
22	3.9E-7	8.1E-8	21	5.6E-10	2.4E-10	43	2.9E-7	1.1E-8	4	1.2E-7	5.2E-8	43
23	4.0E-7	8.9E-8	22	7.0E-10	2.6E-10	38	3.7E-7	1.2E-8	3	1.6E-7	6.0E-8	38
24	5.7E-7	1.2E-7	21	1.9E-9	3.5E-10	19	5.5E-7	1.6E-8	3	-	-	-
25	1.2E-7	8.1E-8	69	8.0E-10	2.4E-10	30	2.2E-7	1.1E-8	5	-	-	-
26	4.5E-7	2.3E-7	51	-	-	-	3.0E-7	3.2E-8	11	-	-	-
27	2.7E-7	9.4E-8	35	5.6E-10	2.8E-10	50	2.9E-7	1.3E-8	4	1.3E-7	6.4E-8	50
28	-	-	-	3.7E-9	5.5E-10	15	7.1E-7	2.5E-8	4	-	-	-
29	5.2E-7	1.4E-7	27	-	-	-	3.3E-7	1.9E-8	6	-	-	-
30	5.8E-7	2.2E-7	38	1.5E-9	6.6E-10	43	3.7E-7	3.0E-8	8	-	-	-
32	-	-	-	-	-	-	3.7E-7	1.7E-8	5	-	-	-
33	4.1E-7	1.5E-7	37	-	-	-	2.7E-7	2.1E-8	8	-	-	-
34	9.1E-7	2.0E-7	22	1.7E-9	5.8E-10	33	6.9E-7	2.7E-8	4	1.7E-7	5.8E-8	34
Sample F2A												
11	2.1E-7	3.6E-8	17	7.1E-10	1.6E-10	22	2.6E-7	1.0E-8	4	4.5E-8	1.0E-8	23
12	3.1E-7	3.8E-8	12	-	-	-	2.6E-7	1.0E-8	4	-	-	-
13	4.0E-7	4.2E-8	11	7.3E-10	1.8E-10	25	4.6E-7	1.2E-8	2	2.4E-7	6.1E-8	25
14	4.0E-7	6.5E-8	16	9.8E-10	2.8E-10	29	2.8E-7	1.8E-8	6	-	-	-
15	4.0E-7	4.1E-8	10	1.2E-9	1.8E-10	15	3.3E-7	1.1E-8	4	-	-	-
16	2.9E-7	3.6E-8	12	3.8E-10	1.5E-10	40	2.0E-7	9.8E-9	5	8.7E-8	3.5E-8	40
17	1.3E-6	6.8E-8	5	7.5E-10	3.0E-10	40	4.4E-7	1.9E-8	4	2.2E-7	8.9E-8	40
18	4.8E-7	7.8E-8	16	2.5E-9	3.4E-10	13	5.9E-7	2.1E-8	4	-	-	-
19	3.0E-7	4.8E-8	16	1.3E-9	2.1E-10	17	2.8E-7	1.4E-8	5	-	-	-
20	3.2E-7	4.3E-8	13	5.7E-10	1.1E-10	20	1.6E-7	7.3E-9	5	-	-	-
21	1.0E-7	3.2E-8	31	1.2E-8	4.8E-10	4	3.5E-6	8.2E-8	2	5.4E-8	2.5E-9	5
22	2.1E-7	3.6E-8	17	2.3E-8	5.6E-10	2	7.2E-6	1.1E-7	2	3.7E-7	1.1E-8	3
23	2.0E-7	2.5E-8	13	9.1E-10	3.8E-10	42	3.5E-7	6.6E-8	19	8.0E-8	3.7E-8	46
24	2.8E-7	3.5E-8	12	3.3E-9	6.1E-10	18	1.1E-6	9.3E-8	8	1.4E-7	2.7E-8	20
25	3.0E-7	3.9E-8	13	3.8E-9	6.7E-10	18	9.9E-7	1.0E-7	11	-	-	-
26	1.5E-7	2.1E-8	14	7.5E-9	3.3E-10	4	2.1E-6	5.7E-8	3	-	-	-
28	8.1E-8	3.9E-8	48	2.4E-8	5.9E-10	2	7.3E-6	1.0E-7	1	2.2E-7	6.4E-9	3
29	2.6E-7	5.3E-8	20	3.5E-8	1.1E-9	3	1.0E-5	1.4E-7	1	-	-	-
30	1.7E-7	2.0E-8	12	7.2E-9	3.5E-10	5	1.8E-6	5.3E-8	3	-	-	-
31	3.6E-7	4.2E-8	12	2.5E-9	6.5E-10	26	6.5E-7	1.1E-7	17	-	-	-
32	7.7E-7	7.5E-8	10	5.1E-9	1.3E-9	26	1.2E-6	2.0E-7	17	-	-	-
33	3.4E-7	5.3E-8	16	1.1E-8	8.0E-10	7	2.7E-6	1.4E-7	5	-	-	-
35	1.6E-7	3.1E-8	20	-	-	-	1.9E-7	8.4E-8	44	-	-	-

Empty spaces (-) are for data with negative NG concentration after blank / atmospheric correction or with 1σ > 100 %.

Table 5.13 NG abundances expressed in cc/g STP in sanidines of samples I1A and I3A.

N°	^{4}He	±1σ	1σ%	^{36}Ar	±1σ	1σ%	^{40}Ar	±1σ	1σ%	^{40}Ar*	1σ	1σ%
Sample I1A												
5	2.2E-8	1.3E-8	58	-	-	-	1.1E-7	1.4E-8	13	-	-	-
10	-	-	-	3.1E-9	1.4E-9	44	1.4E-7	2.8E-8	20	-	-	-
11	1.3E-7	5.9E-8	47	N.A.	N.A.	N.A.	3.9E-7	5.3E-8	14	-	-	-
12	2.9E-7	6.0E-8	21	1.2E-8	4.8E-10	4	3.6E-6	5.4E-8	1	-	-	-
13	2.1E-7	9.7E-8	46	-	-	-	5.7E-7	8.3E-8	15	-	-	-
14	6.9E-7	7.5E-8	11	4.1E-9	4.7E-10	12	1.4E-6	6.8E-8	5	2.3E-7	2.8E-8	12
15	9.2E-7	1.0E-7	11	1.2E-8	6.3E-10	5	3.7E-6	9.8E-8	3	8.3E-8	4.8E-9	6
16	5.1E-7	1.9E-7	38	-	-	-	1.1E-6	1.7E-7	16	-	-	-
17	1.2E-6	1.5E-7	12	4.4E-9	8.8E-10	20	1.3E-6	1.3E-7	10	-	-	-
18	4.2E-7	1.4E-7	33	3.7E-9	8.6E-10	23	4.9E-7	1.2E-7	25	-	-	-
19	8.7E-7	2.0E-7	23	5.5E-9	1.2E-9	21	7.7E-7	1.7E-7	22	-	-	-
20	3.7E-7	1.3E-7	36	2.5E-9	8.3E-10	33	9.8E-7	1.2E-7	12	2.4E-7	8.4E-8	35
21	-	-	-	3.2E-9	6.4E-10	20	1.4E-6	2.8E-7	21	4.1E-7	1.2E-7	29
23	9.7E-7	1.7E-7	18	1.0E-8	6.9E-10	7	3.8E-6	1.0E-7	3	8.1E-7	5.9E-8	7
25	1.1E-6	1.7E-7	15	3.2E-9	2.3E-10	7	1.2E-6	1.0E-7	8	2.3E-7	2.5E-8	11
26	1.5E-6	3.4E-7	22	9.3E-9	1.4E-9	15	2.4E-6	1.7E-7	7	-	-	-
27	1.8E-6	2.8E-7	15	4.2E-9	1.5E-9	36	1.2E-6	1.6E-7	14	-	-	-
28	1.4E-6	2.8E-7	20	3.4E-9	7.6E-10	22	1.0E-6	1.4E-7	14	1.4E-8	3.6E-9	26
29	1.7E-6	3.2E-7	19	3.9E-9	1.3E-9	33	1.1E-6	1.6E-7	14	-	-	-
30	9.1E-7	2.0E-7	22	1.7E-9	8.3E-10	50	6.0E-7	1.0E-7	17	1.0E-7	5.3E-8	53
31	2.4E-6	3.7E-7	15	2.6E-9	1.0E-9	40	1.9E-6	1.9E-7	10	1.2E-6	4.8E-7	41
33	2.6E-6	3.9E-7	15	4.9E-9	1.1E-9	22	8.9E-7	2.0E-7	23	-	-	-
35	2.6E-6	1.2E-7	5	-	-	-	8.3E-7	4.3E-8	5	-	-	-
Sample I3A												
1	-	-	-	2.2E-9	4.2E-10	19	4.9E-7	8.7E-9	2	-	-	-
2	-	-	-	2.9E-9	6.0E-10	21	2.9E-7	1.2E-8	4	-	-	-
10	-	-	-	2.0E-9	5.4E-10	26	1.9E-7	1.0E-8	5	-	-	-
11	3.6E-7	4.1E-8	11	-	-	-	3.7E-7	1.0E-8	3	-	-	-
12	2.5E-7	6.2E-8	25	6.7E-10	2.7E-10	40	5.2E-7	1.7E-8	3	3.2E-7	1.3E-7	40
13	5.1E-7	7.1E-8	14	4.7E-10	3.1E-10	67	4.8E-7	2.0E-8	4	3.4E-7	2.3E-7	67
14	7.2E-7	8.8E-8	12	1.6E-9	2.0E-10	13	3.9E-7	2.5E-8	6	-	-	-
15	5.3E-8	2.8E-8	53	8.7E-10	1.2E-10	14	9.6E-8	7.8E-9	8	-	-	-
16	2.1E-7	5.4E-9	3	1.0E-9	1.0E-10	10	3.2E-7	5.9E-9	2	2.4E-8	2.5E-9	10
17	4.2E-7	7.1E-8	17	2.6E-9	3.7E-10	14	5.9E-7	1.4E-8	2	-	-	-
18	5.6E-7	7.2E-8	13	7.6E-10	3.8E-10	50	4.7E-7	1.3E-8	3	2.4E-7	1.2E-7	50
19	3.9E-7	3.2E-8	8	6.8E-10	1.7E-10	25	3.0E-7	6.1E-9	2	9.5E-8	2.4E-8	25
20	6.8E-7	8.5E-8	13	1.6E-9	4.5E-10	29	4.8E-7	1.6E-8	3	7.1E-9	2.0E-9	29
21	1.8E-7	2.4E-8	13	3.1E-10	1.2E-10	40	2.6E-7	4.4E-9	2	1.6E-7	6.5E-8	40
22	3.3E-7	5.0E-8	15	8.0E-10	2.7E-10	33	2.8E-7	9.7E-9	3	4.2E-8	1.4E-8	34
23	8.1E-8	2.3E-8	29	1.1E-9	1.2E-10	11	2.6E-7	4.4E-9	2	-	-	-
24	2.5E-7	4.9E-8	19	1.5E-8	2.6E-10	2	3.7E-6	9.6E-9	0	-	-	-
25	1.1E-7	4.8E-8	44	8.9E-10	2.6E-10	29	2.4E-7	9.1E-9	4	-	-	-
26	3.8E-7	4.6E-8	12	1.2E-9	2.4E-10	20	3.6E-7	8.5E-9	2	3.7E-9	7.4E-10	20
27	5.5E-7	6.2E-8	11	4.9E-10	3.3E-10	67	4.0E-7	2.8E-8	7	2.5E-7	1.7E-7	67
28	4.4E-7	4.3E-8	10	9.1E-10	2.3E-10	25	3.2E-7	8.2E-9	3	5.0E-8	1.3E-8	25
29	5.0E-7	6.3E-8	13	1.3E-9	3.4E-10	25	3.3E-7	1.2E-8	4	-	-	-
30	5.1E-7	4.4E-8	9	1.6E-9	2.4E-10	14	4.9E-7	8.4E-9	2	-	-	-
31	2.0E-7	2.0E-8	10	4.4E-9	2.4E-10	5	1.2E-6	7.5E-9	1	-	-	-
32	2.2E-7	1.2E-8	6	1.9E-9	1.6E-10	8	5.1E-7	4.6E-9	1	-	-	-
33	3.9E-7	2.1E-8	5	9.6E-9	4.5E-10	5	1.9E-6	9.3E-9	1	-	-	-
34	3.5E-8	1.7E-8	50	1.5E-8	2.6E-10	2	4.1E-6	1.5E-8	0	-	-	-
35	2.8E-7	1.8E-8	6	5.0E-9	3.8E-10	8	8.7E-7	9.4E-9	1	-	-	-
36	1.3E-7	1.1E-8	8	3.9E-9	9.9E-11	3	1.3E-6	6.8E-9	1	1.5E-7	4.0E-9	3
37	3.0E-7	1.8E-8	6	1.7E-9	3.0E-10	18	6.9E-7	1.2E-8	2	1.8E-7	3.2E-8	18
38	7.2E-8	1.5E-8	21	9.5E-10	9.1E-11	10	3.6E-7	8.0E-9	2	7.7E-8	7.5E-9	10
39	7.8E-8	1.2E-8	16	2.2E-9	1.0E-10	5	7.8E-7	1.5E-8	2	1.2E-7	5.9E-9	5
40	2.1E-7	1.4E-8	7	9.6E-10	1.7E-10	18	5.3E-7	2.8E-8	5	2.4E-7	4.5E-8	18
41	8.6E-8	1.5E-8	17	2.4E-10	1.2E-10	50	2.0E-7	2.9E-8	15	1.3E-7	6.7E-8	52
42	9.2E-8	2.9E-8	31	-	-	-	1.7E-7	5.7E-8	34	-	-	-

Empty spaces (-) are for data with negative NG concentration after blank / atmospheric correction or with 1σ > 100 %.

5.5.2.3 $^{40}Ar/^{36}Ar$ isotopic ratios

94 samples yielded $^{40}Ar/^{36}Ar$ ratios that vary between 46.40±22.57 and 1,332±444.53 (Figure 5.27) with analytical uncertainties that range between < 1 % and 75 % (Tables 5.12 - 5.15).

- F1A has the highest variability with ratios of between 130.1±31.9 and 1,332.7±444.5 with a mean of 381.4.

  F2A has ratios of between 223.6±38.8 and 631.7±158 with a mean of 327.1.
- I1A has ratios of between 46.4±22.6 and 749.7±309.1 with a mean of 308.5.
- I3A has the lowest variation with ratios ranging from 90.9±24.6 to 1,021.6±682.5 with a mean of 377.4.

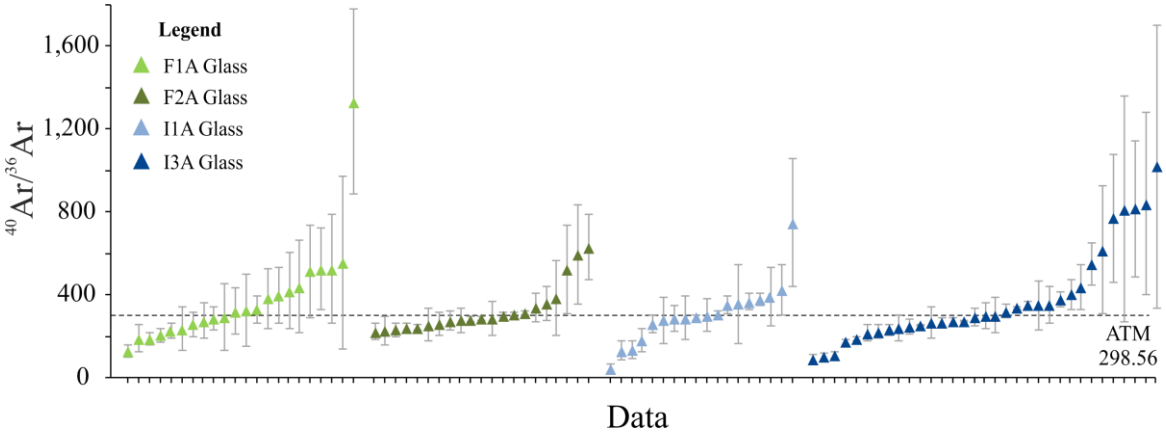

Figure 5.27 Variation of the $^{40}Ar/^{36}Ar$ ratios in sanidine of samples F1A, F2A I1A and I3A. The data are ordered from the lowest to the highest value and reported at the 1σ level. Error bars if not visible are smaller than the symbol used to display the data. ATM (Lee et al., 2006).

5.5.2.4 $^{4}He/^{40}Ar^{*}$ isotopic ratios

It was only possible to determine the $^{4}He/^{40}Ar^{*}$ ratios for 44 samples. The ratios vary from 0.36±0.18 to 103.13±24.17 with analytical uncertainties of between 8 % and 91 % (Tables 5.12 - 5.15).

- F1A has the highest variability with ratios of between 0.36±0.16 and 6.37±2.83 with a mean of 3.10 (Figure 5.28 A).
- F2A has ratios of between 0.36±0.18 and 5.97±2.42 with a mean of 2.57 (Figure 5.28 B).
- I1A has ratios of between 1.20±0.23 and 97.45±32.30 with a mean of 16.32 (Figure 5.28 C – C1).
- I3A has the lowest variation with ratios ranging from 0.66±0.36 to 103.13±24.17 with a mean of 14.20 (Figure 5.28 D – D1).

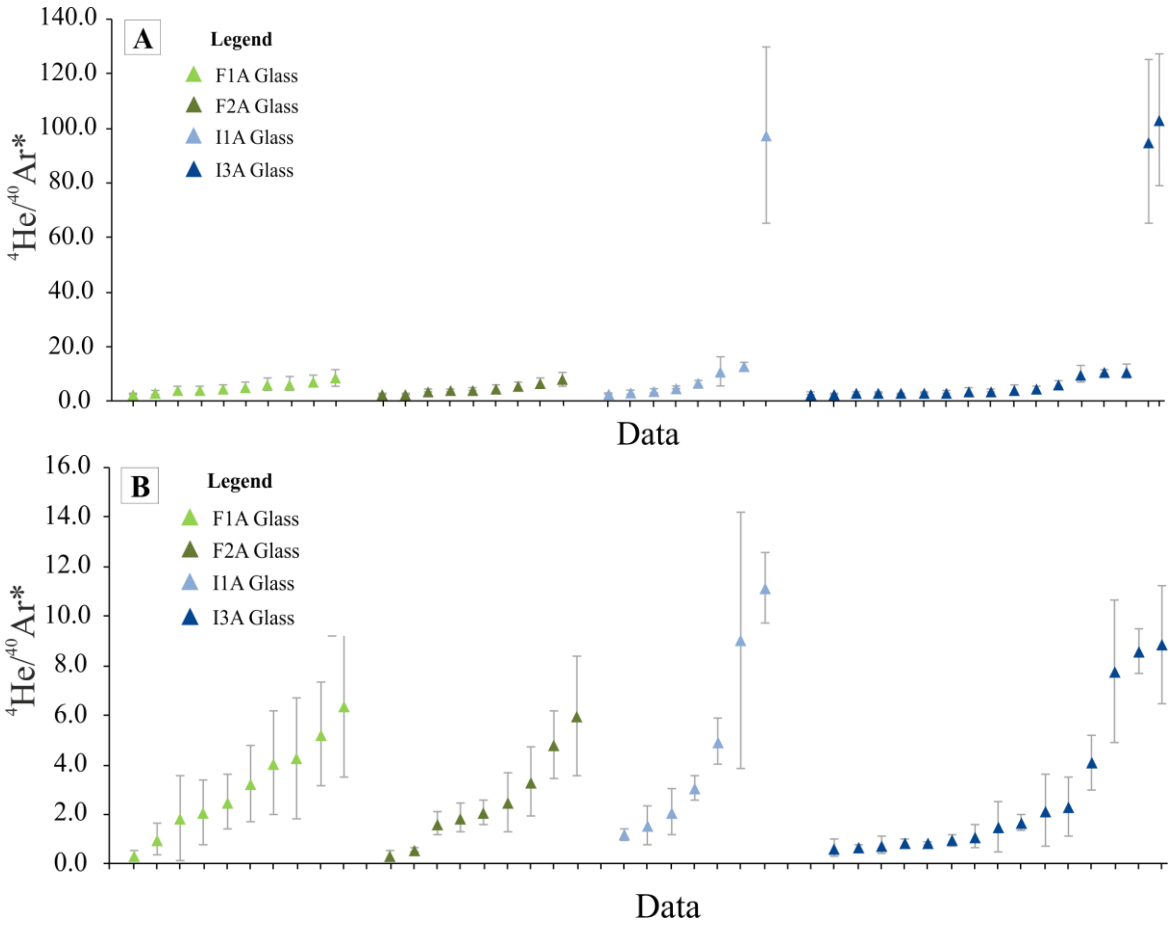

Figure 5.28 A - Variation of the $^{4}He/^{40}Ar^{*}$ ratios in sanidine of samples F1A, F2A, I1A and I3A. B – data with $^{4}He/^{40}Ar^{*}$ ratios of between 0 and 16. The data are ordered from the lowest to the highest value and reported at the 1σ level. Error bars if not visible are smaller than the symbol used to display the data.

Table 5.14 Isotopic ratios in sanidines of samples F1A and F2A.

N°	$^{40}Ar/^{36}Ar$	±1σ	1σ%	$^{4}He/^{40}Ar^{*}$	±1σ	1σ%
Sample F1A						
5	329	175	53	0.99	0.64	64
10	331	64	19	-	-	-
11	323	111	35	-	-	-
12	259	58	23	-	-	-
13	294	161	55	-	-	-
14	1333	445	33	0.36	0.16	45
15	206	35	17	-	-	-
16	227	35	15	-	-	-
17	422	182	43	4.08	2.10	52
18	557	419	75	1.85	1.69	91
19	384	145	38	6.37	2.83	44
20	-	-	-	-	-	-
21	130	32	25	-	-	-
23	-	-	-	-	-	-
25	441	222	50	4.28	2.46	57
26	191	66	34	-	-	-
27	515	222	43	3.23	1.54	48
28	526	198	38	2.51	1.10	44
29	289	55	19	-	-	-
30	277	84	30	-	-	-
31	-	-	-	-	-	-
33	527	265	50	2.10	1.29	61
35	193	30	15	-	-	-
29	-	-	-	-	-	-
30	238	104	44	-	-	-
32	-	-	-	-	-	-
33	-	-	-	-	-	-
34	398	134	34	5.24	2.09	40
Sample F2A						
11	361	81	23	4.81	1.35	28
12	-	-	-	-	-	-
13	632	159	25	1.64	0.45	27
14	288	84	29	-	-	-
15	277	44	16	-	-	-
16	526	212	40	3.31	1.40	42
17	595	239	40	5.97	2.42	41
18	232	32	14	-	-	-
19	224	39	17	-	-	-
20	278	57	21	-	-	-
21	303	14	5	1.89	0.60	32
22	315	9	3	0.56	0.10	18
23	386	178	46	2.48	1.19	48
24	339	68	20	2.07	0.49	24
25	261	54	21	-	-	-
26	283	15	5	-	-	-
28	308	9	3	0.36	0.18	48
29	286	10	3	-	-	-
30	245	14	6	-	-	-
31	257	80	31	-	-	-
32	230	71	31	-	-	-
33	243	21	9	-	-	-
35	-	-	-	-	-	-

Empty spaces (-) are for data derived from NG concentrations with negative values after blank / atmospheric correction or with 1σ > 100 %.

Table 5.15 Isotopic ratios in sanidines of samples I1A and I3A.

N°	$^{40}Ar/^{36}Ar$	±1σ	1σ%	$^{4}He/^{40}Ar^{*}$	±1σ	1σ%
Sample I1A						
5	-	-	-	-	-	-
10	46	23	49	-	-	-
11	-	-	-	-	-	-
12	293	12	4	-	-	-
13	-	-	-	-	-	-
14	354	44	12	3.08	0.51	16
15	305	18	6	11.17	1.42	13
16	-	-	-	-	-	-
17	289	64	22	-	-	-
18	132	45	34	-	-	-
19	139	43	31	-	-	-
20	394	140	35	1.56	0.79	51
21	427	122	29	-	-	-
23	379	28	7	1.20	0.23	19
25	370	41	11	4.94	0.93	19
26	260	43	17	-	-	-
27	278	109	39	-	-	-
28	303	79	26	97.45	32.30	33
29	290	105	36	-	-	-
30	359	190	53	9.04	5.19	57
31	750	309	41	2.10	0.93	44
33	184	58	32	-	-	-
35	-	-	-	-	-	-
Sample I3A						
1	219	41	19	-	-	-
2	101	22	21	-	-	-
10	91	25	27	-	-	-
11	-	-	-	-	-	-
12	772	310	40	0.78	0.37	47
13	1022	682	67	1.51	1.03	68
14	250	35	14	-	-	-
15	111	18	16	-	-	-
16	323	33	10	8.60	0.90	10
17	225	33	14	-	-	-
18	617	309	50	2.30	1.19	52
19	438	110	25	4.10	1.08	26
20	303	87	29	95.27	29.89	31
21	819	328	40	1.11	0.47	42
22	352	118	34	7.81	2.87	37
23	235	26	11	-	-	-
24	253	5	2	-	-	-
25	268	77	29	-	-	-
26	302	61	20	103.13	24.17	23
27	815	547	67	2.17	1.48	68
28	354	89	25	8.86	2.39	27
29	242	61	25	-	-	-
30	296	43	14	-	-	-
31	273	15	5	-	-	-
32	269	23	8	-	-	-
33	192	9	5	-	-	-
34	276	5	2	-	-	-
35	174	14	8	-	-	-
36	338	9	3	0.86	0.07	8
37	403	72	18	1.70	0.32	19
38	379	37	10	0.94	0.22	23
39	351	18	5	0.67	0.11	17
40	552	102	18	0.85	0.17	20
41	841	438	52	0.66	0.36	55
42	-	-	-	-	-	-

Empty spaces (-) are for data derived from NG concentrations with negative values after blank / atmospheric correction or with 1σ > 100 %.

5.6 Ar/Ar dating results

The results of Ar/Ar single grain fusion and step heating analyses of haüyne crystals, pumice glass and sanidine crystals are presented here. When possible the ages are displayed in age spectra and inverse isochron diagrams. Isotopic ratios are also presented in order to show the variations in the isotope concentrations and distributions in different type of materials used for the analysis. All the reported errors are quoted at the 1σ level if not otherwise indicated. Tables 5.16 – 5.22 show the ages and $^{40}Ar/^{36}Ar$ ratios obtained for individual analyses. In the tables the ages are those obtained after recalculation with *ArArReCalc* (Koppers et al., 2002) applying the new age for the GA1550 (99.738±0.104 Ma) and $^{40}K_{tot}$ decay constant ($5.5305±0.0135E^{-10}$) given by Renne et al. (2011). The complete set of Ar isotopes extracted from the samples during the experiments, associated analytical errors, ages, average blank and J values are reported in appendix A4.3.

5.6.1 Haüyne

Single grain total fusion experiments were performed on 8 haüyne crystals recovered from sample I3D. The 8 grains yielded ages ranging from a minimum of 28.88±2.07 Ma to a maximum of 116.95±5.17 Ma with $^{40}Ar/^{36}Ar$ ratios of 2,641±723 and 4,798±1,784, respectively (Table 5.16).

When step heated, the haüyne crystals failed to provide a plateau age or inverse isochron age (Figure 5.29 A - B). The $^{37}Ar/^{39}Ar$ ratios and the $^{38}Ar/^{39}Ar$ ratios constantly increase throughout the experiment. From low to high temperature steps the ages increase from 12.04±2.32 Ma to 286.96±4.95 Ma with $^{40}Ar/^{36}Ar$ ratios of 561±92 and 5,714±173, respectively (Table 5.16 - Figure 5.29).

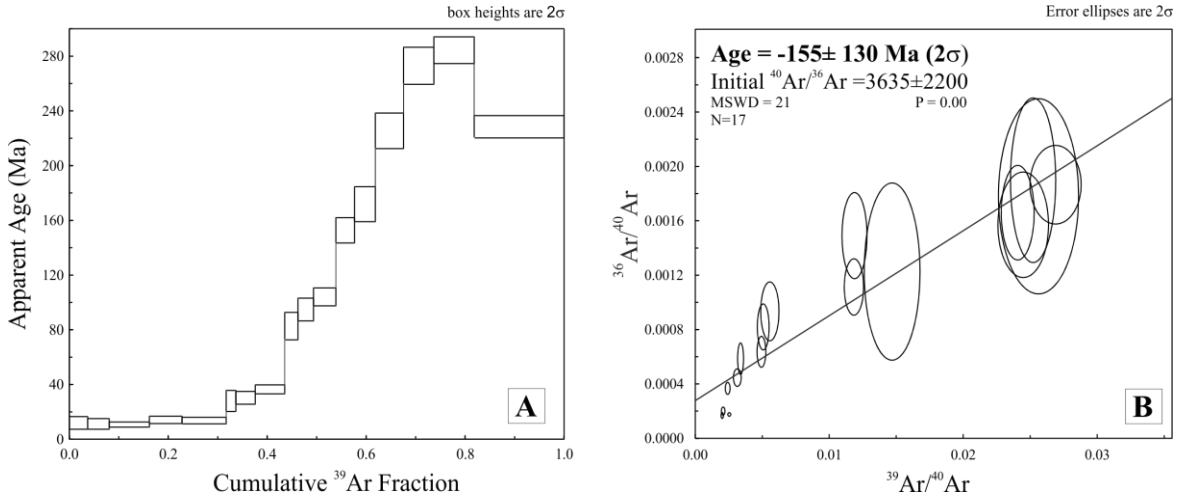

Figure 5.29 Age spectra (A) and inverse isochron (B) for step heating experiments on haüyne crystals of sample I3D.

Table 5.16 Ages and $^{40}Ar/^{36}Ar$ ratios from sample I3D – Haüyne.

Grain	Age (Ma)	±1σ (Ma)	$^{40}Ar/^{36}Ar$	±1σ
Single grain total fusion				
G4	28.88	1.07	2641.32	723.49
G12	44.41	2.12	1563.18	227.63
G3	56.96	2.22	1766.70	192.29
G1	67.67	0.02	1260.02	182.31
G10	79.65	0.04	2860.82	629.98
G2	110.89	7.46	2943.28	1296.11
G11	116.95	5.17	4798.95	1784.43
Step heating				
1	12.04	2.32	561.77	92.56
2	11.31	1.95	526.85	68.63
3	10.85	0.93	536.16	33.95
4	14.27	0.02	636.74	64.27
5	13.79	0.04	602.66	51.62
6	28.26	3.89	815.56	177.12
7	30.56	2.34	670.91	58.28
8	36.84	1.66	898.55	68.39
9	83.52	5.07	1071.55	101.62
10	95.71	4.18	1221.52	103.25
11	105.07	3.30	1572.86	115.04
12	154.12	4.66	1708.11	137.71
13	173.45	6.45	2241.78	133.18
14	227.51	6.55	2725.32	134.43
15	275.49	6.84	5005.11	303.12
16	286.96	4.95	5982.22	316.00
17	230.52	4.09	5714.74	173.74

5.6.2 Pumice glass

When one single grain of pumice glass from F1A was analysed it yielded an age of 0.80±4.11 Ma with a $^{40}Ar/^{36}Ar$ ratio of 303±28 (Table 5.17). Ages of 0.54±0.71 Ma with a $^{40}Ar/^{36}Ar$ ratio of 301±3 and of 0.43±0.44 Ma with a $^{40}Ar/^{36}Ar$ ratio of 303±4 were obtained fusing together 3 and 6 grains, respectively (Table 5.17). A weighted mean age of 0.46±0.75 Ma (2σ) was obtained by combining the results of the three experiments (Figure 5.30 A). Following the same concept an isochron age of 0.34±0.06 Ma (95 % conf. level) with a $^{40}Ar/^{36}Ar$ ratio of 299±14 was obtained for sample F1A (Figure 5.30 B). The weighted mean age and the isochron age are concordant at 2σ confidence level.

Pumice glass from sample I3A failed to provide ages when single or multiple grains were analysed. The ages are all negative and with $^{40}Ar/^{36}Ar$ ratios ranging from 290±4 to 297±4 (Table 5.17).

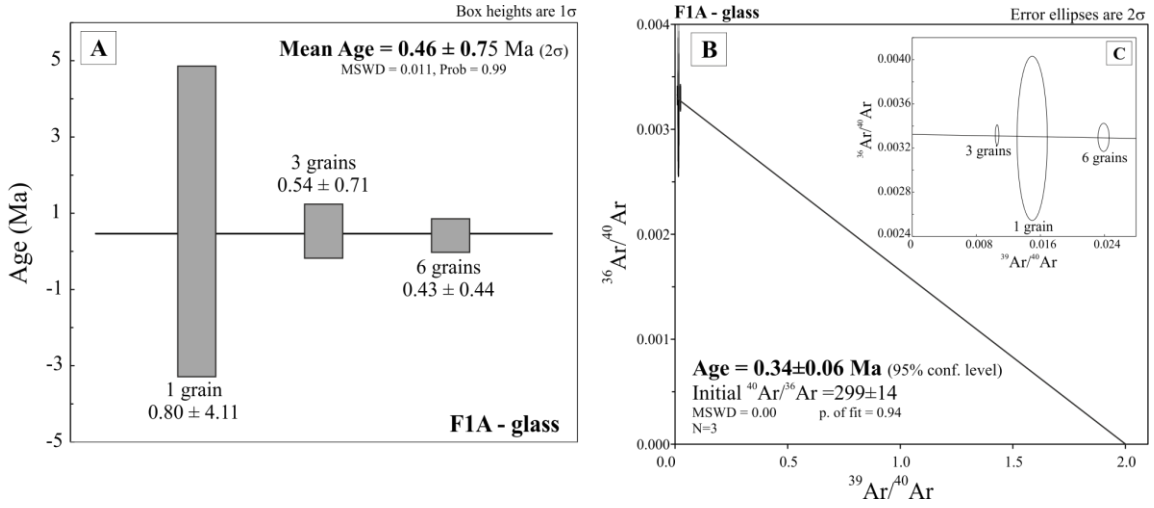

Figure 5.30 Weighted mean age (A) and inverse isochron age (B - C) for total fusion analyses on pumice glass of F1A.

Table 5.17 Ages and $^{40}Ar/^{36}Ar$ ratios of Single grain total fusion from pumice glass particles.

Grain	Age (Ma)	±1σ (Ma)	$^{40}Ar/^{36}Ar$	±1σ
Sample F1A				
G1	0.80	4.11	303.92	28.05
G2-4	0.54	0.71	301.09	3.39
G5-10	0.43	0.44	303.11	4.79
Sample I3A				
G1-6	-5.14	1.41	290.64	4.25
G7	-3.22	2.16	293.95	6.07
G8	-0.61	3.75	296.99	19.27
G9	-2.74	2.75	293.6	9.79
G10	-0.89	2.85	297.83	4.63

When step-heated, pumice glass from sample F1A failed to produce a plateau age or an inverse isochron age (Figure 5.31). All the steps have negative ages with $^{40}Ar/^{36}Ar$ ratios of between 175±16 and 296±4 (Table 5.18). The $^{37}Ar/^{39}Ar$ ratios generally decrease throughout the experiment (Figure 5.32 A) while the $^{38}Ar/^{39}Ar$ ratios tend to increase from low to high temperature steps (Figure 5.32 B).

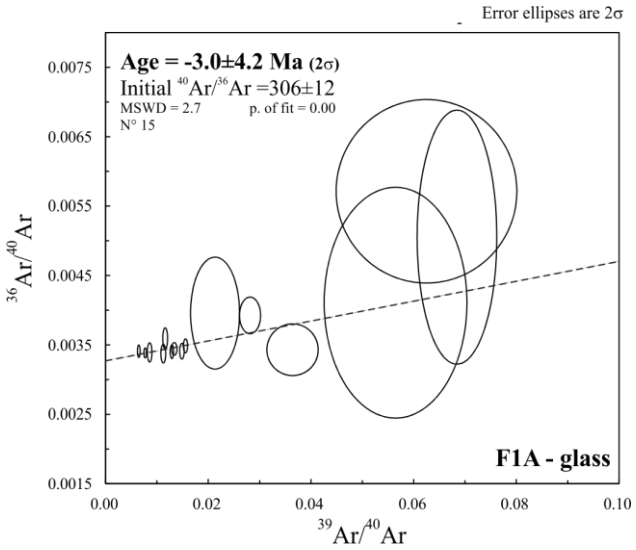

Figure 5.31 Inverse isochron for step heating analysis on pumice glass of sample F1A.

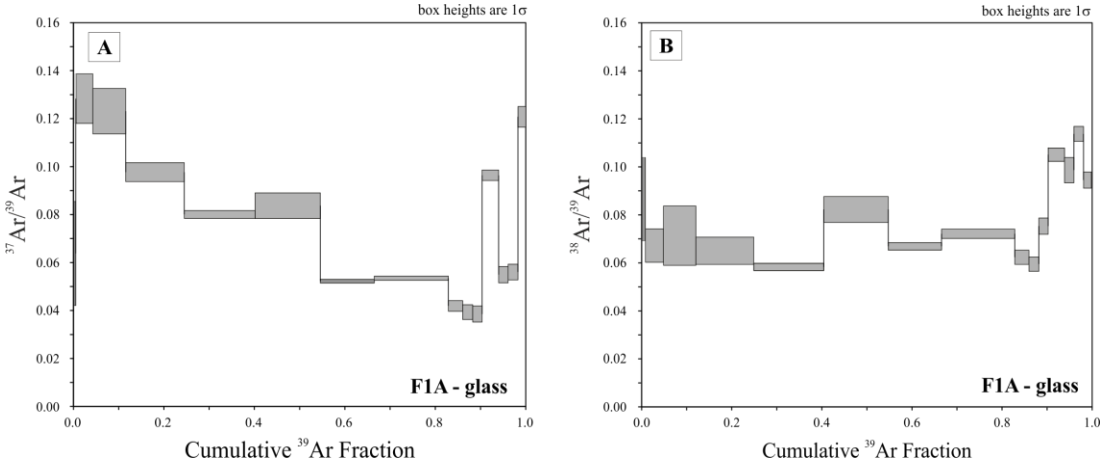

Figure 5.32 Variation of the $^{37}Ar/^{39}Ar$ ratios (A) and of the $^{38}Ar/^{39}Ar$ ratios (B) for step heating analysis on pumice glass of F1A.

When step-heated, pumice glass from sample F2A failed to yield a plateau age. The presence of steps having negative ages (Table 5.18) invalidates the use of the age spectra. These steps have $^{40}Ar/^{36}Ar$ ratios lower than the atmospheric value of 298.56 (Lee et al., 2006) (Table 5.18). In contrast, positive ages are associated with those steps that have $^{40}Ar/^{36}Ar$ ratios higher than 298.56 (Table 5.18). The $^{40}Ar/^{36}Ar$ ratios range from 282±4 to 309±4 (Table 5.18), the $^{37}Ar/^{39}Ar$ ratios are consistent throughout the experiments except for the first two low temperature steps that have much higher values (Figure 5.33 A), the $^{38}Ar/^{39}Ar$ ratios generally increase from low to high temperature steps (Figure 5.33 B).

An inverse isochron age of 0.34±0.07 Ma (95% conf. level) with a $^{40}Ar/^{36}Ar$ ratio of 297±6 (2σ) was obtained by excluding steps 1 and 2 from the calculation (Figure 5.34 A - C). These two steps have higher $^{37}Ar/^{39}Ar$ ratios (> 0.07) with respect to the other steps that are more consistent throughout the experiments (range 0.05 – 0.06) (Table 5.18).

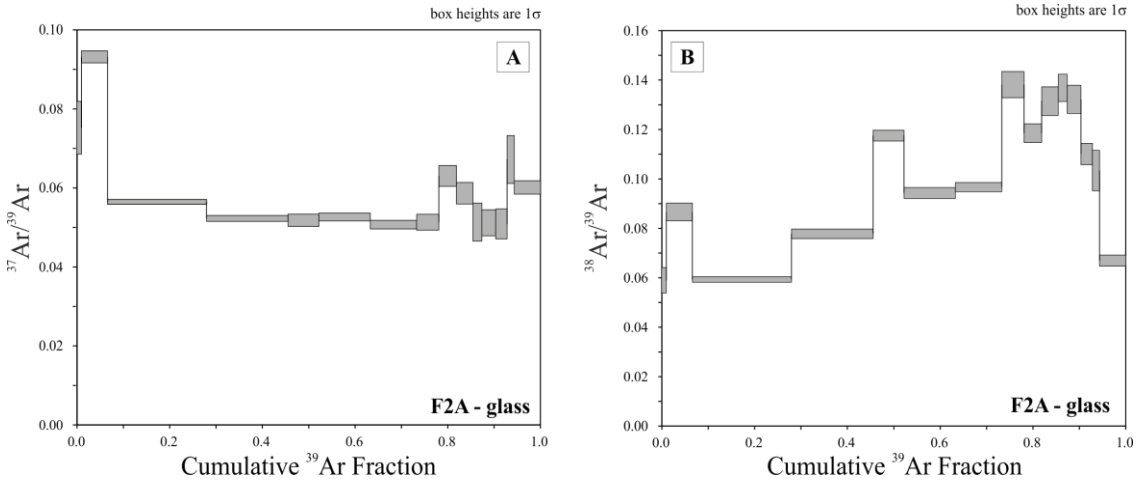

Figure 5.33 Variation of the $^{37}Ar/^{39}Ar$ ratios (A) and of the $^{38}Ar/^{39}Ar$ ratios (B) for step heating analysis on pumice glass of F2A.

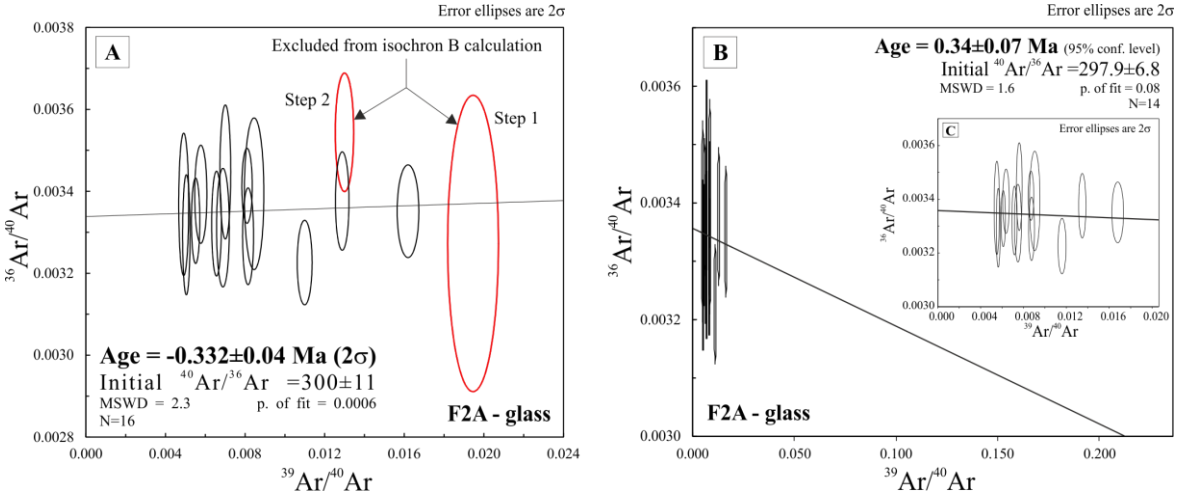

Figure 5.34 A - Inverse isochron for step heating analysis on pumice glass of sample F2A. The age was calculated using all the steps. B - Inverse isochron for step heating analysis on pumice glass of sample F2A with Step 1 and 2 not included in the calculation. The two steps have higher $^{37}Ar/^{39}Ar$ ratios (> 0.07) with respect to the other steps (range 0.05 – 0.06). C - Inset of image B showing in more detail the distribution of the data along the inverse isochron.

When step-heated, pumice glass from sample I1A failed to yield a plateau age. The presence of steps having negative ages (Table 5.19) invalidates the use of the age spectrum. The $^{40}Ar/^{36}Ar$ ratios are between 283±63 and 307±3 (Table 5.19). Those steps with negative ages are those with $^{40}Ar/^{36}Ar$ ratios lower than the atmospheric value of 298.56 (Lee et al., 2006). Positive ages are associated with those steps that have $^{40}Ar/^{36}Ar$ ratios higher than 298.56 (Table 5.19). The $^{37}Ar/^{39}Ar$ ratios are variable throughout the experiment (Figure 5.35 A), the $^{38}Ar/^{39}Ar$ ratios increase from low to high temperature steps (Figure 5.35 B).

An inverse isochron age of 0.32±0.06 Ma (95% conf. level) with a $^{40}Ar/^{36}Ar$ ratio of 298±6 (2σ) was obtained including all the steps in the calculation (Figure 5.36 A - C).

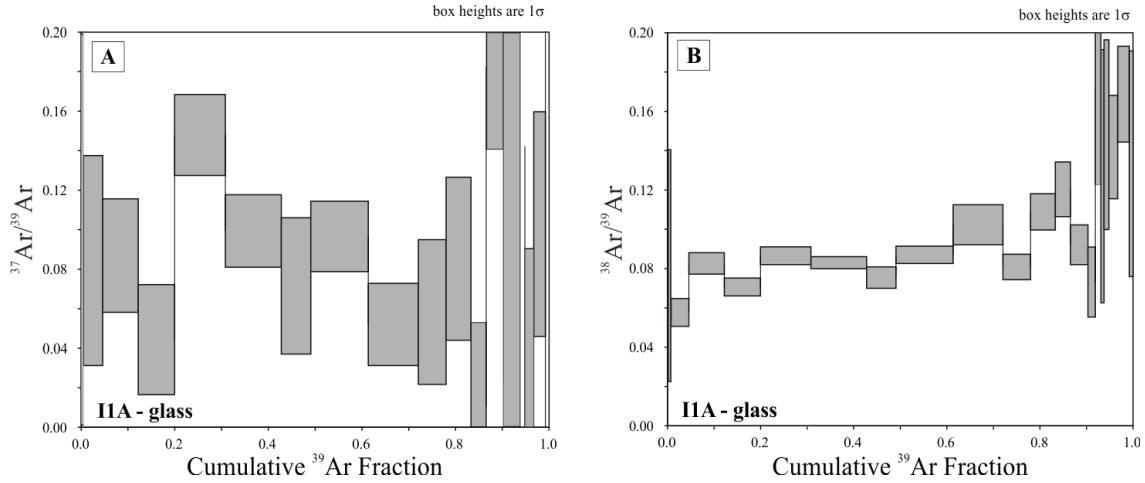

Figure 5.35 Variation of the $^{37}Ar/^{39}Ar$ ratios (A) and of the $^{38}Ar/^{39}Ar$ ratios (B) for step heating analysis on pumice glass of sample F2A.

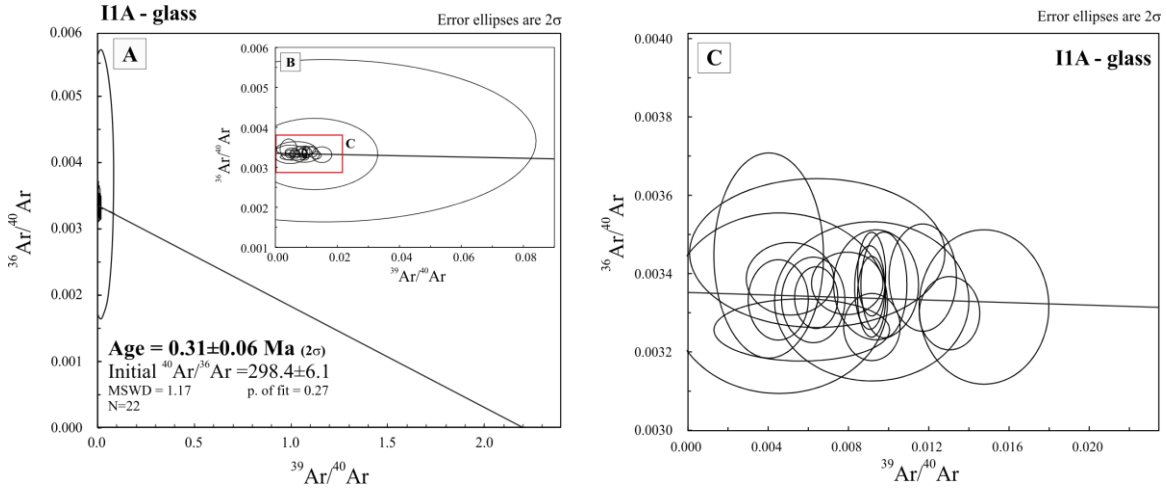

Figure 5.36 Inverse isochron for step heating analysis on pumice glass of sample I1A. A - All the steps are included in the calculation. B and C – Inset of image A showing in more detail the distribution of the data along the inverse isochron.

When step-heated, pumice glass from sample I3A failed to yield a plateau age. The presence of steps having negative ages invalidates the use of the age spectrum (Table 5.19). Those steps having $^{40}Ar/^{36}Ar$ ratios lower than the atmospheric value of 298.56 (Lee et al., 2006) are associated with negative ages. Positive ages are associated with those steps having $^{40}Ar/^{36}Ar$ ratios higher than 298.56 (Table 5.19). The $^{40}Ar/^{36}Ar$ ratios range from 296±4 to 308±5 (Table 5.19), the $^{37}Ar/^{39}Ar$ ratios increase in the central steps while the $^{38}Ar/^{39}Ar$ ratios in the same steps decrease (Figure 5.37 A – B). When the $^{37}Ar/^{39}Ar$ ratios are plotted against the $^{38}Ar/^{39}Ar$ ratios it is clear that two populations of data exist (Figure 5.38). The first is represented by steps 1 to 9 and 14 to 17 and has low $^{37}Ar/^{39}Ar$ ratios and high $^{38}Ar/^{39}Ar$ ratios (Group 1, figure 5.38); the second is represented by steps 10 to 13 and has high $^{39}Ar/^{40}Ar$ and $^{37}Ar/^{39}Ar$ ratios and low $^{38}Ar/^{39}Ar$ ratios (Group 2, Figure 5.38).

An inverse isochron age of -1.0±1.1 Ma (95% confidence level) with a Y-intercept at 303±5 (2σ) was obtained including all the steps in the calculation (Figure 5.39 A). A valid inverse isochron age of 0.29±0.02 Ma (95% confidence level) with a Y-intercept at 299±11 (2σ) (Figure 4.39 B) was obtainable only excluding from the calculation steps 10 to 13 (Group 2, Figure 5.38) and those steps with ^{40}Ar ion count close to 14V (3, 6 and 15).

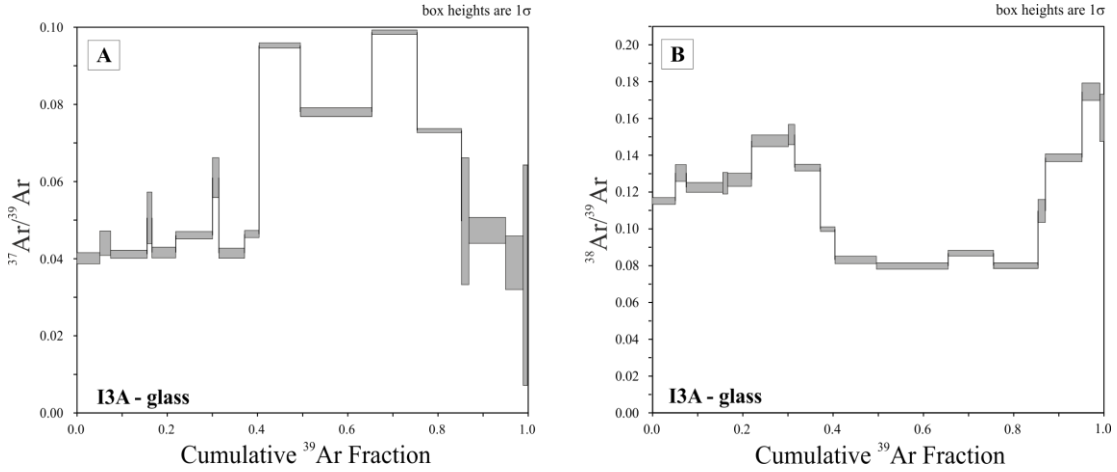

Figure 5.37 Variation of the $^{37}Ar/^{39}Ar$ ratios (A) and of the $^{38}Ar/^{39}Ar$ ratios (B) for step heating analysis on pumice glass of sample I1A. Steps with ratios higher than 0.5 or having negative values are not displayed for clarity.

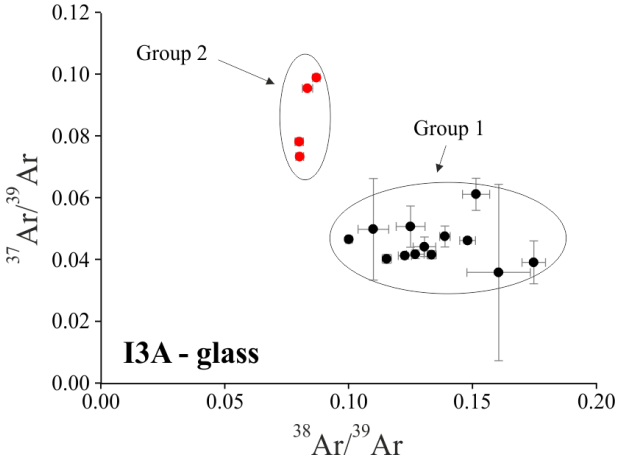

Figure 5.38 Correlation between the $^{37}Ar/^{39}Ar$ and the $^{38}Ar/^{39}Ar$ ratios for pumice glass of sample I3A. It is clear the existence of two populations of data having significantly different ratios (Group 1 and 2). Error bars are displayed at the 1σ level.

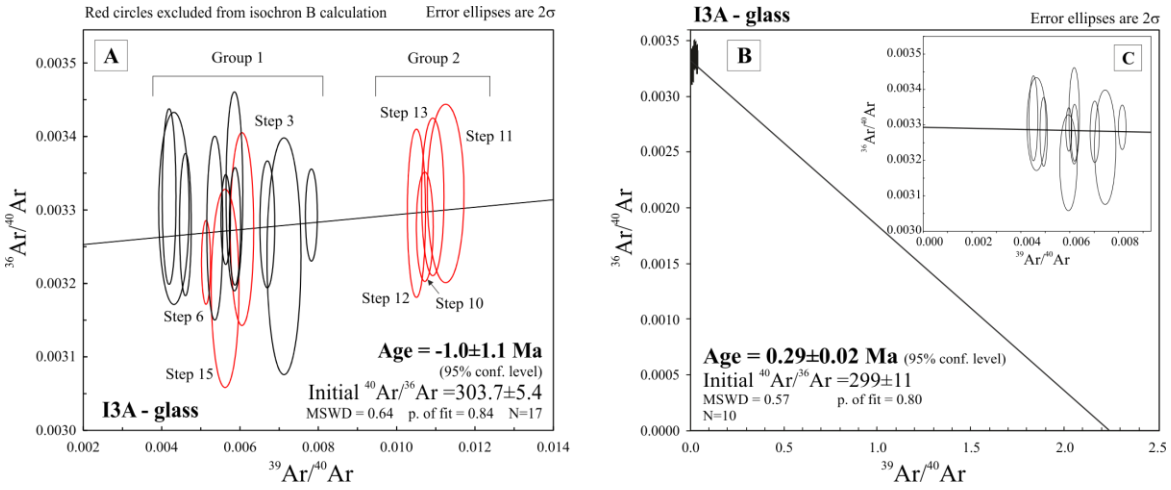

Figure 5.39 Inverse isochron for step heating analysis on pumice glass of sample I3A. A - all the steps are included in the calculation. B - Those steps belonging to Group 2 in Figure 5.43 and those with high ^{40}Ar are excluded from the isochron calculation. C - Inset of image B showing in more detail the distribution of the data along the inverse isochron.

Table 5.18 Ages and $^{40}Ar/^{36}Ar$ ratios for step heating analysis from pumice glass particles.

Step	Age (Ma)	±1σ (Ma)	$^{40}Ar/^{36}Ar$	±1σ
Sample F1A				
1	-5.05	2.18	197.96	29.3
2	-7.68	1.37	175.05	16.55
3	-2.72	2.39	243.49	40.27
4	-0.45	0.83	291.58	12.93
5	-4.14	0.71	254.83	7
6	-5.79	2.87	252.7	21.04
7	-1.77	0.53	286.93	3.37
8	-1.39	0.55	290.58	3.13
9	-0.79	0.63	294.16	3.45
10	-0.81	0.63	293.38	3.98
11	-0.42	0.98	296.48	4.81
12	-0.91	0.76	295.51	2.53
13	-0.97	1.33	294.93	4.91
14	-1.85	1.14	293.39	3.13
15	-4.25	1.09	278.36	4.84
Sample F2A				
1	0.8	1.53	305.56	13.8
2	-3.02	0.9	282.17	4.71
3	-0.02	0.58	298.39	4.11
4	2.26	0.79	309.99	4.05
5	0.87	1.61	301.11	4.75
6	1.47	1.2	303.94	4.46
7	-1.59	0.93	292.97	3.21
8	2.22	2.41	303.6	5.54
9	1.12	1.74	302.01	5.4
10	0.79	1.56	300.49	3.85
11	-0.77	2.91	296.9	6.27
12	-1.51	1.71	294.75	4.25
13	-2.81	1.92	290.1	5.63
14	-1.06	1.79	294.64	6.57
15	-0.42	0.77	296.2	4.31

Table 5.19 Ages and $^{40}Ar/^{36}Ar$ ratios from step heating analysis from pumice glass particles.

Step	Age (Ma)	±1σ (Ma)	$^{40}Ar/^{36}Ar$	±1σ
Sample I1A				
1	4.79	13.07	103.23	315.83
2	0.26	5.92	300	32.8
3	0.47	1.1	301.69	7.33
4	-0.44	1.13	296.66	4.85
5	0.78	0.59	303.15	3.51
6	-0.33	0.97	297.25	3.85
7	-1.08	0.96	294.25	3.78
8	-0.69	0.96	295.02	4.87
9	0.19	0.92	299.34	3.77
10	-0.64	0.82	296.31	2.86
11	1.88	0.78	306.42	3.29
12	0.34	1.01	299.54	2.89
13	0.54	1.44	300.06	4.02
14	-0.47	1.23	296.63	5.04
15	0.45	1.82	300.4	7.49
16	-4.82	5.51	290.19	9.01
17	1.11	4.19	300.82	8.52
18	3.31	1.55	307.13	3.05
19	-1.47	1.52	295.28	3.3
20	0.74	1.87	300.05	3.77
21	-3.21	2.74	289.66	6.51
22	-4.09	13.08	272.96	61.82
Sample I3A				
1	0.57	1.06	300.27	3.18
2	3.78	2	308.34	5.24
3	0.84	1.78	300.85	4.85
4	-0.88	1.89	296.28	4.86
5	0.75	1.12	300.52	2.95
6	2.76	0.91	305.02	2.17
7	0.84	1.72	300.3	3.57
8	0.45	0.89	299.68	2.25
9	0.16	0.65	299.14	2.29
10	0.42	0.57	300.57	2.75
11	-0.41	0.88	296.53	4.36
12	0.08	0.89	298.92	4.18
13	-0.33	0.8	296.94	3.86
14	1.75	1.86	304.24	6.09
15	0.9	1.92	300.74	4.63
16	-0.89	2.33	296.9	4.31
17	-0.12	2.47	298.33	4.75

5.6.3 Sanidine

Single grain total fusion experiments were performed on 7 sanidine crystals from sample F1A. The crystals yielded ages ranging from 0.07±1.37 Ma to 0.72±1.44 Ma with $^{40}Ar/^{36}Ar$ ratios higher than the atmospheric value of 298.56 (Table 5.20).

Single sanidines from I3A yielded ages of 0.26±1.81 Ma and of 0.97±0.58 Ma with $^{40}Ar/^{36}Ar$ ratios of 326±215 and 809±824, respectively (Table 5.20). Ages of 0.75±0.22 Ma and 0.72±0.14 Ma were obtained when 4 grains were fused together during two separate experiments. The $^{40}Ar/^{36}Ar$ ratios are 330±10 and 371±18, respectively (Table 5.20).

A weighted mean age of 0.74±0.24 Ma (2σ) (Figure 5.40 A) and an isochron age of 0.8±1.5 Ma (95% confidence level) with a Y-intercept at 298±35 (2σ) were obtained by combining the results of the 4 experiments done on sample F1A (Figure 5.40 B). The two ages are concordant at the 2σ confidence level.

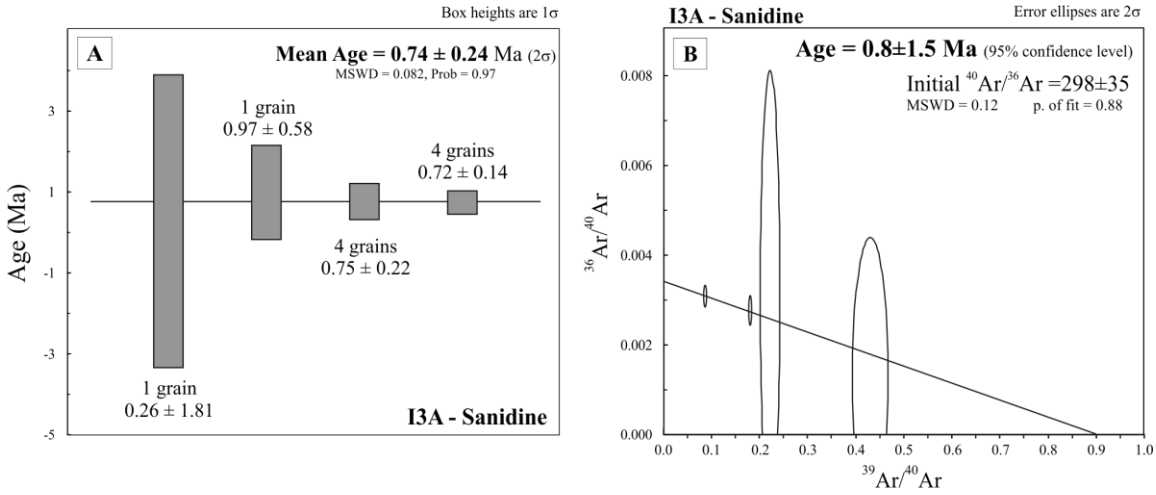

Figure 5.40 Weighted mean age (A) and inverse isochron age (B) for single grain fusion analysis on sanidine of F1A.

Table 5.20 Ages and $^{40}Ar/^{36}Ar$ ratios of single grain total fusion from sanidines

Step	Age (Ma)	±1σ (Ma)	$^{40}Ar/^{36}Ar$	±1σ
Sample F1A				
G1	0.62	0.5	675	688
G2	0.27	0.29	468	280
G3	0.48	0.35	471	200
G4	0.64	1.07	899	3057
G5	0.33	0.45	431	258
G6	0.07	1.37	323	512
G7	0.72	1.42	450	459
Sample I3A				
G1	0.26	1.81	327	216
G2	0.97	0.58	810	825
G3-5	0.75	0.22	330	10
G6-10	0.72	0.14	372	18

When step-heated, sanidine crystals from sample F1A yielded $^{40}Ar/^{36}Ar$ ratios increasing throughout the experiments ranging from 287±10 to 910±140 (Table 5.22). The $^{37}Ar/^{39}Ar$ ratios are extremely variable from step 1 to step 7, while remaining reasonably constant in the second part of the experiment (Figure 5.41 A) and the $^{38}Ar/^{39}Ar$ ratios are pretty constant except for steps 1 and 2 that display extremely high values (Figure 5.41 B).

For F1A was obtained a plateau age of 0.741±0.024 Ma (2σ) comprising 78.3% of the released ^{39}Ar and based on 8 of 15 degassing steps (Figure 5.42 A). The inverse isochron age is 0.79±0.03 Ma (95% confidence level) and has a sub-atmospheric $^{40}Ar/^{36}Ar$ ratio of 258.4±9.6 (2σ) (Figure 5.42 B). The two ages are not concordant at 2σ confidence level.

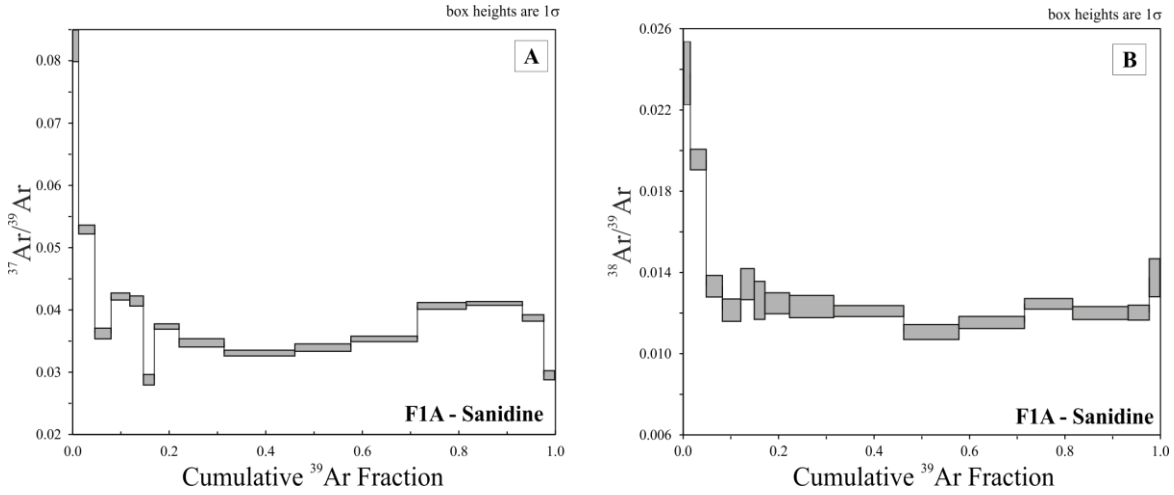

Figure 5.41 Variation of the $^{37}Ar/^{39}Ar$ ratios (A) and of the $^{38}Ar/^{39}Ar$ ratios (B) for step heating analysis on sanidine crystals of sample F1A.

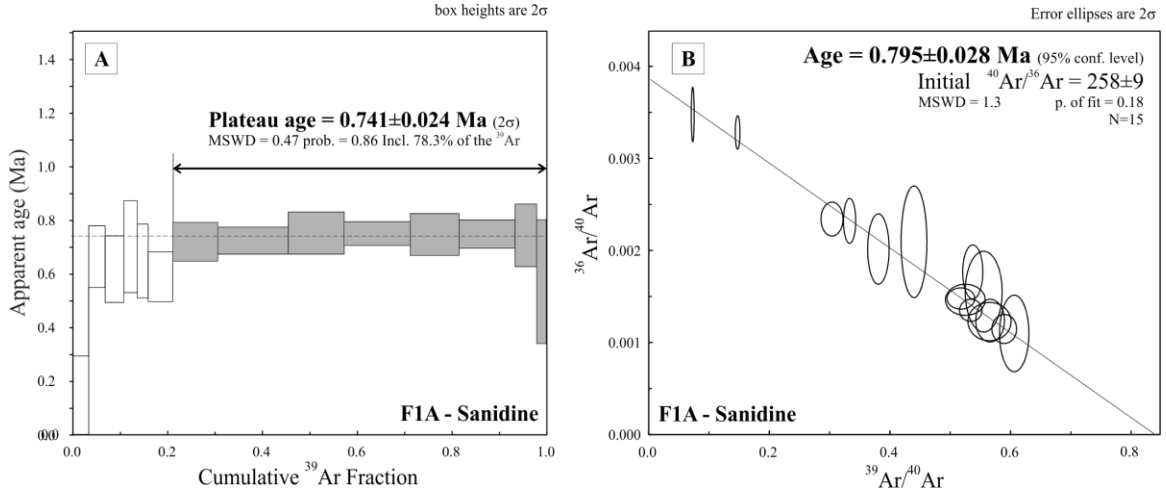

Figure 5.42 Plateau age and inverse isochron age for sanidine crystals from sample F1A.

When step-heated, the sanidine crystals from sample F2A yielded scattered $^{40}Ar/^{36}Ar$ ratios ranging from 350±87 to 2,302±467 (Table 5.21). The $^{38}Ar/^{39}Ar$ ratios slightly decrease throughout the experiment (Figure 5.43 A) and the $^{37}Ar/^{39}Ar$ ratios are extremely variable from step 1 to step 11 whilst somewhat constant (with a slight decrease) in the last five steps of the experiment (Figure 5.43 B).

For F2A it was obtained a plateau age of 0.688±0.021 Ma (2σ) comprising 93.3% of the released ^{39}Ar and based on 9 of 16 degassing steps (Figure 5.44 A). The inverse isochron age is 0.71±0.04 Ma (95% confidence level) and has a $^{40}Ar/^{36}Ar$ ratio of 272±37 (2σ) (Figure 44 B). The two ages are concordant at the 2σ confidence level.

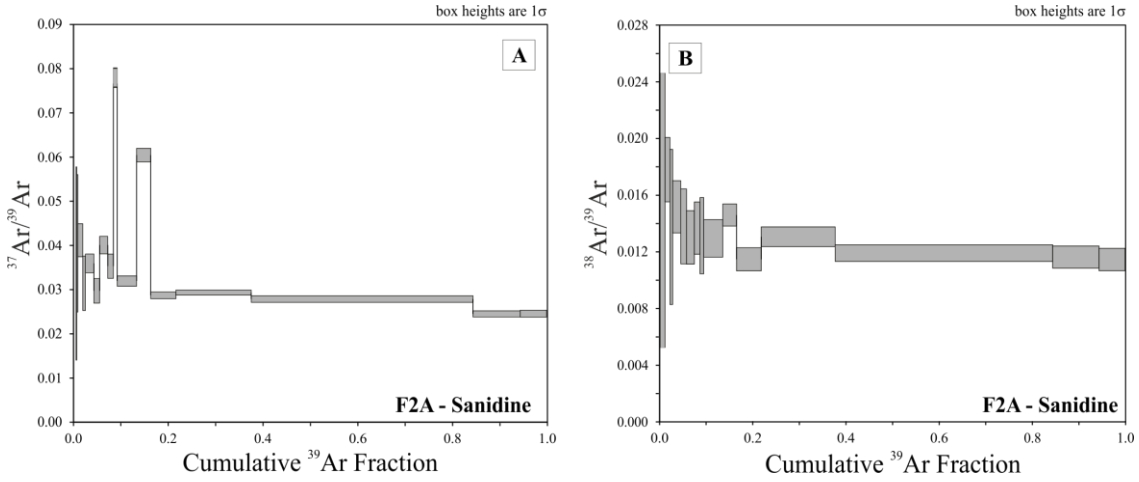

Figure 5.43 Variation of the $^{37}Ar/^{39}Ar$ ratios (A) and of the $^{38}Ar/^{39}Ar$ ratios (B) for step heating analysis on sanidine crystals of sample F2A.

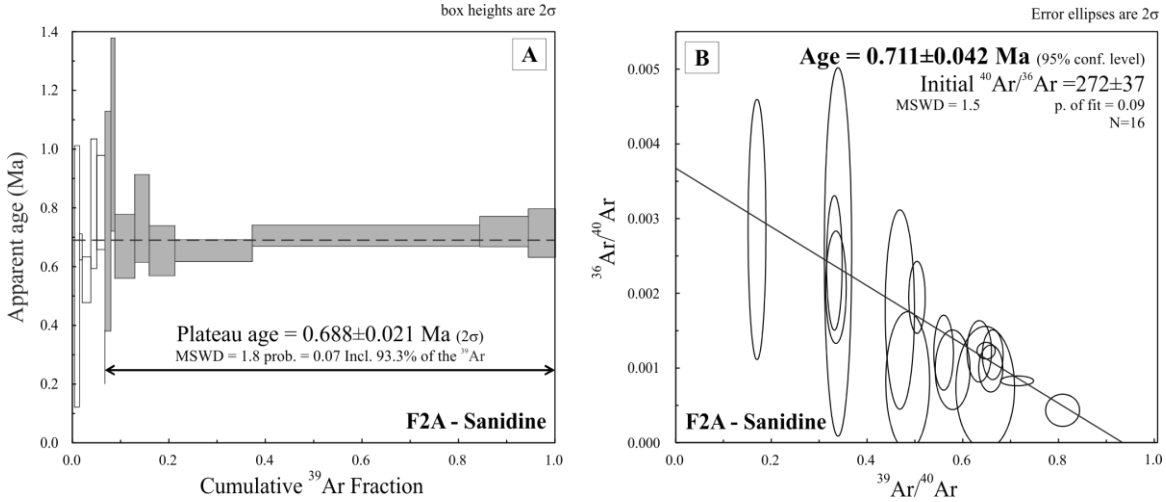

Figure 5.44 Plateau age (A) and inverse isochron age (B) for sanidine crystals from sample F2A.

When step-heated, the sanidine crystals from sample I1A yielded scattered $^{40}Ar/^{36}Ar$ ratios with values ranging from 316±19 to 5,347±7,770 (Table 5.22), the $^{37}Ar/^{39}Ar$ ratios decrease throughout the experiment with step 1 and 2 that have higher values (Figure 5.44 A), the $^{38}Ar/^{39}Ar$ ratios are pretty constant throughout the experiment with only steps 1 and 2 having higher values (Figure 5.45 B).

Sample I1A yielded a plateau age of 0.696±0.030 Ma (2σ) comprising 59.4% of the released ^{39}Ar and based on 4 of 13 degassing steps (Figure 5.46 A). The inverse isochron age is 0.70±0.13 Ma (95 % confidence level) with a $^{40}Ar/^{36}Ar$ ratio of 318±74 (2σ) (Figure 5.46 B). Two ages are concordant at the 2σ confidence level but, the first one is tentatively preferred over the second in representing the age of the eruption of sample I1A due to its better statistics.

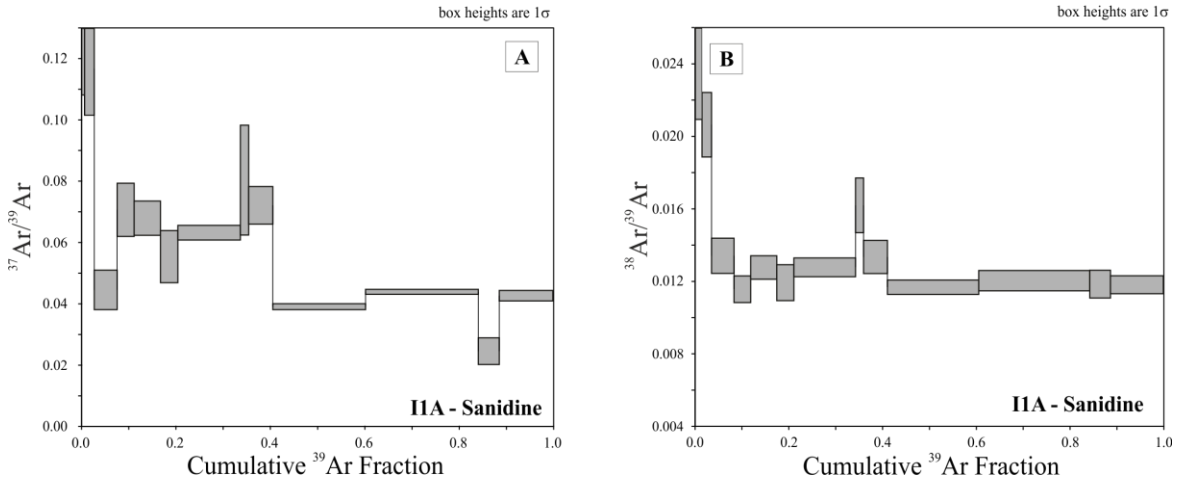

Figure 5.45 Variation of the $^{37}Ar/^{39}Ar$ ratios (A) and of the $^{38}Ar/^{39}Ar$ ratios (B) for step heating analysis on sanidine crystals of sample I1A.

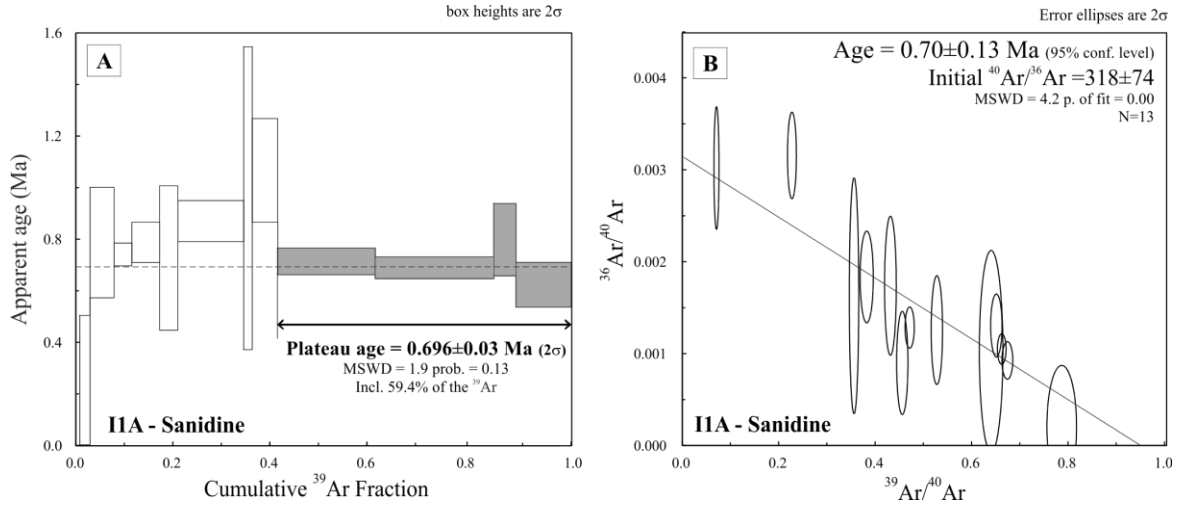

Figure 5.46 Plateau age (A) and inverse isochron age (B) for sanidine crystals from sample F2A.

When step-heated, sanidine crystals from sample I3A yielded $^{40}Ar/^{36}Ar$ ratios ranging from 300±9 to 623±20 (Table 5.22). The $^{37}Ar/^{39}Ar$ ratios and the $^{38}Ar/^{39}Ar$ ratios decrease in the first part of the experiment and then remaining constant in last 3 steps of the experiment (Figure 5.47 A - B).

Sample I3A yielded a plateau age of 0.70±0.03 Ma (2σ) comprising 86.5% of the released ^{39}Ar and based on 5 of 12 degassing steps (Figure 5.48 A). The inverse isochron age is 0.72±0.04 Ma (95% confidence level) and has a $^{40}Ar/^{36}Ar$ ratio of 288.8±8.4 (2σ) (Figure 5.48 B). The two ages are concordant at the 2σ confidence level.

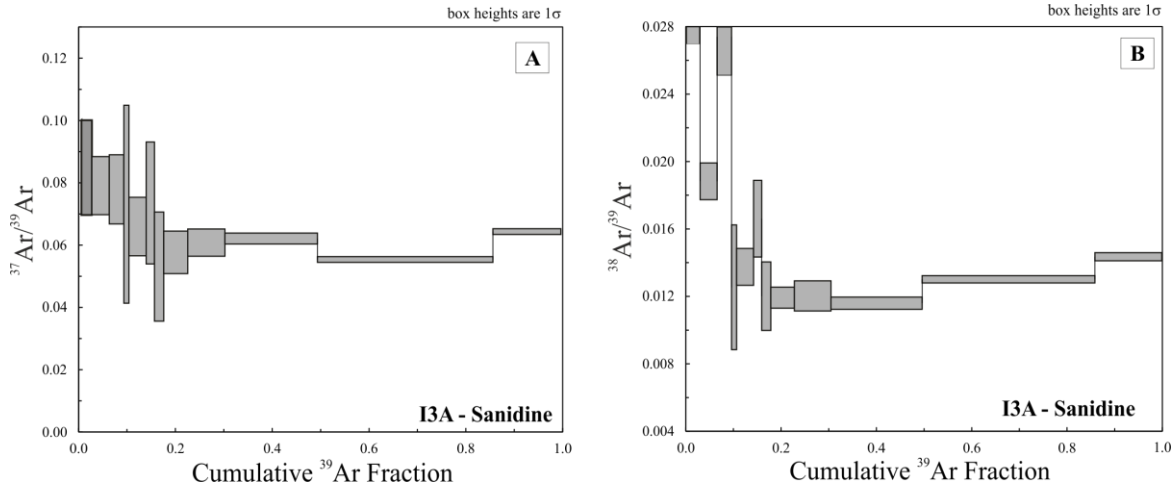

Figure 5.47 Variation of the $^{37}Ar/^{39}Ar$ ratios (A) and of the $^{38}Ar/^{39}Ar$ ratios (B) for step heating analysis on sanidine crystals of sample I3A.

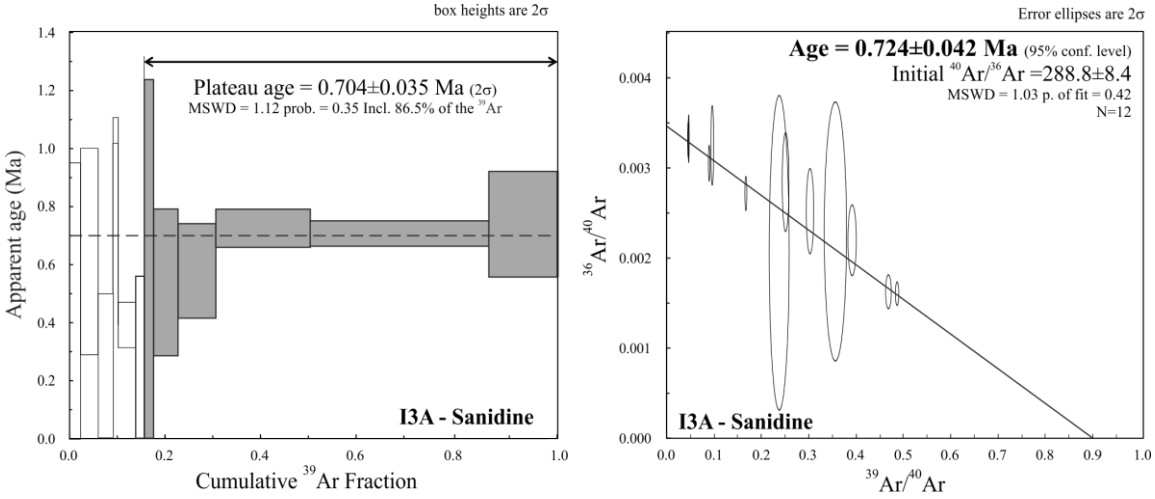

Figure 5.48 Plateau age and inverse isochron age for sanidine crystals from sample I3A.

Table 5.21 Ages and $^{40}Ar/^{36}Ar$ ratios from step heating analysis from sanidines.

Step	Age (Ma)	±1σ (Ma)	$^{40}Ar/^{36}Ar$	±1σ
Sample F1A				
1	-0.34	0.33	287.66	10.06
2	0.09	0.1	304.79	6.9
3	0.66	0.06	427.22	13.74
4	0.61	0.06	430.82	18.54
5	0.7	0.08	496.27	38.46
6	0.64	0.07	644.27	74.4
7	0.59	0.05	566.12	38.41
8	0.71	0.04	683.52	32.26
9	0.72	0.02	676.81	21.6
10	0.75	0.04	814.78	56.49
11	0.75	0.02	741.3	26.99
12	0.74	0.04	808.17	61.93
13	0.74	0.03	872.05	48.98
14	0.74	0.06	910.08	140.64
15	0.57	0.11	477.59	56.51
Sample F2A				
1	0.58	0.83	350.45	87.58
2	0.46	0.59	391.56	154.51
3	0.56	0.22	415.54	63.56
4	0.66	0.23	561	171.49
5	0.55	0.08	514.1	52.03
6	0.81	0.11	1407.88	664.97
7	0.81	0.08	1024.37	228.25
8	0.75	0.19	480.52	70.95
9	1.04	0.16	1251.62	594.49
10	0.66	0.05	817.48	112.11
11	0.76	0.07	829.82	141.21
12	0.65	0.04	849.31	97.94
13	0.65	0.02	811.71	29.85
14	0.7	0.02	1207.41	39.07
15	0.71	0.03	2302.55	467.08
16	0.71	0.04	1007.56	130.08

Table 5.22 Ages and $^{40}Ar/^{36}Ar$ ratios from step heating analysis from sanidines.

Step	Age (Ma)	±1σ (Ma)	$^{40}Ar/^{36}Ar$	±1σ
Sample I1A				
1	0.91	0.76	331.22	30.03
2	0.17	0.17	316.89	19.34
3	0.78	0.11	545.43	60.65
4	0.73	0.14	575.25	102.3
5	0.78	0.09	796.27	153.41
6	0.72	0.14	995.18	444.06
7	0.86	0.04	779.33	55.65
8	0.95	0.29	614.02	198.34
9	1.06	0.1	1112.7	283.86
10	0.71	0.03	1079.85	97.54
11	0.68	0.02	952.71	61.46
12	0.79	0.07	5347.28	7770.37
13	0.62	0.04	765.78	82.1
Sample I3A				
1	0.1	0.44	300.81	9.81
2	0.64	0.18	327.52	8.7
3	0.14	0.32	301.58	7.1
4	1.05	0.59	486.06	168.56
5	0.39	0.17	351.71	27.75
6	0.2	0.36	307.75	17.11
7	0.58	0.32	437.17	112.25
8	0.53	0.13	396.87	30.45
9	0.57	0.08	455.1	33.23
10	0.72	0.03	615.36	29.08
11	0.7	0.02	623.54	20.6
12	0.73	0.09	368.18	10.5

5.6 Discussion

5.6.1 NG geochemistry

5.6.1.1 Glass

5.6.1.1.1 Data variability

From the available data it is clear that pumice glass pieces in this study have retained ^{4}He, ^{36}Ar and $^{40}Ar^{*}$ in different concentrations and proportions, post-eruption.

Looking at the mean abundances of ^{4}He in the two deposits it is possible to observe a decrease from the base to the top of the fall reaching its minimum value in the ignimbrite (Figure 5.49 A). The variability of ^{4}He diminishes from the base of the fall deposit to the upper portion of the ignimbrite (Figure 5.49 A).

$^{40}Ar^{*}$ mean concentration increases from the base to the top of both the fall and the ignimbrite (Figure 5.49 B) from F1A to F2A and from I1A to I3A. In particular, F1A and I1A display similar mean $^{40}Ar^{*}$ abundances while F2A has a lower $^{40}Ar^{*}$ content compared to I3A that has the highest mean $^{40}Ar^{*}$ content with respect to all the other samples (Figure 5.49 B).

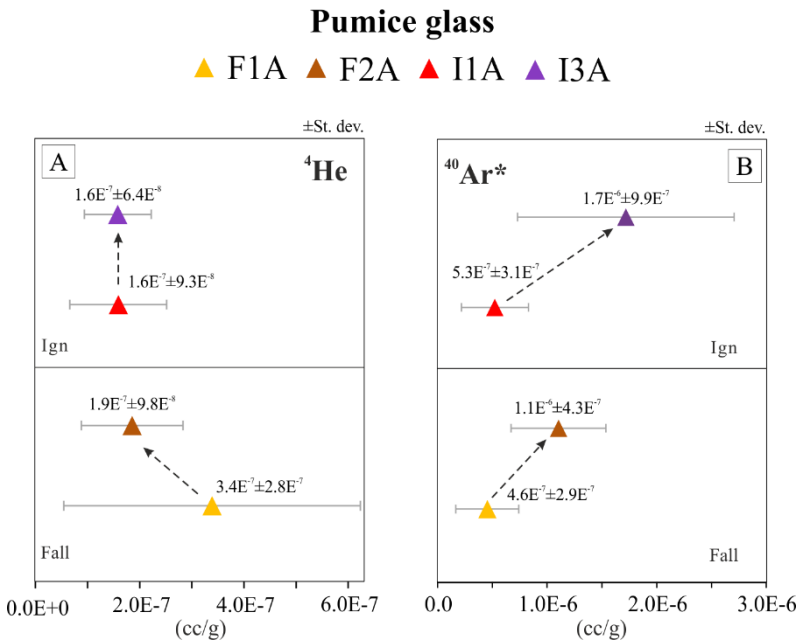

Figure 5.49 Variation of the mean ^{4}He (A) and $^{40}Ar^{*}$ (B) abundances and standard deviations of the means for pumice glasses from F1A, F2A, I1A and I3A with respect to their position in the eruptive sequence. The dotted arrow indicates the direction of the variation from the base to the top within the same deposit.

When $^{40}Ar^*$ is plotted against $^{4}He/^{40}Ar^*$ the data assume a hyperbolic trend (dotted line in Figure 5.50 A - C) with samples collected at the base of both units having, generally, higher $^{4}He/^{40}Ar^*$ ratios and lower $^{40}Ar^*$ content with respect to those collected at the top of the fall and of the ignimbrite (Figure 5.50). Glass particles at the bases of the two deposits display larger spreads in the $^{4}He/^{40}Ar^*$ ratios with respect to the upper portions. Except for one sample, all glass particles from F1A have a clearly distinct $^{4}He/^{40}Ar^*$ ratio with respect to those of F2A (Figure 5.50 A). In the ignimbrite this neat separation doesn't exist. Some particles from I1A have an isotopic ratio similar to those from I3A and vice versa (Figure 5.50 B).

Plotting all the data shows that F1A and I1A display some samples with similar $^{4}He/^{40}Ar^*$ ratios and others with a specific distinct NG signature (higher for samples in F1A and lower for samples in I1A) (Figure 5.50 C). In general the $^{4}He/^{40}Ar^*$ ratio is higher in the F1A than in I1A (Figure 5.50 C - D) and the same is true for F2A and I3A (Figure 5.50 C - D).

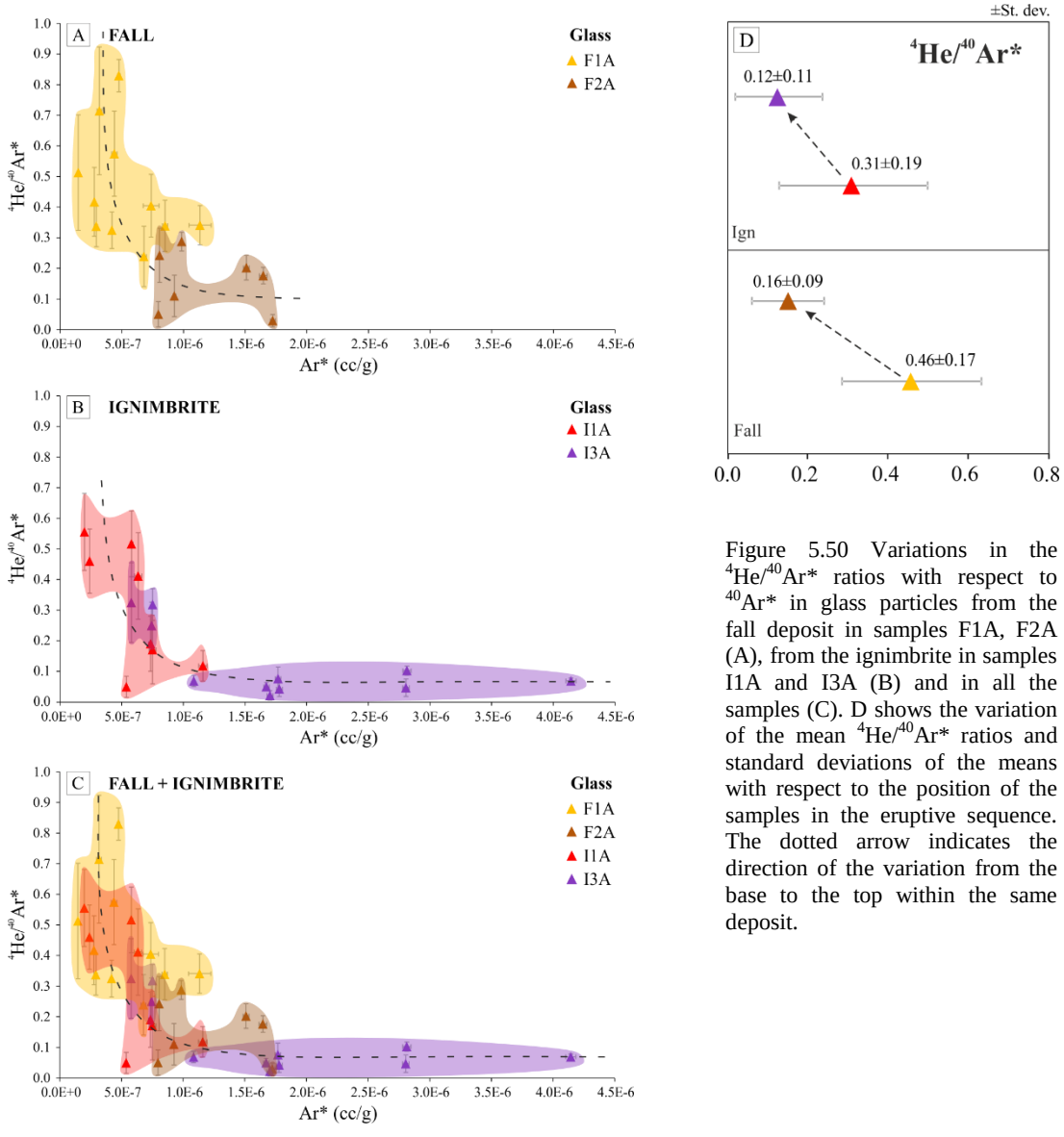

Figure 5.50 Variations in the $^{4}He/^{40}Ar^*$ ratios with respect to $^{40}Ar^*$ in glass particles from the fall deposit in samples F1A, F2A (A), from the ignimbrite in samples I1A and I3A (B) and in all the samples (C). D shows the variation of the mean $^{4}He/^{40}Ar^*$ ratios and standard deviations of the means with respect to the position of the samples in the eruptive sequence. The dotted arrow indicates the direction of the variation from the base to the top within the same deposit.

Analysing the data in more detail indicates that, for the two deposits, there is a separation between glass particles with different $^{40}Ar^*$ contents. There appears to be three populations that have a specific and distinct gas composition (Figure 5.51 A - B):

- Population A: $^{40}Ar^*$ values are lower than $4.5E^{-7}$ cc/g and are only found in the lowermost portions of the two deposits (F1A - Figure 5.51 A; I1A - Figure 5.51 B).
- Population B: $^{40}Ar^*$ values are between $5.0E^{-7}$ cc/g and $1.5E^{-6}$ cc/g and are only found in the base and the top of the fall and the ignimbrite (F1A, F2A - Figure 5.51 A; I1A, I3A - Figure 5.51 B).
- Population C: $^{40}Ar^*$ values are higher than $1.5E^{-6}$ cc/g and are only found in the uppermost portions of the two deposits (F2A - Figure 5.51 A; I3A - Figure 5.51 B).

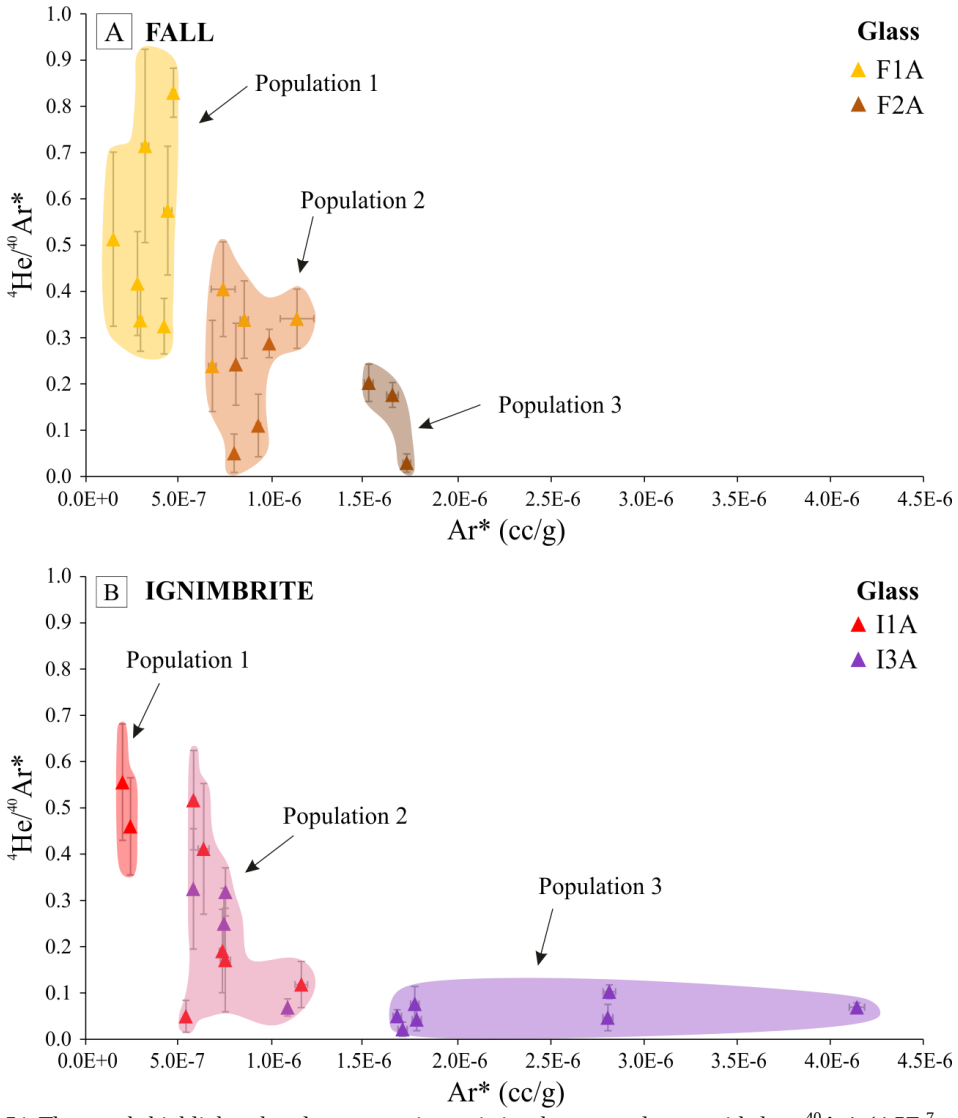

Figure 5.51 The graph highlights the clear separation existing between glasses with low $^{40}Ar^*$ ($4.5E^{-7}$ cc/g) deriving from the base of the deposits (Population 1), with $^{40}Ar^*$ ranging between $5.0E^{-7}$ cc/g and $1.5E^{-6}$ cc/g (Population 2) deriving either from the base and the top of the deposits and glasses that have high $^{40}Ar^*$ content (> $1.5E^{-6}$ cc/g) only from the upper parts of the deposits. Different colours are used to separate and highlight the three different populations.

Plotting $^{40}Ar^*$ against ^{36}Ar indicates that the four samples have a distinct NG signature. The glass particles derived from pumices collected at the base of the two deposits (F1A and I1A) have lower ^{36}Ar contents than do those derived from the upper portions of the units (F2A and I3A) (Figure 5.52).

Plotting the data together yields a positive correlation (correlation coefficient = 0.74). As it is possible to see in Figure 5.52 C and D, I3A has the highest ^{36}Ar content and the highest spread in the ^{36}Ar data while F1A has the lowest ^{36}Ar abundance and the lowest spread in the data. Generally, particles in the fall have lower ^{36}Ar content than those in the ignimbrite.

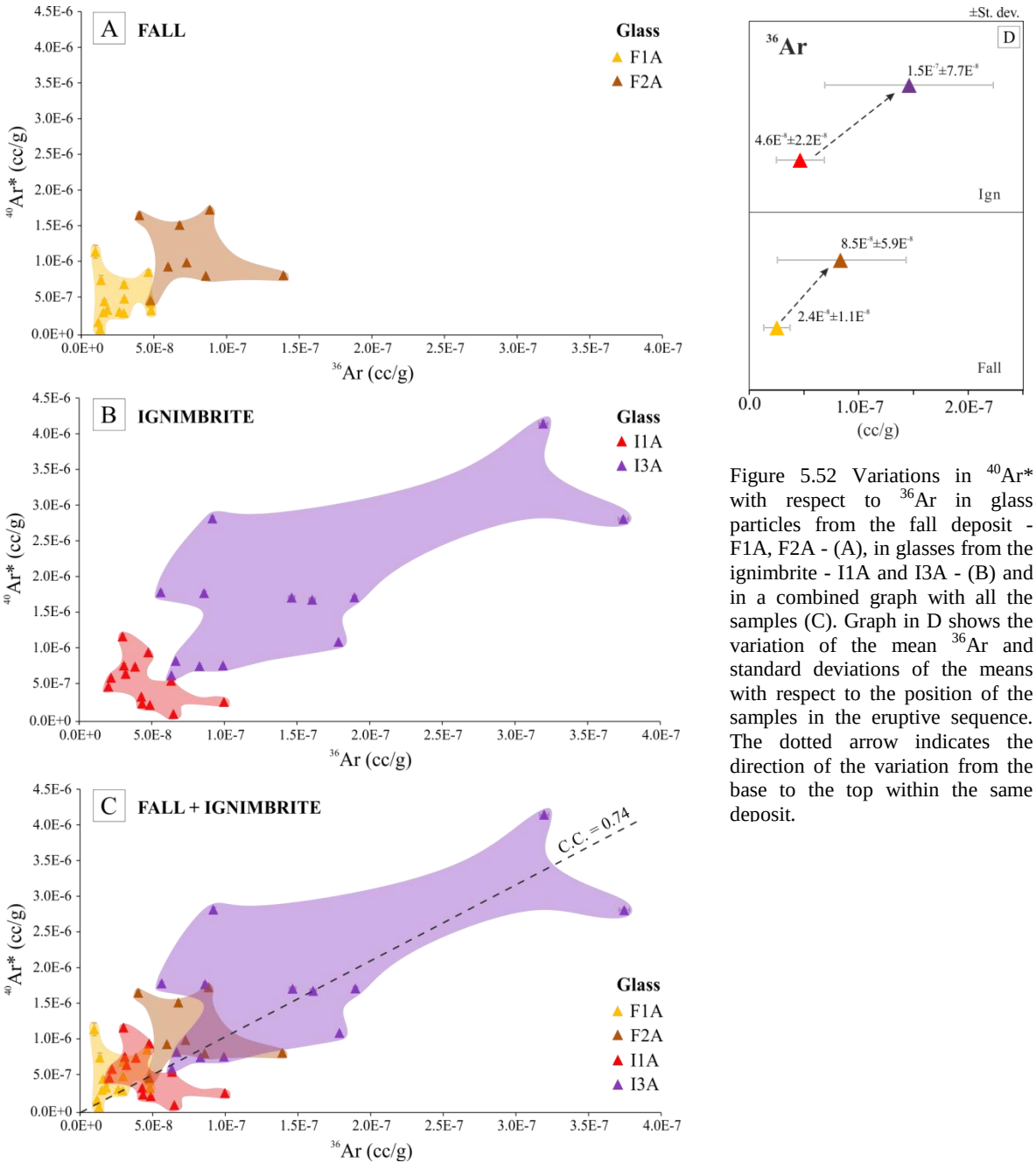

Figure 5.52 Variations in $^{40}Ar^*$ with respect to ^{36}Ar in glass particles from the fall deposit - F1A, F2A - (A), in glasses from the ignimbrite - I1A and I3A - (B) and in a combined graph with all the samples (C). Graph in D shows the variation of the mean ^{36}Ar and standard deviations of the means with respect to the position of the samples in the eruptive sequence. The dotted arrow indicates the direction of the variation from the base to the top within the same deposit.

Individual particles display sub-atmospheric, atmospheric and supra-atmospheric $^{40}Ar/^{36}Ar$ ratios even at the 2σ level (Figure 5.53 A - B). As seen in Figure 5.53 D, the ^{36}Ar increases from the base to the top of each deposit. The $^{40}Ar/^{36}Ar$ ratios are more variable in glass particles glasses derived from the base of the two deposit (F1A, I1A) compared to those samples collected from the upper portions of the units (F2A, I3A) (Figure 5.53 C-D). Only F1A and F2A display glass particles with extremely low $^{40}Ar/^{36}Ar$ ratios of 76, 99 and 125 (Figure 5.53 A).

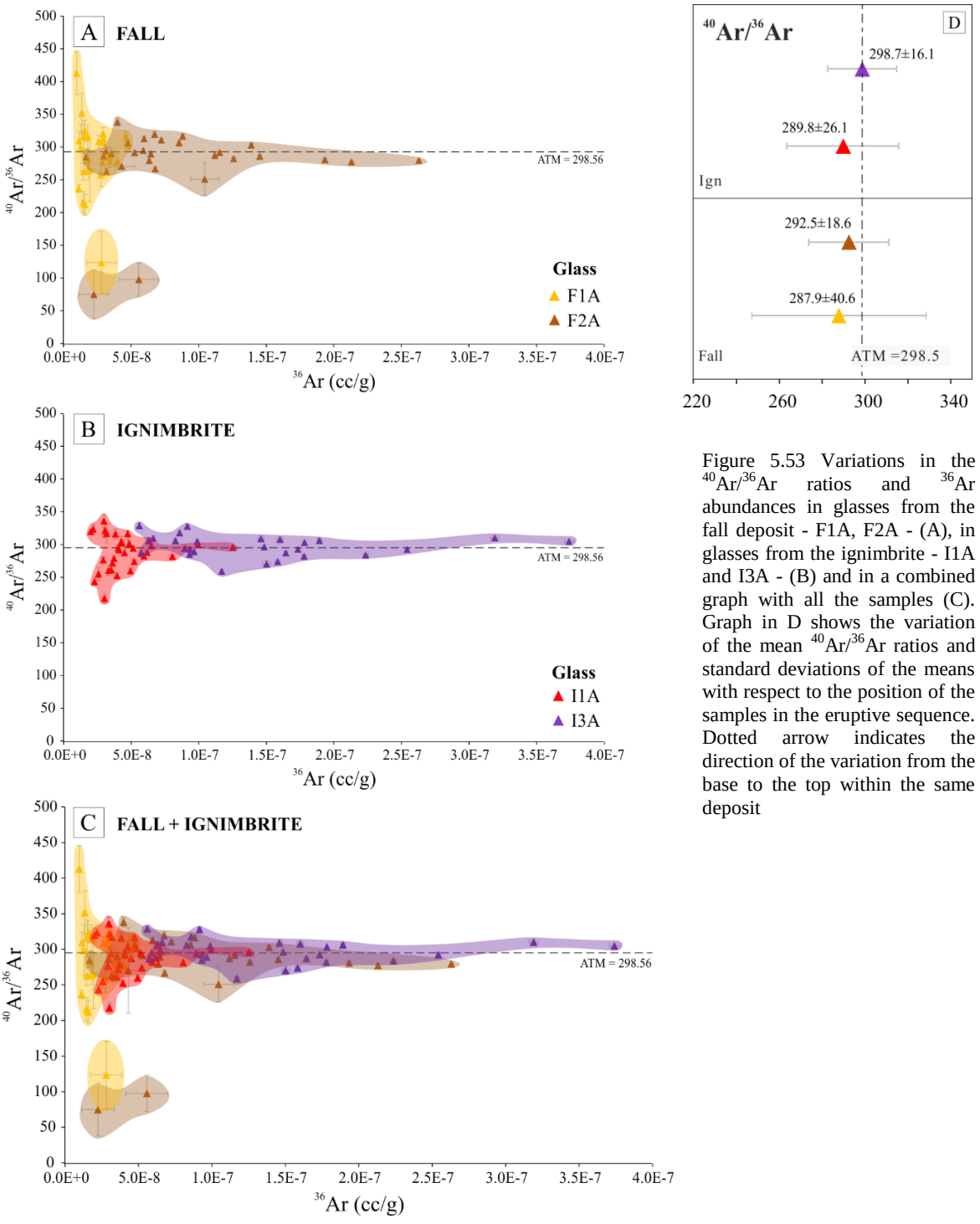

Figure 5.53 Variations in the $^{40}Ar/^{36}Ar$ ratios and ^{36}Ar abundances in glasses from the fall deposit - F1A, F2A - (A), in glasses from the ignimbrite - I1A and I3A - (B) and in a combined graph with all the samples (C). Graph in D shows the variation of the mean $^{40}Ar/^{36}Ar$ ratios and standard deviations of the means with respect to the position of the samples in the eruptive sequence. Dotted arrow indicates the direction of the variation from the base to the top within the same deposit

5.6.1.1.2 Data reliability

A major problem that could affect the reliability of the data from glass particles is related to the determination of the $^{40}Ar^*$, derived using the measured ^{36}Ar to correct the total measured ^{40}Ar for the atmospheric component (assuming atmospheric $^{40}Ar/^{36}Ar$ = 298.56, Lee et al 2006). Because the atmospheric correction is performed on the absolute number given by the $^{40}Ar/^{36}Ar$ ratios, without taking into account the analytical uncertainty associated with the ratios, a portion of the information provided with the analyses is lost.

Following Chapter 4 section 5.6.2, the analytical uncertainties associated with the $^{40}Ar/^{36}Ar$ ratios are discussed in the context of the atmospheric correction. This is intended to determine if the variations of the $^{40}Ar^*$ (and $^{4}He/^{40}Ar^*$ ratios) for the considered samples are real, or, a correction artefact.

In section 5.6.1.1.1 the $^{40}Ar^*$ values and $^{4}He/^{40}Ar^*$ ratios obtained from glass particles in this study are discussed and presented with a pure atmospheric correction ignoring the analytical uncertainties associated with the calculated $^{40}Ar/^{36}Ar$ ratios.

When the $^{40}Ar/^{36}Ar$ ratios with absolute values higher than air are considered at the 1σ level only a few of them are atmospheric within error. Excluding these data from the interpretation the trends observed in Figure 5.50 and 5.52 are still appreciable. The same is true also when the $^{40}Ar/^{36}Ar$ ratios are considered at the 2σ level (Figure 5.54). In this case I1A and F1A have even more similar ^{36}Ar and $^{40}Ar^*$ contents and the difference between glass particles picked from the basal and the top portions of the two deposits are even more distinct (Figure 5.54 A). The hyperbolic trends observed when the $^{4}He/^{40}Ar^*$ ratios are plotted against $^{40}Ar^*$ still exists but is more diffuse due to the few remaining data (Figure 5.54 B-C).

All these lines of evidence support the idea that the variations in the $^{40}Ar^*$ and $^{4}He/^{40}Ar^*$ ratios of glass particles from the two deposits of the Eras Formation are real and not due to an artefact related to an atmospheric correction. Consequently, the data are considered reliable and can now be discussed in the context of volcanic degassing.

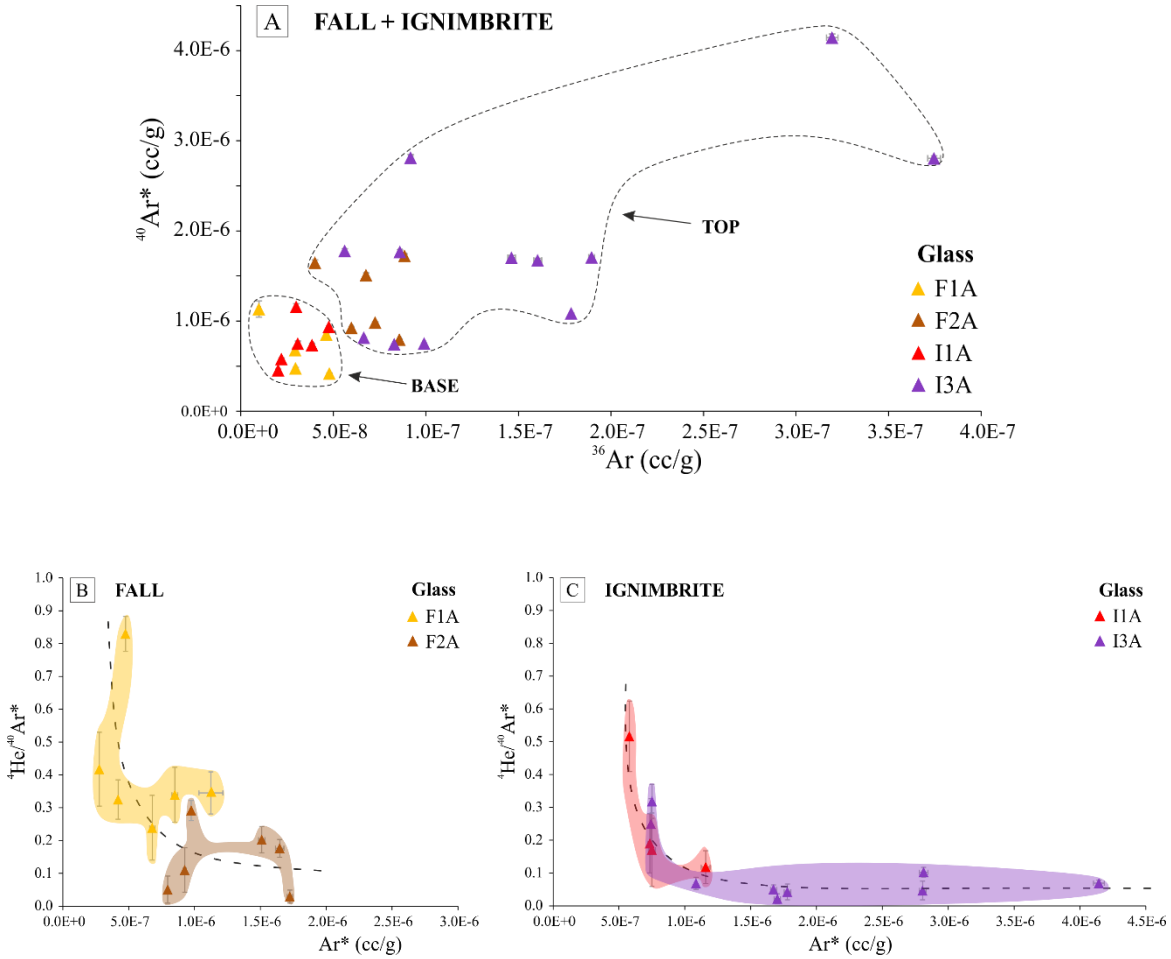

Figure 5.54 Variations in the ^{40}Ar*, ^{36}Ar and ^{4}He/^{40}Ar* in samples with ^{40}Ar/^{36}Ar ratios above the atmospheric value of 298.56 (Lee et al., 2006) even at the 2σ level.

5.6.1.1.3 Factors controlling NG variations

In-keeping with section 4.5.2 of Chapter 4, before starting to discuss the NG data in the context of magmatic degassing it is necessary to carefully evaluate what other external factors could have controlled their abundances in glass particles. The following factors will be carefully scrutinised: presence of micro-crystals, chemical variations and alteration of the glass and sample vesicularity.

Because minerals can retain NG in different concentrations in different structural sites (see section 4.5.2, Chapter 4; Kelley, 2002) their presence in glass particles may alter the abundances of NG measured.

Thin section observations and back-scattered images have shown that glass particles of the same dimension as those used for NG analyses (250 μm) are crystal free with only 2 glass particles (out of 60) having small micro-crystals of biotite. The amount of NG derived from these crystals is likely to be negligible with respect to the total gas trapped in the glass (and bubbles).

The NG contents of the glass particles can vary also in response to changes in the glass composition (see section 4.5.2, Chapter 4) as result of the variability of NG solubility in melt with different concentrations of H_2O and CO_2 (Paonita et al., 2000; Nuccio and Paonita, 2000) and different Si content (e.g. Carroll and Webster, 1994; Carroll and Stolper, 1993; Shibata et al., 1998).

Post-eruptive alteration and hydration of the glass can lead to glass devitrification and/or the formation of secondary minerals (e.g. clays, authigenic feldspars) causing addition, loss and/or redistribution of NG (Fleck et al., 1977; Cerling et al., 1985). In particular, the mobilization of K may result in ^{40}Ar loss impacting on the total amount of Ar measured in samples subject to different degree of alteration (Kaneoka, 1972). However, H_2O and CO_2 were not measured in this study and so it is not possible to identify any influences that they may have had on the solubility of the NG in these samples.

Bulk XRF chemical analyses identify that pumices of suite A have a general homogeneous composition (phonolitic) with only minimal differences (~1%) with respect to their Si and K content (Figure 5.9, Table 5.5). Electron microprobe data of pumice matrices reveal that the glass is trachytic in composition (on a TAS diagram - Le Bas, 1986). According to Woolf et al. (2000), all the glasses classified as trachytic in composition found in the Diego Hernandez Formation (0.37 Ma – 0.17 Ma, nomenclature and ages from Martí et al., 1994) have undergone significant alkali-loss due to post-eruptive hydration. In the specific case of glass particles in this study it is possible to envisage a similar situation. Alteration of the glass is evident looking at the CIA values and

totals derived from the electron microprobe analyses. Alteration indices range from 69 to 71, well above the optimal value for fresh glass (50 according to Nesbit and young, 1982), whilst totals are low and between 90 and 99.5 with mean values of ~ 95.5. The positive correlation between CIA and Si, the negative correlation between CIA and Na, the weak to moderate negative correlation between CIA and K, suggest that alteration and coastal weathering have played a role in modifying the chemical composition of the glasses (Palomar et al., 2017, 2019). Generally speaking CIA, Si and K vary homogeneously within all the four samples (F1A, F2A, I1A and I3A – section 5.4.2). CIA values vary between ~ 60 and 70, SiO_2 variations are of 6 Wt. % in F1A and in F2A and of 5 Wt. % in I1A and I3A and K variations are of between 1.4 Wt. % (F1A) and 2.8 Wt. % (I1A). Based on these data, alteration and weathering have affected all the samples, to the same degree, in modifying their chemistry and possibly promoting the loss of NG from the altered glass structure (Cerling et al., 1985).

However, given the consistency of the trends observed in the NG distribution in glass particles collected in both fall and ignimbritic deposits (Figure 5.50 - 5.53), it is difficult to envisage a process, whereby the NG composition of the glass particles has been determined only by the preferential removal of NG at low temperature, after deposition due to weathering. It seems more likely that the variations in the NG isotopic ratios and abundances are more dependent on the eruptive history of the glass particles rather than solely on post-eruptive alteration processes.

Because NG concentrations in glass particles are mainly influenced by the vesicularity of the glass particles (section 4.5.3 - Chapter 4; e.g. Carroll and Draper, 1994; Sarda and Moreira, 2002), it is important to critically evaluate the variations in the degree of vesicularity of the glass particles. However, in this study it was difficult to directly correlate the NG variations with the degree of vesicularity of individual glass particles, because the vesicularity of pumices is extremely variable during a single eruption, within the same deposit, and even within the same sample (Thomas et al., 1994; Shea et al., 2012). Further, a direct comparison between NG concentrations and vesicularity for each glass particles is not possible because the two types of analyses were done on different samples; specifically, vesicles analyses were conducted on particles prepared as thin sections and thus not suitable for NG analyses. Consequently the role of vesicles in controlling NG variations will be considered as just one of the parameters that could have influenced the degassing behaviour of the samples/their ability to retain NG.

5.6.1.1.4 NG variations in the context of magma degassing

For the Eras eruption limited information are available and so the abundances and the variations of the NG can be interpreted only on the basis of data obtained in this study and theoretical knowledge of NG behaviour in vesiculated glass. The same theoretical principles that were applied to the subaerial basaltic glass particles from Masaya volcano (Chapter 4) are used to investigate the causes of NG variations in phonolitic pumice glass. Although the chemistry of the two are different (basaltic vs. trachytic), the general behaviour of the NG remains the same. For this reason, key concepts already discussed in sections 4.5.3 and 4.5.4 are here introduced and applied but not, again, treated in detail.

From the data it is clear that the mean $^{4}He/^{40}Ar^{*}$ ratio in the fall deposit is controlled by the variation of both ^{4}He and $^{40}Ar^{*}$ while in the ignimbrite it is controlled only by the increase of the $^{40}Ar^{*}$ with the mean ^{4}He content that remains constant (Figure 5.49).

As shown in section 5.6.1.1.1, the glasses at the base of the eruptive sequence have higher $^{4}He/^{40}Ar^{*}$ ratios, lower $^{40}Ar^{*}$ and ^{36}Ar compared to those from the upper portion (Figures 5.50, 5.51 and 5.52). In more detail, the lowermost sections of both the fall and the ignimbrite have higher $^{4}He/^{40}Ar^{*}$ ratios, lower $^{40}Ar^{*}$ and ^{36}Ar than the samples at the top of the two deposits (Figure 5.50, 5.51 and 5.52).

The existence of a group of glass particles with intermediate $^{40}Ar^{*}$ content and variable $^{4}He/^{40}Ar^{*}$ ratios (Population 2, Figure 5.51) may represent glass particles derived from pumices collected between the base and the top of each deposit. This can be plausible considering that the limit between the base and the top of both fall and ignimbrite is quite arbitrary because it was not based specifically on variations in the physical characteristics of the deposits. In this context, the division of glass particles in 3 population with regard to their $^{40}Ar^{*}$ content reflects the stratification of the $^{40}Ar^{*}$ throughout the sequence.

Looking at Figures 5.50 C it is clear that all the glass particles of sample I1A and some of I3A have a NG signature ($^{4}He/^{40}Ar^{*}$ ratio and $^{40}Ar^{*}$) equal to those glass particles from the fall deposit. Considering that the ignimbrite has been deposited by a pyroclastic density current it is possible that glass particles of I1A and I3A, with gas signature similar to F1A and F2A, are from pumices eroded from the lower layer (fall deposit) and incorporated in the ignimbrite. Erosion of the substrate is not unusual for dense pyroclastic flows (e.g. Granadilla Formation, Tenerife - Bryan, 2006; $600\pm14_{2\sigma}$ Ka - Brown et al., 2003). If the glass particles from I1A are considered only derived from re-mixed pumices from the lower fall deposit, the mean $^{4}He/^{40}Ar^{*}$ ratio continuously decreases from the base to the top of the eruptive sequence while the $^{40}Ar^{*}$ (and ^{36}Ar) abundance constantly increases.

Following these considerations possible models are here proposed and discussed with reference to the observations presented earlier in this Chapter.

5.6.1.1.4.1 - Model A) Magma chamber gas signature

Clay et al. (2011) investigated pumice glass particles from the Arico Formation, Tenerife ($668\pm8_{2\sigma}$ Ka - Brown et al., 2003) and found a positive correlation between $^{40}Ar^*$ and ^{36}Ar and suggested a mechanism of air incorporation prior to eruption that acts on all the Ar isotopes not leading to preferential concentration of one of them over another.

If this is also the case for the Eras eruption, the variations in the NG abundances in glass particles from F1A to I3A would reflect primary characteristics of the magma at depth, with the gas signatures inherited from the source region. Such a scenario would require a magma chamber stratified with respect to $^{40}Ar^*$ and ^{36}Ar with the assumption that both isotopes coexist at different levels in different concentrations in the magma chamber. In this case the $^{40}Ar^*$ would be of purely magmatic origin, derived from the assimilation into the magma of old K-rich country rocks enriched in $^{40}Ar^*$ and from hydrothermal fluids, marine and surface water infilling the magma chamber. Similarly, ^{36}Ar would come from country rocks, hydrothermal fluids and marine / meteoric water with an atmospheric Ar composition.

In a simplified model, products emitted during the first stages of the eruption (F1A pumices) would represent the characteristics of the magma residing at more shallow levels. Considering that Ar is preferentially partitioned into bubbles compared to ^{4}He during magma ascent (Carrol and Stolper, 1994) and preferentially lost from the system due to degassing (e.g. passive degassing, open system degassing through the vent), the products originating from magma residing in the upper part of the magma chamber will have high $^{4}He/^{40}Ar^*$ ratios, low $^{40}Ar^*$ and ^{36}Ar and higher ^{4}He (F1A). Products erupted in later stages (F2A, I3A) are those derived from magmas originated at deeper levels and that have experienced less degassing. These will have lower $^{4}He/^{40}Ar^*$ ratios and will be gradually enriched in $^{40}Ar^*$ and ^{36}Ar and relatively depleted in ^{4}He (Figure 5.50 - 5.52).

The high concentrations of $^{40}Ar^*$ and ^{36}Ar in products derived from the deepest portion of the magma chamber (I3A) can be attributed solely to a pure degassing process or related to the intrusion of a more mafic magma enriched in gas into the more evolved phonolitic melt. This phenomena is quite common and well documented in Tenerife (Wolff, 1985) and, in the specific case for the Eras Formation (and other formations e.g. Poris – Brown et al., 1993), it is testified by the co-existence of grey pumices (here investigated for NG - Suite A) and more mafic green and dark-green banded pumices (Suite D) in the ignimbrite.

The high vesicularity (~ 75 Vol %) of glass particles from the ignimbrite could have favoured the retention of high concentration of $^{40}Ar^*$ and ^{36}Ar in the glass even after

eruption. Because sample vesicularity was determined only by inspecting 2D slides prepared as thin sections, an estimation of the effective volume of isolated vesicles that potentially have retained NG after eruption is impossible. For this reason, the relationships between sample vesicularity and amount of NG retained in the glass particles need more dedicated studies and further consideration.

The model here proposed seems to explain the variation of the NG abundances and ratios in glass particles from different levels of the eruptive sequence, although it doesn't take into consideration more complicated models of magma evolution in the magma chamber during eruption (e.g. magma overturn / withdrawal in the magmatic chamber – Wolff, 1985; Blake and Ivey, 1986; Woods and Cowan, 2009) and the fact that pumice glass can degas (e.g. H_20, Cl, S – depending on magma composition and temperature - Hort and Gardner, 2000) and incorporate air after eruption modifying its NG signature (Pinti et al., 1999; Ruzié and Moreira, 2010; Amalberti et al., 2016).

5.6.1.1.4.2 - Model B) Pumice - plume interaction

Several studies have investigated NG elemental and mass fractionation in pumices derived from plinian eruptions (Krummenacher, 1970; Bochsler and Mazor, 1975; Kaneoka, 1980; Pinti et al., 1999; Ruzié and Moreira, 2010) showing significant enrichment in air-derived NG (^{22}Ne, ^{36}Ar) in all the considered pumices and suggesting various and contrasting mechanisms for their incorporation into samples.

Pinti et al. (1999) proposed that diffusion fractionation of atmospheric NG from the air, through a glass shell, happens after pumice quenching (preferential diffusion of air Ne over Ar) while Ruzié and Moreira (2010) have proposed that a kinetic degassing with gas diffusion from the magma into the bubbles, with elemental and isotopic fractionation, occurs before fragmentation. More recently, Amalberti et al. (2016) favoured NG diffusion from air to pumice bubbles, and *vice versa*, and that it may happen during pumice cooling without necessarily implying extreme high temperatures. According to Amalberti et al. (2016), at T = 767 °C, and with the following diffusion coefficients, $D_{Ne} = 5.1 \times 10^{-10}$ cm^2 s^{-1} and $D_{Ar} = 6.2 \times 10^{-11}$ cm^2 s^{-1} at T = 767 °C, Ne diffuses through a 10 μm glass shell in ~ 30 min whilst for Ar it is ~ 4 h. For a bubble wall of 1 μm the rate is even higher with Ne diffusing in ~ 20 s and Ar in ~ 2 min.

Considering an eruption temperature in the range of 850 °C – 750 °C (Thomas et al., 1994), the fact that the pumices are still hot when they move up into the plinian column (Tait et al., 1998) and have a typical rise time of 200 – 300 s (Hort and Gardner, 2000), with previous diffusion rates it is clear that it is possible to add Ar and diffuse ^{4}He (He diffuses even faster than Ar – Amalberti et al., 2016) during pumice cooling when it is still in the plume. $^{40}Ar^*$ would come from degassed magma while ^{36}Ar would be derived mainly from air added during plume rising. Notably, the diffusion coefficients provided by Amalberti et al. (2016) are calculated for a synthetic glass of CMAS composition with SiO_2 of ~ 50 Wt. % and, for this reason, diffusivities for a phonolitic glass (SiO_2 > 60 Wt. % - this study) would be even higher than those obtained in the considered study (> D_{NG} at higher Si content - Carroll, 1991; Roselieb et al., 1992).

Based on these considerations, the hyperbolic trend observed in Figure 5.50 could not represent a pure degassing pattern but could be related to different degrees of $^{40}Ar^*$ (and ^{36}Ar) uptake coupled with elemental diffusion fractionation of ^{4}He and $^{40}Ar^*$. In this case the increase of $^{40}Ar^*$ and ^{36}Ar observed in glass particles in this study would be mainly dependant on the residence time of the pumices within the hot zone of the plume. Here, the NG signature of F1A would be closer to the signature of the magma after fragmentation while the gas composition of F2A and I3A (erupted and deposited in subsequent later

stages of eruption) would reflect a constant addition of $^{40}Ar^*$ and ^{36}Ar and loss of ^{4}He. For this study it is not clear why the mean ^{4}He value decreases in the fall deposit and reaches a constant value in the ignimbrite; this may depend on differences in the ^{4}He diffusion behaviour at different temperatures (Amalberti et al., 2016).

In this discussion it is important to remember that the dimension of the pumices and the position of the glass particle within the pyroclast play an important role on determining the final amount of gas in the sample (and its NG signature). The bigger the size of the pumice the higher the contrast between the rim and the core in term of gas lost due to degassing (Tait et al., 1998; Hort and Gardner, 2000). Small pumices (< 2 cm) and the rims of bigger pumices quench rapidly during their movement in the plume and loses (and possibly uptakes) less gas than the cores of big pumices which remain hotter for longer having more time to degas (Hort and Gardner, 2000). For example, the centre of a pumice with a diameter of 2 cm entering in the atmosphere at T = 850 °C cools to T = 680 °C in 30 - 60 s while the centre of a bigger pumice (> 12 cm in diameter) cools in > 4 x 10^4 s (Hort and Gardner, 2000). The same could be valid for the uptake of NG into the glass particles.

The uptake through diffusion of ^{36}Ar and $^{40}Ar^*$ would be enhanced during the turbulent movement of the pumices in the pyroclastic current, before its deposition, when heated ground water and/or fluids enriched in Ar are admixed to the flow. Possibly, this is another reason why the basal and top portions of the ignimbrite have higher mean ^{36}Ar and $^{40}Ar^*$ abundances compared to the respective parts in the basal fall deposit (Figure 5.52 C).

Since NG diffusion in silicate glass is temperature dependant (Behrens, 2010; Amalberti et al., 2016) it is possible that high temperatures of emplacement of the ignimbrite (unknown for this study but in the range of 200 - 600 °C, Brown and Graham, 2015) and its lower cooling rate compared to a pumice fall (~ 10^{-1} - 10^{-8} °C s^{-1} for an ignimbrite vs. 1 - 10 °C s^{-1} for a pumice of 1 - 5 cm in diameter in a fall deposit – Wallace et al., 2003) could have promoted NG diffusion even after pumice deposition.

Clay et al. (2011) modelled Ar diffusion in 1 mm grains of rhyolitic glass (close to the phonolitic composition of this study) at temperatures of 550 °C and with water contents of between 0.03 Wt. % - 0.85 Wt. %. They found that, over the duration of welding of 1 year and with a cooling rate of 5-20 K/min, there was no appreciable loss of Ar. It may be possible to consider Ar diffusion during ignimbrite emplacement for higher water contents (and thus lower T_g), slower cooling rates and, especially, shorter diffusive lengths in the range of 1-10 μm (typical for pumices - Whitman and Sparks, 1986 - and in the range of those measured in this study).

5.6.1.1.4.3 - Model C)

Because different processes act at different times during glass formation and evolution, sometimes interplaying and superimposing each other, it is possible that a combination of model A and B would work better to explain the NG signatures of glass particles in this study.

The model here suggested considers a chemically stratified magma chamber where a more evolved magma (phonolitic in composition) resides on top of a more primitive / hybrid magma (tephri-phonolitic). This idea is supported by the geochemical models proposed to explain the chemical variability of the volcanic products erupted from the Las Canãdas volcano (Wolff, 1985; Brown et al., 1993; Wolff et al., 2000; Edgar et al., 2002, 2007). In the specific case of the Eras Formation, the appearance of more mafic and banded pumices only in the upper part of the eruptive sequence and their different chemistry compared to the more felsic pumices (see section 5.4.2) are other evidences that support the existence of two chemically different magma reservoirs. I suggest that the increase of the $^{40}Ar^*$ and ^{36}Ar in glass particles from the base to the top of the Eras Formation could reflect primary variations of the volatiles in the magma chamber associated to the different degassing of the magma at various depths (Model A – this study, Clay et al., 2011). Portions of the magma chamber closer to the surface would be more degassed due to the constant release of gas through an open conduit and diffusive degassing while lower portions would preserve a less degassed magma enriched in volatiles coming from a deeper and even more primitive source(basaltic in composition – Wolff, 1985). In this scenario, samples derived from the upper portion of the system (F1A) would be more degassed with low NG abundances and higher $^{4}He/^{40}Ar^*$ ratios compared to samples derived from deeper portions (I3A) that would preserve a less degassed NG signature (high NG abundances, low $^{4}He/^{40}Ar^*$ ratios).

Although primary NG signatures inherited from the magma chamber seems to be preserved in the glass particles, I suggest that the incorporation and diffusion of NG during and after eruption could have concurred in modifying the original gas signature of the pumices (Model B - this study, Pinti et al., 1999; Ruzié and Moreira, 2010; Amalberti et al., 2016). Based on considerations and parameters set out in section 5.6.1.1.4.2, NG fractionation and diffusion in and out from the samples could occur during magma fragmentation in the conduit and during sample cooling when the glass temperature is high enough to allow these phenomena. In particular, I suggest that $^{40}Ar^*$ and ^{36}Ar uptake and diffusion out of ^{4}He from the pumices could happen during sample-plume interaction and during ignimbrite emplacement.

In conclusion, I suggest that the NG signatures of pumice glass of samples from different portions of the Eras Formation reflect the volatile composition and abundance of the magma at depth possibly modified by secondary processes happening during eruption and deposition. In this context, the inverse correlation between $^{40}Ar^*$ and $^{4}He/^{40}Ar^*$ and the increase of $^{40}Ar^*$ and ^{36}Ar throughout the sequence could reflect a combination of the original degassing pattern of the samples coupled with elemental diffusion fractionation of ^{4}He, $^{40}Ar^*$ and $^{36}Ar^*$ syn- and post eruption during sample cooling and deposition.

It is likely that the extent of the uptake and diffusion of NG depend on multiple factors including: the residence time of the pumices within the hot zone of the plume, the initial temperature of the eruption, cooling pattern of samples with different sizes and position of the glass particle in the pumice, temperatures of emplacement of the fall deposit and ignimbrite, bubble wall thickness.

In this context, other processes not considered in this study may need more detailed investigation, dedicated studies and modelling in order to understand their influence on the NG composition of pumice glass particles, these include: magma fragmentation, variation of the temperature and pressure in the eruptive column and within the system during magma up rise.

For all the three models, as already observed for subaerial basaltic glass particles from Masaya volcano (section 4.5.4), different degree of Ar mass fractionation and quenching rate can justify the different $^{40}Ar/^{36}Ar$ ratios and ^{36}Ar abundances in the glasses (Vogel et al., 2006; Morgan et al., 2009; Flude et al., 2018). A single mass fractionation process may be accounted for $^{40}Ar/^{36}Ar$ ratios close to 280 (Krummenacher, 1970; Kaneoka, 1980); lower ratios could be related to a multiple-stage of mass fractionation (Kaneoka, 1980). These may occur prior to magma fragmentation or during pumice cooling through diffusion (see section 4.5.4).

5.6.1.2 Sanidine

5.6.1.2.1 Data variability

From Figure 5.55 it is clear that the majority of the samples display similar ^{4}He (< 7.0E^{-7} cc/g) and ^{36}Ar (< 5.0E^{-9} cc/g) contents. Looking at the data in more detail, it is possible to note that a few crystals from the upper part of the fall deposit (F2A) display higher atmospheric ^{36}Ar with respect to the basal portion (F1A) whilst having similar ^{4}He contents, a feature that is not observed in the ignimbrite deposit. I1A has a ^{4}He content that is much higher than the other samples with values up to 2.61E^{-6} cc/g and not lower than 2.25E^{-8} cc/g.

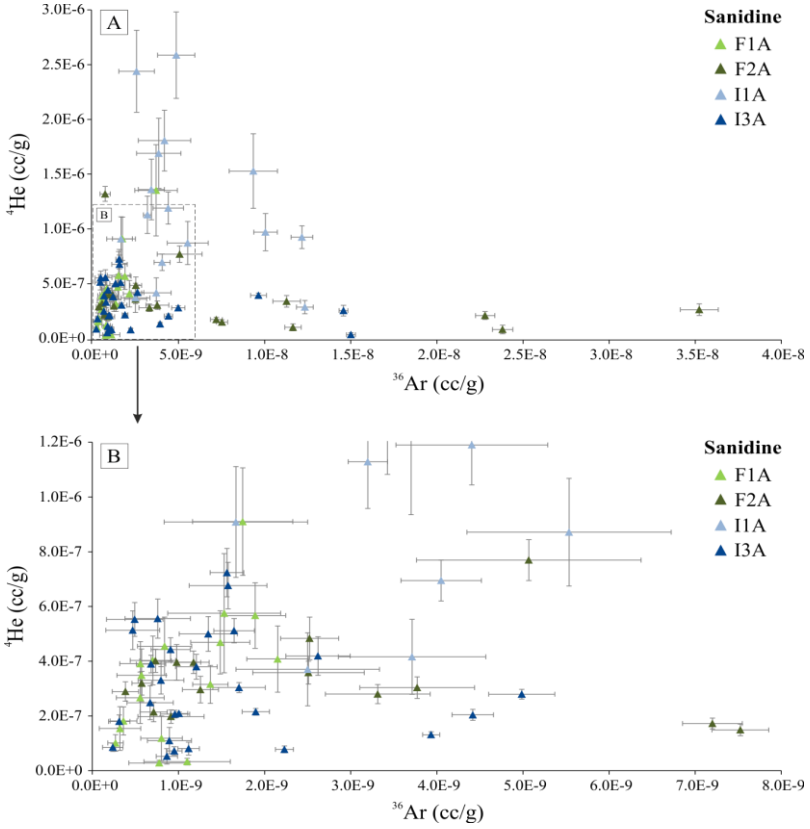

Figure 5.55 A-B Variations in the ^{4}He and ^{36}Ar abundances in in sanidines of samples F1A, F2A, I1A and I3A. Error bars for are at the 1σ level. If not visible they are smaller than the size of the symbol used to display the data. B – Detail of graphs in A highlighting data with ^{36}Ar<5.0E-9 and with ^{4}He<1.3E-6.

When $^{4}He/^{40}Ar^{*}$ ratios are plotted against $^{40}Ar^{*}$ it is possible to distinguish three populations of crystals with distinct NG signatures (Figure 5.56):

- Population 1 has $^{4}He/^{40}Ar^{*}$ ratios > 20 and $^{40}Ar^{*}$ content < $2.0E^{-8}$ cc/g.
- Population 2 has $^{4}He/^{40}Ar^{*}$ < 20 and $^{40}Ar^{*}$ content > $4.0E^{-7}$ Cc/g.
- Population 3 has $^{4}He/^{40}Ar^{*}$ < 2.5 and $^{40}Ar^{*}$ content > $8.0E^{-7}$ Cc/g.

Sanidines collected in the fall deposit show a uniform composition while samples derived from the ignimbrite (I1A, I3A) display a more complex distribution (Figure 5.56 A). F1A and F2A have only crystals that belong to Population 2; I1A has the highest spread in the data with sanidines belonging to Population 1, 2 and 3; I3A shows crystals with NG signatures of Populations 1 and 2.

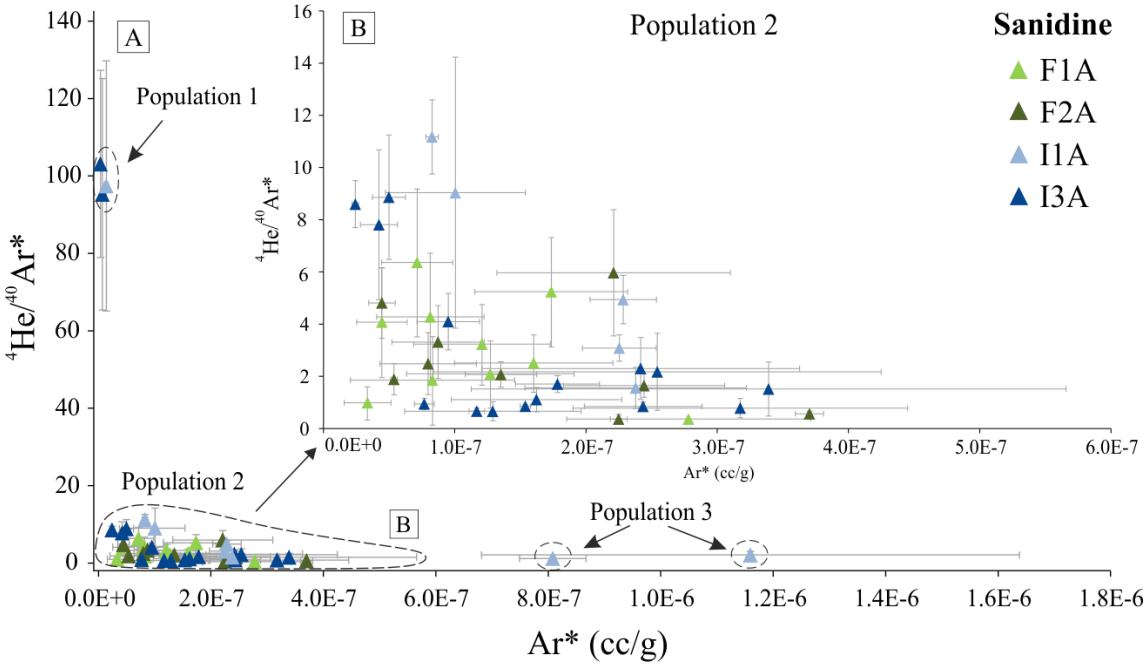

Figure 5.56 A - Variations in the $^{4}He/^{40}Ar^{*}$ ratios with respect to $^{40}Ar^{*}$ in sanidines of samples F1A, F2A, I1A and I3A. Populations 1, 2 and 3 indicate particles having similar NG composition (see text for explanations). B - Inset highlighting the variations of the NG in Population 2. Error bars are at the 1σ level. If not visible they are smaller than the size of the symbol used to display the data.

Despite the apparent homogeneity of Population 2 with respect to $^{4}He/^{40}Ar^{*}$ ratios and $^{40}Ar^{*}$ content, in Figure 5.56 B it is noted that the sanidines of F1A and F2A are more homogeneous whereas in I1A and I3A they are more dispersed. Some of the crystals derived from the ignimbrite (I1A, I3A) have higher $^{4}He/^{40}Ar^{*}$ ratios (> 7.8) with respect to those collected in the fall (≤ 6.4).

Individual crystals display various $^{40}Ar/^{36}Ar$ ratios and ^{36}Ar contents (Figure 5.57). At the 2σ level F1A, I1A and I3A have sub-atmospheric, atmospheric and supra-atmospheric $^{40}Ar/^{36}Ar$ ratios whilst F2A has only crystals with atmospheric $^{40}Ar/^{36}Ar$ ratios. In Figure 5.55, ^{36}Ar contents are very variable in samples F2A, less so in samples I1A and I3A and the least variable in F1A.

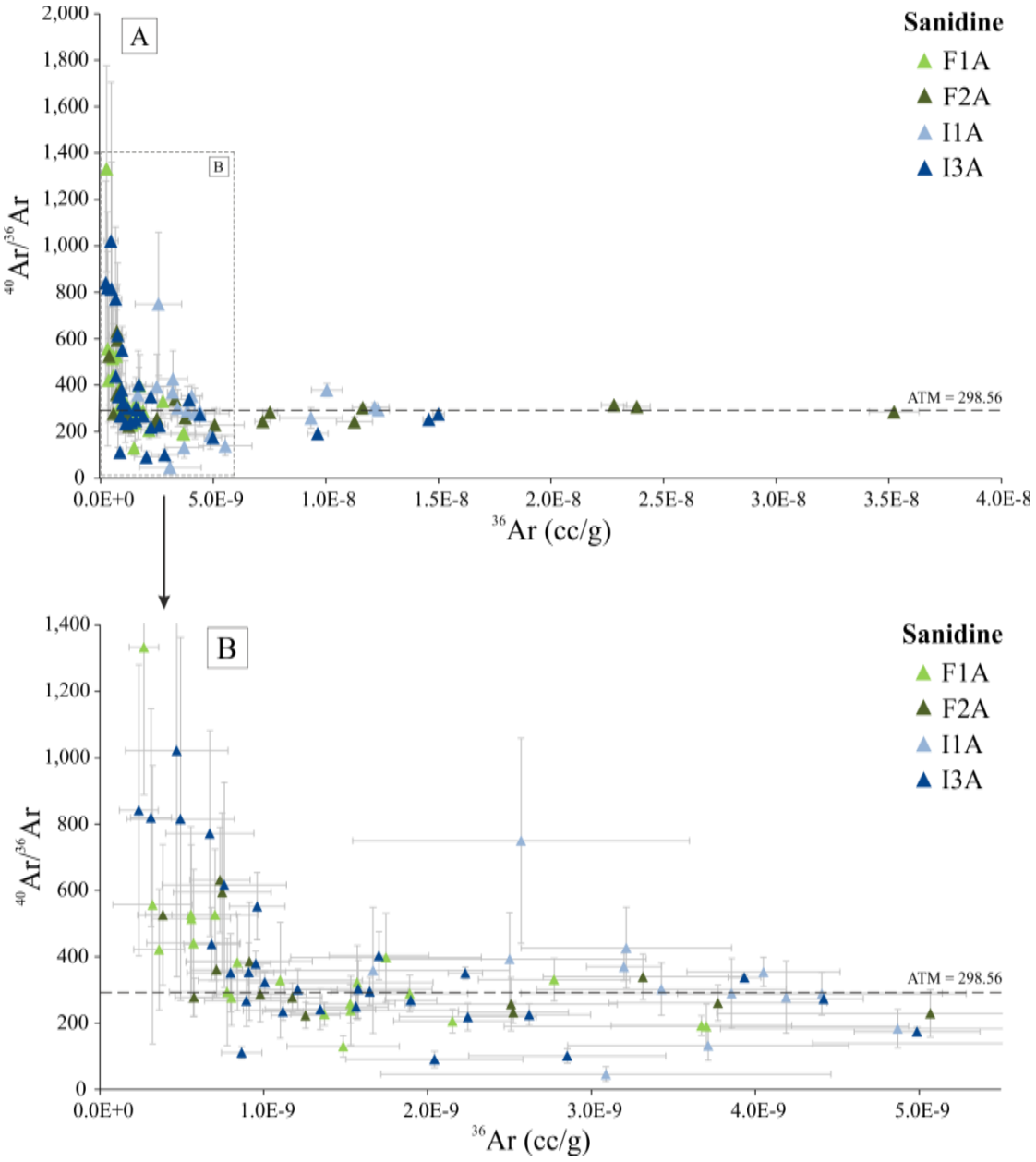

Figure 5.57 Variations in the $^{40}Ar/^{36}Ar$ ratios with respect to ^{36}Ar in sanidines of samples F1A, F2A, I1A and I3A. It is evident that the particles display sub-atmospheric, atmospheric and supra-atmospheric $^{40}Ar/^{36}Ar$ ratios. Error bars are at the 1σ level. ATM is the $^{40}Ar/^{36}Ar$ ratio of the atmosphere and it is equal to 298.56 (Lee et al., 2006).

5.6.1.2.2 Data reliability

The ^{36}Ar measured in the sanidines has, for the majority of the crystals, high 1σ analytical uncertainties (> 40% of the absolute value) and absolute values close to the blank or to the to the minimum detection limit of the mass spectrometer (0.00001 V) (Table A5-4). This is problematic for determining whether the variations in the ^{36}Ar are real or due to a poor measurement. Under these circumstances the $^{40}Ar^*$ and $^{4}He/^{40}Ar^*$ variations observed in the sanidines are not considered to be completely reliable and caution should be applied when considering the information that the sanidines impart relating to magma degassing. This is especially true when the data are discussed including their analytical uncertainties that are derived also by propagating the elevated uncertainties associated to ^{36}Ar measurements.

5.6.1.2.3 NG variations in the context of magma degassing

If the data discussed in paragraph 5.6.1.2.1 are considered as representative of the actual variations of the NG in sanidine crystals the following considerations could be made:

- Crystals from pumices collected at the base and at the top of the fall deposit (F1A, F2A) have homogenous $^{40}Ar^*$ abundances and $^{4}He/^{40}Ar^*$.suggesting that they crystalized under the same magmatic conditions and have experienced the same degassing history.

- The ignimbrite is composed by pumices with a mixed population of crystals with different NG compositions and $^{4}He/^{40}Ar^*$ ratios.

The majority of the sanidines have NG signatures similar to those crystals in pumices collected in the fall deposit (Population 2 in Figure 5.56) indicating a common origin and degassing history. Other crystals have an isotopic signature completely different compared to those of Population 2 and are likely to be xenocrysts (Population 1 and 3 in Figure 5.56). The presence of xenocrysts has been extensively documented in the geological record of Tenerife and in particular in those Formations outcropping along the Banda del Sur area (Edgar et al., 2007).

From thin section analyses slightly altered sanidines with corroded rims were observed in sample I1A. EMPA data highlights that this sample has alkali feldspars with two different chemical compositions (Or_{37}-Or_{51} sanidines, Or_{33}-Or_{35} anorthoclase). It could be possible that crystals with high $^{40}Ar^*$ and ^{4}He and various $^{4}He/^{40}Ar^*$ ratios may have

been derived from small blebs of the less vesiculated dark glass (Suite C, D like) existing in minor amount in some of the grey pumices (Suite A – e.g. I1A).

Crystals with high $^{40}Ar^*$ and low $^{4}He/^{40}Ar^*$ ratios could have been formed from a magma more enriched in $^{40}Ar^*$ (and ^{4}He) while sanidines with low $^{40}Ar^*$ and high $^{4}He/^{40}Ar^*$ may have been recycled within the magma chamber experiencing multiple degassing episodes prior to eruption.

Finally, because the analyses were performed on samples of 250 μm prepared from bigger crystals, it is possible that high $^{40}Ar^*$ abundances may have been derived from portions of the sanidines with undetected micro fluid/melt inclusions hosting higher amounts of $^{40}Ar^*$ (Kelley, 2002).

- The presence of crystals with sub-atmospheric, atmospheric and supra-atmospheric $^{40}Ar/^{36}Ar$ ratios (even at the 2σ level), that are very variable within samples, indicates that the sanidines have not uniformly incorporated ^{36}Ar. F1A crystals have the lowest ^{36}Ar concentration.

In particular non-atmospheric $^{40}Ar/^{36}Ar$ ratios indicate that some crystals are not fully equilibrated with air and/or fully degassed. Supra-atmospheric $^{40}Ar/^{36}Ar$ ratios indicate the presence of $^{40}Ar_E$ hosted in crystal lattice and defects, in fluid and melt inclusions (Esser et al., 1997; Kelley, 2002) or derived from small portions of glass adhering to the sample surface (Clay et al., 2011). The sub-atmospheric $^{40}Ar/^{36}Ar$ ratios detected for some sanidines may be related to a kinetic isotopic mass fractionation during crystallization at depth (Dalrymple, 1969; Matsumoto and Kobayashi, 1995; Ozawa et al., 2006) or simply because the crystals have been formed in areas of the magma chamber with less ^{36}Ar.

The most likely source of ^{36}Ar is water (Hanyu and Kaneoka, 1997; Kaneoka, 1994) either meteoric, marine or hydrothermal although it is not possible to completely exclude that atmospheric Ar has been added during sample preparation through micro-cracks (Ballentine and Barfod, 2000) or may derive from remnant of gas adsorbed on the sample surface. This last point could be probable only because samples for NG analysis were not subjected to a heat lamp, used to expedite the removal of adsorbed Ar from the surfaces of samples/sample chamber.

5.6.2 Ar/Ar ages

5.6.2.1 Haüyne

Haüyne failed to yield geological meaningful ages when both single grain and step heating experiments were performed. All the ages from both experiments (Table 5.23) are higher than the maximum age of the subaerial activity in Tenerife (~ 12 Ma – Old basaltic series, Fuster et al., 1968). Anomalous old ages, extremely high $^{40}Ar/^{36}Ar$ ratios and the particular staircase shape of the age spectra suggest that large amounts of excess ^{40}Ar ($^{40}Ar_E$) have been incorporated within the crystals prior to eruption. Moreover, the continuous and almost exponential increase of the apparent ages from low to high temperature steps (Figure 5.29, Table 5.16) imply a non-homogeneous distribution of the $^{40}Ar_E$ with concentrations increasing from the rim to the core of the Haüynes.

Anomalous old apparent ages and $^{40}Ar_E$ in haüyne have previously documented in studies of similar mineral recovered from the Eifel volcanic Field, Germany (Fuhrmann and Lippolt, 1985; Lippolt et al., 1990). Chemical and petrographic studies performed on haüynes (>250 μm) separated from phonolitic pumices from Tenerife have revealed that these minerals contain thousands of micro melt and fluid inclusions distributed in concentric layers (Cooper et al., 2015). External rims of the mineral are almost inclusion free while the inner portion is characterised by a zone extremely rich in inclusions (Cooper et al., 2015). These observations suggest that the source of $^{40}Ar_E$ is the melt and fluid inclusions that have trapped, during their formation, anomalous high amount of Ar (Kelley, 2002).

Table 5.23 Ages and $^{40}Ar/^{36}Ar$ ratios for Hauyne from I3D.

Step	Age (Ma)	±1σ (Ma)	$^{40}Ar/^{36}Ar$	±1σ
Single grain total fusion				
G4	28.60	1.06	2641.32	723.49
G12	43.99	2.10	1563.18	227.63
G3	56.41	2.20	1766.70	192.29
G1	67.02	5.30	1260.02	182.31
G10	78.89	3.48	2860.82	629.98
G2	109.84	7.39	2943.28	1296.11
G11	115.84	5.12	4798.95	1784.43
Step-heating				
Age spectra	N.A	N.A	N.A	N.A
Isochron	-155	130	3635	1100

5.6.2.2 Glass

5.6.2.2.1 Single fusion

Only pumice glass from F1A yielded sensible positive ages while analyses on single grain or multigrain from I3A failed to provide an age (Table 5.24). Positive ages were obtained from glasses with absolute $^{40}Ar/^{36}Ar$ ratios higher than the atmospheric value of 298.56 (Lee et al., 2006) whereas negative ages, (only from I3A), are correlated to those glasses with absolute $^{40}Ar/^{36}Ar$ ratios lower than the atmosphere (Table 5.25). This is easily explained considering that the $^{40}Ar^*$, used to calculate an Ar/Ar age (see Appendix A1.1), is calculated as follow $^{40}Ar_M^* = [(^{40}Ar/^{36}Ar)_M\text{-}298.56]X^{36}Ar_M$. If the measured $^{40}Ar/^{36}Ar$ ratio is lower than 298.56 the final $^{40}Ar^*$ will be negative impeding calculation an age from the sample.

The fact that positive ages were obtained only from the base of the eruptive sequence (F1A) and negative ages only from the upper part of the ignimbrite (I3A) could be an artefact due to the small amount of analyses done on these samples. In fact, the range of the Ar ratios and isotopes in these experiments don't cover the more realistic variability observed when NG analyses were performed on unirradiated glasses (see section 5.5.1).

Considering only positive ages from F1A the extremely high errors obtained from this sample (1σ are higher than the absolute age) can be attributed to the insufficient amount of ^{39}Ar released during the analyses. The inverse isochron age ($0.34\pm0.06_{(2\sigma)}$ Ma), calculated combining the results of the three experiments from F1A glasses, is more precise but can't be considered reliable due to its meaningless statistics (MSWD = 0) and because all the data are plotted really close to the Y-intercept failing to represent a real mixing line between the radiogenic component and the atmospheric component. For this reason the age must be discarded from further consideration and cannot be used to constraint the time of eruption of the Eras Formation.

Table 5.24 Ar/Ar ages for Single grain total fusion of pumice glass.

Grain	Age (Ma)	±1σ (Ma)	$^{40}Ar/^{36}Ar$	±1σ
F1A				
G1	0.80	4.11	304	56
G2-3	0.54	0.71	301	7
G5-10	0.43	0.44	303	10
Isochron	0.34	0.03	299	14
Weighted mean	0.46	0.37	N.A	N.A
I3A				
G1-6	-5.14	1.41	291	4
G7	-3.22	2.16	294	6
G8	-0.61	3.75	297	19
G9	-2.74	2.75	294	10
G10	-0.89	2.85	298	5

5.6.2.2.2 Step-heating

As seen in section 5.6.2, when step-heated, pumice glasses failed to yield plateau ages. This is related to the presence, in the middle of the experiments, of steps with absolute $^{40}Ar/^{36}Ar$ ratios lower than the atmospheric. As already discussed, this causes an incorrect determination of the $^{40}Ar^*$ making impossible to determine an age for the considered steps.

The samples have $^{37}Ar/^{39}Ar$ ratios in agreement with the Ca/K ratios calculated from electron microprobe data (range 0.04 - 0.22). The $^{38}Ar/^{39}Ar$ ratios are more variable and tend to increase in the last few steps of the analyses (see section 5.6.1.3.1) with values (up to 0.16) that are higher than those observed from chemical analyses (range 0.04 – 0.08). Because high $^{38}Ar/^{39}Ar$ ratios were mostly detected in high temperature steps (F1A, F2A, I1A) it is plausible to hypothesize the existence of two reservoirs hosted in different retentive sites. Low $^{38}Ar/^{39}Ar$ ratios more similar to EMPA data may derive from the glass while high $^{38}Ar/^{39}Ar$ ratios my come from a Cl component hosted in the bubbles.

Amongst the others, I3A shows steps with two clearly distinct $^{37}Ar/^{39}Ar$ and $^{38}Ar/^{39}Ar$ ratios (Figure 5.38). These could be ascribed to significant variations in the Ca, Cl and K content of the glass as demonstrated by the results of microprobe analyses (see section 5.4.3.1) or due to the fact that the two non-isochemical reservoirs are not well mixed like in the other samples. I3A is also the only sample for which some steps measured, values of ^{40}Ar close to the saturation point of the mass spectrometer (14V). This is well in agreement with the high concentrations of atmospheric Ar detected during NG analyses performed on unirradiated glasses (see section 5.5.1.2).

Aside from F1A, all the other samples yielded inverse isochron ages that are concordant at 2σ level and that have $^{40}Ar/^{36}Ar$ ratios of atmospheric value. In these inverse isochrons the majority of the steps are plotted on top of each other's (e.g. I1A, Figure 5.36) really close to the Y-intercept failing to represent a real 2 component mixing line. Moreover, because pumice glass has high surface-area-to-volume ratios it could be particularly subject to Ar recoil (^{37}Ar and ^{39}Ar) that could lead to erroneous young ages ($^{37}Ar_{Ca}$ recoil) or old ages ($^{39}Ar_K$ recoil) (McDougall and Harrison, 1999; Jourdan et al., 2007).

For these reasons, although the ages are precise (0.07 Ma > 2σ < 0.02 Ma), with Y-intercepts at atmospheric values and with fairly good statistics (MSWD range 1.6 – 0.57) their use in determining the eruption age of the Eras formation must be carefully and critically considered.

From field observations, stratigraphically, the age of the Eras Formation should be between $0.735\pm0.01_{(2\sigma)}$ Ma (Helecho Formation - Dávila-Harris, 2009) and $0.668\pm0.008_{(2\sigma)}$ Ma (Arico Formation - Brown et al., 2003). In this context, all the Ar/Ar ages obtained from pumice glasses (Table 5.25) in this study are considerably younger than they should be, even at 2σ confidence level, and must not be considered representative of the true eruption age of the samples. This discrepancy between expected ages and ages recovered from the glasses can be related to K-loss (and thus ^{40}Ar loss) due to alteration and possibly hydration of the glass (see discussion on weathering effects on Ar isotopes in section 5.6.1.1.3).

Table 5.25 Plateau and isochron ages for pumice glass with relative $^{40}Ar/^{36}Ar$ isochron intercepts and MSWD values and weighted mean age.

Sample	Plateau age ±2σ (Ma)	Isochron age ±2σ (Ma)	MSWD	$^{40}Ar/^{36}Ar$	weighted mean age ±2σ (Ma)
F1A	N.A	N.A.	N.A	N.A	
F2A	N.A	0.34±0.007	1.6	298±7	0.295±0.018 MSWD = 1.08 p. = 0.34
I1A	N.A	0.31±0.06	1.17	298±6	
I3A	N.A	0.29±0.02	0.6	299±11	

5.6.2.3 Sanidine

5.6.2.3.1 Single fusion

When single grain total fusion analyses were performed on sanidines highly variable and imprecise Ar/Ar ages were obtained (Table 5.26). This can be attributed to the small amount of ^{39}Ar measured by the mass spectrometer during the analyses that, in turn, is related to the young age of the samples and to the specific small grain size (250 μm) used for the experiments. In a similar way, the small amount of ^{36}Ar measured within the samples can be accountable for the extremely variable and imprecise determination of the $^{40}Ar/^{36}Ar$ ratios of the crystals.

More precise ages (0.72±0.14 Ma, 0.75±0.22 Ma) with more constrained $^{40}Ar/^{36}Ar$ ratios were obtained when multiple grains of sample I3A were melted together (Table 5.26). In this case, the $^{40}Ar/^{36}Ar$ ratios are slightly higher than the atmospheric value of 298.56 (Lee et al., 2006) when considered at the 2σ level. Because the amount of ^{36}Ar released during the analyses is really close to the background level of the mass spectrometer it is difficult to assess if the non-atmospheric $^{40}Ar/^{36}Ar$ ratios are really representative of the presence of $^{40}Ar_E$ in the crystals or are due only to an imprecise determination of the ^{36}Ar isotope. In this context, it is well to remember that small amount of $^{40}Ar_E$ from micro fluid inclusions or from possible xenocrysts could significantly modify the $^{40}Ar/^{36}Ar$ ratios when only a few grains, with minimal amount or ^{36}Ar, are analysed.

The weighted mean age ($0.74\pm0.24_{(2\sigma)}$ Ma) and the isochron age ($0.80\pm1.5_{(2\sigma)}$ Ma) obtained combining the single ages of I3A are not sufficiently precise to be used to frame the Eras Formation into the more general stratigraphical context of the Banda del sur.

Table 5.26 Ar/Ar ages and $^{40}Ar/^{36}Ar$ ratios for single grain total fusion analysis from sanidine crystals

Grain	Age (Ma)	±1σ (Ma)	$^{40}Ar/^{36}Ar$	±1σ
F1A				
G1	0.62	0.50	675	688
G2	0.27	0.29	468	280
G3	0.48	0.35	471	200
G4	0.64	1.07	899	3057
G5	0.33	0.45	431	258
G6	0.07	1.37	323	512
G7	0.72	1.42	450	459
I3A				
G1	0.26	1.81	327	216
G2	0.97	0.58	810	825
G3+4+5	0.75	0.22	330	10
G6+7+8+9+10	0.72	0.14	372	18

5.6.2.3.2 Step-heating

When step-heating results from sanidines are considered it is observed that all the age-spectra have pretty flat plateaus with some low temperature steps rejected from the age calculation. Rejected steps of F2A and I3A have extremely high analytical uncertainties that can be related to the small amount of ^{39}Ar released during the first stages of the analyses. Rejected steps of F1A, with negative or lower apparent ages with respect to the plateau, are associated to the analyses of alteration products probably not completely removed during sample preparation or to a possible ^{40}Ar-loss caused by the alteration of small areas of the sample surface. Rejected steps of I1A with higher apparent ages with respect to the plateau could reflect the presence of $^{40}Ar_E$ released from micro fluid inclusions (not detectable by microscopic observations) (McDougall and Harrison, 1999) or from minor portions of glass attached to the sample surface (Clay et al., 2011).

The plateau ages of F2A ($0.688\pm0.021_{(2\sigma)}$ Ma), I1A ($0.696\pm0.030_{(2\sigma)}$ Ma) and I3A (0.704 ± 0.035 $Ma_{2\sigma}$) are within error each other. F1A has a completely different age (0.74 ± 0.24 $Ma_{2\sigma}$) that is older than those obtained from the other samples. The age errors (2σ) display a clear correlation with the amount of ^{39}Ar released during the analysis. 2σ errors of 0.024 Ma and 0.021 Ma were obtained for F1A and F2A that have released a total ^{39}Ar of 1.96 V and 1.95 V, respectively. 2σ uncertainty of 0.030 Ma and 0.035 Ma are from I1A and I3A, respectively, that have released a total ^{39}Ar of 0.91 V and 0.93 V.

The inverse isochrons ages of F2A ($0.711\pm0.041_{(2\sigma)}$ Ma), I1A ($0.70\pm0.31_{(2\sigma)}$ Ma) and I3A ($0.724\pm0.042_{(2\sigma)}$ Ma) are within error at the 2σ confidence level and concordant with the plateaus ages. The inverse isochron age of F1A ($0.795\pm0.028_{(2\sigma)}$ Ma) is completely different from those obtained from the other samples and non-concordant with the plateau age at the 2σ confidence level.

F2A and I1A display atmospheric $^{40}Ar/^{36}Ar$ ratios (272 ± 37, 318 ± 74) at 2σ level, I3A has a slightly lower value of $289\pm8.4_{2\sigma}$ while F1A has a $^{40}Ar/^{36}Ar$-intercept ($258\pm9_{2\sigma}$) well below the atmospheric value of 298.56. The 2σ errors of the $^{40}Ar/^{36}Ar$ ratios are of between 8.4 and 74. Lower errors are correlated with those samples (F1A, I3A) where the data are well dispersed along the 2-point mixing line that links the atmospheric component (Y-intercept, $^{36}Ar/^{40}Ar$) to the radiogenic component (X-intercept, $^{39}Ar/^{40}Ar$). Larger errors in the $^{40}Ar/^{36}Ar$ ratios of single steps could be related to the extremely low amount of ^{36}Ar released during each stage of the experiments, for some steps the ^{36}Ar is indistinguishable from the background level of the mass spectrometer.

The variations in the absolute $^{40}Ar/^{36}Ar$ ratios, the scatter of the data along the isochrons and the small differences between the plateaus ages and inverse isochrons ages

can be explained by different factors including: heterogeneous distribution of ^{40}Ar within the crystals; possible presence of alteration products (sericite), fluid inclusion and xenocrysts (these last only applicable to I1A and I3A) hosting different amount of Ar isotopes not perfectly atmospheric in composition; ^{40}Ar loss caused by crystal alteration (Sherlock and Arnaud, 1999; Kelley, 2002; Verati and Jourdan, 2014).

Disturbances of the Ar system seem more severe in F1A for which neither a valid plateau age nor an inverse isochron age were obtained. For the other samples (F2A, I1A, I3A) these disturbances seem not to have caused problems in the age determination. This is demonstrated by the concordance between the plateau and isochron ages.

Due to its better statistics (MSWD closer to 1 and higher probability of fit) and higher precision the plateau age of I1A is preferred, tentatively, over the isochron age to represent the eruption age of the sample (Table 5.27). The reliability of the plateau age is guaranteed only because the sample displays an atmospheric $^{40}Ar/^{36}Ar$ ratio within 2σ uncertainty. For F2A and I3A the isochron ages, due to their slightly better statistics, were preferred, tentatively, over the plateau ages to represent the eruption age of the samples (Table 5.27).

The weighted mean age of $0.707\pm0.021_{(2\sigma)}$ Ma (Figure 5.58) calculated from these preferred ages (in bold in Table 5.27) is consistent with the stratigraphy and with ages provided for the upper and lower Formations even at 2σ analytical uncertainty (Figure 5.59). For these reasons, the age of $0.707\pm0.021_{(2\sigma)}$ Ma should be considered representative of the actual eruption age of the Eras Formation.

Table 5.27 Plateau and isochron ages for sanidine crystals with relative $^{39}Ar^*$ comprised within plateau, $^{40}Ar/^{36}Ar$ isochron intercepts and MSWD values and weighted mean age^{+}.

Sample	Plateau age ±2σ (Ma)	MSWD	$^{39}Ar^*$ (%)	Isochron age ±2σ (Ma)	MSWD	$^{40}Ar/^{36}Ar$	weighted mean age^{+} ±2σ (Ma)
F1A	0.740±0.240	0.47	78.3	0.795±0.028	1.3	258±9	**0.707±0.021** MSWD = 0.61 Prob. = 0.54
F2A	0.688±0.021	1.8	93.3	**0.711±0.042**	1.5	272±37	
I1A	**0.696±0.030**	1.9	59.4	0.700±0.130	4.2	318±74	
I3A	0.704±0.035	1.12	86.5	**0.724±0.042**	1.0	289±8	

Note: In bold preferred ages for the considered samples. $^{+}$ The weighted mean is based on preferred ages in bold.

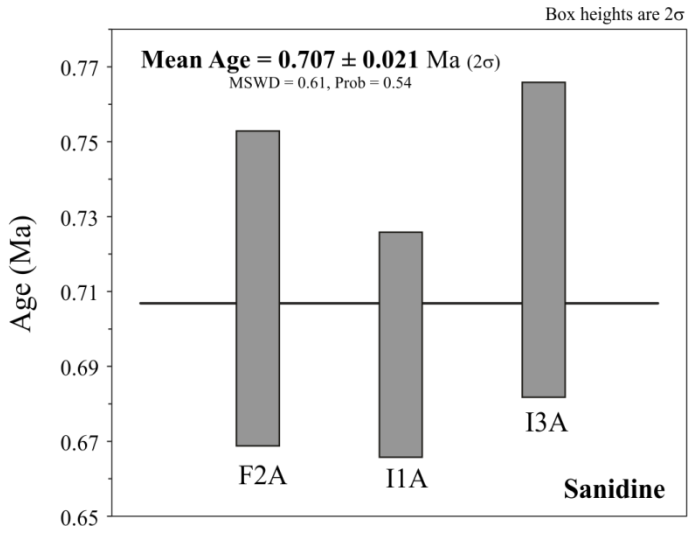

Figure 5.58 Weighted mean age from sanidine preferred ages of samples F2A, I1A and I3A.

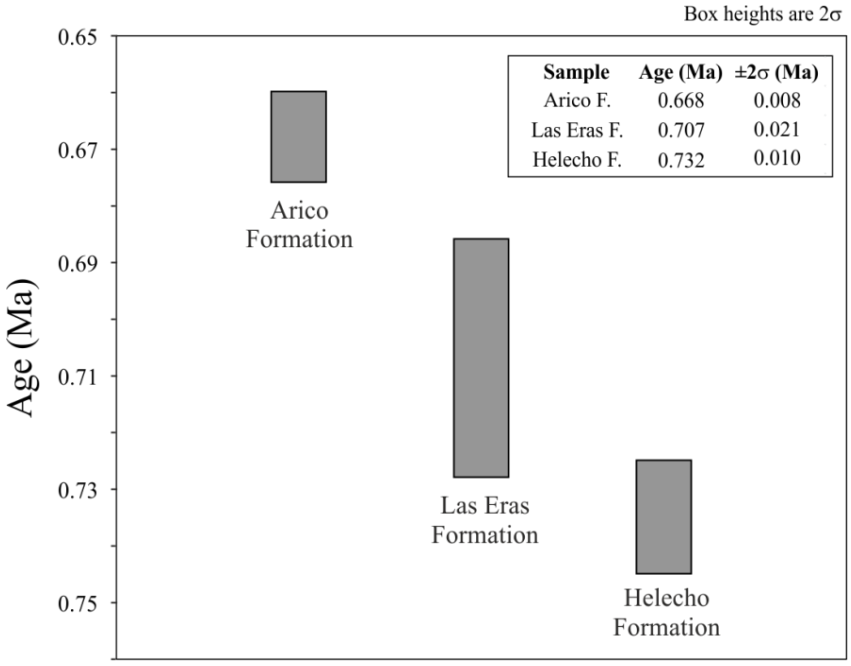

Figure 5.59 Stratigraphic relationships between ages of the Eras Formation (this study) and ages of the Helecho Formation (Dávila-Harris, 2009) and Arico Formation (Brown et al., 2003). All the ages are quoted at the 2σ level.

5.6.3 Ar/Ar ages and relationships with Ar degassing

- Due the high analytical uncertainties of the ^{36}Ar (propagated though to calculate the $^{40}Ar^{*}$) it is difficult to determine if any link exists between degassing histories and Ar ages for the sanidines. Based on the available data no specific relationships were found.
- The sanidines have preserved $^{40}Ar_E$ only to a lesser extent (when the data are considered at 2σ level) and that seem to have not caused problems for the age determination. The presence of a mixture of primary erupted crystals and xenocrysts with extremely high $^{40}Ar_E$ content seems the cause of the poorly constrained age of I1A.
- Sanidines ages are independent from the vesicularity of the samples
- Sanidines and glass particles from the base of the fall deposit (F1A) didn't yield meaningful ages. Crystals and glass particles in this section of the sequence have the lowest ^{36}Ar content.
- Aside from F1A, all the other glass particles yielded comparable young ages despite they show different degassing NG signatures.
- The glass particles in the upper part of the ignimbrite are more enriched in ^{36}Ar and $^{40}Ar^{*}$ compared to those at the base of the eruptive sequence. The high concentration of Ar in this section poses some technical problems during Ar/Ar step-heating experiments. In fact, the release of large amount of atmospheric ^{40}Ar have saturated the detector challenging the correct interpretation of the results of the analyses.
- In glass particles the atmospheric Ar increases throughout the sequence. The large amount of atmospheric Ar in glass particles could represent a serious problem when young samples are used for Ar/Ar dating. The low radiogenic content and the elevated atmospheric Ar produce inverse isochrons that don't really represents a 2-component mixing line generating not completely reliable inverse isochron ages.
- Concentrations of the volatiles in the magma, degassing and gas uptake during pumice cooling and physical characteristics of the samples have a first order control on the amount of NG retained in the glass particles during eruptive events. However, in order to get reliable Ar/Ar ages from pumice glass other processes like syn-eruptive Ar mass fractionation and Ar diffusion during degassing as well as post-depositional weathering and alteration must be better investigated and not underestimated.

It is well to remember that these points are not conclusive and must be treated with care especially because step-heating experiments were not repeated on multiple samples.

5.6.4 The Eras eruption

The Eras Formation records a compositionally zoned multi-component plinian eruption at ~ 700 Ka. The Eras eruption started with the deposition of a plinian fall deposit where grey pumices represent the only juvenile material. These have a homogeneous phonolitic composition with low Ba and high Zr and Nb that suggests that only the more superficial evolved reservoir was tapped during the first phases of the eruption (Wolff et al, 2000). More mafic dark-green and banded pumices with high Ba and low Zr and Nb were erupted during subsequent stages and occur only in the ignimbrite together with grey pumices. According to previous studies (e.g. Wolff et al., 2000; Brown et al., 1993) mafic and banded pumices testify mixing and mingling processes occurred, respectively prior and during the eruption, between a phonolitic magma and a less evolved magma (basaltic to tephritic - Wolff, 1985; Wolff et al., 2000). The higher abundance of mafic pumices in the upper portion of the ignimbrite suggests higher degrees of mixing and mingling during later stages of eruption. Following field and chemical evidences provided in this study it seems plausible that the Eras eruption has been triggered by the intrusion of a mafic magma into a more felsic reservoir. This is concordant with what has been proposed by previous studies for other eruptions of the Banda del Sur Group where felsic, mafic and banded pumices have been found coexisting in ignimbritic deposits (e.g. Wolff et al., 2000; Edgar et al., 2007).

Considering the NG geochemistry of the grey pumices, the increase of the ^{36}Ar and $^{40}Ar^*$ and the decrease of the $^{4}He/^{40}Ar^*$ ratios in glass particles from the base to the top of the eruptive sequence suggests the existence of a highly degassed melt that reside at the top of the magma chamber that progressively become more enriched in gas with depth. Magma degassing at shallow level could have been favoured by the continuous release of gases prior eruption through an open vent or through fault structures. The higher gas abundance in the lower portion of the magma chamber can be attributed to lower degrees of degassing and / or due to the existence of a more mafic gas-rich magma that constantly release gas to the upper phonolitic reservoir. Here, it is well to remember that the variation of the NG abundances in the glass could have also be dependant to fractionation, uptake and diffusion of NG during magma fragmentation, eruption and pumice deposition.

These processes have not influenced the NG composition of the alkali feldspars that seems to have crystalized under the same magmatic and degassing conditions in the magma chamber. The few crystals that display variably NG content and isotopic ratios are likely to be xenocrysts derived from wall rocks or formed at different magmatic conditions.

5.7 Conclusion

For the first time this study has investigated in detail the Eras Formation, one of the minor and least explored pyroclastic sequences of the quaternary volcanism of Tenerife. Here, I focused on understanding the relationships between chemistry, degassing history and Ar/Ar ages of young (< 1 Ma) alkali feldspars and glass recovered from the more felsic juvenile pumices collected in different portions of the eruption.

The Eras Formation ($0.707\pm0.021_{(2\sigma)}$ Ma – weighted mean age from 3 step-heating analyses on sanidines) is the result of a chemically zoned pumice-rich plinian eruption. Different types of pumices were recognised in the basal fall deposit and in the upper ignimbrite. Phonolitic grey, dark-green and dark-green banded pumices show major and trace element variations. The general mineral assemblage is almost the same for all the types of pumices with more mafic banded samples having higher crystal abundances, mafic minerals and feldspathoids compared to grey pumices. These were observed in both fall deposits (pumice fall and ignimbrite) while dark green and dark-green banded samples were found only in the upper ignimbrite.

Grey pumices have a homogeneous population of alkali feldspars (Na-sanidine) with anorthoclase crystals founded only in samples collected at the base of the ignimbrite. This section of the sequence has also 2 populations of crystals with different NG signatures. Feldspars with particularly high $^{40}Ar^*$ or high $^{4}He/^{40}Ar^*$ ratios, interpreted as xenocrysts, were found together with a crystals with more homogeneous NG signature. This last group of sanidines was found in all sections of both fall deposit and ignimbrite.

No relevant information about the degassing history of the sanidine after their eruption were obtained from NG analyses. This observation must be considered with precaution due to the large analytical uncertainties associated to the measurement of the ^{36}Ar, and in turn, to the calculation of the $^{40}Ar^*$ and $^{4}He/^{40}Ar^*$ ratios. Alkali feldspars seem to have recorded the conditions of the magma at depth without being influenced, to a large extent, by syn- and post-eruptive degassing (also during deposition) and by weathering processes happening in the period of time (~700 Ka) elapsed between their deposition and the analyses. This is a great advantage of using sanidines over glass when Ar/Ar ages must be obtained from young samples. However, the presence of the xenocrysts (in ignimbrite deposits), the extremely low ^{36}Ar content (especially at the base of the eruptive sequence) and / or the presence of $^{40}Ar_E$ may preclude an accurate and precise age determination. Kinetic mass fractionation before eruption may be an important process in determining the final amount of ^{36}Ar in the sample with possible strong effects (sub-atmospheric $^{40}Ar/^{36}Ar$ ratio – F1A) on the calculation of the Y-intercept of the inverse isochrons.

Conversely, the glass particles seem more susceptible to syn-eruptive processes such as gas diffusion during pumice cooling and are more affected by post-eruptive meteoric alteration and weathering. Weathering due to the exposure of the pumices to the marine coastal environment seems to have seriously compromised the capacity of the glass to yield reliable ages. All the obtained ages, in fact, are too young (~ 0.3 Ma) and not concordant with Ar/Ar ages provided for upper and lower Formations in previous studies (Brown et al., 1993; Dávila-Harris, 2009. This discordance is attributed to K-loss (and thus ^{40}Ar loss) caused by severe glass alteration (high CIA, low glass totals).

No relationships were found between the positions of the pumices within the eruptive sequence and Ar/Ar ages recovered from pumice glass particles. However, the low amount of ^{36}Ar and the large spread in the ^{40}Ar/^{36}Ar ratios seem to have precluded the possibility to get Ar/Ar ages from glasses at the base of the fall deposit (similarly for the sanidines).

Two models were proposed in order to explain the NG signature of glass particles recovered from different portions of the Formation. These models assume that all the glass particles recovered from the base of the ignimbrite belong to pumices eroded from the lower fall deposit and re-mixed in the ignimbrite. Some of the glass particles in the upper part of the ignimbrite could have as well the same origin. In this context the ^{4}He decrease throughout the sequence while the ^{40}Ar* and ^{36}Ar increase with the result of decreasing the ^{4}He/^{40}Ar* ratios. In the first model the higher ^{4}He/^{40}Ar* ratios in glass particles from the base of the fall indicate great degrees of degassing in the upper portion of the magma reservoir with ^{40}Ar* and ^{36}Ar increasing in the deepest level as result of a minor degassing and / or due to the input of gases from the injection of an hotter gas-rich magma into the upper phonolitic reservoir. In the second model the NG composition of the glass particles is related to the uptake through diffusion of ^{40}Ar* and ^{36}Ar and degassing of ^{4}He during pumice cooling and possibly, during emplacement of the pyroclastic flow. The increase of the two Ar isotopes here considered would be mainly dependant on the residence time of the pumices within the plume; pumices deposited later have uptake higher amount of ^{40}Ar* and ^{36}Ar, and thus will have lower ^{4}He/^{40}Ar* ratios.

Cooling rate of the sample, sample size, position of the glass particle within the sample, bubble walls thickness and bubble connectivity are other factors that may have controlled the diffusion process and the NG abundance in glass particles. A combination of processes listed in the two models seems plausible.

Elemental and mass kinetic elemental and mass fractionation have produced variable ^{4}He/^{40}Ar* ratios and the large spread in the ^{40}Ar/^{36}Ar ratios observed especially at the base of both fall deposit and ignimbrite. The fact that many glasses have sub-atmospheric ^{40}Ar/^{36}Ar ratios have precluded the use of the age spectra during the interpretation of the results of step-heating Ar/Ar analyses.

5.8 Final remarks

With the available data it is not possible to completely discriminate the processes that have influenced the NG composition in pumice glasses recovered from different portions of two completely different pyroclastic deposits and their relationships with Ar/Ar ages and the ability of pumice glass to retain $^{40}Ar_E$. Only with more detailed studies and inputs from other disciplines can the validity of the proposed models be better constrained, tested and verified. For these reasons, I suggest further investigations and a more integrative approach that include:

- Detailed field studies on the real complexity of the Eras Formation.
- Investigations on the abundances of the major volatiles (H_2O, CO_2) within the glass and bubbles (H_2O, CO_2) through Nano-SIMS analyses.
- Better sample characterization in term of effective vesicularity, bubble connectivity, vesicularity variation and distribution throughout the eruptive sequence. Moreover, I see extremely interesting to understand the distribution of mineral phases within the samples in order to determine if and how these have contributed to the total NG gas budget of the glass during pumice cooling. On this regard I propose the application of CT-scan analyses prior NG investigations.
- Quantitative modelling is needed in order to better constrain the residence time of particles in the eruption column and their cooling rate and the influence of these parameters on NG diffusion and fractionation during pumice cooling in the plume and in relation to different emplacement mechanisms and conditions.
- Influence of the lateral variability of the deposit on NG abundances and isotopic ratios.
- More systematic NG and Ar/Ar analyses with multiple types of experiments (single grain fusion and step-heating) on different types of pumices with different chemistry, physical characteristics, from different portions of the deposits and that have undergone to different degree of weathering.

Only after having better constrained these parameters and processes it would be possible to better comprehend how to use pumice glasses for obtaining Ar/Ar ages from young samples.

Chapter 6:
Synthesis

6.1 Introduction

This chapter provides a synthesis of the data discussed in Chapter 3, 4, 5 according to the aims and goals of the thesis set out in Chapter 1. Specific findings of each of the three projects, models for NG degassing during eruption and new Ar/Ar ages are presented and discussed and summarised in Chapter 7.

6.2 Factors controlling NG in volcanic glass

In this study I have investigated which factors influence the NG (^{4}He, ^{22}Ne, ^{36}Ar, ^{40}Ar) abundances and isotopic ratios in subaerial volcanic glass. This was achieved by using different types of glass of different ages, with different chemistry and vesicle content, derived from different deposits, erupted by various explosive activities and with different degrees of weathering (Table 6.1).

Factors controlling NG in volcanic glass can be divided into: primary factors that are related to pre- and syn-eruptive conditions of the magma, and, secondary factors that are linked to post-eruptive processes. These factors act at different times during glass formation and evolution, sometimes interplaying and superimposing each other, and so it is not always possible to definitely discriminate which factors are at work.

Table 6.1 Characteristics of the volcanic glass investigated in this study.

Sample	Composition	SiO_2	Age	Vesicularity	Deposit	Type of eruption	CIA
		Wt. %	Ma	Vol. %			
Glass shard	Rhyolite	$> 70^{+}$	12 - 10.7	0*	Fluvial, Lacustrine	Plinian	$57 - 60^{+}$
Pele's hairs and tears	Basalt	$\sim 51^{++}$	0	0 - 47	loose material	Strombolian	50^{++}
Pumice glass	Phonolite	$\sim 59^{++}$	~ 0.7	67 - 80	pumice fall, ignimbrite	Plinian	$59 - 71^{++}$

$^{+}$Data from XRF bulk analyses
$^{++}$ Data from EMPA
*visually estimated with binocular microscope

6.2.1 Primary factors

Gas variations in the magma chamber

The main factor that controls the abundance of NG in volcanic glass is related to a general change in the gas composition in the magma chamber. This can be related to a degassing event or, in the case of Pele' hairs and tears in this study, can be due to the upward migration of gas-rich magma that increases the amount of NG in the upper magma chamber, in the surface reservoir and, thus, in the final volcanic products.

Chemistry of the magma

A second factor influencing the amount of NG in volcanic glass is the chemistry of the magma. As discussed in previous chapters, NG are more soluble in silica rich magmas due to higher degree of polymerization of the melt and the higher number of vacant sites available for their incorporations (e.g. Carrol and Stolper, 1993).

In this study phonolitic glass (pumice) has higher NG (^{4}He, ^{36}Ar, $^{40}Ar^{*}$) abundance than basaltic glass (Pele's hairs and tears) and this difference is in agreement with solubility controlled NG incorporation in melts. Here, it is necessary to remember that the pumice glass has undergone intense weathering and alteration losing a part of their original NG content. It is likely that even higher NG abundances in pumice glass were trapped within the samples at the time of eruption prior to loss during weathering.

Within the magma chamber itself, the magma also played an important role in modifying the solubility of NG in melt and, in turn, the ability of the glass to incorporate NG. These phenomena were not investigated in this study but were documented in the Eras Formation (Tenerife) where banded pumices were identified. More work would be needed to understand how magma mixing and mingling, prior to eruption, could impact on the final NG signature of the glass.

Glass vesicularity and NG fractionation

Considering the fact that NG segregates into vesicles during magma evolution (Carrol and Stolper, 1994), vesicularity represents an important parameter that controls NG abundances in the glass. Bubbles can form at depth during magma rising, at more surface conditions during fragmentation, and, during second exolution of volatiles after eruption.

Glass shards from the CRBG are "virtually" vesicle free (at the scale of the analyses – 63 μm), based on Ar/Ar dating analyses have atmospheric $^{40}Ar/^{36}Ar$ ratios (at the 2σ

confidence level) and are apparently free from excess ^{40}Ar. On the other hand, pumice glass and Pele's hairs and tears display different vesicularities, variable NG abundances and ratios and have an Ar trapped component that is not always in equilibrium with the atmosphere ($^{40}Ar/^{36}Ar$ < and > than 298.56 - Lee et al., 2006).

These results seem to suggest that at higher degree of fragmentation (ash glass shards) the glass has lost the majority of the NG (e.g. $^{40}Ar^*$) and has an Ar composition more in equilibrium with the atmosphere. Pumice glass, Pele's hairs and tears have undergone minor degrees of fragmentation, and incomplete degassing, and preserve magmatic and atmospheric NG in isolate bubbles.

Accounting for the model proposed for NG trapped in Pele's hairs and tears (section 4.5.3), the variations of the NG abundances in vesiculated glasses can be ascribed to variable degrees of vesiculation of the melt, followed by solubility controlled NG fractionation, between melt and bubbles. In this scenario, the NG signature of a glass particle is determined by the coexistence of vesicles with different NG budgets.

Cooling time, rate and dimension of the glass particles

The rate at which the glass cool from T_e to T_g and finally to T_{amb} is mainly dependent on the residence time of the sample in the eruptive column and the size of the particle. These two factors can influence the final NG composition of the glass and its ability to retain and lose NG, or, exchange with air.

NG abundances vary independently of the shape of the glass particles (e.g. Pele's hairs and tears) while are directly dependant on the size of the sample (e.g. Pumice size). In this study Pele's hairs and tears of uniform size (1- 2 cm), presumably erupted and deposited a few seconds after their extrusion, have experienced really fast quenching (based on the model of Porritt et al., 2012) and have preserved most likely their original NG composition. Conversely, pumice glasses (250 μm) were extracted from larger samples (1 – 10 cm) that have spent, more likely, several minutes (up to 5 min. – Hort and Gardner, 2000) in the plume experiencing longer cooling time and higher degassing (the bigger the sample the longer the time that the core will cool to T_{amb} – Hort and Gardner, 2000). In this context, it is suggested that the time spent in the plume by a sample above T_g must not be underestimated especially when considering syn-eruptive NG diffusion in the glass. It is also important to consider the diffusion length (bubble wall thickness) and the position of the glass particle within the sample, when the results of NG analyses are interpreted, and when the glass is to be considered for Ar/Ar dating (more degassed samples have retained less excess $^{40}Ar_E$ and are more suitable for dating purposes).

6.2.1 Secondary factors

Emplacement mechanism

In this study, no definitive conclusions were determined about the relationship between NG variations, emplacement mechanisms and type of pyroclastic deposit (fall vs. ignimbrite). It is suggested that depositional mechanisms have only a minor impact on NG abundances and isotopic ratios but further work is needed.

Alteration

The alteration of the glass is related to its metastable nature at surface condition and the ease with which it hydrates. Alteration creates devitrification structures that favour degradation of glass to clay minerals and/or the crystallization of secondary minerals (e.g. zeolites). These processes can lead to NG loss and/or NG redistribution.

The process of alteration varies in the context of where the glass is erupted. In samples deposited close to the vent (e.g. Pele's hairs and tears) the glass can alter and become hydrated really quickly (in hours) if exposed to plume acidic gases. In glasses deposited in distal locations as plinian fall and ignimbrite (pumice glass), multiple factors contribute to the modification of NG concentrations in the glass. Hot fluids (hydrothermal/meteoric) circulating in the deposit or derived from pumice cooling may redistribute or introduce significant amount of NG (e.g. ^{36}Ar and $^{40}Ar^{*}$) in the glass, or, promote NG loss (especially He) from its structure; glass exposure to the marine environment (Tenerife pumice glass) accelerates devetrification and hydration favouring NG loss. Hydration may also occur in fluvial and lacustrine environments where ashy glass shards are deposited, or transported, and redeposited after eruption (CRBG glass shards).

In this study alteration was extensively investigated using an appropriate alteration index (CIA – Nesbit and young., 1982) and by comparing the chemistry of samples erupted at different times but exposed to the same weathering conditions. Glass particles collected within 24 h of eruption are pristine and unaltered (Pele's hairs and tears, CIA ~ 50) while much older (~ 0.7 Ma) vesiculated glass has undergone intense weathering and alteration (pumice matrix, CIA ~ 64). There was no particular correlation observed between glass alteration and sample vesicularity when pumices with vesicle contents of between 67 % vol. and 80 % vol. were investigated.

Different degrees of alteration may complicate the interpretation of NG abundances impacting on the production of degassing models (section 6.4) and on the ability of the glass to yield stratigraphically consistent Ar/Ar ages (section 6.3).

In this context, it is suggested that the alteration and hydration of the glass must be always evaluated, taken into consideration and discussed when volcanic glass and NG are used in tandem for unravelling volcanic processes and ages of eruptions. The use of fresh and pristine glass is always preferred over altered phases in order to get more reliable Ar/Ar ages and information on processes governing NG degassing. This is not always possible for old pumices (Eras Formation) but can be attempted for much younger or extremely recent glass when modelling the degassing behaviour of a particular volcanic system using NG (Masaya degassing).

6.3 Atmospheric contamination

Multiple mechanisms have been proposed in to explain the existence of air derived NG (e.g. ^{36}Ar, ^{22}Ne) in volcanic glass (see section 4.5.4).

In this study, it is suggested that in fast quenched subaerial glasses (glass shards, Pele's hairs and tears) the air component is more likely inherited only from the magma chamber while in glass that has experienced more complex degassing and slower cooling rates (big pumices) the air contamination may derive also from the interaction of the glass with hot gases in the plume during cooling. In this case, air NG (e.g. ^{36}Ar, ^{22}Ne) can be uptaken through diffusion during sample movement inside the eruptive column, with total abundances depending on the time spent in the column, and, on the bubble wall thickness (diffusion length). Air derived NG (^{36}Ar, ^{22}Ne) observed in all glasses and inherited from the magma can be derived from wall rock and crater floor materials being assimilated into the melt, from meteoric water and other hot fluids with an air component (hydrothermal, subduction related fluids, marine water) circulating in the reservoir or infilling the magma chamber.

Regarding the Ar system, it is plausible that multiple processes have acted to produce the spread in the $^{40}Ar/^{36}Ar$ ratios and ^{36}Ar abundances observed in different glasses. The different Ar signatures can be ascribed to the inhomogeneous distribution and incorporation of ^{36}Ar within the samples and within the magmatic system, or, to kinetic mass fractionation of the Ar isotopes during magma vesiculation and degassing. These may occur prior to magma fragmentation or during sample cooling through diffusion (e.g. pumice glass). If quenching happens very rapidly after eruption (Pele's hairs and tears, small pumices or rims of big pumices) the degassing and fractionation of ^{40}Ar and ^{36}Ar ceases, and the equilibration of the glass with the atmosphere is impeded, producing non-atmospheric $^{40}Ar/^{36}Ar$ ratios. In this study, it is suggested that different bubbles may have

trapped, during their nucleation and rise, different amount of Ar isotopes (^{40}Ar, ^{36}Ar) in different proportions. It is hypothesized that glass particles that contain a majority of bubbles with an excess of ^{40}Ar* would have a final ^{40}Ar/^{36}Ar ratio higher than 298.56 (atmospheric value - Lee et al., 2006) while particles that contain a majority of bubbles with an excess of ^{36}Ar would have sub-atmospheric ^{40}Ar/^{36}Ar ratios. Atmospheric ratios that are 'normal' and within error of 298.56 may be associated with non-vesicular glass (e.g. glass shards, Pele's tears with no bubbles).

The possibility that there are interferences at mass 36 during NG analyses must be always taken into consideration when air derived Ar is used as a proxy of atmospheric contamination and to calculate the actual amount of ^{40}Ar* trapped in the glass.

Finally, for unirradiated samples it is possible that adsorbed atmospheric Ar has contributed to the total Ar budget measured in the glass because such samples are left to outgas naturally within the vacuum system rather that accelerated degassing of adsorbed gases by infra-red heat-lamp like for samples purely for Ar/Ar dating and not for multi-NG analysis.

6.4 Excess ^{40}Ar ($^{40}Ar_E$)

$^{40}Ar_E$ is the portion of ^{40}Ar that is neither radiogenic nor atmospheric and incorporated into the sample during its formation (McDougall and Harrison, 1999) or from grain boundary fluids during cooling (e.g. Sherlock et al., 1999). For the glass in this study $^{40}Ar_E$ can be derived from:

- Old country rocks (volcanic, plutonic, sedimentary) with high concentration of ^{40}Ar* assimilated into the magma chamber before eruption. Here, any extraneous potassic minerals that are added to the magma chamber will contribute ^{40}Ar that diffused out of the extraneous mineral. This is more of a concern for magmas erupting through K-rich basement rocks rather than through lower-K basaltic rocks.

- Hot fluids circulating in the magmatic system (hydrothermal, subduction related fluids). Here, fluids can 'scavenge' ^{40}Ar diffused out of K-rich minerals in the basement or chamber walls and contribute to the magma.

- Meteoric water (marine, fluvial, ground base water, ice). These can be rich in dissolved atmospheric argon and so could contribute to add ^{40}Ar and also ^{36}Ar to the glass if the magma, after its extrusion, interacts with water from one or more of the mentioned reservoirs.

- Gases enriched in ^{40}Ar incorporated into the glass during cooling. This process may occur in the plume if the glass remain above Tg. In this case the ^{40}Ar diffuses from the plume into the bubbles becoming $^{40}Ar_E$. This process is enhanced in small samples that have thin bubble walls and that stay in the plume for several seconds (e.g. pumices).

- Vapour-phase alteration products. These are secondary minerals derive from post-depositional crystallization of volatiles exsolving from the pyroclasts. These can be enriched in both ^{40}Ar and ^{36}Ar and would contribute to the total Ar budget of the glass if not completely removed from its surface.

6.5 Implication for Ar/Ar dating

Virtually vesicle free glass shards yielded flat age spectra and inverse isochrons with atmospheric $^{40}Ar/^{36}Ar$ ratios (at the 2σ confidence level). The ages returned from both age spectra and the isochron are accurate, precise, comparable at the 2σ level and concordant with the stratigraphy. The glass shards seem not to have suffered ^{40}Ar loss and seem to be free from $^{40}Ar_E$. For these data the majority of the samples have inverse isochrons with data clumping close to the $^{39}Ar/^{40}Ar$ intercept. This is due to the low ^{36}Ar content and the small variation in the ^{39}Ar released for each step of the analysis.

More complicated and unreliable Ar/Ar ages were obtained from vesiculated pumice glass particles. In this case it was impossible to produce any reliable or meaningful age spectra (and relative plateaus ages) due to the presence of steps with negative ages (those having $^{40}Ar/^{36}Ar < 298.56$) in the middle of the experiments. Aside from one sample, pumice glass yielded inverse isochron ages that are concordant at 2σ level and that have $^{40}Ar/^{36}Ar$ ratios of atmospheric value. The ages are much younger (~ 0.3 Ma) than those obtained from the co-existing alkali feldspars (~ 0.7 Ma, stratigraphically consistent age). This discrepancy was attributed to K-loss (and ^{40}Ar loss) due to alteration and possibly hydration of the glass. Pumice glass particles yielded inverse isochrons with the majority of the steps bunched close to the $^{36}Ar/^{40}Ar$ intercept. This indicates that the majority of the Ar is of atmospheric-derived origin with only a minor component is radiogenic.

While the difference in the amount of radiogenic Ar (and thus ^{39}Ar) is only due to the age difference of the samples (~ 12 Ma vs. ~ 0.7 Ma), the difference in the amount of ^{36}Ar trapped in glass shards and pumice glass could be related to the different vesicularity of the samples. The glass shards are "virtually" vesicle free and have quenched really rapidly after eruption while pumice glass particles have higher degree of vesicularity and have

undergone a more complex degassing history. In this scenario it is likely that glass shards have reached atmospheric equilibrium during cooling; pumice glass have a greater chance of preserving from the magma chamber a trapped ^{36}Ar component in the bubbles and have likely incorporated atmospheric Ar though diffusion during cooling. These considerations support the idea that fragmentation, vesicularity and quenching rate have a key role in controlling the amount of trapped Ar (and $^{40}Ar_E$) in volcanic glass.

The non-perfect equilibration of the glass with the atmosphere (sub-atmospheric $^{40}Ar/^{36}Ar$) and the extremely low ^{36}Ar abundances (glass at the base of the pumice fall deposit, glass shards) can be seriously problematic when volcanic glasses are used to extract Ar/Ar ages. Supra-atmospheric ratios can be associated to the presence of $^{40}Ar_E$ in the glass leading to determine erroneous old ages; sub-atmospheric $^{40}Ar/^{36}Ar$ ratios related to an apparent excess of ^{36}Ar can lead to young apparent ages due to an over-correction of the atmospheric ^{40}Ar; extremely low ^{36}Ar abundances can be difficult to measure with sufficient precision during analyses leading to an erroneous under-correction of the atmospheric ^{40}Ar, to erroneous calculation of the $^{40}Ar^*/^{39}Ar$ obtaining old apparent ages.

Glass alteration and hydration are secondary processes that can modify the original abundance of Ar isotopes leading to K-loss (and thus Ar loss) impacting on the Ar/Ar ages (e.g. pumices from the Eras Formation).

^{39}Ar and ^{37}Ar recoil were not investigated in this study but must be seriously considered as a source of errors for the age determination.

In conclusion, before to consider completely reliable Ar/Ar ages obtained from any type of glass, Ar-recoil and Ar loss due to glass alteration and hydration must be always considered and evaluated, respectively, in vacuum-encapsulating the samples in silica vials prior to irradiation and performing EMPA and Nano-SIMS analyses. Moreover, Ar/Ar ages from glass particles must, where possible, always be corroborated with Ar/Ar ages from co-existing k-rich minerals. This comparison will help to assess for the good quality of the ages recovered from the glass.

Following the results of this study, at the moment, alkali feldspars remain the best option to date young pyroclastic deposits. However, Ar kinetic mass fractionation before eruption, the presence of the xenocrysts (in ignimbrite deposits, in basalts), the extremely low ^{36}Ar content of some crystals, and/or the presence of $^{40}Ar_E$, may preclude a correct and precise age determination even when alkali feldspars are dated. But, in particular circumstances (e.g. dating low-K basalt, dating volcanic distal deposit without alkali feldspars), the use of glass shards it is promising in order to obtain precise and accurate Ar/Ar ages for certain types of volcanic deposits (e.g. tuffs).

6.6 NG degassing models

NG trapped in Pele's hairs and tears were used to model the behaviour of a persistent active volcano, Masaya, between 2015 and 2016. In this study, it is proposed that the variation in the NG abundances and isotopic ratios observed in the glass particles are the expression of the upward migration of a gas-rich magma from depth occurred in 2015 that has enriched the upper magmatic reservoir in NG leading to the eruption of more gas rich samples in 2016.

NG trapped in pumice glass were used to model the evolution of a plinian eruption in Tenerife at ~ 0.7 Ma. Two models were proposed: the first attributes the increase of the $^{40}Ar^*$ and ^{36}Ar and the decrease of ^{4}He in pumice glass to a sort of stratification of the magma chamber with respect to NG; the second implies that different amounts of Ar* and ^{36}Ar are incorporated through diffusion in the glass during pumice cooling with elemental diffusion fractionation of ^{4}He and $^{40}Ar^*$, and ^{4}He preferentially lost during the first phases of the eruption. In the second model the amount of NG uptake from the plume and/or lost from the glass is dependent on the residence time of the glass within the hot zone of the plume.

It is likely that what is described in the two models occurred at different stages of glass evolution with diffusion mass fractionation during glass-plume interaction acting only to slightly modify the original NG abundances and ratios inherited from the magma reservoir.

From these considerations it is clear that NG trapped in subaerial erupted glass can be used to study past and present volcanic processes and to monitor long term degassing events (Pele's hairs and tears – Masaya volcano – 1 year of activity) or shorter degassing episodes (pumice glass – Eras plinian eruption, Tenerife – hours/days/weeks of eruption). In order to do that it is important to select specific types of glasses that have retained sufficient NG to be used to trace degassing processes. It is suggested that the more appropriate glasses for this scope are those that have preserved magmatic NG in isolated bubbles. Here again, it is important to stress that the quality of the glass must not be underestimated and investigations on its alteration and hydration state must be undertaken in order to asses for the pristine nature of the sample and the reliability of the information get from NG data.

Chapter 7

Conclusion

In this chapter the key discoveries of this study are summarised as they appear in corresponding chapters. At the end of the chapter are proposed future lines of research in order to continue to investigate those factors controlling NG in volcanic glass, the relationships between Ar degassing, the Ar/Ar system and Ar/Ar ages in volcanic glass.

7.1 Chapter 3 - Ar/Ar dating of silicic volcanic glass interbedding the upper Columbia River Basalt Group (Washington, USA).

- Five new Ar/Ar ages (12.00±0.24 Ma, 11.37±0.15 Ma, 10.67±0.21 Ma, 10.70±0.18 Ma, 10.77±0.18 Ma) were obtained from glass shards derived from silicic tuffs interlayering basaltic lavas of the upper part of the CRBG.
- The ages are accurate, precise, with $^{40}Ar/^{36}Ar$ of atmospheric value at the 2σ confidence level, are consistent with the stratigraphy and in good agreement with those provided for the upper and lower lavas from previous studies.
- When multiple sample aliquots were analysed consistent and reproducible ages were obtained demonstrating that the method used to prepare and analyse the glass is robust.
- From the age spectra and the inverse isochrons the glass shards seem not to have suffered any ^{40}Ar loss and ^{39}Ar recoil and are free from $^{40}Ar_E$.
- The new ages were used to better constrain the timing of the emplacement of the Elephant Mountain Basalt and Pomona Basalt, to critically assess previous Ar/Ar ages from lavas overlain and underlain the ash beds, and, to correlate the interbeds with three major eruptions (CPT V, XI, XIII) of the Bruneau-Jarbidge eruptive centre in the CSRP.
- The use of glass shards in Ar/Ar geochronology is promising for producing reliable and precise indirect Ar/Ar ages for: lava emplacement in volcanic environments for which there are silicic ash-bearing interbeds; distal volcanic deposits where other K-bearing materials are not available; for ash beds overlaying and/or underlying human artefacts helping to understand the relationships between hominoids migrations and civilization with volcanic eruptions.

7.2 Chapter 4 - Noble gases in Pele's hairs and tears: a new tool to track the behaviour of persistent degassing volcano tested using the Masaya volcano (Nicaragua)

- Pele's hairs and tears from Masaya volcano are basaltic in composition, are pristine and the majority of them (99%) are crystal free - only isolated microcrystals of plagioclase and clinopyroxene were observed. The mineral assemblage and the chemistry of the samples have remained the same since the last collection done by Moune et al., (2007).
- Pele's hairs and tears have retained magmatic NG (^{4}He, ^{22}Ne, ^{36}Ar, $^{40}Ar^{*}$) after eruption in a complex mixture of bubbles (vesicularity 0 % to 47 %) of different dimensions (area <0.001 mm^2 up to 45 mm^2) and shapes (round and elongated).
- The NG abundance (^{4}He, ^{22}Ne, ^{36}Ar, $^{40}Ar^{*}$) and isotopic ratios ($^{4}He/^{40}Ar^{*}$, $^{40}Ar/^{36}Ar$) are independent from the shape of the particles while they are function of sample vesicularity and controlled by pre-eruptive solubility and diffusion fractionation of the gas between melt and bubbles.
- The majority of the particles have atmospheric $^{40}Ar/^{36}Ar$ = 298.56 (Lee et al., 2006) with only a few of them displaying higher/lower values. Non-atmospheric $^{40}Ar/^{36}Ar$ ratios were attributed to different degrees of air contamination before eruption, Ar isotopes kinetic fractionation and incomplete Ar degassing.
- The proposed model for the behaviour of the Masaya volcano between 2015 and 2016 attributes the variation in the NG abundances and isotopic ratios to the upward migration of a gas-rich magma from depth occurred in 2015. This is in agreement with previous studies for the same period of time based on long term (2014-2017) data from ground based monitoring system and remote sensing data (Aiuppa et al., 2018).
- It is proposed a wider application of Pele's hairs and tears to continue to monitor the Masaya volcano and extending also their use to other persistent active systems.
- Coupling measurements of NG (He, Ne, Ar isotopes) and major volatiles (H_2O, CO_2, Cl, F) trapped in Pele's hairs and tears with other monitoring techniques (ground based gas sensors, remote sensing) would contribute to better characterise the source of the magma, the chemistry of the reservoirs and the variations of the volatiles at the surface.
- Crushing Pele's hairs and tears and releasing the excess $^{40}Ar^{*}$ retained in the bubbles will leave only virtually 'vesicle free' glass shards. Assessing for the pristine and non-hydrated nature of the glass and using a sufficiently small grain size (e.g. 63 μm) it would be possible to attempt to use this type of glass in Ar/Ar geochronology.

7.3 Chapter 5 - NG behaviour and partitioning in young pumice glass during plinian eruptions and implications for Ar/Ar ages

- The Eras Formation is formed by four types of chemically distinct phonolitic pumices: grey, light-green, dark-green and dark-green banded pumices. These last two types of pumices are absent in the fall deposit. The general mineral assemblage is: alkali feldspar, Mg-rich biotite, sodalite/haüyne, clinopyroxene, Fe–Ti oxides and rare apatite.

With specific reference to grey pumices:

- Alkali-feldspars are Na-sanidine (Or_{37}-Or_{51}) with a few anorthoclase (Or_{33}-Or_{35}) in pumice from the base of the ignimbrite.
- The glass is mainly trachytic in composition with SiO_2 and total alkalis extremely variables (60 - 67 Wt. % and 7.8 - 13 Wt. %, respectively) due to the high grade of alteration (CIA 59 – 71). K_2O content is ~ 6 Wt. %.
- Pumice glass has retained NG (^4He, $^{40}Ar^*$, ^{36}Ar) in different abundances and ratios after eruption. Different degree of $^{40}Ar^*$ and ^4He elemental fractionation have produced variable $^4He/^{40}Ar^*$ ratios in pumices collected in different portions of the two pyroclastic deposits (pumice fall, ignimbrite). $^4He/^{40}Ar^*$ decrease from the base to the top of both deposits and from the base to the top of the eruptive unit.
- Different degrees of Ar mass fractionation coupled with different degrees of air incorporation can justify the range of $^{40}Ar/^{36}Ar$ ratios (atmospheric, supra-atmospheric and sub atmospheric) and ^{36}Ar abundances in the glasses.
- The cooling rate of the glass, pumice size, the position of the glass chip within the pumice, bubble walls thickness and bubble connectivity are important factors in controlling diffusion processes and, thus, the NG abundances and ratios of the glass.
- Two models were proposed in order to explain the NG variations in the glass. The first hypothesizes that the magma chamber is "stratified" with respect to NG with $^{40}Ar^*$ and ^{36}Ar decreasing toward the upper part of the reservoir due to preferential degassing. The second suggests that different amount of $^{40}Ar^*$ and ^{36}Ar are uptake and lost through diffusion during pumice cooling in the plume with elemental diffusion fractionation of ^4He and $^{40}Ar^*$ and ^4He preferentially lost during the first phases of the eruption. The uptake from the plume and/or lost from the glass are dependent on the residence time of the glass within the hot zone of the plume.

- The two proposed models can be combined considering different processes occurring at different stages of pumice formation and evolution.
- Only with more detailed studies and inputs from other disciplines can the validity of the proposed models to be tested and verified. Quantitative modelling is needed in order to better constrain the residence time of particles in the eruption column and their cooling rate and the influence of these parameters on NG diffusion and fractionation during pumice cooling in the plume and in relation to different emplacement mechanisms and conditions.
- Haüyne failed to provide meaningful Ar/Ar ages; pumice glass yielded Ar/Ar ages (~ 0.3 Ma) younger than expected and not concordant with the stratigraphy; sanidines yielded a weighted mean age of 0.707±0.021 Ma consistent with Ar/Ar ages of K-feldspar provided for the upper and lower Formations (Brown et al., 2003; Dávila-Harris, 2009).
- Pumice glass failed to provide Ar/Ar ages most likely because K has been lost (and thus ^{40}Ar loss) due to glass alteration.
- No relationships were observed between Ar degassing and Ar/Ar ages produced from different portions of the eruptive sequence for both sanidines and pumice glass.
- Sub-atmospheric $^{40}Ar/^{36}Ar$ ratios have precluded the use of the age spectra during the interpretation of the results of step-heating Ar/Ar analyses.
- The investigation of NG in pumice glasses is extremely challenging due to the complexity of the phenomena that control sample formation and degassing. Only after having better understood which are the mechanisms that control Ar incorporation and degassing in pumice glass it would be possible to better comprehend how to use pumice glasses for obtaining Ar/Ar ages from young samples.

7.4 Future directions

More detailed studies are required in order to even better understand those factors influencing the NG behaviour and concentration in subaerial volcanic glass and the influence of degassing processes on the quality of Ar/Ar ages when volcanic glass is used to date an eruptive event.

- More systematic NG and Ar/Ar analyses are required using different types of glasses with different chemistry, physical characteristics, from different types of deposits and that have undergone to different degree of weathering.
- Quantitative modelling is needed to better characterise NG (in particular Ar isotopes) diffusion and fractionation during glass cooling after eruption and during sample emplacement.
- Multiple types of experiments (single grain fusion, in vacuo crushing, *in-situ* analyses) must be undertaken in order to investigate the preferential residence site of atmospheric Ar and possible mechanism of ^{36}Ar incorporation.
- More work is needed to determine the influence of sample vesicularity on NG degassing and retention in volcanic glass. In particular, detailed studies could highlight the importance of bubble connectivity and bubble wall thickness in the context of NG degassing. Connected bubbles could work as fast pathways for releasing trapped NG (e.g. excess Ar) during degassing events.
- Different types of glass with different vesicularity, surface areas and of different size must be tested in order to better understand the phenomenon of Ar recoil in volcanic glass.
- Ar/Ar ages must be recovered from volcanic glasses, of different origin (subaerial or submarine), of similar and different types, undergone to different types of weathering and hydration. This could permit to even better understand how, for example, marine, fluvial and meteoric water influence the quality of Ar/Ar ages and ^{36}Ar contamination. Materials with different degrees of alteration must be tested and the results compared.
- Further investigation on how fragmentation processes influence the NG (in particular ^{36}Ar and ^{40}Ar*) degassing and retention in volcanic glass are also required.
- Pele's hairs and tears could be more widely used to monitor other persistent long-term degassing volcanoes such as Kilauea volcano (Hawaii).

References

Ablay, G.J., and Martì, J. (2000). Stratigraphy, structure, and volcanic evolution of the Pico Teide-Pico Viejo formation, Tenerife, Canary Islands. Journal of Volcanology and Geothermal Research, 103, pp. 175-208.

Abramoff, M.D., Magelhaes, P.J., and Ram, S.J. (2004). Image processing with ImageJ. Biophotonics International, 11, p. 36-42.

Aiuppa, A., de Moor, M., Arellano, S., Coppola, D., Francofonte, V., Galle, B., Giudice, G., Liuzzo, M., Mendoza, E., Saballos, J., Tamburello, G., Battaglia, A., Bitetto, M., Laiolo, M., Mastrolia, A., and Moretti, R. (2018). Tracking formation of a lava lake from ground and space: Masaya volcano (Nicaragua), 2015 – 2017. Geochemistry, Geophysics, Geosystems, 19, pp. 496-515.

Álvarez-Valero A.M., Burgess, R., Recio C., de Matos, V., Sánchez-Guillamón, O., Gómez-Ballesteros, M., Recio, G., Fraile-Nuez, E., Sumino, H., Flores, J.A., Ban, M., Geyer, A., Bárcena, M.A., Borrajo, J., and Compaña, J.M. (2018). Noble gas signals in corals predict submarine volcanic eruptions. Chemical Geology, 480, pp. 28-34.

Amalberti, J., Burnard, P., Laporte, D., Tissandier, L., and Neuville, D. R. (2016). Multidiffusion mechanisms for noble gases (He, Ne, Ar) in silicate glasses and melts in the transition temperature domain: Implications for glass polymerization. Geochimica et Cosmochimica Acta, 172, pp. 107-126.

Ancochea, E., Fùster, J.M., Ibarrola, E., Cendrero, A., Coello, J., Hernàn, F., Cantagrel, J.M., and Jamond, C. (1990). Volcanic evolution of the island of Tenerife (Canary Islands) in light of new K-Ar data. Journal of Volcanology and Geothermal Research, 44, pp. 231-249.

Anguita, F. and Hernan, F. (2000). The Canary Islands origin: a unifying model. Journal of Volcanology and Geothermal Research, 103, pp. 1-26.

Araña, V. (1971). Litología y estructura del edificio Cañadas, Tenerife (Islas Canarias). Estudio Geologico, 27, pp. 95-137.

Araña, V. and Ortiz, R. (1991). The Canary Islands: Tectonics, magmatism, and geodynamic framework. In: Kampunzu, A.B., Lubala, R.T. (Eds.) Magmatism in Extensional Structural Settings- the Phanerozoic African Plate, Springer, New York, pp. 209-249.

Atlas, Z., Ryan, J., and Dixon, J. (2011). Multi-stage degassing and volatile flux at Masaya Volcano, Nicaragua. Geophysical Research Abstracts, 13, EGU2011-12727, EGU General Assembly 2011.

Aubry, G.J., Sator, N., Guillot, B. (2013). Vesicularity, bubble formation and noble gas fractionation during MORB degassing, Chemical Geology, 343, pp. 85-98.

Azbel, I. Y. and Tolstikhin, I.N. (1988). Geodynamics, magmatism and degassing of the Earth. Geochimica et Cosmochimica Acta, 54, pp. 139-154.

Baksi, A.K., York, D., and Watkins, N.D. (1967). Age of the Steens Mountain geomagnetic polarity transition. Journal of Geophysical Research, 72(74), pp. 6299-6308, doi:10.1029/JZ072i024p06299.

Ballentine, C.J., and Barfod, D.N. (2000). The origin of air-like noble gases in MORB and OIB. Earth and Planetary Science Letters, 180, pp. 39-48.

Barry, T. L., Kelley, S.P., Reidel, S.P., Camp, V.E., Self, S., Jarboe, N.A., Duncan, R.A., and Renne., P.R. (2013). Eruption chronology of the Columbia River Basalt Group, Geological Society of America, Special Papers, 2497(02), pp. 45-66, doi.org/10.1130/2013.2497(02).

Barry, T.L., Self, S., Kelley, S.P., Reidel, S., Hooper, P., and Widdowson, M. (2012). Response to Baksi, A., 2012, "New $^{40}Ar/^{39}Ar$ dating of the Grande Ronde lavas, Columbia River Basalts, USA: Implications for duration of flood basalt eruption episodes" by Barry et al., 2010 – Discussion. Lithos, 146-147, pp. 300-303.

Barry, T.L., Self, S., Kelley, S.P., Reidel, S., Hooper, P., and Widdowson, M. (2010). New $^{40}Ar/^{39}Ar$ dating of the Grande Ronde lavas, Columbia River Basalts, USA: Implications for duration of flood basalt eruption episodes. Lithos, 118(02-03), pp. 213-222, doi:10.1016/j.lithos.2010.03.014.

Behrens, H. (2010). Noble Gas Diffusion in Silicate Glasses and Melts. Reviews in Mineralogy and Geochemistry, 72(1), pp. 227-267.

Bice, D.C. (1985). Quaternary volcanic stratigraphy of Managua, Nicaragua: Correlation and source assignment for multiple overlapping plinian deposits. Geological Society of America Bulletin, 93, pp. 553-566.

Bice, D. C. (1980). Tephra stratigraphy and physical aspects of recent volcanism near Managua, Nicaragua. Ph.D. Thesis, University of California, Berkeley, USA, 200 p.

Bigazzi, G., Laurenzi, M. A., Soligo, M., and Tuccimei, P. (2008), Multi-method approach to dating glass: The case of Basiluzzo Islet (Aeolian archipelago, Italy), Journal of Volcanology and Geothermal Research, 177(01), pp. 244-250.

Bigazzi, G., Laurenzi, M.A., and Viramonte J.G. (2005). The obsidian from Quiron (Salta Province, Argentina): a new reference glass for fission-track dating. Radiation Measurements, 39, pp. 613-616.

Blake, S. and Ivey, G.N. (1986). Magma-mixing and the dynamics of withdrawal from stratified reservoirs. Journal of Volcanology and Geothermal Research, 27, pp.153-178.

Bochsler, P., and Mazor E. (1975). Excess of atmospheric neon in pumice from the Islands of Lipari. Nature, 257, pp. 474-475.

Bond, D.P.G., and Grasby, S.E. (2017). On the causes of mass extinctions: Palaeogeography, Palaeoclimatology. Palaeoecology, 478, pp. 3-29, doi.org/10.1016/j.palaeo.2016.11.005.

Bonnichsen, B., Leeman, W., Honjo, N., McIntosh, W., and Godchaux, M. (2008). Miocene silicic volcanism in southwestern Idaho: geochronology, geochemistry, and evolution of the central Snake River Plain. Bulletin of Volcanology, 70(3), pp. 315-342, doi:10.1007/s00445-007-0141-6.

Bonnichsen B., and Citron G.P. (1982). The Cougar Point Tuff, south-western Idaho and vicinity: In Bonnichsen B., Breckenridge, R.M. eds, Cenozoic geology of Idaho. Idaho Bureau of Mines and Geology Geological Bulletin, 26, pp. 255-281.

Brooker, R.A., Wartho, J.A., Carroll, M.R., Kelley, S.P., and Draper, D.S. (1998). Preliminary UVLAMP determinations of argon partition coefficients for olivine and clinopyroxene grown from silicate melts. Chemical Geology, 147(1-2), pp. 185-200.

Brown, R.J., and Graham D.M.A. (2015). Chapter 36 - Deposits of Pyroclastic Density Currents. Editor: Haraldur Sigurdsson, The Encyclopedia of Volcanoes (2nd Edition), Academic Press, pp. 631-648.

Brown R.J., and Branney, M.J. (2004). Event-stratigraphy of a caldera-forming ignimbrite eruption on Tenerife: the 273 Ka Poris Formation. Bulletin of Volcanology, 66, pp. 392-416.

Brown, R.J., Blake, S., Thordarson, T., and Self, S. (2014). Pyroclastic edifices record vigorous lava fountains during the emplacement of a flood basalt flow field, Roza Member, Columbia River Basalt Province, USA. Geological Society of America Bulletin, 126, pp. 875-891.

Brown, F.H., Reid, C., and Negash, A. (2009). Possible isotopic fractionation of argon in source obsidians and archeological artifacts from Kulkuletti, Ethiopia. Journal of Archaeological Sciences, 36, pp. 2119-2124.

Brown, R.J., Barry, T.L., Branney, M.J, Pringle, M.S., and Bryan, S.E (2003). The Quaternary pyroclastic succession of the southeast Tenerife, Canary Islands: explosive eruptions, related caldera subsidence, and sector collapse. Geological Magazine, 140(3), pp. 265-288.

Bryan, S.E., and Ferrari, L. (2013). Large igneous provinces and silicic large igneous provinces: Progress in our understanding over the past 25 years. Geological Society of America Bulletin, 125, pp. 1053-1078.

Bryan, S.E., Ukstins Peate, I.A., Self, S., Peate, D., Jerram, D.A., Mawby, M.R., Miller, J., and Marsh, J.S. (2010). The largest volcanic eruptions on earth, Earth-Science Review, 102, pp. 207-229.

Bryan S.E. (2006). Petrology and geochemistry of the Quaternary caldera-forming, phonolitic Granadilla eruption, Tenerife (Canary Islands). Journal of Petrology, 47(8), pp. 1557-1589

Bryan S.E., Martì J., and Leosson M. (2002). Petrology and Geochemistry of the Bandas del Sur Formation, Las Cafiadas Edifice, Tenerife (Canary Islands). Journal of Petrology, 43, pp. 1815-1856.

Bryan, S.E., Cas R., and Martí, J. (2000). The 0.57 Ma plinian eruption of the Granadilla Member, Tenerife (Canary Islands): an example of complexity in eruption dynamics and evolution, Journal of Volcanology and Geothermal Research, 103, pp. 209-238.

Bryan, S.E., Martì, J., and Cas, R.J. (1998). Stratigraphy of the Bandas del Sur Formation: an extracaldera record of Quaternary phonolitic explosive eruptions from the Las Cañadas edifice, Tenerife (Canary Islands). Geological Magazine, 135(5), pp. 605-636.

Bulletin of the Global Volcanism Network. (1970-2018). Report on Masaya (Nicaragua). Smithsonian Institute, 38 (70) - 43(04). Washington, DC.

Burgess, R., and Turner, G. (1998). Laser $^{40}Ar/^{39}Ar$ age determinations of Luna 24 mare basalts. Meteoritics and Planetary Science, 33, pp. 921-935.

Burgess, S.D., Bowring, S., and Shen, S. (2014). High-precision timeline for Earth's most severe extinction: Proceedings of the National Academy of Sciences, 111(9), pp. 3316-3321, doi.org/10.1073/pnas.1317692111.

Burke, K., and Wilson, J.T. (1972), Is the African plate stationary?. Nature, 239, pp. 387-390.

Burnard, P. (2004). Diffusive fractionation of noble gases and helium isotopes during mantle melting. Earth and Planetary Science Letters, 220, pp. 287-295.

Burnard, P. (2001). Correction for volatile fractionation in ascending magmas; noble gas abundances in primary mantle melts. Geochimica et Cosmochimica Acta, 65, pp. 2605-2614.

Burnard, P. (1999). The bubble-by-bubble volatile evolution of two mid-ocean ridge basalts. Earth and Planetary Science Letters. 174, pp. 199-211.

Burnard, P., Graham, D.W., Farley, K.A. (2004). Fractionation of noble gases (He, Ar) during MORB mantle melting: a case study on the southeast Indian ridge. Earth and Planetary Science Letters, 227, p. 457-472.

Burnard, P.G., Graham, D.W., and Farley, K.A. (2002), Noble gas constraints on magmatic gas loss along the Southeast Indian Ridge and the Amsterdam - St. Paul Plateau, Earth and Planetary Science Letters, 203, pp. 131-148.

Burton, M. R., Oppenheimer, C., Horrocks, A., and Francis, P.W. (2000). Remote sensing of CO_2 and H_2O emission rates from Masaya volcano, Nicaragua. Geology, 28(10), pp. 915-918.

Camp, V.E. (2013). Origin of Columbia River Basalt: Passive rise of shallow mantle, or active upwelling of a deep-mantle plume?. in Reidel, S.P., Camp, V.E., et al., eds., The Columbia River Flood Basalt Province, Geological Society of America Special Paper 497, pp. 181-199, doi:10.1130/2013.2497(07).

Camp, V.E., Reidel, S.P., Ross, M.E., Brown, R.J., and Self, S. (2017). Field-trip guide to the vents, dikes, stratigraphy, and structure of the Columbia River Basalt Group, eastern Oregon and southeastern Washington: U.S. Geological Survey Scientific Investigations Report, 5022, pp. 88, doi.org/10.3133/sir20175022N.

Camp, V.E., Ross, M.E., Duncan, R.A., Jarboe, N.A., Coe, S.C., Hanan, B.B., and Johnson, J.A. (2013). The Steens Basalt Earliest lavas of the Columbia River Basalt Group: in Reidel, S.P., Camp, V.E., et al.,

eds., The Columbia River Flood Basalt Province: Geological Society of America Special Paper 497, pp. 87-116, doi: 10.1130/2013.2497(04).

Campbell, I.H. (2005). Large igneous provinces and the mantle plume hypothesis. Elements, 1(5), pp. 265-269, doi.org/10.2113/gselements.1.5.265.

Cannata, C.B., De Rosa, R., Houghton, B., Donato, P., Nudo, A. (2012). Pele's hair: case studies from Kilauea Volcano and Vulcanello (Aeolian Islands). Acta Vulcanologica, Journal of the National Volcanic Group of Italy, 23/24, pp. 1-2.

Cantagrel, J.M., Arnaud, N.O., Ancochea, E., Fúster, J.M., and Huertas, M.J. (1999). Repeated debris avalanches on Tenerife and genesis of Las Cañadas caldera wall (Canary Islands), Geology, 27, pp. 739-742.

Caravantes González, G., Rymer, H., Zurek, J., Ebmeier, S., Blake, S. and Williams-Jones, G., 2019, Structures controlling volcanic activity within Masaya caldera, Nicaragua, Volcanica, v. 2(1), p. 25-44. doi: 10.30909/vol.02.01.2544.

Caravantes González, G. (2013). Geophysical constraints on the structural evolution and hazards of Masaya volcano, Nicaragua. The open University, Ph.D. thesis, 264 p.

Carracedo, J.C., and Perez-Torrado F.J. (2013). Geological and Geodynamic Context of the Teide Volcanic Complex. In: Carracedo J., Troll V. (eds) Teide Volcano. Active Volcanoes of the World. Springer, Berlin, Heidelberg, pp. 23-36.

Carracedo, J.C. and Day, J.S. (2002). Canary Islands, Classic Geology in Europe. Terra Publishing, pp. 294.

Carracedo, J.C., Rodríguez Badiola, E., Guillou, H., Paterne, M., Scaillet, S., Pérez Torrado, F.J., Paris, R., Fra-Paleo U., and Hansen, A. (2007). Eruptive and structural history of Teide Volcano and rift zones of Tenerife, Canary Islands. Geological Science of America Bulletin, 119(9/10), pp. 1027-1051.

Carracedo, J.C., Pérez, F.J.; Ancochea, E.; Meco J.; Hernán, F.; Cubas C.R.; Casillas, R.; Rodriguez, E, and Ahijado, A. (2002). Cenozoic volcanism II: The Canary Islands. In: The Geology of Spain. Ed. By Gibbons, W. and Moreno, T., The Geological Society of London, pp. 439-472.

Carracedo, J.C., Badiola, E.R., Guillou, H., Paterne, M., Scaillet, S., Pérez-Torrado, F.J., Paris, R., Fra-Paleo, U., and Hansen, A. (2007). Eruptive and structural history of Teide Volcano and rift zones of Tenerife, Canary Islands. Geological Science of America Bulletin, 119(9/10), p. 1027-1051.

Carracedo, J.C., Day, S., Guillous, H., Rodriguez, E., Canas, J.A., and Perez, F.J. (1998). Hotspot volcanism close to a passive continental margin. Geological Magazine, 135, pp. 591-604.

Carracedo-Sánchez, M., F., Sarrionandia, J., Arostegui, J., Errandonea-Martin, J.I., and GilIbarguchi, K. (2016). Petrography and geochemistry of achnelithic tephra from Las Herrerías Volcano (Calatrava volcanic field, Spain): Formation of nephelinitic achneliths and post-depositional glass alteration, Journal of Volcanology and Geothermal Research, 327, pp. 484-502.

Carroll, M. R. (1991). Diffusion of Ar in Rhyolite, Orthoclase and Albite Composition Glasses, Earth and Planetary Science Letters, 103(1-4), pp. 156-163.

Carroll, M. R., and Draper, D. S. (1994). Noble gases as trace elements in magmatic processes. Chemical Geology, 117, pp. 37-56.

Carroll, M.R., and Webster, J.D., 1994, Solubilities of sulfur, noble gases, nitrogen, chlorine, and fluorine in magmas. In Volatiles in Magmas (ed. Carroll M.R. and Holloway J.R.). Mineralogical Society of America, 30, pp. 235-279.

Carroll, M.R., and Stolper, E.M. (1993). Noble gas solubilities in silicate melts and glasses: new experimental results for argon and the relationship between solubility and ionic porosity. Geochimica et Cosmochimica Acta, 57, pp. 5039-5051.

Cerling, T.E., Brown, F.H., Bowman, J.R. (1985) Low-temperature alteration of volcanic glass: Hydration, Na, K, ^{18}O and Ar mobility. Chemical Geology, Isotope Geoscience section, 52(3-4), pp. 281-293,

Cheilletz, A., Clark, A.H., Farrar, E., Arroyo Pauca, G., Pichavant, M., and Sandeman, H.A. (1992). Volcano-stratigraphy and $^{40}Ar/^{39}Ar$ geochronology of the Macusani ignimbrite field: monitor of the Miocene geodynamic evolution of the Andes of southeast Peru. Tectonophysics, 205(1-3), pp. 307-327.

Chenet, A.L., Courtillot, V., Fluteau, F., Gerard, M., Quidelleur, X., Khadri, S.F.R., Subbarao, K.V., and Thordarson, T. (2009). Determination of rapid Deccan eruptions across the Cretaceous-Tertiary boundary using paleo-magnetic secular variation: Constraints from analysis of eight new sections and synthesis for a 3500-m-thick composite section. Journal of Geophysical Research, 114, pp. 6103, doi:10.1029/2008JB005644.

Clague, D.A., Davis, A.S., and Dixon, J.E. (2003). Submarine strombolian eruptions on the Gorda mid-ocean ridge. In: White, J.D.L., Smellie, J.L., Clague, J.J. (Eds.), Explosive Subaqueous Volcanism. American Geophysical Union Monograph, 140, pp. 111-128.

Clauer, N. (1981). Strontium and argon isotopes in naturally weathered biotites, muscovites and feldspars, Chemical Geology, 31, pp. 325-334.

Clay, P.L., Busemann, H., Sherlock, S.C., Barry, T.L., Kelley, S.P., and McGarvie, D.W. (2015). $^{40}Ar/^{39}Ar$ ages and residual volatile contents in degassed subaerial and subglacial glassy volcanic rocks from Iceland. Chemical Geology, 403, pp. 99-110,

Clay, P.L., Kelley, S.P., Sherlock, S.C., and Barry, T.L. (2011). Partitioning of excess argon between alkali feldspars and glass in a volcanic system. Chemical Geology, 289, pp. 12-30.

Colgan, J.P., Dumitru, T.A., McWilliams, M., and Miller, E.L. (2006). Timing of Cenozoic volcanism and Basin and Range extension in north western Nevada: New constraints from the northern Pine Forest Range. Geological Society of America Bulletin, 118(1-2), pp. 126-139.

Cooper, L.B., Bachmann, O., and Huber, C. (2015). Volatile budget of Tenerife phonolites inferred from textural zonation of S-rich haüyne. Geology, 43(5), p. 423-426.

Courtillot, V. (1999). Evolutionary Catastrophes: The Science of Mass Extinction. Cambridge University Press, Cambridge, pp. 171.

Courtillot, V.E., and Renne P.R. (2003). On the ages of flood basalt events: Comptes Rendus. Geoscience, 335(1), pp. 113-40. doi:10.1016/S1631-0713(03)00006-3.

Courtillot, V., Fluteau, F., and Besse, J. (2015). Evidence for volcanism triggering extinctions: a short history of IPGP contributions with emphasis on paleomagnetism. In: Schmidt., Anja et al., (eds.), Volcanism and Global Environmental Change, Cambridge University Press, pp. 228-243.

Courtillot, V., and Fluteau, F. (2014). A review of the embedded time scales of flood basalt volcanism with special emphasis on dramatically short magmatic pulses: In Keller, G., Kerr, A. (eds.), Volcanism, Impacts, and Mass Extinctions: Causes and Effects. Geological Society of America Special Paper, 505, pp. 301-317, doi.org/10.1130/2014.2505(15).

Crenshaw, W.B., Williams, S. N., and Stoiber, R.E. (1982). Fault location by radon and mercury detection at an active volcano in Nicaragua. Nature, 300(5890), pp. 345-346.

Dalrymple, G.B. (1969). $^{40}Ar/^{36}Ar$ analyses of historic lava flows. Earth and Planetary Science Letters, 6, pp. 47-55

Dalrymple, M., and Lanphere A. (1971). $^{40}Ar/^{39}Ar$ technique of K-Ar dating: a comparison with the conventional technique. Earth and Planetary Science Letters, 12, pp. 300-308.

Dalrymple, G.B., and Moore, J.G. (1968). Argon-40: excess in submarine pillow basalts from Kilauea volcano, Hawaii. Science, 161(3846), pp. 1132-1135.

Dávila-Harris P., Ellis, B.S., Branney, M.J., Carrasco-Núñez, G. (2013). Lithostratigraphic analysis and geochemistry of a vitric spatter-bearing ignimbrite: the Quaternary Adeje Formation, Cañadas volcano, Tenerife. Bulletin of Volcanology, 75, pp.722.

Dávila-Harris, P. (2009). Explosive ocean-island volcanism: the 1.8-0.7 Ma explosive eruption history of Cañadas volcano recorded by the pyroclastic successions around Adeje and Abona, southern Tenerife, Canary Islands. Ph.D. thesis, 170 p.

De Jong, K., Féraud, G., Ruffet, G., Amouric, M., and Wijbrans, J.R. (2001). Excess argon incorporation in phengite of the Mulhacén Complex: submicroscopic illitization and fluid ingress during late Miocene extension in the Betic Zone, south-eastern Spain. Chemical Geology, 178(1-4), pp. 159-195, doi.org/10.1016/S0009-2541(00)00411-3.

De Moor, J.M., Kern, C., Avard, G., Muller, C., Aiuppa, A., Saballos, J., Ibarra, M.. LaFemina, P., Protti, M., Fischer, T. (2017). A new sulphur and carbon degassing inventory for the Southern Central American Volcanic Arc: The importance of accurate time-series data sets and possible tectonic processes responsible for temporal variations in arc-scale volatile emissions. Geochemistry, Geophysics, Geosystems, 18, pp. 4437-4468, doi.org/10.1002/2017GC007141.

De Moor, J.M., Fischer T.P., Sharp, Z.D., King P.L., Wilke, M., Botcharnikov, R.E., Cottrell, E., Zelenski M., Marty B., Klimm K., Rivard C., Ayalew D., Ramirez C., and Kelley, K.A. (2013). Sulfur degassing at Erta Ale (Ethiopia) and Masaya (Nicaragua) volcanoes: Implications for the degassing processes and oxygen fugacities of basaltic systems. Geochemistry Geophysics Geosystems, 14, pp. 4076- 4108.

Delmelle, P., Stix, J., Baxter, P., Garcia-Alvarez, J., and Barquero, J. (2002). Atmospheric dispersion, environmental effects and potential health hazard associated with the low-altitude gas plume of Masaya volcano, Nicaragua. Bulletin of Volcanology, 64(6), pp. 423-434.

Delmelle, P., Baxter, P., Beaulieu, A., Burton, M., Francis, P., Garcia-Alvarez, J., Horrocks, L., Navarro, M., Oppenheimer, C., Rothery, D., Rymer, H., Amand, K., Stix, John, Strauch, W., and Williams-Jones, G. (1999). Origin, effects of Masaya volcano's continued unrest probed in Nicaragua. Eos, Transactions of the American Geophysical Union, 80(48), pp. 575-581.

Dodson, M.H. (1986). Closure profiles in cooling systems. Material Science Forum, 7, pp. 145-154.

Dong, H., Hall, C.M., Peacor, D.R., and Halliday, A.N. (1995). Mechanisms of argon retention in clays revealed by laser ^{40}Ar-^{39}Ar dating. Science, 267, pp. 355-359, doi:10.1126/science.267.5196.355.

Drake, R.E., Curtis, G.H., Cerling, T.E., Cerling, B.W. and Hampel, J. (1980). KBS Tuff dating and geochronology of tuffaceous sediments in the Koobi Fora and Shungura Formations, East Africa. Nature, 283, pp. 368-372.

Duffell, H. J., Oppenheimer, C., Pyle, D. M., Galle, B., McGonigle, A. J. S., and Burton, M. R. (2003). Changes in gas composition prior to a minor explosive eruption at Masaya volcano, Nicaragua. Journal of Volcanology and Geothermal Research, 126(3-4), pp. 327-339.

Duffield, W.A., Gibson, E.K., and Heiken, G. (1977). Some characteristics of Pele's hair. Journal of resources, U.S Geological Survey, 5, pp. 93-101.

Duncan P. (1983) ^{40}Ar/^{39}Ar radiometric age determinations final report of completed work. Rockwell / Hanford Report, M30-SBB-294449, p. 6.

Duncan p. (1982). ^{40}Ar/^{39}Ar dating of Columbia River Basalts. Rockwell / Hanford Report M29-SBB-258874, p. 10.

Ebinghaus, A., Jolley, D. W., and Hartley, A. J. (2015). Extrinsic forcing of plant ecosystems in a large igneous province: The Columbia River Flood Basalt Province, Washington state, USA. Geology, 43(12), pp. 1107-1110, doi.org/10.1130/G37276.1.

Ebinghaus, A., Hartley, A.J., Jolley, D.W., Hole, M., and Millett, J. (2014), Lava-sediment interaction and drainage-system development in a large igneous province, Washington State, U.S. Journal of Sedimentary Research, 84, pp. 1041-1063, doi:10.2110/jsr.2014.85.

Ellis, B.S., Branney, M.J., Barry, T.L., Barfod, D., Bindeman, I., Wolff, J.A., and Bonnichsen, B. (2012) Geochemical correlation of three large-volume ignimbrites from the Yellowstone hotspot track, Idaho, USA. Bulletin of Volcanology, 74(1), pp. 261-277, doi.org/10.1007/s00445-011-0510-z.

Edgar, C.J., Wolff, J.A., Olin, P.H., Nichols, H.J., Pittari, A., Cas, R., Reiners, P.W, Spell, T.L, and Martí, J. (2007). The late Quaternary Diego Hernández Formation, Tenerife: Volcanology of a complex cycle of voluminous explosive phonolitic eruptions. Journal of Volcanology and Geothermal Research, 160, pp. 59-85.

Edgar, C.J, Wolff, J.A, Nichols, H.J, Cas, R., and Martí, J. (2002). A complex Quaternary ignimbrite-forming phonolitic eruption: the Poris Member of the Diego Hernández Formation (Tenerife, Canary Islands). Journal of Volcanology and Geothermal Research, 118, pp. 99-130.

Ernst, R.E. and Youbi, N. (2017). How Large Igneous Provinces affect global climate, sometimes cause mass extinctions, and represent natural markers in the geological record. Palaeogeography, Palaeoclimatology, Palaeoecology, 478, pp. 30-52. doi.org/10.1016/j.palaeo.2017.03.014.

Esser, R.P., McIntosh, W.C., Heizler, M.T., and Kyle, P.R. (1997). Excess Ar in melt inclusions in zero-age anorthoclase feldspar from Mt. Erebus, Antarctica, as revealed by the ^{40}Ar-^{39}Ar method. Geochimica et Cosmochimica Acta, 61, pp. 3789-3801.

Evernden, J.F. and James, G.T. (1964). Potassium-argon dates and the Tertiary floras of North America: American Journal of Science, v. 262, p. 945-974, doi:10.2475/ajs.262.8.945.

Fearn, S., McPhail, D.S., and Oakley, V. (2004). Room temperature corrosion of museum glass: an investigation using low-energy SIMS. Applied Surface Science, 231-232, pp. 510-514.

Fecht, K.R., Reidel, S.P., and Tallman, A. (1987). Paleodrainage of the Columbia River System on the Columbia Plateau of Washington State: a summary. Washington Division of Geology and Earth Resources Bulletin, 77, pp. 219-248.

Fisher, D. (1971). Incorporation of Ar in east pacific basalts. Earth and Planetary Science Letters, 12, pp. 321-324.

Fisher, R.V., and Schmincke, H.U. (1969). Pyroclastic rocks. Springer-Verlag, Berlin, New York, pp. 472.

Fleck, R.J., Sutter, J.F. and Elliot, D.H. (1977). Interpretation of discordant ^{40}Ar/^{39}Ar age spectra of Mesozoic tholeiites from Antarctica. Geochimica et Cosmochimica Acta, 41, pp. 15-32.

Flude, S., Tuffen, H., and Sherlock, S.C. (2018). Spatially heterogeneous argon-isotope systematics and apparent ^{40}Ar/^{39}Ar ages in perlitised obsidian. Chemical Geology, 480, pp. 44-57.

Flude, S., McGarvie, D.W., Burgess, R., and Tindle, A.G. (2010). Rhyolites at Kerlingarfjöll, Iceland: the evolution and lifespan of silicic central volcanoes. Bulletin of Volcanology, 72, pp. 523-538.

Flude, S., Burgess, R. and McGarvie, D., 2008, Silicic volcanism at Ljósufjöll, Iceland: Insights into evolution and eruptive history from Ar-Ar dating, Journal of Volcanology and Geothermal Research, 169, pp. 154-175, 10.1016/j.jvolgeores.2007.08.019.

Foland, K.A., Fleming, T.H., Heimann, A., and Elliot, D.H. (1993). Potassium-Argon dating of fine-grained basalts with massive Ar Loss - application of the $^{40}Ar/^{39}Ar$ technique to plagioclase and glass from the Kirkpatrick Basalt, Antarctica. Chemical Geology, 107, pp. 173-190.

Foland, K.A., Hubacher, F.A., and Arehart, G.B. (1992). $^{40}Ar/^{39}Ar$ dating of very fine-grained samples: An encapsulated-vial procedure to overcome the problem of ^{39}Ar recoil loss. Chemical Geology, 102, pp. 269-276, doi: 10.1016/0009-2541(92)90161-W.

Fuhrmann, U., and Lippolt, H.J. (1985). Excess argon and dating of Quaternary Eifel volcanism: The Schellkopf alkali phonolite - East Eifel. Geology Paläont. Mh., H., 8, pp. 484-497.

Funkhouser, J. G., and Naughton, J. J. (1968). Radiogenic helium and argon in ultramafic inclusions from Hawaii, Journal of Geophysical Research, 73(14), pp. 4601- 4607.

Fúster, J.M. (1975). Las Islas Canarias: un ejemplo de evolucion temporal y espacial del vulcanismo oceanico. Estern Geology, 31, pp. 439-463.

Fúster, J.M., Araña, V., Brändle, J.L., Navarro, J.M., Alonso, V., and Aparicio, A. (1968). Geology and volcanology of the Canary Islands: Tenerife. Instituto Lucas Mallada, CSIC, Madrid.

Gradstein, F., Ogg, J., and Smith, A. (2004). A Geologic Time Scale. Cambridge, UK, Cambridge University Press, pp. 589.

Graham, D.W. (2002). Noble gas isotope geochemistry of mid-ocean ridge and ocean islands basalts: characterization of mantle source reservoirs. In: Porcelli, D., Ballentine, C.J., Wieler, R. (Eds.), Noble Gases in Geochemistry and Cosmochemistry, Review. Mineral Geochemistry, 47, pp. 247-305.

Guillou, H., Carracedo, J.C., Paris, R., and Pérez-Torrado, F.J. (2004). K/Ar ages and magnetic stratigraphy of the Miocene-Pliocene shield volcanoes of Tenerife, Canary Islands: Implications for the early evolution of Tenerife and the Canarian hotspot age progression. Earth and Planetary Science Letters, 222, pp. 599-614.

Hall, C.M. (2013). Direct measurement of recoil effects on $^{40}Ar/^{39}Ar$ standards, Geological Society, London, Special Publications, 378, pp. 53-62. In Jourdan, F., Mark, D. F. and Verati, C., (eds) 2014. Advances in $^{40}Ar/^{39}Ar$ Dating: from Archaeology to Planetary Sciences. Geological Society, London, Special Publications, 378.

Halton, A.M. (2011). Paleocene-Eocene Time-Stratigraphic Calibration in the North Atlantic Igneous Province with Focus on the Faroes-Shetland Basin Area, Ph.D. thesis, The Open University, 331 p.

Hanyu T., and Kaneoka, I. (1997). Magmatic processes revealed by noble gas signatures: the case of Unzen Volcano. Japan Geochemical Journal, 31, pp. 395-405.

Harpel, C.J., Kyle, P.R., Dunbar, N.W. (2008). Englacial tephrostratigraphy of Erebus volcano Antarctica. Journal of Volcanology and Geothermal Research, 177(3), pp. 549-568.

Harris, A. (2009). The pit-craters and pit-crater-filling lavas of Masaya volcano. Bulletin of Volcanology, 71(5), pp. 541-558.

Harris, A.J.L., Flynn L.P., Rothery, D.A., Oppenheimer C., and Sherman, S.B. (1999). Mass flux measurements at active lava lakes: Implications for magma recycling. Journal of Geophysical Research, 104(B4), pp. 7117-7136,

Heiken, G. (1972). Morphology and petrography of volcanic ashes. Geological Society of America Bulletin, 83, pp. 1961-1988.

Heiken, G., and Wohletz, K. (1985). Volcanic Ash. University of California Press, Berkeley, pp. 246.

Heizler, M.T., and Harrison, T.M. (1988). Multiple trapped argon isotope components revealed by $^{40}Ar/^{39}Ar$ isochron analysis. Geochimica et Cosmochimica Acta, 52, pp. 1295-1303.

Henderson, A.L., Najman, Y., Parrish, R., Mark, D.F., and Foster, G. (2011). Constraints on the timing of India-Eurasia collision: a re-evaluation of evidence from the Indus Basin sedimentary rocks of the Indus-Tsangpo Suture Zone, Ladakh, India. Earth Science Reviews, 106, pp. 265-292.

Henry, C.D., Castor, S.B., Starkel, W.A., Ellis, B.S., Wolff, J.A., Laravie, J.A., McIntosh, W.C., and Heizler, M.T. (2017). Geology and evolution of the McDermitt caldera, northern Nevada and southeastern Oregon, western USA. Geosphere, 13(4), pp. 1066-1112, doi:10.1130/GES01454.1.

Henry, C.D., Castor, S.B., McIntosh, W.C., Heizler, M.T., Cuney, M., and Chemillac, R. (2006). Timing of oldest Steens Basalt magmatism from precise dating of silicic volcanic rocks, McDermitt caldera and northwest Nevada volcanic field [abs]. Eos (Transactions, American Geophysical Union), Fall Meeting Supplement, 44C, p. 8.

Hoernle, K., and Carracedo, J.C. (2009). Canary Islands, geology. In: Gillespie, R.G. and Clague, D.A. (eds) Encyclopedia of islands (encyclopedias of the natural world). University of California Press, USA, pp. 133-143.

Hoernle, K., and Schmincke, H.U. (1993). The role of partial melting in the 15 Ma geochemical evolution of Gran Canaria: a blob model for the Canary hotspot. Journal of Petrology, 34, pp. 599-626.

Hoernle, K., Zhang, Y.S., and Graham, D. (1995). Seismic and geochemical evidence for large-scale mantle upwelling beneath the eastern Atlantic and western and central Europe. Nature, 374, pp. 34-39.

Hofmann, C., Féraud, G. and Courtillot V. (2000). $^{40}Ar/^{39}Ar$ dating of mineral separates and whole rocks from the Western Ghats lava pile: further constraints on duration and age of the Deccan traps. Earth and Planetary Science Letters, 180, pp. 13-27.

Holmgren, D. (1970). K-Ar dates and paleomagnetics of the type Yakima Basalt, central Washington: in Gilmour, E.H., and Stradling, D.F., eds., Proceedings of the Second Columbia River Basalt Symposium: Cheney, Washington, Eastern Washington State College Press, pp. 189-199.

Hooper, P.R., (2000). Chemical discrimination of Columbia River basalt flows. Geochemistry, Geophysics, Geosystems, 1(6), doi: 10.1029/2000GC000040.

Hooper, P.R., and Hawkesworth, C.J. (1993). Isotopic and geochemical constraints on the origin and evolution of the Columbia River Basalts. Journal of Petrology, 34, pp. 1203-1246.

Hooper, P.R., Binger, G.B., and Lees, K.R. (2002). Ages of the Steens and Columbia River Food Basalts and their relationship to extension-related calc-alkaline volcanism in eastern Oregon. Geological Society of America Bulletin, 114(1), pp. 43-50.

Qiu, H., Wu, H., Yun, J., Feng, Z., Xu, Y., Mei, L., Wijbrans, J. R. (2011). High-precision $^{40}Ar/^{39}Ar$ age of the gas emplacement into the Songliao Basin. Geology, 39(5), pp. 451-454, doi.org/10.1130/G31885.1.

Huertas, M.J., Arnaud, N.O., Ancochea, E., Cantagrel, J.M., Fúster, J.M. (2002). $^{40}Ar/^{39}Ar$ of main pyroclastic units from the Cañadas volcanic edifice (Tenerife, Canary Islands) and their bearing on structural evolution. Journal of Volcanology and Geothermal Research, 115, pp. 351-365.

Jambon, A., Weber, H., and Braun, O. (1986). Solubility of He, Ne, Ar, Kr and Xe in a basalt melt in the range 1250-1600 °C: geochemical implications. Geochimica et Cosmochimica Acta, 50, pp. 401-408.

Jarboe, N.A., Coe, R.S., Renne, P.R., and Glen, J.M.G. (2010). The age of the Steens reversal and the Columbia River Basalt Group, Chemical Geology, 274(3-4), pp. 158-168, doi:10.1016/j.chemgeo.2010.04.001.

Jarboe, N.A., Coe, R.S., Renne, P.R., Glen, J.M.G., and Mankinen, E.A. (2008). Quickly erupted volcanic sections of the Steens Basalt, Columbia River Basalt Group: Secular variation, tectonic rotation, and the Steens Mountain reversal. Geochemistry Geophysics Geosystems, 9(11), doi:10.1029/2008GC002067.

Jolley, D.W. (1997). Palaeosurface palynofloras of the Skye lava field and the age of the British Tertiary volcanic province. In: Widdowson, M. (ed.) Palaeosurfaces: Recognition, Reconstruction and Palaeoenvironmental Interpretation. Geological Society, London, Special Publications, 120(1), pp. 67-94, doi.org/10.1144/GSL.SP.1997.120.01.06.

Jolley, D.W., and Widdowson, M. (2005). North Atlantic rift eruptions drive Eocene climate cooling, Lithos, 79, pp. 355-366.

Jolley, D.W., and Bell, B.R. (2002). The evolution of the North Atlantic Igneous Province and the opening of the NE Atlantic rift: In Jolley D.W. (ed.), The North Atlantic Igneous Province: Stratigraphy, Tectonic, Volcanic and Magmatic Processes. Geological Society, Special Publication, 197(1), pp. 1-13, doi.org/10.1144/GSL.SP.2002.197.01.01.

Jolley, D.W., Widdowson, M. and Self, S. (2008). Volcanogenic nutrient fluxes and plant ecosystems in large igneous provinces: An example from the Columbia River Basalt Group. Journal of the Geological Society, London, v. 165, p. 955-966, doi.org/10.1144/0016-76492006-199.

Jolley, D.W., Clarke, B. and Kelley, S.P. (2002). Paleogene time scale miscalibration: Evidence from the dating of the North Atlantic Igneous province. Geology, 30(1), pp. 7-10.

Jourdan, F., and Renne, P.R. (2007). Age calibration of the Fish Canyon sanidine $^{40}Ar/^{39}Ar$ dating standard using primary K-Ar standards. Geochimica et Cosmochimica Acta, 71, pp. 387-402, doi:10.1016/j.gca.2006.09.002.

Jourdan, F., Matzel, J.P., and Renne, P.R. (2007). ^{39}Ar and ^{37}Ar recoil loss during neutron irradiation of sanidine and plagioclase. Geochimica et Cosmochimica Acta, 71, pp. 2791-2808, doi:10.1016/J.GCA.2007.03.017.

Jourdan, F., Feraud, G., Bertrand, H., Kampunzu, A. B., Tshoso, G., Watkeys, M. K. and Le Gall, B. (2005). The Karoo large igneous province: brevity, origin, and relation with mass extinction questioned by new $^{40}Ar/^{39}Ar$ age data. Geology, 33, pp. 745-748.

Kaneoka, I. (1994). The effect of water on noble gas signatures of volcanic materials. In: Matsuda, J. Ed. , Noble Gas Geochemistry and Cosmochemistry, Terra publication, Tokyo, pp. 205-215.

Kaneoka, I., (1980). Rare gas isotopes and mass fractionation: An indicator of gas transport into or from a magma. Earth and Planetary Science Letters, 48(2), pp. 284-292.

Kaneoka, I. (1972), The effect of hydration on the K/Ar ages of volcanic rocks. Earth and Planetary Science Letters, 14, pp. 216-220.

Kaneoka, I. (1969). The use of obsidian for K-Ar dating. Recent Developments in Mass Spectroscopy, 675, pp. 514-521.

Kelley, S.P. (2007). The geochronology of large igneous provinces, terrestrial impact craters, and their relationship to mass extinctions on Earth. Journal of the Geological Society, London, 164, pp. 923-936, doi: http://dx.doi.org/10.1144/0016-76492007-026.

Kelley, S.P. (2002). Excess argon in K-Ar and Ar-Ar geochronology. Chemical Geology, 188(1-2), pp. 1-22, doi.org/10.1016/S0009-2541(02)00064-5.

Kelley, S.P., Reddy, S.M., and Maddock, R. (1994). $^{40}Ar/^{39}Ar$ laser probe investigation of a pseudotachylyte vein from the Moine Thrust Zone, Scotland. Geology, 22, pp. 443-446.

Kelley, S.P., and Bluck, B. J (1989). Detrital mineral ages from the Southern Uplands using ^{40}Ar-^{39}Ar laser probe, Journal of the Geological Society, 146, pp. 401-403.

Kelley, S.P., Turner G., Butterfield, A.W. and Shepherd, T.J. (1986). The source and significance of argon isotopes in fluid inclusions from areas of mineralization, Earth and Planetary Science Letters, 79, pp. 303-318.

Koppers, A.A.P. (2002). ArArCalc-software for $^{40}Ar/^{39}Ar$ age calculations. Computer Geoscience, 28(5), p. 605-619, doi.org/10.1016/S0098-3004(01)00095-4.

Koppers, A.A.P., Staudigel, H., and Wijbrans, J.R. (2000). Dating crystalline groundmass separates of altered Cretaceous seamount basalts by the $^{40}Ar/^{39}Ar$ incremental heating technique. Chemical Geology, 166 (1-2), pp. 139-158, doi.org/10.1016/S0009-2541(99)00188-6.

Krummenacher, D. (1970). Isotopic composition of argon in modern surface volcanic rocks. Earth and Planetary Science Letters, 8, pp. 109-117.

Kuiper, K.F., Deino, A., Hilgen, F.J., Krijgsman, W., Renne, P.R., and Wijbrans, J.R. (2008). Synchronizing rock clocks of Earth history. Science, 320(5875), pp. 500-504, doi:10 .1126/science.1154339.

Kutterolf, S., Freundt, A., Perez, W., Wehrmann, H., and Schmincke, H.U. (2007). Late Pleistocene to Holocene temporal succession and magnitudes of highly-explosive volcanic eruptions in West-Central Nicaragua. Journal of Volcanology and Geothermal Research, 163(1-4), pp. 55-82.

Ladle, G.H. (1978). Scanning electron microscopy and petrography of glassy particles produced by lava fountains eruptions. Lunar and Planetary Institute 325, Houston, pp. 203.

Layer, P.W., and Gardner, G.E., 2001, Excess argon in Mount St. Helens plagioclase as a recorder of magmatic processes. Geophysical Research Letters, 28(22), pp. 4279-4282, doi: 10.1029/2001GL013855.

Le Bas, M.J., Le Maitre, R.W., Streckeisen, B., and Zanettina, A. (1986). Chemical classification of volcanic rocks based on the total alkali-silica diagram. Journal of Petrology, 27, pp. 745-750.

Lee, J.Y., Marti, K., Severinghaus, J.P., Kawamura, K., Yoo, H.S., Lee, J.B., and Kim, J.S. (2006). A redetermination of the isotopic abundances of atmospheric Ar, Geochimica et Cosmochimica Acta, 70(17), pp. 4507-4512, doi.org/10.1016/j.gca.2006.06.1563.

Lees, K. (1994). Magmatic and tectonic changes through time in the Neogene volcanic rocks of the Vale area, Oregon, northwestern U.S.A. Ph.D. thesis, Milton Keynes, UK, The Open University, 283 p.

Lippolt, H.J., Troesch, M., and Hess, J.C. (1990). Excess argon and dating of Quaternary Eifel volcanism, IV. Common argon with high and lower-than-atmospheric $^{40}Ar/^{36}Ar$ ratios in phonolitic rocks, East Eifel, F.R.G. Earth and Planetary Science Letters, 101(1), pp. 19-33.

Liu, L., and Stegman, D.R. (2012). Origin of Columbia River flood basalt controlled by propagating rupture of the Farallon slab, Nature, 482(7385), pp. 386-389, doi.org/10.1038/nature10749.

Long, M.D., Till, C.B., Druken, K.A., Carlson, R.W., Wagner, L.S., Fouch, M.J., and Kincaid, C. (2012). Mantle dynamics beneath the Pacific Northwest and the generation of voluminous back-arc volcanism. Geochemistry, Geophysics, Geosystems, 13(1), p. 22, doi.org/10.1029/2012GC004189.

Lovera O.M., Richter F.M., and Harrison T.M. (1989). The $^{40}Ar/^{39}Ar$ thermochronometry for slowly cooled samples having a distribution of diffusion domain sizes. Journal of Geophysical Research, 94, pp. 917-935.

Ludwig, K., (2003). Isoplot/Ex3.00. The Geochronological Toolkit for Excel. University of California Berkeley, Berkeley Geochronology Center, Special Publication, 1a.

Lux, G. (1987). The behaviour of noble gases in silicate liquids: solution, diffusion, bubbles and surface effects, with applications to natural samples. Geochimica et Cosmochimica Acta, 51, pp. 1549-1560.

Mackin, J.H. (1961). A stratigraphic section in the Yakima Basalt and the Ellensburg Formation in south-central Washington. Department of Conservation, Washington Division of Mines and Geology, Report of Investigations, 19, pp. 4-35.

Macpherson, C.G, Hilton, D.R., Mertz, D.F., and Dunai T.J. (2005). Sources, degassing, and contamination of CO_2, H_2O, He, Ne, and Ar in basaltic glasses from Kolbeinsey Ridge, North Atlantic. Geochimica et Cosmochimica Acta, 69(24), pp. 5729-5746.

Maher, C. (2006). An investigation of depositional mechanisms of pyroclastic density currents using anisotropy of magnetic susceptibility (AMS) and a detailed stratigraphic study of the La Caleta Formation, Tenerife. Ph.D. thesis, University of Leicester, UK.

Mahood, G.A., and Benson, T.R. (2017). Using $^{40}Ar/^{39}Ar$ ages of intercalated silicic tuffs to date flood basalts: Precise ages for Steens Basalt Member of the Columbia River Basalt Group. Earth and Planetary Science Letters, 459, pp. 340-351, doi:10.1016/j.epsl.2016.11.038.

Mark, D.F., Barfod, D., Stuart, F.M., and Imlach, J. (2009). The ARGUS multicollector noble gas mass spectrometer: performance for $^{40}Ar/^{39}Ar$ geochronology. Geochemistry, Geophysics, Geosystems, 10, pp. 1-9.

Martí, J., Geyer, A., Folch, A., and Gottsmann, J. (2008). A review on collapse calderas modelling. In Gottsmann, J.A., Martí, J. "Caldera Volcanism: analysis, modelling and response". Developments in Volcanology, Elsevier., 10, pp. 233-283.

Martí, J., Mitjavila, J., and Araña, V. (1994). Stratigraphy, structure, age and origin of the Cañadas Caldera (Tenerife, Canary Islands). Geological Magazine, 131, pp. 715-727

Martin, R.S., Sawyer, G.M., Spampinato, L., Salerno, G.G., Ramirez, C., Ilyinskaya, E., Witt, M.L.I., Mather, T.A., Watson, I.M., Phillips, J.C., and Oppenheimer, C. (2010). A total volatile inventory for Masaya Volcano, Nicaragua. Journal of Geophysical Research, 115(9): B09215.

Martin, R.S., Mather, T.A., Pyle, D.M., Power, M., Allen, A.G., Aiuppa, A., Horwell, C.J., and Ward, E.P.W. (2008). Composition-resolved size distributions of volcanic aerosols in the Mt. Etna plumes. Journal of Geophysics, 113, D17211, doi.org/10.1029/2007JD009648.

Marvin, A., Lanphere, G., and Dalrymple B. (1971). A test of the $^{40}Ar/^{39}Ar$ age spectrum technique on some terrestrial materials. Earth and Planetary Science Letters, 12(4), pp. 359-372.

Mastin, L.G. (2001). Eject! A Simple Calculator of Ballistic Trajectories for Blocks Ejected During Volcanic Eruptions. USGS Open-File Report 01-45, Reston, VA.

Matsumoto, A., and Kobayashi, T. (1995). K-Ar age-determination of late Quaternary volcanic rocks using the mass fractionation correction procedure - application to the younger Ontake volcano, Central Japan. Chemical Geology, 125, pp. 123-135.

Mauri, G. (2009). Multi-scale analysis of multiparameter geophysical and geochemical data from active volcanic systems. Ph.D. Thesis, Simon Fraser University, Burnaby (Canada).

Mauri, G., Williams-Jones, G., Saracco, G., and Zurek, J.M. (2012). A geochemical and geophysical investigation of the hydrothermal complex of Masaya volcano, Nicaragua. Journal of Volcanology and Geothermal Research, 227-228, pp. 15-31.

May, P.R. (1971). Pattern of Triassic-Jurassic diabase dikes around the North Atlantic in the context of the pre-drift position of the continents. Geological Society American Bulletin, 82, pp. 1285-1292.

McBirney, A. (1956). The Nicaragua Volcano Masaya and its Caldera. Eos Transactions, American Geophysical Union, 37, pp. 83-96.

McDougall I. (1994). dating of rhyolitic glass in the Tonga forearc (hole 841b). Proceedings of the Ocean Drilling Program, Scientific Results, 135.

McDougall, I., and Wellman, P. (2011). Calibration of GA1550 biotite standard for K/Ar and $^{40}Ar/^{39}Ar$ dating. Chemical Geology, 280, pp. 19-25.

McDougall, I., and Harrison, T.M., (eds) (1999). Geochronology and Thermochronology by the $^{40}Ar/^{39}Ar$ method, 2nd edition, Oxford University Press, New York, 269 p.

McGarvie, D.W., Stevenson, J.A., Burgess, R., Tuffen, H., and Tindle, A. (2007). Volcano-ice interactions at Prestahnúkur, Iceland: rhyolite eruption during the last interglacial-glacial transition, Annals of Glaciology, 45, pp. 38-47.

McKee, E.H., Swanson, D.A., and Wright, T.L. (1977). Duration and volume of Columbia River basalt volcanism, Washington, Oregon, and Idaho. Geological Society of America, Abstracts with Programs, 9, pp. 463.

Menyailov, I. A., Nikitina, L. P., Shapar, V. N., and Pilipenko, V. P. (1986). Temperature increase and chemical change of fumarolic gases at Momotombo volcano, Nicaragua, in 1982-1985: Are these indicators of a possible eruption?. Journal of Geophysical Research, 91, pp. 12199-12214.

Merrihue, C., and Turner, G. (1966). Potassium-argon dating by activation with fast neutrons. Journal of Geophysical Research, 71, pp. 2852-2857.

Métaxian, J. P., Lesage, P. and Dorel, J. (1997). Permanent tremor of Masaya Volcano, Nicaragua: Wave field analysis and source location. Journal of Geophysical Research, 102 (B10), pp. 22529-22545.

Min, K., Mundil, R., Renne, P.R., and Ludwig, K.R. (2000). A test for systematic errors in $^{40}Ar/^{39}Ar$ geochronology through comparison with U/Pb analysis of a 1.1 Ga rhyolite. Geochimica et Cosmochimica Acta, 64, pp. 73-98, doi: 10.1016/S0016-7037(99)00204-5

Moreira, M.A., and Kurz M.D. (2013). Noble Gases as Tracers of Mantle Processes and Magmatic Degassing, pp. 371-391. In: Burnard P. (eds) The Noble Gases as Geochemical Tracers. Advances in Isotope Geochemistry, Springer, Berlin, Heidelberg.

Moreira, M., and Sarda, P. (2000). Noble gas constraints on degassing process. Earth and Planetary Science Letters, 176, pp. 375-386.

Morgan, L.E., Renne, P.R., Taylor, R.E., and Wolde Gabriel, G. (2009). Archaeological age constraints from extrusion ages of obsidian: Examples from the Middle Awash, Ethiopia. Quaternary Geochronology, 4(3), pp. 193-203, doi.org/10.1016/j.quageo.2009.01.001.

Moune, S., Gauthier, P.-J., and Delmelle, P. (2010), Trace elements in the particulate phase of the plume of Masaya volcano, Nicaragua. Journal of Volcanology and Geothermal Research, 193(3-4), pp. 232-244.

Moune, S., Faure, F., Gauthier, P.J., and Sims, K.W.W. (2007). Pele's hairs and tears: natural probe of volcanic plume. Journal of Volcanology and Geothermal Research, 164, pp. 244-253, doi.org/10.1016/j.jvolgeores.2007.05.007.

Muenow D. W. (1973). High temperature mass spectrometric gas-release studies of Hawaiian volcanic glass: Pele's tears. Geochimica et Cosmochimica Acta, 37(6), pp. 1551- 1561.

Nesbitt, H.W., and Young, G.M. (1982). Early Proterozoic climates and plate motions inferred from major element chemistry of lutites, Nature, 299, pp. 715-717.

Nomade, S., Knight, K.B., Beutel, E., Renne, P. and Verati, C., Féraud, G., Marzoli, A., Youbi, N., and Bertrand, H. (2007). Chronology of the Central Atlantic Magmatic Province: implications for the Central Atlantic rifting processes and the Triassic-Jurassic biotic crisis. Palaeogeography, Palaeoclimatology, Palaeoecology, 246, pp. 326-344.

Nuccio, P.M., and Paonita, A. (2000). Investigation of the noble gas solubility in H_2O-CO_2 bearing silicate liquids at moderate pressure II: the extended ionic porosity (EIP) model. Earth and Planetary Science Letters, 183, pp. 499-512.

Nyland, R.E., Panter, K.S., Rocchi, S., Di Vincenzo, G., Del Carlo, P., Tiepolo, M., Field, B., and Gorsevski, P. (2013). Volcanic activity and its link to glaciation cycles: Single-grain age and geochemistry of Early to Middle Miocene volcanic glass from ANDRILL AND-2A core, Antarctica. Journal of Volcanology and Geothermal Research, 250, pp. 106-128.

Ozawa, A., Tagami, T., and Kamata, H. (2006). Argon isotopic composition of some Hawaiian historical lavas. Chemical Geology, 226, pp. 66-72.

Ozima, M., and Podosek, P.A. (2002). Noble gas geochemistry, 2nd eds. Cambridge University Press, Cambridge, pp. 286.

Palomar, T., de la Fuente, D., Morcillo, M., Alvarez de Buergo, M., Vilarigues, M. (2019), Early stages of glass alteration in the coastal atmosphere. Building and Environment, 147, pp. 305-313.

Palomar, T., Chabas, A., Bastidas, D.M., de la Fuente, D., and Verney-Carron, A. (2017). Effect of marine aerosols on the alteration of silicate glasses. Journal of Non-Crystalline Solids, 471, pp. 328-337.

Palomar, T., and Llorente, I. (2016). Decay processes of silicate glasses in river and marine aquatic environments. Journal of Non-Crystalline Solids, 449, pp. 20-28.

Paonita, A. (2005). Noble gas solubility in silicate melts: a review of experimentation and theory, and implications regarding magma degassing processes. Annals of Geophysics, 48, pp. 647-669.

Paonita, A., Gigli G., Gozzi, D., Nuccio, P.M., Trigila, R., 2000, Investigation of He solubility in H2O-CO2 bearing silicate liquids at moderate pressure: an experimental method. Earth and Planetary Science letters, 181, pp. 595-604.

Pasteels, N., Kolios, A., Boven, A., and Saliba, E. (1986). Applicability of the K-Ar method to whole-rock samples of acid lava and pumice: case of the upper pleistocene domes and pyroclasts on Kos Island, Aegean sea, Greece. Chemical Geology, 57, pp. 145-154.

Pérez, W. and Freundt, A. (2006), The youngest highly explosive basaltic eruptions from Masaya Caldera (Nicaragua): Stratigraphy and hazard assessment, Geological Society of America Special Papers, 412, pp. 189-207.

Pérez, W., Freundt, A., Kutterolf, S., and Schmincke, H.U. (2009). The Masaya Triple Layer: A 2100 year old basaltic multi-episodic Plinian eruption from the Masaya Caldera Complex (Nicaragua). Journal of Volcanology and Geothermal Research, 179 (3-4), pp. 191-205.

Pinti, D., Wada, N. and Matsuda, J. (1999), Neon excess in pumice: volcanological implications. Journal of Volcanology and Geothermal Research, 88, pp. 279-289.

Polyak, V., McIntosh, W., Guven, N., and Provencio, P. (1998). Age and origin of Carlsbad cavern and related caves from $^{40}Ar/^{39}Ar$ of alunite. Science, 279, pp. 1919-1922.

Porritt, L.A., Russell, J.K., and Quane, S.L., (2012). Pele's tears and spheres: examples from Kilauea Iki. Earth and Planetary Science Letters, 333-334, pp. 171-180, doi.org/10.1016/j.epsl.2012.03.031.

Ramos, F.C., Wolff, J.A., Starkel, W., Eckberg, A., Tollstrup, D.L., and Scott, S. (2013). Insights into the petrogenetic histories of Columbia River flood basalts from strontium isotope ratio variations in plagioclase phenocrysts, in Reidel, S.P., Camp, V.E., Ross, M.E., Wolff, J.A., Martin, B.S., Tolan, T.L., and Wells, R.E., eds., The Columbia River Flood Basalt Province. Geological Society of America Special Paper, 497, doi:10.1130/2013.2497(09).

Ramos, F.C., Wolff, J.A., and Tollstrup, D.L. (2005). Sr isotope disequilibrium in Columbia River flood basalts: Evidence for rapid shallow-level open-system processes, Geology, 33(6), pp. 457-460, doi.org/10.1130/G21512.1.

Rampino, M.R. and Self, S. (1992). Volcanic winter and accelerated glaciation following the Toba super-eruption. Nature, 359, pp. 50-52.

Reichow, M.K., Saunders, A.D., White, R.V., Al'Mukhamedov, A.I., and Medvedev, A.Y. (2005). Geochemistry and petrogenesis of basalts from the West Siberian Basin: an extension of the Permo-Triassic Siberian Traps, Russia. Lithos, 9, pp. 425-452.

Reidel, S.P., and Tolan, T.L. (2013). The late Cenozoic evolution of the Columbia River system in the Columbia River Flood Basalt Province: in Reidel, S.P., Camp, V.E., et al., eds., The Columbia River

Flood Basalt Province, Geological Society of America Special Paper 497, 2497, pp. 201-213, doi: 10.1130/2013.2497(08).

Reidel, S.P., and Tolan, T.L., 1992, Eruption and emplacement of flood basalt: An example from the large-volume Teepee Butte Member, Columbia River Basalt Group: Geological Society of America Bulletin, v. 104, p. 1650-1671.

Reidel, S.P., and Fecht, K.R. (1987). The Huntzinger flow: Evidence of surface mixing of the Columbia River Basalt and its petrogenetic implication. Geological Society of America Bulletin, 98, pp. 664-677.

Reidel, S.P., Camp, V.E., Tolan, T.L., and Martin, B.S. (2013). The Columbia River flood basalt province: Stratigraphy, areal extent, volume, and physical volcanology. Geological Society of America Special Papers, 497(1), pp. 1-43, doi.org/10.1130/2013.2497(01).

Reidel, S.P., Tolan, T.L., Hooper, P.R., Beeson, M.H., Fecht, K.R., Bentley, R.D., and Anderson, J.L. (1989). The Grande Ronde Basalt, Columbia River Basalt Group; stratigraphic descriptions and correlations in Washington, Oregon, and Idaho, in Reidel, S.P., and Hooper, P.R., eds., Volcanism and Tectonism in the Columbia River Flood Basalt Province: Geological Society of America Special Paper, 239, pp. 21-53, doi.org/10.1130/SPE239-p21.

Renne, P.R., and Norman, E.B. (2001). Determination of the half-life of ^{37}Ar by mass spectrometry. Physical Review, Nuclear Physics, 63(4), pp. 47302-473023.

Renne, P.R., Mulcahy, S.R., Cassata, W.S., Morgan, L.E., Kelley, S.P., Hlusko, L.J., and Njau, J.K. (2012). Retention of inherited Ar by Alkali Feldspar xenocrysts in a magma: Kinetic constraints from Ba zoning profiles, Geochimica et Cosmochimica Acta, 93, pp. 129-142, doi: 10.1016/j.gca.2012.06.029.

Renne, P.R., Balco, G., Ludwig, K.R., Mundil, R., and Min, K. (2011). Response to the comment by W.H. Schwarz et al. on "Joint determination of ^{40}K decay constants and ^{40}Ar*/^{40}K for the Fish Canyon sanidine standard, and improved accuracy for ^{40}Ar/^{39}Ar geochronology" by P.R. Renne et al. (2010): Geochimica et Cosmochimica Acta, 75(17), pp. 5097-5100, doi: 10.1016/j.gca.2011.06.021.

Renne, P.R., Mundil, R., Balco, G., Min, K., and Ludwig, K.R. (2010). Joint determination of ^{40}K decay constants and ^{40}Ar*/^{40}K for the Fish Canyon sanidine standard, and improved accuracy for ^{40}Ar/^{39}Ar geochronology. Geochimica et Cosmochimica Acta, 74(18), pp. 5349-5367.

Renne, P.R., Swisher, C.C., Deino, A.L., Karner, D., Owens, B.T.L., and De Paolo, D.J., 1998, Intercalibration of standards, absolute ages and uncertainties in ^{40}Ar/^{39}Ar dating. Chemical Geology, 145(1-2), pp. 117-152, doi:10.1016/S0009-2541(97) 00159-9.

Renne, P.R, Sharp, W.D., Deino, A.L., Orsi, G., and Civetta, L. (1997), ^{40}Ar/^{39}Ar dating into the historical realm: Calibration against Pliny the Younger. Science, 277, pp. 1279-1280.

Richter, D.H., Eaton, J.P., Murata, K.J., Ault, W.U., and Krivoy, H.L. (1970). Chronological narrative of the 1959-1960 eruption of Kilaueau Volcano, Hawaii. U.S. Geological Survey, 73, pp. 537.

Roche, O., van Wyk de Vries B., and Druitt T.H. (2001). Sub-surface structures and collapse mechanisms of summit pit craters. Journal of Volcanology and Geothermal Research, 105(1-2), pp. 1-18.

Rodehorst, U., Schmincke, H.U. and Sumita, M. (1998). Geochemistry and petrology of Pleistocene ash units erupted at Las Cañadas edifice (Tenerife). Proceedings of the Ocean Drilling Program, Scientific Results, 157, pp. 315-28.

Roselieb, K., Rammensee, W., Btittner, H., and Rosenhauer, M. (1992). Solubility and diffusion of noble gases in vitreous albite. Chemical Geology, 96, pp. 241-266.

Ruzie, L. and Moreira M. (2010). Magma degassing process during Plinian eruptions. Journal of Volcanological and Geothermal Research, 192, pp. 142-150.

Rymer, H., van Wyk de Vries, B., Stix, J., and Williams-Jones, G. (1998). Pit crater structure and processes governing persistent activity at Masaya volcano, Nicaragua. Bulletin of Volcanology, 59(5), pp. 345 - 355.

Sarda, P., and Moreira, M. (2002). Vesiculation and vesicle loss in mid-ocean ridge basalt glasses: He, Ne, Ar elemental fractionation and pressure influence. Geochimica et Cosmochimica Acta, 66(8), pp. 1449-1458.

Sarda, P., and Graham, D. W. (1990). Mid-ocean ridge popping rocks: Implications for degassing at ridge crests. Earth and Planetary Science Letters, 97, pp. 268-289.

Schmincke, H.U. (1979). Age and crustal structure of the Canary Islands. A discussion. Journal of Geophysics, 46, pp. 217-224.

Schmincke, H.U. (1967). Stratigraphy and petrography of four Upper Yakima basalt flows in south-central Washington. Geological Society of America Bulletin, 78(11), pp. 1385-1422.

Schwanethal, J. (2006). ArMaDiLo instruction Manual, 11 p.

Self, S., Coffin, M.F., Rampino, M.R., and Wolff, J.A. (2015). Large Igneous Provinces and Flood Basalt Volcanism. The Encyclopedia of Volcanoes, Elsevier, pp. 441-455, doi: 10.1016/B978-0-12-385938-9.00024-9.

Self, S., Widdowson, M., Thordarson, T., and Jay, A.E. (2006). Volatile fluxes during flood basalt eruptions and potential effects on the global environment: A Deccan perspective. Earth and Planetary Science Letters, 248(1-2), pp. 517-531, doi: 10.1016/j.epsl.2006.05.041.

Self, S., Keszthelyi, L., and Thordarson, T. (1998). The importance of pahoehoe. Annual Review, Earth and Planetary Science Letters, 26, pp. 81-110.

Shea, T., Gurioli, L. and Houghton R. (2012). Transitions between fall phases and pyroclastic density currents during the AD 79 eruption at Vesuvius: building a transient conduit model from the textural and volatile record. Bulletin of volcanology, 74, pp. 2363-2381.

Shea, T., Houghton, B.F., Gurioli, L., Cashman, K.V., Hammer, J.E., and Hobden, B. (2010). Textural studies of vesicles in volcanic rocks: an integrated methodology. Journal of Volcanological and Geothermal Research, 190, pp. 271 - 289.

Sherlock S.C. and Kelley, S. (2002). Excess argon evolution in HP-LT rocks: a UVLAMP study of phengite and K-free minerals, NW Turkey. Chemical Geology, 182.

Sherlock, S.C., and Arnaud, N.O. (1999). Flat plateau and impossible isochrons: Apparent ^{40}Ar-^{39}Ar geochronology in a high-pressure terrain. Geochimica et Cosmochimica Acta, 63(18), pp. 2835-2838, doi: 10.1016/S0016-7037(99)00116-7.

Sherlock, S.C., Strachan, R.A., and Jones, K.A. (2009). High spatial resolution ^{40}Ar/^{39}Ar dating of pseudotachylites: geochronological evidence for multiple phases of faulting within basement gneisses of the Outer Hebrides. Journal of the Geological Society, 166(6), pp. 1049-1059.

Sherlock S.C., Kelley, S., Zalasiewicz, J.A., Schofield, D.I., Evans, J.A., Merriman, R.J., and Kemp, S. (2003). Precise dating of low-temperature deformation: strain-fringe analysis by ^{40}Ar/^{39}Ar laserprobe. Geology, 31, pp. 219-222.

Sherlock, S.C., Kelley, S., Simon, I., Nigel H., and Aral, H. (1999). ^{40}Ar-^{39}Ar and Rb-Sr geochronology of high-pressure metamorphism and exhumation history of the Tavsanli Zone, NW Turkey. Contributions to Mineralogy and Petrology, 137, pp. 46-58.

Sheth, H. (2016). Giant plagioclase basalts: Continental flood basalt-induced remobilization of anorthositic mushes in a deep crustal sill complex. Geological Society of America Bulletin, 128(5-6), pp. 916-925, doi: 10.1130/B31404.1.

Shibata, T., Takahashi, E., and Matsuda, J. (1998). Solubility of neon, argon, krypton, and xenon in binary and ternary silicate systems: a new view of noble gas solubility. Geochimica et Cosmochimica Acta, 62, pp. 1241-1253.

Shimozuru, K. (1994). Physical parameters governing the formation of Pele's hair and tears. Bulletin of Volcanology, 56, pp. 217-219, doi.org/10.1007/BF00279606.

Smith, N.J., and Kokelaar, B.P. (2013). Proximal record of the 273 Ka Poris caldera-forming eruption, Las Cañadas, Tenerife. Bulletin of volcanology, 75(768).

Smith, G.A. (1988). Sedimentology of proximal to distal volcaniclastics dispersed across an active foldbelt: Ellensburg Formation (late Miocene), Central Washington. Sedimentology, 35(6), pp. 953-977, doi:10.1111/j.1365-3091.1988.tb01740.x.

Smith, G.A. (1987). The influence of explosive volcanism on fluvial sedimentation: the Deschutes Formation (Neogene) in Central Oregon. Journal of Sedimentary Petrology, 57(4), pp. 613-629, doi.org/10.1306/212f8bbb-2b24-11d7-8648000102c1865d.

Spadaro, F., Lefèvre, R.A., Ausset, P. (2002). Experimental rapid alteration of basaltic glass: implications for the origins of atmospheric particulates. Geology, 30, pp. 671-674.

Spampinato, L., and Salerno, G. (2012). Heat and SO_2 Emission Rates at Active Volcanoes - The Case Study of Masaya, Nicaragua. New Achievements in Geoscience book, Chapter 5, pp. 107-130.

Spray, J.G., Kelley, S.P., and Reimold, W.U. (1995). Laser probe $^{40}Ar/^{39}Ar$ dating of coesite- and stishovite-bearing pseudotachylytes and the age of the Vredefort impact event. Meteoritics, 30, pp. 335-343.

Steiger, R.H., and Jäger, E. (1977). Subcommission on geochronology: Convention on the use of decay constants in geo- and cosmochronology. Earth and Planetary Science Letters, 36(3), pp. 359-362, doi.org/10.1016/0012-821X(77)90060-7.

Stephens, K.J. and Wauthier, C. (2018). Satellite geodesy captures offset magma supply associated with lava lake appearance at Masaya Volcano, Nicaragua. Geophysical Research Letters, 45(6), pp. 2669–2678, doi: 10.1002/2017gl076769.

Stix, J. (2007). Stability and instability of quiescently active volcanoes: The case of Masaya, Nicaragua. Geology, 35(6), pp. 535-538.

Stix, J., de Moor, J. M., Rüdiger, J., Alan, A., Corrales, E., D'Arcy, F., Diaz, J., and Liotta, M. (2018). Using drones and miniaturized instrumentation to study degassing at Turrialba and Masaya volcanoes, Central America. Journal of Geophysical Research, Solid Earth, 123, pp. 6501-6520. https://doi.org/10.1029/2018JB015655

Stock, M., Taylor, R., and Gernon, T. (2012). Triggering of major eruptions recorded by actively forming cumulates, Scientific reports, 2, pp. 731.

Stoenner, R.W., Schaeffer, O.A., and Katcoff, S. (1965). Half-lives of ^{37}Ar, ^{39}Ar, and ^{42}Ar. Science, 148, pp. 1325-1328.

Stoiber, R.E., Williams, S.N., and Huebert, B.J. (1986). Sulfur and halogen gases at Masaya caldera complex, Nicaragua: Total flux and variations with time. Journal of Geophysical Research, 91(B12), pp. 12215-12231.

Stovall, W.K., Houghton, B.F., Hammer, J.E., Fagents, S.A., and Swanson, D.A. (2012). Vesiculation of high fountaining Hawaiian eruptions: episodes 15 and 16 of 1959 Kilauea Iki. Bulletin of Volcanology, 74, pp. 441-455, doi.org/10.1007/s00445-011-0531-7.

Stroncik, N.A., and Niedermann, S. (2016). He, Ne and Ar isotope signatures of mid-ocean ridge basalts and their implications for upper mantle structure: a case study from the mid-Atlantic Ridge at 4-12°S. Geochimica et Cosmochimica Acta, 183, pp. 94-105.

Sumino, H., Ikehata, K., Shimizu, A., Nagao, K., and Nakada, S. (2008). Magmatic processes of Unzen volcano revealed by excess argon distribution in zero-age plagioclase phenocrysts. Journal of Volcanology and Geothermal Research, 175(1-2), pp. 189-207.

Swanson, D.A., Wright, T.L., Hooper, P.R., and Bentley, R.D. (1979). Revisions in Stratigraphic Nomenclature of the Columbia River Basalt Group: U.S. Geological Survey Bulletin, 1457G, 59 p.

Swindle, T. D. (2002). Noble Gases in the Moon and Meteorites: Radiogenic Components and Early Volatile Chronologies. Reviews in Mineralogy and Geochemistry, 47, pp. 101-124.

Tait, S., Thomas, R., Gardner, J., and Jaupart, C. (1998). Constraints on cooling rates and permeabilities of pumice in an explosive eruption jet from colour and magnetic mineralogy. Journal of Volcanology and Geothermal Research, 86, pp. 79-91.

Thomas, N., Jaupert, C., and Vergniolle, S. (1994), On the vesicularity of pumice. Journal of Geophysics Research, 99(15), pp. 633-644.

Tobin, T.S., Bitz, C.M., and Archer, D. (2017). Modelling climatic effects of carbon dioxide emissions from Deccan Traps volcanic eruptions around the Cretaceous-Paleogene boundary. Palaeogeography, Palaeoclimatology, Palaeoecology, 478, pp. 139-148, doi: 10.1016/j.palaeo.2016.05.028.

Toutain, J.P., Quisefit, J.P., Briole, P., Aloupogiannis, P., Blanc, P., and Robaye, G. (1995). Mineralogy and chemistry of solid aerosols emitted from Mount Etna. Geochemical Journal of Japan, 29, pp. 163-173. doi.org/10.2343/geochemj.29.163.

Turner, G. (1977). Potassium-argon chronology of the moon. Physics and Chemistry of the Earth, 10(3), pp. 145-195.

Turner, G., Knott, S. F., Ash, R. D., and Gilmour, J. D. (1997). Ar/Ar chronology of the Martian meteorite ALH84001: Evidence for the timing of the early bombardment of Mars. Geochimica et Cosmochimica Acta, v. 61, p. 3835-3850.

Turrin, B. D., Swisher, C. C., and Deino, A. L. (2010). Mass discrimination monitoring and intercalibration of dual collectors in noble gas mass spectrometer systems. Geochemistry, Geophysics, Geosystems, 11.

U.S. Energy Research and Development Administration (1976). Preliminary Feasibility Study on Storage of Radioactive Wastes in Columbia River Basalts: U.S. Energy Research and Engineering Division Report ARH-ST-137 under contract E(45-1)-2130, 183 p.

Van Wyk de Vries, B. (1993). Tectonics and magma evolution of Nicaraguan volcanic systems. Ph.D. Thesis, The Open University, Milton Keynes (UK).

Verati, C., and Jourdan F., 2014, Modelling Effect of Sericitization of Plagioclase on the $^{40}K/^{40}Ar$ and $^{40}Ar/^{39}Ar$ Chronometers: Implication for Dating Basaltic Rocks and Mineral Deposits. Geological Society, London, Special Publications, 378(1), pp. 155-74, doi:10.1144/SP378.14.

Villa, I. M. (1997). Direct determination of ^{39}Ar recoil distance. Geochimica et Cosmochimica Acta, 61, pp. 689-691.

Villemant, B., Salaün, A., and Staudacher, T. (2009). Evidence for a homogeneous primary magma at piton de la Fournaise (la Reunion): a geochemical study of matrix glass, melt inclusions and Pele's hair of the 1998-2008 eruptive activity. Journal of volcanology and geothermal research, 184, pp. 79-92.

Villermaux E., 2012, The formation of filamentary structures from molten silicates: Pele's hair, angel hair, and blown clinker, Comptes Rendus Mécanique, v. 340(8), p. 555-564,

Vogel, N., Nomade, S., Negash, A., and Renne, P.R. (2006). Forensic $^{40}Ar/^{39}Ar$ dating: a provenance study of Middle Stone Age obsidian artifacts from Ethiopia: Journal of Archaeological Science, 33(12), pp. 1749-1765, doi: 10.1016/j.jas.2006.03.008.

Walker, J.A. (1989). Caribbean arc tholeiites, Journal of Geophysics Research, 94(10), pp. 539-10,548.

Walker, J.A., Williams, S.N., Kalamarides, R.I., and Feigenson, M.D. (1993). Shallow open-system evolution of basaltic magma beneath a subduction zone volcano - The Masaya Caldera Complex, Nicaragua. Journal of Volcanology and Geothermal Research, 56(4), pp. 379-400.

Walker, G.P.L., and Croasdale, R. (1972). Characteristics of some basaltic pyroclastics. Bulletin of Volcanology, 35 (2), pp. 303-317, doi.org/10.1007/BF02596957.

Wallace P.J., Dufek J., Anderson A.T., and Zhang, Y. (2003). Cooling rates of Plinian-fall and pyroclastic-flow deposits in the Bishop Tuff: inferences from water speciation in quartz-hosted glass inclusions, Bulletin of Volcanology, 65(2-3), pp. 105-123.

Wang, S., Zai, M., Hu, s., Sang H., and Qiu, J. (1986). $^{40}Ar/^{39}Ar$ age spectrum for biotite separated from Qingyuan tonalite, NE China. Scientia Geologica Sinica, 1, pp. 97-100.

Warren, C.J., Kelley, S.P., Sherlock, S.C., and McDonald, C.S. (2012). Metamorphic rocks seek meaningful cooling rate: Interpreting $^{40}Ar/^{39}Ar$ ages in an exhumed ultra-high pressure terrane. Lithos, 155, pp. 30-48.

Whattman, S.A., and Stern, R.J. (2016). Arc magmatic evolution and the construction of continental crust at the Central American Volcanic Arc system. International Geology Review, 58(6), pp. 653-686.

Whitman, A.G., and Sparks, R.S.J. (1986). Pumice. Bulletin of Volcanology, 48, p. 209-233.

Wignall, P.B. (2001). Large igneous provinces and mass extinctions. Earth Science Reviews, 53(1-2), pp. 1-33, doi.org/10.1016/S0012-8252(00)00037-4.

Wilkinson, M. (2013), Understanding Extraneous Argon in Silicic Volcanic Products using $^{40}Ar/^{39}Ar$ Laser probe Geochronology. Ph.D. thesis, The Open University, 450 p.

Williams, S.N. (1983). Geology and eruptive mechanisms of Masaya Caldera Complex, Nicaragua. Ph.D. Thesis, Dartmouth College, Hanover (USA), 216 p.

Williams-Jones, G., Rymer, H., and Rothery, D.A. (2003). Gravity changes and passive SO_2 degassing at the Masaya caldera complex, Nicaragua. Journal of Volcanology and Geothermal Research, 123(1-2), pp. 137-160.

Wilson, M. (1997). Thermal evolution of the central Atlantic passive margins: Continental break-up above a Mesozoic super-plume. Journal of Geological Society of London, 154, pp. 491-495.

Wolff, J.A. (2009). The origin of coarse antecrysts in flood basalt lavas: a LA-MC-ICPMS Sr-isotope microanalytical study of the Columbia River Basalts. Geological Society of America Abstracts with Programs, 45(7), p. 894.

Wolff, J.A. (1985). Zonation, mixing and eruption of silica undersaturated alkaline magma: a case study from Tenerife, Canary Islands. Geological Magazine, 122, pp. 623-640

Wolff, J.A., and Storey, M. (1984). Zoning in highly alkaline magma bodies. Geological Magazine, 121, pp. 563-575.

Wolff, J.A., and Ramos, F.C. (2013). Source materials for the main phase of the Columbia River Basalt Group: Geochemical evidence and implications for magma storage and transport, in Reidel, S.P., Camp, V.E. et al., eds., The Columbia River Flood Basalt Province. Geological Society of America Special Papers, 497(11), pp. 273-291, doi:10.1130/2013.2497(11).

Wolff, J.A., Ramos, F.C., Hart, G.L., Patterson, J.D., and Brandon, A.D. (2008). Columbia River flood basalts from a centralized crustal magmatic system. Nature Geoscience, v. 1, p. 177- 180, doi.org/10.1038/ngeo124.

Wolff, J.A., Grandy, J.S. and Larson, P.B. (2000). Interaction of mantle-derived magma with island crust? Trace element and oxygen isotope data from the Diego Hernández Formation, Las Cañadas, Tenerife. Journal of Volcanology and Geothermal Research, 103, pp. 343-366.

Woods, A.W., and Cowan, A. (2009). Magma mixing triggered during volcanic eruptions. Earth and Planetary Science Letters, 288(1–2), pp. 132-137.

Yamamoto, J., and Burnard, P.G. (2005). Solubility controlled noble gas fractionation during magmatic degassing: Implications for noble gas compositions of primary melts of OIB and MORB. Geochimica et Cosmochimica Acta, 69(3), pp. 727-734,

York, D. (1969). Least squares fitting of a straight line with correlated errors. Earth and Planetary Science Letters, v. 5, p. 320-324, doi.org/10.1016/S0012-821X(68)80059-7.

Young, E.D., Galy, A., and Nagahara, H. (2002). Kinetic and equilibrium mass dependent isotope fractionation laws in nature and their geochemical and cosmochemical significance. Geochimica et Cosmochimica Acta, 66, pp. 1095-1104.

Zimanowski, B., Büttner, R., Lorenz, V., and Häfele, H.G. (1997). Fragmentation of basaltic melt in the course of explosion volcanism. Journal of Geophysics Research, 102, pp. 803-814, doi.org/10.1029/96JB02935.

Zimmerman, J.L. (1972). L'eau et les gaz dans les principals familles de silicates. Science de la Terre Memoir, 22, pp. 1-188.

Appendix A1:

The Ar/Ar dating technique

A1.1 Introduction

Since its formalisation as an isotope dating method (Merrihue and Turner, 1966), the Ar/Ar technique has become one of the most important and widely tools for dating geological materials. It has been successfully used to date volcanic deposits and timing of eruptions (Renne et al., 1997, Bigazzi et al., 2008), metamorphic rocks and metamorphic events (Warren et al., 2012); detrital minerals in sediments (Henderson et al., 2011), cave deposits (Polyak et al., 1998), clay minerals (Clauer et al., 2012), pseudotachylytes in fault zones (Kelley et al., 1994) and terrestrial sand grains (Kelley and Bluck, 1989). Extra-terrestrial samples like lunar soil grains (Burgess and Turner, 1998), meteorite impacts (Spray et al., 1995), Martian rocks (Turner et al., 1997) and moon rocks (Turner, 1977; Swindle, 2002) have also been dated with success.

The application of the Ar/Ar dating technique brought some new important advantages in determining the age of a rocks compared to the old K/Ar method. The introduction of the laser ablation technique to extract Ar isotopes from the sample has permitted to measure the parent-daughter ratio in the same aliquot of the sample. This has allowed a reduction of the sample size up to milligrams of material increasing the possibility to analyse even more homogeneous samples (McDougall & Harrison, 1999). In particular, the use of the in-situ laser ablation has permitted to extract Ar isotopes with a spatial resolution of 2-3 μm (Kelley et al., 1994) enabling the dating of complicated samples with complex cooling histories (Sherlock and Arnaud, 1999). This was not possible with the old K/Ar technique where the parent and daughter isotopes were measured with different techniques within two different sample aliquots (up to a few g in size) not always homogeneous with respect to their composition and geological history (McDougall & Harrison, 1999).

Compared to the K/Ar technique where only single grain fusion was possible, in the Ar/Ar technique the use of the laser ablation permitted the application of the step-heating practice. This allows an incremental heating of the sample by increasing the laser power step by step during the experiment. The release of Ar isotopes trapped within different reservoirs (crystal lattice, fluid or melt inclusions) happen at different temperatures and thus, at different stages of the analysis. The identification of the variations of the Ar

isotopic signal during the experiment permits a better interpretation of the Ar/Ar ages. The combination of these advantages with the improvement of the mass spectrometers have increased both the accuracy and the precision of the Ar/Ar method against the previous K/Ar technique.

In the following paragraphs are briefly presented physical principles and theoretical aspects of this powerful technique. Source of errors, correction factors and data presentation are also discussed. Further detailed information can be found in Dalrymple & Lanphere (1971), Lanphere & Dalrymple (1971), Kelley et al. (1994), McDougall & Harrison (1999), Kelley (2002).

A1.2 Argon and its isotopes: *definition and nomenclature*

Argon is a noble gas with atomic number 18. It has five isotopes: three are natural stable isotopes (^{36}Ar, ^{38}Ar, ^{40}Ar) with an atmospheric concentration of 0.3336±0.0004 % ^{36}Ar, 0.0629±0.0001 % ^{38}Ar and 99.6035±0.0004 % for ^{40}Ar and relative ratio of $^{40}Ar/^{36}Ar$ = 298.56± 0.15, $^{38}Ar/^{36}Ar$ = 0.1886±0.0002 (Lee et al., 2006); the remaining two isotopes (^{37}Ar, ^{39}Ar) are unstable and are only produced from neutron interactions with Ca, Cl and K during irradiation within a nuclear reactor. ^{39}Ar decays to ^{39}K by beta-emission with a half-life of 269±3 years (Stoenner et al., 1965) while ^{37}Ar decays with a half-life of 34.95±0.08 days (Renne and Norman, 2001).
In the Ar/Ar dating it is usual to distinguish:

Atmospheric Argon (Ar_{atm}): argon with isotopic composition of the present-day atmosphere ($^{40}Ar/^{36}Ar$ and 298.56±0.31 - Lee et al., 2006).

Radiogenic Argon ($^{40}Ar^*$): argon formed by in situ decay of ^{40}K (half-life of 1.25 Ga). For terrestrial sample it is calculated as follow: $^{40}Ar^* = {}^{40}Ar_{total} - (^{36}Ar_{atm} \times 298.56)$. Where $^{40}Ar_{total}$ is the total ^{40}Ar measured, $^{36}Ar_{atm}$ is the atmospheric ^{36}Ar.

Cosmogenic argon: argon produced by cosmic-ray interactions with Ca, Ti, Fe. It must be corrected only for analysis of extra-terrestrial material

Neutron-induced argon: argon produced by the interaction of neutron with Cl, Ca, K during irradiation in a nuclear reactor.

Trapped argon: argon which is trapped in a rock or mineral at the time of its formation or during a subsequent event. For terrestrial samples it has an atmospheric composition.

Extraneous argon (*inherited and excess*): portion of $^{40}Ar/^{36}Ar$ in excess with respect to the atmospheric value. It can derive from various processes.

Inherited argon: argon introduced into rocks or minerals during their formation by contamination from older material.

Excess argon ($^{40}Ar_E$): portion of ^{40}Ar neither radiogenic nor atmospheric incorporated into the sample during processes not related to the in-situ decay of ^{40}K.

A1.3 Theoretical basis of the Ar/Ar dating:

The Ar/Ar technique represents a variation of the K/Ar technique and it is founded on the same assumptions of the previous method:

1) The decay of ^{40}K must be independent of its physical state and not affected by differences in temperature and pressure.

2) The natural $^{40}K/K$ ratio must be a constant.

3) All radiogenic $^{40}Ar^*$ measured in the sample must result from in situ decay of ^{40}K.

4) If a non-radiogenic ^{40}Ar is detected inside the sample it must be corrected for. These corrections are easy for terrestrial samples where the constant $^{40}Ar/^{36}Ar$ ratio for contaminating atmospheric argon is 298.56±0.31 (Lee et al., 2006). In extra-terrestrial samples (especially meteorites) the $^{40}Ar/^{36}Ar$ ratio is not accurately known and the corrections are more difficult.

5) The sample, in order to be dated, must be a K-bearing material that has accumulated and retained sufficient radiogenic $^{40}Ar^*$ through time. In particular, the sample must have remained in a closed system since the event being dated.
   This assumption is sometimes invalid due to the processes of gain and loss of the argon or potassium during complex geological and thermal events. For this reason, this assumption is commonly violated in geological samples.

Like the K/Ar method, the Ar/Ar is based on the physical principle of the constant decay of the unstable parent isotope ^{40}K (half-life of 1.25 Ga) to the more stable daughter isotope ^{40}Ar. This process involves a series of decay reactions that transform 89.52% of the total ^{40}K in ^{40}Ca (by β^- emission) and the remaining 10.48% in radiogenic argon $^{40}Ar^*$ (by orbital electron capture).

The main difference between the Ar/Ar and the K/Ar technique is how the parent-daughter ratio is measured and thus the age of the sample determined. In the K/Ar technique the age is directly calculated by measuring the two isotopes in separate aliquots of the sample through different techniques (flame photometry and mass spectrometry). In the Ar/Ar technique the parent-daughter ratio is measured (through mass spectrometry) in the same aliquot of sample only after its irradiation in a nuclear reactor. Fast neutrons, generated by the reactor, are incorporated inside the structure of ^{39}K atoms that are transformed into the ^{39}Ar atoms by protons emission. The amount of ^{39}Ar, produced during this process, depends on the original content of ^{39}K within the sample, duration of the irradiation and dose of radiation received by the sample. As the natural ratio of $^{40}K/^{39}K$ is constant, the ratio between radiogenic $^{40}Ar^*$ (produced by the decay of ^{40}K) and ^{39}Ar (produced by irradiation of ^{39}K) is constant. Therefore, the $^{40}Ar^*/^{40}K$ ratio is proportional to the $^{40}Ar^*/^{39}Ar$ ratio, and the following equation for the age calculation can be applied:

$$age = \frac{1}{\lambda} In\left\{\left(\frac{^{40}Ar^*}{^{39}Ar}\right)J + 1\right\}$$ Where:

λ represents the total decay constant for ^{40}K. It comprises the decay of ^{40}K to ^{40}Ar by electron capture and gamma emission, the decay of ^{40}Ar to ^{40}Ca by beta emissions and the decay of ^{40}K to ^{40}Ar by electron capture.

J represents the irradiation parameter calculated from standard minerals of known age (derived from K/Ar dating) irradiated together with the unknown-age sample. The J value depends on the duration of the irradiation, the neutron flux and the neutron capture cross section.

A1.4 Source of errors:

When an age is obtained its precision is expressed through the total age error (2σ). The 2σ account for internal analytical error (1σ) coming from isotope measurements and external errors coming from other sources. The internal analytical error is mainly function of the amount of Ar isotopes extracted during the analysis; the higher this value, the smaller the associated 1σ error. External errors can be attributed to errors coming from the calculation of J-value, K/Ar age of the standard, atmospheric argon concentration, interference reaction of Ca, K and Cl, standard intercalibration and decay constant. The analytical error associated with laboratory measurements and external errors (2σ) can be calculated using the following equation:

$$\sigma_t^2 = \frac{J^2\sigma_R^2 + R^2\sigma_J^2}{\lambda^2\left(1+RJ\right)^2}$$

σ_t is the final error on the age, R is the $^{40}Ar^*/^{39}Ar$ ratio, λ is the combined decay constant of ^{40}K, J is the irradiation parameter, σ_R is the error on the $^{40}Ar^*/^{39}Ar$ ratio as measured and σ_J is the error on the J value.

Where:

In the next paragraphs are briefly explained the external sources of error in age calculation and basic concept for their reduction. For detailed explanation of error sources and corrections applied prior the age calculation see McDougal and Harrison (1999).

Atmospheric contamination

Subtraction of atmospheric derived ^{40}Ar from the total amount of measured ^{40}Ar is routinely done in order to determine the right abundance of $^{40}Ar^*$ (radiogenic) for age calculation. This correction is necessary because geological samples trap ^{40}Ar with atmospheric composition when they enter in contact with a reservoir with an atmospheric Ar ratio (water, atmosphere, country rock) during cooling events. The $^{40}Ar/^{36}Ar$ = 298.56±0.15 value (Lee et al., 2006) is used to correct for atmospheric content. This correction is also made in order to subtract any contribution of atmospheric argon coming from the vacuum system (McDougal and Harrison, 1999).

J-value

The J parameter represents the flux of neutrons received by the sample during the irradiation. Its value must be sufficiently high to produce enough $^{39}Ar^*$ for allowing precise measuring during the analysis and low enough to reduce interference reactions from Ca, K and Cl. The J value must be also selected in function of the age of the sample and of its K/Ca ratio. In order to monitor and evaluate the J value, a standard mineral of known age is irradiated together with the unknown age sample. J value uncertainty can be reduced by constraining the geometry of the standard relative to the unknown and analysing more flux monitor aliquots per standard location (McDougal and Harrison, 1999).

Interference reactions

During the irradiation process, atoms of ^{36}Ar, ^{37}Ar, ^{38}Ar, ^{39}Ar and ^{40}Ar are produced by the interaction of fast neutrons with atoms of Ca, K and Cl. These reactions have to be corrected in order to know the real amount of Ar isotopes naturally occurring inside the sample. Most of them, however, could be neglected because have low production rates in relation to the purpose of Ar-dating. The amount of these interferences varies with the

value of the J parameter and with the position of the sample inside the reactor. To reduce these unwanted reactions it is possible to shield the sample with a cadmium/aluminium foil or selecting an appropriate J-value for each irradiation process. A complete list of these reactions can be found in McDougal and Harrison (1999).

Correction for K:

Neutron-induced reactions on K produce ^{37}Ar, ^{38}Ar, ^{39}Ar and ^{40}Ar. The only necessary correction is for ^{40}Ar production because the amount of the other isotopes respect to the ^{40}Ar is very low for terrestrial samples and thus negligible. It is important to determine the ^{40}Ar from K in order to establish the right concentration of $^{40}Ar^*$ in the sample. The total of ^{40}Ar produced by K is detected measuring its concentration in a K_2SO_4 salt irradiated together with the unknown sample.

Correction for Ca:

During the irradiation process the ^{38}Ar, ^{40}Ar, ^{37}Ar, ^{36}Ar and ^{39}Ar isotopes are produced by Ca. If corrections for ^{38}Ar and ^{40}Ar are negligible in terrestrial samples this is not true for ^{37}Ar, ^{36}Ar and ^{39}Ar especially when the K/Ca ratio of the sample is very low. Because the ^{37}Ar is only produced by Ca (apart a negligible quantity from ^{39}K) it is used to correct the abundance of the other two major interference-derived isotopes (^{36}Ar and ^{39}Ar). The correction for the ^{39}Ar and ^{36}Ar produced from irradiation of Ca are done using the measured ^{37}Ar concentration and a correction value determined from CaF_2 salt irradiated together the unknown.

Correction for Cl:

^{36}Ar and ^{38}Ar derive also from the decay of ^{36}Cl and ^{38}Cl respectively produced by neutron interaction with ^{35}Cl and ^{37}Cl. Because of the slow decay of ^{36}Cl to ^{36}Ar (half-life $3x10^5$ years), the amount of ^{36}Ar produced from the ^{36}Cl decay would not cause an increase in ^{36}Ar sufficient to introduce a significant error in the application of the atmospheric ^{40}Ar based upon ^{36}Ar. Moreover the Cd shielding of the reactor contribute to reduce the production of these interfering isotopes. For this reason correction for ^{36}Ar is done only if the analysis are conducted after one year since the irradiation. The amount of ^{36}Ar is detected on KCl salts irradiated together with the unknown.

Mass spectrometer discrimination

Another correction applied to each isotope after the analysis is related to any mass-dependant bias introduced by the ionization of the sample in the mass spectrometer. This correction is known as mass discrimination correction and it changes in function of the design and components of mass spectrometer. The mass discrimination refers to the difference between the known isotopic ratio of a sample (calibration gas) and the ratio actually given by the machine for that sample. The calibration gas can be a mixture of gasses (^{40}Ar, ^{38}Ar, ^{36}Ar, He, Ne, Kr, Xe) with standard ratios derived from a calibration bottle or can derive from an online-air pipette which permits some of the air outside the machine to be analysed. The mass discrimination correction is always done for all the samples but becomes particularly relevant for samples with low concentrations of ^{40}Ar*. Any variation in the mass discrimination can have a profound effect on the calculated ^{40}Ar/^{39}Ar age (Turrin et al., 2010).

Standard

As previously mentioned, it is necessary to irradiate together with the unknown, a standard sample of known age in order to evaluate the J value. The age of the standard is usually obtained cross-calibrating the ages obtained from different dating techniques (e.g. K/Ar, U/Pb, astronomical polarity time scale). This means that the precision of Ar/Ar technique is limited by an external parameter represented by the precision of the age of the standard mineral. The most used international standards are: hornblende Hb3gr and MMhb1, biotite GA1550 (McDougall and Wellman, 2011) and sanidines from Fish Canyon Tuff (Jourdan and Renne, 2007), Taylor Creek and Alder Creek (McDougall and Harrison, 1999).

Decay constant

The determination of the decay constant (λ) of ^{40}K is one of the main problems, and source of errors, that affect the precision of the Ar/Ar method. A lot of scientists have tried to determine, with a reasonable precision, a good value for the ^{40}K decay constant but different results have been obtained by different methodologies, selection criteria and statistical techniques (e.g. Steiger and Jager, 1977; Min et al, 2000; Renne et al., 2010; 2011). For many years the decay constant proposed by Steiger & Jäger (1977) – λ=5.543±0.010E^{-10} - has been accepted and routinely used by the Ar-dating community. More recently, after a critical revaluation of the decay constant, the new value of λ=5.5305±0.0135E^{-10} (Renne et al., 2011) is becoming more widely used.

Recoil of ^{39}Ar

Another source of errors comes from the ^{39}Ar recoil when very fine grain size samples (clays or basalts) are irradiated (Koppers et al., 2000; Jourdan et al., 2007). The collision of a fast neutron with a ^{39}K nucleus cause the expulsion of a ^{39}Ar nucleus causing a recoil effect of the same atom into the sample. This phenomenon causes a redistribution of ^{39}Ar inside the sample or, in some cases, a partial loss of it. When this happens, the ^{40}Ar/^{39}Ar ratio increase and anomalous apparent age are obtained during analysis. ^{39}Ar recoil (and ^{37}Ar if it is also present) recoil can be minimised by in vacuum-encapsulating the samples, in silica vials, prior to irradiation (Dong et al., 1995; Hall et al., 2013).

A1.5 Data presentation

After having applied all the corrections, the results are plotted in graphs in order to better interpret the age of the sample and evaluate possible disturbances of the Ar-system. Age spectrum and inverse isochron diagrams are the standards to display Ar/Ar results. A detailed explanation and a list of examples can be found in McDougall & Harrison (1999).

A1.5.1 Age spectrum

During step heating experiments a series ^{40}Ar/^{39}Ar ratios are acquired for each gas fraction released. These ratios, each of them corresponding to an apparent age of the sample, are plotted in an age spectrum diagram with the ^{40}Ar/^{39}Ar ratios on the ordinate and the cumulative percentage of ^{39}Ar released during the experiment on the abscissa. The determination of age of the sample

If the sample is remained in a closed system since its formation, without any thermal and chemical disturbances, the ^{40}Ar/^{39}Ar ratios should be uniform for each step of the experiment and the resulting shape of the age spectrum will be flat forming a 'plateau'. According to Fleck et al. (1977) a 'plateau' is "*a sequence of concordant steps with similar apparent ages scattered with a 95% confidence level, for a 50 % minimum proportion of total ^{39}Ar release*". Once a plateau is defined, the age of the rock is calculated as the error-weighted mean of the steps comprising the plateau. A key assumption for the application of the age-spectra is that the sample has an initial trapped atmospheric ^{40}Ar/^{36}Ar ratio.

If the analysed sample comes from an open system, such as a metamorphic or hydrothermal environment, the shape of the age spectra will be more complicated and possibly the apparent ages do not form a plateau (McDougall & Harrison, 1999). If the sample has experienced Ar loss the age spectrum will have a step-up shape with ages

increasing from low-temperature to high-temperature extraction steps (McDougall & Harrison, 1999). Otherwise if the sample has incorporated $^{40}Ar_E$ the age spectra may have a 'U'-shape reflecting the decrepitation of fluid inclusions at low temperatures and melt / solid inclusions at high temperature during mineral breakdown (McDougall & Harrison, 1999). Other disturbances of the Ar/Ar system can derive from grain size distribution (Lovera et al., 1989), argon recoil (Villa et al., 1997), effect of mixing between different gas reservoirs (Wang et al., 1980), slow cooling (Dodson, 1986) and phase changing during laboratory analysis (Zimmerman, 1972). In these circumstances the interpretation of the age spectrum is more problematic because the 'plateau method' is not immediately applicable to define an age. For this reason it is always better to compare the age spectra with isochrons and interpret the relative ages in light of the information given by the two graphic solutions (McDougall & Harrison, 1999).

A1.5.2 Inverse isochron

Contrariwise to the age-spectra where the plateau age assumes that the sample has an atmospheric component, the isochron age is free of any assumption given by the initial trapped Ar. The age is only calculated starting from the $^{39}Ar/^{40}Ar$ and $^{36}Ar/^{40}Ar$ ratios.
Using inverse isochrons it is possible to identify, for each step of the step-heating experiment, those measurements dominated by a radiogenic or trapped component. Data with a high radiogenic component are plotted close to the $^{39}Ar/^{40}Ar$ axis (X axis), whereas those with a high trapped argon are plotted close to the $^{36}Ar/^{40}Ar$ axis (Y axis). The age of the sample is given by the X-intercept (^{39}Ar) and the amount of the ^{40}Ar trapped within the sample is given by the Y-intercept. If the trapped argon/radiogenic argon ratio remains the same for all the measurements, all data points are plotted on top of each other or in a close clump. In this situation, a precise determination of the age of the sample is not always possible because the large error associate to the intercepts. A meaningful isochron, and thus a reliable age, is obtained when the ratio vary along the experiment reflecting some mixing between radiogenic and atmospheric component. If the gas released during the analysis is only composed by a mixture of atmospheric and radiogenic argon, the Y-intercept of the isochron will results at 1/298.56. In this case, all the trapped ^{40}Ar has an atmospheric origin. If the Y-intercept is lower than 1/298.56, $^{40}Ar_E$ is present in addition to atmospheric argon. Once the amount of $^{40}Ar_E$ is detected with the isochron method, it is possible to correct the age spectrum steps for excess ^{40}Ar. Uncorrected disturbed spectra can become plateaux after correction (Heizler and Harrison, 1988).

Appendix A2 – Data from Chapter 3

A2.1 Ar/Ar data of glass shards from the CRBG

Ar/Ar data (expressed in V) of step -heating analysis of sample BJ-1-10 (Analytical uncertainties are at the 1sigma level)

Step	40Ar	+/-	39Ar	+/-	38Ar	+/-	37Ar	+/-	36Ar	+/-	40Ar*/39Ar	+/-	Age (Ma)	+/- (Ma)	39Ar/40Ar	+/-	36Ar/40Ar	+/-
1	0.20831	0.00218	0.18224	0.00128	0.00233	0.00007	-0.00692	0.01057	0.00030	0.00002	0.65473	0.03987	11.23	0.68	0.87483	0.01102	0.00143	0.00011
2	0.24215	0.00285	0.20558	0.00250	0.00288	0.00007	0.02076	0.01057	0.00030	0.00002	0.74114	0.03734	12.71	0.64	0.84896	0.01436	0.00124	0.00010
3	0.20192	0.00146	0.23964	0.00124	0.00296	0.00010	-0.01154	0.01058	0.00017	0.00002	0.63168	0.02954	10.83	0.50	1.18679	0.01058	0.00084	0.00011
4	0.23057	0.00059	0.27700	0.00076	0.00341	0.00009	0.00693	0.01058	0.00017	0.00002	0.64441	0.02500	11.05	0.43	1.20135	0.00450	0.00076	0.00010
5	0.30891	0.00155	0.40826	0.00168	0.00510	0.00012	0.00693	0.01058	0.00019	0.00002	0.61446	0.01746	10.54	0.30	1.32164	0.00856	0.00063	0.00007
6	0.25304	0.00149	0.32610	0.00137	0.00404	0.00007	-0.00693	0.01059	0.00015	0.00002	0.64038	0.01490	10.98	0.25	1.28873	0.00933	0.00059	0.00006
7	0.09937	0.00064	0.13762	0.00057	0.00164	0.00008	0.03467	0.01059	0.00005	0.00002	0.61995	0.05029	10.63	0.86	1.38493	0.01058	0.00047	0.00023
8	0.27764	0.00125	0.39559	0.00185	0.00489	0.00009	-0.00231	0.01059	0.00013	0.00002	0.60609	0.01224	10.40	0.21	1.42483	0.00925	0.00046	0.00005
9	0.26706	0.00121	0.37285	0.00084	0.00479	0.00013	-0.01156	0.01060	0.00013	0.00002	0.61271	0.01879	10.51	0.32	1.39613	0.00705	0.00048	0.00009
10	0.62653	0.00218	0.88153	0.00287	0.01126	0.00017	0.03470	0.01060	0.00027	0.00002	0.62028	0.00843	10.64	0.14	1.40701	0.00670	0.00043	0.00004
11	0.21107	0.00119	0.29822	0.00128	0.00383	0.00010	0.02083	0.01061	0.00006	0.00002	0.64697	0.02358	11.10	0.40	1.41289	0.01001	0.00029	0.00011
Blank	0.00654	0.00016	0.00008	0.00002	0.00003	0.00001	0.00014	0.00002	0.00004	0.00001	J value =		0.009443135±0.0000472157					

Ar/Ar data (expressed in V) of step-heating analysis of sample SRD-1-2 (Analytical uncertainties are at the 1sigma level)

Step	40Ar	+/-	39Ar	+/-	38Ar	+/-	37Ar	+/-	36Ar	+/-	40Ar*/39Ar	+/-	Age (Ma)	+/- (Ma)	39Ar/40Ar	+/-	36Ar/40Ar	+/-
1	0.17532	0.00157	0.12387	0.00113	0.00149	0.00006	0.01644	0.00844	0.00032	0.00003	0.64783	0.08000	11.30	1.39	0.70652	0.00903	0.00182	0.00019
2	0.30939	0.00185	0.28995	0.00165	0.00373	0.00007	0.01644	0.00845	0.00045	0.00003	0.60530	0.03442	10.56	0.60	0.93719	0.00773	0.00145	0.00011
3	0.35622	0.00316	0.37537	0.00281	0.00484	0.00010	0.02125	0.00845	0.00042	0.00003	0.61720	0.02770	10.77	0.48	1.05376	0.01221	0.00117	0.00009
4	0.21778	0.00158	0.27080	0.00179	0.00354	0.00007	0.00686	0.00845	0.00015	0.00002	0.63772	0.02725	11.13	0.47	1.24346	0.01221	0.00069	0.00011
5	0.41290	0.00342	0.52346	0.00259	0.00643	0.00012	0.03566	0.00846	0.00034	0.00002	0.59297	0.01177	10.35	0.20	1.26775	0.01222	0.00083	0.00004
6	0.34552	0.00136	0.46679	0.00264	0.00609	0.00010	0.02127	0.00846	0.00020	0.00002	0.61410	0.01591	10.72	0.28	1.35095	0.00932	0.00057	0.00007
7	0.42248	0.00126	0.59071	0.00254	0.00780	0.00019	0.03088	0.00846	0.00021	0.00002	0.60673	0.01251	10.59	0.22	1.39819	0.00731	0.00051	0.00006
8	0.24895	0.00128	0.33394	0.00167	0.00449	0.00013	0.01647	0.00846	0.00010	0.00002	0.65746	0.02190	11.47	0.38	1.34138	0.00961	0.00040	0.00010
9	0.23107	0.00054	0.32433	0.00076	0.00420	0.00007	0.01648	0.00847	0.00011	0.00002	0.61261	0.02205	10.69	0.38	1.40358	0.00462	0.00047	0.00010
10	0.99956	0.00306	1.43266	0.00478	0.01817	0.00032	0.06457	0.00847	0.00039	0.00002	0.61732	0.00579	10.77	0.10	1.43329	0.00650	0.00039	0.00002
11	0.38807	0.00210	0.55188	0.00210	0.00698	0.00013	0.04053	0.00847	0.00019	0.00002	0.59927	0.01364	10.46	0.24	1.42210	0.00942	0.00050	0.00006
Blank	0.00546	0.00013	0.00006	0.00002	0.00002	0.00002	0.00012	0.00002	0.00004	0.00001	J value =		0.009606513±0.0000480326					

Ar/Ar data (expressed in V) of step-heating analysis of sample MA-1-5M_1 (Analytical uncertainties are at the 1sigma level)

Step	40Ar	+/-	39Ar	+/-	38Ar	+/-	37Ar	+/-	36Ar	+/-	40Ar*/39Ar	+/-	Age (Ma)	+/- (Ma)	39Ar/40Ar	+/-	36Ar/40Ar	+/-
1	0.02416	0.00040	0.01143	0.00027	0.00017	0.00003	-0.20453	0.18203	0.00012	0.00005	-1.02115	-1.31536	-20.94	22.49	0.47317	0.01351	0.00497	0.00209
2	0.05111	0.00062	0.02506	0.00026	0.00037	0.00004	-0.20458	0.18207	0.00019	0.00005	-0.22457	-0.63481	-5.46	10.78	0.49037	0.00783	0.00372	0.00104
3	0.05671	0.00071	0.03220	0.00035	0.00037	0.00004	0.32925	0.18215	0.00001	0.00005	1.68148	0.49476	28.30	8.26	0.56784	0.00945	0.00015	0.00094
4	0.04565	0.00043	0.03257	0.00040	0.00042	0.00002	0.11571	0.18219	0.00003	0.00005	1.17088	0.48882	19.75	8.20	0.71345	0.01106	0.00055	0.00117
5	0.08905	0.00083	0.04515	0.00033	0.00055	0.00005	-0.31166	0.18227	0.00031	0.00005	-0.06709	-0.35293	-2.06	5.98	0.50699	0.00600	0.00346	0.00060
6	0.09895	0.00073	0.08517	0.00050	0.00110	0.00005	-0.09797	0.18231	0.00013	0.00005	0.69976	0.18712	11.83	3.15	0.86074	0.00811	0.00133	0.00054
7	0.12781	0.00067	0.13510	0.00050	0.00179	0.00008	-0.09802	0.18240	0.00019	0.00005	0.52217	0.11797	8.84	1.99	1.05702	0.00675	0.00150	0.00042
8	0.09456	0.00053	0.10274	0.00054	0.00129	0.00007	-0.09804	0.18244	0.00012	0.00005	0.56638	0.14673	9.58	2.47	1.08650	0.00830	0.00129	0.00053
9	0.18652	0.00098	0.20275	0.00094	0.00261	0.00007	-0.20508	0.18252	0.00022	0.00005	0.59574	0.07877	10.08	1.33	1.08700	0.00764	0.00118	0.00029
10	0.15046	0.00056	0.16729	0.00075	0.00211	0.00007	-0.20513	0.18257	0.00019	0.00005	0.55994	0.09019	9.47	1.52	1.11188	0.00648	0.00126	0.00034
11	0.25780	0.00107	0.28357	0.00070	0.00347	0.00008	-0.52646	0.18265	0.00040	0.00005	0.49288	0.05636	8.34	0.95	1.09996	0.00532	0.00153	0.00021
12	0.33472	0.00155	0.39898	0.00231	0.00504	0.00011	0.33023	0.18269	0.00018	0.00005	0.70549	0.04035	11.93	0.68	1.19199	0.00882	0.00053	0.00016
13	0.16837	0.00093	0.20616	0.00128	0.00250	0.00007	-0.20537	0.18277	0.00017	0.00005	0.57012	0.07757	9.64	1.31	1.22447	0.01021	0.00101	0.00032
14	0.19319	0.00114	0.22794	0.00092	0.00275	0.00011	0.11610	0.18281	0.00011	0.00005	0.70993	0.07022	12.00	1.18	1.17987	0.00846	0.00054	0.00028
15	0.13925	0.00072	0.16926	0.00074	0.00214	0.00004	-0.31277	0.18292	0.00020	0.00005	0.47217	0.08933	7.99	1.51	1.21552	0.00825	0.00143	0.00036
16	0.13691	0.00090	0.14803	0.00072	0.00177	0.00006	-0.09963	0.18540	0.00011	0.00005	0.69853	0.10924	11.81	1.84	1.08119	0.00887	0.00082	0.00039
Blank	0.00756	0.00015	0.00008	0.00002	0.00002	0.00002	0.00012	0.00002	0.00004	0.00001		J value =	0.009310776±0.0000597					

Ar/Ar data (expressed in V) of step-heating analysis of sample MA-1-5M_2 (Analytical uncertainties are at the 1sigma level)

Step	40Ar	+/-	39Ar	+/-	38Ar	+/-	37Ar	+/-	36Ar	+/-	40Ar*/39Ar	+/-	Age (Ma)	+/- (Ma)	39Ar/40Ar	+/-	36Ar/40Ar	+/-
1	0.02416	0.00040	0.01143	0.00027	0.00017	0.00003	-0.20453	0.18203	0.00012	0.00005	-1.02115	-1.31536	-20.94	22.49	0.47317	0.01351	0.00497	0.00209
2	0.05111	0.00062	0.02506	0.00026	0.00037	0.00004	-0.20458	0.18207	0.00019	0.00005	-0.22457	-0.63481	-5.46	10.78	0.49037	0.00783	0.00372	0.00104
3	0.05671	0.00071	0.03220	0.00035	0.00037	0.00004	0.32925	0.18215	0.00001	0.00005	1.68148	0.49476	28.30	8.26	0.56784	0.00945	0.00015	0.00094
4	0.04565	0.00043	0.03257	0.00040	0.00042	0.00002	0.11571	0.18219	0.00003	0.00005	1.17088	0.48882	19.75	8.20	0.71345	0.01106	0.00055	0.00117
5	0.08905	0.00083	0.04515	0.00033	0.00055	0.00005	-0.31166	0.18227	0.00031	0.00005	-0.06709	-0.35293	-2.06	5.98	0.50699	0.00600	0.00346	0.00060
6	0.09895	0.00073	0.08517	0.00050	0.00110	0.00005	-0.09797	0.18231	0.00013	0.00005	0.69976	0.18712	11.83	3.15	0.86074	0.00811	0.00133	0.00054
7	0.12781	0.00067	0.13510	0.00050	0.00179	0.00008	-0.09802	0.18240	0.00019	0.00005	0.52217	0.11797	8.84	1.99	1.05702	0.00675	0.00150	0.00042
8	0.09456	0.00053	0.10274	0.00054	0.00129	0.00007	-0.09804	0.18244	0.00012	0.00005	0.56638	0.14673	9.58	2.47	1.08650	0.00830	0.00129	0.00053
9	0.18652	0.00098	0.20275	0.00094	0.00261	0.00007	-0.20508	0.18252	0.00022	0.00005	0.59574	0.07877	10.08	1.33	1.08700	0.00764	0.00118	0.00029
10	0.15046	0.00056	0.16729	0.00075	0.00211	0.00007	-0.20513	0.18257	0.00019	0.00005	0.55994	0.09019	9.47	1.52	1.11188	0.00648	0.00126	0.00034
Blank	0.00761	0.00016	0.00080	0.00003	0.00003	0.00001	0.00012	0.00002	0.00004	0.00001		J value =	0.0092792±0.0000464					

values excluded from the isochron age calculation

Ar/Ar data (expressed in V) of step-heating analysis of sample AR-1-6A_1 (Analytical uncertainties are at the 1sigma level)

Step	40Ar	+/-	39Ar	+/-	38Ar	+/-	37Ar	+/-	36Ar	+/-	40Ar*/39Ar	+/-	Age (Ma)	+/- (Ma)	39Ar/40Ar	+/-	36Ar/40Ar	+/-
1	0.29935	0.00080	0.35911	0.00129	0.00442	0.00019	0.01808	0.00014	0.00010	0.00002	0.75070	0.01820	12.99	0.31	1.19964	0.00539	0.00033	0.00007
2	0.11666	0.00121	0.15952	0.00148	0.00198	0.00011	0.00889	0.00014	0.00001	0.00002	0.70860	0.04144	12.26	0.71	1.36738	0.01902	0.00010	0.00018
3	0.09547	0.00109	0.14158	0.00100	0.00161	0.00011	0.00748	0.00014	0.00004	0.00002	0.58469	0.04614	10.12	0.80	1.48296	0.01995	0.00045	0.00023
4	0.23394	0.00158	0.34162	0.00314	0.00439	0.00006	0.01728	0.00014	0.00003	0.00002	0.65865	0.02026	11.40	0.35	1.46029	0.01667	0.00013	0.00009
5	0.40425	0.00218	0.57825	0.00153	0.00689	0.00019	0.02842	0.00014	0.00005	0.00003	0.67485	0.01655	11.68	0.29	1.43042	0.00861	0.00012	0.00008
6	0.35862	0.00154	0.53248	0.00239	0.00674	0.00020	0.02321	0.00014	0.00001	0.00002	0.66882	0.01275	11.58	0.22	1.48478	0.00922	0.00002	0.00006
7	0.34005	0.00167	0.50356	0.00286	0.00601	0.00021	0.02342	0.00014	0.00000	0.00002	0.67631	0.01371	11.71	0.24	1.48083	0.01113	-0.00001	-0.00006
8	0.24883	0.00155	0.35403	0.00184	0.00418	0.00021	0.01569	0.00014	0.00005	0.00002	0.66041	0.01895	11.43	0.33	1.42276	0.01155	0.00020	0.00009
9	0.34342	0.00206	0.50497	0.00205	0.00598	0.00026	0.02495	0.00014	0.00001	0.00003	0.67542	0.01898	11.69	0.33	1.47041	0.01065	0.00002	0.00009
10	0.33702	0.00169	0.48851	0.00212	0.00579	0.00026	0.02384	0.00014	0.00002	0.00001	0.67878	0.00900	11.75	0.16	1.44952	0.00962	0.00005	0.00004
11	0.34650	0.00358	0.44228	0.00245	0.00524	0.00020	0.02229	0.00014	0.00015	0.00004	0.68316	0.02893	11.82	0.50	1.27642	0.01497	0.00043	0.00012
12	0.08434	0.00168	0.11124	0.00070	0.00119	0.00007	0.00608	0.00014	0.00005	0.00002	0.61625	0.05974	10.67	1.03	1.31896	0.02757	0.00063	0.00026
Blank	0.00426	0.00040	0.00010	0.00009	0.00001	0.00002	0.00015	0.00004	0.00002	0.00002		J value =	0.009531765±0.0000477					

Ar/Ar data (expressed in V) of step-heating analysis of sample AR-1-6A_2 (Analytical uncertainties are at the 1sigma level)

Step	40Ar	+/-	39Ar	+/-	38Ar	+/-	37Ar	+/-	36Ar	+/-	40Ar*/39Ar	+/-	Age (Ma)	+/- (Ma)	39Ar/40Ar	+/-	36Ar/40Ar	+/-
1	0.37525	0.00252	0.47614	0.00273	0.00604	0.00016	0.02401	0.00018	0.00025	0.00003	0.63224	0.02076	10.91	0.36	1.26886	0.01120	0.00066	0.00008
2	0.16880	0.00162	0.23576	0.00148	0.00278	0.00019	0.01185	0.00018	0.00006	0.00002	0.63766	0.02918	11.00	0.50	1.39669	0.01605	0.00037	0.00013
3	0.49005	0.00197	0.72360	0.00275	0.00835	0.00037	0.03311	0.00018	0.00007	0.00002	0.64992	0.00986	11.21	0.17	1.47657	0.00816	0.00014	0.00005
4	0.48229	0.00197	0.71225	0.00190	0.00779	0.00032	0.03229	0.00018	0.00004	0.00002	0.66186	0.00985	11.42	0.17	1.47682	0.00720	0.00008	0.00005
5	0.46443	0.00267	0.69272	0.00296	0.00841	0.00038	0.03288	0.00018	0.00007	0.00002	0.64188	0.01066	11.08	0.18	1.49154	0.01067	0.00014	0.00005
6	0.60742	0.00388	0.88281	0.00362	0.01061	0.00025	0.03957	0.00018	0.00009	0.00002	0.65610	0.00910	11.32	0.16	1.45337	0.01103	0.00016	0.00004
7	0.48400	0.00243	0.71627	0.00188	0.00839	0.00028	0.03677	0.00018	0.00004	0.00003	0.66103	0.01367	11.40	0.23	1.47991	0.00839	0.00007	0.00007
8	0.34490	0.00177	0.50167	0.00219	0.00600	0.00017	0.02447	0.00018	0.00002	0.00002	0.67649	0.01398	11.67	0.24	1.45454	0.00982	0.00005	0.00006
9	0.43938	0.00203	0.63995	0.00279	0.00799	0.00018	0.03053	0.00018	-0.00002	0.00001	0.69736	0.00781	12.03	0.13	1.45648	0.00926	-0.00005	-0.00003
10	0.36665	0.00207	0.52470	0.00233	0.00622	0.00016	0.02997	0.00018	0.00006	0.00002	0.66632	0.01354	11.50	0.23	1.43106	0.01027	0.00016	0.00006
Blank	0.00435	0.00038	0.00006	0.00009	0.00001	0.00002	0.00014	0.00004	0.00003	0.00002		J value =	0.009500195±0.0000475					

Ar/Ar data (expressed in V) of step-heating analysis of sample AR-1-6A_3 (Analytical uncertainties are at the 1sigma level)

Step	40Ar	+/-	39Ar	+/-	38Ar	+/-	37Ar	+/-	36Ar	+/-	40Ar*/39Ar	+/-	Age (Ma)	+/- (Ma)	39Ar/40Ar	+/-	36Ar/40Ar	+/-
1	0.24476	0.00229	0.32297	0.00095	0.00376	0.00014	0.01530	0.00007	0.00016	0.00003	0.60760	0.03028	10.45	0.51	1.31955	0.01294	0.00066	0.00013
2	0.34213	0.00262	0.49208	0.00246	0.00589	0.00022	0.02258	0.00007	0.00006	0.00002	0.65851	0.01507	11.32	0.26	1.43828	0.01315	0.00018	0.00007
3	0.39015	0.00110	0.56028	0.00163	0.00701	0.00025	0.02885	0.00007	0.00006	0.00003	0.66494	0.01716	11.43	0.29	1.43607	0.00582	0.00015	0.00008
4	0.24540	0.00159	0.36772	0.00193	0.00417	0.00014	0.01777	0.00007	0.00000	0.00002	0.66585	0.01917	11.45	0.33	1.49844	0.01250	0.00001	0.00009
5	0.34190	0.00191	0.50653	0.00179	0.00597	0.00018	0.02228	0.00007	0.00002	0.00002	0.66279	0.01404	11.40	0.24	1.48154	0.00980	0.00006	0.00007
6	0.53598	0.00177	0.73880	0.00249	0.00843	0.00027	0.03588	0.00007	0.00018	0.00004	0.65392	0.01703	11.24	0.29	1.37842	0.00651	0.00033	0.00008
7	0.19762	0.00129	0.29823	0.00194	0.00358	0.00019	0.01487	0.00007	0.00000	0.00002	0.66000	0.02343	11.35	0.40	1.50913	0.01393	0.00001	0.00011
8	0.21344	0.00226	0.32512	0.00194	0.00367	0.00009	0.01557	0.00007	-0.00001	0.00001	0.66342	0.01554	11.41	0.27	1.52327	0.01851	-0.00004	-0.00007
9	0.22859	0.00110	0.34412	0.00157	0.00423	0.00020	0.01642	0.00007	-0.00002	0.00002	0.67968	0.02010	11.69	0.34	1.50544	0.00998	-0.00008	-0.00010
10	0.29217	0.00140	0.42758	0.00119	0.00467	0.00020	0.02021	0.00007	0.00001	0.00002	0.67546	0.01622	11.61	0.28	1.46350	0.00811	0.00004	0.00008
11	0.23942	0.00556	0.35042	0.00141	0.00423	0.00020	0.01622	0.00007	0.00005	0.00004	0.63870	0.03873	10.98	0.66	1.46363	0.03451	0.00022	0.00017
Blank	0.00370	0.00027	0.00009	0.00007	0.00001	0.00002	0.00009	0.00003	0.00002	0.00002		J value =	0.00946862±0.0000473					

values excluded from the isochron age calculation

Ar/Ar data (expressed in V) of step-heating analysis of sample PRD-1-2A (Analytical uncertainties are at the 1sigma level)

Step	40Ar	+/-	39Ar	+/-	38Ar	+/-	37Ar	+/-	36Ar	+/-	40Ar*/39Ar	+/-	Age (Ma)	+/- (Ma)	39Ar/40Ar	+/-	36Ar/40Ar	+/-
1	0.27270	0.00206	0.28822	0.00173	0.00376	0.00009	0.03276	0.00900	0.00021	0.00002	0.73322	0.02676	12.63	0.46	1.05691	0.01021	0.00075	0.00009
2	0.54926	0.00374	0.66356	0.00422	0.00821	0.00016	0.01843	0.00900	0.00022	0.00002	0.72904	0.01323	12.56	0.23	1.20812	0.01126	0.00040	0.00004
3	0.29565	0.00104	0.39176	0.00107	0.00484	0.00014	0.02322	0.00901	0.00007	0.00002	0.70276	0.01897	12.11	0.33	1.32507	0.00589	0.00023	0.00008
4	0.27109	0.00127	0.35952	0.00197	0.00448	0.00008	0.01366	0.00901	0.00006	0.00002	0.70367	0.01534	12.13	0.26	1.32619	0.00956	0.00022	0.00006
5	0.25356	0.00205	0.35247	0.00134	0.00433	0.00012	0.00410	0.00901	0.00002	0.00002	0.69974	0.01604	12.06	0.28	1.39007	0.01244	0.00009	0.00007
6	0.22602	0.00112	0.30927	0.00070	0.00350	0.00012	0.01367	0.00902	0.00004	0.00002	0.69155	0.01722	11.92	0.30	1.36837	0.00749	0.00018	0.00008
7	0.17398	0.00091	0.24025	0.00077	0.00292	0.00010	0.01846	0.00902	0.00002	0.00002	0.70005	0.02203	12.06	0.38	1.38094	0.00849	0.00011	0.00010
8	0.21373	0.00154	0.27801	0.00102	0.00364	0.00008	-0.00068	0.00902	0.00008	0.00002	0.67809	0.01961	11.69	0.34	1.30077	0.01051	0.00040	0.00008
9	0.26242	0.00168	0.37173	0.00093	0.00441	0.00011	-0.00068	0.00903	0.00003	0.00002	0.67826	0.02028	11.69	0.35	1.41655	0.00974	0.00013	0.00009
10	0.32719	0.00171	0.44859	0.00249	0.00564	0.00011	0.04244	0.00903	0.00004	0.00002	0.70074	0.01277	12.08	0.22	1.37103	0.01044	0.00013	0.00005
11	0.12605	0.00167	0.15891	0.00132	0.00201	0.00007	0.00411	0.00903	0.00004	0.00002	0.71209	0.03478	12.27	0.60	1.26066	0.01970	0.00034	0.00014
Blank	0.00513	0.00013	0.00006	0.00002	0.00002	0.00002	0.00012	0.00002	0.00004	0.00001		J value =	0.009491765±0.0000474588					

Ar/Ar data (expressed in V) of step-heating analysis of sample U-1-2 (Analytical uncertainties are at the 1sigma level)

Step	40Ar	+/-	39Ar	+/-	38Ar	+/-	37Ar	+/-	36Ar	+/-	40Ar*/39Ar	+/-	Age (Ma)	+/- (Ma)	39Ar/40Ar	+/-	36Ar/40Ar	+/-
1	1.94218	0.00886	0.11255	0.00034	0.00174	0.00014	0.02521	0.00618	0.00227	0.00006	11.22370	0.18192	183.90	2.83	0.05795	0.00032	0.00117	0.00003
2	0.96173	0.00259	0.06500	0.00020	0.00098	0.00004	0.01584	0.00618	0.00116	0.00003	9.48238	0.15098	156.57	2.39	0.06759	0.00028	0.00120	0.00003
3	1.20353	0.00325	0.08362	0.00061	0.00131	0.00006	0.00646	0.00618	0.00139	0.00004	9.43232	0.16582	155.78	2.62	0.06948	0.00054	0.00115	0.00003
4	1.12973	0.00517	0.07863	0.00053	0.00116	0.00007	0.02524	0.00618	0.00104	0.00003	10.40224	0.15215	171.06	2.39	0.06960	0.00057	0.00092	0.00003
5	1.36805	0.00791	0.09412	0.00080	0.00134	0.00006	-0.00294	0.00619	0.00102	0.00003	11.29422	0.16112	185.00	2.51	0.06880	0.00071	0.00075	0.00002
6	1.50320	0.00641	0.13504	0.00065	0.00187	0.00007	0.02056	0.00619	0.00102	0.00003	8.88602	0.09391	147.11	1.49	0.08984	0.00058	0.00068	0.00002
7	1.31770	0.00809	0.11799	0.00084	0.00158	0.00008	0.01117	0.00619	0.00064	0.00003	9.55273	0.12450	157.68	1.97	0.08955	0.00084	0.00048	0.00002
8	1.81479	0.00634	0.17683	0.00101	0.00220	0.00008	0.00647	0.00619	0.00069	0.00004	9.09898	0.09330	150.49	1.48	0.09744	0.00065	0.00038	0.00002
9	1.63097	0.00753	0.19197	0.00100	0.00236	0.00005	0.02529	0.00620	0.00055	0.00002	7.63348	0.06501	127.09	1.04	0.11771	0.00082	0.00034	0.00001
10	3.01229	0.01330	0.38222	0.00091	0.00449	0.00010	0.05352	0.00620	0.00066	0.00003	7.36787	0.04591	122.81	0.74	0.12689	0.00064	0.00022	0.00001
11	6.91085	0.04240	1.02469	0.00390	0.01204	0.00021	0.13357	0.00620	0.00096	0.00003	6.46592	0.04899	108.22	0.80	0.14827	0.00107	0.00014	0.00000
12	1.98663	0.00723	0.28801	0.00127	0.00345	0.00012	0.02060	0.00620	0.00020	0.00002	6.69484	0.04478	111.93	0.73	0.14497	0.00083	0.00010	0.00001
Blank	0.00697	0.00017	0.00007	0.00002	0.00003	0.00002	0.00011	0.00002	0.00004	0.00001		J value =	0.00946745±0.0000473373					

values excluded from the isochron age calculation

Appendix A3- Data from Chapter 4

A3.1 Electron microprobe data

Analytical Conditions :
Date : 7-Mar-2017
Analysis Parameters :

Sp	Elements	Xtal	Position
Sp4	S Ka		LPET
Sp4	K Ka		LPET
Sp3	Fe Ka		LLIF
Sp3	Mn Ka		LLIF
Sp2	Si Ka		LTAP
Sp2	Mg Ka		LTAP
Sp5	Cl Ka		PET
Sp5	P Ka		PET
Sp4	Ca Ka		LPET
Sp1	Na Ka		TAP
Sp1	Al Ka		TAP
Sp5	Ti Ka		PET

Standard Name :
S On Barite
K , Si, Al On fspr-In5
Fe On Haematite
Mn, Ca On Bustamite
Mg On for-BM4
Cl On sylv-BM4
P On apa-BM4
Na On jad-BM4
Ti On rut-BM4

Beam Size : 10 µm

Major element (Wt %) from electron microprobe analyses of sample KS15-03 (N° 33)

SiO_2	Na_2O	K_2O	CaO	MgO	MnO	FeO	Al_2O_3	TiO_2	Cl	P_2O_5	SO_3	Total	CIA
50.14	2.94	1.44	8.85	4.87	0.25	13.16	13.48	1.51	0.09	0.35	0.00	97.07	50.47
50.22	2.92	1.41	8.85	4.97	0.24	13.67	13.37	1.36	0.01	0.38	0.00	97.40	50.36
50.26	2.94	1.41	8.93	4.92	0.24	13.49	13.40	1.37	0.06	0.35	0.00	97.37	50.22
50.54	3.21	1.45	8.85	4.85	0.25	13.43	13.48	1.24	0.02	0.33	0.01	97.66	49.94
50.96	3.09	1.43	8.84	4.91	0.26	13.39	13.76	1.30	0.06	0.37	0.01	98.38	50.74
51.00	2.91	1.43	8.99	4.87	0.26	13.55	13.71	1.32	0.09	0.32	0.00	98.44	50.70
51.09	3.23	1.50	8.83	4.78	0.24	13.24	13.89	1.21	0.05	0.37	0.00	98.42	50.60
51.10	2.94	1.44	8.93	4.94	0.25	13.56	13.74	1.34	0.04	0.34	0.00	98.62	50.79
51.11	2.84	1.45	8.87	4.92	0.24	13.65	13.71	1.25	0.07	0.37	0.01	98.47	51.02
51.13	2.89	1.43	8.94	4.87	0.25	13.22	13.68	1.31	0.04	0.37	0.00	98.12	50.78
51.16	3.06	1.43	8.93	4.89	0.25	13.39	13.86	1.38	0.02	0.35	0.02	98.74	50.81
51.18	3.03	1.45	8.87	4.88	0.25	13.70	13.79	1.26	0.07	0.40	0.00	98.89	50.81
51.19	2.93	1.46	8.88	4.84	0.25	13.71	13.58	1.25	0.03	0.35	0.00	98.45	50.58
51.25	2.86	1.43	8.85	4.80	0.23	13.54	13.66	1.18	0.03	0.32	0.02	98.18	50.97
51.26	2.85	1.44	8.90	4.88	0.24	13.64	13.85	1.39	0.02	0.35	0.01	98.82	51.22
51.30	2.99	1.45	8.85	4.81	0.25	13.47	13.68	1.32	0.07	0.35	0.02	98.56	50.72
51.37	3.00	1.44	8.90	4.89	0.27	13.15	13.61	1.38	0.04	0.34	0.00	98.39	50.50
51.37	3.02	1.42	8.93	4.90	0.25	13.52	13.83	1.34	0.06	0.37	0.03	99.03	50.85
51.39	3.03	1.44	8.86	4.85	0.25	13.20	13.77	1.30	0.05	0.35	0.03	98.52	50.81
51.40	3.02	1.45	8.90	4.83	0.26	13.53	13.71	1.26	0.01	0.39	0.01	98.77	50.63
51.45	2.98	1.43	8.90	4.90	0.26	13.26	13.93	1.28	0.05	0.31	0.00	98.75	51.14
51.45	3.08	1.44	8.92	4.90	0.25	13.44	13.81	1.34	0.01	0.35	0.00	99.01	50.68
51.48	2.99	1.45	8.95	4.92	0.24	13.70	13.66	1.30	0.10	0.37	0.01	99.16	50.50
51.52	2.91	1.47	8.85	4.82	0.23	13.48	13.87	1.26	0.07	0.32	0.01	98.81	51.18
51.55	2.79	1.42	8.93	4.93	0.24	13.40	13.70	1.30	0.09	0.35	0.01	98.70	51.04
51.58	3.04	1.47	8.79	4.79	0.23	13.17	13.74	1.27	0.04	0.38	0.00	98.49	50.81
51.58	3.00	1.44	8.88	4.86	0.25	13.41	13.83	1.32	0.06	0.37	0.00	99.00	50.94
51.63	2.95	1.43	8.91	4.86	0.25	13.56	13.66	1.30	0.02	0.36	0.00	98.92	50.69
51.65	3.04	1.44	8.91	4.89	0.23	13.49	13.77	1.31	0.05	0.33	0.00	99.13	50.70
51.66	2.97	1.45	8.84	4.80	0.23	13.63	13.77	1.25	0.03	0.38	0.01	99.02	50.94
51.66	2.95	1.42	8.89	4.89	0.24	13.64	13.69	1.34	0.03	0.35	0.01	99.11	50.80
51.73	2.95	1.43	8.90	4.84	0.25	13.37	13.82	1.39	0.07	0.40	0.00	99.15	51.00
51.81	2.81	1.45	8.90	4.87	0.27	13.36	13.76	1.22	0.01	0.34	0.00	98.79	51.11

Major element (Wt %) from electron microprobe analyses of sample KS03-11L (N° 53)

SiO_2	Na_2O	K_2O	CaO	MgO	MnO	FeO	Al_2O_3	TiO_2	Cl	P_2O_5	SO_3	Total	CIA
50.95	3.20	1.41	9.03	4.74	0.25	12.93	13.52	1.25	0.03	0.39	0.04	97.74	49.78
51.01	3.06	1.39	9.06	5.02	0.27	14.03	13.64	1.25	0.01	0.35	0.00	99.08	50.24
51.08	2.86	1.46	8.87	4.78	0.24	13.49	13.52	1.23	0.02	0.39	0.03	97.98	50.62
51.21	2.96	1.43	8.97	4.84	0.23	13.65	13.84	1.29	0.07	0.37	0.00	98.86	50.88
51.34	3.11	1.45	8.87	4.89	0.24	13.56	13.90	1.33	0.00	0.36	0.00	99.05	50.86
51.38	2.98	1.48	8.97	4.87	0.26	13.58	13.91	1.38	0.04	0.38	0.00	99.23	50.88
51.38	3.29	1.45	8.87	4.93	0.23	13.29	13.81	1.38	0.03	0.33	0.02	99.00	50.36
51.38	2.90	1.45	8.91	4.90	0.24	13.46	13.76	1.33	0.11	0.36	0.02	98.82	50.93
51.47	3.07	1.44	8.93	4.84	0.24	13.42	13.90	1.36	0.04	0.42	0.00	99.14	50.84
51.48	3.31	1.43	8.89	4.90	0.28	13.69	13.91	1.25	0.03	0.35	0.02	99.55	50.51
51.50	3.09	1.42	8.85	4.95	0.23	13.38	13.89	1.32	0.04	0.34	0.00	99.00	50.97
51.50	2.97	1.43	8.93	4.91	0.23	13.35	13.69	1.29	0.11	0.37	0.01	98.78	50.67
51.50	2.93	1.43	8.90	4.88	0.24	13.19	13.75	1.36	0.02	0.36	0.01	98.58	50.91
51.51	3.08	1.46	8.83	4.87	0.25	13.50	13.82	1.25	0.05	0.33	0.00	98.95	50.83
51.52	2.89	1.46	8.82	4.85	0.24	13.45	13.79	1.26	0.02	0.31	0.00	98.63	51.15
51.54	3.05	1.43	8.92	4.87	0.25	13.33	13.78	1.35	0.00	0.32	0.00	98.84	50.70
51.56	2.82	1.44	8.94	4.82	0.26	13.31	13.80	1.31	0.08	0.38	0.00	98.70	51.11
51.58	2.80	1.44	8.89	4.93	0.26	13.44	13.84	1.44	0.03	0.33	0.00	98.96	51.32
51.59	2.97	1.42	8.95	4.89	0.26	13.41	13.76	1.29	0.05	0.37	0.01	98.98	50.77
51.61	3.20	1.44	8.85	4.85	0.23	13.40	13.90	1.34	0.02	0.35	0.00	99.19	50.75
51.63	2.94	1.44	8.79	4.85	0.24	13.20	13.80	1.40	0.04	0.40	0.00	98.74	51.17
51.63	2.99	1.43	8.91	4.86	0.26	13.61	13.71	1.35	0.04	0.39	0.04	99.22	50.70
51.64	3.23	1.44	8.90	4.89	0.24	13.64	13.85	1.29	0.05	0.37	0.01	99.54	50.51
51.64	3.08	1.45	8.87	4.96	0.23	13.42	13.68	1.29	0.02	0.34	0.00	98.98	50.52
51.65	2.88	1.42	8.83	4.85	0.27	13.36	13.89	1.38	0.03	0.36	0.00	98.92	51.41
51.66	2.99	1.44	8.94	4.90	0.23	13.47	13.92	1.32	0.03	0.40	0.01	99.31	51.01
51.66	3.15	1.47	8.90	4.85	0.23	13.51	13.73	1.28	0.04	0.35	0.02	99.18	50.39
51.67	3.18	1.42	8.85	4.89	0.23	13.24	13.79	1.26	0.00	0.34	0.00	98.88	50.62
51.69	3.11	1.42	8.86	4.89	0.25	13.59	13.85	1.35	0.04	0.37	0.00	99.40	50.84
51.70	3.02	1.41	8.87	4.97	0.24	13.59	13.91	1.34	0.03	0.35	0.03	99.47	51.12
51.70	2.88	1.41	8.91	4.87	0.24	13.40	13.69	1.28	0.08	0.38	0.03	98.88	50.91
51.70	3.02	1.45	8.82	4.77	0.24	13.07	13.86	1.35	0.03	0.33	0.01	98.65	51.05
51.71	3.01	1.43	8.89	4.82	0.25	13.16	13.82	1.31	0.00	0.32	0.00	98.73	50.90
51.72	3.12	1.44	8.84	4.91	0.26	13.29	13.77	1.39	0.06	0.31	0.02	99.13	50.68
51.72	2.91	1.45	8.81	4.85	0.25	13.44	13.84	1.37	0.05	0.33	0.01	99.02	51.24
51.75	2.83	1.40	8.80	4.85	0.26	13.01	13.71	1.32	0.01	0.36	0.00	98.31	51.27
51.78	3.04	1.44	8.90	4.85	0.23	13.40	13.67	1.23	0.04	0.32	0.02	98.94	50.54
51.79	3.11	1.45	8.91	4.82	0.23	13.53	13.93	1.37	0.00	0.40	0.00	99.54	50.84
51.83	2.99	1.41	8.80	4.94	0.24	13.50	13.80	1.33	0.04	0.35	0.00	99.23	51.11
51.87	2.91	1.44	8.84	4.83	0.25	13.44	13.70	1.23	0.07	0.30	0.00	98.89	50.95
51.88	3.15	1.44	8.84	4.92	0.26	13.28	13.78	1.28	0.04	0.41	0.01	99.29	50.64
51.91	3.06	1.44	8.86	4.93	0.24	13.37	13.88	1.24	0.05	0.35	0.01	99.34	50.95
51.93	2.88	1.43	8.82	4.83	0.24	13.12	13.99	1.34	0.04	0.37	0.02	99.02	51.59
51.98	2.79	1.43	8.86	4.90	0.25	13.36	13.86	1.36	0.03	0.33	0.00	99.15	51.45
51.99	3.07	1.42	8.76	4.78	0.24	12.91	13.85	1.23	0.10	0.34	0.00	98.68	51.11
52.02	3.13	1.48	8.71	4.71	0.27	13.18	13.97	1.33	0.07	0.38	0.02	99.29	51.19
52.06	2.77	1.42	8.76	4.91	0.24	13.02	13.91	1.35	0.05	0.35	0.00	98.83	51.79
52.19	2.96	1.40	8.81	4.89	0.24	13.42	13.75	1.23	0.09	0.41	0.00	99.39	51.08
52.25	3.03	1.51	8.66	4.68	0.23	12.84	13.49	1.23	0.04	0.35	0.00	98.31	50.54
52.26	3.11	1.51	8.69	4.76	0.24	13.11	13.89	1.34	0.03	0.35	0.03	99.31	51.07
52.32	3.12	1.42	8.73	4.85	0.25	13.29	13.87	1.31	0.05	0.37	0.01	99.58	51.11
52.58	3.08	1.51	8.59	4.74	0.22	12.97	13.91	1.36	0.05	0.36	0.00	99.33	51.35
52.88	3.17	1.57	8.47	4.63	0.21	12.53	13.95	1.38	0.05	0.32	0.00	99.16	51.36

Major element (Wt %) from electron microprobe analyses of sample KS13-4L (N° 20)

SiO_2	Na_2O	K_2O	CaO	MgO	MnO	FeO	Al_2O_3	TiO_2	Cl	P_2O_5	SO_3	Total	CIA
50.17	2.82	1.41	8.87	4.87	0.25	13.32	13.63	1.42	0.01	0.37	0.01	97.14	50.99
50.78	2.97	1.49	8.69	4.80	0.23	13.09	13.60	1.35	0.06	0.39	0.00	97.46	50.84
50.30	3.18	1.43	8.90	4.87	0.25	13.29	13.55	1.33	0.02	0.36	0.00	97.48	50.07
50.67	2.96	1.45	8.82	4.82	0.22	13.55	13.54	1.46	0.03	0.38	0.01	97.90	50.58
50.80	3.08	1.43	8.89	4.84	0.23	13.39	13.59	1.33	0.03	0.35	0.04	98.00	50.35
50.67	3.04	1.44	8.91	4.89	0.25	13.61	13.67	1.35	0.01	0.32	0.01	98.16	50.52
51.13	2.91	1.44	8.82	4.78	0.25	13.49	13.53	1.42	0.06	0.32	0.00	98.16	50.67
51.24	2.88	1.45	8.89	4.84	0.25	13.32	13.74	1.28	0.00	0.37	0.00	98.25	50.96
51.57	2.85	1.45	8.79	4.76	0.26	13.07	13.79	1.31	0.11	0.35	0.00	98.31	51.30
50.74	3.02	1.43	8.84	4.87	0.24	13.85	13.72	1.29	0.00	0.35	0.01	98.37	50.80
51.15	3.11	1.46	8.92	4.84	0.23	13.11	13.84	1.33	0.08	0.35	0.00	98.43	50.64
51.67	3.04	1.45	8.84	4.82	0.25	13.22	13.48	1.34	0.03	0.34	0.01	98.46	50.28
51.48	2.99	1.45	8.87	4.79	0.26	13.54	13.73	1.30	0.00	0.37	0.00	98.76	50.78
51.96	2.93	1.43	8.70	4.84	0.21	13.13	13.88	1.27	0.02	0.36	0.03	98.76	51.52
51.27	3.10	1.45	8.81	4.90	0.25	13.63	13.77	1.26	0.01	0.35	0.00	98.78	50.76
51.48	2.94	1.45	8.90	4.80	0.25	13.63	13.78	1.21	0.05	0.39	0.01	98.90	50.91
51.36	3.06	1.46	8.88	4.83	0.25	13.59	13.68	1.37	0.04	0.39	0.00	98.92	50.52
51.38	2.96	1.43	8.89	4.88	0.24	13.57	13.76	1.41	0.09	0.38	0.02	99.00	50.89
51.15	3.20	1.43	8.95	4.89	0.25	13.54	13.78	1.46	0.03	0.33	0.00	99.03	50.37
51.47	3.10	1.44	8.91	4.91	0.25	13.77	13.78	1.37	0.04	0.33	0.00	99.38	50.61

A3.2 Vesicularity calculation: Areas of bubbles and glass of Pele's hairs and tears

Sample KS15-03_1

Bubbles µm²	Glass µm²	Total µm²
10096		
99		
123597		
17854		
285		
1964		
153895	351602	505497
30 %	70 %	100 %

Sample KS15-03_2

Bubbles µm²	Glass µm²	Total µm²
924		
682		
864		
176		
257		
1287		
236		
422		
4848	280226	285074
2 %	98 %	100 %

Sample KS15-03_3

Bubbles µm²	Glass µm²	Total µm²
16294		
2169		
6309		
322		
1035		
3309		
2324		
25185		
10081		
1677		
3101		
343		
72150	882035	954185
8 %	92 %	100 %

Sample KS15-03_4

Bubbles µm²	Glass µm²	Total µm²
780		
955		
1934		
501		
4961		
3937		
125		
917		
2454		
1330		
610		
50		
458		
627		
647		
1660		
385		
1550		
1876		
25757	411727	437483
6 %	94 %	100 %

Sample KS15-03_5

Bubbles µm²	Glass µm²	Total µm²
24803		
11001		
11690		
16765		
17600		
627		
98083		
187		
6450		
39843		
1137		
226		
2081		
7358		
481		
8412		
0.27		
0.27		
1365		
5743		
741		
4308		
1238		
9087		
603		
971		
1108		
271908	1291568	1563476
17 %	83 %	100 %

Sample KS15-03_6

Bubbles µm²	Glass µm²	Total µm²
364		
171		
12657		
3877		
387		
3266		
411		
118		
7583		
28835	444828	473663
6 %	94 %	100 %

Sample KS15-03_7

Bubbles µm²	Glass µm²	Total µm²
2424		
201		
446		
24948		
14102		
257		
6983		
6790		
18268		
8109		
18330		
15537		
13395		
0.13		
129792	376010	505802
26 %	74 %	100 %

Sample KS15-03_8

Bubbles µm²	Glass µm²	Total µm²
18929		
7363		
17929		
28097		
20212		
26310		
24230		
2685		
3431		
12898		
6102		
2653		
5683		
883		
4922		
2708		
32101		
2354		
303		
0.18		
735		
326		
855		
1597		
12105		
6868		
4795		
302		
743		
5522		
6728		
1038		
3056		
264463	670387	670387
39 %	61 %	100 %

Sample KS15-03_9

Bubbles µm²	Glass µm²	Total µm²
12596		
521		
16162		
93028		
0.24		
0.48		
4949		
204		
0.24		
1083		
29780		
7582		
0.24		
165907	445558	611466
27 %	73 %	100 %

Sample KS15-03_10

Bubbles µm²	Glass µm²	Total µm²
114031		
7638		
27043		
19918		
866		
1821		
9020		
180336	1239737	1420073
13 %	87 %	100 %

Sample KS16-03_1

Bubbles µm²	Glass µm²	Total µm²
531		
6859		
151		
2028		
5683		
2510		
1502		
13825		
33090	491183	524273
6 %	94 %	100 %

Sample KS16-03_2

Bubbles µm²	Glass µm²	Total µm²
18158		
8293		
296		
16377		
90		
140		
1427		
1978		
46760	395591	442350
11 %	89 %	100 %

Sample KS16-03_3

Bubbles µm²	Glass µm²	Total µm²
204		
376		
9072		
1232		
1175		
918		
10045		
360		
4263		
1194		
4874		
8142		
1770		
31873		
219		
7739		
534		
2449		
91		
86531	779177	865707
10 %	90 %	100 %

Sample KS16-03_4

Bubbles µm²	Glass µm²	Total µm²
1249		
5474		
22		
4886		
70		
43		
2589		
2253		
1010		
104		
13583		
23978		
21509		
4945		
81717	143401	225118
36 %	64 %	100 %

Sample KS16-03_5

Bubbles µm²	Glass µm²	Total µm²
0	69150	69150
0 %	100 %	100 %

Sample KS16-03_6

Bubbles µm²	Glass µm²	Total µm²
222		
11187		
4578		
263		
55493		
30797		
850		
6396		
6648		
39101		
2698		
423		
17139		
158		
175953	193788	369740
48 %	52 %	100 %

Sample KS16-03_7

Bubbles µm²	Glass µm²	Total µm²
7613		
6826		
1893		
2317		
1442		
1376		
3353		
2070		
1936		
1561		
1962		
1512		
1399		
768		
876		
2705		
5159		
739		
120323		
2741		
168571	1047137	1215708
14 %	86 %	100 %

KS16-03_8

Bubbles µm²	Glass µm²	Total µm²
1286		
37625		
4349		
4347		
9193		
56800	382445	439246
13 %	87 %	100 %

Sample KS16-03_9

Bubbles µm²	Glass µm²	Total µm²
4869		
2027		
8793		
5942		
3690		
16920		
3737		
2689		
4551		
1136		
2315		
2595		
2289		
1658		
23222		
206		
4364		
177623		
5013		
273640	516061	789701
30 %	70 %	100 %

Sample KS16-03_10

Bubbles µm²	Glass µm²	Total µm²
126807		
8124		
119620		
173		
8504		
10334		
193675		
467238	582768	1050006
44 %	56 %	100 %

Sample KS16-13_1

Bubbles µm^2	Glass µm^2	Total µm^2
5758		
4481		
4344		
23285		
16911		
1787		
7386		
488		
346		
5160		
8576		
5298		
7509		
513		
1059		
717		
93617	323631	417248
22 %	78 %	100 %

Sample KS16-13_3

Bubbles µm^2	Glass µm^2	Total µm^2
388		
14609		
264		
605		
166		
16032	636144	652177
3 %	98 %	100 %

Sample KS16-13_2

Bubbles µm^2	Glass µm^2	Total µm^2
20224		
4797		
643		
6556		
386		
425		
257		
0.09		
0.19		
0.28		
49962		
4484		
4453		
541		
10809		
465		
7194		
747		
227		
16443		
337		
585		
3773		
1802		
1578		
6082		
5507		
7316		
1189		
9649		
2957		
7777		
410		
2014		
328		
2199		
6020		
1750		
874		
300		
1584		
2666		
2794		
1119		
1726		
3951		
680		
1052		
550		
2281		
2165		
328		
211954	731247	943201
22 %	78 %	100 %

Sample KS16-13_4

Bubbles µm²	Glass µm²	Total µm²
7402		
8927		
10469		
11228		
587		
4061		
135		
8423		
822		
1708		
166		
4307		
8929		
25197		
4867		
4372		
5391		
893		
6725		
6358		
3308		
31258		
12922		
5911		
1846		
1860		
3444		
867		
6563		
20692		
7011		
2693		
648		
666		
2539		
192		
430		
1852		
7534		
10666		
3577		
1654		
6176		
1771		
165		
300		
415		
1842		
359		
769		
13199		
6078		
24432		
1415		
306021	985562	1291583
24 %	76 %	100 %

Sample KS16-13_5

Bubbles µm²	Glass µm²	Total µm²
5123		
99		
7905		
599		
332		
47		
1136		
307		
959		
293		
1430		
243		
831		
611		
5839		
1.03		
0.26		
0.52		
0.26		
0.52		
0.26		
0.52		
1.03		
25757	602687	628444
4 %	96 %	100 %

Sample KS16-13_6

Bubbles µm²	Glass µm²	Total µm²
60		
336		
506		
430		
718		
7590		
6573		
12930		
723		
92		
29958	148667	178625
17 %	83 %	100 %

Sample KS16-13_8

Bubbles µm^2	Glass µm^2	Total µm^2
3999		
91		
82		
405		
516		
3531		
3132		
3117		
2403		
421		
1482		
1105		
1247		
5662		
561		
2439		
2837		
33029	439552	472581
7 %	93 %	100 %

Sample KS16-13_9

Bubbles µm^2	Glass µm^2	Total µm^2
25946		
5688		
10824		
36617		
6618		
9046		
2095		
8132		
104967	189302	294269
36 %	64 %	100 %

Sample KS16-13_10

Bubbles µm^2	Glass µm^2	Total µm^2
6620	318189	324809
2 %	98 %	100 %

A3.3 NG analysis

NG Analyses of Pele's hairs and tears

Sample	Grain	Date	Weight (g)	4He (v)	± (v)	22Ne (v)	± (v)	36Ar (v)	± (v)	40Ar (v)	± (v)
KS-03-10S	1	21/07/2016	0.00133	0.00048	0.00018	0.00120	0.00014	N.A.	N.A.	1.53	0.00448
KS-03-10S	2	21/07/2016	0.00144	-0.00006	0.00014	0.00032	0.00016	N.A.	N.A.	0.11	0.00112
KS-03-10S	4	21/07/2016	0.00110	0.00210	0.00011	0.00070	0.00014	N.A.	N.A.	3.57	0.00429
KS-03-10S	5	21/07/2016	0.00052	0.00007	0.00016	0.00050	0.00014	N.A.	N.A.	3.09	0.00169
KS-03-10S	6	21/07/2016	0.00017	0.00086	0.00017	-0.00011	0.00014	N.A.	N.A.	0.37	0.00170
KS-03-10S	7	21/07/2016	0.00039	0.00094	0.00023	0.00022	0.00014	N.A.	N.A.	0.64	0.00185
KS-03-10S	8	23/10/2016	0.00336	0.00604	0.00077	0.00303	0.00019	N.A.	N.A.	**13.92**	**0.04259**
KS-03-10S	9	23/10/2016	0.00348	0.00239	0.00076	0.00250	0.00022	N.A.	N.A.	4.25	0.04304
KS-03-10S	10	23/10/2016	0.00589	0.02290	0.00087	0.00939	0.00023	N.A.	N.A.	**13.86**	**0.00541**
KS-03-10S	11	23/10/2016	0.00146	0.00122	0.00087	0.00059	0.00017	N.A.	N.A.	0.18	0.00565
KS-03-10S	12	23/10/2016	0.00090	0.00147	0.00088	0.00017	0.00017	N.A.	N.A.	3.74	0.01206
KS-03-10S	13	23/10/2016	0.00108	0.00310	0.00087	0.00048	0.00017	N.A.	N.A.	8.99	0.00930
KS-03-10S	14	23/10/2016	0.00204	0.00296	0.00089	0.00177	0.00019	N.A.	N.A.	7.36	0.01363
KS-03-10S	15	25/10/2016	0.00050	0.00158	0.00031	0.00079	0.00019	N.A.	N.A.	0.29	0.00427
KS-03-10S	16	25/10/2016	0.00109	0.00778	0.00033	0.00215	0.00019	N.A.	N.A.	**13.87**	**0.00399**
KS-03-10S	18	25/10/2016	0.00093	0.00006	0.00030	0.00008	0.00018	N.A.	N.A.	1.82	0.00680
KS-03-10S	19	25/10/2016	0.00058	0.00099	0.00033	0.00048	0.00018	N.A.	N.A.	1.41	0.00523
KS-03-10S	20	25/10/2016	0.00046	0.00125	0.00026	0.00036	0.00018	N.A.	N.A.	1.02	0.00531
KS-03-10S	21	25/10/2016	0.00034	-0.00036	0.00043	-0.00015	0.00019	N.A.	N.A.	**13.86**	**0.00403**
KS-03-11L	1	18/07/2016	0.00306	0.00195	0.00021	0.00200	0.00017	N.A.	N.A.	**13.87**	**0.00171**
KS-03-11L	2	18/07/2016	0.00058	0.00003	0.00019	-0.00015	0.00016	N.A.	N.A.	0.08	0.00152
KS-03-11L	3	18/07/2016	0.00058	0.00154	0.00018	0.00033	0.00016	N.A.	N.A.	1.37	0.00165
KS-03-11L	4	18/07/2016	0.00148	0.00014	0.00017	0.00138	0.00017	N.A.	N.A.	1.60	0.00261
KS-03-11L	5	18/07/2016	0.00055	0.00157	0.00016	0.00096	0.00017	N.A.	N.A.	2.85	0.00555
KS-03-11L	6	18/07/2016	0.00033	0.00104	0.00015	0.00031	0.00017	N.A.	N.A.	1.33	0.00171
KS-03-11L	7	18/07/2016	0.00058	0.00004	0.00015	0.00142	0.00017	N.A.	N.A.	0.96	0.00209
KS-03-11L	8	19/07/2016	0.00064	0.00060	0.00056	0.00072	0.00019	N.A.	N.A.	4.72	0.00391
KS-03-11L	9	19/07/2016	0.00044	0.00014	0.00057	0.00055	0.00019	N.A.	N.A.	0.51	0.00306
KS-03-11L	10	19/07/2016	0.00047	0.00030	0.00056	0.00023	0.00020	N.A.	N.A.	1.72	0.00366
KS-03-11L	11	19/07/2016	0.00035	0.00036	0.00061	0.00028	0.00019	N.A.	N.A.	0.32	0.00306
KS-03-11L	12	19/07/2016	0.00033	0.00054	0.00056	0.00064	0.00020	N.A.	N.A.	2.59	0.00355
KS-03-11L	14	19/07/2016	0.00040	0.00140	0.00057	0.00060	0.00020	N.A.	N.A.	0.67	0.00292
KS-03-11L	17	03/02/2017	0.00227	0.00244	0.00076	0.00061	0.00030	0.04139	0.00037	**11.65**	**0.01267**
KS-03-11L	18	03/02/2017	0.00181	0.00157	0.00073	0.00109	0.00031	0.01021	0.00037	3.43	0.00522
KS-03-11L	19	03/02/2017	0.00375	0.00482	0.00081	0.00215	0.00032	0.01040	0.00015	2.91	0.00528
KS-03-11L	20	03/02/2017	0.00233	0.00568	0.00074	0.00131	0.00031	0.04724	0.00020	**12.99**	**0.01165**
KS-03-11L	21	03/02/2017	0.00123	0.00253	0.00076	0.00067	0.00031	0.01074	0.00024	3.47	0.00713
KS-03-11L	22	06/02/2017	0.00094	0.00176	0.00056	0.00246	0.00025	0.01830	0.00017	5.52	0.00557
KS-03-11L	23	06/02/2017	0.00083	0.00026	0.00052	0.00135	0.00025	0.00031	0.00012	0.12	0.00245
KS-03-11L	25	06/02/2017	0.00083	0.00128	0.00052	0.00070	0.00028	0.00622	0.00017	1.91	0.00289
KS-03-11L	26	06/02/2017	0.00043	0.00021	0.00055	0.00021	0.00024	0.00301	0.00013	0.72	0.00316
KS-03-11L	27	06/02/2017	0.00072	0.00165	0.00051	0.00196	0.00026	0.00129	0.00013	0.38	0.00297
KS-03-11L	28	06/02/2017	0.00386	0.00543	0.00058	0.00124	0.00025	0.03860	0.00018	**11.12**	**0.00513**
KS-03-11L	29	03/10/2018	0.00469	0.00085	0.00025	0.00040	0.00011	0.00427	0.00003	1.27	0.00177
KS-03-11L	30	03/10/2018	0.00362	0.00171	0.00026	0.00122	0.00011	0.01215	0.00009	3.38	0.00221
KS-03-11L	31	03/10/2018	0.00424	0.00042	0.00024	0.00033	0.00010	0.00019	0.00002	0.02	0.00063
KS-03-11L	32	03/10/2018	0.00273	0.00066	0.00025	0.00043	0.00011	0.00013	0.00003	0.03	0.00059
KS-03-11L	33	03/10/2018	0.00340	0.00044	0.00024	0.00016	0.00011	0.00014	0.00002	0.02	0.00066
KS-03-11L	34	03/10/2018	0.00356	0.00116	0.00024	0.00060	0.00011	0.00169	0.00004	0.49	0.00078
KS-03-11L	35	03/10/2018	0.00205	0.00106	0.00023	0.00033	0.00011	0.01169	0.00012	3.23	0.00176

NG Analyses of Pele's hairs and tears (cc)

Sample	Grain	4He	±	22Ne	±	36Ar	±	40Ar	±
KS15-03	1	1.08E-10	4.53E-12	2.64E-11	2.12E-12	N.A.	N.A.	7.67E-10	5.32E-12
KS15-03	2	1.23E-10	4.74E-12	1.70E-11	2.20E-12	N.A.	N.A.	**1.88E-08**	**5.45E-12**
KS15-03	3	7.34E-11	5.25E-12	1.73E-11	1.95E-12	N.A.	N.A.	**1.88E-08**	**5.11E-12**
KS15-03	4	4.48E-11	4.74E-12	6.11E-12	1.87E-12	N.A.	N.A.	5.93E-09	6.26E-12
KS15-03	5	2.09E-11	4.74E-12	4.24E-13	2.12E-12	N.A.	N.A.	4.22E-11	5.02E-12
KS15-03	6	6.92E-11	4.94E-12	1.38E-11	2.46E-12	N.A.	N.A.	4.47E-09	1.45E-11
KS15-03	7	6.45E-11	4.64E-12	2.04E-11	2.12E-12	N.A.	N.A.	4.69E-09	2.54E-11
KS15-03	9	3.11E-11	5.36E-12	1.87E-11	1.78E-12	N.A.	N.A.	**1.88E-08**	**4.57E-12**
KS15-03	10	1.82E-11	5.67E-12	1.36E-12	1.78E-12	N.A.	N.A.	7.04E-09	1.55E-11
KS15-03	11	2.04E-10	5.97E-12	6.13E-11	3.14E-12	N.A.	N.A.	1.89E-08	4.57E-12
KS15-03	12	1.63E-11	5.36E-12	6.53E-12	1.87E-12	N.A.	N.A.	7.27E-11	4.81E-12
KS15-03	13	1.96E-11	5.67E-12	1.02E-12	1.78E-12	N.A.	N.A.	5.09E-10	5.47E-12
KS15-03	14	2.39E-11	6.59E-12	-7.63E-13	2.97E-12	N.A.	N.A.	3.20E-09	4.60E-12
KS15-03	15	1.82E-11	6.70E-12	1.17E-11	3.05E-12	N.A.	N.A.	5.67E-10	3.45E-12
KS15-03	16	9.51E-11	7.31E-12	5.43E-12	2.97E-12	N.A.	N.A.	**1.88E-08**	**3.70E-12**
KS15-03	17	3.11E-11	6.49E-12	1.70E-13	3.22E-12	N.A.	N.A.	1.83E-09	6.64E-12
KS15-03	18	4.88E-11	7.11E-12	5.17E-12	2.88E-12	N.A.	N.A.	2.10E-09	6.94E-12
KS15-03	19	1.63E-11	6.70E-12	4.32E-12	2.97E-12	N.A.	N.A.	3.90E-09	6.57E-12
KS15-03	20	1.29E-11	7.00E-12	-1.53E-12	2.97E-12	N.A.	N.A.	5.60E-11	3.50E-12
KS15-03	21	3.26E-11	2.75E-12	8.66E-12	1.68E-12	4.85E-11	3.00E-13	**1.42E-08**	**3.75E-11**
KS15-03	23	2.35E-11	2.75E-12	1.75E-12	1.68E-12	7.20E-13	2.76E-13	1.49E-10	3.15E-11
KS15-03	24	2.66E-13	2.39E-12	1.01E-11	1.68E-12	1.58E-11	3.36E-13	4.45E-09	3.17E-11
KS15-03	25	2.00E-11	2.66E-12	8.52E-12	1.68E-12	1.61E-11	3.00E-13	4.18E-09	3.23E-11
KS15-03	27	9.04E-12	2.66E-12	4.96E-12	1.75E-12	2.69E-12	2.76E-13	5.89E-10	3.15E-11
KS15-03	28	1.79E-11	2.57E-12	1.99E-11	3.56E-12	1.28E-12	1.68E-13	2.50E-10	1.42E-11
KS15-03	29	1.73E-11	3.19E-12	1.88E-11	3.56E-12	2.44E-11	2.64E-13	6.96E-09	1.51E-11
KS15-03	30	1.80E-11	2.75E-12	8.38E-13	3.56E-12	1.13E-12	1.92E-13	1.26E-10	1.42E-11
KS15-03	31	2.54E-11	2.75E-12	3.56E-12	3.49E-12	7.56E-13	1.56E-13	1.63E-10	1.42E-11
KS15-03	32	2.15E-11	4.18E-12	2.57E-12	1.45E-12	2.45E-11	1.72E-13	7.39E-09	5.37E-12
KS15-03	33	1.93E-11	4.03E-12	1.85E-12	1.45E-12	4.09E-12	9.26E-14	1.19E-09	2.16E-12
KS15-03	34	6.48E-12	4.32E-12	3.96E-12	1.52E-12	1.32E-14	7.94E-14	2.04E-11	1.57E-12
KS15-03	35	3.34E-11	4.32E-12	1.98E-12	1.45E-12	1.18E-11	1.72E-13	3.66E-09	2.72E-12
KS15-03	37	9.66E-12	4.47E-12	4.55E-12	1.45E-12	6.79E-12	1.06E-13	2.04E-09	2.41E-12
KS15-03	38	2.02E-12	4.18E-12	5.93E-13	1.45E-12	3.84E-13	7.94E-14	1.10E-10	1.58E-12
KS15-03	39	7.93E-12	4.32E-12	-1.65E-12	1.45E-12	0.00E+00	9.26E-14	2.75E-11	1.54E-12
KS15-03	41	-4.90E-12	4.18E-12	3.23E-12	1.45E-12	1.61E-12	1.06E-13	5.69E-10	1.66E-12
KS15-03	42	-1.87E-12	4.18E-12	1.78E-12	1.45E-12	0.00E+00	9.26E-14	1.16E-11	1.54E-12
KS15-03	43	-4.90E-12	4.18E-12	1.98E-13	1.52E-12	1.15E-12	9.26E-14	3.11E-10	1.69E-12
KS15-03	44	-7.21E-13	4.18E-12	1.19E-12	1.45E-12	4.10E-13	9.26E-14	1.19E-10	1.58E-12

NG Analyses of Pele's hairs and tears (cc/g)

Sample	Grain	4He	±	% ±	22Ne	±	% ±	36Ar	±	% ±	40Ar	±	% ±	40Ar*	±	% ±
KS15-03	1	4.05E-08	1.70E-09	4	9.91E-09	7.97E-10	8	N.A.	N.A.	N.A.	2.88E-07	2.00E-09	0.7	N.A.	N.A.	N.A.
KS15-03	2	3.43E-08	1.32E-09	4	4.74E-09	6.16E-10	13	N.A.	N.A.	N.A.	**5.25E-06**	**1.52E-09**	**0.0**	N.A.	N.A.	N.A.
KS15-03	3	3.03E-08	2.17E-09	7	7.15E-09	8.06E-10	11	N.A.	N.A.	N.A.	**7.78E-06**	**2.11E-09**	**0.0**	N.A.	N.A.	N.A.
KS15-03	4	3.01E-08	3.18E-09	11	4.10E-09	1.25E-09	31	N.A.	N.A.	N.A.	3.98E-06	4.20E-09	0.1	N.A.	N.A.	N.A.
KS15-03	5	1.27E-08	2.89E-09	23	2.59E-10	1.29E-09	500	N.A.	N.A.	N.A.	2.57E-08	3.06E-09	11.9	N.A.	N.A.	N.A.
KS15-03	6	2.93E-08	2.09E-09	7	5.86E-09	1.04E-09	18	N.A.	N.A.	N.A.	1.89E-06	6.16E-09	0.3	N.A.	N.A.	N.A.
KS15-03	7	2.22E-08	1.59E-09	7	6.99E-09	7.29E-10	10	N.A.	N.A.	N.A.	1.61E-06	8.71E-09	0.5	N.A.	N.A.	N.A.
KS15-03	9	7.76E-09	1.34E-09	17	4.65E-09	4.44E-10	10	N.A.	N.A.	N.A.	**4.70E-06**	**1.14E-09**	**0.0**	N.A.	N.A.	N.A.
KS15-03	10	2.00E-08	6.23E-09	31	1.49E-09	1.96E-09	131	N.A.	N.A.	N.A.	7.73E-06	1.71E-08	0.2	N.A.	N.A.	N.A.
KS15-03	11	1.03E-07	3.02E-09	3	3.10E-08	1.58E-09	5	N.A.	N.A.	N.A.	9.52E-06	2.31E-09	0.0	N.A.	N.A.	N.A.
KS15-03	12	1.36E-08	4.46E-09	33	5.44E-09	1.55E-09	29	N.A.	N.A.	N.A.	6.06E-08	4.01E-09	6.6	N.A.	N.A.	N.A.
KS15-03	13	1.34E-08	3.88E-09	29	6.97E-10	1.22E-09	175	N.A.	N.A.	N.A.	3.48E-07	3.74E-09	1.1	N.A.	N.A.	N.A.
KS15-03	14	2.37E-08	6.53E-09	28	-7.56E-10	2.94E-09	-389	N.A.	N.A.	N.A.	3.17E-06	4.55E-09	0.1	N.A.	N.A.	N.A.
KS15-03	15	1.02E-08	3.76E-09	37	6.57E-09	1.72E-09	26	N.A.	N.A.	N.A.	3.19E-07	1.94E-09	0.6	N.A.	N.A.	N.A.
KS15-03	16	7.92E-08	6.09E-09	8	4.52E-09	2.47E-09	55	N.A.	N.A.	N.A.	**1.57E-05**	**3.08E-09**	**0.0**	N.A.	N.A.	N.A.
KS15-03	17	2.75E-08	5.74E-09	21	1.50E-10	2.85E-09	1900	N.A.	N.A.	N.A.	1.62E-06	5.87E-09	0.4	N.A.	N.A.	N.A.
KS15-03	18	6.51E-08	9.48E-09	15	6.90E-09	3.84E-09	56	N.A.	N.A.	N.A.	2.80E-06	9.25E-09	0.3	N.A.	N.A.	N.A.
KS15-03	19	2.01E-08	8.27E-09	41	5.34E-09	3.66E-09	69	N.A.	N.A.	N.A.	4.81E-06	8.11E-09	0.2	N.A.	N.A.	N.A.
KS15-03	20	1.37E-08	7.45E-09	54	-1.62E-09	3.16E-09	-194	N.A.	N.A.	N.A.	5.95E-08	3.72E-09	6.2	N.A.	N.A.	N.A.
KS15-03	21	2.67E-08	2.25E-09	8	7.10E-09	1.37E-09	19	3.98E-08	2.46E-10	1	**1.16E-05**	**3.07E-08**	**0.3**	**-2.69E-07**	**-2.46E-09**	**1**
KS15-03	23	1.59E-08	1.86E-09	12	1.18E-09	1.13E-09	96	4.86E-10	1.86E-10	38	1.01E-07	2.13E-08	21.2	-4.47E-08	-2.60E-08	58
KS15-03	24	2.71E-10	2.44E-09	900	1.03E-08	1.71E-09	17	1.61E-08	3.43E-10	2	4.54E-06	3.23E-08	0.7	-2.61E-07	-8.10E-09	3
KS15-03	25	3.78E-08	5.02E-09	13	1.61E-08	3.16E-09	20	3.04E-08	5.66E-10	2	7.89E-06	6.09E-08	0.8	-1.19E-06	-3.27E-08	3
KS15-03	27	1.17E-08	3.45E-09	29	6.44E-09	2.27E-09	35	3.49E-09	3.58E-10	10	7.66E-07	4.10E-08	5.4	-2.77E-07	-4.28E-08	15
KS15-03	28	2.27E-08	3.25E-09	14	2.52E-08	4.51E-09	18	1.63E-09	2.13E-10	13	3.17E-07	1.79E-08	5.7	-1.69E-07	-3.26E-08	19
KS15-03	29	1.57E-08	2.90E-09	18	1.71E-08	3.24E-09	19	2.22E-08	2.40E-10	1	6.33E-06	1.38E-08	0.2	-2.98E-07	-4.60E-09	2
KS15-03	30	2.77E-08	4.23E-09	15	1.29E-09	5.48E-09	425	1.74E-09	2.95E-10	17	1.93E-07	2.18E-08	11.3	-3.25E-07	-8.63E-08	27
KS15-03	31	4.54E-08	4.90E-09	11	6.36E-09	6.24E-09	98	1.35E-09	2.79E-10	21	2.90E-07	2.54E-08	8.7	-1.13E-07	-3.43E-08	30
KS15-03	32	3.48E-09	6.77E-10	19	4.17E-10	2.35E-10	56	3.97E-09	2.79E-11	1	1.20E-06	8.71E-10	0.1	1.14E-08	1.13E-10	1
KS15-03	33	2.86E-09	5.97E-10	21	2.73E-10	2.15E-10	79	6.05E-10	1.37E-11	2	1.77E-07	3.20E-10	0.2	-3.89E-09	-1.25E-10	3
KS15-03	34	2.33E-09	1.56E-09	67	1.42E-09	5.45E-10	38	4.76E-12	2.86E-11	600	7.34E-09	5.64E-10	7.7	5.92E-09	5.02E-08	849
KS15-03	35	4.51E-09	5.83E-10	13	2.67E-10	1.95E-10	73	1.59E-09	2.32E-11	1	4.94E-07	3.67E-10	0.1	1.95E-08	4.02E-10	2
KS15-03	37	2.31E-09	1.07E-09	46	1.09E-09	3.47E-10	32	1.62E-09	2.53E-11	2	4.89E-07	5.77E-10	0.1	3.95E-09	8.73E-11	2
KS15-03	38	9.99E-10	2.07E-09	207	2.94E-10	7.18E-10	244	1.90E-10	3.93E-11	21	5.43E-08	7.84E-10	1.4	-2.39E-09	-6.99E-10	29
KS15-03	39	1.03E-09	5.64E-10	55	-2.15E-10	1.89E-10	-88	0.00E+00	1.21E-11	0	3.59E-09	2.01E-10	5.6	0.00	0.00	0.00
KS15-03	41	-2.29E-09	1.95E-09	-85	1.51E-09	6.78E-10	45	7.54E-10	4.95E-11	7	2.66E-07	7.75E-10	0.3	4.09E-08	3.79E-09	9
KS15-03	42	-4.05E-10	9.05E-10	-223	3.85E-10	3.14E-10	81	0.00E+00	2.00E-11	0	2.52E-09	3.33E-10	13.2	0.00	0.00	0.00
KS15-03	43	-8.97E-10	7.65E-10	-85	3.62E-11	2.78E-10	767	2.11E-10	1.70E-11	8	5.69E-08	3.09E-10	0.5	-6.02E-09	-6.85E-10	11
KS15-03	44	-1.66E-10	9.61E-10	-580	2.73E-10	3.33E-10	122	9.43E-11	2.13E-11	23	2.73E-08	3.64E-10	1.3	-9.00E-10	-2.88E-10	32

NG Analyses of Pele's hairs and tears

Sample	Grain	40Ar/36Ar	±	% ±	He/Ar*	±	% ±
KS15-03	1	N.A.	N.A.	N.A.	N.A.	N.A.	N.A.
KS15-03	2	N.A.	N.A.	N.A.	N.A.	N.A.	N.A.
KS15-03	3	N.A.	N.A.	N.A.	N.A.	N.A.	N.A.
KS15-03	4	N.A.	N.A.	N.A.	N.A.	N.A.	N.A.
KS15-03	5	N.A.	N.A.	N.A.	N.A.	N.A.	N.A.
KS15-03	6	N.A.	N.A.	N.A.	N.A.	N.A.	N.A.
KS15-03	7	N.A.	N.A.	N.A.	N.A.	N.A.	N.A.
KS15-03	9	N.A.	N.A.	N.A.	N.A.	N.A.	N.A.
KS15-03	10	N.A.	N.A.	N.A.	N.A.	N.A.	N.A.
KS15-03	11	N.A.	N.A.	N.A.	N.A.	N.A.	N.A.
KS15-03	12	N.A.	N.A.	N.A.	N.A.	N.A.	N.A.
KS15-03	13	N.A.	N.A.	N.A.	N.A.	N.A.	N.A.
KS15-03	14	N.A.	N.A.	N.A.	N.A.	N.A.	N.A.
KS15-03	15	N.A.	N.A.	N.A.	N.A.	N.A.	N.A.
KS15-03	16	N.A.	N.A.	N.A.	N.A.	N.A.	N.A.
KS15-03	17	N.A.	N.A.	N.A.	N.A.	N.A.	N.A.
KS15-03	18	N.A.	N.A.	N.A.	N.A.	N.A.	N.A.
KS15-03	19	N.A.	N.A.	N.A.	N.A.	N.A.	N.A.
KS15-03	20	N.A.	N.A.	N.A.	N.A.	N.A.	N.A.
KS15-03	21	**291.8**	**2.0**	**1**	**-9.93E-02**	**-8.41E-03**	**8**
KS15-03	23	206.7	90.5	44	-3.55E-01	-2.11E-01	59
KS15-03	24	282.3	6.3	2	-1.04E-03	-9.34E-03	900
KS15-03	25	259.4	5.2	2	-3.17E-02	-4.30E-03	14
KS15-03	27	219.3	25.4	12	-4.24E-02	-1.41E-02	33
KS15-03	28	194.8	27.8	14	-1.34E-01	-3.24E-02	24
KS15-03	29	285.1	3.1	1	-5.28E-02	-9.78E-03	19
KS15-03	30	111.5	22.8	20	-8.52E-02	-2.61E-02	31
KS15-03	31	215.1	48.2	22	-4.03E-01	-1.30E-01	32
KS15-03	32	301.4	2.1	1	3.07E-01	5.97E-02	19
KS15-03	33	292.1	6.6	2	-7.34E-01	-1.55E-01	21
KS15-03	34	1541.5	9249.9	600	3.94E-01	3.36E+00	851
KS15-03	35	310.8	4.5	1	2.32E-01	3.03E-02	13
KS15-03	37	301.0	4.7	2	5.84E-01	2.71E-01	46
KS15-03	38	286.0	59.3	21	-4.18E-01	-8.75E-01	209
KS15-03	39	0.00	0.00	0.00	0.00	0.00	0.00
KS15-03	41	352.7	23.2	7	-5.60E-02	-4.81E-02	86
KS15-03	42	0.00	0.00	0.00	0.00	0.00	0.00
KS15-03	43	270.0	21.8	8	1.49E-01	1.28E-01	86
KS15-03	44	289.0	65.4	23	1.84E-01	1.07E+00	581

NG Analyses of Pele's hairs and tears

Sample	Grain	Date	Weight (g)	4He (v)	± (v)	22Ne (v)	± (v)	36Ar (v)	± (v)	40Ar (v)	± (v)
KS-03-10S	1	21/07/2016	0.00133	0.00048	0.00018	0.00120	0.00014	N.A.	N.A.	1.53	0.00448
KS-03-10S	2	21/07/2016	0.00144	-0.00006	0.00014	0.00032	0.00016	N.A.	N.A.	0.11	0.00112
KS-03-10S	4	21/07/2016	0.00110	0.00210	0.00011	0.00070	0.00014	N.A.	N.A.	3.57	0.00429
KS-03-10S	5	21/07/2016	0.00052	0.00007	0.00016	0.00050	0.00014	N.A.	N.A.	3.09	0.00169
KS-03-10S	6	21/07/2016	0.00017	0.00086	0.00017	-0.00011	0.00014	N.A.	N.A.	0.37	0.00170
KS-03-10S	7	21/07/2016	0.00039	0.00094	0.00023	0.00022	0.00014	N.A.	N.A.	0.64	0.00185
KS-03-10S	8	23/10/2016	0.00336	0.00604	0.00077	0.00303	0.00019	N.A.	N.A.	**13.92**	**0.04259**
KS-03-10S	9	23/10/2016	0.00348	0.00239	0.00076	0.00250	0.00022	N.A.	N.A.	4.25	0.04304
KS-03-10S	10	23/10/2016	0.00589	0.02290	0.00087	0.00939	0.00023	N.A.	N.A.	**13.86**	**0.00541**
KS-03-10S	11	23/10/2016	0.00146	0.00122	0.00087	0.00059	0.00017	N.A.	N.A.	0.18	0.00565
KS-03-10S	12	23/10/2016	0.00090	0.00147	0.00088	0.00017	0.00017	N.A.	N.A.	3.74	0.01206
KS-03-10S	13	23/10/2016	0.00108	0.00310	0.00087	0.00048	0.00017	N.A.	N.A.	8.99	0.00930
KS-03-10S	14	23/10/2016	0.00204	0.00296	0.00089	0.00177	0.00019	N.A.	N.A.	7.36	0.01363
KS-03-10S	15	25/10/2016	0.00050	0.00158	0.00031	0.00079	0.00019	N.A.	N.A.	0.29	0.00427
KS-03-10S	16	25/10/2016	0.00109	0.00778	0.00033	0.00215	0.00019	N.A.	N.A.	**13.87**	**0.00399**
KS-03-10S	18	25/10/2016	0.00093	0.00006	0.00030	0.00008	0.00018	N.A.	N.A.	1.82	0.00680
KS-03-10S	19	25/10/2016	0.00058	0.00099	0.00033	0.00048	0.00018	N.A.	N.A.	1.41	0.00523
KS-03-10S	20	25/10/2016	0.00046	0.00125	0.00026	0.00036	0.00018	N.A.	N.A.	1.02	0.00531
KS-03-10S	21	25/10/2016	0.00034	-0.00036	0.00043	-0.00015	0.00019	N.A.	N.A.	**13.86**	**0.00403**
KS-03-11L	1	18/07/2016	0.00306	0.00195	0.00021	0.00200	0.00017	N.A.	N.A.	**13.87**	**0.00171**
KS-03-11L	2	18/07/2016	0.00058	0.00003	0.00019	-0.00015	0.00016	N.A.	N.A.	0.08	0.00152
KS-03-11L	3	18/07/2016	0.00058	0.00154	0.00018	0.00033	0.00016	N.A.	N.A.	1.37	0.00165
KS-03-11L	4	18/07/2016	0.00148	0.00014	0.00017	0.00138	0.00017	N.A.	N.A.	1.60	0.00261
KS-03-11L	5	18/07/2016	0.00055	0.00157	0.00016	0.00096	0.00017	N.A.	N.A.	2.85	0.00555
KS-03-11L	6	18/07/2016	0.00033	0.00104	0.00015	0.00031	0.00017	N.A.	N.A.	1.33	0.00171
KS-03-11L	7	18/07/2016	0.00058	0.00004	0.00015	0.00142	0.00017	N.A.	N.A.	0.96	0.00209
KS-03-11L	8	19/07/2016	0.00064	0.00060	0.00056	0.00072	0.00019	N.A.	N.A.	4.72	0.00391
KS-03-11L	9	19/07/2016	0.00044	0.00014	0.00057	0.00055	0.00019	N.A.	N.A.	0.51	0.00306
KS-03-11L	10	19/07/2016	0.00047	0.00030	0.00056	0.00023	0.00020	N.A.	N.A.	1.72	0.00366
KS-03-11L	11	19/07/2016	0.00035	0.00036	0.00061	0.00028	0.00019	N.A.	N.A.	0.32	0.00306
KS-03-11L	12	19/07/2016	0.00033	0.00054	0.00056	0.00064	0.00020	N.A.	N.A.	2.59	0.00355
KS-03-11L	14	19/07/2016	0.00040	0.00140	0.00057	0.00060	0.00020	N.A.	N.A.	0.67	0.00292
KS-03-11L	17	03/02/2017	0.00227	0.00244	0.00076	0.00061	0.00030	0.04139	0.00037	**11.65**	**0.01267**
KS-03-11L	18	03/02/2017	0.00181	0.00157	0.00073	0.00109	0.00031	0.01021	0.00037	3.43	0.00522
KS-03-11L	19	03/02/2017	0.00375	0.00482	0.00081	0.00215	0.00032	0.01040	0.00015	2.91	0.00528
KS-03-11L	20	03/02/2017	0.00233	0.00568	0.00074	0.00131	0.00031	0.04724	0.00020	**12.99**	**0.01165**
KS-03-11L	21	03/02/2017	0.00123	0.00253	0.00076	0.00067	0.00031	0.01074	0.00024	3.47	0.00713
KS-03-11L	22	06/02/2017	0.00094	0.00176	0.00056	0.00246	0.00025	0.01830	0.00017	5.52	0.00557
KS-03-11L	23	06/02/2017	0.00083	0.00026	0.00052	0.00135	0.00025	0.00031	0.00012	0.12	0.00245
KS-03-11L	25	06/02/2017	0.00083	0.00128	0.00052	0.00070	0.00028	0.00622	0.00017	1.91	0.00289
KS-03-11L	26	06/02/2017	0.00043	0.00021	0.00055	0.00021	0.00024	0.00301	0.00013	0.72	0.00316
KS-03-11L	27	06/02/2017	0.00072	0.00165	0.00051	0.00196	0.00026	0.00129	0.00013	0.38	0.00297
KS-03-11L	28	06/02/2017	0.00386	0.00543	0.00058	0.00124	0.00025	0.03860	0.00018	**11.12**	**0.00513**
KS-03-11L	29	03/10/2018	0.00469	0.00085	0.00025	0.00040	0.00011	0.00427	0.00003	1.27	0.00177
KS-03-11L	30	03/10/2018	0.00362	0.00171	0.00026	0.00122	0.00011	0.01215	0.00009	3.38	0.00221
KS-03-11L	31	03/10/2018	0.00424	0.00042	0.00024	0.00033	0.00010	0.00019	0.00002	0.02	0.00063
KS-03-11L	32	03/10/2018	0.00273	0.00066	0.00025	0.00043	0.00011	0.00013	0.00003	0.03	0.00059
KS-03-11L	33	03/10/2018	0.00340	0.00044	0.00024	0.00016	0.00011	0.00014	0.00002	0.02	0.00066
KS-03-11L	34	03/10/2018	0.00356	0.00116	0.00024	0.00060	0.00011	0.00169	0.00004	0.49	0.00078
KS-03-11L	35	03/10/2018	0.00205	0.00106	0.00023	0.00033	0.00011	0.01169	0.00012	3.23	0.00176

NG Analyses of Pele's hairs and tears (cc)

Sample	Grain	4He	±	22Ne	±	36Ar	±	40Ar	±
KS-03-10S	1	1.23E-11	4.63E-12	1.17E-10	1.36E-11	N.A.	N.A.	2.24E-09	6.54E-12
KS-03-10S	2	-1.54E-12	3.60E-12	3.11E-11	1.56E-11	N.A.	N.A.	1.57E-10	1.64E-12
KS-03-10S	4	5.40E-11	2.83E-12	6.81E-11	1.36E-11	N.A.	N.A.	5.21E-09	6.26E-12
KS-03-10S	5	1.80E-12	4.11E-12	4.87E-11	1.36E-11	N.A.	N.A.	4.52E-09	2.47E-12
KS-03-10S	6	2.21E-11	4.37E-12	-1.07E-11	1.36E-11	N.A.	N.A.	5.34E-10	2.48E-12
KS-03-10S	7	2.42E-11	5.91E-12	2.14E-11	1.36E-11	N.A.	N.A.	9.29E-10	2.70E-12
KS-03-10S	8	6.10E-11	7.78E-12	2.99E-11	1.88E-12	N.A.	N.A.	**2.48E-08**	**7.58E-11**
KS-03-10S	9	2.41E-11	7.68E-12	2.47E-11	2.17E-12	N.A.	N.A.	7.56E-09	7.66E-11
KS-03-10S	10	2.31E-10	8.79E-12	9.28E-11	2.27E-12	N.A.	N.A.	**2.47E-08**	**9.63E-12**
KS-03-10S	11	1.23E-11	8.79E-12	5.83E-12	1.68E-12	N.A.	N.A.	3.24E-10	1.01E-11
KS-03-10S	12	1.48E-11	8.89E-12	1.68E-12	1.68E-12	N.A.	N.A.	6.66E-09	2.15E-11
KS-03-10S	13	3.13E-11	8.79E-12	4.74E-12	1.68E-12	N.A.	N.A.	1.60E-08	1.66E-11
KS-03-10S	14	2.99E-11	8.99E-12	1.75E-11	1.88E-12	N.A.	N.A.	1.31E-08	2.43E-11
KS-03-10S	15	1.63E-11	3.19E-12	6.70E-12	1.61E-12	N.A.	N.A.	3.02E-09	4.40E-11
KS-03-10S	16	8.01E-11	3.40E-12	1.82E-11	1.61E-12	N.A.	N.A.	**1.43E-07**	**4.11E-11**
KS-03-10S	18	6.18E-13	3.09E-12	6.78E-13	1.53E-12	N.A.	N.A.	1.88E-08	7.00E-11
KS-03-10S	19	1.02E-11	3.40E-12	4.07E-12	1.53E-12	N.A.	N.A.	1.45E-08	5.39E-11
KS-03-10S	20	1.29E-11	2.68E-12	3.05E-12	1.53E-12	N.A.	N.A.	1.05E-08	5.47E-11
KS-03-10S	21	-3.71E-12	4.43E-12	-1.27E-12	1.61E-12	N.A.	N.A.	**1.43E-07**	**4.15E-11**
KS-03-11L	1	5.01E-11	5.40E-12	1.9E-10	1.7E-11	N.A.	N.A.	**2.02E-08**	**2.50E-12**
KS-03-11L	2	7.71E-13	4.88E-12	-1.5E-11	1.6E-11	N.A.	N.A.	1.17E-10	2.22E-12
KS-03-11L	3	3.96E-11	4.63E-12	3.2E-11	1.6E-11	N.A.	N.A.	2.01E-09	2.41E-12
KS-03-11L	4	3.60E-12	4.37E-12	1.3E-10	1.7E-11	N.A.	N.A.	2.34E-09	3.81E-12
KS-03-11L	5	4.03E-11	4.11E-12	9.3E-11	1.7E-11	N.A.	N.A.	4.17E-09	8.10E-12
KS-03-11L	6	2.67E-11	3.86E-12	3.0E-11	1.7E-11	N.A.	N.A.	1.94E-09	2.50E-12
KS-03-11L	7	1.03E-12	3.86E-12	1.4E-10	1.7E-11	N.A.	N.A.	1.41E-09	3.05E-12
KS-03-11L	8	1.54E-11	1.44E-11	7.0E-11	1.8E-11	N.A.	N.A.	6.90E-09	5.71E-12
KS-03-11L	9	3.60E-12	1.46E-11	5.4E-11	1.8E-11	N.A.	N.A.	7.42E-10	4.47E-12
KS-03-11L	10	7.71E-12	1.44E-11	2.2E-11	1.9E-11	N.A.	N.A.	2.51E-09	5.34E-12
KS-03-11L	11	9.25E-12	1.57E-11	2.7E-11	1.8E-11	N.A.	N.A.	4.66E-10	4.47E-12
KS-03-11L	12	1.39E-11	1.44E-11	6.2E-11	1.9E-11	N.A.	N.A.	3.78E-09	5.18E-12
KS-03-11L	14	3.60E-11	1.46E-11	5.8E-11	1.9E-11	N.A.	N.A.	9.80E-10	4.26E-12
KS-03-11L	17	2.16E-11	6.73E-12	4.3E-12	2.1E-12	4.97E-11	4.44E-13	**1.41E-08**	**1.53E-11**
KS-03-11L	18	1.39E-11	6.47E-12	7.6E-12	2.2E-12	1.23E-11	4.44E-13	4.14E-09	6.32E-12
KS-03-11L	19	4.27E-11	7.18E-12	1.5E-11	2.2E-12	1.25E-11	1.80E-13	3.52E-09	6.39E-12
KS-03-11L	20	5.03E-11	6.56E-12	9.1E-12	2.2E-12	5.67E-11	2.40E-13	**1.57E-08**	**1.41E-11**
KS-03-11L	21	2.24E-11	6.73E-12	4.7E-12	2.2E-12	1.29E-11	2.88E-13	4.20E-09	8.63E-12
KS-03-11L	22	1.56E-11	4.96E-12	1.7E-11	1.7E-12	2.20E-11	2.04E-13	6.68E-09	6.74E-12
KS-03-11L	23	2.30E-12	4.61E-12	9.4E-12	1.7E-12	3.72E-13	1.44E-13	1.50E-10	2.96E-12
KS-03-11L	25	1.13E-11	4.61E-12	4.9E-12	2.0E-12	7.46E-12	2.04E-13	2.31E-09	3.50E-12
KS-03-11L	26	1.86E-12	4.87E-12	1.5E-12	1.7E-12	3.61E-12	1.56E-13	8.74E-10	3.82E-12
KS-03-11L	27	1.46E-11	4.52E-12	1.4E-11	1.8E-12	1.55E-12	1.56E-13	4.59E-10	3.59E-12
KS-03-11L	28	4.81E-11	5.14E-12	8.7E-12	1.7E-12	4.63E-11	2.16E-13	**1.35E-08**	**6.21E-12**
KS-03-11L	29	1.12E-11	3.28E-12	2.50E-12	6.88E-13	5.87E-12	4.12E-14	1.80E-09	2.51E-12
KS-03-11L	30	2.25E-11	3.42E-12	7.63E-12	6.88E-13	1.67E-11	1.24E-13	4.79E-09	3.13E-12
KS-03-11L	31	5.52E-12	3.15E-12	2.06E-12	6.25E-13	2.61E-13	2.75E-14	3.35E-11	8.93E-13
KS-03-11L	32	8.67E-12	3.28E-12	2.69E-12	6.88E-13	1.79E-13	4.12E-14	3.73E-11	8.36E-13
KS-03-11L	33	5.78E-12	3.15E-12	1.00E-12	6.88E-13	1.92E-13	2.75E-14	3.48E-11	9.35E-13
KS-03-11L	34	1.52E-11	3.15E-12	3.75E-12	6.88E-13	2.32E-12	5.50E-14	6.96E-10	1.11E-12
KS-03-11L	35	1.39E-11	3.02E-12	2.06E-12	6.88E-13	1.61E-11	1.65E-13	4.58E-09	2.49E-12

NG Analyses of Pele's hairs and tears (cc/g)

Sample	Grain	4He	±	% ±	22Ne	±	% ±	36Ar	±	% ±	40Ar	±	% ±	40Ar*	±	% ±
KS-03-10S	1	9.28E-09	3.48E-09	38	8.78E-08	1.02E-08	12	N.A.	N.A.	N.A.	1.68E-06	4.92E-09	0.3	N.A.	N.A.	N.A.
KS-03-10S	2	-1.07E-09	2.50E-09	-233	2.16E-08	1.08E-08	50	N.A.	N.A.	N.A.	1.09E-07	1.14E-09	1.0	N.A.	N.A.	N.A.
KS-03-10S	4	4.91E-08	2.57E-09	5	6.19E-08	1.24E-08	20	N.A.	N.A.	N.A.	4.73E-06	5.69E-09	0.1	N.A.	N.A.	N.A.
KS-03-10S	5	3.46E-09	7.91E-09	229	9.36E-08	2.62E-08	28	N.A.	N.A.	N.A.	8.69E-06	4.75E-09	0.1	N.A.	N.A.	N.A.
KS-03-10S	6	1.30E-07	2.57E-08	20	-6.30E-08	8.01E-08	-127	N.A.	N.A.	N.A.	3.14E-06	1.46E-08	0.5	N.A.	N.A.	N.A.
KS-03-10S	7	6.19E-08	1.52E-08	24	5.49E-08	3.49E-08	64	N.A.	N.A.	N.A.	2.38E-06	6.93E-09	0.3	N.A.	N.A.	N.A.
KS-03-10S	8	1.82E-08	2.31E-09	13	8.91E-09	5.59E-10	6	N.A.	N.A.	N.A.	**7.38E-06**	**2.26E-08**	**0.3**	N.A.	N.A.	N.A.
KS-03-10S	9	6.94E-09	2.21E-09	32	7.10E-09	6.25E-10	9	N.A.	N.A.	N.A.	2.17E-06	2.20E-08	1.0	N.A.	N.A.	N.A.
KS-03-10S	10	3.93E-08	1.49E-09	4	1.58E-08	3.86E-10	2	N.A.	N.A.	N.A.	**4.19E-06**	**1.63E-09**	**0.0**	N.A.	N.A.	N.A.
KS-03-10S	11	8.44E-09	6.02E-09	71	3.99E-09	1.15E-09	29	N.A.	N.A.	N.A.	2.22E-07	6.89E-09	3.1	N.A.	N.A.	N.A.
KS-03-10S	12	1.65E-08	9.88E-09	60	1.87E-09	1.87E-09	100	N.A.	N.A.	N.A.	7.40E-06	2.39E-08	0.3	N.A.	N.A.	N.A.
KS-03-10S	13	2.90E-08	8.14E-09	28	4.39E-09	1.56E-09	35	N.A.	N.A.	N.A.	1.48E-05	1.53E-08	0.1	N.A.	N.A.	N.A.
KS-03-10S	14	1.47E-08	4.41E-09	30	8.57E-09	9.20E-10	11	N.A.	N.A.	N.A.	6.43E-06	1.19E-08	0.2	N.A.	N.A.	N.A.
KS-03-10S	15	3.25E-08	6.39E-09	20	1.34E-08	3.22E-09	24	N.A.	N.A.	N.A.	6.05E-06	8.80E-08	1.5	N.A.	N.A.	N.A.
KS-03-10S	16	7.35E-08	3.12E-09	4	1.67E-08	1.48E-09	9	N.A.	N.A.	N.A.	**1.31E-04**	**3.77E-08**	**0.0**	N.A.	N.A.	N.A.
KS-03-10S	18	6.65E-10	3.32E-09	500	7.29E-10	1.64E-09	225	N.A.	N.A.	N.A.	2.02E-05	7.53E-08	0.4	N.A.	N.A.	N.A.
KS-03-10S	19	1.76E-08	5.86E-09	33	7.02E-09	2.63E-09	38	N.A.	N.A.	N.A.	2.51E-05	9.29E-08	0.4	N.A.	N.A.	N.A.
KS-03-10S	20	2.80E-08	5.82E-09	21	6.64E-09	3.32E-09	50	N.A.	N.A.	N.A.	2.29E-05	1.19E-07	0.5	N.A.	N.A.	N.A.
KS-03-10S	21	-1.09E-08	1.30E-08	-119	-3.74E-09	4.74E-09	-127	N.A.	N.A.	N.A.	**4.20E-04**	**1.22E-07**	**0.0**	N.A.	N.A.	N.A.
KS-03-11L	1	1.64E-08	1.76E-09	11	6.36E-08	5.41E-09	9	N.A.	N.A.	N.A.	**6.62E-06**	**8.16E-10**	**0.0**	N.A.	N.A.	N.A.
KS-03-11L	2	1.33E-09	8.42E-09	633	-2.52E-08	2.68E-08	-107	N.A.	N.A.	N.A.	2.02E-07	3.83E-09	1.9	N.A.	N.A.	N.A.
KS-03-11L	3	6.82E-08	7.98E-09	12	5.54E-08	2.68E-08	48	N.A.	N.A.	N.A.	3.46E-06	4.15E-09	0.1	N.A.	N.A.	N.A.
KS-03-11L	4	2.43E-09	2.95E-09	121	9.07E-08	1.12E-08	12	N.A.	N.A.	N.A.	1.58E-06	2.57E-09	0.2	N.A.	N.A.	N.A.
KS-03-11L	5	7.34E-08	7.48E-09	10	1.70E-07	3.01E-08	18	N.A.	N.A.	N.A.	7.58E-06	1.47E-08	0.2	N.A.	N.A.	N.A.
KS-03-11L	6	8.10E-08	1.17E-08	14	9.14E-08	5.01E-08	55	N.A.	N.A.	N.A.	5.89E-06	7.57E-09	0.1	N.A.	N.A.	N.A.
KS-03-11L	7	1.77E-09	6.65E-09	375	2.38E-07	2.85E-08	12	N.A.	N.A.	N.A.	2.43E-06	5.26E-09	0.2	N.A.	N.A.	N.A.
KS-03-11L	8	2.41E-08	2.25E-08	93	1.09E-07	2.89E-08	26	N.A.	N.A.	N.A.	1.08E-05	8.92E-09	0.1	N.A.	N.A.	N.A.
KS-03-11L	9	8.18E-09	3.33E-08	407	1.22E-07	4.20E-08	35	N.A.	N.A.	N.A.	1.69E-06	1.02E-08	0.6	N.A.	N.A.	N.A.
KS-03-11L	10	1.64E-08	3.06E-08	187	4.76E-08	4.14E-08	87	N.A.	N.A.	N.A.	5.35E-06	1.14E-08	0.2	N.A.	N.A.	N.A.
KS-03-11L	11	2.64E-08	4.48E-08	169	7.78E-08	5.28E-08	68	N.A.	N.A.	N.A.	1.33E-06	1.28E-08	1.0	N.A.	N.A.	N.A.
KS-03-11L	12	4.21E-08	4.36E-08	104	1.89E-07	5.90E-08	31	N.A.	N.A.	N.A.	1.14E-05	1.57E-08	0.1	N.A.	N.A.	N.A.
KS-03-11L	14	9.00E-08	3.66E-08	41	1.46E-07	4.87E-08	33	N.A.	N.A.	N.A.	2.45E-06	1.07E-08	0.4	N.A.	N.A.	N.A.
KS-03-11L	17	9.52E-09	2.97E-09	31	1.88E-09	9.23E-10	49	2.19E-08	1.96E-10	1	**6.21E-06**	**6.75E-09**	**0.1**	**-3.3E-07**	**-4.1E-09**	**1**
KS-03-11L	18	7.69E-09	3.57E-09	46	4.21E-09	1.20E-09	28	6.77E-09	2.45E-10	4	2.29E-06	3.49E-09	0.2	2.69E-07	1.38E-08	5
KS-03-11L	19	1.14E-08	1.91E-09	17	4.00E-09	5.96E-10	15	3.33E-09	4.80E-11	1	9.38E-07	1.70E-09	0.2	-5.56E-08	-1.14E-09	2
KS-03-11L	20	2.16E-08	2.81E-09	13	3.93E-09	9.29E-10	24	2.43E-08	1.03E-10	0	**6.75E-06**	**6.05E-09**	**0.1**	**-5.18E-07**	**-3.14E-09**	**1**
KS-03-11L	21	1.82E-08	5.47E-09	30	3.80E-09	1.76E-09	46	1.05E-08	2.34E-10	2	3.41E-06	7.01E-09	0.2	2.86E-07	9.05E-09	3
KS-03-11L	22	1.66E-08	5.28E-09	32	1.83E-08	1.86E-09	10	2.34E-08	2.17E-10	1	7.10E-06	7.17E-09	0.1	1.30E-07	1.71E-09	1
KS-03-11L	23	2.78E-09	5.55E-09	200	1.14E-08	2.10E-09	19	4.48E-10	1.73E-10	39	1.81E-07	3.57E-09	2.0	4.73E-08	2.59E-08	55
KS-03-11L	25	1.37E-08	5.55E-09	41	5.89E-09	2.36E-09	40	8.99E-09	2.46E-10	3	2.78E-06	4.21E-09	0.2	9.65E-08	3.73E-09	4
KS-03-11L	26	4.33E-09	1.13E-08	262	3.41E-09	3.90E-09	114	8.40E-09	3.63E-10	4	2.03E-06	8.89E-09	0.4	-4.74E-07	-2.90E-08	6
KS-03-11L	27	2.03E-08	6.28E-09	31	1.90E-08	2.52E-09	13	2.15E-09	2.17E-10	10	6.38E-07	4.99E-09	0.8	-4.10E-09	-5.85E-10	14
KS-03-11L	28	1.25E-08	1.33E-09	11	2.24E-09	4.52E-10	20	1.20E-08	5.60E-11	0	**3.49E-06**	**1.61E-09**	**0.0**	**-9.75E-08**	**-6.45E-10**	**1**
KS-03-11L	29	2.38E-09	7.00E-10	29	5.33E-10	1.47E-10	28	1.25E-09	8.79E-12	1	3.83E-07	5.35E-10	0.1	9.74E-09	9.77E-11	1
KS-03-11L	30	6.21E-09	9.44E-10	15	2.11E-09	1.90E-10	9	4.61E-09	3.42E-11	1	1.32E-06	8.65E-10	0.1	-5.42E-08	-5.68E-10	1
KS-03-11L	31	1.30E-09	7.44E-10	57	4.87E-10	1.47E-10	30	6.16E-11	6.48E-12	11	7.91E-09	2.11E-10	2.7	-1.05E-08	-1.58E-09	15
KS-03-11L	32	3.18E-09	1.20E-09	38	9.85E-10	2.52E-10	26	6.54E-11	1.51E-11	23	1.37E-08	3.06E-10	2.2	-5.88E-09	-1.92E-09	33
KS-03-11L	33	1.70E-09	9.27E-10	55	2.94E-10	2.02E-10	69	5.66E-11	8.08E-12	14	1.02E-08	2.75E-10	2.7	-6.65E-09	-1.35E-09	20
KS-03-11L	34	4.28E-09	8.86E-10	21	1.05E-09	1.93E-10	18	6.52E-10	1.54E-11	2	1.95E-07	3.10E-10	0.2	6.71E-10	2.25E-11	3
KS-03-11L	35	6.79E-09	1.47E-09	22	1.01E-09	3.36E-10	33	7.84E-09	8.04E-11	1	2.23E-06	1.22E-09	0.1	-1.06E-07	-1.54E-09	1

NG Analyses of Pele's hairs and tears

Sample	Grain	40Ar/36Ar	±	% ±	He/Ar*	±	% ±
KS-03-10S	1	N.A.	N.A.	N.A.	N.A.	N.A.	N.A.
KS-03-10S	2	N.A.	N.A.	N.A.	N.A.	N.A.	N.A.
KS-03-10S	4	N.A.	N.A.	N.A.	N.A.	N.A.	N.A.
KS-03-10S	5	N.A.	N.A.	N.A.	N.A.	N.A.	N.A.
KS-03-10S	6	N.A.	N.A.	N.A.	N.A.	N.A.	N.A.
KS-03-10S	7	N.A.	N.A.	N.A.	N.A.	N.A.	N.A.
KS-03-10S	8	N.A.	N.A.	N.A.	N.A.	N.A.	N.A.
KS-03-10S	9	N.A.	N.A.	N.A.	N.A.	N.A.	N.A.
KS-03-10S	10	N.A.	N.A.	N.A.	N.A.	N.A.	N.A.
KS-03-10S	11	N.A.	N.A.	N.A.	N.A.	N.A.	N.A.
KS-03-10S	12	N.A.	N.A.	N.A.	N.A.	N.A.	N.A.
KS-03-10S	13	N.A.	N.A.	N.A.	N.A.	N.A.	N.A.
KS-03-10S	14	N.A.	N.A.	N.A.	N.A.	N.A.	N.A.
KS-03-10S	15	N.A.	N.A.	N.A.	N.A.	N.A.	N.A.
KS-03-10S	16	N.A.	N.A.	N.A.	N.A.	N.A.	N.A.
KS-03-10S	18	N.A.	N.A.	N.A.	N.A.	N.A.	N.A.
KS-03-10S	19	N.A.	N.A.	N.A.	N.A.	N.A.	N.A.
KS-03-10S	20	N.A.	N.A.	N.A.	N.A.	N.A.	N.A.
KS-03-10S	21	N.A.	N.A.	N.A.	N.A.	N.A.	N.A.
KS-03-11L	1	N.A.	N.A.	N.A.	N.A.	N.A.	N.A.
KS-03-11L	2	N.A.	N.A.	N.A.	N.A.	N.A.	N.A.
KS-03-11L	3	N.A.	N.A.	N.A.	N.A.	N.A.	N.A.
KS-03-11L	4	N.A.	N.A.	N.A.	N.A.	N.A.	N.A.
KS-03-11L	5	N.A.	N.A.	N.A.	N.A.	N.A.	N.A.
KS-03-11L	6	N.A.	N.A.	N.A.	N.A.	N.A.	N.A.
KS-03-11L	7	N.A.	N.A.	N.A.	N.A.	N.A.	N.A.
KS-03-11L	8	N.A.	N.A.	N.A.	N.A.	N.A.	N.A.
KS-03-11L	9	N.A.	N.A.	N.A.	N.A.	N.A.	N.A.
KS-03-11L	10	N.A.	N.A.	N.A.	N.A.	N.A.	N.A.
KS-03-11L	11	N.A.	N.A.	N.A.	N.A.	N.A.	N.A.
KS-03-11L	12	N.A.	N.A.	N.A.	N.A.	N.A.	N.A.
KS-03-11L	14	N.A.	N.A.	N.A.	N.A.	N.A.	N.A.
KS-03-11L	17	**283.7**	**2.6**	**3**	**-2.93E-02**	**-9.13E-03**	**31**
KS-03-11L	18	338.3	12.3	12	2.86E-02	1.34E-02	47
KS-03-11L	19	281.9	4.1	4	-2.05E-01	-3.47E-02	17
KS-03-11L	20	**277.3**	**1.2**	**1**	**-4.17E-02**	**-5.44E-03**	**13**
KS-03-11L	21	325.8	7.3	7	6.38E-02	1.93E-02	30
KS-03-11L	22	304.1	2.8	3	1.28E-01	4.07E-02	32
KS-03-11L	23	404.1	156.6	157	5.87E-02	1.22E-01	207
KS-03-11L	25	309.3	8.5	8	1.42E-01	5.78E-02	41
KS-03-11L	26	242.1	10.5	11	-9.12E-03	-2.39E-02	262
KS-03-11L	27	296.7	30.0	30	-4.95E+00	-1.69E+00	34
KS-03-11L	28	**290.4**	**1.4**	**1**	**-1.28E-01**	**-1.37E-02**	**11**
KS-03-11L	29	306.3	2.2	2	2.44E-01	7.19E-02	29
KS-03-11L	30	286.8	2.1	2	-1.15E-01	-1.75E-02	15
KS-03-11L	31	128.4	13.9	14	-1.24E-01	-7.34E-02	59
KS-03-11L	32	208.7	48.4	48	-5.40E-01	-2.70E-01	50
KS-03-11L	33	181.1	26.3	26	-2.56E-01	-1.49E-01	58
KS-03-11L	34	299.6	7.1	7	6.38E+00	1.34E+00	21
KS-03-11L	35	285.1	2.9	3	-6.43E-02	-1.40E-02	22

NG Analyses of Pele's hairs and tears

Sample	Grain	Date	Weight (g)	4He (v)	± (v)	22Ne (v)	± (v)	36Ar (v)	± (v)	40Ar (v)	± (v)
KS-13-4L	2	22/07/2016	0.00463	0.00366	0.00019	0.00359	0.00005	N.A.	N.A.	**13.87**	**0.00165**
KS-13-4L	3	20/10/2016	0.00061	0.00191	0.00070	0.00072	0.00011	N.A.	N.A.	1.06	0.02918
KS-13-4L	4	20/10/2016	0.00076	0.00247	0.00068	0.00424	0.00014	N.A.	N.A.	1.48	0.02900
KS-13-4L	5	20/10/2016	0.00231	0.00550	0.00071	0.00229	0.00012	N.A.	N.A.	1.28	0.02911
KS-13-4L	6	20/10/2016	0.00101	0.00015	0.00069	0.00048	0.00014	N.A.	N.A.	0.24	0.02896
KS-13-4L	7	20/10/2016	0.00077	0.00045	0.00066	0.00062	0.00012	N.A.	N.A.	0.17	0.02929
KS-13-4L	8	07/11/2016	0.00109	0.00059	0.00079	0.00108	0.00023	N.A.	N.A.	0.03	0.00246
KS-13-4L	9	07/11/2016	0.00156	0.00042	0.00080	0.00147	0.00024	N.A.	N.A.	**13.82**	**0.00247**
KS-13-4L	10	07/11/2016	0.00041	0.00004	0.00081	0.00034	0.00024	N.A.	N.A.	0.27	0.00257
KS-13-4L	11	07/11/2016	0.00092	0.00029	0.00078	0.00117	0.00027	N.A.	N.A.	0.05	0.00263
KS-13-4L	12	07/11/2016	0.00127	0.00034	0.00080	0.00024	0.00024	N.A.	N.A.	0.08	0.00246
KS-13-4L	13	07/11/2016	0.00062	-0.00037	0.00078	-0.00016	0.00023	N.A.	N.A.	0.34	0.00251
KS-13-4L	14	12/02/2017	0.00720	0.02340	0.00065	0.00792	0.00031	0.21899	0.00144	**13.79**	**0.00697**
KS-13-4L	15	12/02/2017	0.00194	0.00542	0.00063	0.00185	0.00016	0.08621	0.00048	**13.75**	**0.00269**
KS-13-4L	16	12/02/2017	0.00172	0.00064	0.00064	0.00137	0.00017	0.00739	0.00017	2.25	0.00349
KS-13-4L	17	12/02/2017	0.00165	0.00158	0.00067	0.00082	0.00016	0.00330	0.00006	0.94	0.00384
KS-13-4L	18	12/02/2017	0.00480	0.00450	0.00065	0.00285	0.00018	0.09701	0.00025	**13.74**	**0.00296**
KS-13-4L	20	12/02/2017	0.00275	0.00216	0.00064	0.00009	0.00015	0.00391	0.00008	1.20	0.00399
KS-13-4L	21	15/02/2017	0.00126	0.00243	0.0005	0.00073	0.00022	0.0026	0.0001	0.80	0.0139
KS-13-4L	22	15/02/2017	0.00162	0.00092	0.0005	0.00112	0.00020	0.0013	0.0001	0.48	0.0138
KS-13-10L	1	09/11/2016	0.00325	0.00495	0.00046	0.00317	0.00030	N.A.	N.A.	**13.70**	**0.03353**
KS-13-10L	2	09/11/2016	0.00228	0.00254	0.00047	0.00094	0.00029	N.A.	N.A.	**13.72**	**0.03352**
KS-13-10L	3	09/11/2016	0.00097	0.00170	0.00043	0.00061	0.00030	N.A.	N.A.	**13.76**	**0.03391**
KS-13-10L	4	09/11/2016	0.00164	0.00314	0.00043	-0.00005	0.00030	N.A.	N.A.	7.40	0.03633
KS-13-10L	5	09/11/2016	0.00176	0.00243	0.00043	0.00090	0.00029	N.A.	N.A.	**13.71**	**0.03353**
KS-13-10L	7	09/11/2016	0.00125	0.00037	0.00042	0.00256	0.00033	N.A.	N.A.	3.82	0.03427
KS-13-10L	8	11/11/2016	0.00120	0.00098	0.00060	0.00103	0.00017	N.A.	N.A.	0.30	0.00310
KS-13-10L	9	11/11/2016	0.00098	0.00104	0.00060	0.00123	0.00018	N.A.	N.A.	2.22	0.00862
KS-13-10L	10	11/11/2016	0.00156	-0.00025	0.00060	0.00155	0.00020	N.A.	N.A.	5.90	0.01520
KS-13-10L	11	11/11/2016	0.00081	0.00019	0.00063	0.00100	0.00019	N.A.	N.A.	0.51	0.00318
KS-13-10L	12	11/11/2016	0.00176	0.00113	0.00059	0.00031	0.00019	N.A.	N.A.	0.28	0.00304
KS-13-10L	13	11/11/2016	0.00064	0.00020	0.00064	-0.00006	0.00018	N.A.	N.A.	0.15	0.00298
KS-13-10L	15	01/02/2017	0.00339	0.00102	0.00031	0.00159	0.00027	0.00602	0.00009	1.98	0.00176
KS-13-10L	16	01/02/2017	0.00083	0.00018	0.00031	0.00051	0.00026	0.00103	0.00005	0.30	0.00123
KS-13-10L	17	01/02/2017	0.00087	0.00018	0.00030	0.00008	0.00026	0.00879	0.00022	2.57	0.00693
KS-13-10L	18	01/02/2017	0.00265	0.00653	0.00035	0.00239	0.00026	0.08869	0.00041	**13.82**	**0.00264**
KS-13-10L	19	01/02/2017	0.00083	0.00011	0.00040	0.00022	0.00026	0.00175	0.00006	0.51	0.00125
KS-13-10L	20	01/02/2017	0.00055	0.00081	0.00032	0.00011	0.00025	0.00070	0.00006	0.18	0.00132
KS-13-10L	21	01/02/2017	0.00319	0.00280	0.00032	0.00147	0.00027	0.03316	0.00046	9.87	0.00632

NG Analyses of Pele's hairs and tears (cc)

Sample	Grain	4He	±	22Ne	±	36Ar	±	40Ar	±
KS-13-4L	2	9.41E-11	4.88E-12	3.49E-10	4.87E-12	N.A.	N.A.	2.03E-08	2.41E-12
KS-13-4L	3	1.93E-11	7.07E-12	7.11E-12	1.09E-12	N.A.	N.A.	1.89E-09	5.19E-11
KS-13-4L	4	2.49E-11	6.87E-12	4.19E-11	1.38E-12	N.A.	N.A.	2.64E-09	5.16E-11
KS-13-4L	5	5.56E-11	7.17E-12	2.26E-11	1.19E-12	N.A.	N.A.	2.28E-09	5.18E-11
KS-13-4L	6	1.52E-12	6.97E-12	4.74E-12	1.38E-12	N.A.	N.A.	4.22E-10	5.15E-11
KS-13-4L	7	4.55E-12	6.67E-12	6.13E-12	1.19E-12	N.A.	N.A.	2.96E-10	5.21E-11
KS-13-4L	8	6.08E-12	8.14E-12	9.16E-12	1.95E-12	N.A.	N.A.	3.51E-11	3.35E-12
KS-13-4L	9	4.33E-12	8.24E-12	1.25E-11	2.04E-12	N.A.	N.A.	1.88E-08	3.36E-12
KS-13-4L	10	4.12E-13	8.34E-12	2.88E-12	2.04E-12	N.A.	N.A.	3.71E-10	3.50E-12
KS-13-4L	11	2.99E-12	8.03E-12	9.92E-12	2.29E-12	N.A.	N.A.	6.34E-11	3.58E-12
KS-13-4L	12	3.50E-12	8.24E-12	2.04E-12	2.04E-12	N.A.	N.A.	1.13E-10	3.35E-12
KS-13-4L	13	-3.81E-12	8.03E-12	-1.36E-12	1.95E-12	N.A.	N.A.	4.69E-10	3.41E-12
KS-13-4L	14	2.07E-10	5.76E-12	5.53E-11	2.17E-12	2.63E-10	1.73E-12	1.67E-08	8.43E-12
KS-13-4L	15	4.80E-11	5.58E-12	1.29E-11	1.12E-12	1.03E-10	5.76E-13	1.66E-08	3.25E-12
KS-13-4L	16	5.67E-12	5.67E-12	9.57E-12	1.19E-12	8.87E-12	2.04E-13	2.72E-09	4.22E-12
KS-13-4L	17	1.40E-11	5.94E-12	5.73E-12	1.12E-12	3.96E-12	7.20E-14	1.14E-09	4.65E-12
KS-13-4L	18	3.99E-11	5.76E-12	1.99E-11	1.26E-12	1.16E-10	3.00E-13	1.66E-08	3.58E-12
KS-13-4L	20	1.91E-11	5.67E-12	6.29E-13	1.05E-12	4.69E-12	9.60E-14	1.46E-09	4.83E-12
KS-13-4L	21	2.15E-11	4.34E-12	5.10E-12	1.54E-12	3.06E-12	1.68E-13	9.74E-10	1.68E-11
KS-13-4L	22	8.15E-12	4.52E-12	7.82E-12	1.40E-12	1.57E-12	1.32E-13	5.83E-10	1.67E-11
KS-13-10L	1	5.10E-11	4.74E-12	2.69E-11	2.54E-12	N.A.	N.A.	1.86E-08	4.56E-11
KS-13-10L	2	2.62E-11	4.84E-12	7.97E-12	2.46E-12	N.A.	N.A.	1.87E-08	4.56E-11
KS-13-10L	3	1.75E-11	4.43E-12	5.17E-12	2.54E-12	N.A.	N.A.	1.87E-08	4.61E-11
KS-13-10L	4	3.23E-11	4.43E-12	-4.24E-13	2.54E-12	N.A.	N.A.	1.01E-08	4.94E-11
KS-13-10L	5	2.50E-11	4.43E-12	7.63E-12	2.46E-12	N.A.	N.A.	1.86E-08	4.56E-11
KS-13-10L	7	3.81E-12	4.33E-12	2.17E-11	2.80E-12	N.A.	N.A.	5.19E-09	4.66E-11
KS-13-10L	8	1.01E-11	6.18E-12	8.73E-12	1.44E-12	N.A.	N.A.	4.11E-10	4.22E-12
KS-13-10L	9	1.07E-11	6.18E-12	1.04E-11	1.53E-12	N.A.	N.A.	3.02E-09	1.17E-11
KS-13-10L	10	-2.58E-12	6.18E-12	1.31E-11	1.70E-12	N.A.	N.A.	8.02E-09	2.07E-11
KS-13-10L	11	1.96E-12	6.49E-12	8.48E-12	1.61E-12	N.A.	N.A.	6.88E-10	4.32E-12
KS-13-10L	12	1.16E-11	6.08E-12	2.63E-12	1.61E-12	N.A.	N.A.	3.75E-10	4.13E-12
KS-13-10L	13	2.06E-12	6.59E-12	-5.09E-13	1.53E-12	N.A.	N.A.	2.07E-10	4.05E-12
KS-13-10L	15	9.04E-12	2.75E-12	1.11E-11	1.89E-12	7.22E-12	1.08E-13	2.40E-09	2.13E-12
KS-13-10L	16	1.59E-12	2.75E-12	3.56E-12	1.82E-12	1.24E-12	6.00E-14	3.65E-10	1.49E-12
KS-13-10L	17	1.59E-12	2.66E-12	5.59E-13	1.82E-12	1.05E-11	2.64E-13	3.12E-09	8.39E-12
KS-13-10L	18	5.79E-11	3.10E-12	1.67E-11	1.82E-12	1.06E-10	4.92E-13	1.67E-08	3.19E-12
KS-13-10L	19	9.75E-13	3.54E-12	1.54E-12	1.82E-12	2.10E-12	7.20E-14	6.15E-10	1.51E-12
KS-13-10L	20	7.18E-12	2.84E-12	7.68E-13	1.75E-12	8.40E-13	7.20E-14	2.13E-10	1.60E-12
KS-13-10L	21	2.48E-11	2.84E-12	1.03E-11	1.89E-12	3.98E-11	5.52E-13	1.19E-08	7.65E-12

NG Analyses of Pele's hairs and tears (cc/g)

Sample	Grain	4He	±	% ±	22Ne	±	% ±	36Ar	±	% ±	40Ar	±	% ±	40Ar*	±	% ±
KS-13-4L	2	2.03E-08	1.05E-09	5	7.54E-08	1.05E-09	1	N.A.	N.A.	N.A.	**4.37E-06**	**5.20E-10**	**0**	N.A.	N.A.	N.A.
KS-13-4L	3	3.16E-08	1.16E-08	37	1.17E-08	1.78E-09	15	N.A.	N.A.	N.A.	3.10E-06	8.51E-08	3	N.A.	N.A.	N.A.
KS-13-4L	4	3.28E-08	9.04E-09	28	5.51E-08	1.82E-09	3	N.A.	N.A.	N.A.	3.47E-06	6.79E-08	2	N.A.	N.A.	N.A.
KS-13-4L	5	2.40E-08	3.10E-09	13	9.79E-09	5.13E-10	5	N.A.	N.A.	N.A.	9.88E-07	2.24E-08	2	N.A.	N.A.	N.A.
KS-13-4L	6	1.50E-09	6.90E-09	460	4.70E-09	1.37E-09	29	N.A.	N.A.	N.A.	4.18E-07	5.10E-08	12	N.A.	N.A.	N.A.
KS-13-4L	7	5.90E-09	8.66E-09	147	7.96E-09	1.54E-09	19	N.A.	N.A.	N.A.	3.84E-07	6.77E-08	18	N.A.	N.A.	N.A.
KS-13-4L	8	5.58E-09	7.47E-09	134	8.40E-09	1.79E-09	21	N.A.	N.A.	N.A.	3.22E-08	3.07E-09	10	N.A.	N.A.	N.A.
KS-13-4L	9	2.77E-09	5.28E-09	190	7.99E-09	1.30E-09	16	N.A.	N.A.	N.A.	**1.20E-05**	**2.15E-09**	**0**	N.A.	N.A.	N.A.
KS-13-4L	10	1.00E-09	2.03E-08	2025	7.03E-09	4.96E-09	71	N.A.	N.A.	N.A.	9.04E-07	8.52E-09	1	N.A.	N.A.	N.A.
KS-13-4L	11	3.25E-09	8.73E-09	269	1.08E-08	2.49E-09	23	N.A.	N.A.	N.A.	6.89E-08	3.89E-09	6	N.A.	N.A.	N.A.
KS-13-4L	12	2.76E-09	6.49E-09	235	1.60E-09	1.60E-09	100	N.A.	N.A.	N.A.	8.92E-08	2.63E-09	3	N.A.	N.A.	N.A.
KS-13-4L	13	-6.15E-09	1.30E-08	-211	-2.19E-09	3.15E-09	-144	N.A.	N.A.	N.A.	7.56E-07	5.51E-09	1	N.A.	N.A.	N.A.
KS-13-4L	14	2.88E-08	8.00E-10	3	7.68E-09	3.01E-10	4	3.65E-08	2.40E-10	1	**2.32E-06**	**1.17E-09**	**0**	**-8.58E-06**	**-7.99E-08**	**1**
KS-13-4L	15	2.48E-08	2.88E-09	12	6.66E-09	5.76E-10	9	5.33E-08	2.97E-10	1	**8.58E-06**	**1.68E-09**	**0**	**-7.34E-06**	**-5.78E-08**	**1**
KS-13-4L	16	3.30E-09	3.30E-09	100	5.56E-09	6.90E-10	12	5.16E-09	1.19E-10	2	1.58E-06	2.46E-09	0	4.28E-08	1.39E-09	3
KS-13-4L	17	8.48E-09	3.60E-09	42	3.47E-09	6.77E-10	20	2.40E-09	4.36E-11	2	6.88E-07	2.82E-09	0	-2.83E-08	-7.36E-10	3
KS-13-4L	18	8.31E-09	1.20E-09	14	4.15E-09	2.62E-10	6	2.43E-08	6.25E-11	0	**3.46E-06**	**7.46E-10**	**0**	**-3.78E-06**	**-1.38E-08**	**0**
KS-13-4L	20	6.96E-09	2.06E-09	30	2.29E-10	3.81E-10	167	1.71E-09	3.49E-11	2	5.29E-07	1.76E-09	0	2.01E-08	5.84E-10	3
KS-13-4L	21	1.71E-08	3.45E-09	20	4.05E-09	1.22E-09	30	2.43E-09	1.33E-10	5	7.73E-07	1.34E-08	2	4.76E-08	3.78E-09	8
KS-13-4L	22	5.03E-09	2.79E-09	55	4.83E-09	8.62E-10	18	9.70E-10	8.15E-11	8	3.60E-07	1.03E-08	3	7.02E-08	8.57E-09	12
KS-13-10L	1	1.57E-08	1.46E-09	9	8.27E-09	7.83E-10	9	N.A.	N.A.	N.A.	**5.73E-06**	**1.40E-08**	**0**	N.A.	N.A.	N.A.
KS-13-10L	2	1.15E-08	2.12E-09	19	3.50E-09	1.08E-09	31	N.A.	N.A.	N.A.	**8.18E-06**	**2.00E-08**	**0**	N.A.	N.A.	N.A.
KS-13-10L	3	1.81E-08	4.57E-09	25	5.33E-09	2.62E-09	49	N.A.	N.A.	N.A.	**1.93E-05**	**4.75E-08**	**0**	N.A.	N.A.	N.A.
KS-13-10L	4	1.97E-08	2.70E-09	14	-2.59E-10	1.55E-09	-600	N.A.	N.A.	N.A.	6.14E-06	3.01E-08	0	N.A.	N.A.	N.A.
KS-13-10L	5	1.42E-08	2.52E-09	18	4.34E-09	1.40E-09	32	N.A.	N.A.	N.A.	**1.06E-05**	**2.59E-08**	**0**	N.A.	N.A.	N.A.
KS-13-10L	7	3.05E-09	3.46E-09	114	1.74E-08	2.24E-09	13	N.A.	N.A.	N.A.	4.15E-06	3.73E-08	1	N.A.	N.A.	N.A.
KS-13-10L	8	8.41E-09	5.15E-09	61	7.28E-09	1.20E-09	17	N.A.	N.A.	N.A.	3.43E-07	3.51E-09	1	N.A.	N.A.	N.A.
KS-13-10L	9	1.09E-08	6.31E-09	58	1.06E-08	1.56E-09	15	N.A.	N.A.	N.A.	3.08E-06	1.20E-08	0	N.A.	N.A.	N.A.
KS-13-10L	10	-1.65E-09	3.96E-09	-240	8.43E-09	1.09E-09	13	N.A.	N.A.	N.A.	5.14E-06	1.33E-08	0	N.A.	N.A.	N.A.
KS-13-10L	11	2.42E-09	8.01E-09	332	1.05E-08	1.99E-09	19	N.A.	N.A.	N.A.	8.49E-07	5.34E-09	1	N.A.	N.A.	N.A.
KS-13-10L	12	6.61E-09	3.45E-09	52	1.49E-09	9.15E-10	61	N.A.	N.A.	N.A.	2.13E-07	2.35E-09	1	N.A.	N.A.	N.A.
KS-13-10L	13	3.22E-09	1.03E-08	320	-7.95E-10	2.39E-09	-300	N.A.	N.A.	N.A.	3.23E-07	6.33E-09	2	N.A.	N.A.	N.A.
KS-13-10L	15	2.67E-09	8.10E-10	30	3.28E-09	5.56E-10	17	2.13E-09	3.186E-11	1	7.07E-07	6.28E-10	0	7.10E-08	1.50E-09	2
KS-13-10L	16	1.92E-09	3.31E-09	172	4.29E-09	2.19E-09	51	1.49E-09	7.229E-11	5	4.39E-07	1.79E-09	0	-5.21E-09	-3.58E-10	7
KS-13-10L	17	1.83E-09	3.06E-09	167	6.42E-10	2.09E-09	325	1.21E-08	3.034E-10	3	3.58E-06	9.64E-09	0	-3.90E-08	-1.39E-09	4
KS-13-10L	18	2.18E-08	1.17E-09	5	6.30E-09	6.85E-10	11	4.02E-08	1.857E-10	0	**6.31E-06**	**1.21E-09**	**0**	**-5.68E-06**	**-3.72E-08**	**1**
KS-13-10L	19	1.17E-09	4.27E-09	364	1.85E-09	2.19E-09	118	2.53E-09	8.675E-11	3	7.41E-07	1.82E-09	0	-1.47E-08	-7.16E-10	5
KS-13-10L	20	1.30E-08	5.15E-09	40	1.40E-09	3.17E-09	227	1.53E-09	1.309E-10	9	3.88E-07	2.90E-09	1	-6.85E-08	-8.32E-09	12
KS-13-10L	21	7.78E-09	8.89E-10	11	3.22E-09	5.91E-10	18	1.25E-08	1.73E-10	1	3.74E-06	2.40E-09	0	2.04E-08	4.00E-10	2

NG Analyses of Pele's hairs and tears

Sample	Grain	40Ar/36Ar	±	% ±	He/Ar*	±	% ±
KS-13-4L	2	N.A.	N.A.	N.A.	N.A.	N.A.	N.A.
KS-13-4L	3	N.A.	N.A.	N.A.	N.A.	N.A.	N.A.
KS-13-4L	4	N.A.	N.A.	N.A.	N.A.	N.A.	N.A.
KS-13-4L	5	N.A.	N.A.	N.A.	N.A.	N.A.	N.A.
KS-13-4L	6	N.A.	N.A.	N.A.	N.A.	N.A.	N.A.
KS-13-4L	7	N.A.	N.A.	N.A.	N.A.	N.A.	N.A.
KS-13-4L	8	N.A.	N.A.	N.A.	N.A.	N.A.	N.A.
KS-13-4L	9	N.A.	N.A.	N.A.	N.A.	N.A.	N.A.
KS-13-4L	10	N.A.	N.A.	N.A.	N.A.	N.A.	N.A.
KS-13-4L	11	N.A.	N.A.	N.A.	N.A.	N.A.	N.A.
KS-13-4L	12	N.A.	N.A.	N.A.	N.A.	N.A.	N.A.
KS-13-4L	13	N.A.	N.A.	N.A.	N.A.	N.A.	N.A.
KS-13-4L	14	63.5	0.4	0	**-3.36E-03**	**-9.83E-05**	**3**
KS-13-4L	15	160.8	0.9	1	**-3.37E-03**	**-3.93E-04**	**12**
KS-13-4L	16	306.9	7.1	7	7.71E-02	7.71E-02	100
KS-13-4L	17	286.8	5.3	5	**-3.00E-01**	**-1.27E-01**	**42**
KS-13-4L	18	142.8	0.4	0	-2.20E-03	-3.18E-04	14
KS-13-4L	20	310.3	6.4	6	3.47E-01	1.03E-01	30
KS-13-4L	21	318.1	18.3	18	3.59E-01	7.79E-02	22
KS-13-4L	22	370.9	32.9	33	7.17E-02	4.07E-02	57
KS-13-10L	1	N.A.	N.A.	N.A.	N.A.	N.A.	N.A.
KS-13-10L	2	N.A.	N.A.	N.A.	N.A.	N.A.	N.A.
KS-13-10L	3	N.A.	N.A.	N.A.	N.A.	N.A.	N.A.
KS-13-10L	4	N.A.	N.A.	N.A.	N.A.	N.A.	N.A.
KS-13-10L	5	N.A.	N.A.	N.A.	N.A.	N.A.	N.A.
KS-13-10L	7	N.A.	N.A.	N.A.	N.A.	N.A.	N.A.
KS-13-10L	8	N.A.	N.A.	N.A.	N.A.	N.A.	N.A.
KS-13-10L	9	N.A.	N.A.	N.A.	N.A.	N.A.	N.A.
KS-13-10L	10	N.A.	N.A.	N.A.	N.A.	N.A.	N.A.
KS-13-10L	11	N.A.	N.A.	N.A.	N.A.	N.A.	N.A.
KS-13-10L	12	N.A.	N.A.	N.A.	N.A.	N.A.	N.A.
KS-13-10L	13	N.A.	N.A.	N.A.	N.A.	N.A.	N.A.
KS-13-10L	15	331.9	5.0	5	3.76E-02	1.14E-02	30
KS-13-10L	16	295.1	14.4	14	-3.69E-01	-6.35E-01	172
KS-13-10L	17	295.3	7.4	7	**-4.70E-02**	**-7.83E-02**	**167**
KS-13-10L	18	157.1	0.7	1	-3.84E-03	-2.07E-04	5
KS-13-10L	19	292.7	10.1	10	-7.97E-02	-2.90E-01	364
KS-13-10L	20	253.7	21.8	22	-1.91E-01	-7.88E-02	41
KS-13-10L	21	300.2	4.2	4	3.82E-01	4.43E-02	12

Calibration data (average of 6 measurements)

He cc/V	Ne cc/V	36Ar cc/V	40Ar cc/V	Date
2.57E-08	9.73E-08	N.A.	1.46E-09	20/01/2016
1.01E-08	9.88E-09	N.A.	1.78E-09	11/10/2016
1.03E-08	8.48E-09	N.A.	1.36E-09	24/10/2016
8.86E-09	6.98E-09	1.20E-09	1.21E-09	31/01/2017
1.44E-08	6.59E-09	1.32E-09	1.48E-09	19/06/2018
1.31E-08	6.25E-09	1.37E-09	1.42E-09	25/09/2018
				03/10/2018

Daily blank values (V) used to correct data of sample KS15-03

	Date	4He	±	22Ne	±	36Ar	±	40Ar	±
Mean	27/10/2017	0.00338	0.00017	0.00056	0.00004	NA	NA	0.01819	0.00029
St. Dev.	27/10/2018	0.00042	0.00004	0.00022	0.00003	NA	NA	0.00360	0.00009
Mean (1 data)	02/11/2017	0.00417	0.00013	0.00083	0.00007	NA	NA	0.02148	0.00025
Mean	03/11/2017	0.00304	0.00017	0.00041	0.00005	NA	NA	0.01342	0.00048
St. Dev.	03/11/2018	0.00051	0.00005	0.00021	0.00002	NA	NA	0.00334	0.00022
Mean	05/11/2017	0.00225	0.00015	0.00059	0.00006	NA	NA	0.02499	0.00041
St. Dev.	05/11/2018	0.00063	0.00006	0.00034	0.00003	NA	NA	0.00248	0.00013
Mean	09/02/2018	0.00347	0.00018	0.00045	0.00006	0.00020	0.00003	0.04612	0.00047
St. Dev.	09/02/2019	0.00027	0.00005	0.00013	0.00003	0.00019	0.00001	0.02342	0.00015
Mean	15/02/2018	0.00367	0.00016	0.00064	0.00004	0.00016	0.00003	0.04557	0.00051
St. Dev.	15/02/2019	0.00029	0.00007	0.00050	0.00001	0.00012	0.00001	0.01169	0.00013
Mean	19/06/2019	0.00299	0.00007	0.00046	0.00002	0.00006	0.00001	0.01036	0.00012
St. Dev.	19/06/2020	0.00028	0.00001	0.00022	0.00001	0.00004	0.00000	0.00104	0.00003

Daily blank values (V) used to correct data of sample KS16-03

Run No	Date	4He		22Ne		36Ar		40Ar	
Mean	18/07/2017	0.00375	0.00010	0.00035	0.00003	NA	NA	0.01697	0.00033
St. Dev.	18/07/2018	0.00014	0.00003	0.00016	0.00001	NA	NA	0.00144	0.00014
Mean	19/07/2017	0.00341	0.00015	0.00043	0.00003	NA	NA	0.01790	0.00039
St. Dev.	19/07/2018	0.00055	0.00005	0.00019	0.00001	NA	NA	0.00278	0.00046
Mean	21/07/2017	0.00368	0.00011	0.00074	0.00005	NA	NA	0.01842	0.00036
St. Dev.	21/07/2018	0.00009	0.00004	0.00013	0.00002	NA	NA	0.00100	0.00011
Mean	23/10/2017	0.00248	0.00015	0.00035	0.00004	NA	NA	0.09450	0.00089
St. Dev..	23/10/2018	0.00075	0.00007	0.00018	0.00001	NA	NA	0.01521	0.00044
Mean	25/10/2017	0.00547	0.00013	0.00049	0.00005	NA	NA	0.01987	0.00054
St. Dev.	25/10/2018	0.00024	0.00002	0.00017	0.00001	NA	NA	0.00395	0.00021
Mean	03/02/2018	0.00534	0.00015	0.00035	0.00004	0.00012	0.00003	0.02590	0.00036
St. Dev.	03/02/2019	0.00073	0.00007	0.00030	0.00001	0.00007	0.00002	0.00428	0.00010
Mean	06/02/2018	0.00347	0.00016	0.00049	0.00004	0.00011	0.00002	0.01630	0.00031
St. Dev.	06/02/2019	0.00051	0.00005	0.00024	0.00002	0.00011	0.00001	0.00240	0.00014
Mean	03/10/2019	0.00286	0.00005	0.00025	0.00002	-0.00003	0.00002	0.01257	0.00009
St. Dev.	03/10/2020	0.00023	0.00002	0.00010	0.00000	0.00002	0.00001	0.00059	0.00002

Daily blank values (V) used to correct data of sample KS16-03

Run No	Date	4He	±	22Ne	±	36Ar	±	40Ar	±
Mean	22/07/2017	0.00351	0.00015	0.00003	0.00002	NA	NA	0.02733	0.00049
St. Dev.	22/07/2018	0.00005	0.00003	0.00001	0.00000	NA	NA	0.00085	0.00017
Mean	20/10/2017	0.00591	0.00025	0.00052	0.00006	NA	NA	0.03926	0.00139
St. Dev.	20/10/2018	0.00066	0.00006	0.00010	0.00003	NA	NA	0.00673	0.00030
Mean	07/11/2017	0.00350	0.00017	0.00063	0.00007	NA	NA	0.02375	0.00049
St. Dev.	07/11/2018	0.00078	0.00006	0.00022	0.00002	NA	NA	0.00162	0.00012
Mean	09/11/2017	0.00330	0.00018	0.00056	0.00003	NA	NA	0.14617	0.00124
St. Dev.	09/11/2018	0.00041	0.00005	0.00029	0.00001	NA	NA	0.03352	0.00035
Mean	11/11/2017	0.00335	0.00016	0.00036	0.00005	NA	NA	0.02292	0.00027
St. Dev.	11/11/2018	0.00059	0.00003	0.00017	0.00003	NA	NA	0.00294	0.00010
Mean	12/02/2018	0.00412	0.00016	0.00039	0.00004	0.00018	0.00002	0.03534	0.00048
St. Dev.	12/02/2019	0.00063	0.00006	0.00015	0.00001	0.00005	0.00001	0.00255	0.00021
Mean	15/02/2018	0.00386	0.00018	0.00031	0.00004	0.00017	0.00002	0.04414	0.00065
St. Dev.	15/02/2019	0.00047	0.00006	0.00020	0.00001	0.00011	0.00001	0.01379	0.00017
Mean	01/02/2018	0.00405	0.00017	0.00030	0.00004	0.00002	0.00001	0.00562	0.00028
St. Dev.	01/02/2019	0.00029	0.00006	0.00025	0.00001	0.00003	0.00000	0.00102	0.00010

Appendix A4 - Data from Chapter 5

A4.1 Electron microprobe data

Analytical Conditions :

Sp	Elements	Position
Sp3	Fe Ka	LLIF
Sp3	Mn Ka	LLIF
Sp2	Na Ka	LTAP
Sp2	Mg Ka	LTAP
Sp1	Si Ka	TAP
Sp5	Ca Ka	PET
Sp4	K Ka	LPET
Sp4	Ti Ka	LPET
Sp4	Cl Ka	LPET
Sp1	Al Ka	TAP

Standard Name :

Fe On Haematite

Mn, Ca On Bustamite

Na On jad-BM4

Mg On for-BM4

Si, K , Al On fspr-In5

Ti On Rutile

Cl On sylv-BM4

Beam Size : 1 µm

Electron microprobe raw data of selected glass particles from sample F1A (Wt %)

SiO2	Na2O	K2O	CaO	MgO	MnO	FeO	Al2O3	TiO2	Cl	Total	CIA
59.97	6.88	6.12	0.55	0.23	0.24	2.96	20.99	0.62	0.31	98.87	60.77
58.08	5.44	5.93	0.62	0.26	0.30	2.41	20.65	0.51	0.27	94.46	63.27
59.27	5.23	5.96	0.69	0.22	0.38	3.50	20.28	0.57	0.27	96.38	63.06
58.56	5.74	6.13	0.46	0.26	0.34	2.63	20.20	0.39	0.30	95.00	62.10
59.03	5.69	5.99	0.73	0.23	0.19	2.68	20.32	0.46	0.27	95.60	62.08
58.82	5.41	5.75	0.36	0.24	0.12	2.79	20.73	0.60	0.28	95.11	64.28
59.49	5.68	6.05	0.69	0.28	0.34	2.59	20.12	0.64	0.25	96.12	61.83
59.69	5.33	6.13	0.58	0.31	0.20	2.64	20.67	0.57	0.23	96.35	63.19
59.08	6.23	5.79	0.43	0.25	0.32	2.51	20.05	0.32	0.36	95.33	61.69
59.16	5.20	6.65	1.01	0.34	0.16	2.44	19.52	0.67	0.20	95.34	60.28
59.43	5.00	6.29	0.82	0.32	0.20	3.23	19.51	0.77	0.18	95.74	61.70
58.86	4.74	6.66	0.56	0.28	0.28	2.79	19.75	0.51	0.31	94.75	62.28
59.04	4.76	6.41	0.67	0.27	0.23	2.97	20.03	0.46	0.18	95.01	62.85
58.60	5.22	6.11	0.49	0.34	0.21	2.84	19.64	0.61	0.19	94.26	62.43
60.02	5.92	6.06	0.63	0.23	0.30	2.09	20.40	0.54	0.35	96.52	61.80
59.78	5.67	6.05	0.75	0.24	0.18	2.50	20.28	0.46	0.21	96.13	61.92
59.15	4.90	6.66	0.49	0.26	0.13	2.84	19.83	0.54	0.29	95.11	62.20
59.53	4.99	6.03	0.71	0.35	0.21	2.63	20.24	0.69	0.19	95.58	63.31
59.98	4.59	6.34	0.88	0.29	0.17	2.88	20.34	0.51	0.25	96.23	63.27
59.24	4.73	6.15	0.82	0.37	0.12	2.59	20.04	0.71	0.26	95.02	63.14
59.53	5.42	5.85	0.42	0.30	0.18	2.82	19.97	0.70	0.26	95.46	63.08
58.98	5.00	5.79	0.43	0.25	0.22	3.43	19.57	0.60	0.17	94.45	63.56
59.44	5.05	6.37	0.66	0.29	0.20	2.30	19.86	0.76	0.24	95.16	62.18
60.00	5.29	6.33	0.55	0.38	0.17	2.52	20.02	0.53	0.23	96.02	62.19
60.12	5.78	5.57	0.55	0.24	0.26	2.66	20.16	0.50	0.32	96.17	62.88
59.70	4.74	6.58	0.64	0.34	0.27	2.44	19.95	0.53	0.24	95.43	62.52
59.62	5.29	5.65	0.38	0.21	0.32	2.94	20.16	0.44	0.29	95.30	64.04
60.60	5.44	5.85	0.52	0.32	0.14	2.77	20.43	0.54	0.25	96.85	63.37
60.40	5.81	5.45	0.52	0.27	0.36	2.54	20.45	0.39	0.32	96.51	63.45
59.89	5.47	6.15	0.58	0.36	0.18	2.25	20.06	0.58	0.15	95.69	62.18
60.30	5.17	6.03	0.73	0.32	0.23	3.14	19.58	0.61	0.23	96.33	62.14
59.33	5.82	5.74	0.52	0.26	0.30	2.59	19.58	0.38	0.24	94.75	61.84
59.38	4.77	6.25	0.74	0.28	0.23	2.21	19.91	0.69	0.29	94.77	62.87
59.95	5.62	5.91	0.76	0.33	0.12	2.37	19.69	0.61	0.15	95.52	61.57
60.48	5.69	5.63	0.82	0.27	0.09	2.67	19.96	0.51	0.24	96.36	62.18
59.26	4.31	5.94	0.65	0.25	0.23	3.17	19.72	0.51	0.33	94.38	64.40
59.68	5.63	5.85	0.35	0.29	0.37	2.24	19.85	0.52	0.24	95.03	62.66
59.52	5.26	5.56	0.91	0.23	0.22	2.55	19.55	0.49	0.29	94.58	62.50
59.22	4.91	6.34	0.45	0.28	0.36	1.75	20.11	0.46	0.23	94.10	63.22
60.53	4.64	6.11	0.76	0.31	0.25	3.26	19.38	0.64	0.28	96.17	62.74
60.20	4.70	6.34	0.77	0.33	0.22	2.82	19.29	0.68	0.23	95.58	62.03
59.28	3.68	6.32	0.37	0.24	0.28	2.92	20.08	0.59	0.34	94.09	65.94
59.32	5.02	5.80	0.31	0.24	0.30	2.28	19.93	0.62	0.30	94.13	64.17
60.65	4.52	6.31	0.63	0.28	0.20	2.64	20.09	0.50	0.23	96.06	63.68
59.88	3.78	6.34	1.18	0.33	0.20	2.51	19.60	0.77	0.23	94.82	63.43
60.40	4.51	6.14	0.60	0.23	0.22	2.85	19.80	0.51	0.35	95.61	63.77
59.95	4.32	6.14	0.39	0.24	0.17	2.89	19.99	0.47	0.26	94.81	64.82
60.23	4.95	6.40	0.72	0.30	0.31	1.67	19.75	0.67	0.23	95.22	62.07
60.74	4.55	6.75	0.30	0.30	0.17	2.49	19.81	0.69	0.22	96.02	63.07
60.39	4.65	5.47	0.45	0.28	0.24	2.45	20.35	0.76	0.24	95.29	65.82
60.18	4.81	5.96	0.45	0.28	0.13	2.62	19.73	0.53	0.22	94.91	63.75
61.23	4.94	5.81	0.74	0.29	0.21	2.53	20.11	0.49	0.17	96.54	63.64
59.90	4.33	6.67	0.65	0.33	0.21	2.37	19.28	0.50	0.16	94.40	62.33
59.13	3.53	5.96	0.74	0.27	0.21	3.05	19.45	0.57	0.24	93.17	65.53
60.41	3.77	6.06	0.73	0.23	0.34	3.08	19.58	0.53	0.33	95.07	64.96
59.63	3.34	6.09	0.61	0.31	0.28	2.87	19.74	0.62	0.28	93.76	66.29
60.30	4.42	6.14	0.50	0.25	0.24	2.10	19.90	0.45	0.27	94.56	64.28
61.38	4.63	5.74	0.45	0.30	0.12	2.87	19.83	0.63	0.24	96.17	64.70
60.27	4.26	6.16	0.49	0.30	0.29	2.27	19.66	0.47	0.27	94.43	64.31
60.24	2.82	6.51	0.81	0.33	0.25	3.27	19.19	0.64	0.22	94.27	65.43
60.41	3.52	5.55	0.90	0.27	0.30	2.76	19.94	0.57	0.26	94.47	66.67
60.88	3.91	6.49	0.85	0.30	0.16	2.14	19.60	0.62	0.24	95.19	63.53
59.77	3.41	6.15	0.66	0.24	0.26	2.27	19.80	0.50	0.33	93.39	65.96
59.89	3.72	6.12	0.60	0.30	0.20	2.19	19.35	0.73	0.31	93.40	64.95
60.33	3.22	5.86	0.36	0.27	0.21	2.94	20.07	0.51	0.29	94.05	68.01
61.83	4.19	6.39	0.70	0.34	0.32	2.58	19.27	0.59	0.19	96.38	63.08
59.09	3.05	5.73	0.53	0.23	0.19	2.80	19.45	0.42	0.34	91.82	67.63
59.88	3.22	5.79	0.52	0.27	0.19	2.72	19.64	0.51	0.27	93.01	67.33
60.71	3.45	5.61	0.55	0.25	0.25	3.12	19.27	0.48	0.29	93.98	66.72
59.18	3.00	5.51	0.51	0.30	0.16	2.55	19.39	0.48	0.25	91.33	68.25
60.14	3.28	5.74	0.56	0.29	0.30	2.19	19.54	0.52	0.17	92.72	67.10
59.50	2.94	5.18	0.72	0.25	0.22	2.02	19.59	0.64	0.28	91.34	68.91
60.53	2.35	6.16	0.54	0.29	0.21	2.55	19.50	0.48	0.27	92.87	68.30
60.45	2.54	5.66	0.61	0.32	0.11	2.47	18.12	0.68	0.17	91.13	67.29

Electron microprobe raw data of selected glass particles from sample F2A (Wt %)

SiO2	Na2O	K2O	CaO	MgO	MnO	FeO	Al2O3	TiO2	Cl	Total	CIA
60.74	2.13	5.07	0.49	0.34	0.07	2.92	17.85	0.62	0.28	90.51	69.89
59.10	2.81	5.70	0.53	0.35	0.25	2.13	18.97	0.64	0.16	90.64	67.73
60.29	2.71	5.71	0.58	0.34	0.15	2.34	18.20	0.65	0.23	91.20	66.91
57.67	4.14	6.33	0.55	0.23	0.18	1.87	19.71	0.48	0.34	91.50	64.14
60.55	2.31	6.29	0.54	0.34	0.09	1.71	18.93	0.83	0.14	91.73	67.44
59.91	2.76	5.75	0.57	0.34	0.15	2.35	19.05	0.69	0.19	91.75	67.72
60.10	2.59	6.21	0.88	0.36	0.18	1.83	18.85	0.60	0.20	91.78	66.07
58.51	4.68	6.13	0.58	0.36	0.21	1.66	19.17	0.66	0.17	92.13	62.73
58.77	4.04	6.28	0.51	0.34	0.18	2.12	19.29	0.68	0.19	92.41	64.04
58.63	3.83	6.31	0.56	0.35	0.22	2.49	19.20	0.60	0.23	92.43	64.21
59.66	3.17	6.05	0.57	0.41	0.15	2.53	19.08	0.62	0.21	92.46	66.09
58.62	4.09	5.91	0.85	0.36	0.31	2.32	19.21	0.68	0.15	92.51	63.91
57.85	4.72	5.84	0.57	0.25	0.26	2.92	19.28	0.55	0.29	92.52	63.40
61.04	2.36	5.97	0.44	0.30	0.29	2.59	18.85	0.62	0.21	92.67	68.25
60.14	3.23	5.53	0.70	0.41	0.27	2.13	19.38	0.74	0.15	92.67	67.20
59.36	3.54	6.22	0.63	0.35	0.16	2.17	19.39	0.71	0.19	92.71	65.11
60.48	3.02	5.48	0.75	0.34	0.20	3.03	18.73	0.61	0.20	92.85	66.94
60.25	3.35	5.99	0.72	0.36	0.13	2.49	18.96	0.64	0.25	93.14	65.33
59.91	3.26	6.04	0.44	0.32	0.13	2.93	19.47	0.56	0.20	93.26	66.66
58.96	4.54	6.43	0.45	0.36	0.10	2.11	19.40	0.72	0.20	93.27	62.95
58.76	4.26	6.57	0.80	0.36	0.18	2.30	19.15	0.76	0.14	93.28	62.22
59.11	3.78	6.74	0.47	0.34	0.22	1.97	19.78	0.68	0.19	93.28	64.28
60.74	3.24	5.85	0.67	0.33	0.23	2.02	19.52	0.68	0.20	93.48	66.67
58.43	5.26	5.80	0.51	0.40	0.19	2.05	20.02	0.64	0.21	93.49	63.37
59.14	4.76	6.00	0.89	0.34	0.16	2.39	19.13	0.64	0.17	93.61	62.15
59.25	5.44	5.51	0.58	0.34	0.22	1.95	19.63	0.53	0.17	93.62	63.00
59.53	3.92	6.52	0.80	0.43	0.21	2.35	19.06	0.68	0.18	93.69	62.90
60.27	2.75	6.31	0.58	0.37	0.15	3.21	19.15	0.81	0.20	93.80	66.52
57.54	5.85	6.11	0.93	0.36	0.19	2.54	19.56	0.59	0.19	93.87	60.28
58.68	5.45	6.03	0.62	0.35	0.16	2.63	19.05	0.70	0.20	93.88	61.16
58.41	5.60	6.09	0.83	0.34	0.24	2.73	18.94	0.59	0.12	93.90	60.20
58.39	5.39	6.11	0.59	0.36	0.14	2.18	19.98	0.66	0.16	93.96	62.30
59.27	5.68	5.85	0.42	0.36	0.19	2.10	19.36	0.61	0.14	93.98	61.83
59.17	4.66	6.23	0.68	0.35	0.16	2.78	19.02	0.76	0.26	94.07	62.18
58.92	5.38	6.01	0.65	0.34	0.14	1.93	19.72	0.78	0.21	94.09	62.09
60.00	4.70	6.12	0.69	0.38	0.21	2.13	19.06	0.63	0.18	94.11	62.35
59.20	4.72	5.96	0.52	0.36	0.17	2.81	19.53	0.67	0.19	94.13	63.55
58.65	5.32	6.29	0.72	0.36	0.17	2.70	19.07	0.65	0.22	94.15	60.73
59.41	4.29	6.07	0.73	0.33	0.18	2.94	19.45	0.63	0.17	94.19	63.69
58.83	4.97	6.06	0.84	0.35	0.24	2.16	19.78	0.79	0.21	94.23	62.50
58.93	5.27	5.99	0.47	0.25	0.19	2.44	20.01	0.50	0.24	94.28	63.04
60.20	3.73	6.58	0.77	0.36	0.08	2.35	19.28	0.78	0.19	94.32	63.50
58.84	5.48	5.85	0.62	0.35	0.22	2.87	19.42	0.60	0.18	94.43	61.91
59.84	4.97	5.92	0.36	0.34	0.21	2.61	19.44	0.57	0.18	94.43	63.34
58.98	4.94	6.19	0.73	0.31	0.07	3.04	19.30	0.67	0.24	94.48	61.94
59.77	5.10	6.11	0.68	0.36	0.24	2.15	19.21	0.73	0.17	94.50	61.77
58.62	4.84	6.25	0.87	0.32	0.20	2.56	19.98	0.66	0.24	94.52	62.55
59.86	4.82	6.27	0.66	0.36	0.08	2.25	19.31	0.76	0.21	94.56	62.17
58.91	5.48	6.00	0.84	0.40	0.20	2.24	19.66	0.60	0.24	94.58	61.48
59.40	5.70	5.74	0.45	0.35	0.16	2.52	19.35	0.74	0.17	94.58	61.94
58.75	5.25	6.36	0.56	0.36	0.29	2.77	19.34	0.72	0.22	94.61	61.38
59.91	4.48	6.05	0.63	0.40	0.26	2.44	19.57	0.74	0.16	94.62	63.68
59.85	4.89	6.52	1.00	0.32	0.12	1.97	19.17	0.60	0.20	94.63	60.70
58.19	5.57	6.33	0.71	0.32	0.11	3.03	19.56	0.68	0.17	94.66	60.80
59.62	5.00	5.65	0.77	0.37	0.11	2.84	19.33	0.79	0.20	94.69	62.86
59.81	4.62	5.86	0.45	0.31	0.19	2.39	20.19	0.76	0.17	94.75	64.88
59.00	5.72	6.28	0.70	0.36	0.23	2.47	19.11	0.71	0.19	94.76	60.08
59.58	4.82	5.94	0.62	0.40	0.18	3.08	19.27	0.67	0.21	94.77	62.87
59.57	5.78	6.04	0.52	0.33	0.17	2.29	19.37	0.73	0.19	94.99	61.08
59.14	5.66	5.98	0.78	0.42	0.25	2.39	19.63	0.77	0.13	95.15	61.25
59.98	5.32	6.15	0.52	0.29	0.30	2.42	19.45	0.60	0.21	95.23	61.86

Electron microprobe raw data of selected glass particles from sample F2A (Wt %)

SiO2	Na2O	K2O	CaO	MgO	MnO	FeO	Al2O3	TiO2	Cl	Total	CIA
59.77	4.76	6.17	0.66	0.32	0.17	3.05	19.61	0.60	0.15	95.26	62.85
59.31	5.60	6.02	0.59	0.37	0.18	2.39	19.82	0.82	0.19	95.28	61.88
59.47	5.44	5.93	0.58	0.34	0.23	3.02	19.36	0.72	0.19	95.29	61.83
59.79	5.08	5.97	0.59	0.43	0.20	2.64	19.69	0.74	0.24	95.36	62.85
60.48	4.69	6.08	0.84	0.36	0.16	2.34	19.43	0.86	0.14	95.39	62.60
59.57	5.62	5.69	0.90	0.37	0.23	2.53	19.53	0.75	0.22	95.42	61.53
59.43	5.32	6.30	0.80	0.35	0.16	3.01	19.23	0.65	0.19	95.43	60.76
59.03	5.61	6.17	0.81	0.40	0.25	2.45	19.85	0.78	0.14	95.50	61.19
59.91	5.61	6.35	0.89	0.34	0.13	2.39	19.03	0.70	0.21	95.54	59.69
60.82	5.29	5.97	0.58	0.36	0.21	2.24	19.31	0.61	0.18	95.56	61.99
58.59	5.18	6.50	0.77	0.34	0.27	2.88	20.12	0.75	0.19	95.59	61.77
60.00	5.78	5.96	0.78	0.38	0.26	2.35	19.25	0.66	0.17	95.59	60.59
60.26	6.02	6.03	0.50	0.37	0.27	1.97	19.20	0.78	0.19	95.60	60.47
59.27	5.49	6.37	0.57	0.35	0.26	3.05	19.37	0.69	0.21	95.63	60.91
58.91	5.24	6.48	0.74	0.33	0.26	3.09	19.68	0.69	0.23	95.64	61.23
59.99	5.60	5.93	0.94	0.36	0.21	2.33	19.52	0.60	0.20	95.69	61.02
59.73	4.97	6.02	0.78	0.40	0.24	2.56	20.03	0.81	0.19	95.74	62.99
59.20	5.74	6.20	0.58	0.22	0.29	2.39	20.32	0.53	0.32	95.79	61.88
59.99	4.94	6.23	0.67	0.37	0.27	2.86	19.73	0.58	0.18	95.82	62.50
59.78	5.57	6.54	0.51	0.32	0.26	2.65	19.47	0.51	0.22	95.83	60.67
60.03	5.59	6.05	0.56	0.38	0.27	2.68	19.67	0.54	0.16	95.95	61.72
60.34	4.97	6.05	0.74	0.37	0.26	2.90	19.56	0.66	0.17	96.01	62.45
59.80	5.15	6.75	0.57	0.35	0.23	2.86	19.43	0.68	0.20	96.02	60.91
60.98	4.36	5.93	0.44	0.37	0.10	2.84	20.16	0.77	0.21	96.16	65.26
60.36	5.32	6.89	0.35	0.32	0.27	2.85	19.10	0.64	0.17	96.28	60.33
59.79	4.96	6.41	0.50	0.35	0.26	2.77	20.50	0.67	0.17	96.38	63.33
59.84	5.12	6.16	0.86	0.32	0.27	2.92	20.12	0.64	0.19	96.44	62.37
60.48	5.19	6.21	0.73	0.37	0.26	2.53	19.96	0.67	0.19	96.59	62.20
59.67	5.02	6.14	0.70	0.39	0.18	4.03	19.65	0.71	0.16	96.65	62.36
61.48	4.55	6.29	0.85	0.40	0.20	2.74	19.33	0.63	0.18	96.66	62.31
60.42	5.26	6.58	0.66	0.34	0.12	2.60	20.24	0.63	0.20	97.04	61.82
59.52	4.71	6.11	0.65	0.35	0.20	2.52	19.43	0.67	0.20	94.34	62.96

Electron microprobe raw data of selected glass particles from sample I1A (Wt %)

SiO2	Na2O	K2O	CaO	MgO	MnO	FeO	Al2O3	TiO2	Cl	Total	CIA
58.49	4.70	5.24	0.88	0.40	0.07	2.10	18.76	0.73	0.12	91.48	63.42
59.82	3.45	6.33	0.53	0.35	0.25	2.43	18.71	0.63	0.22	92.73	64.47
60.13	3.36	6.09	0.52	0.36	0.27	1.83	19.80	0.70	0.22	93.27	66.51
59.40	4.79	6.06	0.71	0.37	0.16	1.84	19.52	0.80	0.19	93.85	62.81
59.59	4.86	5.51	0.58	0.36	0.10	2.20	19.83	0.76	0.17	93.97	64.42
59.11	5.19	6.21	0.47	0.39	0.18	2.26	19.53	0.77	0.18	94.29	62.20
58.89	5.14	5.93	1.09	0.37	0.13	2.22	19.83	0.70	0.20	94.49	61.99
60.05	5.11	5.81	0.91	0.38	0.20	1.84	19.45	0.85	0.26	94.84	62.18
60.24	4.67	6.34	0.81	0.38	0.12	2.26	19.11	0.80	0.13	94.85	61.78
59.11	5.14	6.27	0.97	0.36	0.12	2.24	19.78	0.71	0.16	94.87	61.50
59.62	5.07	5.93	0.64	0.39	0.07	2.42	19.89	0.68	0.19	94.90	63.08
60.33	4.59	5.70	0.89	0.35	0.08	2.39	19.62	0.86	0.23	95.04	63.70
59.11	5.27	5.82	0.83	0.42	0.27	2.43	19.99	0.79	0.18	95.11	62.64
59.79	5.89	6.17	0.76	0.33	0.18	1.91	19.36	0.60	0.18	95.16	60.16
60.33	5.63	5.90	1.09	0.35	0.07	2.26	18.97	0.57	0.20	95.38	60.05
60.13	4.57	6.12	0.76	0.34	0.09	2.86	19.71	0.72	0.15	95.46	63.25
60.38	4.81	5.82	0.51	0.37	0.28	2.45	19.79	0.82	0.23	95.46	63.98
60.62	4.77	5.72	0.71	0.39	0.17	2.66	19.63	0.64	0.18	95.48	63.67
60.54	5.40	5.87	0.86	0.39	0.13	2.57	19.28	0.79	0.10	95.93	61.38
61.06	4.37	6.01	0.90	0.37	0.11	2.42	19.80	0.71	0.20	95.96	63.71
60.15	4.86	5.88	0.91	0.39	0.21	2.64	19.97	0.78	0.20	95.99	63.16
61.09	4.65	5.73	1.07	0.52	0.21	2.35	19.51	0.75	0.17	96.05	63.02
59.83	5.42	5.84	0.72	0.33	0.22	2.97	19.95	0.65	0.19	96.11	62.48
61.24	4.61	6.48	0.68	0.41	0.20	1.63	19.95	0.71	0.22	96.12	62.89
60.44	4.82	5.74	0.86	0.39	0.16	3.12	19.94	0.62	0.15	96.24	63.58
60.68	5.03	5.91	0.94	0.36	0.13	2.71	19.76	0.68	0.16	96.38	62.45
60.55	5.02	5.87	1.09	0.33	0.24	3.04	19.58	0.61	0.21	96.55	62.04
61.14	5.98	5.76	0.59	0.38	0.23	2.34	19.65	0.80	0.15	97.02	61.44
60.91	5.33	5.95	0.77	0.36	0.23	2.68	19.95	0.66	0.20	97.04	62.34
61.06	6.10	4.29	0.85	0.33	0.25	2.59	19.20	0.91	0.14	95.72	63.07
61.07	5.57	5.24	0.73	0.37	0.24	2.52	19.20	0.68	0.12	95.73	62.47
61.23	4.63	6.09	0.81	0.33	0.19	2.79	18.52	0.64	0.17	95.41	61.64
58.28	5.98	6.01	0.95	0.38	0.14	2.92	19.24	0.79	0.12	94.80	59.80
61.41	4.18	6.24	0.81	0.40	0.12	2.94	19.55	0.80	N.A.	96.45	63.50
61.41	4.61	5.09	0.88	0.35	0.14	2.89	19.39	0.79	N.A.	95.53	64.71
61.43	3.91	5.06	0.82	0.37	0.17	3.01	19.26	0.81	N.A.	94.84	66.29
60.46	2.96	6.62	0.70	0.36	0.24	2.41	19.29	0.86	N.A.	93.90	65.25
61.51	4.06	5.14	0.76	0.36	0.21	2.67	19.17	0.90	N.A.	94.79	65.80
61.52	4.79	6.09	0.71	0.33	0.24	2.66	19.13	0.76	N.A.	96.23	62.28
61.61	4.12	6.06	0.78	0.36	0.30	2.88	19.02	0.80	N.A.	95.92	63.46
61.64	2.66	5.27	0.81	0.39	0.25	2.79	19.55	0.84	N.A.	94.19	69.11
61.77	4.55	5.30	0.90	0.42	0.24	2.55	19.07	0.74	N.A.	95.53	63.95
61.77	5.65	5.94	0.59	0.35	0.22	2.78	19.77	0.78	N.A.	97.86	61.88
60.78	4.76	5.98	0.81	0.39	0.28	2.70	19.67	0.88	N.A.	96.24	63.01
61.79	5.21	6.40	0.82	0.39	0.12	3.03	19.73	0.65	N.A.	98.15	61.34
61.81	4.09	5.11	0.78	0.40	0.12	3.03	18.87	0.92	N.A.	95.13	65.42
61.82	5.23	5.22	1.14	0.47	0.25	3.19	19.41	0.78	N.A.	97.51	62.61
62.00	4.69	6.09	0.77	0.34	0.28	2.74	19.35	0.68	N.A.	96.92	62.63
62.05	4.44	5.14	0.75	0.36	0.23	2.73	19.62	0.73	N.A.	96.04	65.49
62.13	4.75	5.12	0.84	0.37	0.25	2.92	19.46	0.76	N.A.	96.58	64.51
62.26	3.77	6.51	0.77	0.35	0.18	2.86	19.80	0.72	N.A.	97.23	64.17
62.26	4.47	5.39	0.80	0.36	0.30	2.84	19.48	0.82	N.A.	96.72	64.63
62.28	3.89	6.06	0.83	0.38	0.21	2.91	19.51	0.78	N.A.	96.85	64.42
60.33	3.75	6.03	0.67	0.35	0.22	2.57	19.24	0.66	N.A.	93.81	64.80
62.35	4.64	6.10	0.83	0.38	0.15	2.78	19.44	0.80	N.A.	97.47	62.70
64.46	5.01	4.20	0.79	0.36	0.22	2.88	19.35	0.74	N.A.	98.00	65.94
62.65	4.98	6.54	0.92	0.40	0.16	2.74	19.36	0.67	N.A.	98.41	60.89
62.80	4.49	5.18	0.78	0.36	0.17	2.97	19.47	0.90	N.A.	97.12	65.07
62.90	3.70	5.44	0.72	0.32	0.19	3.02	19.44	0.76	N.A.	96.51	66.36
58.00	3.66	6.31	0.76	0.30	0.24	2.50	18.92	0.84	N.A.	91.54	63.80
58.73	4.31	5.80	0.62	0.36	0.20	2.76	19.03	0.63	N.A.	92.43	63.94
58.84	5.87	6.03	0.76	0.32	0.15	2.94	19.26	0.88	N.A.	95.05	60.34
58.91	5.50	6.04	0.81	0.38	0.21	2.66	19.04	0.71	N.A.	94.25	60.67
59.07	5.91	6.15	1.28	0.51	0.19	2.88	19.22	0.76	N.A.	95.97	59.05
59.09	5.85	6.11	1.33	0.64	0.23	3.50	19.14	1.13	N.A.	97.01	59.02
59.24	4.93	6.17	0.80	0.33	0.16	3.02	19.32	0.70	N.A.	94.67	61.86
59.25	5.06	5.97	0.67	0.39	0.22	2.66	19.04	0.98	N.A.	94.24	61.94
59.62	4.37	6.68	0.82	0.41	0.20	2.68	18.58	0.64	N.A.	94.00	61.02
59.66	5.01	6.03	0.82	0.36	0.13	2.86	19.14	0.52	N.A.	94.53	61.75
59.70	5.45	6.46	0.85	0.31	0.26	2.84	19.16	0.58	N.A.	95.61	60.01
59.74	5.86	6.22	0.89	0.35	0.11	2.74	18.96	0.75	N.A.	95.61	59.38
59.82	5.09	6.62	0.69	0.34	0.20	3.09	18.94	0.49	N.A.	95.29	60.43
59.94	3.59	6.56	0.79	0.34	0.10	2.72	19.56	0.82	N.A.	94.43	64.11
59.97	5.66	6.20	0.74	0.31	0.18	2.67	19.03	0.56	N.A.	95.31	60.17
63.00	5.58	6.31	0.91	0.40	0.17	2.78	19.07	0.73	N.A.	98.93	59.83
60.06	4.76	5.64	0.82	0.35	0.27	2.59	19.37	0.76	N.A.	94.61	63.32
60.11	5.80	5.99	0.77	0.38	0.21	2.86	19.22	0.75	N.A.	96.08	60.49

Electron microprobe raw data of selected glass particles from sample I3A (Wt %)

SiO2	Na2O	K2O	CaO	MgO	MnO	FeO	Al2O3	TiO2	Cl	Total	CIA
57.91	3.23	5.06	0.37	0.19	0.23	3.47	18.82	0.46	0.34	90.09	68.49
58.05	3.45	4.85	0.51	0.24	0.25	2.61	19.67	0.62	0.25	90.49	69.07
59.94	2.37	5.23	0.65	0.22	0.22	2.76	18.85	0.33	0.33	90.90	69.56
60.65	2.32	5.95	0.29	0.21	0.20	3.18	17.87	0.47	0.44	91.57	67.61
58.06	3.97	5.49	0.48	0.26	0.22	2.94	19.56	0.47	0.29	91.74	66.31
61.30	2.54	5.24	0.55	0.22	0.28	3.02	17.98	0.62	0.38	92.12	68.34
59.16	3.52	5.51	0.62	0.46	0.18	2.61	19.93	0.41	0.36	92.76	67.38
59.42	3.84	5.89	0.36	0.24	0.21	2.62	19.43	0.51	0.32	92.82	65.82
62.05	2.09	5.24	0.31	0.18	0.35	2.72	19.27	0.58	0.42	93.20	71.61
59.72	4.59	5.30	0.49	0.24	0.35	2.28	20.07	0.49	0.35	93.87	65.91
61.79	3.45	5.66	0.62	0.24	0.14	2.25	19.39	0.46	0.30	94.30	66.59
61.26	2.83	6.01	0.64	0.21	0.31	3.17	18.98	0.60	0.40	94.41	66.69
59.23	4.78	6.16	0.43	0.28	0.27	2.29	20.59	0.57	0.32	94.92	64.42
59.40	4.74	6.14	0.52	0.26	0.27	2.95	19.80	0.61	0.29	94.99	63.46
59.59	5.05	6.44	0.56	0.25	0.28	2.61	19.58	0.53	0.30	95.19	61.90
60.18	2.89	6.46	0.57	0.22	0.31	3.81	20.13	0.45	0.27	95.30	66.99
59.21	4.98	6.27	0.87	0.22	0.35	2.70	20.09	0.51	0.31	95.50	62.37
60.06	4.22	6.40	0.41	0.28	0.28	2.99	20.07	0.48	0.35	95.53	64.53
61.04	4.95	5.13	0.52	0.25	0.26	2.55	20.48	0.39	0.28	95.86	65.89
60.16	5.61	5.56	0.55	0.24	0.24	2.31	20.37	0.60	0.23	95.87	63.48
59.91	3.98	6.31	0.56	0.19	0.29	3.42	20.37	0.51	0.41	95.94	65.25
60.17	5.87	5.62	0.38	0.25	0.24	2.53	20.24	0.57	0.29	96.16	63.03
60.42	5.08	5.70	0.71	0.24	0.23	2.96	19.97	0.55	0.30	96.16	63.48
60.75	4.45	6.26	0.63	0.24	0.37	3.02	19.76	0.51	0.31	96.28	63.54
59.60	5.94	5.90	0.53	0.27	0.37	2.68	20.27	0.52	0.24	96.32	62.10
59.91	5.31	5.80	0.55	0.21	0.40	2.75	20.67	0.56	0.27	96.42	63.93
60.10	4.81	6.71	0.59	0.26	0.27	2.82	20.05	0.51	0.31	96.42	62.34
60.45	5.35	5.46	0.45	0.24	0.32	2.93	20.41	0.55	0.25	96.42	64.45
60.25	5.34	5.64	0.63	0.22	0.31	3.13	20.20	0.48	0.26	96.46	63.50
61.12	4.21	6.12	0.48	0.32	0.21	2.86	20.31	0.56	0.30	96.48	65.26
59.79	5.79	5.78	0.56	0.25	0.29	3.03	20.25	0.55	0.32	96.61	62.54
60.84	4.64	6.19	0.61	0.25	0.39	2.70	20.13	0.55	0.31	96.61	63.76
59.85	5.26	5.48	0.46	0.28	0.20	3.73	20.48	0.51	0.36	96.62	64.65
60.89	4.76	6.15	0.37	0.23	0.20	2.70	20.66	0.53	0.32	96.80	64.68
60.32	4.28	6.17	0.88	0.24	0.26	3.59	20.31	0.47	0.30	96.82	64.19
60.63	4.80	6.36	0.47	0.25	0.31	3.03	20.31	0.54	0.30	97.00	63.59
61.00	5.63	5.63	0.55	0.26	0.33	2.46	20.29	0.57	0.32	97.04	63.21
60.23	5.69	5.74	0.74	0.26	0.32	2.55	20.82	0.42	0.30	97.06	63.11
62.23	4.19	5.89	0.37	0.40	0.16	2.65	20.45	0.48	0.27	97.09	66.18
61.13	5.79	5.14	0.35	0.28	0.15	3.04	20.32	0.68	0.29	97.18	64.30
61.19	5.69	6.10	0.44	0.24	0.20	2.25	20.38	0.48	0.31	97.26	62.50
59.81	5.53	5.69	0.63	0.26	0.22	4.15	20.24	0.59	0.28	97.40	63.07
60.70	5.81	5.75	0.74	0.22	0.28	2.63	20.45	0.55	0.31	97.44	62.44
60.91	5.23	6.26	0.65	0.26	0.25	2.79	20.30	0.49	0.38	97.52	62.58
60.88	5.11	6.37	0.45	0.27	0.17	3.42	20.17	0.53	0.32	97.68	62.83
61.90	4.54	6.28	0.62	0.20	0.32	2.90	20.18	0.47	0.31	97.72	63.82
60.46	5.86	5.66	0.52	0.25	0.29	3.00	20.87	0.49	0.33	97.73	63.42
60.64	5.99	6.11	0.63	0.24	0.30	2.63	20.39	0.50	0.34	97.76	61.56
59.83	6.25	5.63	0.76	0.22	0.24	3.45	20.61	0.54	0.26	97.81	61.98
60.42	4.98	6.02	0.74	0.28	0.37	3.37	20.89	0.52	0.30	97.88	64.02
60.56	5.94	5.95	0.52	0.29	0.25	3.01	20.49	0.63	0.28	97.91	62.28
60.64	5.72	5.92	0.69	0.22	0.39	3.12	20.39	0.55	0.28	97.91	62.32
59.85	6.22	6.55	0.59	0.23	0.32	2.93	20.33	0.57	0.33	97.92	60.34
61.16	5.49	6.22	0.46	0.25	0.25	3.27	20.10	0.41	0.35	97.96	62.29
60.37	5.79	6.51	0.69	0.25	0.24	2.99	20.24	0.59	0.31	97.98	60.91
60.37	5.59	6.11	0.53	0.26	0.37	3.20	20.78	0.49	0.31	98.01	62.95
61.40	5.73	5.81	0.42	0.25	0.28	3.28	20.24	0.49	0.29	98.20	62.86
60.01	5.97	6.29	0.52	0.24	0.34	3.20	20.79	0.60	0.30	98.27	61.93
61.58	5.88	5.67	0.49	0.25	0.26	2.45	21.07	0.49	0.29	98.44	63.64
61.03	5.53	6.43	0.62	0.26	0.22	2.99	20.57	0.54	0.34	98.54	62.05
61.35	4.93	6.39	0.35	0.22	0.22	3.38	21.05	0.39	0.30	98.58	64.33
60.80	6.31	6.13	0.47	0.24	0.40	3.09	20.34	0.56	0.26	98.59	61.17
60.91	5.36	6.35	0.57	0.23	0.43	3.41	20.70	0.52	0.33	98.81	62.77
62.49	5.33	6.37	0.60	0.23	0.28	2.77	20.08	0.50	0.26	98.91	62.01
61.25	5.98	5.67	0.57	0.23	0.27	3.34	20.87	0.45	0.33	98.95	63.07
61.78	5.06	6.32	0.75	0.29	0.32	2.87	20.83	0.47	0.30	98.99	63.20
61.62	6.04	5.99	0.73	0.29	0.25	3.07	20.51	0.55	0.23	99.26	61.65
61.43	6.38	6.18	0.83	0.22	0.28	2.51	20.82	0.51	0.31	99.46	60.86

Electron microprobe raw data of selected sanidines from sample F1A (Wt %)

Crystal	Na2O	K2O	CaO	MgO	MnO	FeO	Al2O3	SiO2	TiO2	Cl	Total
	7.49	6.08	0.39	0.00	0.00	0.45	19.63	67.18	0.00	0.00	101.21
1	7.58	6.09	0.50	0.03	0.02	0.22	19.90	68.08	0.00	0.03	102.44
	7.63	6.03	0.29	0.00	0.00	0.26	19.15	66.90	0.00	0.01	100.26
	7.46	6.11	0.41	0.00	0.00	0.41	19.73	67.01	0.00	0.01	101.14
2	7.50	6.04	0.50	0.00	0.00	0.28	19.81	67.19	0.18	0.02	101.52
	7.47	5.70	0.57	0.00	0.02	0.45	19.98	67.59	0.11	0.01	101.88
3	7.01	6.88	0.22	0.02	0.00	0.32	19.73	67.55	0.12	0.00	101.85
	7.25	6.74	0.34	0.01	0.00	0.36	19.76	67.52	0.06	0.02	102.06
	7.26	6.39	0.29	0.00	0.01	0.42	19.38	67.41	0.21	0.00	101.37
4	7.03	6.60	0.33	0.00	0.00	0.35	19.44	67.75	0.01	0.00	101.52
	7.69	5.82	0.44	0.00	0.15	0.44	20.13	67.33	0.11	0.00	102.11
	7.60	5.49	0.83	0.00	0.04	0.31	19.86	67.17	0.12	0.04	101.46
	8.27	5.29	0.76	0.01	0.05	0.39	19.85	67.46	0.03	0.04	102.14
5	7.81	5.17	0.77	0.00	0.04	0.37	20.12	67.18	0.13	0.00	101.58
	7.02	6.18	0.42	0.00	0.00	0.56	19.57	67.31	0.00	0.03	101.08
	7.73	5.38	0.67	0.01	0.05	0.32	19.94	67.83	0.04	0.01	101.99
6	7.62	5.69	0.54	0.00	0.00	0.38	19.84	67.35	0.00	0.00	101.43
	7.75	5.53	0.53	0.01	0.00	0.36	19.69	66.94	0.04	0.02	100.86
	6.90	7.18	0.23	0.02	0.02	0.33	19.49	66.51	0.00	0.08	100.76
7	6.98	7.16	0.23	0.01	0.07	0.42	19.48	67.69	0.03	0.00	102.06
	6.85	6.71	0.28	0.00	0.00	0.35	19.76	67.71	0.15	0.00	101.82
8	7.43	6.21	0.39	0.00	0.00	0.20	19.45	66.59	0.04	0.03	100.34
	7.94	5.47	0.71	0.00	0.05	0.23	19.79	66.88	0.05	0.02	101.13
	7.26	6.30	0.28	0.00	0.07	0.45	19.14	68.91	0.06	0.00	102.47
9	7.34	5.97	0.48	0.00	0.03	0.25	19.82	66.72	0.00	0.00	100.60
	8.04	5.50	0.66	0.00	0.00	0.29	19.84	67.93	0.04	0.00	102.30
	7.48	6.40	0.44	0.02	0.00	0.25	19.49	67.41	0.00	0.00	101.50
10	7.91	5.77	0.56	0.00	0.00	0.32	20.04	67.45	0.17	0.00	102.21
	7.08	6.32	0.29	0.00	0.00	0.55	19.76	67.08	0.14	0.01	101.23
	7.03	6.73	0.27	0.00	0.01	0.39	19.45	66.79	0.09	0.00	100.76
11	7.43	5.85	0.37	0.02	0.03	0.35	19.55	66.54	0.05	0.01	100.20
	7.19	6.15	0.31	0.02	0.00	0.37	19.01	64.97	0.02	0.02	98.05
	7.26	6.62	0.00	0.00	0.04	0.23	19.41	67.08	0.03	0.00	100.65
12	7.46	6.50	0.54	0.00	0.00	0.35	19.38	66.09	0.00	0.05	100.37
	7.64	6.07	0.34	0.01	0.00	0.56	19.75	67.92	0.00	0.00	102.29
	6.95	5.94	0.31	0.00	0.04	0.11	21.80	64.70	0.06	0.04	99.95

Electron microprobe raw data of selected sanidines from sample F1A (Wt %)

Crystal	Na2O	K2O	CaO	MgO	MnO	FeO	Al2O3	SiO2	TiO2	Cl	Total
13	7.30	6.71	0.31	0.00	0.07	0.60	19.67	67.40	0.04	0.00	102.11
	7.52	6.39	0.58	0.00	0.04	0.22	19.46	66.01	0.02	0.02	100.26
	7.86	5.92	0.54	0.00	0.00	0.37	19.81	67.67	0.06	0.00	102.24
	7.79	5.68	0.63	0.02	0.00	0.54	19.94	67.63	0.08	0.00	102.33
14	7.78	6.10	0.68	0.00	0.09	0.27	20.03	67.42	0.02	0.00	102.41
	7.75	6.40	0.26	0.02	0.00	0.40	19.85	66.17	0.00	0.01	100.87
	6.98	6.31	0.30	0.00	0.00	0.14	19.32	67.36	0.05	0.00	100.46
15	7.35	6.67	0.18	0.00	0.00	0.18	19.28	66.17	0.09	0.02	99.94
	6.93	6.52	0.48	0.00	0.02	0.70	19.00	67.16	0.00	0.00	100.81
	7.07	6.68	0.06	0.01	0.03	0.42	18.72	67.00	0.12	0.02	100.10
	7.04	6.77	0.14	0.00	0.00	0.67	18.95	67.93	0.04	0.00	101.53
16	7.67	6.15	0.47	0.00	0.01	0.92	19.69	66.75	0.00	0.00	101.66
	8.03	5.96	1.08	0.00	0.00	0.46	19.73	66.94	0.05	0.00	102.25
	7.50	6.07	0.54	0.00	0.02	0.19	19.80	67.65	0.00	0.04	101.81
17	7.37	6.02	0.30	0.00	0.02	0.98	19.26	68.25	0.04	0.02	102.25
	7.30	6.31	0.37	0.01	0.00	0.27	18.80	66.57	0.05	0.00	99.68
	7.54	5.73	0.34	0.01	0.06	0.50	19.23	67.69	0.04	0.00	101.14
	7.59	5.83	0.61	0.00	0.03	0.34	19.54	66.32	0.06	0.03	100.35
18	7.44	6.10	0.34	0.01	0.06	0.45	19.81	66.97	0.09	0.00	101.26
	7.62	5.89	0.48	0.00	0.00	0.01	19.46	67.04	0.00	0.00	100.51
	7.75	5.88	0.53	0.00	0.00	0.36	19.59	66.67	0.13	0.00	100.91
	7.60	5.74	0.50	0.00	0.00	0.22	19.66	66.93	0.04	0.00	100.68
19	6.73	7.18	0.32	0.01	0.04	0.66	19.34	67.59	0.03	0.00	101.91
	7.12	7.27	0.08	0.00	0.03	0.21	19.08	67.26	0.00	0.03	101.08
	6.92	7.09	0.12	0.00	0.00	0.39	19.30	66.42	0.05	0.00	100.30
	7.10	6.64	0.21	0.00	0.00	0.47	18.35	66.46	0.03	0.00	99.26
20	7.87	5.72	0.42	0.00	0.00	0.32	19.43	68.59	0.01	0.01	102.36
	7.30	6.34	0.17	0.00	0.03	0.34	19.40	67.56	0.05	0.03	101.21
	7.55	5.57	0.43	0.00	0.12	0.30	19.51	67.09	0.14	0.00	100.70
21	7.85	5.29	0.51	0.00	0.03	0.56	19.74	66.57	0.02	0.02	100.60
	8.19	5.19	0.39	0.00	0.01	0.43	19.64	67.75	0.02	0.00	101.61
	8.35	5.27	0.51	0.00	0.00	0.69	19.41	67.16	0.03	0.02	101.44
	7.73	5.49	0.59	0.00	0.00	0.27	19.54	66.77	0.00	0.02	100.41
22	7.23	6.49	0.23	0.00	0.08	0.31	19.31	67.79	0.12	0.00	101.56
	7.68	5.95	0.51	0.00	0.02	0.33	19.88	67.64	0.01	0.00	102.03
	7.32	6.64	0.41	0.00	0.01	0.25	19.21	66.32	0.13	0.01	100.30
23	7.35	6.37	0.47	0.01	0.00	0.46	20.11	66.20	0.04	0.00	101.00
	7.83	6.12	0.29	0.01	0.07	0.20	19.64	68.27	0.00	0.04	102.47
	7.51	6.25	0.66	0.01	0.00	0.19	19.22	66.90	0.00	0.01	100.74
24	7.49	6.53	0.32	0.00	0.00	0.42	18.94	65.87	0.06	0.01	99.65
	7.65	5.95	0.27	0.00	0.04	0.20	19.88	66.34	0.01	0.01	100.35
	7.36	6.45	0.28	0.01	0.00	0.18	19.35	66.52	0.07	0.03	100.25
25	8.02	5.68	0.63	0.00	0.03	0.32	20.08	67.53	0.08	0.01	102.39
	7.93	5.57	0.70	0.00	0.03	0.53	19.94	67.07	0.01	0.00	101.79

Electron microprobe raw data of selected sanidines from sample F2A (Wt %)

Crystal	Na2O	K2O	CaO	MgO	MnO	FeO	Al2O3	SiO2	TiO2	Cl	Total
	7.66	5.89	0.35	0.000	0.00	0.28	19.53	67.08	0.04	0.01	100.84
1	7.24	6.43	0.27	0.010	0.00	0.29	19.59	67.60	0.02	0.00	101.46
	7.36	6.57	0.32	0.003	0.04	0.43	19.61	66.63	0.06	0.11	101.13
	7.22	6.37	0.33	0.000	0.08	0.29	19.52	66.57	0.01	0.04	100.41
2	6.73	6.91	0.34	0.006	0.00	0.41	19.12	64.86	0.15	0.02	98.54
	7.01	6.76	0.31	0.000	0.00	0.30	19.66	66.94	0.00	0.04	101.01
	7.24	6.03	0.37	0.000	0.02	0.42	19.32	67.25	0.02	0.02	100.67
3	7.36	6.16	0.28	0.005	0.04	0.23	19.41	66.16	0.00	0.00	99.64
	7.28	6.14	0.37	0.003	0.05	0.32	19.32	65.89	0.12	0.02	99.51
	6.93	6.57	0.27	0.000	0.05	0.40	19.50	68.22	0.14	0.01	102.08
4	7.06	6.54	0.30	0.010	0.06	0.22	19.36	65.39	0.04	0.00	98.98
	7.17	6.27	0.26	0.023	0.00	0.46	19.39	67.62	0.03	0.04	101.28
5	7.23	6.73	0.28	0.000	0.00	0.35	19.40	67.25	0.07	0.04	101.35
	6.91	6.45	0.45	0.000	0.02	0.38	18.89	65.51	0.08	0.04	98.72
	7.10	6.19	0.34	0.000	0.09	0.39	19.46	66.11	0.00	0.01	99.69
6	7.43	6.28	0.27	0.016	0.00	0.20	19.48	66.84	0.02	0.01	100.56
	7.59	5.80	0.40	0.000	0.00	0.45	19.65	67.36	0.05	0.00	101.30
	6.80	6.47	0.37	0.008	0.08	0.49	18.91	65.11	0.09	0.00	98.32
7	7.28	6.73	0.28	0.014	0.00	0.14	19.27	66.80	0.00	0.00	100.52
	7.36	6.40	0.33	-0.003	0.00	0.45	19.19	65.04	0.12	0.01	98.91
	7.52	5.54	0.48	-0.001	0.00	0.33	19.46	65.31	0.00	0.00	98.63
8	7.86	5.50	0.55	0.000	0.07	0.25	19.53	66.53	0.00	0.02	100.30
	7.41	6.26	0.38	0.000	0.00	0.46	19.39	65.34	0.08	0.02	99.35
	7.13	5.98	0.40	0.019	0.07	0.18	19.27	63.84	0.10	0.01	97.00
9	7.60	5.82	0.37	0.003	0.00	0.37	19.50	66.13	0.02	0.01	99.81
	7.67	5.94	0.36	0.000	0.00	0.18	19.66	66.43	0.00	0.10	100.33
	7.05	6.77	0.30	-0.004	0.00	0.36	19.47	66.54	0.08	0.02	100.58
10	7.13	6.38	0.32	0.004	0.03	0.22	19.28	65.05	0.12	0.04	98.57
	7.21	6.65	0.34	0.020	0.00	0.40	19.20	68.11	0.00	0.00	101.94
11	7.07	6.20	0.42	0.000	0.00	0.34	19.09	65.28	0.01	0.00	98.43
	7.34	6.44	0.25	0.000	0.00	0.15	19.36	66.51	0.07	0.00	100.12
	7.03	6.54	0.27	0.017	0.00	0.40	19.23	65.83	0.14	0.00	99.58
12	7.27	6.42	0.28	0.018	0.07	0.33	19.27	66.84	0.04	0.07	100.59
	7.14	6.72	0.31	0.000	0.00	0.31	19.26	65.54	0.00	0.00	99.27
	7.06	6.30	0.24	0.009	0.09	0.25	19.05	65.62	0.15	0.08	98.86
13	6.87	6.39	0.40	0.035	0.00	0.29	19.05	66.47	0.08	0.00	99.59
	7.36	6.50	0.24	0.004	0.04	0.22	19.60	68.49	0.15	0.00	102.61
	7.86	5.63	0.50	-0.003	0.09	0.42	19.42	66.89	0.00	0.00	100.80
14	7.75	6.06	0.39	0.000	0.00	0.46	19.51	66.62	0.00	0.00	100.79
	7.45	6.58	0.33	0.014	0.00	0.33	19.67	67.74	0.14	0.00	102.24
	7.28	6.22	0.36	-0.004	0.01	0.57	19.75	66.47	0.11	0.00	100.75
15	7.63	5.71	0.52	0.000	0.04	0.36	19.52	65.92	0.13	0.00	99.83
	7.55	5.83	0.55	-0.004	0.00	0.38	19.87	67.09	0.11	0.00	101.38

Electron microprobe raw data of selected sanidines from sample F2A (Wt %)

Crystal	Na2O	K2O	CaO	MgO	MnO	FeO	Al2O3	SiO2	TiO2	Cl	Total
	7.66	5.89	0.35	0.000	0.00	0.28	19.53	67.08	0.04	0.01	100.84
1	7.24	6.43	0.27	0.010	0.00	0.29	19.59	67.60	0.02	0.00	101.46
	7.36	6.57	0.32	0.003	0.04	0.43	19.61	66.63	0.06	0.11	101.13
	7.22	6.37	0.33	0.000	0.08	0.29	19.52	66.57	0.01	0.04	100.41
2	6.73	6.91	0.34	0.006	0.00	0.41	19.12	64.86	0.15	0.02	98.54
	7.01	6.76	0.31	0.000	0.00	0.30	19.66	66.94	0.00	0.04	101.01
	7.24	6.03	0.37	0.000	0.02	0.42	19.32	67.25	0.02	0.02	100.67
3	7.36	6.16	0.28	0.005	0.04	0.23	19.41	66.16	0.00	0.00	99.64
	7.28	6.14	0.37	0.003	0.05	0.32	19.32	65.89	0.12	0.02	99.51
	6.93	6.57	0.27	0.000	0.05	0.40	19.50	68.22	0.14	0.01	102.08
4	7.06	6.54	0.30	0.010	0.06	0.22	19.36	65.39	0.04	0.00	98.98
	7.17	6.27	0.26	0.023	0.00	0.46	19.39	67.62	0.03	0.04	101.28
5	7.23	6.73	0.28	0.000	0.00	0.35	19.40	67.25	0.07	0.04	101.35
	6.91	6.45	0.45	0.000	0.02	0.38	18.89	65.51	0.08	0.04	98.72
	7.10	6.19	0.34	0.000	0.09	0.39	19.46	66.11	0.00	0.01	99.69
6	7.43	6.28	0.27	0.016	0.00	0.20	19.48	66.84	0.02	0.01	100.56
	7.59	5.80	0.40	0.000	0.00	0.45	19.65	67.36	0.05	0.00	101.30
	6.80	6.47	0.37	0.008	0.08	0.49	18.91	65.11	0.09	0.00	98.32
7	7.28	6.73	0.28	0.014	0.00	0.14	19.27	66.80	0.00	0.00	100.52
	7.36	6.40	0.33	-0.003	0.00	0.45	19.19	65.04	0.12	0.01	98.91
	7.52	5.54	0.48	-0.001	0.00	0.33	19.46	65.31	0.00	0.00	98.63
8	7.86	5.50	0.55	0.000	0.07	0.25	19.53	66.53	0.00	0.02	100.30
	7.41	6.26	0.38	0.000	0.00	0.46	19.39	65.34	0.08	0.02	99.35
	7.13	5.98	0.40	0.019	0.07	0.18	19.27	63.84	0.10	0.01	97.00
9	7.60	5.82	0.37	0.003	0.00	0.37	19.50	66.13	0.02	0.01	99.81
	7.67	5.94	0.36	0.000	0.00	0.18	19.66	66.43	0.00	0.10	100.33
	7.05	6.77	0.30	-0.004	0.00	0.36	19.47	66.54	0.08	0.02	100.58
10	7.13	6.38	0.32	0.004	0.03	0.22	19.28	65.05	0.12	0.04	98.57
	7.21	6.65	0.34	0.020	0.00	0.40	19.20	68.11	0.00	0.00	101.94
11	7.07	6.20	0.42	0.000	0.00	0.34	19.09	65.28	0.01	0.00	98.43
	7.34	6.44	0.25	0.000	0.00	0.15	19.36	66.51	0.07	0.00	100.12
	7.03	6.54	0.27	0.017	0.00	0.40	19.23	65.83	0.14	0.00	99.58
12	7.27	6.42	0.28	0.018	0.07	0.33	19.27	66.84	0.04	0.07	100.59
	7.14	6.72	0.31	0.000	0.00	0.31	19.26	65.54	0.00	0.00	99.27
	7.06	6.30	0.24	0.009	0.09	0.25	19.05	65.62	0.15	0.08	98.86
13	6.87	6.39	0.40	0.035	0.00	0.29	19.05	66.47	0.08	0.00	99.59
	7.36	6.50	0.24	0.004	0.04	0.22	19.60	68.49	0.15	0.00	102.61
	7.86	5.63	0.50	-0.003	0.09	0.42	19.42	66.89	0.00	0.00	100.80
14	7.75	6.06	0.39	0.000	0.00	0.46	19.51	66.62	0.00	0.00	100.79
	7.45	6.58	0.33	0.014	0.00	0.33	19.67	67.74	0.14	0.00	102.24
	7.28	6.22	0.36	-0.004	0.01	0.57	19.75	66.47	0.11	0.00	100.75
15	7.63	5.71	0.52	0.000	0.04	0.36	19.52	65.92	0.13	0.00	99.83
	7.55	5.83	0.55	-0.004	0.00	0.38	19.87	67.09	0.11	0.00	101.38

Electron microprobe raw data of selected sanidines from sample F2A (Wt %)

Mineral	Na2O	K2O	CaO	MgO	MnO	FeO	Al2O3	SiO2	TiO2	Cl	Total
	6.98	6.29	0.47	0.000	0.03	0.30	19.20	66.59	0.10	0.02	99.98
16	7.56	6.14	0.52	0.000	0.03	0.63	19.14	66.73	0.00	0.00	100.74
	7.53	5.98	0.27	0.000	0.00	0.27	18.92	66.76	0.04	0.00	99.78
	7.26	6.03	0.45	0.010	0.00	0.36	19.08	66.86	0.06	0.00	100.10
17	7.73	5.69	0.29	0.000	0.07	0.49	19.40	67.51	0.08	0.00	101.27
	7.62	6.14	0.34	0.010	0.01	0.18	19.62	66.33	0.02	0.00	100.27
	7.62	5.88	0.18	0.000	0.00	0.50	19.63	66.86	0.05	0.00	100.72
18	7.40	6.20	0.34	0.010	0.00	0.49	19.98	68.45	0.00	0.00	102.88
	7.60	6.17	0.21	0.000	0.00	0.05	19.13	67.08	0.00	0.01	100.25
19	7.51	6.29	0.21	0.010	0.02	0.20	19.71	67.37	0.03	0.02	101.37
	7.93	5.18	0.49	0.000	0.00	0.24	19.40	65.88	0.12	0.00	99.25
	7.40	6.05	0.53	0.000	0.00	0.46	19.04	67.18	0.00	0.00	100.67
20	7.83	5.43	0.44	0.010	0.01	0.28	19.28	66.56	0.11	0.00	99.95
	8.04	5.48	0.48	0.000	0.03	0.57	19.17	66.29	0.00	0.00	100.06
	7.50	6.06	0.33	0.000	0.00	0.06	19.11	65.94	0.03	0.01	99.04
21	7.33	6.21	0.49	0.000	0.05	0.43	19.06	64.91	0.06	0.02	98.57
	7.51	6.77	0.18	0.000	0.12	0.67	18.63	64.48	0.00	0.02	98.37
22	7.95	5.45	0.45	0.010	0.00	0.28	18.63	64.93	0.09	0.00	97.79
	7.57	6.46	0.29	0.000	0.00	0.25	19.80	65.15	0.06	0.00	99.59
	7.45	6.17	0.39	0.000	0.01	0.29	19.52	66.18	0.11	0.00	100.13
23	7.49	5.71	0.69	0.020	0.06	0.19	18.93	65.73	0.05	0.03	98.88
	7.11	5.75	0.46	0.010	0.06	0.44	18.74	64.77	0.03	0.00	97.37
	7.62	6.12	0.35	0.000	0.11	0.40	19.08	66.26	0.05	0.00	99.99
24	7.60	6.44	0.26	0.000	0.08	0.68	19.67	64.88	0.09	0.10	99.80
	7.34	6.27	0.35	0.010	0.00	0.28	19.35	65.64	0.00	0.00	99.24
25	7.00	6.37	0.22	0.010	0.11	0.29	18.93	64.29	0.00	0.00	97.23
	7.44	6.12	0.34	0.020	0.00	0.36	19.70	66.97	0.00	0.00	100.95
	7.56	5.83	0.52	0.000	0.07	0.44	19.85	66.61	0.11	0.00	100.99
26	7.71	6.54	0.26	0.010	0.07	0.35	19.09	64.47	0.07	0.00	98.58
	7.32	6.39	0.20	0.020	0.03	0.19	19.12	64.78	0.11	0.00	98.16
	7.41	6.15	0.33	0.020	0.04	0.11	18.72	64.26	0.05	0.00	97.08
27	7.54	5.78	0.60	0.010	0.05	0.41	19.82	65.95	0.00	0.03	100.20
	7.55	6.05	0.33	0.000	0.09	0.33	19.64	64.58	0.06	0.02	98.66
	7.43	6.64	0.22	0.000	0.00	0.46	19.05	65.10	0.05	0.00	98.94
28	7.29	6.63	0.39	0.020	0.00	0.24	19.46	65.56	0.02	0.00	99.60
	7.36	6.61	0.44	0.000	0.04	0.18	19.14	65.12	0.08	0.00	98.97
	7.31	6.87	0.28	0.000	0.00	0.32	18.99	64.79	0.00	0.00	98.56

Electron microprobe raw data of selected sanidines from sample I1A (Wt %)

Crystal	Na2O	K2O	CaO	MgO	MnO	FeO	Al2O3	SiO2	TiO2	Cl	Total
1	7.24	6.06	0.37	0.00	0.00	0.26	19.44	65.72	0.00	0.00	99.08
	7.89	6.22	0.27	0.00	0.01	0.28	19.36	65.18	0.00	0.00	99.21
2	7.81	5.27	0.72	0.01	0.00	0.22	19.64	66.19	0.04	0.00	99.91
	8.28	4.64	0.91	0.01	0.00	0.42	20.37	66.40	0.20	0.02	101.24
3	6.42	5.88	0.48	0.00	0.01	0.21	19.28	66.10	0.05	0.00	98.42
	7.27	6.54	0.30	0.02	0.07	0.39	19.30	66.90	0.03	0.01	100.83
	7.15	6.35	0.27	0.00	0.08	0.39	19.20	67.50	0.00	0.00	100.93
4	7.37	6.47	0.25	0.00	0.02	0.26	19.38	67.92	0.02	0.00	101.69
	7.56	5.98	0.43	0.00	0.03	0.29	19.91	66.84	0.05	0.04	101.13
	7.60	5.80	0.41	0.01	0.00	0.41	20.14	67.20	0.04	0.02	101.61
5	7.44	5.52	0.69	0.01	0.00	0.48	19.76	67.19	0.19	0.03	101.31
	7.70	5.53	0.58	0.00	0.13	0.35	19.71	65.93	0.11	0.05	100.07
6	7.83	5.46	0.61	0.01	0.00	0.34	19.65	65.28	0.03	0.02	99.21
	7.71	5.24	0.70	0.00	0.00	0.28	19.87	65.68	0.00	0.00	99.48
7	6.92	6.05	0.32	0.00	0.00	0.23	19.55	67.53	0.05	0.03	100.67
	7.14	5.88	0.39	0.00	0.06	0.39	19.78	66.76	0.03	0.00	100.43
	7.90	5.89	0.44	0.00	0.04	0.31	19.78	67.38	0.13	0.00	101.88
8	7.66	6.40	0.33	0.00	0.00	0.36	19.41	67.04	0.00	0.05	101.25
	6.88	6.30	0.30	0.00	0.09	0.26	19.52	66.25	0.02	0.07	99.69
	6.94	6.02	0.34	0.00	0.03	0.38	19.48	66.40	0.00	0.00	99.59
9	7.92	4.73	0.95	0.00	0.00	0.44	19.95	66.32	0.19	0.01	100.52
	8.05	4.74	1.04	0.00	0.00	0.21	20.78	67.63	0.05	0.00	102.50
10	7.21	6.74	0.22	0.00	0.00	0.26	19.49	66.11	0.13	0.00	100.15
	7.26	6.92	0.17	0.00	0.02	0.25	19.14	64.32	0.04	0.00	98.12
11	7.11	6.85	0.24	0.00	0.10	0.30	18.99	65.73	0.00	0.01	99.32
	6.86	6.85	0.17	0.00	0.00	0.43	19.12	65.22	0.00	0.00	98.65
	6.89	7.00	0.21	0.00	0.00	0.32	19.19	66.93	0.06	0.00	100.60
12	7.04	6.81	0.15	0.00	0.01	0.22	19.42	67.42	0.08	0.00	101.14
	7.08	6.84	0.23	0.00	0.00	0.40	19.33	66.63	0.04	0.00	100.56
	7.01	6.89	0.17	0.00	0.03	0.34	19.53	68.11	0.00	0.01	102.10
13	6.93	6.58	0.34	0.00	0.12	0.19	19.36	64.64	0.01	0.00	98.18
	7.47	6.10	0.27	0.00	0.00	0.32	19.52	67.52	0.00	0.02	101.22
	7.81	6.15	0.39	0.00	0.05	0.38	19.22	64.81	0.09	0.00	98.89

Electron microprobe raw data of selected sanidines from sample I1A (Wt %)

Crystal	Na2O	K2O	CaO	MgO	MnO	FeO	Al2O3	SiO2	TiO2	Cl	Total
	7.31	6.43	0.19	0.00	0.00	0.55	18.80	67.18	0.08	0.00	100.55
14	7.30	6.28	0.52	0.00	0.07	0.24	19.62	68.06	0.16	0.00	102.25
	7.11	6.49	0.47	0.00	0.00	0.06	19.69	67.88	0.06	0.02	101.78
	7.24	6.51	0.24	0.00	0.00	0.36	19.63	67.59	0.03	0.00	101.60
15	7.03	6.63	0.38	0.00	0.00	0.28	19.07	67.49	0.10	0.00	100.99
	7.23	6.62	0.12	0.00	0.00	0.05	18.53	67.08	0.06	0.01	99.70
	7.39	6.05	0.47	0.01	0.00	0.51	19.33	66.42	0.05	0.01	100.22
16	7.52	6.59	0.16	0.01	0.00	0.34	18.99	66.90	0.07	0.01	100.60
	6.84	6.53	0.22	0.00	0.00	0.11	18.99	67.20	0.00	0.00	99.89
	7.60	5.53	0.51	0.00	0.03	0.55	19.37	66.06	0.02	0.00	99.67
17	7.64	5.15	0.72	0.00	0.03	0.13	19.48	66.84	0.04	0.01	100.06
	7.51	4.68	0.93	0.02	0.01	0.24	19.77	66.72	0.08	0.00	99.97
	7.17	5.28	0.49	0.00	0.00	0.50	19.96	66.18	0.11	0.01	99.69
18	6.82	5.18	0.87	0.00	0.01	0.11	20.11	66.09	0.02	0.00	99.22
	6.62	4.87	0.92	0.01	0.00	0.34	19.76	64.80	0.05	0.02	97.39
	7.93	4.78	0.71	0.00	0.00	0.28	20.23	68.23	0.05	0.00	102.21
18	8.34	5.01	0.83	0.00	0.02	0.07	20.84	67.31	0.09	0.01	102.51
	8.31	4.78	0.68	0.02	0.00	0.48	20.22	67.19	0.05	0.00	101.72
	7.59	4.67	0.81	0.01	0.02	0.22	19.92	65.08	0.11	0.00	98.43
20	8.08	4.53	0.95	0.02	0.11	0.29	20.06	66.54	0.15	0.00	100.73
	8.38	4.70	1.01	0.00	0.12	0.33	20.05	67.02	0.07	0.03	101.71
	7.65	4.94	0.86	0.01	0.00	0.09	20.22	65.48	0.16	0.02	99.43
21	7.31	5.97	0.45	0.02	0.00	0.27	19.32	67.25	0.01	0.00	100.59
	7.52	5.79	0.34	0.00	0.05	0.13	19.29	66.73	0.00	0.03	99.88
	7.65	6.06	0.29	0.01	0.00	0.36	19.93	66.45	0.02	0.00	100.78
22	7.17	6.13	0.60	0.00	0.08	0.20	19.78	66.51	0.02	0.00	100.49
	7.71	5.89	0.45	0.00	0.00	0.00	19.80	65.95	0.07	0.01	99.88
	7.06	6.14	0.69	0.00	0.00	0.37	19.54	67.46	0.00	0.00	101.27
23	7.85	5.64	0.43	0.00	0.00	0.67	19.53	65.33	0.01	0.00	99.46
	7.93	5.41	0.59	0.01	0.00	0.16	19.47	65.52	0.03	0.01	99.11
	8.07	5.62	0.58	0.00	0.00	0.34	19.93	67.61	0.00	0.00	102.14
24	7.84	5.35	0.30	0.00	0.00	0.43	19.68	67.04	0.03	0.01	100.69
	7.17	5.85	0.27	0.00	0.12	0.03	19.60	67.05	0.06	0.01	100.14
	7.07	6.47	0.51	0.02	0.00	0.03	19.35	66.72	0.05	0.00	100.23
25	7.24	6.37	0.38	0.00	0.00	0.33	19.43	68.01	0.04	0.04	101.85
	7.28	6.25	0.23	0.00	0.08	0.16	18.90	67.61	0.00	0.00	100.52
26	7.33	6.27	0.21	0.01	0.00	0.67	18.89	65.18	0.00	0.00	98.56
	7.65	5.47	1.27	0.00	0.00	0.58	19.45	65.06	0.09	0.01	99.58
	6.91	6.55	0.30	0.00	0.02	0.00	18.55	68.04	0.01	0.01	100.39
27	7.18	6.46	0.30	0.00	0.08	0.70	18.74	65.88	0.05	0.00	99.40
	7.01	6.48	0.21	0.01	0.03	0.00	18.66	68.10	0.06	0.00	100.57

Electron microprobe raw data of selected sanidines from sample I3A (Wt %)

Crystal	Na2O	K2O	CaO	MgO	MnO	FeO	Al2O3	SiO2	TiO2	Cl	Total
1	7.42	6.83	0.24	0.00	0.00	0.32	19.73	67.46	0.16	0.07	102.22
	7.75	6.02	0.27	0.00	0.00	0.37	19.32	66.08	0.05	0.01	99.86
2	6.19	6.78	0.30	0.01	0.00	0.23	18.84	66.09	0.12	0.01	98.57
	7.02	6.64	0.22	0.00	0.00	0.37	19.50	67.42	0.07	0.01	101.24
	7.33	6.37	0.29	0.00	0.02	0.36	20.26	66.99	0.02	0.04	101.66
3	7.02	6.65	0.19	0.00	0.06	0.19	19.92	68.72	0.01	0.00	102.76
	6.89	7.00	0.21	0.00	0.07	0.59	19.85	66.22	0.10	0.07	100.99
	7.75	6.31	0.18	0.00	0.02	0.22	19.33	67.82	0.14	0.02	101.78
4	7.18	6.52	0.25	0.02	0.00	0.39	19.60	68.00	0.05	0.03	102.03
	6.73	6.73	0.27	0.01	0.09	0.33	19.19	67.07	0.14	0.00	100.55
	7.44	6.55	0.22	0.01	0.00	0.37	19.39	67.09	0.00	0.00	101.07
5	7.06	7.36	0.16	0.00	0.00	0.34	19.87	66.92	0.08	0.00	101.80
	6.84	6.48	0.31	0.01	0.00	0.32	19.26	66.81	0.03	0.01	100.06
	7.13	6.00	0.35	0.01	0.00	0.38	19.26	65.00	0.09	0.00	98.21
6	7.35	6.19	0.37	0.02	0.00	0.61	19.48	66.98	0.07	0.00	101.08
	7.47	5.81	0.44	0.00	0.01	0.34	19.76	67.90	0.12	0.00	101.83
	7.72	5.81	0.41	0.00	0.00	0.40	19.30	65.86	0.10	0.05	99.65
	7.95	5.98	0.37	0.00	0.00	0.60	19.73	66.23	0.11	0.06	101.04
7	7.00	6.19	0.41	0.00	0.04	0.32	19.51	65.34	0.02	0.04	98.87
	7.44	6.16	0.33	0.00	0.00	0.41	19.27	67.53	0.07	0.00	101.22
	7.47	6.47	0.21	0.00	0.00	0.38	18.74	64.07	0.06	0.00	97.40
8	7.39	6.42	0.32	0.01	0.00	0.32	19.20	65.47	0.04	0.07	99.21
	7.59	6.46	0.29	0.00	0.00	0.18	19.46	65.88	0.00	0.00	99.85
	7.41	6.21	0.37	0.00	0.00	0.43	19.98	67.03	0.00	0.00	101.42
9	7.26	6.50	0.27	0.01	0.00	0.36	19.16	66.91	0.07	0.00	100.54
	7.50	6.54	0.16	0.00	0.00	0.32	19.18	68.04	0.01	0.01	101.77
	6.36	6.77	0.25	0.00	0.00	0.38	19.11	66.86	0.04	0.06	99.83
10	7.31	6.76	0.27	0.00	0.05	0.45	19.43	66.39	0.03	0.02	100.71
	7.49	6.64	0.29	0.00	0.00	0.28	19.67	67.70	0.00	0.00	102.08
11	7.48	6.59	0.20	0.00	0.00	0.30	19.96	67.12	0.00	0.00	101.66
	8.06	5.67	0.40	0.01	0.00	0.33	19.65	65.64	0.03	0.02	99.79
	7.59	6.49	0.21	0.01	0.00	0.24	19.41	66.98	0.04	0.00	100.97
12	7.41	6.59	0.21	0.00	0.04	0.37	19.26	67.01	0.06	0.00	100.94
	6.87	6.68	0.32	0.00	0.00	0.38	19.77	68.49	0.11	0.01	102.62

A4.2 NG data

NG analysis of glass particles from sample F1A

N°	date	weight (g)	4He (v)	±	36Ar (v)	±	40Ar (v)	±
1	27/09/2017	0.000040	-0.00130	0.00013	0.00114	0.00005	0.30961	0.00946
2	27/09/2017	0.000021	-0.00097	0.00012	0.00034	0.00005	0.08622	0.00945
3	27/09/2017	0.000046	-0.00130	0.00011	0.00050	0.00005	0.14253	0.00945
4	27/09/2017	0.000058	-0.00121	0.00010	0.00074	0.00005	0.22305	0.00945
5	28/09/2017	0.000043	0.00234	0.00007	0.00041	0.00001	0.09271	0.00028
8	28/09/2017	0.000037	-0.00183	0.00025	0.00087	0.00033	0.10312	0.00353
11	15/12/2017	0.000033	0.00060	0.00010	0.00055	0.00004	0.10937	0.00191
12	15/12/2017	0.000053	0.00092	0.00009	0.00191	0.00003	0.49843	0.00203
13	15/12/2017	0.000073	0.00033	0.00012	0.00090	0.00004	0.26090	0.00419
16	15/12/2017	0.000112	0.00265	0.00016	0.00348	0.00007	1.02034	0.00766
18	15/12/2017	0.000033	0.00268	0.00017	0.00096	0.00006	0.23180	0.00752
19	15/12/2017	0.000086	0.00051	0.00010	0.00237	0.00007	0.68404	0.00748
21	16/12/2017	0.000035	0.00034	0.00014	0.00108	0.00003	0.32371	0.00305
22	16/12/2017	0.000053	0.00075	0.00016	0.00083	0.00004	0.20410	0.00307
23	16/12/2017	0.000029	0.00011	0.00014	0.00045	0.00003	0.09106	0.00303
24	16/12/2017	0.000034	0.00042	0.00014	0.00066	0.00003	0.16298	0.00303
25	16/12/2017	0.000075	0.00052	0.00014	0.00231	0.00003	0.66304	0.00332
26	16/12/2017	0.000093	0.00076	0.00014	0.00467	0.00003	1.33749	0.00327
27	16/12/2017	0.000039	0.00059	0.00014	0.00065	0.00003	0.19759	0.00303
28	16/12/2017	0.000062	0.00066	0.00014	0.00189	0.00003	0.48877	0.00309
29	16/12/2017	0.000036	0.00049	0.00014	0.00068	0.00004	0.20038	0.00305
30	16/12/2017	0.000038	0.00088	0.00015	0.00039	0.00003	0.15058	0.00305
31	16/12/2017	0.000033	0.00057	0.00014	0.00160	0.00004	0.47258	0.00305
32	16/12/2017	0.000027	0.00116	0.00016	0.00051	0.00003	0.13394	0.00307
33	16/12/2017	0.000033	0.00059	0.00014	0.00047	0.00004	0.15453	0.00305
34	16/12/2017	0.000023	0.00054	0.00014	0.00096	0.00004	0.24961	0.00303
35	16/12/2017	0.000025	0.00015	0.00014	0.00126	0.00003	0.35820	0.00313

NG analysis of glass particles from sample F1A (cc)

N°	4He	±	36Ar	±	40Ar	±
9	-1.57E-11	1.57E-12	1.37E-12	6.01E-14	3.91E-10	1.20E-11
10	-1.17E-11	1.45E-12	4.08E-13	6.01E-14	1.09E-10	1.19E-11
11	-1.57E-11	1.33E-12	6.01E-13	6.01E-14	1.80E-10	1.19E-11
12	-1.46E-11	1.21E-12	8.89E-13	6.01E-14	2.82E-10	1.19E-11
13	2.83E-11	8.47E-13	4.92E-13	1.20E-14	1.17E-10	3.54E-13
14	-2.21E-11	3.02E-12	1.04E-12	3.96E-13	1.30E-10	4.46E-12
15	1.00E-11	1.67E-12	5.25E-13	3.82E-14	1.12E-10	1.96E-12
16	1.54E-11	1.50E-12	1.82E-12	2.86E-14	5.10E-10	2.08E-12
17	5.51E-12	2.00E-12	8.59E-13	3.82E-14	2.67E-10	4.29E-12
18	4.43E-11	2.67E-12	3.32E-12	6.68E-14	1.05E-09	7.85E-12
19	4.48E-11	2.84E-12	9.16E-13	5.73E-14	2.37E-10	7.70E-12
20	8.52E-12	1.67E-12	2.26E-12	6.68E-14	7.01E-10	7.66E-12
21	5.68E-12	2.34E-12	1.03E-12	2.86E-14	3.32E-10	3.12E-12
22	1.25E-11	2.67E-12	7.92E-13	3.82E-14	2.09E-10	3.14E-12
23	1.84E-12	2.34E-12	4.30E-13	2.86E-14	9.33E-11	3.10E-12
24	7.01E-12	2.34E-12	6.30E-13	2.86E-14	1.67E-10	3.10E-12
25	8.68E-12	2.34E-12	2.20E-12	2.86E-14	6.79E-10	3.40E-12
26	1.27E-11	2.34E-12	4.46E-12	2.86E-14	1.37E-09	3.35E-12
27	9.85E-12	2.34E-12	6.20E-13	2.86E-14	2.02E-10	3.10E-12
28	1.10E-11	2.34E-12	1.80E-12	2.86E-14	5.01E-10	3.16E-12
29	8.18E-12	2.34E-12	6.49E-13	3.82E-14	2.05E-10	3.12E-12
30	1.47E-11	2.50E-12	3.72E-13	2.86E-14	1.54E-10	3.12E-12
31	9.52E-12	2.34E-12	1.53E-12	3.82E-14	4.84E-10	3.12E-12
32	1.94E-11	2.67E-12	4.87E-13	2.86E-14	1.37E-10	3.14E-12
33	9.85E-12	2.34E-12	4.49E-13	3.82E-14	1.58E-10	3.12E-12
34	9.02E-12	2.34E-12	9.16E-13	3.82E-14	2.56E-10	3.10E-12
35	2.50E-12	2.34E-12	1.20E-12	2.86E-14	3.67E-10	3.21E-12

NG analysis of glass particles from sample F1A (cc/g)

N°	4He	±	% ±	36Ar	±	% ±	40Ar	±	% ±	40Ar*	±	% ±
9	-3.93E-07	3.93E-08	-10	3.42E-08	1.50E-09	4.4	9.78E-06	2.99E-07	3.06	-4.40E-07	-2.35E-08	5.3
10	-5.59E-07	6.91E-08	-12	1.94E-08	2.86E-09	14.7	5.19E-06	5.69E-07	10.96	-6.18E-07	-1.13E-07	18.3
11	-3.42E-07	2.89E-08	-8	1.31E-08	1.31E-09	10.0	3.92E-06	2.60E-07	6.63	1.74E-08	2.09E-09	12.0
12	-2.52E-07	2.09E-08	-8	1.53E-08	1.04E-09	6.8	4.86E-06	2.06E-07	4.24	2.84E-07	2.27E-08	8.0
13	6.58E-07	1.97E-08	3	1.15E-08	2.79E-10	2.4	2.72E-06	8.23E-09	0.30	-6.95E-07	-1.71E-08	2.5
14	-5.98E-07	8.17E-08	-14	2.82E-08	1.07E-08	37.9	3.52E-06	1.21E-07	3.42	-4.91E-06	-1.87E-06	38.1
15	3.04E-07	5.06E-08	17	1.59E-08	1.16E-09	7.3	3.39E-06	5.93E-08	1.75	-1.35E-06	-1.01E-07	7.5
16	2.90E-07	2.84E-08	10	3.44E-08	5.40E-10	1.6	9.63E-06	3.92E-08	0.41	-6.38E-07	-1.03E-08	1.6
17	7.55E-08	2.74E-08	36	1.18E-08	5.23E-10	4.4	3.66E-06	5.88E-08	1.61	1.47E-07	6.95E-09	4.7
18	3.95E-07	2.39E-08	6	2.97E-08	5.97E-10	2.0	9.33E-06	7.00E-08	0.75	4.76E-07	1.02E-08	2.1
19	1.36E-06	8.60E-08	6	2.78E-08	1.74E-09	6.3	7.19E-06	2.33E-07	3.24	-1.10E-06	-7.72E-08	7.0
20	9.90E-08	1.94E-08	20	2.63E-08	7.77E-10	3.0	8.15E-06	8.91E-08	1.09	2.93E-07	9.24E-09	3.1
21	1.62E-07	6.68E-08	41	2.95E-08	8.18E-10	2.8	9.47E-06	8.93E-08	0.94	6.79E-07	1.99E-08	2.9
22	2.36E-07	5.04E-08	21	1.49E-08	7.20E-10	4.8	3.94E-06	5.93E-08	1.50	-5.19E-07	-2.62E-08	5.0
23	6.33E-08	8.06E-08	127	1.48E-08	9.87E-10	6.7	3.22E-06	1.07E-07	3.33	-1.21E-06	-8.99E-08	7.5
24	2.06E-07	6.88E-08	33	1.85E-08	8.42E-10	4.5	4.91E-06	9.13E-08	1.86	-6.22E-07	-3.06E-08	4.9
25	1.16E-07	3.12E-08	27	2.94E-08	3.82E-10	1.3	9.05E-06	4.53E-08	0.50	2.77E-07	3.86E-09	1.4
26	1.36E-07	2.51E-08	18	4.79E-08	3.08E-10	0.6	1.47E-05	3.60E-08	0.24	4.20E-07	2.89E-09	0.7
27	2.53E-07	5.99E-08	24	1.59E-08	7.34E-10	4.6	5.19E-06	7.96E-08	1.53	4.40E-07	2.14E-08	4.9
28	1.78E-07	3.77E-08	21	2.91E-08	4.62E-10	1.6	8.07E-06	5.10E-08	0.63	-6.13E-07	-1.05E-08	1.7
29	2.27E-07	6.49E-08	29	1.80E-08	1.06E-09	5.9	5.70E-06	8.68E-08	1.52	3.18E-07	1.93E-08	6.1
30	3.87E-07	6.59E-08	17	9.80E-09	7.54E-10	7.7	4.06E-06	8.22E-08	2.03	1.13E-06	9.02E-08	8.0
31	2.88E-07	7.08E-08	25	4.63E-08	1.16E-09	2.5	1.47E-05	9.47E-08	0.65	8.51E-07	2.20E-08	2.6
32	7.17E-07	9.90E-08	14	1.80E-08	1.06E-09	5.9	5.08E-06	1.16E-07	2.29	-3.02E-07	-1.91E-08	6.3
33	2.99E-07	7.08E-08	24	1.36E-08	1.16E-09	8.5	4.80E-06	9.47E-08	1.97	7.37E-07	6.44E-08	8.7
34	3.92E-07	1.02E-07	26	3.98E-08	1.66E-09	4.2	1.11E-05	1.35E-07	1.21	-7.79E-07	-3.38E-08	4.3
35	1.00E-07	9.35E-08	93	4.81E-08	1.15E-09	2.4	1.47E-05	1.28E-07	0.87	3.12E-07	7.92E-09	2.5

NG analysis of glass particles from sample F1A

N°	40Ar/36Ar	±	% ±	4He/40Ar*	±	% ±
9	285.72	15.27	5.3	0.89	1.01E-01	11
10	266.78	48.93	18.3	0.90	2.00E-01	22
11	299.89	35.98	12.0	-19.67	-2.89E+00	15
12	317.10	25.29	8.0	-0.89	-1.02E-01	11
13	237.89	5.85	2.5	-0.95	-3.67E-02	4
14	124.70	47.49	38.1	0.12	4.93E-02	40
15	213.38	15.96	7.5	-0.22	-4.09E-02	18
16	280.02	4.54	1.6	-0.45	-4.51E-02	10
17	311.07	14.70	4.7	0.51	1.88E-01	37
18	314.62	6.75	2.1	0.83	5.32E-02	6
19	259.10	18.25	7.0	-1.24	-1.17E-01	9
20	309.71	9.75	3.1	0.34	6.71E-02	20
21	321.63	9.43	2.9	0.24	9.86E-02	41
22	263.87	13.32	5.0	-0.46	-9.99E-02	22
23	217.14	16.18	7.5	-0.05	-6.70E-02	127
24	264.98	13.01	4.9	-0.33	-1.12E-01	34
25	308.00	4.29	1.4	0.42	1.12E-01	27
26	307.32	2.11	0.7	0.32	5.99E-02	18
27	326.19	15.86	4.9	0.57	1.39E-01	24
28	277.50	4.74	1.7	-0.29	-6.17E-02	21
29	316.20	19.21	6.1	0.71	2.09E-01	29
30	414.31	32.96	8.0	0.34	6.42E-02	19
31	316.94	8.18	2.6	0.34	8.38E-02	25
32	281.81	17.79	6.3	-2.38	-3.60E-01	15
33	352.81	30.82	8.7	0.40	1.02E-01	25
34	279.00	12.11	4.3	-0.50	-1.32E-01	26
35	305.05	7.74	2.5	0.32	2.99E-01	93

NG analysis of glass particles from sample F2A

N°	date	weight (g)	4He (v)	±	36Ar (v)	±	40Ar (v)	±
1	28/09/2017	0.000078	-0.00161	0.00074	0.00281	0.00062	0.72575	0.00390
2	28/09/2017	0.000068	-0.00134	0.00074	0.00128	0.00062	0.09249	0.00422
3	28/09/2017	0.000072	-0.00152	0.00074	0.00628	0.00062	1.50544	0.00371
4	28/09/2017	0.000052	-0.00115	0.00074	0.00242	0.00062	0.22710	0.00404
6	08/10/2017	0.000044	0.00125	0.00018	0.00782	0.00003	2.07120	0.00613
7	08/10/2017	0.000050	0.00120	0.00018	0.00167	0.00003	0.53911	0.00306
8	08/10/2017	0.000054	0.00120	0.00018	0.00306	0.00003	0.77952	0.00290
9	08/10/2017	0.000053	0.00063	0.00018	0.00855	0.00005	2.29168	0.00400
10	08/10/2017	0.000036	0.00091	0.00018	0.00203	0.00003	0.61913	0.00277
11	17/12/2017	0.000082	0.00034	0.00023	0.00604	0.00007	1.82598	0.00229
12	17/12/2017	0.000109	0.00040	0.00024	0.00577	0.00005	1.54003	0.00150
13	17/12/2017	0.000039	0.00063	0.00023	0.00452	0.00004	1.30762	0.00142
14	17/12/2017	0.000043	0.00054	0.00024	0.00943	0.00003	2.51831	0.00275
15	17/12/2017	0.000086	0.00195	0.00026	0.00256	0.00006	0.70867	0.00242
16	17/12/2017	0.000081	-0.00017	0.00027	0.00322	0.00005	0.94288	0.00304
17	17/12/2017	0.000072	0.00044	0.00027	0.00451	0.00006	1.31994	0.00298
18	17/12/2017	0.000076	0.00110	0.00027	0.00421	0.00005	1.14911	0.00289
20	17/12/2017	0.000086	0.00105	0.00013	0.00285	0.00005	0.78530	0.00269
23	17/12/2017	0.000092	0.00060	0.00014	0.00571	0.00005	1.57608	0.00274
24	17/12/2017	0.000071	0.00017	0.00014	0.00638	0.00005	1.83035	0.00302
25	17/12/2017	0.000045	0.00018	0.00013	0.00595	0.00004	1.57232	0.00261
26	17/12/2017	0.000062	0.00139	0.00015	0.00109	0.00004	0.29054	0.00258
27	17/12/2017	0.000066	-0.00005	0.00014	0.01006	0.00009	2.69264	0.00311
28	17/12/2017	0.000066	0.00052	0.00014	0.00448	0.00006	1.21388	0.00268
29	18/12/2017	0.000056	0.00095	0.00010	0.00426	0.00003	1.23913	0.00151
30	18/12/2017	0.000052	0.00031	0.00009	0.00174	0.00003	0.42865	0.00115
31	18/12/2017	0.000064	0.00070	0.00009	0.00753	0.00003	2.02476	0.00104
33	18/12/2017	0.000076	0.00066	0.00008	0.00922	0.00008	2.51862	0.00479
34	18/12/2017	0.000062	0.00092	0.00007	0.00194	0.00002	0.52066	0.00073

NG analysis of glass particles from sample F2A (cc)

N°	4He	±	36Ar	±	40Ar	±
5	-1.95E-11	8.95E-12	3.38E-12	7.45E-13	9.17E-10	4.93E-12
6	-1.62E-11	8.95E-12	1.54E-12	7.45E-13	1.17E-10	5.33E-12
7	-1.84E-11	8.95E-12	7.54E-12	7.45E-13	1.90E-09	4.69E-12
8	-1.39E-11	8.95E-12	2.91E-12	7.45E-13	2.87E-10	5.11E-12
9	1.51E-11	2.18E-12	9.39E-12	3.60E-14	2.62E-09	7.75E-12
10	1.45E-11	2.18E-12	2.01E-12	3.60E-14	6.81E-10	3.87E-12
11	1.45E-11	2.18E-12	3.68E-12	3.60E-14	9.85E-10	3.66E-12
12	7.62E-12	2.18E-12	1.03E-11	6.01E-14	2.90E-09	5.05E-12
13	1.10E-11	2.18E-12	2.44E-12	3.60E-14	7.82E-10	3.50E-12
14	4.11E-12	2.78E-12	7.25E-12	8.41E-14	2.31E-09	2.89E-12
15	4.84E-12	2.90E-12	6.93E-12	6.01E-14	1.95E-09	1.90E-12
16	7.62E-12	2.78E-12	5.43E-12	4.80E-14	1.65E-09	1.79E-12
17	6.53E-12	2.90E-12	1.13E-11	3.60E-14	3.18E-09	3.47E-12
18	2.36E-11	3.15E-12	3.07E-12	7.21E-14	8.96E-10	3.06E-12
19	-2.06E-12	3.27E-12	3.87E-12	6.01E-14	1.19E-09	3.84E-12
20	7.35E-12	4.51E-12	4.30E-12	5.73E-14	1.35E-09	3.05E-12
21	1.84E-11	4.51E-12	4.02E-12	4.77E-14	1.18E-09	2.96E-12
22	1.75E-11	2.17E-12	2.72E-12	4.77E-14	8.04E-10	2.76E-12
23	1.00E-11	2.34E-12	5.45E-12	4.77E-14	1.61E-09	2.81E-12
24	2.84E-12	2.34E-12	6.09E-12	4.77E-14	1.87E-09	3.09E-12
25	3.01E-12	2.17E-12	5.68E-12	3.82E-14	1.61E-09	2.67E-12
26	2.32E-11	2.50E-12	1.04E-12	3.82E-14	2.98E-10	2.64E-12
27	-8.35E-13	2.34E-12	9.60E-12	8.59E-14	2.76E-09	3.19E-12
28	8.68E-12	2.34E-12	4.28E-12	5.73E-14	1.24E-09	2.74E-12
29	1.59E-11	1.67E-12	4.07E-12	2.86E-14	1.27E-09	1.55E-12
30	5.18E-12	1.50E-12	1.66E-12	2.86E-14	4.39E-10	1.18E-12
31	1.17E-11	1.50E-12	7.19E-12	2.86E-14	2.07E-09	1.07E-12
32	1.10E-11	1.34E-12	8.80E-12	7.64E-14	2.58E-09	4.91E-12
33	1.54E-11	1.17E-12	1.85E-12	1.91E-14	5.33E-10	7.48E-13

NG analysis of glass particles from sample F2A (cc/g)

N°	4He	±	% ±	36Ar	±	% ±	40Ar	±	% ±	40Ar*	±	% ±
5	-2.50E-07	1.15E-07	-46	4.33E-08	9.55E-09	22.1	1.18E-05	6.32E-08	0.54	-1.16E-06	-2.56E-07	22.1
6	-2.38E-07	1.32E-07	-55	2.26E-08	1.10E-08	48.4	1.72E-06	7.84E-08	4.56	-5.03E-06	-2.45E-06	48.7
7	-2.55E-07	1.24E-07	-49	1.05E-07	1.03E-08	9.9	2.64E-05	6.51E-08	0.25	-4.86E-06	-4.80E-07	9.9
8	-2.68E-07	1.72E-07	-64	5.59E-08	1.43E-08	25.6	5.52E-06	9.82E-08	1.78	-1.12E-05	-2.87E-06	25.7
9	3.44E-07	4.95E-08	14	2.13E-07	8.19E-10	0.4	5.95E-05	1.76E-07	0.30	-4.25E-06	-2.06E-08	0.5
10	2.90E-07	4.36E-08	15	4.01E-08	7.21E-10	1.8	1.36E-05	7.73E-08	0.57	1.65E-06	3.10E-08	1.9
11	2.69E-07	4.03E-08	15	6.81E-08	6.67E-10	1.0	1.82E-05	6.79E-08	0.37	-2.08E-06	-2.18E-08	1.0
12	1.44E-07	4.11E-08	29	1.94E-07	1.13E-09	0.6	5.46E-05	9.54E-08	0.17	-3.21E-06	-1.96E-08	0.6
13	3.06E-07	6.05E-08	20	6.77E-08	1.00E-09	1.5	2.17E-05	9.72E-08	0.45	1.51E-06	2.33E-08	1.5
14	5.02E-08	3.39E-08	68	8.85E-08	1.03E-09	1.2	2.81E-05	3.53E-08	0.13	1.72E-06	2.01E-08	1.2
15	4.44E-08	2.66E-08	60	6.36E-08	5.51E-10	0.9	1.79E-05	1.74E-08	0.10	-1.13E-06	-9.85E-09	0.9
16	1.95E-07	7.13E-08	37	1.39E-07	1.23E-09	0.9	4.24E-05	4.60E-08	0.11	8.06E-07	7.18E-09	0.9
17	1.52E-07	6.75E-08	44	2.63E-07	8.38E-10	0.3	7.40E-05	8.08E-08	0.11	-4.64E-06	-1.56E-08	0.3
18	2.74E-07	3.66E-08	13	3.58E-08	8.38E-10	2.3	1.04E-05	3.56E-08	0.34	-2.62E-07	-6.21E-09	2.4
19	-2.54E-08	4.03E-08	-159	4.77E-08	7.41E-10	1.6	1.47E-05	4.74E-08	0.32	4.53E-07	7.19E-09	1.6
20	1.02E-07	6.26E-08	61	5.98E-08	7.95E-10	1.3	1.88E-05	4.24E-08	0.23	9.26E-07	1.25E-08	1.3
21	2.42E-07	5.93E-08	25	5.29E-08	6.28E-10	1.2	1.55E-05	3.89E-08	0.25	-3.00E-07	-3.64E-09	1.2
22	2.04E-07	2.52E-08	12	3.16E-08	5.55E-10	1.8	9.35E-06	3.20E-08	0.34	-9.13E-08	-1.63E-09	1.8
23	1.09E-07	2.54E-08	23	5.92E-08	5.19E-10	0.9	1.75E-05	3.05E-08	0.17	-1.41E-07	-1.26E-09	0.9
24	4.00E-08	3.29E-08	82	8.58E-08	6.72E-10	0.8	2.64E-05	4.36E-08	0.16	7.96E-07	6.38E-09	0.8
25	6.68E-08	4.82E-08	72	1.26E-07	8.48E-10	0.7	3.58E-05	5.94E-08	0.17	-1.89E-06	-1.31E-08	0.7
26	3.74E-07	4.04E-08	11	1.68E-08	6.16E-10	3.7	4.80E-06	4.26E-08	0.89	-2.10E-07	-7.94E-09	3.8
27	-1.27E-08	3.54E-08	-280	1.45E-07	1.30E-09	0.9	4.18E-05	4.83E-08	0.12	-1.65E-06	-1.49E-08	0.9
28	1.32E-07	3.54E-08	27	6.48E-08	8.68E-10	1.3	1.88E-05	4.16E-08	0.22	-5.06E-07	-6.87E-09	1.4
29	2.83E-07	2.98E-08	11	7.26E-08	5.11E-10	0.7	2.27E-05	2.76E-08	0.12	9.85E-07	7.04E-09	0.7
30	9.95E-08	2.89E-08	29	3.19E-08	5.51E-10	1.7	8.44E-06	2.27E-08	0.27	-1.09E-06	-1.91E-08	1.7
31	1.83E-07	2.35E-08	13	1.12E-07	4.47E-10	0.4	3.24E-05	1.66E-08	0.05	-1.13E-06	-4.52E-09	0.4
32	1.45E-07	1.76E-08	12	1.16E-07	1.00E-09	0.9	3.39E-05	6.46E-08	0.19	-6.29E-07	-5.59E-09	0.9
33	2.48E-07	1.89E-08	8	2.99E-08	3.08E-10	1.0	8.60E-06	1.21E-08	0.14	-3.16E-07	-3.29E-09	1.0

NG analysis of glass particles from sample F2A

N°	40Ar/36Ar	±	% ±	4He/40Ar*	±	% ±
5	271.71	59.97	22.1	0.21	1.10E-01	51
6	76.02	36.98	48.7	0.05	3.49E-02	74
7	252.19	24.91	9.9	0.05	2.61E-02	50
8	98.73	25.35	25.7	0.02	1.66E-02	69
9	278.64	1.35	0.5	-0.08	-1.16E-02	14
10	339.62	6.40	1.9	0.18	2.67E-02	15
11	268.00	2.81	1.0	-0.13	-1.94E-02	15
12	281.98	1.72	0.6	-0.04	-1.28E-02	29
13	320.86	4.95	1.5	0.20	4.02E-02	20
14	318.04	3.71	1.2	0.03	1.97E-02	68
15	280.79	2.45	0.9	-0.04	-2.36E-02	60
16	304.35	2.71	0.9	0.24	8.86E-02	37
17	280.95	0.94	0.3	-0.03	-1.46E-02	44
18	291.23	6.90	2.4	-1.05	-1.42E-01	14
19	308.05	4.89	1.6	-0.06	-8.90E-02	159
20	314.05	4.24	1.3	0.11	6.76E-02	61
21	292.89	3.56	1.2	-0.81	-1.98E-01	25
22	295.67	5.29	1.8	-2.23	-2.79E-01	13
23	296.18	2.64	0.9	-0.77	-1.81E-01	23
24	307.85	2.47	0.8	0.05	4.13E-02	82
25	283.56	1.96	0.7	-0.04	-2.55E-02	72
26	286.02	10.80	3.8	-1.78	-2.03E-01	11
27	287.21	2.59	0.9	0.01	2.15E-02	280
28	290.75	3.95	1.4	-0.26	-7.01E-02	27
29	312.12	2.23	0.7	0.29	3.03E-02	11
30	264.35	4.61	1.7	-0.09	-2.65E-02	29
31	288.54	1.16	0.4	-0.16	-2.09E-02	13
32	293.12	2.60	0.9	-0.23	-2.80E-02	12
33	287.99	3.00	1.0	-0.78	-6.03E-02	8

NG analysis of glass particles from sample I1A

N°	date	weight (g)	4He (v)	±	36Ar (v)	±	40Ar (v)	±
3	08/10/2017	0.000102	0.00079	0.00018	0.00765	0.00004	2.16957	0.00298
4	08/10/2017	0.000055	-0.00057	0.00020	0.00197	0.00002	0.59072	0.00284
5	08/10/2017	0.000047	0.00045	0.00019	0.00106	0.00003	0.33683	0.00271
6	08/10/2017	0.000062	0.00068	0.00018	0.00185	0.00003	0.44251	0.00278
8	08/10/2017	0.000109	0.00084	0.00019	0.00400	0.00004	1.14065	0.00271
9	08/10/2017	0.000069	0.00130	0.00018	0.00352	0.00004	0.91930	0.00297
10	28/11/2017	0.000032	0.00009	0.00018	0.00104	0.00003	0.25827	0.00087
11	28/11/2017	0.000068	-0.00014	0.00017	0.00287	0.00004	0.82640	0.00078
12	28/11/2017	0.000031	0.00018	0.00017	0.00078	0.00003	0.18958	0.00079
13	28/11/2017	0.000037	0.00026	0.00017	0.00111	0.00004	0.33990	0.00073
14	28/11/2017	0.000022	0.00023	0.00018	0.00065	0.00002	0.13496	0.00071
15	28/11/2017	0.000056	0.00031	0.00017	0.00161	0.00002	0.42424	0.00112
16	28/11/2017	0.000030	0.00017	0.00018	0.00125	0.00003	0.36262	0.00101
17	28/11/2017	0.000035	0.00050	0.00017	0.00109	0.00005	0.32909	0.00109
18	28/11/2017	0.000041	0.00033	0.00018	0.00198	0.00003	0.49002	0.00113
19	28/11/2017	0.000047	0.00036	0.00017	0.00176	0.00004	0.53019	0.00085
20	28/11/2017	0.000075	-0.00019	0.00017	0.00474	0.00005	1.34705	0.00226
21	28/11/2017	0.000037	0.00045	0.00017	0.00083	0.00002	0.19266	0.00068
22	28/11/2017	0.000046	0.00048	0.00017	0.00159	0.00002	0.39558	0.00064
23	28/11/2017	0.000050	0.00082	0.00017	0.00107	0.00002	0.32971	0.00078
24	28/11/2017	0.000084	0.00021	0.00006	0.00506	0.00006	1.38866	0.00330
25	28/11/2017	0.000066	0.00026	0.00006	0.00382	0.00004	1.02767	0.00340
26	28/11/2017	0.000104	0.00044	0.00007	0.01269	0.00009	3.57502	0.00262
27	28/11/2017	0.000089	0.00013	0.00009	0.00549	0.00009	1.59865	0.00325
28	28/11/2017	0.000090	0.00013	0.00007	0.00328	0.00004	0.87138	0.00208
29	28/11/2017	0.000073	0.00114	0.00007	0.00288	0.00004	0.80953	0.00245
30	28/11/2017	0.000128	0.00061	0.00007	0.00643	0.00004	1.80417	0.00450
31	28/11/2017	0.000048	0.00093	0.00008	0.00170	0.00003	0.44038	0.00214
32	28/11/2017	0.000082	0.00003	0.00014	0.00161	0.00005	0.49036	0.00202
33	28/11/2017	0.000092	0.00041	0.00014	0.00722	0.00006	1.93710	0.00664
34	28/11/2017	0.000085	0.00062	0.00014	0.00340	0.00005	0.94583	0.00217
35	28/11/2017	0.000069	0.00092	0.00014	0.00304	0.00004	0.83250	0.00452

NG analysis of glass particles from sample I1A (cc)

N°	4He	±	36Ar	±	40Ar	±
3	1.13E-11	2.57E-12	1.02E-11	5.32E-14	3.06E-09	4.20E-12
4	-8.15E-12	2.86E-12	2.62E-12	2.66E-14	8.33E-10	4.01E-12
5	6.44E-12	2.72E-12	1.41E-12	3.99E-14	4.75E-10	3.82E-12
6	9.73E-12	2.57E-12	2.46E-12	3.99E-14	6.24E-10	3.92E-12
7	1.20E-11	2.72E-12	5.32E-12	5.32E-14	1.61E-09	3.82E-12
8	2.38E-11	3.29E-12	3.62E-12	4.11E-14	9.97E-10	3.22E-12
9	1.64E-12	3.29E-12	1.07E-12	3.08E-14	2.80E-10	9.43E-13
10	-2.56E-12	3.11E-12	2.95E-12	4.11E-14	8.96E-10	8.46E-13
11	3.29E-12	3.11E-12	8.02E-13	3.08E-14	2.06E-10	8.56E-13
12	4.75E-12	3.11E-12	1.14E-12	4.11E-14	3.68E-10	7.91E-13
13	4.20E-12	3.29E-12	6.68E-13	2.06E-14	1.46E-10	7.70E-13
14	5.66E-12	3.11E-12	1.66E-12	2.06E-14	4.60E-10	1.21E-12
15	3.11E-12	3.29E-12	1.29E-12	3.08E-14	3.93E-10	1.09E-12
16	9.13E-12	3.11E-12	1.12E-12	5.14E-14	3.57E-10	1.18E-12
17	6.03E-12	3.29E-12	2.04E-12	3.08E-14	5.31E-10	1.23E-12
18	6.58E-12	3.11E-12	1.81E-12	4.11E-14	5.75E-10	9.21E-13
19	-3.47E-12	3.11E-12	4.87E-12	5.14E-14	1.46E-09	2.45E-12
20	8.22E-12	3.11E-12	8.53E-13	2.06E-14	2.09E-10	7.37E-13
21	8.77E-12	3.11E-12	1.63E-12	2.06E-14	4.29E-10	6.94E-13
22	1.50E-11	3.11E-12	1.10E-12	2.06E-14	3.57E-10	8.46E-13
23	3.84E-12	1.10E-12	5.20E-12	6.17E-14	1.51E-09	3.58E-12
24	4.75E-12	1.10E-12	3.93E-12	4.11E-14	1.11E-09	3.69E-12
25	8.04E-12	1.28E-12	1.30E-11	9.25E-14	3.88E-09	2.84E-12
26	2.38E-12	1.64E-12	5.64E-12	9.25E-14	1.73E-09	3.52E-12
27	2.38E-12	1.28E-12	3.37E-12	4.11E-14	9.45E-10	2.25E-12
28	2.08E-11	1.28E-12	2.96E-12	4.11E-14	8.78E-10	2.66E-12
29	1.11E-11	1.28E-12	6.61E-12	4.11E-14	1.96E-09	4.88E-12
30	1.70E-11	1.46E-12	1.75E-12	3.08E-14	4.77E-10	2.32E-12
31	5.48E-13	2.56E-12	1.66E-12	5.14E-14	5.32E-10	2.19E-12
32	7.49E-12	2.56E-12	7.42E-12	6.17E-14	2.10E-09	7.20E-12
33	1.13E-11	2.56E-12	3.50E-12	5.14E-14	1.03E-09	2.35E-12
34	1.68E-11	2.56E-12	3.13E-12	4.11E-14	9.02E-10	4.90E-12

NG analysis of glass particles from sample I1A (cc/g)

N°	4He	±	% ±	36Ar	±	% ±	40Ar	±	% ±	40Ar*	±	% ±
3	1.11E-07	2.52E-08	23	9.97E-08	5.21E-10	0.5	3.00E-05	4.12E-08	0.14	2.41E-07	1.30E-09	0.5
4	-1.48E-07	5.20E-08	-35	4.76E-08	4.83E-10	1.0	1.51E-05	7.28E-08	0.48	9.36E-07	1.05E-08	1.1
5	1.37E-07	5.78E-08	42	3.00E-08	8.48E-10	2.8	1.01E-05	8.13E-08	0.80	1.16E-06	3.41E-08	2.9
6	1.57E-07	4.15E-08	26	3.97E-08	6.43E-10	1.6	1.01E-05	6.32E-08	0.63	-1.77E-06	-3.08E-08	1.7
7	1.10E-07	2.49E-08	23	4.88E-08	4.88E-10	1.0	1.48E-05	3.51E-08	0.24	1.98E-07	2.04E-09	1.0
8	3.44E-07	4.77E-08	14	5.24E-08	5.96E-10	1.1	1.44E-05	4.67E-08	0.32	-1.22E-06	-1.44E-08	1.2
9	5.14E-08	1.03E-07	200	3.34E-08	9.64E-10	2.9	8.75E-06	2.95E-08	0.34	-1.23E-06	-3.56E-08	2.9
10	-3.76E-08	4.57E-08	-121	4.34E-08	6.05E-10	1.4	1.32E-05	1.24E-08	0.09	2.20E-07	3.07E-09	1.4
11	1.06E-07	1.00E-07	94	2.59E-08	9.95E-10	3.8	6.63E-06	2.76E-08	0.42	-1.09E-06	-4.23E-08	3.9
12	1.28E-07	8.39E-08	65	3.08E-08	1.11E-09	3.6	9.96E-06	2.14E-08	0.21	7.51E-07	2.71E-08	3.6
13	1.91E-07	1.49E-07	78	3.04E-08	9.35E-10	3.1	6.65E-06	3.50E-08	0.53	-2.42E-06	-7.55E-08	3.1
14	1.01E-07	5.55E-08	55	2.96E-08	3.67E-10	1.2	8.21E-06	2.17E-08	0.26	-6.12E-07	-7.77E-09	1.3
15	1.04E-07	1.10E-07	106	4.28E-08	1.03E-09	2.4	1.31E-05	3.65E-08	0.28	3.14E-07	7.59E-09	2.4
16	2.61E-07	8.87E-08	34	3.20E-08	1.47E-09	4.6	1.02E-05	3.38E-08	0.33	6.34E-07	2.92E-08	4.6
17	1.47E-07	8.02E-08	55	4.96E-08	7.52E-10	1.5	1.30E-05	2.99E-08	0.23	-1.87E-06	-2.86E-08	1.5
18	1.40E-07	6.61E-08	47	3.85E-08	8.75E-10	2.3	1.22E-05	1.96E-08	0.16	7.35E-07	1.67E-08	2.3
19	-4.63E-08	4.14E-08	-89	6.50E-08	6.85E-10	1.1	1.95E-05	3.27E-08	0.17	7.19E-08	7.68E-10	1.1
20	2.22E-07	8.39E-08	38	2.31E-08	5.56E-10	2.4	5.64E-06	1.99E-08	0.35	-1.24E-06	-3.02E-08	2.4
21	1.91E-07	6.75E-08	35	3.55E-08	4.47E-10	1.3	9.32E-06	1.51E-08	0.16	-1.29E-06	-1.63E-08	1.3
22	3.00E-07	6.21E-08	21	2.20E-08	4.11E-10	1.9	7.15E-06	1.69E-08	0.24	5.80E-07	1.09E-08	1.9
23	4.57E-08	1.30E-08	29	6.19E-08	7.34E-10	1.2	1.79E-05	4.26E-08	0.24	-5.68E-07	-6.87E-09	1.2
24	7.20E-08	1.66E-08	23	5.95E-08	6.23E-10	1.0	1.69E-05	5.58E-08	0.33	-8.86E-07	-9.73E-09	1.1
25	7.73E-08	1.23E-08	16	1.25E-07	8.90E-10	0.7	3.73E-05	2.73E-08	0.07	-1.88E-07	-1.34E-09	0.7
26	2.67E-08	1.85E-08	69	6.34E-08	1.04E-09	1.6	1.95E-05	3.96E-08	0.20	5.39E-07	8.90E-09	1.7
27	2.64E-08	1.42E-08	54	3.75E-08	4.57E-10	1.2	1.05E-05	2.51E-08	0.24	-6.90E-07	-8.58E-09	1.2
28	2.85E-07	1.75E-08	6	4.06E-08	5.63E-10	1.4	1.20E-05	3.64E-08	0.30	-8.77E-08	-1.25E-09	1.4
29	8.71E-08	9.99E-09	11	5.16E-08	3.21E-10	0.6	1.53E-05	3.81E-08	0.25	-1.39E-07	-9.31E-10	0.7
30	3.54E-07	3.04E-08	9	3.64E-08	6.43E-10	1.8	9.95E-06	4.83E-08	0.49	-9.25E-07	-1.69E-08	1.8
31	6.68E-09	3.12E-08	467	2.02E-08	6.27E-10	3.1	6.48E-06	2.67E-08	0.41	4.56E-07	1.43E-08	3.1
32	8.14E-08	2.78E-08	34	8.07E-08	6.70E-10	0.8	2.28E-05	7.82E-08	0.34	-1.26E-06	-1.14E-08	0.9
33	1.33E-07	3.01E-08	23	4.11E-08	6.05E-10	1.5	1.21E-05	2.77E-08	0.23	-2.15E-07	-3.20E-09	1.5
34	2.44E-07	3.71E-08	15	4.53E-08	5.96E-10	1.3	1.31E-05	7.10E-08	0.54	-4.44E-07	-6.32E-09	1.4

NG analysis of glass particles from sample I1A

N°	40Ar/36Ar	±	% ±	4He/40Ar*	±	% ±
3	300.98	1.63	0.5	0.46	1.05E-01	23
4	318.22	3.57	1.1	-0.16	-5.56E-02	35
5	337.23	9.92	2.9	0.12	5.00E-02	42
6	253.85	4.41	1.7	-0.09	-2.35E-02	27
7	302.63	3.11	1.0	0.56	1.26E-01	23
8	275.39	3.25	1.2	-0.28	-3.94E-02	14
9	261.86	7.61	2.9	-0.04	-8.38E-02	200
10	303.63	4.24	1.4	-0.17	-2.08E-01	121
11	256.29	9.92	3.9	-0.10	-9.17E-02	95
12	322.90	11.66	3.6	0.17	1.12E-01	65
13	218.94	6.83	3.1	-0.08	-6.19E-02	78
14	277.86	3.53	1.3	-0.17	-9.07E-02	55
15	305.90	7.39	2.4	0.33	3.49E-01	106
16	318.36	14.64	4.6	0.41	1.41E-01	34
17	260.97	4.00	1.5	-0.08	-4.30E-02	55
18	317.65	7.24	2.3	0.19	9.00E-02	47
19	299.67	3.20	1.1	-0.64	-5.76E-01	89
20	244.76	5.96	2.4	-0.18	-6.78E-02	38
21	262.34	3.33	1.3	-0.15	-5.25E-02	35
22	324.92	6.12	1.9	0.52	1.08E-01	21
23	289.39	3.50	1.2	-0.08	-2.30E-02	29
24	283.68	3.12	1.1	-0.08	-1.88E-02	23
25	297.06	2.12	0.7	-0.41	-6.56E-02	16
26	307.05	5.07	1.7	0.05	3.43E-02	69
27	280.14	3.48	1.2	-0.04	-2.06E-02	54
28	296.40	4.21	1.4	-3.25	-2.05E-01	6
29	295.87	1.98	0.7	-0.63	-7.20E-02	11
30	273.16	5.00	1.8	-0.38	-3.37E-02	9
31	321.16	10.06	3.1	0.01	6.84E-02	467
32	282.91	2.54	0.9	-0.06	-2.20E-02	34
33	293.34	4.37	1.5	-0.62	-1.40E-01	23
34	288.77	4.11	1.4	-0.55	-8.39E-02	15

NG analysis of glass particles from sample I3A

N°	date	weight (g)	4He (v)	±	36Ar (v)	±	40Ar (v)	±
1	09/10/2017	0.000171	0.00127	0.00016	0.03276	0.00014	9.07135	0.00529
2	09/10/2017	0.000048	0.00064	0.00017	0.00208	0.00004	0.56467	0.00077
3	09/10/2017	0.000047	0.00094	0.00013	0.01130	0.00011	3.31710	0.00553
4	09/10/2017	0.000055	0.00092	0.00015	0.00410	0.00003	1.18275	0.00084
6	09/10/2017	0.000053	0.00028	0.00016	0.00224	0.00003	0.69703	0.00144
7	09/10/2017	0.000124	0.00069	0.00016	0.01621	0.00008	4.49221	0.00382
8	09/10/2017	0.000053	0.00066	0.00015	0.00358	0.00006	0.99635	0.00106
9	09/10/2017	0.000060	0.00060	0.00016	0.00437	0.00004	1.19579	0.00100
10	28/11/2017	0.000039	0.00028	0.00017	0.01421	0.00013	4.12432	0.00933
11	28/11/2017	0.000046	0.00048	0.00019	0.01002	0.00009	2.70910	0.00336
12	28/11/2017	0.000058	0.00059	0.00018	0.00468	0.00004	1.36485	0.00197
13	28/11/2017	0.000038	0.00051	0.00017	0.00346	0.00004	0.96469	0.00179
14	28/11/2017	0.000049	0.00001	0.00017	0.00785	0.00007	2.14795	0.00223
15	28/11/2017	0.000032	0.00028	0.00017	0.00291	0.00005	0.79054	0.00098
16	28/11/2017	0.000045	0.00043	0.00018	0.00780	0.00006	2.09618	0.00268
17	29/11/2017	0.000047	0.00010	0.00013	0.00304	0.00003	0.89611	0.00229
18	29/11/2017	0.000059	-0.00012	0.00013	0.01088	0.00009	3.17345	0.00201
19	29/11/2017	0.000032	0.00032	0.00014	0.00494	0.00005	1.28878	0.00061
20	29/11/2017	0.000038	0.00028	0.00014	0.00318	0.00004	0.96236	0.00106
21	29/11/2017	0.000038	0.00034	0.00014	0.00556	0.00010	1.43153	0.00160
22	29/11/2017	0.000034	0.00035	0.00014	0.00209	0.00003	0.60991	0.00064
23	29/11/2017	0.000027	0.00017	0.00014	0.00308	0.00003	0.76030	0.00254
25	18/12/2017	0.000064	0.00014	0.00010	0.00981	0.00014	2.83588	0.00491
26	18/12/2017	0.000044	0.00076	0.00011	0.00423	0.00005	1.29779	0.00164
28	18/12/2017	0.000072	0.00036	0.00010	0.01210	0.00016	3.48430	0.00591
29	18/12/2017	0.000089	0.00087	0.00010	0.01387	0.00007	3.84918	0.00337
30	18/12/2017	0.000083	0.00037	0.00010	0.01553	0.00005	4.40892	0.00320

NG analysis of glass particles from sample I3A (cc)

N°	4He	±	36Ar	±	40Ar	±
4	1.82E-11	2.29E-12	4.35E-11	1.86E-13	1.28E-08	7.46E-12
5	9.15E-12	2.43E-12	2.76E-12	5.32E-14	7.96E-10	1.09E-12
6	1.34E-11	1.86E-12	1.50E-11	1.46E-13	4.68E-09	7.80E-12
7	1.32E-11	2.15E-12	5.45E-12	3.99E-14	1.67E-09	1.18E-12
8	4.01E-12	2.29E-12	2.98E-12	3.99E-14	9.83E-10	2.03E-12
9	9.87E-12	2.29E-12	2.15E-11	1.06E-13	6.34E-09	5.39E-12
10	9.44E-12	2.15E-12	4.76E-12	7.97E-14	1.41E-09	1.49E-12
11	8.58E-12	2.29E-12	5.81E-12	5.32E-14	1.69E-09	1.41E-12
12	5.12E-12	3.11E-12	1.46E-11	1.34E-13	4.47E-09	1.01E-11
13	8.77E-12	3.47E-12	1.03E-11	9.25E-14	2.94E-09	3.64E-12
14	1.08E-11	3.29E-12	4.81E-12	4.11E-14	1.48E-09	2.14E-12
15	9.32E-12	3.11E-12	3.56E-12	4.11E-14	1.05E-09	1.94E-12
16	1.83E-13	3.11E-12	8.07E-12	7.20E-14	2.33E-09	2.42E-12
17	5.12E-12	3.11E-12	2.99E-12	5.14E-14	8.57E-10	1.06E-12
18	7.86E-12	3.29E-12	8.02E-12	6.17E-14	2.27E-09	2.91E-12
19	1.83E-12	2.38E-12	3.13E-12	3.08E-14	9.71E-10	2.48E-12
20	-2.19E-12	2.38E-12	1.12E-11	9.25E-14	3.44E-09	2.18E-12
21	5.85E-12	2.56E-12	5.08E-12	5.14E-14	1.40E-09	6.61E-13
22	5.12E-12	2.56E-12	3.27E-12	4.11E-14	1.04E-09	1.15E-12
23	6.21E-12	2.56E-12	5.72E-12	1.03E-13	1.55E-09	1.73E-12
24	6.39E-12	2.56E-12	2.15E-12	3.08E-14	6.61E-10	6.94E-13
25	3.11E-12	2.56E-12	3.17E-12	3.08E-14	8.24E-10	2.75E-12
26	2.34E-12	1.67E-12	9.36E-12	1.34E-13	2.90E-09	5.03E-12
27	1.27E-11	1.84E-12	4.04E-12	4.77E-14	1.33E-09	1.68E-12
28	6.01E-12	1.67E-12	1.15E-11	1.53E-13	3.57E-09	6.05E-12
29	1.45E-11	1.67E-12	1.32E-11	6.68E-14	3.94E-09	3.45E-12
30	6.18E-12	1.67E-12	1.48E-11	4.77E-14	4.52E-09	3.28E-12

NG analysis of glass particles from sample I3A (cc/g)

N°	4He	±	% ±	36Ar	±	% ±	40Ar	±	% ±	40Ar*	±	% ±
4	1.06E-07	1.34E-08	13	2.55E-07	1.09E-09	0.4	7.48E-05	4.36E-08	0.06	-1.20E-06	-5.16E-09	0.4
5	1.91E-07	5.07E-08	27	5.76E-08	1.11E-09	1.9	1.66E-05	2.26E-08	0.14	-6.02E-07	-1.16E-08	1.9
6	2.86E-07	3.96E-08	14	3.20E-07	3.11E-09	1.0	9.95E-05	1.66E-07	0.17	4.14E-06	4.09E-08	1.0
7	2.39E-07	3.90E-08	16	9.91E-08	7.25E-10	0.7	3.03E-05	2.15E-08	0.07	7.51E-07	5.52E-09	0.7
8	7.56E-08	4.32E-08	57	5.62E-08	7.52E-10	1.3	1.85E-05	3.83E-08	0.21	1.78E-06	2.41E-08	1.4
9	7.96E-08	1.85E-08	23	1.74E-07	8.57E-10	0.5	5.11E-05	4.34E-08	0.09	-7.75E-07	-3.88E-09	0.5
10	1.78E-07	4.05E-08	23	8.98E-08	1.50E-09	1.7	2.65E-05	2.82E-08	0.11	-2.88E-07	-4.83E-09	1.7
11	1.43E-07	3.81E-08	27	9.68E-08	8.86E-10	0.9	2.81E-05	2.35E-08	0.08	-7.90E-07	-7.26E-09	0.9
12	1.31E-07	7.96E-08	61	3.75E-07	3.43E-09	0.9	1.15E-04	2.59E-07	0.23	2.81E-06	2.64E-08	0.9
13	1.91E-07	7.55E-08	40	2.24E-07	2.01E-09	0.9	6.38E-05	7.92E-08	0.12	-3.02E-06	-2.73E-08	0.9
14	1.86E-07	5.67E-08	31	8.30E-08	7.09E-10	0.9	2.55E-05	3.68E-08	0.14	7.43E-07	6.44E-09	0.9
15	2.45E-07	8.17E-08	33	9.36E-08	1.08E-09	1.2	2.75E-05	5.11E-08	0.19	-4.27E-07	-5.00E-09	1.2
16	3.73E-09	6.34E-08	1700	1.65E-07	1.47E-09	0.9	4.75E-05	4.93E-08	0.10	-1.65E-06	-1.48E-08	0.9
17	1.60E-07	9.71E-08	61	9.35E-08	1.61E-09	1.7	2.68E-05	3.32E-08	0.12	-1.13E-06	-1.95E-08	1.7
18	1.75E-07	7.31E-08	42	1.78E-07	1.37E-09	0.8	5.05E-05	6.46E-08	0.13	-2.71E-06	-2.11E-08	0.8
19	3.89E-08	5.05E-08	130	6.65E-08	6.56E-10	1.0	2.07E-05	5.28E-08	0.26	8.16E-07	8.32E-09	1.0
20	-3.72E-08	4.03E-08	-108	1.90E-07	1.57E-09	0.8	5.83E-05	3.69E-08	0.06	1.71E-06	1.42E-08	0.8
21	1.83E-07	7.99E-08	44	1.59E-07	1.61E-09	1.0	4.37E-05	2.07E-08	0.05	-3.72E-06	-3.77E-08	1.0
22	1.35E-07	6.73E-08	50	8.60E-08	1.08E-09	1.3	2.75E-05	3.02E-08	0.11	1.77E-06	2.23E-08	1.3
23	1.63E-07	6.73E-08	41	1.50E-07	2.71E-09	1.8	4.08E-05	4.56E-08	0.11	-4.07E-06	-7.34E-08	1.8
24	1.88E-07	7.52E-08	40	6.32E-08	9.07E-10	1.4	1.94E-05	2.04E-08	0.10	5.79E-07	8.33E-09	1.4
25	1.15E-07	9.47E-08	82	1.17E-07	1.14E-09	1.0	3.05E-05	1.02E-07	0.33	-4.49E-06	-4.62E-08	1.0
26	3.65E-08	2.61E-08	71	1.46E-07	2.09E-09	1.4	4.54E-05	7.86E-08	0.17	1.70E-06	2.45E-08	1.4
27	2.88E-07	4.17E-08	14	9.18E-08	1.08E-09	1.2	3.02E-05	3.82E-08	0.13	2.81E-06	3.34E-08	1.2
28	8.35E-08	2.32E-08	28	1.60E-07	2.12E-09	1.3	4.96E-05	8.41E-08	0.17	1.67E-06	2.23E-08	1.3
29	1.63E-07	1.88E-08	11	1.49E-07	7.51E-10	0.5	4.43E-05	3.88E-08	0.09	-1.14E-07	-5.85E-10	0.5
30	7.44E-08	2.01E-08	27	1.79E-07	5.75E-10	0.3	5.44E-05	3.95E-08	0.07	1.09E-06	3.58E-09	0.3

NG analysis of glass particles from sample I3A

N°	40Ar/36Ar	±	% ±	4He/40Ar*	±	% ±
4	293.86	1.27	0.4	-0.09	-1.12E-02	13
5	288.10	5.55	1.9	-0.32	-8.44E-02	27
6	311.53	3.08	1.0	0.07	9.57E-03	14
7	306.15	2.25	0.7	0.32	5.20E-02	16
8	330.23	4.48	1.4	0.04	2.43E-02	57
9	294.10	1.47	0.5	-0.10	-2.38E-02	23
10	295.36	4.96	1.7	-0.62	-1.41E-01	23
11	290.40	2.67	0.9	-0.18	-4.83E-02	27
12	306.05	2.88	0.9	0.05	2.84E-02	61
13	285.10	2.59	0.9	-0.06	-2.50E-02	40
14	307.52	2.67	0.9	0.25	7.63E-02	31
15	294.00	3.44	1.2	-0.57	-1.92E-01	33
16	288.53	2.59	0.9	0.00	-3.84E-02	1700
17	286.46	4.93	1.7	-0.14	-8.58E-02	61
18	283.38	2.21	0.8	-0.06	-2.70E-02	42
19	310.83	3.17	1.0	0.05	6.19E-02	130
20	307.56	2.55	0.8	-0.02	-2.36E-02	108
21	275.10	2.79	1.0	-0.05	-2.15E-02	44
22	319.11	4.03	1.3	0.08	3.81E-02	50
23	271.49	4.89	1.8	-0.04	-1.65E-02	41
24	307.72	4.43	1.4	0.32	1.30E-01	40
25	260.30	2.68	1.0	-0.03	-2.11E-02	82
26	310.20	4.46	1.4	0.02	1.53E-02	71
27	329.22	3.91	1.2	0.10	1.49E-02	15
28	308.99	4.12	1.3	0.05	1.39E-02	28
29	297.79	1.53	0.5	-1.43	-1.64E-01	12
30	304.64	1.01	0.3	0.07	1.85E-02	27

Daily blank mean values (V) used to correct NG data from glass particles

Data	4He	±	36Ar	±	40Ar	±
September						
27/09/2017	0.00549	0.00006	0.00010	0.00001	0.01958	0.00015
28/09/2017	0.00463	0.00006	0.00086	0.00001	0.01390	0.00018
29/09/2017	0.00570	0.00005	0.00020	0.00001	0.00783	0.00008
Mean	0.00528	0.00006	0.00038	0.00001	0.01377	0.00014
St. dev.	0.00046	0.00000	0.00034	0.00000	0.00480	0.00004
October						
08/10/2017	0.00211	0.00004	0.00005	0.00001	0.01026	0.00009
09/10/2017	0.00279	0.00006	0.00005	0.00001	0.00830	0.00006
10/10/2017	0.00234	0.00004	0.00003	0.00000	0.00630	0.00006
Mean	0.00242	0.00005	0.00004	0.00000	0.00829	0.00007
St. dev.	0.00028	0.00001	0.00001	0.00000	0.00162	0.00001
November						
22/11/2017	0.00173	0.00005	0.00009	0.00001	0.01641	0.00014
23/11/2017	0.00258	0.00005	0.00010	0.00001	0.01869	0.00014
24/11/2017	0.00244	0.00004	0.00005	0.00001	0.00963	0.00009
27/11/2017	0.00217	0.00004	0.00011	0.00001	0.03342	0.00025
28/11/2017	0.00181	0.00004	0.00003	0.00001	0.00937	0.00009
29/11/2017	0.00156	0.00004	0.00005	0.00001	0.00756	0.00009
Mean	0.00205	0.00004	0.00007	0.00001	0.01584	0.00013
St. dev.	0.00038	0.00001	0.00003	0.00000	0.00882	0.00006
December						
15/12/2017	0.00225	0.00004	0.00013	0.00001	0.03752	0.00023
16/12/2017	0.00193	0.00005	0.00011	0.00001	0.02421	0.00015
17/12/2017	0.00196	0.00005	0.00009	0.00001	0.01894	0.00013
18/12/2017	0.00198	0.00004	0.00009	0.00001	0.01293	0.00008
19/12/2017	0.00190	0.00005	0.00005	0.00001	0.01460	0.00010
Mean	0.00200	0.00005	0.00009	0.00001	0.02164	0.00014
St. dev.	0.00012	0.00000	0.00003	0.00000	0.00885	0.00005

Calibration data used for NG analysis on Glass particles (mean values from 6 measurements)

4He cc/V	36Ar cc/V	40Ar cc/V	Date
1.21E-08	1.20E-09	1.26E-09	September 2017
1.43E-08	1.33E-09	1.41E-09	October 2017
1.83E-08	1.03E-09	1.08E-09	November 2017
1.67E-08	9.54E-10	1.02E-09	December 2017

NG analysis of sanidines from sample F1A

N°	date	weight (g)	4He (v)	±	36Ar (v)	±	40Ar (v)	±
4	27/09/2017	0.000120	0.00033	0.00012	0.00011	0.00005	0.03441	0.00945
5	27/09/2017	0.000130	0.00002	0.00012	0.00030	0.00005	0.09439	0.00947
6	27/09/2017	0.000130	-0.00007	0.00012	0.00017	0.00005	0.05212	0.00945
7	27/09/2017	0.000220	-0.00012	0.00010	0.00028	0.00005	0.06884	0.00945
10	27/09/2017	0.000170	0.00040	0.00013	0.00011	0.00005	0.03073	0.00945
11	24/11/2017	0.000344	0.00191	0.00057	0.00009	0.00003	0.11375	0.00137
12	24/11/2017	0.000086	0.00192	0.00057	0.00018	0.00003	0.03523	0.00131
13	24/11/2017	0.000150	0.00259	0.00057	0.00020	0.00003	0.04314	0.00131
14	24/11/2017	0.000199	0.00198	0.00056	0.00007	0.00003	0.02800	0.00131
15	24/11/2017	0.000128	0.00108	0.00056	0.00004	0.00003	0.02114	0.00131
16	24/11/2017	0.000098	0.00244	0.00057	0.00008	0.00003	0.02911	0.00133
17	24/11/2017	0.000123	0.00130	0.00057	0.00003	0.00003	0.04324	0.00131
18	24/11/2017	0.000090	0.00231	0.00057	0.00013	0.00003	0.01604	0.00133
19	24/11/2017	0.000084	0.00171	0.00057	0.00000	0.00003	0.01186	0.00132
20	24/11/2017	0.000108	0.00206	0.00057	0.00006	0.00003	0.02510	0.00131
21	24/11/2017	0.000025	0.00185	0.00057	0.00009	0.00003	0.01629	0.00135
22	24/11/2017	0.000129	0.00276	0.00057	0.00007	0.00003	0.03420	0.00132
23	24/11/2017	0.000117	0.00258	0.00057	0.00008	0.00003	0.03994	0.00131
24	24/11/2017	0.000087	0.00270	0.00057	0.00016	0.00003	0.04388	0.00131
25	24/11/2017	0.000128	0.00083	0.00057	0.00010	0.00003	0.02628	0.00133
26	24/11/2017	0.000045	0.00111	0.00057	-0.00001	0.00003	0.01240	0.00131
27	24/11/2017	0.000111	0.00162	0.00057	0.00006	0.00003	0.03001	0.00132
28	24/11/2017	0.000056	0.00058	0.00056	0.00020	0.00003	0.03655	0.00131
29	24/11/2017	0.000073	0.00209	0.00056	-0.00001	0.00003	0.02231	0.00130
30	24/11/2017	0.000047	0.00148	0.00056	0.00007	0.00003	0.01583	0.00131
32	24/11/2017	0.000082	0.00060	0.00057	0.00003	0.00003	0.02763	0.00131
33	24/11/2017	0.000068	0.00153	0.00057	0.00000	0.00003	0.01671	0.00132
34	24/11/2017	0.000053	0.00264	0.00057	0.00009	0.00003	0.03397	0.00131

NG analysis of sanidines from sample F1A (cc)

N°	4He	±	36Ar	±	40Ar	±
4	3.99E-12	1.45E-12	1.32E-13	6.01E-14	4.35E-11	1.19E-11
5	2.42E-13	1.45E-12	3.60E-13	6.01E-14	1.19E-10	1.20E-11
6	-8.47E-13	1.45E-12	2.04E-13	6.01E-14	6.59E-11	1.19E-11
7	-1.45E-12	1.21E-12	3.36E-13	6.01E-14	8.70E-11	1.19E-11
10	4.84E-12	1.57E-12	1.32E-13	6.01E-14	3.88E-11	1.19E-11
11	3.49E-11	1.04E-11	9.25E-14	3.08E-14	1.23E-10	1.49E-12
12	3.51E-11	1.04E-11	1.85E-13	3.08E-14	3.82E-11	1.42E-12
13	4.73E-11	1.04E-11	2.06E-13	3.08E-14	4.68E-11	1.42E-12
14	3.62E-11	1.02E-11	7.20E-14	3.08E-14	3.04E-11	1.42E-12
15	1.97E-11	1.02E-11	4.11E-14	3.08E-14	2.29E-11	1.42E-12
16	4.46E-11	1.04E-11	8.22E-14	3.08E-14	3.16E-11	1.44E-12
17	2.38E-11	1.04E-11	3.08E-14	3.08E-14	4.69E-11	1.42E-12
18	4.22E-11	1.04E-11	1.34E-13	3.08E-14	1.74E-11	1.44E-12
19	3.12E-11	1.04E-11	0.00E+00	3.08E-14	1.29E-11	1.43E-12
20	3.76E-11	1.04E-11	6.17E-14	3.08E-14	2.72E-11	1.42E-12
21	3.38E-11	1.04E-11	9.25E-14	3.08E-14	1.77E-11	1.46E-12
22	5.04E-11	1.04E-11	7.20E-14	3.08E-14	3.71E-11	1.43E-12
23	4.71E-11	1.04E-11	8.22E-14	3.08E-14	4.33E-11	1.42E-12
24	4.93E-11	1.04E-11	1.64E-13	3.08E-14	4.76E-11	1.42E-12
25	1.52E-11	1.04E-11	1.03E-13	3.08E-14	2.85E-11	1.44E-12
26	2.03E-11	1.04E-11	-1.03E-14	3.08E-14	1.34E-11	1.42E-12
27	2.96E-11	1.04E-11	6.17E-14	3.08E-14	3.25E-11	1.43E-12
28	1.06E-11	1.02E-11	2.06E-13	3.08E-14	3.96E-11	1.42E-12
29	3.82E-11	1.02E-11	-1.03E-14	3.08E-14	2.42E-11	1.41E-12
30	2.70E-11	1.02E-11	7.20E-14	3.08E-14	1.72E-11	1.42E-12
32	1.10E-11	1.04E-11	3.08E-14	3.08E-14	3.00E-11	1.42E-12
33	2.80E-11	1.04E-11	0.00E+00	3.08E-14	1.81E-11	1.43E-12
34	4.82E-11	1.04E-11	9.25E-14	3.08E-14	3.68E-11	1.42E-12

NG analysis of sanidines from sample F1A (cc/g)

N°	4He	±	% ±	36Ar	±	% ±	40Ar	±	% ±	40Ar*	±	% ±
6	3.33E-08	1.21E-08	36	1.10E-09	5.00E-10	45	3.62E-07	9.95E-08	27	3.36E-08	1.79E-08	53
7	1.86E-09	1.12E-08	600	2.77E-09	4.62E-10	17	9.17E-07	9.21E-08	10	8.99E-08	1.75E-08	19
8	-6.51E-09	1.12E-08	-171	1.57E-09	4.62E-10	29	5.07E-07	9.19E-08	18	3.77E-08	1.30E-08	35
9	-6.60E-09	5.50E-09	-83	1.53E-09	2.73E-10	18	3.95E-07	5.43E-08	14	-6.10E-08	-1.37E-08	23
10	2.85E-08	9.25E-09	33	7.77E-10	3.53E-10	45	2.28E-07	7.02E-08	31	-3.62E-09	-1.99E-09	55
11	1.01E-07	3.03E-08	30	2.69E-10	8.97E-11	33	3.58E-07	4.32E-09	1	2.78E-07	9.28E-08	33
12	4.08E-07	1.21E-07	30	2.15E-09	3.59E-10	17	4.44E-07	1.65E-08	4	-1.98E-07	-3.39E-08	17
13	3.15E-07	6.94E-08	22	1.37E-09	2.06E-10	15	3.12E-07	9.47E-09	3	-9.75E-08	-1.49E-08	15
14	1.82E-07	5.14E-08	28	3.62E-10	1.55E-10	43	1.53E-07	7.14E-09	5	4.46E-08	1.92E-08	43
15	1.54E-07	7.99E-08	52	3.21E-10	2.41E-10	75	1.79E-07	1.11E-08	6	8.31E-08	6.26E-08	75
16	4.55E-07	1.06E-07	23	8.39E-10	3.15E-10	38	3.22E-07	1.47E-08	5	7.14E-08	2.70E-08	38
17	1.93E-07	8.47E-08	44	2.51E-10	2.51E-10	100	3.81E-07	1.15E-08	3	3.06E-07	3.06E-07	100
18	4.69E-07	1.16E-07	25	1.49E-09	3.43E-10	23	1.93E-07	1.60E-08	8	-2.50E-07	-6.13E-08	25
19	3.72E-07	1.24E-07	33	0.00E+00	3.67E-10	0	1.53E-07	1.70E-08	11	0.00E+00	0.00E+00	0
20	3.48E-07	9.64E-08	28	5.71E-10	2.86E-10	50	2.52E-07	1.31E-08	5	8.14E-08	4.09E-08	50
21	1.35E-06	4.17E-07	31	3.70E-09	1.23E-09	33	7.06E-07	5.85E-08	8	-3.99E-07	-1.37E-07	34
22	3.91E-07	8.07E-08	21	5.58E-10	2.39E-10	43	2.87E-07	1.11E-08	4	1.21E-07	5.20E-08	43
23	4.03E-07	8.90E-08	22	7.03E-10	2.64E-10	38	3.70E-07	1.21E-08	3	1.60E-07	6.03E-08	38
24	5.67E-07	1.20E-07	21	1.89E-09	3.55E-10	19	5.47E-07	1.63E-08	3	-1.77E-08	-3.36E-09	19
25	1.18E-07	8.14E-08	69	8.03E-10	2.41E-10	30	2.23E-07	1.13E-08	5	-1.72E-08	-5.24E-09	30
26	4.51E-07	2.31E-07	51	-2.28E-10	6.85E-10	-300	2.99E-07	3.16E-08	11	3.67E-07	1.10E-06	300
27	2.67E-07	9.38E-08	35	5.56E-10	2.78E-10	50	2.93E-07	1.29E-08	4	1.27E-07	6.38E-08	50
28	1.89E-07	1.83E-07	97	3.67E-09	5.51E-10	15	7.08E-07	2.54E-08	4	-3.89E-07	-5.99E-08	15
29	5.23E-07	1.40E-07	27	-1.41E-10	4.22E-10	-300	3.31E-07	1.93E-08	6	3.73E-07	1.12E-06	300
30	5.75E-07	2.18E-07	38	1.53E-09	6.56E-10	43	3.65E-07	3.02E-08	8	-9.20E-08	-4.02E-08	44
31	1.34E-07	1.27E-07	95	3.76E-10	3.76E-10	100	3.65E-07	1.73E-08	5	2.53E-07	2.53E-07	100
32	4.11E-07	1.53E-07	37	0.00E+00	4.54E-10	0	2.66E-07	2.10E-08	8	0.00E+00	0.00E+00	0
34	9.10E-07	1.96E-07	22	1.75E-09	5.82E-10	33	6.95E-07	2.68E-08	4	1.74E-07	5.83E-08	34

NG analysis of sanidines from sample F1A

N°	40Ar/36Ar	±	% ±	4He/40Ar*	±	% ±
6	329.09	174.77	53	0.99	0.64	64
7	331.00	64.39	19	0.02	0.12	600
8	322.54	111.44	35	-0.17	-0.30	175
9	258.65	58.26	23	0.11	0.09	86
10	293.90	161.29	55	-7.86	-5.01	64
11	1332.73	444.53	33	0.36	0.16	45
12	206.38	35.24	17	-2.06	-0.70	34
13	227.45	34.81	15	-3.24	-0.87	27
14	421.79	181.84	43	4.08	2.10	52
15	557.29	419.39	75	1.85	1.69	91
16	383.70	144.95	38	6.37	2.83	44
17	1519.84	1520.54	100	0.63	0.69	109
18	130.11	31.90	25	-1.87	-0.65	35
19	0.00	0.00	0.00	0.00	0.00	0.00
20	441.12	221.76	50	4.28	2.46	57
21	190.86	65.56	34	-3.39	-1.56	46
22	515.18	221.69	43	3.23	1.54	48
23	526.44	198.17	38	2.51	1.10	44
24	289.19	54.91	19	-32.00	-9.09	28
25	277.11	84.31	30	-6.88	-5.17	75
26	-1307.54	-3925.06	300	1.23	3.74	305
27	527.41	264.72	50	2.10	1.29	61
28	192.70	29.72	15	-0.49	-0.48	98
29	-2352.52	-7058.90	300	1.40	4.22	301
30	238.46	104.09	44	-6.25	-3.61	58
31	971.17	972.26	100	0.53	0.73	138
32	0.00	0.00	0.00	0.00	0.00	0.00
34	398.00	133.55	34	5.24	2.09	40

NG analysis of sanidines from sample F2A

N°	date	weight (g)	4He (v)	±	36Ar (v)	±	40Ar (v)	±
11	09/10/2017	0.000168	0.00252	0.00042	0.00009	0.00002	0.03063	0.00119
12	09/10/2017	0.000164	0.00350	0.00043	-0.00001	0.00002	0.02975	0.00119
13	09/10/2017	0.000145	0.00407	0.00043	0.00008	0.00002	0.04762	0.00119
14	09/10/2017	0.000095	0.00263	0.00043	0.00007	0.00002	0.01897	0.00119
15	09/10/2017	0.000147	0.00407	0.00042	0.00013	0.00002	0.03398	0.00119
16	09/10/2017	0.000173	0.00350	0.00043	0.00005	0.00002	0.02478	0.00120
17	09/10/2017	0.000089	0.00821	0.00042	0.00005	0.00002	0.02802	0.00120
18	09/10/2017	0.000079	0.00267	0.00043	0.00015	0.00002	0.03285	0.00119
19	09/10/2017	0.000127	0.00263	0.00043	0.00012	0.00002	0.02528	0.00123
20	09/10/2017	0.000179	0.00313	0.00042	0.00010	0.00002	0.02639	0.00120
21	27/11/2017	0.000173	0.00096	0.00030	0.00196	0.00008	0.56353	0.01311
22	27/11/2017	0.000147	0.00168	0.00029	0.00326	0.00008	0.97324	0.01476
23	27/11/2017	0.000214	0.00232	0.00029	0.00019	0.00008	0.06954	0.01309
24	27/11/2017	0.000152	0.00233	0.00029	0.00049	0.00009	0.15770	0.01310
25	27/11/2017	0.000139	0.00231	0.00030	0.00051	0.00009	0.12633	0.01343
26	27/11/2017	0.000250	0.00204	0.00029	0.00183	0.00008	0.49168	0.01311
28	27/11/2017	0.000139	0.00062	0.00030	0.00322	0.00008	0.94054	0.01316
29	27/11/2017	0.000103	0.00148	0.00030	0.00353	0.00011	0.95833	0.01327
30	27/11/2017	0.000267	0.00252	0.00029	0.00187	0.00009	0.43382	0.01313
31	27/11/2017	0.000127	0.00249	0.00029	0.00031	0.00008	0.07561	0.01313
32	27/11/2017	0.000071	0.00299	0.00029	0.00035	0.00009	0.07620	0.01309
33	27/11/2017	0.000103	0.00191	0.00030	0.00113	0.00008	0.26059	0.01310
35	27/11/2017	0.000169	0.00147	0.00029	0.00001	0.00008	0.02970	0.01308

NG analysis of sanidines from sample F2A (cc)

N°	4He	±	36Ar	±	40Ar	±
11	3.60E-11	6.01E-12	1.20E-13	2.66E-14	4.32E-11	1.68E-12
12	5.01E-11	6.15E-12	-1.33E-14	2.66E-14	4.20E-11	1.68E-12
13	5.82E-11	6.15E-12	1.06E-13	2.66E-14	6.72E-11	1.68E-12
14	3.76E-11	6.15E-12	9.30E-14	2.66E-14	2.68E-11	1.68E-12
15	5.82E-11	6.01E-12	1.73E-13	2.66E-14	4.79E-11	1.68E-12
16	5.01E-11	6.15E-12	6.64E-14	2.66E-14	3.49E-11	1.69E-12
17	1.17E-10	6.01E-12	6.64E-14	2.66E-14	3.95E-11	1.69E-12
18	3.82E-11	6.15E-12	1.99E-13	2.66E-14	4.63E-11	1.68E-12
19	3.76E-11	6.15E-12	1.59E-13	2.66E-14	3.57E-11	1.73E-12
20	5.72E-11	7.67E-12	1.03E-13	2.06E-14	2.86E-11	1.30E-12
21	1.75E-11	5.48E-12	2.02E-12	8.22E-14	6.11E-10	1.42E-11
22	3.07E-11	5.30E-12	3.35E-12	8.22E-14	1.06E-09	1.60E-11
23	4.24E-11	5.30E-12	1.95E-13	8.22E-14	7.54E-11	1.42E-11
24	4.26E-11	5.30E-12	5.04E-13	9.25E-14	1.71E-10	1.42E-11
25	4.22E-11	5.48E-12	5.24E-13	9.25E-14	1.37E-10	1.46E-11
26	3.73E-11	5.30E-12	1.88E-12	8.22E-14	5.33E-10	1.42E-11
28	1.13E-11	5.48E-12	3.31E-12	8.22E-14	1.02E-09	1.43E-11
29	2.70E-11	5.48E-12	3.63E-12	1.13E-13	1.04E-09	1.44E-11
30	4.60E-11	5.30E-12	1.92E-12	9.25E-14	4.70E-10	1.42E-11
31	4.55E-11	5.30E-12	3.19E-13	8.22E-14	8.20E-11	1.42E-11
32	5.46E-11	5.30E-12	3.60E-13	9.25E-14	8.26E-11	1.42E-11
33	3.49E-11	5.48E-12	1.16E-12	8.22E-14	2.83E-10	1.42E-11
35	2.69E-11	5.30E-12	1.03E-14	8.22E-14	3.22E-11	1.42E-11

NG analysis ofsanidines from sample F2A (cc/g)

N°	4He	±	% ±	36Ar	±	% ±	40Ar	±	% ±	40Ar*	±	% ±
11	2.15E-07	3.58E-08	17	7.12E-10	1.58E-10	22	2.57E-07	9.99E-09	4	4.46E-08	1.01E-08	23
13	3.05E-07	3.75E-08	12	-8.10E-11	1.62E-10	-200	2.56E-07	1.02E-08	4	2.80E-07	5.60E-07	200
14	4.02E-07	4.24E-08	11	7.33E-10	1.83E-10	25	4.63E-07	1.16E-08	2	2.44E-07	6.14E-08	25
15	3.96E-07	6.47E-08	16	9.79E-10	2.80E-10	29	2.82E-07	1.77E-08	6	-1.07E-08	-3.14E-09	29
16	3.96E-07	4.09E-08	10	1.18E-09	1.81E-10	15	3.26E-07	1.14E-08	4	-2.49E-08	-3.92E-09	16
17	2.89E-07	3.56E-08	12	3.84E-10	1.54E-10	40	2.02E-07	9.78E-09	5	8.73E-08	3.52E-08	40
18	1.32E-06	6.75E-08	5	7.47E-10	2.99E-10	40	4.44E-07	1.90E-08	4	2.21E-07	8.89E-08	40
19	4.83E-07	7.79E-08	16	2.52E-09	3.36E-10	13	5.86E-07	2.12E-08	4	-1.67E-07	-2.31E-08	14
20	2.96E-07	4.84E-08	16	1.26E-09	2.09E-10	17	2.81E-07	1.37E-08	5	-9.42E-08	-1.63E-08	17
21	3.19E-07	4.29E-08	13	5.74E-10	1.15E-10	20	1.60E-07	7.27E-09	5	-1.17E-08	-2.39E-09	21
22	1.01E-07	3.17E-08	31	1.16E-08	4.75E-10	4	3.53E-06	8.22E-08	2	5.38E-08	2.53E-09	5
23	2.09E-07	3.60E-08	17	2.28E-08	5.60E-10	2	7.18E-06	1.09E-07	2	3.70E-07	1.07E-08	3
24	1.98E-07	2.48E-08	13	9.13E-10	3.84E-10	42	3.52E-07	6.63E-08	19	7.98E-08	3.68E-08	46
25	2.80E-07	3.49E-08	12	3.31E-09	6.09E-10	18	1.12E-06	9.34E-08	8	1.35E-07	2.73E-08	20
26	3.04E-07	3.94E-08	13	3.77E-09	6.66E-10	18	9.85E-07	1.05E-07	11	-1.41E-07	-2.90E-08	21
27	1.49E-07	2.12E-08	14	7.53E-09	3.29E-10	4	2.13E-06	5.68E-08	3	-1.15E-07	-5.88E-09	5
28	8.15E-08	3.94E-08	48	2.38E-08	5.92E-10	2	7.34E-06	1.03E-07	1	2.25E-07	6.41E-09	3
29	2.63E-07	5.32E-08	20	3.52E-08	1.10E-09	3	1.01E-05	1.40E-07	1	-4.33E-07	-1.48E-08	3
30	1.72E-07	1.98E-08	12	7.20E-09	3.47E-10	5	1.76E-06	5.33E-08	3	-3.88E-07	-2.21E-08	6
31	3.58E-07	4.17E-08	12	2.51E-09	6.48E-10	26	6.45E-07	1.12E-07	17	-1.04E-07	-3.23E-08	31
32	7.69E-07	7.46E-08	10	5.07E-09	1.30E-09	26	1.16E-06	2.00E-07	17	-3.50E-07	-1.08E-07	31
33	3.39E-07	5.32E-08	16	1.13E-08	7.99E-10	7	2.74E-06	1.38E-07	5	-6.25E-07	-5.42E-08	9
34	1.59E-07	3.14E-08	20	6.08E-11	4.87E-10	800	1.91E-07	8.39E-08	44	1.72E-07	1.38E-06	801

NG analysis of sanidines from sample F2A

N°	40Ar/36Ar	±	% ±	4He/40Ar*	±	% ±
11	361.18	81.48	23	4.81	1.35	28
12	-3157.22	-6315.71	200	1.09	2.18	200
13	631.71	158.71	25	1.64	0.45	27
14	287.60	84.13	29	-36.90	-12.36	34
15	277.39	43.77	16	-15.92	-3.00	19
16	525.96	211.92	40	3.31	1.40	42
17	594.73	239.25	40	5.97	2.42	41
18	232.41	32.11	14	-2.90	-0.61	21
19	223.57	38.82	17	-3.15	-0.75	24
20	278.27	57.08	21	-27.42	-6.72	25
21	303.18	14.24	5	1.89	0.60	32
22	314.80	9.08	3	0.56	0.10	18
23	385.94	178.00	46	2.48	1.19	48
24	339.37	68.41	20	2.07	0.49	24
25	261.20	53.81	21	-2.15	-0.52	24
26	283.31	14.51	5	-1.30	-0.20	15
27	308.00	8.78	3	0.36	0.18	48
28	286.27	9.76	3	-0.61	-0.12	21
29	244.63	13.91	6	-0.44	-0.06	13
30	257.19	80.00	31	-3.45	-1.15	33
31	229.57	70.99	31	-2.20	-0.71	32
32	243.17	21.11	9	-0.54	-0.10	18
33	3131.77	25092.13	801	0.92	7.39	801

NG analysis of sanidines from sample I1A

N°	date	weight (g)	4He (v)	±	36Ar (v)	±	40Ar (v)	±
5	29/09/2017	0.000140	0.00026	0.00015	-0.00005	0.00008	0.01184	0.00158
10	29/09/2017	0.000070	-0.00017	0.00015	0.00018	0.00008	0.00794	0.00157
11	22/11/2017	0.000083	0.00057	0.00027	0.00000	0.00003	0.02972	0.00407
12	22/11/2017	0.000085	0.00133	0.00028	0.00102	0.00004	0.28376	0.00424
13	22/11/2017	0.000053	0.00061	0.00028	0.00002	0.00003	0.02792	0.00407
14	22/11/2017	0.000066	0.00251	0.00027	0.00026	0.00003	0.08734	0.00413
15	22/11/2017	0.000049	0.00248	0.00028	0.00058	0.00003	0.16796	0.00441
16	22/11/2017	0.000026	0.00072	0.00027	-0.00003	0.00003	0.02627	0.00408
17	22/11/2017	0.000035	0.00228	0.00028	0.00015	0.00003	0.04106	0.00407
18	22/11/2017	0.000036	0.00082	0.00027	0.00013	0.00003	0.01631	0.00407
19	22/11/2017	0.000026	0.00124	0.00028	0.00014	0.00003	0.01850	0.00408
20	22/11/2017	0.000037	0.00075	0.00027	0.00009	0.00003	0.03360	0.00407
21	23/11/2017	0.000016	0.00029	0.00042	0.00005	0.00001	0.02024	0.00416
23	23/11/2017	0.000045	0.00239	0.00042	0.00044	0.00003	0.15812	0.00431
25	23/11/2017	0.000045	0.00278	0.00042	0.00014	0.00001	0.04912	0.00417
26	23/11/2017	0.000022	0.00184	0.00041	0.00020	0.00003	0.04924	0.00355
27	23/11/2017	0.000027	0.00267	0.00041	0.00011	0.00004	0.02904	0.00410
28	23/11/2017	0.000027	0.00201	0.00041	0.00009	0.00002	0.02583	0.00355
29	23/11/2017	0.000024	0.00222	0.00042	0.00009	0.00003	0.02477	0.00356
30	23/11/2017	0.000037	0.00184	0.00041	0.00006	0.00003	0.02042	0.00356
31	23/11/2017	0.000020	0.00267	0.00041	0.00005	0.00002	0.03555	0.00356
33	23/11/2017	0.000019	0.00269	0.00041	0.00009	0.00002	0.01568	0.00355
35	23/11/2017	0.000018	0.00257	0.00012	0.00002	0.00002	0.01370	0.00071

NG analysis of sanidines from sample I1A (cc)

N°	4He	±	36Ar	±	40Ar	±
5	3.15E-12	1.81E-12	-6.01E-14	9.61E-14	1.50E-11	2.00E-12
10	-2.06E-12	1.81E-12	2.16E-13	9.61E-14	1.00E-11	1.98E-12
11	1.04E-11	4.93E-12	0.00E+00	3.08E-14	3.22E-11	4.41E-12
12	2.43E-11	5.12E-12	1.05E-12	4.11E-14	3.08E-10	4.60E-12
13	1.11E-11	5.12E-12	2.06E-14	3.08E-14	3.03E-11	4.41E-12
14	4.59E-11	4.93E-12	2.67E-13	3.08E-14	9.47E-11	4.48E-12
15	4.53E-11	5.12E-12	5.96E-13	3.08E-14	1.82E-10	4.78E-12
16	1.32E-11	4.93E-12	-3.08E-14	3.08E-14	2.85E-11	4.42E-12
17	4.17E-11	5.12E-12	1.54E-13	3.08E-14	4.45E-11	4.41E-12
18	1.50E-11	4.93E-12	1.34E-13	3.08E-14	1.77E-11	4.41E-12
19	2.27E-11	5.12E-12	1.44E-13	3.08E-14	2.01E-11	4.42E-12
20	1.37E-11	4.93E-12	9.25E-14	3.08E-14	3.64E-11	4.41E-12
21	5.30E-12	7.67E-12	5.14E-14	1.03E-14	2.19E-11	4.51E-12
23	4.37E-11	7.67E-12	4.52E-13	3.08E-14	1.71E-10	4.67E-12
25	5.08E-11	7.67E-12	1.44E-13	1.03E-14	5.33E-11	4.52E-12
26	3.36E-11	7.49E-12	2.06E-13	3.08E-14	5.34E-11	3.85E-12
27	4.88E-11	7.49E-12	1.13E-13	4.11E-14	3.15E-11	4.44E-12
28	3.67E-11	7.49E-12	9.25E-14	2.06E-14	2.80E-11	3.85E-12
29	4.06E-11	7.67E-12	9.25E-14	3.08E-14	2.69E-11	3.86E-12
30	3.36E-11	7.49E-12	6.17E-14	3.08E-14	2.21E-11	3.86E-12
31	4.88E-11	7.49E-12	5.14E-14	2.06E-14	3.85E-11	3.86E-12
33	4.91E-11	7.49E-12	9.25E-14	2.06E-14	1.70E-11	3.85E-12
35	4.70E-11	2.19E-12	2.06E-14	2.06E-14	1.49E-11	7.70E-13

NG analysis ofsanidines from sample I1A (cc/g)

N°	4He	±	% ±	36Ar	±	% ±	40Ar	±	% ±	40Ar*	±	% ±
11	2.25E-08	1.30E-08	58	-4.29E-10	6.86E-10	-160	1.07E-07	1.43E-08	13	2.35E-07	3.77E-07	161
12	-2.94E-08	2.59E-08	-88	3.09E-09	1.37E-09	44	1.43E-07	2.83E-08	20	-7.79E-07	-3.79E-07	49
13	1.25E-07	5.94E-08	47	0.00E+00	3.72E-10	0	3.88E-07	5.32E-08	14	0.00E+00	0.00E+00	0
14	2.86E-07	6.02E-08	21	1.23E-08	4.84E-10	4	3.62E-06	5.41E-08	1	-6.43E-08	-2.70E-09	4
15	2.10E-07	9.65E-08	46	3.88E-10	5.82E-10	150	5.71E-07	8.32E-08	15	4.55E-07	6.86E-07	151
16	6.95E-07	7.47E-08	11	4.05E-09	4.67E-10	12	1.43E-06	6.78E-08	5	2.25E-07	2.81E-08	12
17	9.25E-07	1.04E-07	11	1.22E-08	6.29E-10	5	3.72E-06	9.76E-08	3	8.27E-08	4.80E-09	6
18	5.06E-07	1.90E-07	38	-1.19E-09	1.19E-09	-100	1.10E-06	1.70E-07	16	1.45E-06	1.47E-06	101
19	1.19E-06	1.46E-07	12	4.41E-09	8.81E-10	20	1.27E-06	1.26E-07	10	-4.37E-08	-9.75E-09	22
20	4.16E-07	1.37E-07	33	3.71E-09	8.57E-10	23	4.91E-07	1.23E-07	25	-6.17E-07	-2.10E-07	34
21	8.71E-07	1.97E-07	23	5.54E-09	1.19E-09	21	7.71E-07	1.70E-07	22	-8.81E-07	-2.71E-07	31
22	3.70E-07	1.33E-07	36	2.50E-09	8.34E-10	33	9.84E-07	1.19E-07	12	2.38E-07	8.44E-08	35
23	3.31E-07	4.80E-07	145	3.21E-09	6.43E-10	20	1.37E-06	2.82E-07	21	4.12E-07	1.18E-07	29
24	9.70E-07	1.71E-07	18	1.01E-08	6.85E-10	7	3.81E-06	1.04E-07	3	8.08E-07	5.93E-08	7
25	1.13E-06	1.71E-07	15	3.20E-09	2.28E-10	7	1.18E-06	1.00E-07	8	2.28E-07	2.53E-08	11
26	1.53E-06	3.40E-07	22	9.35E-09	1.40E-09	15	2.43E-06	1.75E-07	7	-3.64E-07	-6.06E-08	17
27	1.81E-06	2.77E-07	15	4.19E-09	1.52E-09	36	1.17E-06	1.65E-07	14	-8.45E-08	-3.30E-08	39
28	1.36E-06	2.77E-07	20	3.43E-09	7.62E-10	22	1.04E-06	1.43E-07	14	1.40E-08	3.65E-09	26
29	1.69E-06	3.20E-07	19	3.86E-09	1.29E-09	33	1.12E-06	1.61E-07	14	-3.22E-08	-1.17E-08	36
30	9.09E-07	2.02E-07	22	1.67E-09	8.34E-10	50	5.98E-07	1.04E-07	17	1.01E-07	5.32E-08	53
31	2.44E-06	3.75E-07	15	2.57E-09	1.03E-09	40	1.93E-06	1.93E-07	10	1.16E-06	4.78E-07	41
32	2.59E-06	3.94E-07	15	4.87E-09	1.08E-09	22	8.95E-07	2.03E-07	23	-5.59E-07	-1.77E-07	32
33	2.61E-06	1.22E-07	5	1.14E-09	1.14E-09	100	8.25E-07	4.28E-08	5	4.84E-07	4.85E-07	100

NG analysis of sanidines from sample F1A

N°	40Ar/36Ar	±	% ±	4He/40Ar*	±	% ±
9	-249.12	-399.98	161	0.10	0.16	171
10	46.41	22.57	49	0.04	0.04	101
11	0.00	0.00	0.00	0.00	0.00	0.00
12	293.35	12.31	4	-4.45	-0.95	21
13	1472.04	2218.46	151	0.46	0.73	158
14	354.22	44.17	12	3.08	0.51	16
15	305.36	17.71	6	11.17	1.42	13
16	-923.36	0.00	0	0.35	0.38	108
17	288.64	64.43	22	-27.24	-6.94	25
18	132.30	44.97	34	-0.67	-0.32	47
19	139.34	42.85	31	-0.99	-0.38	38
20	393.67	139.62	35	1.56	0.79	51
21	426.85	122.41	29	0.80	1.19	148
22	378.94	27.82	7	1.20	0.23	19
23	369.97	41.05	11	4.94	0.93	19
24	259.61	43.21	17	-4.20	-1.17	28
25	278.38	108.59	39	-21.37	-8.96	42
26	302.63	79.07	26	97.45	32.30	33
27	290.21	105.35	36	-52.52	-21.50	41
28	358.87	190.03	53	9.04	5.19	57
29	749.73	309.15	41	2.10	0.93	44
30	183.71	58.28	32	-4.62	-1.63	35
31	722.31	0.00	0	5.39	5.40	100

NG analysis of sanidines from sample I3A

N°	date	weight (g)	4He (v)	±	36Ar (v)	±	40Ar (v)	±
1	29/09/2017	0.000230	-0.00026	0.00015	0.00043	0.00008	0.08946	0.00159
2	29/09/2017	0.000160	-0.00008	0.00017	0.00038	0.00008	0.03655	0.00157
10	29/09/2017	0.000200	-0.00066	0.00016	0.00034	0.00009	0.02938	0.00159
11	09/10/2017	0.000145	0.00368	0.00042	0.00002	0.00002	0.03762	0.00106
12	09/10/2017	0.000099	0.00172	0.00043	0.00005	0.00002	0.03636	0.00119
13	09/10/2017	0.000085	0.00305	0.00042	0.00003	0.00002	0.02888	0.00122
14	09/10/2017	0.000068	0.00344	0.00042	0.00008	0.00001	0.01882	0.00119
15	09/10/2017	0.000215	0.00079	0.00042	0.00014	0.00002	0.01464	0.00119
16	10/10/2017	0.000132	0.00193	0.00005	0.00010	0.00001	0.03041	0.00055
17	10/10/2017	0.000071	0.00208	0.00035	0.00014	0.00002	0.02974	0.00068
18	10/10/2017	0.000070	0.00272	0.00035	0.00004	0.00002	0.02325	0.00067
19	10/10/2017	0.000156	0.00425	0.00035	0.00008	0.00002	0.03303	0.00067
20	10/10/2017	0.000059	0.00279	0.00035	0.00007	0.00002	0.01999	0.00066
21	10/10/2017	0.000213	0.00268	0.00035	0.00005	0.00002	0.03859	0.00067
22	10/10/2017	0.000100	0.00231	0.00035	0.00006	0.00002	0.01988	0.00069
23	10/10/2017	0.000214	0.00121	0.00035	0.00018	0.00002	0.03989	0.00067
24	10/10/2017	0.000103	0.00183	0.00035	0.00113	0.00002	0.26969	0.00070
25	10/10/2017	0.000104	0.00080	0.00035	0.00007	0.00002	0.01766	0.00067
26	10/10/2017	0.000110	0.00292	0.00035	0.00010	0.00002	0.02842	0.00066
27	10/10/2017	0.000081	0.00313	0.00035	0.00003	0.00002	0.02305	0.00160
28	10/10/2017	0.000117	0.00362	0.00035	0.00008	0.00002	0.02665	0.00068
29	10/10/2017	0.000079	0.00276	0.00035	0.00008	0.00002	0.01823	0.00068
30	10/10/2017	0.000113	0.00404	0.00035	0.00014	0.00002	0.03901	0.00067
31	23/11/2017	0.000128	0.00143	0.00014	0.00055	0.00003	0.14265	0.00089
32	23/11/2017	0.000195	0.00230	0.00013	0.00036	0.00003	0.09184	0.00082
33	23/11/2017	0.000113	0.00243	0.00013	0.00106	0.00005	0.19307	0.00097
34	23/11/2017	0.000200	0.00038	0.00019	0.00292	0.00005	0.76358	0.00277
35	23/11/2017	0.000134	0.00205	0.00013	0.00065	0.00005	0.10750	0.00116
36	19/12/2017	0.000311	0.00224	0.00018	0.00119	0.00003	0.38106	0.00194
37	19/12/2017	0.000169	0.00281	0.00017	0.00028	0.00005	0.10708	0.00191
38	19/12/2017	0.000227	0.00090	0.00019	0.00021	0.00002	0.07555	0.00168
39	19/12/2017	0.000295	0.00126	0.00020	0.00064	0.00003	0.21301	0.00421
40	19/12/2017	0.000182	0.00206	0.00014	0.00017	0.00003	0.08903	0.00468
41	19/12/2017	0.000173	0.00081	0.00014	0.00004	0.00002	0.03192	0.00468
42	19/12/2017	0.000089	0.00045	0.00014	0.00000	0.00002	0.01359	0.00467

NG analysis of sanidines from sample I3A (cc)

N°	4He	±	36Ar	±	40Ar	±
1	-3.15E-12	1.81E-12	5.16E-13	9.61E-14	1.13E-10	2.01E-12
2	-9.68E-13	2.06E-12	4.56E-13	9.61E-14	4.62E-11	1.98E-12
10	-7.98E-12	1.94E-12	4.08E-13	1.08E-13	3.71E-11	2.01E-12
11	5.26E-11	6.01E-12	2.66E-14	2.66E-14	5.31E-11	1.49E-12
12	2.46E-11	6.15E-12	6.64E-14	2.66E-14	5.13E-11	1.68E-12
13	4.36E-11	6.01E-12	3.99E-14	2.66E-14	4.07E-11	1.72E-12
14	4.92E-11	6.01E-12	1.06E-13	1.33E-14	2.65E-11	1.68E-12
15	1.13E-11	6.01E-12	1.86E-13	2.66E-14	2.06E-11	1.68E-12
16	2.76E-11	7.15E-13	1.33E-13	1.33E-14	4.29E-11	7.76E-13
17	2.98E-11	5.01E-12	1.86E-13	2.66E-14	4.19E-11	9.59E-13
18	3.89E-11	5.01E-12	5.32E-14	2.66E-14	3.28E-11	9.45E-13
19	6.08E-11	5.01E-12	1.06E-13	2.66E-14	4.66E-11	9.45E-13
20	3.99E-11	5.01E-12	9.30E-14	2.66E-14	2.82E-11	9.31E-13
21	3.83E-11	5.01E-12	6.64E-14	2.66E-14	5.44E-11	9.45E-13
22	3.30E-11	5.01E-12	7.97E-14	2.66E-14	2.80E-11	9.73E-13
23	1.73E-11	5.01E-12	2.39E-13	2.66E-14	5.63E-11	9.45E-13
24	2.62E-11	5.01E-12	1.50E-12	2.66E-14	3.80E-10	9.87E-13
25	1.14E-11	5.01E-12	9.30E-14	2.66E-14	2.49E-11	9.45E-13
26	4.18E-11	5.01E-12	1.33E-13	2.66E-14	4.01E-11	9.31E-13
27	4.48E-11	5.01E-12	3.99E-14	2.66E-14	3.25E-11	2.26E-12
28	5.18E-11	5.01E-12	1.06E-13	2.66E-14	3.76E-11	9.59E-13
29	3.95E-11	5.01E-12	1.06E-13	2.66E-14	2.57E-11	9.59E-13
30	5.78E-11	5.01E-12	1.86E-13	2.66E-14	5.50E-11	9.45E-13
31	2.61E-11	2.56E-12	5.65E-13	3.08E-14	1.55E-10	9.65E-13
32	4.20E-11	2.38E-12	3.70E-13	3.08E-14	9.96E-11	8.89E-13
33	4.44E-11	2.38E-12	1.09E-12	5.14E-14	2.09E-10	1.05E-12
34	6.94E-12	3.47E-12	3.00E-12	5.14E-14	8.28E-10	3.00E-12
35	3.75E-11	2.38E-12	6.68E-13	5.14E-14	1.17E-10	1.26E-12
36	4.09E-11	3.29E-12	1.22E-12	3.08E-14	4.13E-10	2.10E-12
37	5.13E-11	3.11E-12	2.88E-13	5.14E-14	1.16E-10	2.07E-12
38	1.64E-11	3.47E-12	2.16E-13	2.06E-14	8.19E-11	1.82E-12
39	2.30E-11	3.65E-12	6.58E-13	3.08E-14	2.31E-10	4.56E-12
40	3.76E-11	2.56E-12	1.75E-13	3.08E-14	9.65E-11	5.07E-12
41	1.48E-11	2.56E-12	4.11E-14	2.06E-14	3.46E-11	5.07E-12
42	8.22E-12	2.56E-12	0.00E+00	2.06E-14	1.47E-11	5.06E-12

NG analysis of sanidines from sample I3A (cc/g)

N°	4He	±	% ±	36Ar	±	% ±	40Ar	±	% ±	40Ar*	±	% ±
1	-1.37E-08	7.89E-09	-58	2.25E-09	4.18E-10	19	4.91E-07	8.74E-09	2	-1.79E-07	-3.34E-08	19
2	-6.05E-09	1.29E-08	-213	2.85E-09	6.01E-10	21	2.89E-07	1.24E-08	4	-5.63E-07	-1.21E-07	21
10	-3.99E-08	9.68E-09	-24	2.04E-09	5.41E-10	26	1.86E-07	1.00E-08	5	-4.24E-07	-1.15E-07	27
11	3.63E-07	4.14E-08	11	1.83E-10	1.83E-10	100	3.66E-07	1.03E-08	3	3.11E-07	3.11E-07	100
12	2.49E-07	6.21E-08	25	6.71E-10	2.68E-10	40	5.18E-07	1.70E-08	3	3.18E-07	1.27E-07	40
13	5.13E-07	7.07E-08	14	4.69E-10	3.13E-10	67	4.79E-07	2.02E-08	4	3.39E-07	2.27E-07	67
14	7.24E-07	8.83E-08	12	1.56E-09	1.95E-10	13	3.90E-07	2.47E-08	6	-7.65E-08	-1.07E-08	14
15	5.26E-08	2.79E-08	53	8.65E-10	1.24E-10	14	9.60E-08	7.81E-09	8	-1.62E-07	-2.67E-08	16
16	2.09E-07	5.42E-09	3	1.01E-09	1.01E-10	10	3.25E-07	5.88E-09	2	2.43E-08	2.47E-09	10
17	4.19E-07	7.05E-08	17	2.62E-09	3.74E-10	14	5.91E-07	1.35E-08	2	-1.92E-07	-2.77E-08	14
18	5.56E-07	7.15E-08	13	7.59E-10	3.80E-10	50	4.68E-07	1.35E-08	3	2.42E-07	1.21E-07	50
19	3.90E-07	3.21E-08	8	6.81E-10	1.70E-10	25	2.99E-07	6.06E-09	2	9.51E-08	2.39E-08	25
20	6.76E-07	8.49E-08	13	1.58E-09	4.50E-10	29	4.78E-07	1.58E-08	3	7.10E-09	2.04E-09	29
21	1.80E-07	2.35E-08	13	3.12E-10	1.25E-10	40	2.56E-07	4.44E-09	2	1.62E-07	6.50E-08	40
22	3.30E-07	5.01E-08	15	7.97E-10	2.66E-10	33	2.80E-07	9.73E-09	3	4.23E-08	1.42E-08	34
23	8.09E-08	2.34E-08	29	1.12E-09	1.24E-10	11	2.63E-07	4.42E-09	2	-7.08E-08	-7.96E-09	11
24	2.54E-07	4.86E-08	19	1.46E-08	2.58E-10	2	3.69E-06	9.58E-09	0	-6.60E-07	-1.18E-08	2
25	1.10E-07	4.81E-08	44	8.94E-10	2.56E-10	29	2.39E-07	9.09E-09	4	-2.76E-08	-7.95E-09	29
26	3.80E-07	4.55E-08	12	1.21E-09	2.42E-10	20	3.64E-07	8.46E-09	2	3.68E-09	7.41E-10	20
27	5.53E-07	6.18E-08	11	4.92E-10	3.28E-10	67	4.01E-07	2.79E-08	7	2.54E-07	1.71E-07	67
28	4.43E-07	4.28E-08	10	9.09E-10	2.27E-10	25	3.21E-07	8.20E-09	3	4.99E-08	1.26E-08	25
29	5.00E-07	6.34E-08	13	1.35E-09	3.36E-10	25	3.25E-07	1.21E-08	4	-7.63E-08	-1.93E-08	25
30	5.11E-07	4.43E-08	9	1.65E-09	2.35E-10	14	4.87E-07	8.36E-09	2	-4.69E-09	-6.75E-10	14
31	2.04E-07	2.00E-08	10	4.42E-09	2.41E-10	5	1.21E-06	7.54E-09	1	-1.11E-07	-6.08E-09	5
32	2.15E-07	1.22E-08	6	1.90E-09	1.58E-10	8	5.11E-07	4.56E-09	1	-5.61E-08	-4.70E-09	8
33	3.93E-07	2.10E-08	5	9.64E-09	4.55E-10	5	1.85E-06	9.31E-09	1	-1.03E-06	-4.87E-08	5
34	3.47E-08	1.74E-08	50	1.50E-08	2.57E-10	2	4.14E-06	1.50E-08	0	-3.42E-07	-5.99E-09	2
35	2.79E-07	1.77E-08	6	4.99E-09	3.84E-10	8	8.70E-07	9.38E-09	1	-6.19E-07	-4.81E-08	8
36	1.32E-07	1.06E-08	8	3.93E-09	9.92E-11	3	1.33E-06	6.76E-09	1	1.54E-07	3.96E-09	3
37	3.04E-07	1.84E-08	6	1.70E-09	3.04E-10	18	6.87E-07	1.23E-08	2	1.78E-07	3.20E-08	18
38	7.24E-08	1.53E-08	21	9.51E-10	9.06E-11	10	3.61E-07	8.02E-09	2	7.68E-08	7.52E-09	10
39	7.80E-08	1.24E-08	16	2.23E-09	1.05E-10	5	7.83E-07	1.55E-08	2	1.17E-07	5.95E-09	5
40	2.07E-07	1.41E-08	7	9.60E-10	1.69E-10	18	5.30E-07	2.79E-08	5	2.44E-07	4.49E-08	18
41	8.55E-08	1.48E-08	17	2.38E-10	1.19E-10	50	2.00E-07	2.93E-08	15	1.29E-07	6.72E-08	52
42	9.24E-08	2.87E-08	31	0.00E+00	2.31E-10	0	1.66E-07	5.69E-08	34	0.00E+00	0.00E+00	0

NG analysis of sanidines from sampleI3A

N°	40Ar/36Ar	±	% ±	4He/40Ar*	±	% ±
8	218.87	40.91	19	0.08	0.05	61
9	101.19	21.74	21	0.01	0.02	214
10	90.91	24.56	27	0.09	0.03	36
11	1996.21	1997.01	100	1.17	1.17	101
12	771.74	309.73	40	0.78	0.37	47
13	1021.63	682.45	67	1.51	1.03	68
14	249.66	34.97	14	-9.47	-1.76	19
15	110.98	18.24	16	-0.32	-0.18	56
16	322.73	32.80	10	8.60	0.90	10
17	225.44	32.62	14	-2.19	-0.49	22
18	616.85	308.94	50	2.30	1.19	52
19	438.16	109.90	25	4.10	1.08	26
20	303.06	87.17	29	95.27	29.89	31
21	819.07	327.94	40	1.11	0.47	42
22	351.63	117.84	34	7.81	2.87	37
23	235.19	26.43	11	-1.14	-0.35	31
24	253.28	4.53	2	-0.38	-0.07	19
25	267.74	77.17	29	-3.99	-2.09	52
26	301.61	60.73	20	103.13	24.17	23
27	815.39	546.54	67	2.17	1.48	68
28	353.53	88.84	25	8.86	2.39	27
29	241.83	61.13	25	-6.55	-1.85	28
30	295.71	42.55	14	-108.99	-18.31	17
31	273.49	15.01	5	-1.84	-0.21	11
32	269.01	22.55	8	-3.84	-0.39	10
33	192.06	9.11	5	-0.38	-0.03	7
34	275.74	4.83	2	-0.10	-0.05	50
35	174.39	13.55	8	-0.45	-0.05	10
36	337.66	8.68	3	0.86	0.07	8
37	403.26	72.37	18	1.70	0.32	19
38	379.36	37.10	10	0.94	0.22	23
39	350.96	17.85	5	0.67	0.11	17
40	552.23	101.68	18	0.85	0.17	20
41	841.47	438.45	52	0.66	0.36	55
42	0.00	0.00	0.00	0.00	0.00	0.00

Calibration data used for NG analysis on Sanidines
(mean values from 6 measurements)

4He cc/V	36Ar cc/V	40Ar cc/V	Date
1.21E-08	1.20E-09	1.26E-09	September 2017
1.43E-08	1.33E-09	1.41E-09	October 2017
1.83E-08	1.03E-09	1.08E-09	November 2017
1.67E-08	9.54E-10	1.02E-09	December 2017

Daily blank mean values (V) used to correct NG data from Sanidines

Data	4He	±	36Ar	±	40Ar	±
September						
27/09/2017	0.00549	0.00006	0.00010	0.00001	0.01958	0.00015
29/09/2017	0.00570	0.00005	0.00020	0.00001	0.00783	0.00008
Mean	0.00560	0.00006	0.00015	0.00001	0.01371	0.00012
St. dev.	0.00010	0.00001	0.00005	0.00000	0.00588	0.00004
October						
09/10/2017	0.00279	0.00006	0.00005	0.00001	0.00830	0.00006
10/10/2017	0.00234	0.00004	0.00003	0.00000	0.00630	0.00006
Mean	0.00257	0.00005	0.00004	0.00000	0.00730	0.00006
St. dev.	0.00023	0.00001	0.00001	0.00000	0.00100	0.00000
November						
22/11/2017	0.00173	0.00005	0.00009	0.00001	0.01641	0.00014
23/11/2017	0.00258	0.00005	0.00010	0.00001	0.01869	0.00014
24/11/2017	0.00244	0.00004	0.00005	0.00001	0.00963	0.00009
27/11/2017	0.00217	0.00004	0.00011	0.00001	0.03342	0.00025
Mean	0.00223	0.00005	0.00009	0.00001	0.01954	0.00015
St. dev.	0.00033	0.00001	0.00002	0.00000	0.00868	0.00006
December						
19/12/2017	0.00190	0.00005	0.00005	0.00001	0.01460	0.00010

A4.2 Ar/Ar data of Glass shards and sanidines from the Eras Formation

Ar/Ar data (expressed in V) of single fusion analysis from Hauyne crystals (Analytical uncertainties are at the 1sigma level)

Grain	40Ar	+/-	39Ar	+/-	38Ar	+/-	37Ar	+/-	36Ar	+/-	40Ar*/39Ar	+/-	Age (Ma)	+/- (Ma)	39Ar/40Ar	+/-	36Ar/40Ar	+/-
4	0.20832	0.00057	0.00419	0.00005	0.00012	0.00003	0.00426	0.00011	0.00008	0.00002	44.09	1.65	28.60	1.06	0.02012	0.00027	0.00038	0.00010
12	0.13869	0.00078	0.00165	0.00005	0.00009	0.00003	0.00483	0.00011	0.00009	0.00001	68.10	3.29	43.99	2.10	0.01188	0.00040	0.00064	0.00009
3	0.20973	0.00093	0.00199	0.00006	0.00011	0.00004	0.00486	0.00011	0.00012	0.00001	87.64	3.47	56.41	2.20	0.00948	0.00031	0.00057	0.00006
1	0.11251	0.00061	0.00082	0.00005	0.00003	0.00003	0.00268	0.00011	0.00009	0.00001	104.43	8.41	67.02	5.30	0.00731	0.00049	0.00079	0.00011
10	0.28074	0.00164	0.00204	0.00007	0.00013	0.00004	0.00704	0.00011	0.00010	0.00002	123.32	5.56	78.89	3.48	0.00726	0.00027	0.00035	0.00008
2	0.14441	0.00104	0.00075	0.00004	0.00005	0.00003	0.00354	0.00011	0.00005	0.00002	173.21	12.01	109.84	7.39	0.00519	0.00025	0.00034	0.00015
11	0.27882	0.00099	0.00143	0.00005	0.00010	0.00003	0.00717	0.00011	0.00006	0.00002	182.97	8.35	115.84	5.12	0.00513	0.00020	0.00021	0.00008
Blank	0.00514	0.00014	0.00002	0.00002	0.00003	0.00002	0.00004	0.00002	0.00003	0.00002	J value = 0.000362435 +/- 1.81217E-06							

Ar/Ar data (expressed in V) of step-heating analysis from U-1-2 (Analytical uncertainties are at the 1sigma level)

Step	40Ar	+/-	39Ar	+/-	38Ar	+/-	37Ar	+/-	36Ar	+/-	40Ar*/39Ar	+/-	Age (Ma)	+/- (Ma)	39Ar/40Ar	+/-	36Ar/40Ar	+/-
step1	0.10568	0.00134	0.00271	0.00012	0.00012	0.00002	0.00168	0.00020	0.00019	0.00003	18.29	3.54	11.92	2.30	0.02562	0.00122	0.00178	0.00029
step2	0.12539	0.00130	0.00316	0.00008	0.00011	0.00002	0.00213	0.00020	0.00024	0.00003	17.19	2.98	11.20	1.94	0.02522	0.00069	0.00190	0.00025
step3	0.21868	0.00183	0.00588	0.00016	0.00020	0.00001	0.00269	0.00020	0.00041	0.00003	16.48	1.41	10.74	0.92	0.02689	0.00078	0.00187	0.00012
step4	0.19589	0.00193	0.00479	0.00014	0.00022	0.00002	0.00348	0.00020	0.00031	0.00003	21.70	2.07	14.13	1.34	0.02448	0.00077	0.00157	0.00016
step5	0.26964	0.00221	0.00649	0.00012	0.00023	0.00003	0.00438	0.00020	0.00045	0.00004	20.97	1.83	13.66	1.19	0.02407	0.00050	0.00166	0.00014
step6	0.09626	0.00117	0.00141	0.00008	0.00009	0.00002	0.00202	0.00020	0.00012	0.00003	43.14	5.98	27.99	3.85	0.01470	0.00085	0.00123	0.00027
step7	0.23967	0.00188	0.00285	0.00009	0.00017	0.00002	0.00506	0.00020	0.00036	0.00003	46.68	3.61	30.27	2.32	0.01189	0.00038	0.00149	0.00013
step8	0.36525	0.00152	0.00433	0.00011	0.00028	0.00002	0.00787	0.00020	0.00041	0.00003	56.37	2.56	36.49	1.64	0.01185	0.00029	0.00111	0.00008
step9	0.34955	0.00175	0.00195	0.00010	0.00024	0.00003	0.00889	0.00020	0.00033	0.00003	129.46	8.04	82.72	5.02	0.00557	0.00028	0.00093	0.00009
step10	0.44661	0.00133	0.00227	0.00008	0.00029	0.00003	0.01115	0.00020	0.00037	0.00003	148.86	6.67	94.80	4.14	0.00508	0.00018	0.00082	0.00007
step11	0.66667	0.00330	0.00330	0.00009	0.00044	0.00003	0.01779	0.00020	0.00042	0.00003	163.84	5.30	104.07	3.27	0.00495	0.00013	0.00064	0.00005
step12	0.80781	0.00173	0.00274	0.00007	0.00052	0.00003	0.02130	0.00020	0.00047	0.00004	243.65	7.69	152.67	4.62	0.00339	0.00009	0.00059	0.00005
step13	0.96805	0.00238	0.00304	0.00012	0.00060	0.00005	0.02547	0.00020	0.00043	0.00003	275.71	10.75	171.83	6.39	0.00314	0.00012	0.00045	0.00003
step14	1.71173	0.00339	0.00415	0.00012	0.00087	0.00004	0.03957	0.00020	0.00063	0.00003	367.19	11.26	225.40	6.50	0.00243	0.00007	0.00037	0.00002
step15	2.13506	0.00349	0.00445	0.00012	0.00092	0.00006	0.05065	0.00030	0.00043	0.00003	450.70	12.06	272.96	6.78	0.00209	0.00006	0.00020	0.00001
step16	2.92754	0.00726	0.00591	0.00011	0.00113	0.00006	0.07784	0.00030	0.00049	0.00003	471.01	8.78	284.34	4.91	0.00202	0.00004	0.00017	0.00001
step17	5.18471	0.05554	0.01320	0.00020	0.00227	0.00007	0.12358	0.00030	0.00091	0.00003	372.36	7.04	228.39	4.05	0.00255	0.00005	0.00017	0.00001
Blank	0.00826	0.00016	0.00005	0.00004	0.00002	0.00002	0.00006	0.00002	0.00006	0.00001	J value = 0.000362435 +/- 1.81217E-06							

Ar/Ar data (expressed in V) of single fusion analysis from glass particles (Analytical uncertainties are at the 1sigma level)

Grain	40Ar	+/-	39Ar	+/-	38Ar	+/-	37Ar	+/-	36Ar	+/-	40Ar*/39Ar	+/-	Age (Ma)	+/- (Ma)	39Ar/40Ar	+/-	36Ar/40Ar	+/-
F1A1	0.06989	0.00018	0.00106	0.00005	0.00009	0.00002	0.00010	0.00004	0.00023	0.00002	1.17	6.00	0.79	4.07	0.01512	0.00077	0.00329	0.00030
F1A2-4	0.96332	0.00562	0.01034	0.00006	0.00079	0.00004	0.00198	0.00004	0.00320	0.00003	0.78	1.04	0.53	0.71	0.01073	0.00009	0.00332	0.00004
F1A5-10	0.24852	0.00129	0.00598	0.00006	0.00027	0.00002	0.00044	0.00004	0.00082	0.00001	0.62	0.65	0.42	0.44	0.02405	0.00029	0.00330	0.00005
Blank	0.00564	0.00012	0.00003	0.00002	0.00001	0.00002	0.00005	0.00002	0.00004	0.00001	J value = 0.000376413 +/- 1.88206E-06							
I3A1-6	7.60023	0.03443	0.02699	0.00015	0.00559	0.00008	0.00119	0.00007	0.02615	0.00015	-7.67	-2.10	-5.14	1.41	0.00355	0.00002	0.00344	0.00003
I3A7	1.20226	0.00316	0.00392	0.00008	0.00086	0.00005	0.00019	0.00007	0.00409	0.00004	-4.81	-3.21	-3.22	2.16	0.00326	0.00007	0.00340	0.00004
I3A8	0.37419	0.00066	0.00218	0.00005	0.00032	0.00003	0.00023	0.00007	0.00126	0.00004	-0.90	-5.59	-0.61	3.75	0.00583	0.00014	0.00337	0.00011
I3A9	1.07162	0.00177	0.00443	0.00011	0.00080	0.00003	0.00019	0.00007	0.00365	0.00006	-4.09	-4.11	-2.74	2.75	0.00413	0.00011	0.00341	0.00006
I3A10	3.16593	0.00574	0.00580	0.00012	0.00216	0.00004	0.00031	0.00007	0.01063	0.00008	-1.33	-4.26	-0.89	2.85	0.00183	0.00004	0.00336	0.00003
Blank	0.00564	0.00012	0.00003	0.00002	0.00001	0.00002	0.00005	0.00002	0.00004	0.00001	J value = 0.000371171 +/- 1.85585E-06							

Ar/Ar data (expressed in V) of step-heating analysis from F1A glass particles (Analytical uncertainties are at the 1sigma level)

Step	40Ar	+/-	39Ar	+/-	38Ar	+/-	37Ar	+/-	36Ar	+/-	40Ar*/39Ar	+/-	Age (Ma)	+/- (Ma)	39Ar/40Ar	+/-	36Ar/40Ar	+/-
step1	0.03661	0.00139	0.00251	0.00007	0.00022	0.00004	0.00016	0.00005	0.00018	0.00003	-7.43	-3.21	-5.05	2.18	0.06844	0.00317	0.00505	0.00075
step2	0.51533	0.04297	0.03221	0.00255	0.00217	0.00014	0.00414	0.00005	0.00294	0.00013	-11.29	-2.01	-7.68	1.37	0.06251	0.00719	0.00571	0.00054
step3	1.02584	0.06693	0.05794	0.00443	0.00414	0.00064	0.00714	0.00005	0.00421	0.00064	-4.00	-3.51	-2.72	2.39	0.05648	0.00568	0.00411	0.00068
step4	2.84652	0.11185	0.10367	0.00414	0.00676	0.00052	0.01015	0.00005	0.00976	0.00020	-0.66	-1.22	-0.45	0.83	0.03642	0.00204	0.00343	0.00015
step5	4.44998	0.10089	0.12526	0.00243	0.00732	0.00012	0.01005	0.00005	0.01746	0.00027	-6.10	-1.04	-4.14	0.71	0.02815	0.00084	0.00392	0.00011
step6	5.39831	0.35521	0.11513	0.00730	0.00949	0.00014	0.00966	0.00005	0.02136	0.00109	-8.51	-4.22	-5.79	2.87	0.02133	0.00195	0.00396	0.00033
step7	6.12131	0.02826	0.09534	0.00091	0.00639	0.00013	0.00500	0.00005	0.02133	0.00023	-2.60	-0.78	-1.77	0.53	0.01558	0.00017	0.00349	0.00004
step8	9.80805	0.07659	0.13132	0.00184	0.00949	0.00022	0.00705	0.00005	0.03375	0.00025	-2.05	-0.82	-1.39	0.55	0.01339	0.00021	0.00344	0.00004
step9	1.93992	0.00829	0.02506	0.00024	0.00157	0.00007	0.00106	0.00005	0.00659	0.00007	-1.16	-0.92	-0.79	0.63	0.01292	0.00013	0.00340	0.00004
step10	1.20134	0.01010	0.01787	0.00016	0.00107	0.00005	0.00071	0.00005	0.00409	0.00004	-1.19	-0.92	-0.81	0.63	0.01488	0.00018	0.00341	0.00005
step11	1.47197	0.01062	0.01656	0.00026	0.00125	0.00005	0.00064	0.00005	0.00496	0.00007	-0.62	-1.45	-0.42	0.98	0.01125	0.00019	0.00337	0.00005
step12	3.79263	0.02450	0.02926	0.00034	0.00308	0.00007	0.00283	0.00005	0.01283	0.00007	-1.34	-1.11	-0.91	0.76	0.00771	0.00010	0.00338	0.00003
step13	1.95383	0.02181	0.01679	0.00031	0.00166	0.00008	0.00093	0.00005	0.00662	0.00008	-1.43	-1.95	-0.97	1.33	0.00859	0.00019	0.00339	0.00006
step14	2.66540	0.00938	0.01725	0.00028	0.00196	0.00004	0.00097	0.00005	0.00908	0.00009	-2.72	-1.68	-1.85	1.14	0.00647	0.00011	0.00341	0.00004
step15	1.22050	0.00684	0.01417	0.00022	0.00134	0.00004	0.00171	0.00005	0.00438	0.00007	-6.25	-1.60	-4.25	1.09	0.01161	0.00019	0.00359	0.00006
Blank	0.00766	0.00018	0.00006	0.00002	0.00004	0.00001	0.00008	0.00002	0.00006	0.00001	J value =0.000376413 +/- 1.88206E-06							

Ar/Ar data (expressed in V) of step-heating analysis from F2A glass particles (Analytical uncertainties are at the 1sigma level)

Step	40Ar	+/-	39Ar	+/-	38Ar	+/-	37Ar	+/-	36Ar	+/-	40Ar*/39Ar	+/-	Age (Ma)	+/- (Ma)	39Ar/40Ar	+/-	36Ar/40Ar	+/-
step1	0.21896	0.00233	0.00426	0.00010	0.00025	0.00002	0.00032	0.00003	0.00072	0.00003	1.18	2.27	0.80	1.53	0.01946	0.00052	0.00327	0.00015
step2	1.83581	0.01691	0.02386	0.00027	0.00207	0.00008	0.00223	0.00003	0.00651	0.00009	-4.47	-1.34	-3.02	0.90	0.01300	0.00019	0.00354	0.00006
step3	5.60972	0.06255	0.09083	0.00073	0.00541	0.00009	0.00514	0.00004	0.01880	0.00015	-0.03	-0.85	-0.02	0.58	0.01619	0.00022	0.00335	0.00005
step4	6.81043	0.06622	0.07489	0.00074	0.00584	0.00013	0.00392	0.00004	0.02197	0.00019	3.35	1.17	2.26	0.79	0.01100	0.00015	0.00323	0.00004
step5	4.30007	0.02993	0.02824	0.00038	0.00332	0.00004	0.00147	0.00004	0.01428	0.00020	1.29	2.38	0.87	1.61	0.00657	0.00010	0.00332	0.00005
step6	5.78712	0.05166	0.04718	0.00050	0.00446	0.00009	0.00249	0.00004	0.01904	0.00022	2.17	1.78	1.47	1.20	0.00815	0.00011	0.00329	0.00005
step7	5.23839	0.03207	0.04244	0.00050	0.00411	0.00006	0.00216	0.00004	0.01788	0.00016	-2.36	-1.37	-1.59	0.93	0.00810	0.00011	0.00341	0.00004
step8	4.02601	0.04044	0.02033	0.00023	0.00281	0.00010	0.00105	0.00004	0.01326	0.00020	3.29	3.57	2.22	2.41	0.00505	0.00008	0.00329	0.00006
step9	2.35288	0.02437	0.01621	0.00026	0.00192	0.00005	0.00102	0.00004	0.00779	0.00011	1.66	2.57	1.12	1.74	0.00689	0.00013	0.00331	0.00006
step10	2.74672	0.01628	0.01516	0.00022	0.00199	0.00008	0.00089	0.00004	0.00914	0.00010	1.16	2.31	0.79	1.56	0.00552	0.00009	0.00333	0.00004
step11	1.67185	0.02735	0.00822	0.00010	0.00113	0.00004	0.00042	0.00004	0.00563	0.00008	-1.14	-4.31	-0.77	2.91	0.00492	0.00010	0.00337	0.00007
step12	2.18146	0.01488	0.01260	0.00026	0.00167	0.00006	0.00065	0.00004	0.00740	0.00009	-2.23	-2.52	-1.51	1.71	0.00578	0.00013	0.00339	0.00005
step13	1.49719	0.01558	0.01049	0.00013	0.00116	0.00004	0.00054	0.00004	0.00516	0.00008	-4.16	-2.83	-2.81	1.92	0.00701	0.00011	0.00345	0.00007
step14	0.78404	0.01268	0.00663	0.00011	0.00069	0.00005	0.00045	0.00004	0.00266	0.00004	-1.57	-2.65	-1.06	1.79	0.00846	0.00020	0.00339	0.00008
step15	1.86922	0.01554	0.02408	0.00017	0.00162	0.00005	0.00145	0.00004	0.00631	0.00008	-0.62	-1.13	-0.42	0.77	0.01288	0.00014	0.00338	0.00005
Blank	0.01654	0.00034	0.00005	0.00002	0.00003	0.00001	0.00005	0.00002	0.00009	0.00001	J value =0.000374665 +/- 1.87333E-06							

Ar/Ar data (expressed in V) of step-heating analysis from I3A glass particles (Analytical uncertainties are at the 1sigma level)

Step	40Ar	+/-	39Ar	+/-	38Ar	+/-	37Ar	+/-	36Ar	+/-	40Ar*/39Ar	+/-	Age (Ma)	+/- (Ma)	39Ar/40Ar	+/-	36Ar/40Ar	+/-
step1	6.47601	0.05630	0.04339	0.00033	0.00501	0.00007	0.00174	0.00006	0.02157	0.00013	0.85	1.58	0.57	1.06	0.00670	0.00008	0.00333	0.00004
step2	3.60368	0.04869	0.02026	0.00044	0.00265	0.00007	0.00089	0.00006	0.01169	0.00012	5.64	2.99	3.78	2.00	0.00562	0.00014	0.00324	0.00006
step3	11.36228	0.16723	0.06877	0.00095	0.00844	0.00014	0.00283	0.00006	0.03777	0.00025	1.26	2.66	0.84	1.78	0.00605	0.00012	0.00332	0.00005
step4	1.57543	0.01008	0.00923	0.00012	0.00115	0.00005	0.00047	0.00006	0.00532	0.00008	-1.31	-2.82	-0.88	1.89	0.00586	0.00009	0.00338	0.00006
step5	7.62040	0.05186	0.04476	0.00033	0.00568	0.00015	0.00186	0.00006	0.02536	0.00018	1.11	1.67	0.75	1.12	0.00587	0.00006	0.00333	0.00003
step6	13.48684	0.04866	0.06924	0.00058	0.01025	0.00020	0.00319	0.00006	0.04422	0.00027	4.12	1.36	2.76	0.91	0.00513	0.00005	0.00328	0.00002
step7	2.59077	0.00649	0.01194	0.00016	0.00181	0.00006	0.00073	0.00006	0.00863	0.00010	1.26	2.57	0.84	1.72	0.00461	0.00006	0.00333	0.00004
step8	8.59400	0.02355	0.04845	0.00040	0.00647	0.00007	0.00201	0.00006	0.02868	0.00020	0.66	1.33	0.45	0.89	0.00564	0.00005	0.00334	0.00003
step9	3.50129	0.01662	0.02740	0.00018	0.00274	0.00003	0.00127	0.00002	0.01170	0.00007	0.25	0.98	0.16	0.65	0.00782	0.00006	0.00334	0.00003
step10	7.25965	0.03852	0.07782	0.00049	0.00649	0.00015	0.00742	0.00002	0.02415	0.00018	0.62	0.85	0.42	0.57	0.01072	0.00009	0.00333	0.00003
step11	12.00401	0.11212	0.13507	0.00192	0.01082	0.00017	0.01055	0.00002	0.04048	0.00046	-0.61	-1.31	-0.41	0.88	0.01125	0.00019	0.00337	0.00005
step12	8.10446	0.06099	0.08515	0.00042	0.00741	0.00012	0.00841	0.00002	0.02711	0.00032	0.11	1.33	0.08	0.89	0.01051	0.00009	0.00335	0.00005
step13	7.65904	0.06957	0.08366	0.00048	0.00672	0.00012	0.00613	0.00002	0.02579	0.00024	-0.50	-1.19	-0.33	0.80	0.01092	0.00012	0.00337	0.00004
step14	1.96775	0.02089	0.01402	0.00032	0.00154	0.00008	0.00070	0.00023	0.00647	0.00011	2.62	2.77	1.75	1.86	0.00713	0.00018	0.00329	0.00007
step15	12.88267	0.14027	0.06902	0.00077	0.00959	0.00010	0.00327	0.00023	0.04284	0.00047	1.35	2.86	0.90	1.92	0.00536	0.00008	0.00333	0.00005
step16	7.95328	0.06993	0.03334	0.00049	0.00583	0.00013	0.00130	0.00023	0.02679	0.00031	-1.33	-3.47	-0.89	2.33	0.00419	0.00007	0.00337	0.00005
step17	1.87290	0.01564	0.00808	0.00029	0.00130	0.00009	0.00029	0.00023	0.00628	0.00009	-0.18	-3.70	-0.12	2.47	0.00431	0.00016	0.00335	0.00005
Blank	0.01182	0.00023	0.00009	0.00002	0.00004	0.00002	0.00007	0.00002	0.00008	0.00001	J value =0.000371171 +/- 1.85585E-06							

Ar/Ar data (expressed in V) of step-heating analysis from I1A glass particles (Analytical uncertainties are at the 1sigma level)

Step	40Ar	+/-	39Ar	+/-	38Ar	+/-	37Ar	+/-	36Ar	+/-	40Ar*/39Ar	+/-	Age (Ma)	+/- (Ma)	39Ar/40Ar	+/-	36Ar/40Ar	+/-
step1	0.00207	0.00586	-0.00055	0.00079	0.00001	0.00003	-0.00016	0.00048	0.00002	0.00002	7.13	19.48	4.79	13.07	-0.26539	-0.84351	0.00969	0.02964
step2	0.09596	0.00587	0.00119	0.00080	0.00010	0.00003	0.00054	0.00048	0.00032	0.00003	0.39	8.81	0.26	5.92	0.01238	0.00834	0.00333	0.00036
step3	0.61538	0.00614	0.00908	0.00081	0.00053	0.00004	0.00077	0.00048	0.00204	0.00005	0.70	1.63	0.47	1.10	0.01475	0.00132	0.00331	0.00008
step4	1.72347	0.00656	0.01684	0.00081	0.00140	0.00006	0.00147	0.00048	0.00581	0.00009	-0.66	-1.68	-0.44	1.13	0.00977	0.00047	0.00337	0.00006
step5	1.32168	0.00683	0.01723	0.00081	0.00122	0.00005	0.00077	0.00048	0.00436	0.00005	1.16	0.88	0.78	0.59	0.01304	0.00062	0.00330	0.00004
step6	2.65711	0.00882	0.02409	0.00081	0.00209	0.00008	0.00357	0.00048	0.00894	0.00011	-0.49	-1.44	-0.33	0.97	0.00906	0.00031	0.00336	0.00004
step7	2.88934	0.00949	0.02646	0.00082	0.00220	0.00004	0.00264	0.00048	0.00982	0.00012	-1.60	-1.42	-1.08	0.96	0.00916	0.00028	0.00340	0.00004
step8	1.19476	0.00609	0.01398	0.00082	0.00106	0.00004	0.00100	0.00048	0.00405	0.00006	-1.02	-1.43	-0.69	0.96	0.01170	0.00069	0.00339	0.00006
step9	2.97520	0.00876	0.02724	0.00085	0.00238	0.00009	0.00264	0.00048	0.00994	0.00012	0.28	1.37	0.19	0.92	0.00916	0.00029	0.00334	0.00004
step10	2.98075	0.00870	0.02367	0.00217	0.00243	0.00009	0.00124	0.00048	0.01006	0.00009	-0.96	-1.23	-0.64	0.82	0.00794	0.00073	0.00337	0.00003
step11	1.43706	0.00679	0.01318	0.00082	0.00107	0.00005	0.00077	0.00048	0.00469	0.00005	2.80	1.16	1.88	0.78	0.00917	0.00058	0.00326	0.00004
step12	1.83909	0.00710	0.01176	0.00081	0.00128	0.00006	0.00101	0.00048	0.00614	0.00005	0.51	1.50	0.34	1.01	0.00639	0.00044	0.00334	0.00003
step13	1.15123	0.00271	0.00719	0.00074	0.00087	0.00005	0.00008	0.00030	0.00384	0.00005	0.80	2.13	0.54	1.44	0.00625	0.00064	0.00333	0.00004
step14	0.89471	0.00258	0.00839	0.00077	0.00078	0.00005	0.00153	0.00030	0.00302	0.00005	-0.69	-1.83	-0.47	1.23	0.00938	0.00086	0.00337	0.00006
step15	0.37749	0.00155	0.00346	0.00075	0.00025	0.00003	0.00008	0.00030	0.00126	0.00003	0.67	2.71	0.45	1.82	0.00916	0.00198	0.00333	0.00008
step16	0.66067	0.00181	0.00266	0.00074	0.00046	0.00005	0.00008	0.00030	0.00228	0.00007	-7.16	-8.17	-4.82	5.51	0.00403	0.00112	0.00345	0.00011
step17	0.33288	0.00155	0.00151	0.00073	0.00019	0.00003	0.00032	0.00030	0.00111	0.00003	1.65	6.24	1.11	4.19	0.00455	0.00221	0.00332	0.00009
step18	0.41057	0.00141	0.00233	0.00073	0.00035	0.00003	-0.00040	0.00030	0.00134	0.00001	4.92	2.31	3.31	1.55	0.00568	0.00179	0.00326	0.00003
step19	0.83171	0.00175	0.00423	0.00074	0.00060	0.00004	0.00008	0.00030	0.00282	0.00003	-2.18	-2.25	-1.47	1.52	0.00509	0.00089	0.00339	0.00004
step20	1.22017	0.00226	0.00550	0.00075	0.00093	0.00005	0.00057	0.00030	0.00407	0.00005	1.10	2.78	0.74	1.87	0.00450	0.00061	0.00333	0.00004
step21	0.28293	0.00150	0.00182	0.00074	0.00024	0.00004	-0.00040	0.00030	0.00098	0.00002	-4.77	-4.07	-3.21	2.74	0.00645	0.00260	0.00345	0.00008
step22	0.02631	0.00125	0.00041	0.00073	0.00005	0.00003	0.00105	0.00030	0.00010	0.00002	-6.08	-19.39	-4.09	13.08	0.01544	0.02789	0.00366	0.00083
Blank	0.00807	0.00017	0.00050	0.00003	0.00003	0.00002	0.00013	0.00002	0.00004	0.00002	J value =0.000372918 +/- 1.86459E-06							

Ar/Ar data (expressed in V) of single fusion analysis from sanidines (Analytical uncertainties are at the 1sigma level)

Grain	40Ar	+/-	39Ar	+/-	38Ar	+/-	37Ar	+/-	36Ar	+/-	40Ar*/39Ar	+/-	Age (Ma)	+/- (Ma)	39Ar/40Ar	+/-	36Ar/40Ar	+/-
F1A1	0.00961	0.00030	0.00578	0.00011	0.00005	0.00003	0.00019	0.00005	0.00001	0.00001	0.93	0.75	0.62	0.50	0.60125	0.02206	0.00148	0.00151
F1A2	0.01135	0.00035	0.01014	0.00015	0.00010	0.00003	0.00011	0.00005	0.00002	0.00001	0.41	0.43	0.27	0.29	0.89282	0.03053	0.00214	0.00128
F1A3	0.01613	0.00035	0.00823	0.00010	0.00009	0.00003	0.00023	0.00005	0.00003	0.00001	0.72	0.53	0.48	0.35	0.50987	0.01269	0.00212	0.00090
F1A4	0.00384	0.00038	0.00271	0.00004	0.00005	0.00003	0.00007	0.00005	0.00000	0.00001	0.95	1.61	0.63	1.07	0.70517	0.07114	0.00111	0.00378
F1A5	0.01046	0.00044	0.00649	0.00015	0.00013	0.00002	0.00011	0.00005	0.00002	0.00001	0.50	0.67	0.33	0.45	0.62058	0.02952	0.00232	0.00139
F1A6	0.00461	0.00035	0.00327	0.00003	0.00004	0.00003	0.00011	0.00005	0.00001	0.00002	0.11	2.06	0.07	1.37	0.71103	0.05385	0.00310	0.00491
F1A7	0.00642	0.00030	0.00203	0.00007	0.00002	0.00003	0.00011	0.00005	0.00001	0.00001	1.06	2.13	0.71	1.42	0.31673	0.01856	0.00222	0.00226
Blank	0.00585	0.00013	0.00002	0.00002	0.00002	0.00002	0.00004	0.00002	0.00004	0.00001	J value = 0.000369424 +/- 1.84712E-06							
I3A1	0.01120	0.00031	0.00248	0.00006	0.00004	0.00003	0.00011	0.00005	0.00003	0.00002	0.39	2.72	0.26	1.79	0.22129	0.00829	0.00306	0.00202
I3A2	0.01152	0.00031	0.00496	0.00011	0.00007	0.00003	0.00019	0.00005	0.00001	0.00001	1.47	0.88	0.96	0.58	0.43034	0.01534	0.00124	0.00126
I3A3	0.33818	0.00176	0.02881	0.00021	0.00054	0.00004	0.00060	0.00005	0.00102	0.00003	1.13	0.34	0.74	0.22	0.08518	0.00076	0.00303	0.00010
I3A4	0.17247	0.00069	0.03118	0.00023	0.00046	0.00003	0.00176	0.00005	0.00046	0.00002	1.09	0.22	0.72	0.14	0.18080	0.00150	0.00269	0.00013
Blank	0.00585	0.00013	0.00002	0.00002	0.00002	0.00002	0.00004	0.00002	0.00004	0.00001	J value = 0.000364182 +/- 1.82091E-06							

Ar/Ar data (expressed in V) of step-heating analysis from F1A sanidines (Analytical uncertainties are at the 1sigma level)

Step	40Ar	+/-	39Ar	+/-	38Ar	+/-	37Ar	+/-	36Ar	+/-	40Ar*/39Ar	+/-	Age (Ma)	+/- (Ma)	39Ar/40Ar	+/-	36Ar/40Ar	+/-
step1	0.19408	0.00216	0.01421	0.00011	0.00034	0.00002	0.00115	0.00004	0.00067	0.00002	-0.52	-0.49	-0.34	0.33	0.07321	0.00098	0.00348	0.00012
step2	0.44623	0.00304	0.06587	0.00055	0.00129	0.00003	0.00349	0.00004	0.00146	0.00003	0.14	0.15	0.09	0.10	0.14761	0.00159	0.00328	0.00007
step3	0.21974	0.00367	0.06681	0.00120	0.00089	0.00003	0.00242	0.00004	0.00051	0.00001	0.99	0.09	0.66	0.06	0.30404	0.00745	0.00234	0.00008
step4	0.23012	0.00230	0.07668	0.00057	0.00093	0.00004	0.00324	0.00004	0.00053	0.00002	0.92	0.09	0.61	0.06	0.33321	0.00414	0.00232	0.00010
step5	0.14610	0.00224	0.05565	0.00063	0.00075	0.00004	0.00231	0.00004	0.00029	0.00002	1.05	0.13	0.70	0.08	0.38090	0.00727	0.00202	0.00016
step6	0.08031	0.00173	0.04461	0.00029	0.00056	0.00004	0.00129	0.00004	0.00012	0.00001	0.97	0.10	0.64	0.07	0.55547	0.01252	0.00155	0.00018
step7	0.18908	0.00208	0.10162	0.00064	0.00127	0.00005	0.00380	0.00004	0.00033	0.00002	0.88	0.07	0.59	0.05	0.53742	0.00682	0.00177	0.00012
step8	0.35085	0.00638	0.18423	0.00334	0.00227	0.00009	0.00641	0.00004	0.00051	0.00002	1.07	0.05	0.71	0.04	0.52509	0.01348	0.00146	0.00007
step9	0.56003	0.00668	0.28990	0.00396	0.00351	0.00006	0.00960	0.00003	0.00083	0.00002	1.08	0.04	0.72	0.02	0.51766	0.00938	0.00148	0.00005
step10	0.40571	0.00780	0.22927	0.00398	0.00254	0.00007	0.00780	0.00003	0.00050	0.00003	1.12	0.06	0.75	0.04	0.56512	0.01464	0.00123	0.00009
step11	0.50960	0.00381	0.27219	0.00331	0.00314	0.00007	0.00963	0.00003	0.00069	0.00002	1.12	0.03	0.75	0.02	0.53412	0.00762	0.00135	0.00005
step12	0.35385	0.00410	0.20035	0.00254	0.00250	0.00004	0.00816	0.00003	0.00044	0.00003	1.11	0.06	0.74	0.04	0.56619	0.00972	0.00124	0.00009
step13	0.39024	0.00492	0.23007	0.00151	0.00276	0.00007	0.00945	0.00003	0.00045	0.00002	1.12	0.04	0.74	0.03	0.58956	0.00837	0.00115	0.00006
step14	0.14479	0.00193	0.08776	0.00084	0.00106	0.00003	0.00340	0.00003	0.00016	0.00002	1.11	0.09	0.74	0.06	0.60609	0.00994	0.00110	0.00017
step15	0.10013	0.00187	0.04405	0.00030	0.00061	0.00004	0.00130	0.00003	0.00021	0.00002	0.85	0.17	0.57	0.11	0.43998	0.00874	0.00209	0.00025
Blank	0.00931	0.00020	0.00007	0.00002	0.00002	0.00001	0.00004	0.00002	0.00005	0.00001	J value =0.000369424 +/- 1.84712E-06							

Ar/Ar data (expressed in V) of step-heating analysis from F2A sanidines (Analytical uncertainties are at the 1sigma level)

Step	40Ar	+/-	39Ar	+/-	38Ar	+/-	37Ar	+/-	36Ar	+/-	40Ar*/39Ar	+/-	Age (Ma)	+/- (Ma)	39Ar/40Ar	+/-	36Ar/40Ar	+/-
step1	0.01901	0.00052	0.00324	0.00011	0.00009	0.00002	0.00012	0.00004	0.00005	0.00001	0.87	1.25	0.58	0.83	0.17043	0.00762	0.00285	0.00071
step2	0.01341	0.00037	0.00455	0.00009	0.00007	0.00002	0.00018	0.00004	0.00003	0.00001	0.70	0.89	0.46	0.59	0.33962	0.01166	0.00255	0.00101
step3	0.05987	0.00082	0.01988	0.00029	0.00035	0.00002	0.00082	0.00004	0.00014	0.00002	0.85	0.33	0.56	0.22	0.33204	0.00665	0.00241	0.00037
step4	0.02479	0.00051	0.01162	0.00020	0.00016	0.00003	0.00037	0.00004	0.00004	0.00001	1.00	0.35	0.66	0.23	0.46880	0.01250	0.00178	0.00054
step5	0.06887	0.00075	0.03475	0.00030	0.00053	0.00003	0.00125	0.00004	0.00013	0.00001	0.83	0.12	0.55	0.08	0.50459	0.00703	0.00195	0.00020
step6	0.03728	0.00128	0.02412	0.00043	0.00033	0.00003	0.00072	0.00003	0.00003	0.00001	1.22	0.16	0.81	0.11	0.64716	0.02504	0.00071	0.00034
step7	0.05768	0.00140	0.03340	0.00028	0.00044	0.00003	0.00134	0.00003	0.00006	0.00001	1.22	0.12	0.81	0.08	0.57908	0.01489	0.00098	0.00022
step8	0.07037	0.00166	0.02360	0.00027	0.00032	0.00002	0.00083	0.00003	0.00015	0.00002	1.13	0.28	0.75	0.19	0.33532	0.00880	0.00208	0.00031
step9	0.03297	0.00124	0.01600	0.00014	0.00021	0.00002	0.00123	0.00003	0.00003	0.00001	1.57	0.25	1.04	0.16	0.48530	0.01872	0.00080	0.00038
step10	0.12751	0.00117	0.08093	0.00111	0.00105	0.00005	0.00259	0.00003	0.00016	0.00002	1.00	0.08	0.66	0.05	0.63469	0.01046	0.00122	0.00017
step11	0.10433	0.00123	0.05846	0.00054	0.00085	0.00002	0.00354	0.00003	0.00013	0.00002	1.14	0.11	0.76	0.07	0.56035	0.00838	0.00121	0.00021
step12	0.15786	0.00166	0.10465	0.00087	0.00120	0.00004	0.00301	0.00003	0.00019	0.00002	0.98	0.06	0.65	0.04	0.66291	0.00889	0.00118	0.00014
step13	0.48234	0.00379	0.31307	0.00283	0.00409	0.00010	0.00921	0.00003	0.00059	0.00002	0.97	0.03	0.65	0.02	0.64906	0.00778	0.00123	0.00005
step14	1.29173	0.01872	0.92188	0.01246	0.01099	0.00022	0.02576	0.00003	0.00107	0.00003	1.05	0.03	0.70	0.02	0.71368	0.01415	0.00083	0.00003
step15	0.24266	0.00318	0.19625	0.00241	0.00229	0.00007	0.00482	0.00003	0.00011	0.00002	1.08	0.04	0.71	0.03	0.80873	0.01452	0.00043	0.00009
step16	0.16720	0.00188	0.11013	0.00120	0.00126	0.00004	0.00272	0.00003	0.00017	0.00002	1.07	0.06	0.71	0.04	0.65870	0.01030	0.00099	0.00013
Blank	0.00786	0.00018	0.00012	0.00002	0.00004	0.00001	0.00006	0.00002	0.00006	0.00001								

Ar/Ar data (expressed in V) of step-heating analysis from I1A sanidines (Analytical uncertainties are at the 1sigma level)

Step	40Ar	+/-	39Ar	+/-	38Ar	+/-	37Ar	+/-	36Ar	+/-	40Ar*/39Ar	+/-	Age (Ma)	+/- (Ma)	39Ar/40Ar	+/-	36Ar/40Ar	+/-
step1	0.08712	0.00120	0.00622	0.00017	0.00016	0.00002	0.00117	0.00029	0.00026	0.00002	1.38	1.15	0.91	0.76	0.07137	0.00215	0.00302	0.00027
step2	0.08326	0.00039	0.01897	0.00030	0.00039	0.00003	0.00222	0.00029	0.00026	0.00002	0.25	0.25	0.17	0.17	0.22779	0.00377	0.00316	0.00019
step3	0.11607	0.00115	0.04443	0.00048	0.00060	0.00004	0.00198	0.00029	0.00021	0.00002	1.18	0.16	0.78	0.11	0.38282	0.00558	0.00183	0.00020
step4	0.07634	0.00070	0.03298	0.00023	0.00038	0.00002	0.00233	0.00029	0.00013	0.00002	1.11	0.21	0.73	0.14	0.43195	0.00496	0.00174	0.00031
step5	0.09747	0.00061	0.05149	0.00034	0.00066	0.00003	0.00350	0.00029	0.00012	0.00002	1.18	0.14	0.78	0.09	0.52823	0.00482	0.00126	0.00024
step6	0.05258	0.00056	0.03369	0.00038	0.00040	0.00003	0.00187	0.00029	0.00005	0.00002	1.09	0.21	0.72	0.14	0.64071	0.01000	0.00100	0.00045
step7	0.25818	0.00158	0.12183	0.00067	0.00156	0.00006	0.00771	0.00029	0.00033	0.00002	1.31	0.06	0.86	0.04	0.47187	0.00389	0.00128	0.00009
step8	0.04482	0.00036	0.01598	0.00013	0.00026	0.00002	0.00129	0.00029	0.00007	0.00002	1.44	0.44	0.95	0.29	0.35651	0.00400	0.00163	0.00053
step9	0.10285	0.00080	0.04696	0.00033	0.00063	0.00004	0.00339	0.00029	0.00009	0.00002	1.60	0.15	1.06	0.10	0.45655	0.00480	0.00090	0.00023
step10	0.26794	0.00163	0.18070	0.00055	0.00211	0.00007	0.00708	0.00018	0.00025	0.00002	1.07	0.04	0.71	0.03	0.67440	0.00459	0.00093	0.00008
step11	0.33101	0.00148	0.21938	0.00071	0.00264	0.00012	0.00965	0.00018	0.00035	0.00002	1.04	0.03	0.68	0.02	0.66275	0.00367	0.00105	0.00007
step12	0.05204	0.00074	0.04096	0.00030	0.00049	0.00003	0.00101	0.00018	0.00001	0.00001	1.20	0.11	0.79	0.07	0.78709	0.01256	0.00019	0.00027
step13	0.15991	0.00083	0.10419	0.00055	0.00123	0.00005	0.00445	0.00018	0.00021	0.00002	0.94	0.06	0.62	0.04	0.65156	0.00482	0.00131	0.00014
Blank	0.01030	0.00027	0.00007	0.00003	0.00003	0.00002	0.00007	0.00002	0.00006	0.00002			J value =0.000365929 +/- 1.82965E-06					

Ar/Ar data (expressed in V) of step-heating analysis from I3A sanidines (Analytical uncertainties are at the 1sigma level)

Step	40Ar	+/-	39Ar	+/-	38Ar	+/-	37Ar	+/-	36Ar	+/-	40Ar*/39Ar	+/-	Age (Ma)	+/- (Ma)	39Ar/40Ar	+/-	36Ar/40Ar	+/-
step1	0.42249	0.00188	0.02063	0.00017	0.00063	0.00004	0.00175	0.00031	0.00140	0.00005	0.15	0.66	0.10	0.44	0.04884	0.00046	0.00332	0.00011
step2	0.37151	0.00230	0.03372	0.00019	0.00064	0.00004	0.00267	0.00031	0.00113	0.00003	0.97	0.27	0.64	0.18	0.09077	0.00076	0.00305	0.00008
step3	0.59545	0.00302	0.02839	0.00028	0.00078	0.00006	0.00221	0.00031	0.00197	0.00005	0.21	0.49	0.14	0.32	0.04767	0.00053	0.00332	0.00008
step4	0.04122	0.00125	0.00991	0.00023	0.00012	0.00004	0.00073	0.00031	0.00008	0.00003	1.60	0.89	1.05	0.59	0.24042	0.00920	0.00206	0.00071
step5	0.13169	0.00134	0.03356	0.00023	0.00046	0.00004	0.00222	0.00032	0.00037	0.00003	0.59	0.26	0.39	0.17	0.25483	0.00312	0.00284	0.00022
step6	0.16455	0.00155	0.01609	0.00015	0.00027	0.00004	0.00118	0.00032	0.00053	0.00003	0.31	0.55	0.20	0.36	0.09781	0.00129	0.00325	0.00018
step7	0.05016	0.00137	0.01800	0.00016	0.00022	0.00004	0.00096	0.00032	0.00011	0.00003	0.88	0.49	0.58	0.32	0.35876	0.01028	0.00229	0.00059
step8	0.15251	0.00131	0.04641	0.00034	0.00055	0.00003	0.00268	0.00032	0.00038	0.00003	0.81	0.19	0.53	0.13	0.30431	0.00345	0.00252	0.00019
step9	0.18378	0.00151	0.07235	0.00039	0.00087	0.00006	0.00440	0.00032	0.00040	0.00003	0.87	0.12	0.57	0.08	0.39369	0.00388	0.00220	0.00016
step10	0.38278	0.00151	0.17989	0.00071	0.00209	0.00006	0.01118	0.00032	0.00062	0.00003	1.10	0.05	0.72	0.03	0.46995	0.00263	0.00163	0.00008
step11	0.69837	0.00202	0.34086	0.00048	0.00444	0.00007	0.01889	0.00032	0.00112	0.00004	1.07	0.03	0.70	0.02	0.48808	0.00157	0.00160	0.00005
step12	0.77971	0.00248	0.13204	0.00057	0.00190	0.00003	0.00850	0.00012	0.00212	0.00006	1.12	0.14	0.73	0.09	0.16935	0.00091	0.00272	0.00008
Blank	0.01104	0.00023	0.00020	0.00003	0.00004	0.00002	0.00007	0.00002	0.00007	0.00001	J value =0.000364182 +/- 1.82091E-06							